MATURATION AND AGEING IN BIOMINERALS WITH APPLICATION TO ENAMEL MATURATION

By

ANASTASIOS G. PAPADIAMANTIS

A thesis submitted to The University of Birmingham

for the degree of

Doctor of Philosophy

School of Geography, Earth and Environmental Sciences

College of Life and Environmental Sciences

The University of Birmingham

May 2016

Abstract

Dental enamel consists mainly of calcium-deficient hydroxyapatite (CDHA). The formation and evolution of enamel is a progressive and complex process the final stage of which is post-eruptive maturation (PEM), when mineralisation is completed following tooth eruption and exposure to oral fluids. Although PEM is directly correlated with decrease in caries susceptibility, a complete model to describe the whole process does not exist. Several reports have recently suggested that the previously observed caries decline, which started with the introduction of F^- in drinking water and dental products, has stopped and is in some cases in reverse. New research approaches are therefore needed, which will focus on caries prevention and not treatment.

This project monitored the *in vitro* effects of simulated PEM on the physicochemical properties of dental enamel and proposed a model which describes the whole process. For this purpose, primary and permanent bovine enamel was tested, using a suitably designed demineralisation/remineralisation laboratory protocol as well as characterisation techniques. The results were applied to the synthesis of enamel proxies, which could mimic the physicochemical properties of dental enamel; these proxies were evaluated for their potential to be used as enamel substitutes in dental research.

For my parents Despoina & Georgios

For their unselfish and unconditional love

and for their sacrifices, which brought me where I am today

Για τους γονείς μου Δέσποινα και Γιώργο

Για την ανιδιοτελή και άνευ όρων αγάπη τους

και για τις θυσίες τους, που με έφεραν εδώ που είμαι σήμερα

Acknowledgments

The creation and completion of a PhD thesis is not an individual achievement, but the joined and hard effort of a community of people, whom I would like to thank.

First of all, I would like to express my sincere thanks and gratitude to my supervisors **Prof Eugenia Valsami-Jones** and **Prof Richard J.M. Lynch** for their excellent guidance, support and help. During the last 4 years Prof Valsami-Jones has been a constant inspiration, mentor and friend and the person who has influenced me the most, during my "scientific life". Above all, I would like to thank her for her trust and patience and for always believing in me. Prof Lynch has also been a great mentor and friend and his way of thinking and vision has allowed me to see things differently, opened up my mind and helped me generate new ideas.

I would also like to acknowledge and thank my secondary supervisor **Dr Ivan Sansom** for his scientific help and guidance and for always being there and doing his best to solve any issues I had. I would also like to thank my friend and scientific mentor **Dr James Bowen**. Without his knowledge, help and advice this thesis would never reach completion. I will never forget our brainstorming discussions, which I hope we repeat in the future.

I wish to also acknowledge and thank present and past members our group (Sophie, Adam, Maria, Ruth to name a few) for the moments we shared, the good times we had and their support and help over the years.

Special mention goes to **Dr Georgina Kaklamani** and **Dr Steven Emery**. Dr Kaklamani for being one of the main reasons I am here today and Dr Emery for the long discussions during the days, and mainly nights, which made my working days more interesting and fun.

Finally, I would like to thank **Vicky** for always being by my side during the good and the bad. Without your energy, inspiration and presence I would have never made it!

Table of Contents

List of Figures

Page intentionally left blank

List of Tables

Page intentionally left blank

List of Abbreviations

α-TCP	Alpha Tricalcium Phosphate
AAS	Atomic Absorption Spectroscopy
AC	Acid Challenge
ACP	Amorphous Calcium Phosphate
AFM	Atomic Force Microscopy
AI	Amelogenesis Imperfecta
Am	Ameloblasts
ANOVA	Analysis of Variance
AS	Artificial Saliva
β-TCMP	Whitlockite
β-TCP	Beta Tricalcium Phosphate
BET	Brunauer, Emmett and Teller Surface Area Analyser
BF	Background Fluoride
BS	Beam Splitter
C-AFM	Contact Mode Atomic Force Microscopy
CDHA	Calcium Deficient Hydroxyapatite
CH	Carbohydrates
CNC	Cranial Neural Crest
DCPA	Dicalcium Phosphate Anhydrous
DCPD	Dicalcium Phosphate Dihydrate, Mineral Brushite
EDJ	Dentino-Enamel Junction
EH	Enamel Hypoplasia
FA	Fluorapatite
FD-HA	Freeze Dried Hydroxyapatite
FFT	Fast Fourier Transformation
FTIR	Fourier Transform Infrared Spectrometry
fHA	Fluoridated Hydroxyapatite
HA	Hydroxyapatite
HD-HA	Heat Dried Hydroxyapatite

HP	Helium Pycnometry
HME	Hypomineralised Enamel
IC	Ion Chromatography
IC-AFM	Tapping Mode Atomic Force Microscopy
IR	Infrared
MI	Micro Indentation
MIF	Michelson Interferometer
MIH	Molar Incisor Hypomineralisation
MCPA	Monocalcium Phosphate Anhydrous
MCPM	Monocalcium Phosphate Monohydrate
MP	Mercury Porosimetry
NC-AFM	Non-Contact Mode Atomic Force Microscopy
NE	Normal Enamel
OCP	Octacalcium Phosphate
OEE	Outer Enamel Epithelium
OXA	Oxyapatite
PEM	Post Eruptive Maturation
PF	Plaque Fluid
PL	Papillary Layer
RA	Ruffle-Ended Ameloblasts
SA	Smooth-Ended Ameloblasts
SEM	Scanning Electron Microscopy
SI	Stratum Intermedium
SR	Stellate Reticulum
TCP	Tricalcium Phosphate
TTCP	Tetracalcium Phosphate, Mineral Hilgenstockite
TEM	Transmission Electron Microscopy
VH	Vickers Hardness
XRD	X-Ray Diffractometry

1. Introduction & Literature Review

1.1 Thesis Outline

The current thesis is divided into 7 Chapters.

Chapter 1 provides a general background to the experimental work in the project. Besides summarising the general knowledge on enamel structure, formation and maturation, it also presents a discussion on calcium phosphates, and their potential role in the post-eruptive maturation (PEM) process and/or as enamel proxies. The Chapter concludes with a review of the research performed and the motivation behind the work presented.

Chapter 2 offers details on the materials and experimental protocols used in this work, while describing the basic principles and settings for the analytical techniques used.

Chapter 3 studies the mechanism behind PEM. It comprises of a pH-cycling study the purpose of which is to decode the mechanism and describe the kinetics behind the PEM process.

Chapter 4 studies the effects of PEM process on primary enamel and compares it to permanent enamel.

Chapter 5 investigates the synthesis, pelleting and characterisation of hydroxyapatite (HA), with the aim to develop an enamel proxy.

Chapter 6 presents the application of an artificial PEM pH-cycling model on synthetic HA pellets and describes the observed changes in their physicochemical properties.

Chapter 7 provides a summary of the project, the conclusions of the present study, its contribution to knowledge and discusses future research challenges.

1.2 Application of Research

The current project studied the mechanism behind PEM and the replication of the process using appropriately prepared synthetic proxies. The need for the current study was based on the fact that PEM is directly correlated with caries vulnerability and its decrease over time (1-3). Caries has negative impact on the quality of life of both adults (4-6) and children (7-9); it also has an effect on the economic productivity (4, 10) and the national health budget in general (10-13). Following F^- introduction in water fluoridation and dental hygiene in general during the 70s, a significant and continuous decline in caries incidence was observed (14-16). However more recently, there have been reports suggesting that, the modern way of life, has caused caries decline to stop (17, 18) and, in some cases, is in reverse (18, 19). As a result, the need for caries prevention, rather than treatment, is of utmost importance. New research approaches and clinical applications are therefore necessary and provide the focus for the current project. Recent improvements in the resolution of analytical techniques in combination with better understanding of the factors affecting the physicochemical changes taking place during PEM and caries, offer a good basis for new paths to be studied and new approaches to be applied.

1.2.1 Research Applications

The current work could help dental and materials research in various ways. By developing *in vitro* pH-cycling models which realistically mimic the oral cavity, it provides a novel *in vitro* experimental approach, which mimics PEM. Studying the mechanism behind PEM enables the development and testing of new approaches and dental products that could support the maturation process and prevent caries.

By producing synthetic proxies for enamel, it offers a substitute to bovine enamel that has less natural variation and more reliable and reproducible composition, while being readily available when needed. Finally, by replicating the physicochemical enamel properties it brings forward new biocompatible dental materials, free from the biological hazards of natural materials.

1.2.2 Clinical Applications

Besides the research applications just mentioned, the long-term aim of the current work is to assist dental professionals to intervene with the PEM process by developing new products and treatments that could be used during every day oral health care and caries prevention. At the same time, the synthetic proxies could be used, following further research, as biocompatible enamel substitutes and/or fillings. Current fillings may lead to secondary caries formation at the interface with the enamel due to plaque accumulation leading to enamel demineralisation, which is more intense the narrower the exposed area is (20, 21). On the other hand, HA based fillings could protect the enamel from demineralising by reducing the undersaturation of the topical environment through simultaneous dissolution and release of Ca^{2+}, PO_4^{3-} and potentially F^- and/or metal elements (22).

1.3 Tooth Structure

1.3.1 The Human Dentition

The human dentition develops in two separate stages. The first consisting of 20 teeth in total, is called the primary (or deciduous) dentition and can be observed during childhood (Figure 1-1a) (23). Eruption of the primary dentition begins at around 6 months of age and completes around the age of 3 (24-27). The second, called the secondary (or permanent) dentition comprises of 32 teeth in total (Figure 1-1b) (23). Permanent teeth begin to erupt around the age of 6 (when primary teeth begin to shed) and the whole process is nearly complete by the age of 12 (26, 27). The last 4 permanent teeth to erupt are the 3rd molars (wisdom teeth), which appear inside the oral cavity usually between the ages of 17 to 22 years (28). The intermediate period when both primary and permanent teeth are present is called the mixed dentition (27).

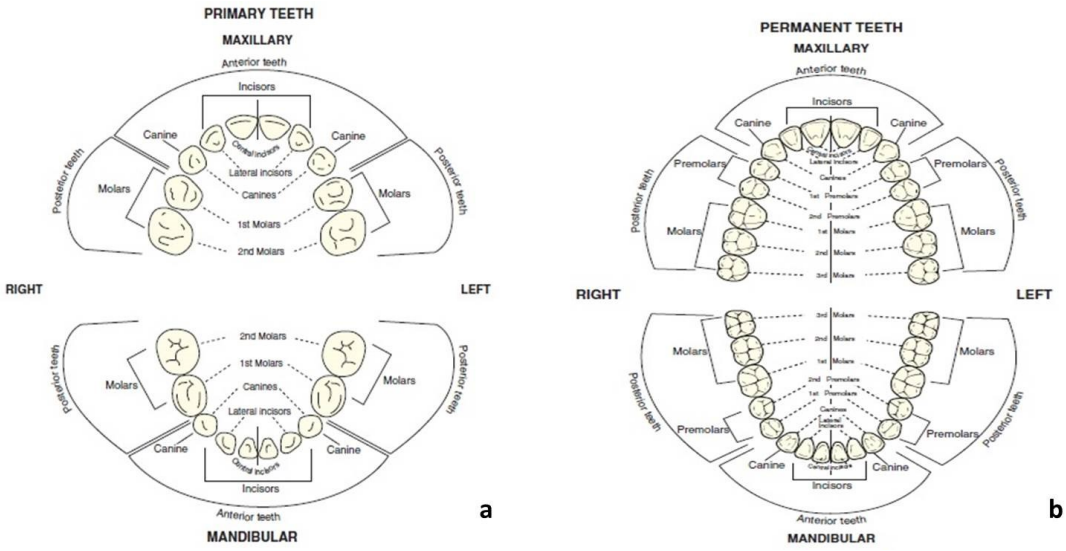

Figure 1-1: The a. primary and b. permanent human dentition. Reprinted by permission from Lippincott, Williams & Wilkins: Woelfel's Dental Anatomy, 8th edition, from reference (23), copyright (2011).

1.3.2 General Tooth Structure

The human tooth consists of 4 different structures (Figure 1-2); the two outermost being the enamel and the cementum. Dental enamel is the white outermost always visible part of the tooth, while the cementum is the dull yellow external layer of the root of the tooth that is usually covered by the gums. Beneath these two layers exists the dentine; a yellowish, usually non-visible, layer. The innermost structure is the pulp, which is a soft tissue containing the blood and nerve circulation of the tooth (23).

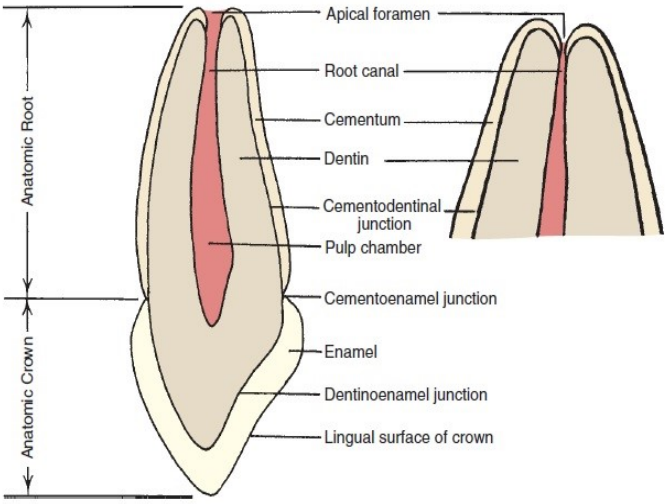

Figure 1-2: Schematic of a maxillary human incisor depicting the different structures. As can be seen the dentine covers the majority of the tooth and covers the pulp chamber and the pulp itself. Reprinted by permission from Lippincott, Williams & Wilkins: Woelfel's Dental Anatomy, 8th edition, from reference (23), copyright (2011).

Enamel, cementum and dentine are hard, highly mineralised tissues. Human enamel is the hardest tissue of the human body and consists of 80-90% by volume of calcium deficient HA (CDHA, reader is referred to section 1.4.4 for further details), with the rest being organic material (e.g. collagen) and water (29-32). Cementum is far softer than the enamel, which can be explained by the fact that it consists of 40-50% of HA and 50-60% of organic material and water (23, 33). Finally, dentine lies somewhere between enamel and cementum as it consists of 70% mineral, 18% organic material and 12% water (23, 31, 32).

1.3.3 Dental Enamel Structure

Dental enamel is comprised of biological apatite (or bio-apatite), which is a form of carbonated CDHA (32, 34). Similar to bone (Figure 1-3) (35), enamel is a biomaterial which is formed in 7 different hierarchical levels ranging from the nanometre up to the micrometre scale (Figure 1-4) (32, 35-38). The structural units of permanent enamel are bio-apatite crystallites, which have an average thickness of 26 nm and a width of 13 nm; while their length ranges from 100 nm to 1 μm (Figures 1-4, 1-5) (32, 36, 37, 39, 40). Bio-apatite crystallites come together to form nano-fibrils (Figure 1-6), which then align to form larger fibrils and even larger fibres. The next stage is for these fibres to come together to form enamel prisms, which are packed together hence forming the interprismatic space between them as well. Finally, the prisms create prism bands which are positioned parallel to each other so as to produce a homogeneous structure throughout the entire volume of the enamel. These structural arrangements also influence the variations in the physicochemical properties of the enamel (32, 36, 37, 41) and the direction of caries progression since the rate of enamel demineralisation increases moving from the surface to the dentino-enamel junction (EDJ) when the acid attack takes place perpendicular to the natural surface of the tooth (42); since CDHA dissolution takes place in the direction of the crystallites' *c* axis (43).

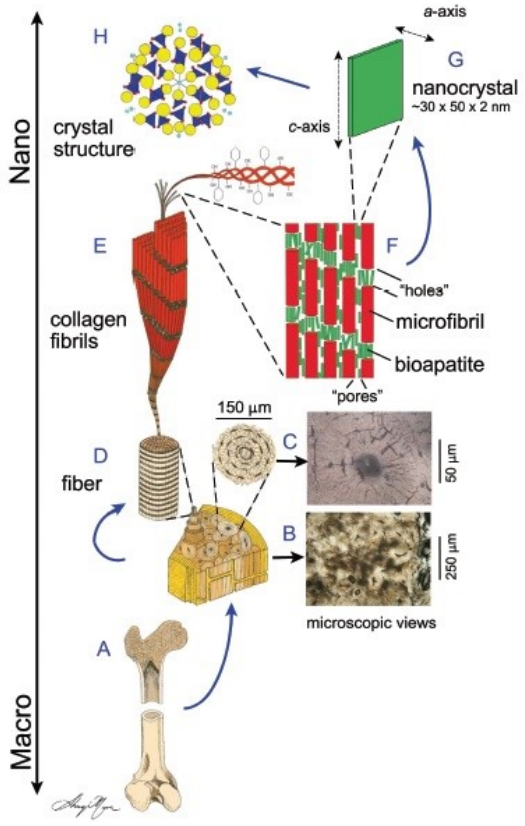

Figure 1-3: The 7 hierarchical levels of cortical bone. The bone (longitudinal section, a; cross-section, b) consists of cylindrical osteons (c) and collagen fibres (d). The latter form the structural framework of the bone and consist of a large amount of collagen fibrils (e), which in turn are the sum of a large amount of microfibrils (f). Microfibrils come together when 5 collagen molecules are bundled together, with bioapatite crystallites formed in the holes created between adjacent microfibrils (f). Bioapatite crystallites, contrary to HA and fluorapatite, are carbonated Ca-deficient apatites which form platelets and are only about 2-3 unit cells thick (g). The crystal structure of fluorapatite as can be seen down the *c*-axis (Ca^{2+}: Yellow spheres, PO_4^{3-}: Dark blue tetrahedra, OH^-: Light blue, O^{2-}: Red spheres) (h). Reprinted by permission from the Mineralogical Society of America from reference (35), copyright (2008).

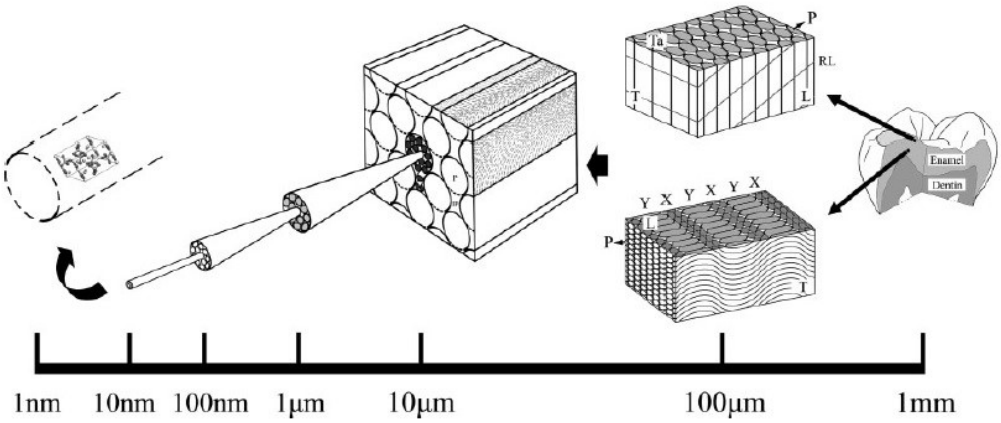

Figure 1-4: Schematic of the hierarchical structure of dental enamel. The building blocks of the entire enamel structure are tracked down to the nanoscale and are hexagonal HA crystals. These crystals come together to form nano-fibrils, which align lengthways and bundle so as to form mineral fibres. Moving to the mesoscale the (~10 µm) the fibres create the prisms. Many prisms together build prism bands, which are arranged in several ways within the macroscopic enamel, providing the necessary mechanical and physical properties. Reprinted by permission from Journal of Tissue Engineering and Regenerative Medicine from reference (37), copyright (2007).

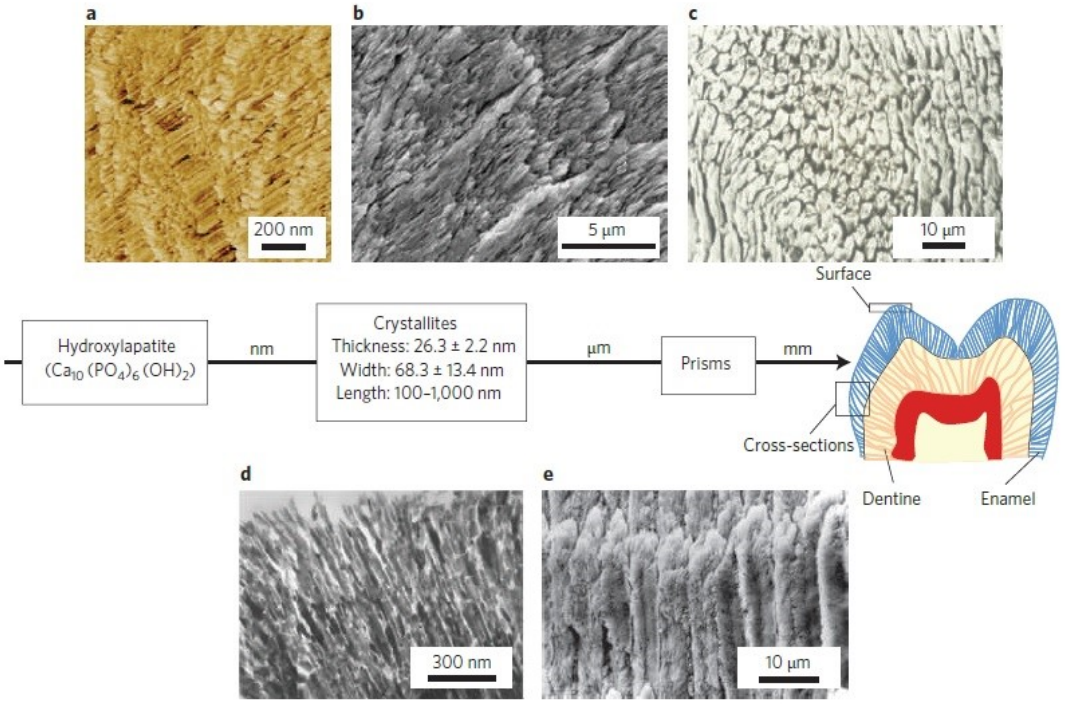

Figure 1-5: Atomic Force Microscope (a), Scanning Electron Microscope (b, c, e) and Transmission Electron Microscope (d) images depicting the hierarchical structure of dental enamel. HA nano-crystallites (a, b, d) come together and form the enamel prisms (c, e), which form the macroscopic enamel layer. Reprinted by permission from Macmillan Publishers Ltd: Nature Nanotechnology from reference (36), copyright (2010).

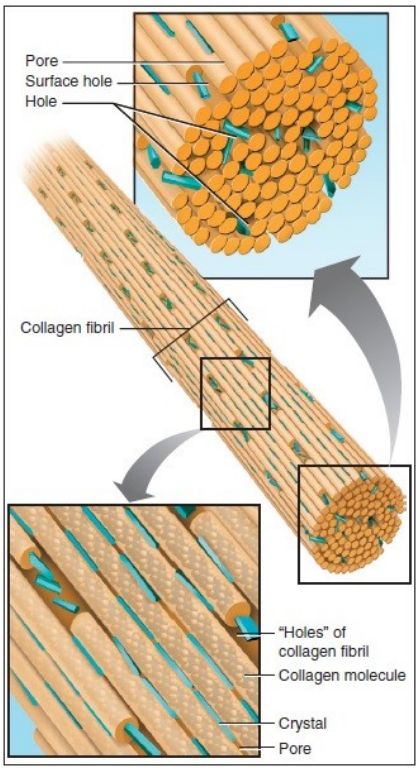

Figure 1-6: Nanofibrils are created through the formation of bioapatite crystallites in the "holes" existing beyween the various collagen bundles. Reprinted by permission from Elsevier Health Science Books: from Ten Cate's oral histology: development, structure, and function (44), copyright (2013).

1.3.4 Enamel Formation & Maturation

Enamel formation and maturation is a complex process, which can be divided into three different stages. The first, called the secretory stage, involves the formation of partially mineralised enamel through complex interactions of enamel specific proteins and an organic matrix (45-47). During the second stage, called the pre-eruptive maturation, the newly formed enamel mineralises rapidly with simultaneous decrease in the organic content (48, 49). Pre-eruptive maturation and the secretory stage constitute the process of amelogenesis, which is followed by the third and final stage, called the post-eruptive maturation (PEM). PEM takes place as soon as the tooth erupts inside the oral cavity. During this stage the enamel becomes fully mineralised through its interaction with the fluids inside the oral cavity (50-52).

1.3.4.1 Enamel Formation

Enamel formation (Figure 1-7) is initiated by the ameloblasts, which are columnar epithelial cells and originate from cells residing in the cranial neural crest (CNC). These cells then enter the underlying connective tissue and form the ectomesenchyme, which displays characteristics from both tissues. During tooth formation, the interactions inside the ectomesenchyme form two types of columnar cells, the ameloblasts and the odontoblasts. Cells, of each type are connected by intercellular junctions and form two completely separate extracellular spaces in which the enamel and dentine form (34, 45, 53, 54).

Following the formation of the EDJ (53, 55), the ameloblasts secret an aprismatic enamel layer and then differentiate by initialising a single Tomes' process (Figure 1-8) on their secretory surface, which will eventually determine the structure of the developing enamel (56-58). The mineral deposition takes place through an organic matrix, which comprises of proteins secreted by the ameloblasts (59-63). The enamel crystallites, during the secretory stage, extend mainly in length and far less in thickness and width. The more the ameloblasts secret proteins the longer the enamel crystallites become, while the shapes of the Tomes'

processes control the orientation of the proteins of the organic matrix and thus the alignment of the HA crystallites (53, 64-66).

At the same time, the Tomes' processes are responsible for the formation and organisation of rod and inter-rod enamel; the crystals of which have similar structure but different orientation (Figure 1-9). Similar to ameloblasts, Tomes' processes contain secretory and non-secretory surfaces. The former are responsible for rod formation, while the latter forms the inter-rod enamel (53, 58, 67, 68). As a result, the shape and location of both the rod and inter-rod components of mature enamel are directed by the secretory part of the enamel formation and maturation process (Figure 1-10). The enamel produced during this stage is soft and translucent and contains only 10-20% of calcium phosphates, with the rest being fluid and proteins of the organic matrix. After the developing enamel reaches its full local thickness and ameloblasts have completed their secretory activities, the secretion stage finishes and the ameloblasts undergo a series of cytological changes, in order to prepare for the maturation stage (47, 53, 69).

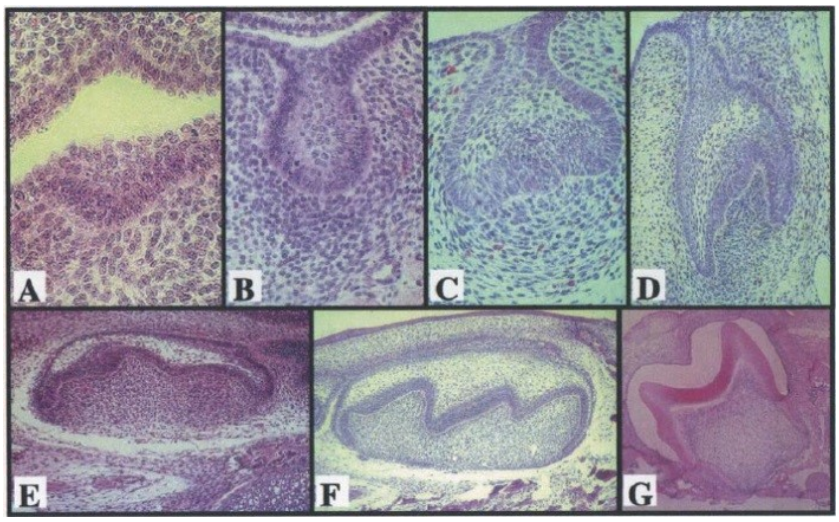

Figure 1-7: Different stages of tooth formation up to the stage of the beginning of mineralisation. The images refer to a developing mouse molar. Reprinted by permission of Prof J. Simmer: Journal of Dental Education from reference (53), copyright (2001).

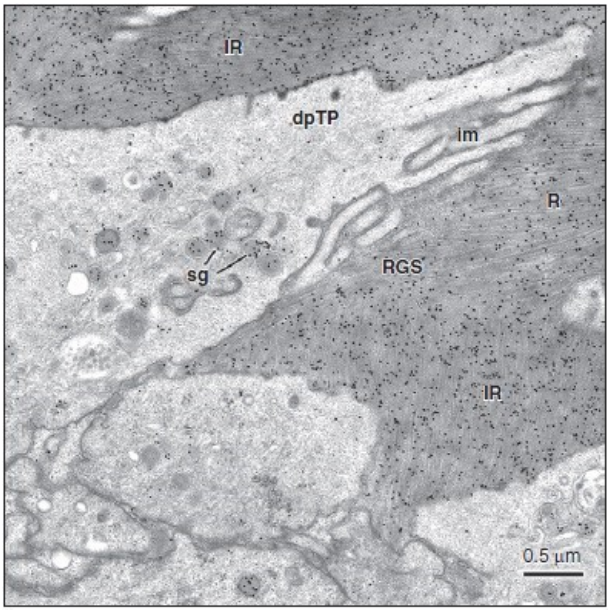

Figure 1-8: Tomes' processes define the junction between newly formed enamel and the ameloblasts. As the ameloblasts fend off from the newly formed enamel layer, their end closer to the enamel layer changes and acquires a "wedge shaped" form and keeps secreting proteins so as to build the organic matrix. At the same time its shape controls the alignment of the secreted proteins, hence the alignment of the newly formed enamel crystallites. These "wedge shaped" differentiations of the ameloblasts, along with their functions are called Tomes' processes. Reprinted by permission from Elsevier Health Science Books: Ten Cate's oral histology: development, structure, and function from reference (44), copyright (2013).

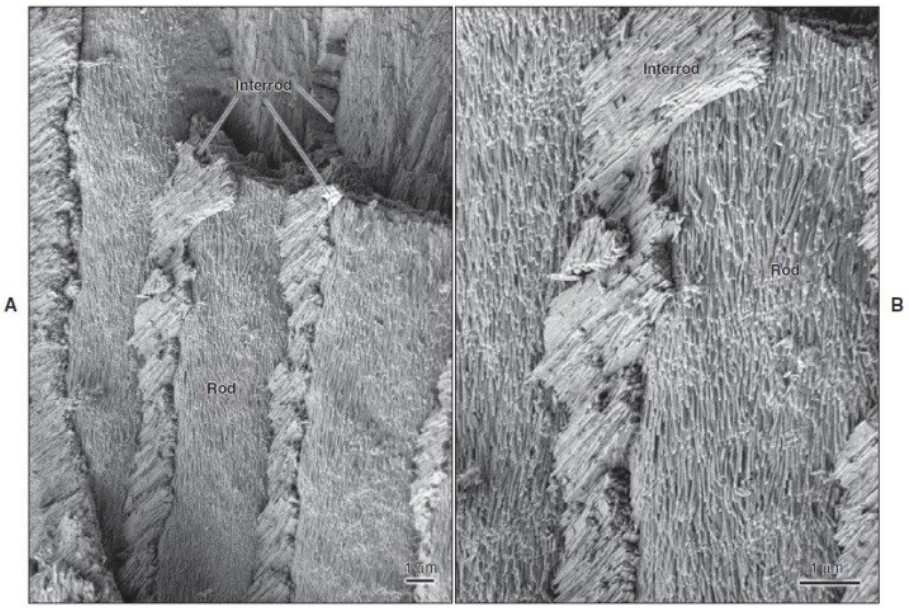

Figure 1-9: SEM images of rod and interred enamel crystals. Reprinted by permission from Elsevier Health Science Books: Ten Cate's oral histology: development, structure, and function from reference (44), copyright (2013).

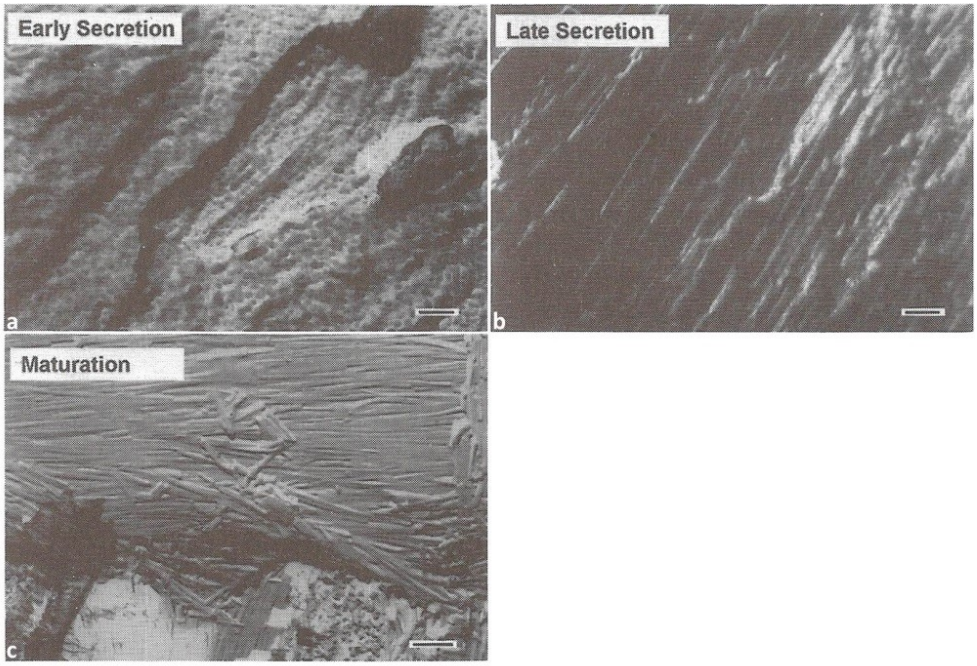

Figure 1-10: TEM images of the different stages of amelogenesis in a rat incisor. Early (a) and late (b) secretion and maturation stages (c). The co-linear spheres which can be seen during the secretory stages denote sites of nucleation inside the organic matrix. These spheres are not visible in the maturation stage, in which organised prisms containing large crystals can be seen. Reprinted by permission from Wiley & Sons Ltd: Ciba Foundation Symposium from reference (30), copyright (2007).

1.3.4.2 Enamel Maturation

1.3.4.2.1 Pre-eruptive Maturation

During the pre-eruptive maturation stage the already aligned crystallites begin to grow in width and thickness, which leads to subsequent changes in the physicochemical properties of the enamel (30, 49, 53). In order for the maturation stage to take place, the ameloblasts go through several morphological and functional changes (30, 49, 53, 70-74). To begin with, ameloblasts shorten by about 50% at the beginning of the maturation stage (30, 70, 72, 74) and undergo membrane specialisations, which are expressed through changes in the morphology of their distal ends; switching from ruffle to smooth ended (Figure 1-11).

The ameloblasts turn into transporters and move Ca^{2+}, PO_4^{3-}, F^- and HCO_3^- ions into the matrix and remove H_2O and organic material (49, 53, 71, 73, 74). At the same time, the pH of the environment surrounding the enamel fluctuates between the critical pH area (around 5.5) and 7.2 (53, 71, 75), with HCO_3^- acting as a buffer which raises the pH values (49). As a result, both the organic matrix and the less acid resistant enamel crystallites (e.g. those with high CO_3^{2-}) dissolve and are substituted by more stable crystallites of apatitic nature, which leads to mineral content increase of up to 70% by volume (48, 53). When the process is completed the tooth erupts inside the oral cavity and PEM is initiated.

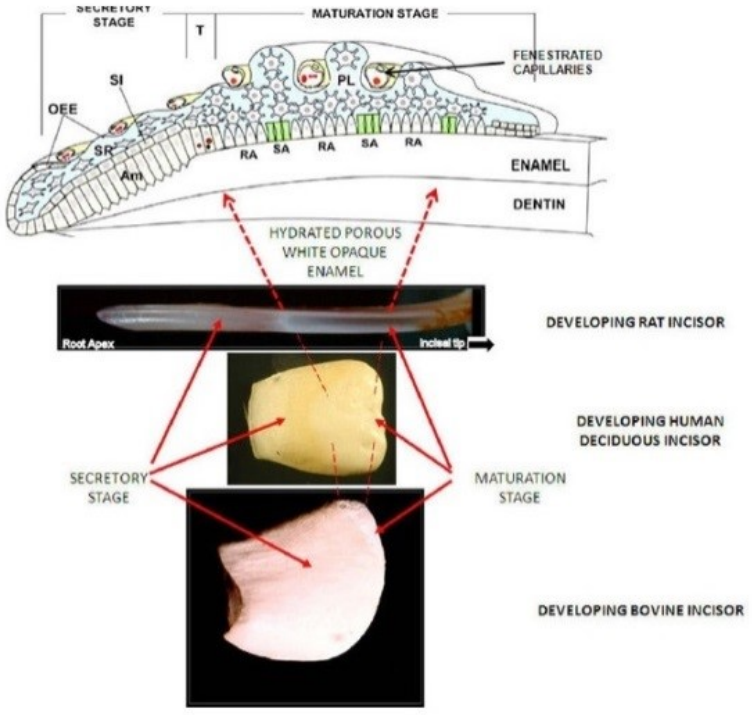

Figure 1-11: Schematic of a developing rat incisor, along with images of rat, human and bovine incisors showing the positions and appearances of secretory and maturation stages. Key: ameloblasts (Am), stratum intermedium (SI), stellate reticulum (SR), outer enamel epithelium (OEE), ruffle-ended ameloblasts (RA), smooth-ended ameloblasts (SA) and the papillary layer (PL). Original figure reprinted with permission from the American Physiological Society: American Journal of Physiology: Cell Physiology from reference (71), copyright (2010). Modified figure reprinted by permission from C. Robinson form reference (74), copyright (2014).

1.3.4.2.2 Post-eruptive Maturation

PEM is the third and final stage of enamel formation and maturation and begins as soon as the tooth erupts inside the oral cavity. During this stage significant physicochemical changes take place, while the mineral content of the enamel increases to 80%-90% by volume (29, 30). Although the mechanism governing the process is not fully understood, it has been suggested that sequential cycles of demineralisation challenges and remineralisation treatments are responsible (76, 77). Demineralisation challenges result in enamel dissolution with simultaneous loss of impurities like CO_3^{2-}, Mg^{2+} and Na^{+}, which enhance its solubility (78, 79). During remineralisation, reprecipitation of more stable apatitic phases like HA, fHA and FA takes place (reader is referred to section 1.4 for further information), through the uptake of Ca^{2+}, PO_4^{3-}, F^{-} (52, 80-82) and possibly other elements (e.g. Sr^{2+}, Zn^{2+}) (27, 83-85).

Post-eruptive enamel maturation is considered to be mainly a surface phenomenon, with most changes taking place in the upper 100 μm (86-88). This is evident by the precipitation of a distinct prismless layer (Figure 1-12) (89-93), which is less soluble and permeable than the underlying enamel (94-97). At the same time, an increase in the Ca/P ratio is observed, which is attributed to the calcification of hypomineralised areas that are present inside the enamel during eruption (95, 98-100). This is achieved through the precipitation of more stable and less soluble apatitic phases (e.g. HA) (78, 79), the significant increase in the width of the enamel crystallites (65, 89, 101) and the deposition of material filling the interstices of the underlying enamel prisms (91-93, 102, 103); which also result in significant hardness increase (104-107), a reduction in porosity (76, 108, 109) and the incorporation of F^{-} (52) and possibly metal species (e.g. Zn^{2+}, Sr^{2+}) (27, 83-85).

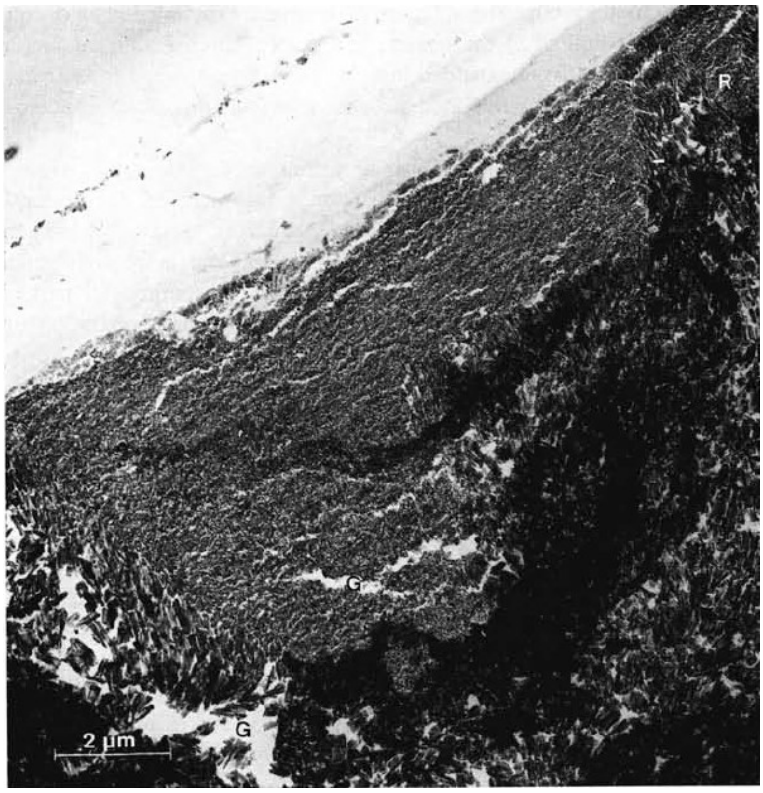

Figure 1-12: Precipitation of an amorphous prismless layer on the surface of the enamel following immersion into a non-F^- calcifying solution. Deposition of material inside the bulk of the enamel can also be observed. Reprinted by permission from Karger Publishers AG: Caries Research from reference (91), copyright (2009).

1.3.5 Dental Enamel Pathology

Enamel diseases and pathological conditions may be of systemic origin or the result of the interaction of the enamel with the oral environment and the effects of modern lifestyle and healthcare. Diseases which are of systemic origin are amelogenesis imperfecta (AI), enamel hypoplasia (EH) and molar incisor hypomineralisation (MIH), while on the second category are dental caries and dental erosion. A combination of both is dental fluorosis which is the result of excessive F^- administration and could be of both systemic and post-eruptive origin.

1.3.5.1 Molar Incisor Hypomineralisation (MIH)

MIH (Figure 1-13) is a developmental enamel defect of systemic origin, which affects the permanent first molars and the incisors (110-112). MIH is the result of incomplete mineralisation, which happens due to ameloblast malfunction during the transition from the secretory to the maturation stage (82, 112, 113) due to health or environmental factors (110, 112, 114). As a result, high CO_3^{2-} and decreased Ca^{2+} and PO_4^{3-} content (110, 115) is observed. Teeth affected by MIH are soft, with varying porosity and have white-yellow or yellow-brown chalk-like appearance (82, 110, 112, 113). Diagnosis is performed through the presence of demarcated opacities, post-eruptive breakdown and demarcates restorations (110-112). Recently it has been suggested to treat MIH using an artificial PEM treatment (82, 113).

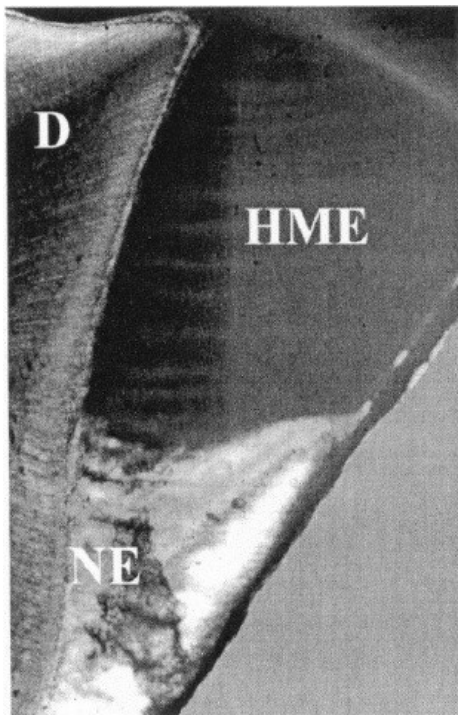

Figure 1-13: Incompletely mineralised enamel (HME) found on the buccal surface of a human tooth. A well-defined border is observed between HME and normal enamel (NE). Reprinted by permission from ScienceDirect: Archives of Oral Biology from reference (115), copyright (2001).

1.3.5.2 Dental Fluorosis

As it is the best anti-caries agent, F^- has been administered extensively both systemically and topically (116-121). As a result, F^- is being absorbed by the enamel either through the blood circulation, during enamel formation and early mineralisation, or through the surface of the enamel during PEM (118). Systemic administration is achieved through water fluoridation and F^- containing tablets and salts, while topical through F^- containing dentifrices and mouthrinses (120). Despite its positive effects when dosed correctly, extensive F^- administration may disrupt the enamel mineralisation process and lead to fluorosis (116-122). In such case, the enamel remains hypomineralised, having increased porosity and an opaque appearance. In extreme cases, the enamel has a chalky appearance and breaks down post-eruptively exposing the underlying dentine (116, 118, 119). Although the mechanism behind fluorosis is not clear, it has been suggested that F^- ions break down the organic matrix present during enamel formation, not allowing the necessary Ca^{2+} to be deposited (117, 119).

All of the above have led to a huge debate regarding the need for both systemic and topical F^- administration. As PEM is mainly a surface phenomenon and may be enhanced through topical F^- administration (123-125), in combination with the proposal that pre-eruptive systemic fluoride administration can lead to both increased surface fluoride concentration (126) and increased, in terms of width, crystallite sizes (127) led to the initial conclusion that systemic administration is highly significant during enamel formation and the pre-eruptive maturation period and should be stopped after the teeth have fully erupted (128, 129). This is based on the acceptance that the main effect of F^- is of topical nature, even when systemic administration takes place; because the systemically administered F^- is released through the saliva, which results in topical effects on the enamel (130, 131). As a result, simultaneous systemic and topical F^- administration may lead to excessive amounts of F^- reaching the surface of the enamel.

1.3.5.3 Dental Erosion

Dental erosion is a condition which is the result of the interaction of the surface enamel with non-bacterial acids, originating from either acidic foods and/or beverages or are of systemic origin (e.g. backflow of gastric contents) (132-134). During erosion, dissolution of the enamel (bio-apatite) takes place. As a result surface lesions are created which soften the enamel (Figure 1-14) (132). Erosion can be the result of H^+, originating from the hydrolysis of acids, or by chelating anions (135). Visible results are enamel discoloration and shape changes. If allowed to progress, the bulk of the enamel wares off, layer by layer exposing the dentine and causing severe pain (132, 135, 136).

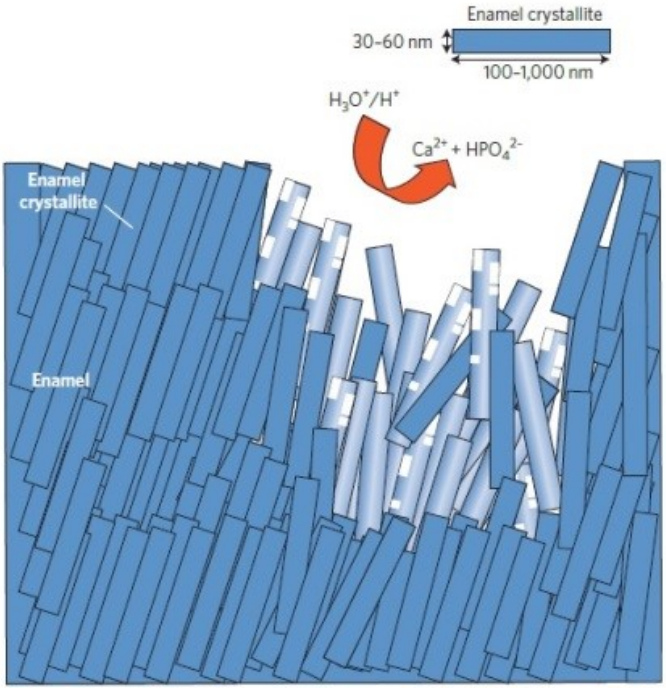

Figure 1-14: Dental erosion is caused by low pH (pH: 1-4) caused either by acidic foods and drinks or gastric juices. The result is the dissolution of the surface of the enamel and the release of Ca^{2+} and HPO_4^{2-} ions. Reprinted by permission from Macmillan Publishers Ltd: Nature Nanotechnology from reference (36), copyright (2010).

1.3.5.4 Dental Caries

Dental caries is one of the most common chronic diseases globally; and the most common chronic disease and the main reason of oral pain and tooth loss of children (6-11 years old) and adolescents (12-19 years old). Caries is highly common in adults as well, with nine out of ten having experienced tooth decay and is considered to be four times more common than asthma and seven than hay fever (17, 137). It is defined as localised destruction of the dental hard tissues (enamel, dentine, cementum) and can affect both the root and crown (root and coronal caries respectively) of primary and permanent teeth (19).

Caries is formed (Figure 1-15) from the interaction of acid producing bacteria (e.g. *Streptococcus mutans*, *Streptococcus sobrinus* and *Lactobacillus spp*) within the teeth and saliva (36, 138). This is achieved through the pellicle, a layer full of proteins, which is formed following the interaction of the tooth with the oral fluids (36). The aforementioned bacteria colonise the surface and form a biofilm called dental plaque.

The bacteria metabolise dietary carbohydrates (CH) and produce lactic and other organic acids (e.g. acetic acid, phosphoric acid) (139, 140), which then hydrolyse and form H^+. As a result, the local pH at and near the plaque-tooth interface decreases and if it falls below a critical value (around pH 5.5) the enamel starts to demineralise. Demineralisation commences underneath the surface of the tooth, while a white mark becomes observable on the surface of the enamel (white-spot lesion) due to the increase in porosity observed topically (141). During the whole process Ca^{2+} and PO_4^{3-} are released along with some other elements, which are lost during enamel dissolution (e.g. Mg^{2+}, CO_3^{2-}) (Figure 1-19) (19, 36, 138). Initially, due to remineralising agents present inside the oral fluids (e.g. Ca^{2+}, F^-), reprecipitation of material takes place onto the surface of the enamel. As a result, a pseudo-intact surface layer is observed on top of the white-spot lesion, although if the process is allowed to evolve

cavitation will eventually take place (19). The outcome relies on the balance between the rates of the demineralisation and remineralisation processes taking place simultaneously in the affected area. If the demineralisation rate is higher, the partially demineralised crystallites will not be able to be remineralised through the deposition of calcium phosphates from the saliva and cavitation will take place. In the opposite case, the lesion will be fully remineralised (arrested lesion) (142).

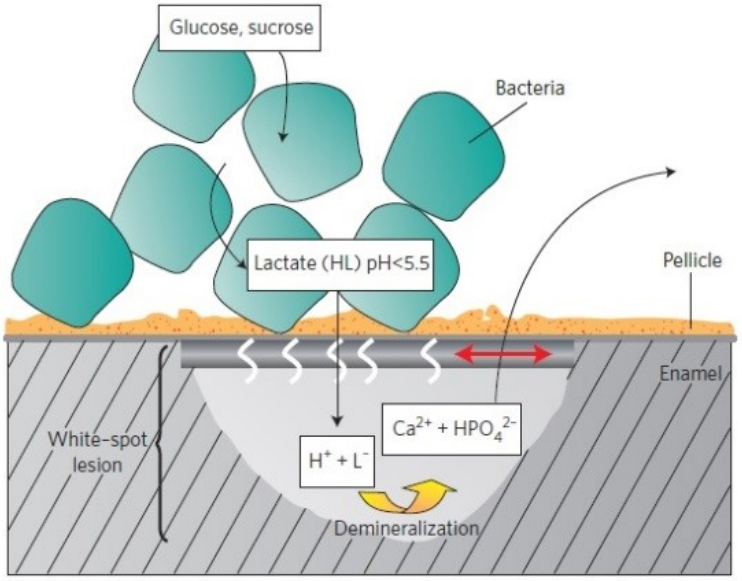

Figure 1-15: Schematic representing dental caries formation. Bacteria colonise the pellicle and metabolise sugar and carbohydrates (CH) creating lactate, which in turn dissociated into H^+ ions that diffuse through the enamel and demineralise it from underneath the surface. Reprinted by permission from Macmillan Publishers Ltd: Nature Nanotechnology from reference (36), copyright (2010).

Caries progression is based on several factors like salivary flow and composition, exposure to fluoride and other remineralisation or demineralisation agents, consumption of dietary sugars, oral hygiene and environmental pollution. During the early stages the lesions created may be remineralised and not progress into cavitation. In order to do so, action is needed through the uptake of mineralising agents, such as Ca^{2+}, PO_4^{3-} and mainly F^-, which can lead to the formation of more stable apatitic phases like F^- bearing HA and FA (143, 144).

1.4 Biogenic Apatites

The body's calcified tissues consist of both organic and inorganic components, mainly proteins and minerals respectively. The inorganic part, which is called a biomineral, must fulfil the dual role of structural support (bones) or mechanical grinding (teeth) and that of phosphorous reservoir, which is present in several biomolecules (e.g. DNA, RNA) and plays a significant role in many biological processes (e.g. ATP formation) and especially biomineral formation (32, 35, 145-147).

Biogenic apatites are the biologically produced analogue of HA, which is a sub-category of calcium orthophosphates, and comprise the main mineral component of bones and teeth. The apatite structure is highly versatile and can accommodate a large portion of the periodic table (148, 149), which results in a wide range of physicochemical properties and increased chemical adaptability. Since apatites contain 80%, 99% and 50% per weight of the body's phosphorus, calcium and magnesium respectively (35, 150), while being readily soluble makes them an important reservoir for Ca^{2+} and PO_4^{3-} (35).

In general, calcium orthophosphates are minerals containing Ca^{2+} arranged around a network of PO_4^{3-} groups which provides the stability of the whole structure. The parameters usually used to characterise these minerals are Ca/P ratio, solubility and basicity/acidity (Table 1-1) (151, 152). So far, there are 13 known non-substituted calcium orthophosphates (Table 1-1) with Ca/P ratio ranging from 0.5 to 2.0 (31). Those presented below are of great importance in dental research since it has been suggested that they exist during enamel formation and/or both pre-eruptive and PEM (95, 98, 99, 153, 154).

Calcium Orthophosphate Type	Chemical Formula	Ca/P	Solubility (25°C), log(Ks)	Solubility (25°C, g l^{-1})	pH stability range in aqueous solutions at 25°C
Amorphous Calcium Phosphate (ACP)	$Ca_xH_y(PO_4)_z \cdot nH_2O$, n = 3 - 4.5	1.2-2.2	N/A	N/A	~5-12 (always metastable)
α-Tricalcium Phosphate (α-TCP)	α-$Ca_3(PO_4)_2$	1.5	25.5	~0.0025	Cannot be precipitated from aqueous solutions*
β-Tricalcium Phosphate (β-TCP)	β-$Ca_3(PO_4)_2$	1.5	28.9	~0.0005	Cannot be precipitated from aqueous solutions*
Hydroxyapatite (HA)	$Ca_{10}(PO_4)_6(OH)_2$	1.67	116.8	~0.0003	9.5-12.0
Calcium Deficient Hydroxyapatite (CDHA)	$Ca_{10-x}(HPO_4)_x(PO_4)_{6-x}(OH)_{2-x}$, 0 < x < 1	1.5-1.67	~85.1	~0.0094	6.5-9.5
Fluorapatite (FA)	$Ca_{10}(PO_4)_6F_2$	1.67	120.0	~0.0002	7.0-12.0
Octacalcium Phosphate (OCP)	$Ca_8(HPO_4)_2(PO_4)_4 \cdot 5H_2O$	1.33	96.6	~0.0081	5.5-7.0
Monocalcium Phosphate Monohydrate (MCPM)	$Ca(H_2PO_4)_2 \cdot H_2O$	0.5	1.14	~18	0.0-2.0
Monocalcium Phosphate Anhydrous (MCPA)	$Ca(H_2PO_4)_2$	0.5	1.14	~17	Stable > 100°C
Dicalcium Phosphate Dihydrate (DCPD), Mineral Brushite	$CaHPO_4 \cdot 2H_2O$	1.0	6.59	~0.0880	2.0-6.0
Dicalcium Phosphate Anhydrous (DCPA), Mineral Monetite	$CaHPO_4$	1.0	6.90	0.0480	Stable > 100°C
Oxyapatite (OXA)	$Ca_{10}(PO_4)_6O$	1.67	~69.0	~0.0870	Cannot be precipitated from aqueous solutions*
Tetracalcium Phosphate (TTCP),Mineral Hilgenstockite	$Ca_4(PO_4)_2O$	2.0	38-44	~0.0007	Cannot be precipitated from aqueous solutions*

Table 1-1: **The 13 known non-substituted calcium orthophosphates and the main parameters used to describe them. ACP, α-TCP, β-TCP (and its Mg^{2+} substituted form whitlockite), HA, CDHA, FA, OCP and DCPD are those which are going to be described in more detail below and can be traced as biogenic forms in bones and/or teeth. Adapted by permission from Multidisciplinary Digital Publishing Institute: Materials from reference (155), copyright (2013).**

*** Cannot be precipitated using wet precipitation synthesis routes, but through thermal transformation and solid-state reactions of precursor phases.**

1.4.1 Amorphous Calcium Phosphates (ACPs)

ACPs have the general formula $Ca_xH_y(PO_4)_z \cdot nH_2O$, $3 \leq n \leq 4.5$ and are considered, in many cases, to act as precursors for bioapatite (156-159). ACPs have Ca/P ratio between 1.2 and 2.2 and present varying chemical, but similar physical properties (160). The unit cell of ACPs is called a Posner's cluster ($Ca_9(PO_4)_6$) (Figure 1-16) and comprises of a central Ca^{2+} cation, which is surrounded by six PO_4^{3-} anions; and the structure is surrounded by the eight remaining Ca^{2+} ions (160, 161). ACP is proposed to be present in forming and maturing human tooth along with HA (157, 162, 163).

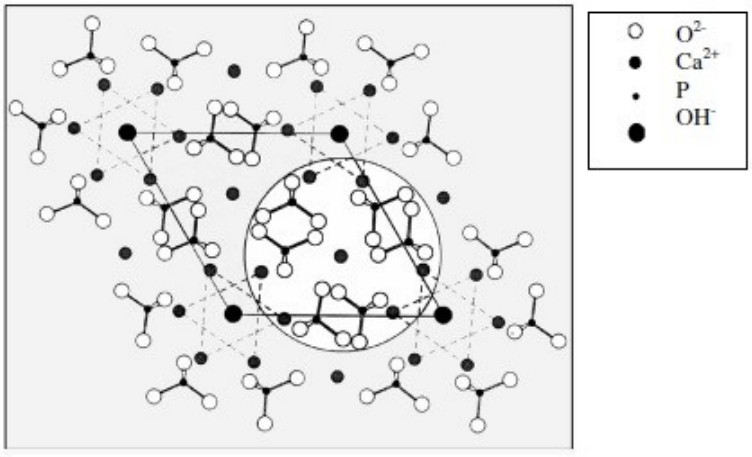

Figure 1-16: Schematic depicting the structure of amorphous calcium phosphate Posner's cluster. Reprinted by permission from Acta Materialia Inc: Acta Biomaterialia from reference (164), copyright (2010).

ACPs can be synthesised using mainly wet precipitation (165-172) or mechanical (173-175) and thermal techniques (176-178). Crystallite properties (e.g. size, stoichiometry) can be manipulated by modifying the experimental conditions (e.g. temperature, reactants) (164, 168). The ACPs synthesised using low temperatures are those which act as precursors during more stable calcium orthophosphate production. This is due to their lower surface energy, which leads to the initial random packing of the Ca^{2+} and PO_4^{3-} clusters to form the ACP particles (179); while the degree of amorphisation is proportional to the Ca^{2+} and PO_4^{3-} concentrations inside the solutions (145, 160).

ACP synthesis can happen for a wide pH range (6.5-13), but not in acidic environments (166, 167). This suggests that ACPs could, initially, be part of the enamel formation process (157) and subsequently mineralise during their interaction with the fluids of the environment (180, 181). This idea is also supported by the greater presence of ACPs in bone during the early stages of mineralisation (166, 182, 183). At the same time, biogenic ACPs are always linked with an organic matrix, while stabilisation of the mineral is attributed to the presence of inorganic ions (e.g. Mg^{2+}, F^-, CO_3^{2-}) (184, 185), which, in combination with the subsequent remineralisation process, could explain their incorporation inside the enamel (79, 84, 85, 126,

127, 186, 187). Biomedical applications of ACPs are in self-setting calcium orthophosphates (188) developed for caries prevention and remineralisation (189-191) and surgery (192, 193).

1.4.2 Tricalcium Phosphate (TCP)

TCPs ($Ca_3(PO_4)_2$) are found in three different polymorphs: β-TCP which is the most common and exists at low temperatures and the high temperature α-TCP and a'-TCP. α- and β-TCP differ in terms of crystal structure, which results in slight differences in density and solubility; with β-TCP being less soluble. a'-TCP can exist only at temperatures over 1430ºC, else it transforms almost instantly to α-TCP. β-TCP is stable at room temperature and if heated above 1225ºC can also transform to α-TCP (194). These differences also affect their biological properties and possible clinical applications. It is also notable that pure β-TCP never occurs naturally in biological calcification. Only the Mg-substituted (β-$(Ca,Mg)_3(PO4)_2$; β-TCMP, whitlockite) form, which is less soluble than β-TCP (195), has been traced during pathological conditions (e.g. urinary stones, dental caries) (145, 194).

1.4.2.1 α-Tricalcium Phosphate

There are several ways to synthesise α-TCP, such as thermal transformation of precursors with a molar Ca/P ratio of about 1.5 (e.g. CDHA, ACP, β-TCP) (196-199), solid state reaction of a mixture of solid precursors (200), self-propagating high-temperature synthesis (201) and combustion synthesis (202). The simplest way, though, is by thermal transformation of β-TCP following calcination above 1230ºC (196). Although α-TCP is not generally preferred in biomedical applications due to its low stability, it has been used during self-setting calcium orthophosphate formulations (188) and in artificial bone grafts (203, 204).

1.4.2.2 β-Tricalcium Phosphate

β-TCP can be synthesised either using high temperature thermal decomposition of CDHA (see section 1.4.4) or solid-state interaction of acidic calcium orthophosphates (145). Of high interest is the formation through the calcination of HA (199, 205), which could directly affect the HA phase and thermal stability during its use as bone or enamel substitute (206-208). Besides high temperature synthesis, β-TCP can be also produced using lower temperatures (~150ºC) either by wet precipitation and synthesis in organic media (e.g. ethylene glycol) or through amorphous precursors (209, 210). Same as α-TCP, β-TCP has been used during self-setting calcium orthophosphate formulations (188) and bone grafts (Figure 1-17) (211, 212). Other uses include drug delivery (213), toothpastes (214) and vitamin and food supplements (215, 216).

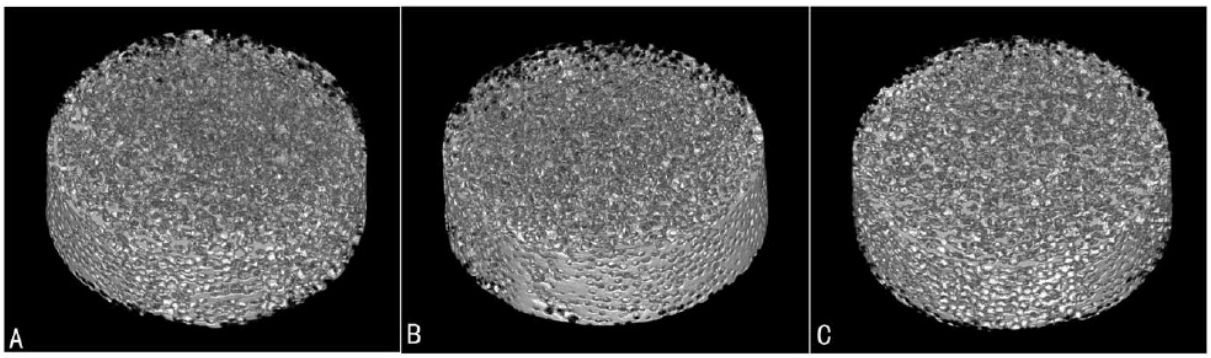

Figure 1-17: Micro-CT images of porous β-TCP scaffolds with different interconnections sizes of a. 100 µm, b. 120µm and c. 150 µm. Reprinted by permission from Macmillan Publishers Ltd: Scientific Reports from reference (217), copyright (2015).

1.4.3 Hydroxyapatite (HA)

HA ($Ca_{10}(PO_4)_6(OH)_2$) is a naturally occurring mineral and one of the most stable and least soluble calcium orthophosphates (Table 1-1). Although it is chemically similar to biological apatite, it never occurs in stoichiometric form in biological systems (145). Stoichiometric HA has a Ca/P ratio of 1.667 and can be synthesised using various methods like microemulsion and emulsion techniques (218), wet precipitation (219, 220), plasma spray (221) and solution spray (222) dry methods, sol-gel methods (223-225), solid state mixing (226, 227), hydrolysis (228, 229), patterning process (230, 231) and hydrothermal methods (232).

HA precipitated at ambient temperatures is poorly crystalline and crystallises in the monoclinic space group $P2_1/b$ (233, 234) and in its non-stoichiometric form it is equivalent to CDHA (234). Recent studies have shown that, with the use of biopolymers, the morphology (shape, size) of the synthesised HA crystals can be controlled to mimic that of enamel (235, 236). Calcination of HA using temperatures above 250ºC results in phase transition to the hexagonal space group $P6_3/m$ with the unit cell having average dimensions of α = 9.417 Å and c = 6.875 Å (Figure 1-18) (234, 237, 238). While high-temperature calcination results in more dense and crystalline material (239, 240), for temperatures up to 500ºC no significant changes in the degree of crystallinity are observed (Figure 1-19) (220, 241).

Of high significance is also the thermal stability of the produced HA. High temperature calcination of nonstoichiometric HA may lead to its decomposition and transformation into secondary phases (CaO, TCP) (Figure 1-19) depending on the original Ca/P ratio. For ratios between 1.50 and 1.67 decomposition into either α-TCP (242) or β-TCP (243, 244) is favoured, while for values between 1.67 and 2.00 HA decomposes into CaO and P_2O_5 and possibly $Ca_4(PO_4)_2O$ (245-247). The latter is hard to detect due to the overlapping of its peaks with those of HA in XRD patterns (247).

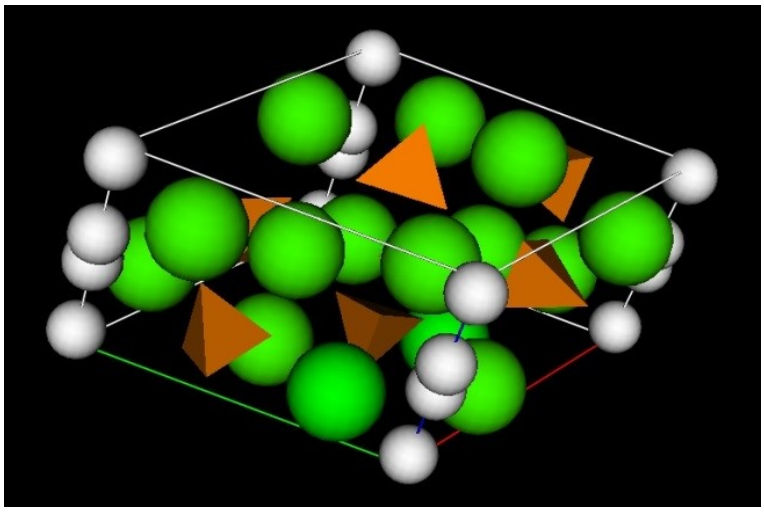

Figure 1-18: Schematic representation of a HA unit cell as produced by XRD data and the Rietveld analysis using the GSAS-II software. The green spheres correspond to Ca^{2+} atoms, the white to OH^- and the pyramids to the PO_4^{3-} tetrahedra.

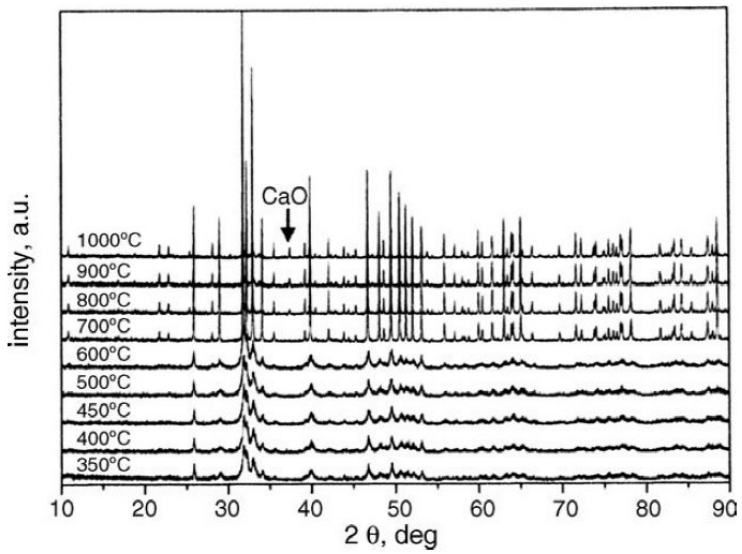

Figure 1-19: Changes in the crystallinity of HA through calcination at different temperatures as observed using XRD. Up to 500ºC no significant changes can be observed. From 600ºC upwards the crystallinity of HA begins to increase significantly as the well-defined pattern of the XRDs show. Reprinted by permission from Elsevier Ltd: Journal of the European Ceramic Society from reference (241), copyright (2006).

The thermal stability of HA is significant and for that reason it is widely used in orthopaedic (248-250) and dental (251-254) science, which means that mimicking the mechanical properties of natural bone and teeth is essential. HA has been also used as "bone-building" supplements (255), as additives in toothpastes, as a remineralising (256, 257), polishing and whitening agent (258, 259) and to reduce dental hypersensitivity (260, 261); as well as in HA liquid chromatography (262-264) and as drug delivery agents (265-267).

1.4.4 Calcium Deficient Hydroxyapatite (CDHA)

CDHA ($Ca_{10-x}(HPO_4)_x(PO_4)_{6-x}(OH)_{2-x}$, $0 < x < 1$) is a form of poorly crystalline HA with low Ca/P ratio (Table 1-1). Although this variation has been mainly attributed to the loss of Ca^{2+} (268), it is evident from its chemical formula that some OH^- deficiency and PO_4^{3-} protonation also exists adding up to the available ionic vacancies in the crystal structure (234, 268).

CDHA can be synthesised using various techniques (269-271) and, as already stated in paragraph 1.4, its biological form is the main constituent of bone and teeth (145, 234, 272, 273). It is produced through the ionic substitution of Ca^{2+} by Zn^{2+}, K^+, Mg^{2+} and Sr^{2+} and due to its similarity with its biogenic counterpart has been proposed to be used as a bone substitute (270, 274, 275) and for drug delivery purposes (276).

1.4.5 Fluorapatite (FA)

FA ($Ca_{10}(PO_4)_6F_2$) can be synthesised using the techniques mentioned earlier for HA, with the addition of the desired amount of F^- usually in the form of NaF (145, 234). Depending on the amount of F^- used, partially F-substituted HA (fHA, $Ca_{10}(PO_4)_6(OH)_{2-x}F_x$, $0 < x < 2$) can be also formed (277-279). Fluoride incorporation in the HA structure reduces the apatite solubility and increases its stability and hardness through changes in crystallite orientation and decreases in the lattice parameters, crystallite sizes and aspect ratio (280, 281). Although it would be expected that FA would be the most stable, hardest and least soluble of the calcium phosphates; and that fHA would lie somewhere between HA and FA, it has been suggested that substitution of OH^- by F^- between 50% and 60% provides the most stable material (80, 282). This is probably due to the hydrogen bonds created between the OH^- present in the HA structure and the incorporated F^- (283) and the disordered structure of HA (Figure 1-20) in which the H^+ of the disordered OH^- lies further from the structural triangle of Ca^{2+} atoms along the *c* axis than in the ordered structure (Figure 1-20c, d). Substitution of the

more energetically stable ordered OH^- (Figure 1-20a, e) from F^-, which is then located in the centre of the triangle (Figure 1-20b); will result to changes in the inter-atomic distances until both the normal Ca^{2+} to F^- distances are reached and the disordered OH^- are stabilised (284, 285).

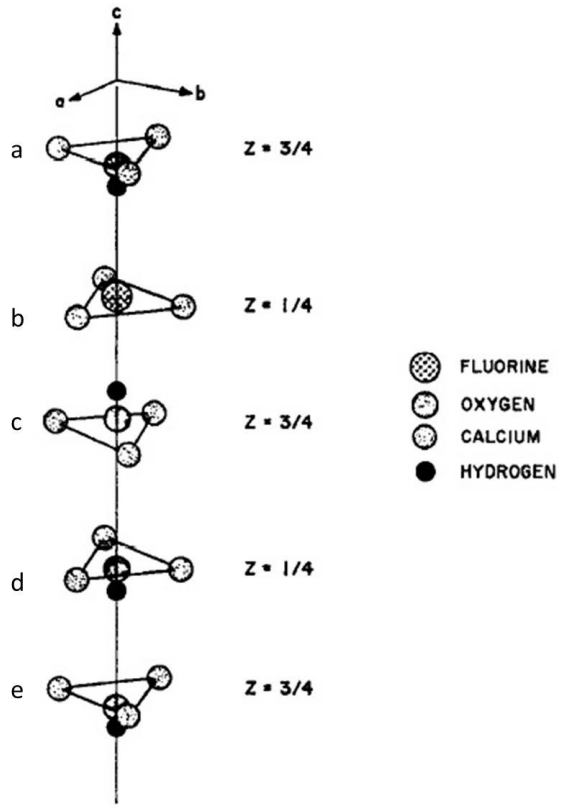

Figure 1-20: Schematic representation of the HA Ca^{2+} structural triangles observed on the *c-axis*. The observed triangles correspond to the ordered (a, e) and disordered (c, d) HA structure and the F^- substituted triangle (b). Reprinted by permission from ScienceDirect: Archives of Oral Biology from reference (285), copyright (1966).

FA does not occur naturally in biological systems. This is probably because the amount of F^- needed to produce FA would cause significant toxic damage to the organisms (234, 286, 287). On the other hand, hard tissues always contain a small amount of F^-, with the highest concentrations observed in cementum and dentine, followed by bone and enamel (234). The effects of F^- on the physicochemical properties of the hard tissues, has led to extensive use in caries prevention and lesion remineralisation mainly through water fluoridation and systemic absorption and subsequent release into the saliva, which results in topical application (121, 288-291); and in biomedical applications in general (292-294).

1.4.6 Octacalcium Phosphate (OCP)

OCP ($Ca_8(HPO_4)_2(PO_4)_4 \cdot 5H_2O$) has been suggested to act as precursor during the formation of other apatitic phases like CDHA and HA (295-297). OCP can also form through precipitation (298, 299) and can have Ca/P ratio between 1.26 and 1.48 (298). OCP is highly unstable and hydrolyses into either HA (295) or CDHA (298); especially with the presence of ionic substitutions like Sr^{2+} and Mg^{2+} which create an intermediate phase named "collapsed OCP" (300). Supporting this hypothesis is the proposal that OCP acts as a starting phase during enamel and bone formation, due to its chemical and structural similarity with HA (301-305). As a result, OCP has been widely used in bone regeneration and in bone grafts for osseointegration (306-309). At the same time, OCP has been used as a precursor for the epitaxial growth of HA during controlled enamel remineralisation, which can be accelerated with the presence of a small amount of F^- (Figure 1-21) (310-312).

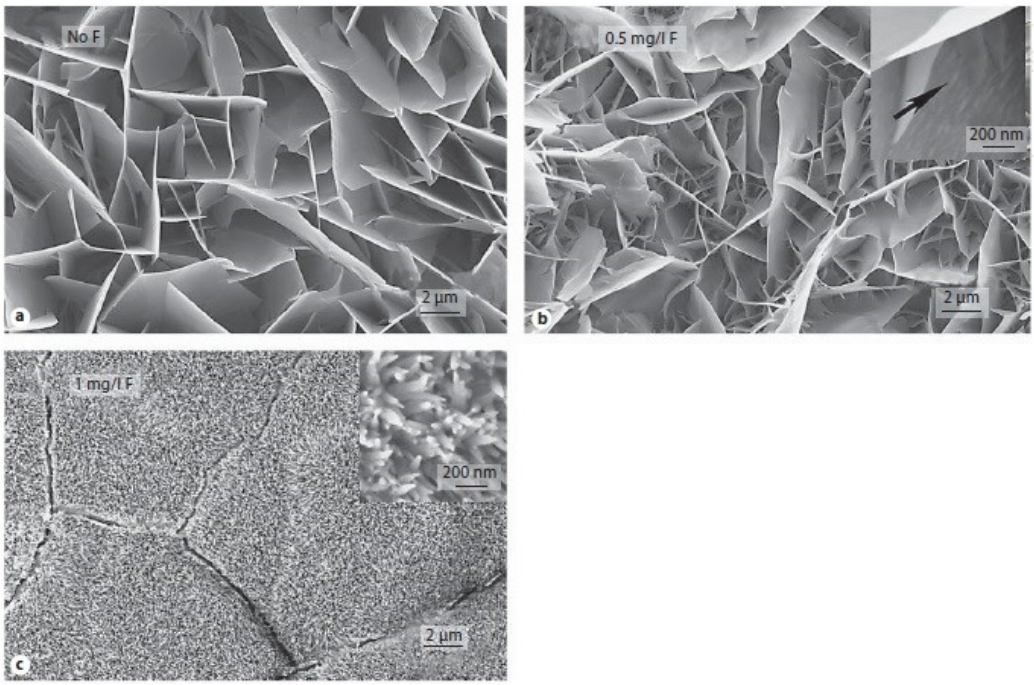

Figure 1-21: Coating deposited on the surface of the enamel, following remineralisation for 16 hours with a. 0 ppm, b. 0.5 ppm and c. 1.0 ppm of F^-. The OCP flake-like structure observed when no F^- is present changes progressively to the needle-like structure of fHA with increasing F^- presence. Reprinted by permission from Karger Publishers AG: Caries Research from reference (312), copyright (2009).

1.4.7 Dicalcium Phosphate Dihydrate, Mineral Brushite (DCPD)

DCPD ($CaHPO_4 \cdot 2H_2O$) has been also suggested to act as a precursor of HA and dental enamel (313, 314). DCPD has a Ca/P ration of 1.0 and can be synthesised using wet (315) or gel (316) precipitation under acidic conditions (pH: 2-6). DCPD can then hydrolyse in HA (228) following the reaction:

$$10\ CaHPO_4 \cdot 2H_2O \rightarrow Ca_{10}(PO_4)_6(OH)_2 + 18\ H_2O + 12\ H^+ + 4\ PO_4^{3-}$$

DCPD is also found in pathological calcifications (e.g. dental calculi) and in some carious lesions; and has been observed as an intermediate phase during bone mineralisation and enamel dissolution taking place during erosion (272).

1.5 Literature Review

1.5.1 Post-Eruptive Enamel Maturation

Many of the studies describing PEM can be traced back to the 60s and early 70s, the time when the idea of PEM became widely accepted. Besides the universal acknowledgement of its significance, a complete model to describe the process has not been defined. This is because during the 70s research interest moved to the effects of F^- on enamel properties and caries incidence, which left the PEM study inconclusive. Since then, most of the studies on this subject are either indirect or incidental (113, 317, 318). From the existing studies, various categorisations can be made, with most appropriate being that distinguishing between the physical and chemical changes of enamel properties.

It has been suggested that following eruption inside the oral cavity, the surface of the enamel enters into sequential demineralisation and remineralisation cycles due to its interaction with the oral fluids (319-322). As a result, surface dissolution of the initial bio-apatite takes place with the simultaneous loss of impurities which enhance enamel solubility like CO_3^{2-}, Mg^{2+} and Na^+ (78, 79, 187) and is followed by the precipitation of more stable apatitic phases like

HA, fHA and FA in the form of a prismless surface layer (80, 81, 323, 324). This is achieved through the filling of the interstitial spaces between the enamel prisms during remineralisation, which exist inside the enamel shortly after eruption and the uptake of Ca^{2+}, PO_4^{3-} and F^- from the oral environment (52, 102, 325). As a result, increase of Ca/P ratio (79, 95, 98-100, 154, 323) and F^- concentration on the surface of the enamel is observed. Fluoride is either incorporated in the crystal structure (326-330) or deposited as CaF_2 on the surface (331-333) of the enamel as is suggested during *in vitro* sequential demineralisation and remineralisation experiments.

Although the effects of PEM are seen primarily on the surface of the enamel, which led to the conclusion that PEM is mainly of surface nature, the underlying enamel is affected as well (78, 79, 95, 98). The structural changes observed during PEM have been attributed to a linear increase in crystallite width with post-eruptive age and is the result of the precipitation of less soluble phases (40, 101, 103, 334, 335); while some of the precipitated material also fills the interstices between the enamel prisms (91-93, 102). As a result, the sequential dissolution and reprecipitation cycles lead to significant decrease in solubility (336, 337), porosity (76, 91, 108, 109) and hence permeability (319, 338-340) of the enamel, as well as to significant hardness increase (104-107, 341).

Besides the research performed directly on post-eruptive enamel maturation, several studies investigated its effect on caries incidence and other enamel diseases such as MIH. Crombie et al. recently suggested that it would be possible to prevent MIH using an artificial maturation process, which would lead to mineralisation and stabilisation of the affected enamel (82, 113). Most studies, though, have focussed on the relationship between PEM and the decrease in caries incidence. Shortly after eruption an increased caries susceptibility has been observed for both humans (327, 342, 343) and animals (1, 344, 345), which is followed by rapid

decrease and has been attributed to PEM and the absorption of Ca^{2+} and PO_4^{3-} present in the oral fluids (1, 346, 347); while F^- administration significantly enhances the whole process (348-351).

Besides F^-, and because the enamel has the ability to adsorb various elements (352, 353), extended research has been performed into the effects of naturally occurring compositional impurities (e.g. Sr^{2+}, Zn^{2+}, N^{3-}, Mg^{2+}) and those acquired during post-eruptive life through the environment (e.g. Cu^{2+}, Cd^{2+}, Pb^{2+}) on the properties of the enamel and caries incidence. Elements linked with environmental pollution (Cu^{2+}, Cd^{2+}, Pb^{2+}) (354-356) and the presence of the organic content (e.g. Mg^{2+}, N^{3-}, Cl^-) (79, 357-359) have been identified as caries inducing agents which destabilise the enamel structure. On the other hand, several elements (e.g. Sr^{2+}, Zn^{2+}) have been found to have a strong positive post-eruptive effect either through incorporation inside the enamel structure, or through the enhancement of F^- activity (360-364).

1.5.2 The Use of Synthetic Hydroxyapatite as Enamel Substitute

Although there have been several studies using synthetic HA as an enamel substitute (236, 365, 366), none has studied the potential to use pelleted HA to study PEM. This is because, so far, it has not been possible to directly replicate the mechanical properties of the enamel through HA precipitation and pelleting (367-369). HA sintering could in principle improve properties like density, flexural strength and hardness, but could also lead to chemical deterioration due to HA decomposition into β-TCP and CaO (370-372). The replication of the physicochemical properties of enamel could lead to a synthetic material which could be used to study the process of PEM and help design more accurate clinical studies.

Currently, the majority of the studies concerning the use of synthetic HA in dental science have been limited to attempts to repair the surface of the enamel following carious attacks using HA particles of various sizes (365, 373-378), as additives in dentifrices for remineralisation, polishing and whitening purposes (256-258, 379, 380) and as coatings for dental implants (381-385). Other than that, HA has been used in comparative and simulation studies with dental enamel, in studies of their structural properties and uptake of several species (trace elements, CO_3^{2-}) (386-393), biomimetic enamel synthesis (376, 377, 394) and in dissolution studies (395).

Lately, there have been studies demonstrating that it is possible to synthesise HA which can be thermally stable up to 1200ºC (206, 242-244, 396, 397). As a result, it is possible to prepare pure and chemically doped HA powders and pellets, which remain stable after sintering at high temperatures; these are compositionally closer to enamel. However - to the author's knowledge - no studies, so far, have taken advantage of these new approaches for the design and development of novel enamel proxies.

1.6 Aims & Objectives

The initial aim of this project was to study the effects of PEM on the physicochemical properties of tooth-related biogenic apatites and to study one of the proposed models (398) behind post-eruptive dental enamel maturation. As stated in paragraph 1.5.1, although extended study has been performed regarding the changes on enamel properties, a complete model to describe the whole process does not exist. At the same time, most of the studies can be traced back to the 50s and 60s, when the analytical techniques available today were either less developed or unavailable. The development of a complete PEM model could in the future be validated through carefully planned clinical studies, which can then be used for the *in vivo* accurate monitoring of the PEM effects on dental enamel.

The objectives in this case were:

- To modify the available experimental techniques and develop a simple *in vitro* procedure to realistically mimic the processes taking place between the plaque and the enamel, with the intention to simulate the PEM process and study proposed models for PEM using immature-like and prematured permanent bovine enamel.
- To analyse the treated enamel using state-of-the-art experimental techniques and test whether the results support the proposed PEM process.
- To test whether post-eruptive enamel maturation could take place in primary enamel.
- To study the effects of a simulated *in vitro* PEM experimental procedure on the physicochemical properties of dental enamel.

Following the analysis of enamel, the project aimed to address the problems described in paragraph 1.5.2 and more specifically the lack of synthetic enamel proxies, which can mimic both the physical and chemical properties of bovine enamel and to further investigate if it is possible to replicate the process of PEM using the novel synthetic materials. Production of such a material can be used instead of enamel primarily for research purposes; e.g. during *in vitro* experiments, during which the PEM process can be significantly accelerated and can help plan targeted clinical trials. Enamel proxies could also be used in the development of dental materials for the inhibition of secondary caries formation.

The objectives in this case were:

- To take advantage of the newly available approaches during HA synthesis to develop an experimental method leading to the production of thermally stable synthetic HA pellets with physicochemical properties similar to those of enamel.
- To apply the modified *in vitro* experimental procedure used for enamel, to test whether simulated PEM can take place in synthetic HA pellets.
- To test whether the changes in the physicochemical properties of synthetic HA pellets during simulated PEM are similar to those of enamel.

2. Materials & Methods

Chapter 2 describes the materials, experimental methods and analytical techniques used, and is divided into three subsections. Firstly, the materials used during all experimental work are introduced and a justification for their use is presented. Secondly, the preparation and/or synthesis methods for each of the materials used are described, along with the experimental methods used to artificially mature these materials. Finally, the third part describes the analytical techniques employed to monitor potential changes on the physicochemical properties of each material.

2.1 Materials

Although human enamel would be the best material to use to study the effects of artificial PEM, difficulties in obtaining it in sufficient quantity led to the use of bovine enamel which is widely considered to be the best proxy for human enamel (399-404), as described in section 2.1.1. Section 2.1.2 introduces the reader to the synthetic material developed as part of the work presented here.

2.1.1 Dental Enamel

During this study both primary and permanent bovine incisors were used as substitutes for extracted human teeth, the quality of which is often low due to extensive caries and other potential dental defects (399). Human enamel composition is significantly affected by F^- exposure (topical and systemic), environmental factors (e.g. diet, urban vs. rural pollution) and age (e.g. PEM) (399, 403-405).

Bovine teeth, on the other hand, are easier to acquire and present similar radiodensity (Figure 2-1) (105, 406, 407), chemical composition, Ca/P ratio and F^- uptake (408-411) with human enamel; and similar physical properties (e.g. tensile strength, modulus of elasticity) (412, 413). As far as hardness is concerned, human teeth are considered to be harder than bovine, although Fonseca et al. (2008) found that hardness was significantly higher for younger, but similar for older teeth (105). In the case of caries experiments the lesions created have similar mineral distribution to those of human origin (400, 401, 414, 415). Finally, bovine teeth are bigger, flatter and allow preparation of specimens with larger surface areas and more uniform enamel thickness, which correspond to higher experimental surfaces and makes them more suitable during experiments where a flat surface is needed (e.g. hardness monitoring) (399) or when destructive analytical techniques are employed (e.g. transverse micro-radiography) (415). The more balanced diet and the shorter life span of cattle, which keep the environmental influences low, in combination with the lack of cariogenic challenges and the low exposure to F^- make bovine enamel more homogeneous and results in a less variable response to demineralisation challenges and remineralisation treatments (403, 415, 416).

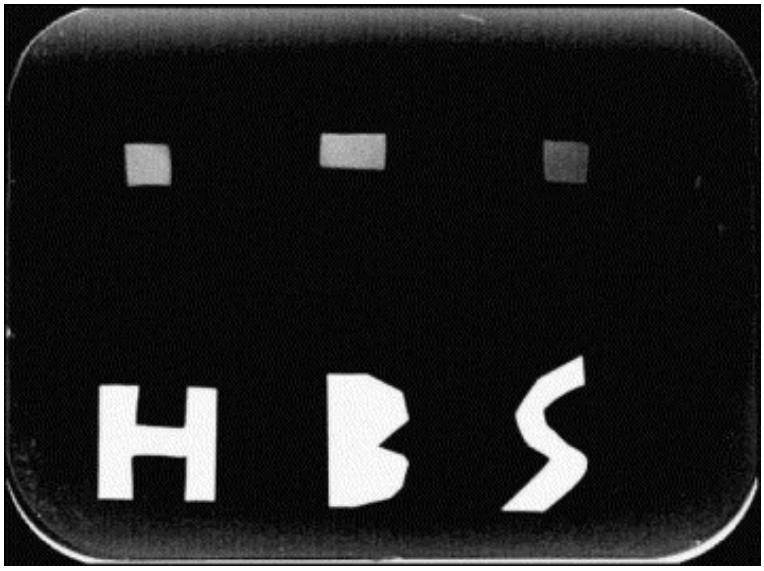

Figure 2-1: Radiodensities of human (H), bovine (B) and porcine (S) enamel. The radiodensities of human and bovine enamel are similar and higher than porcine enamel. Reprinted by permission from ScienceDirect Ltd: Archives of Oral Biology from reference (406), copyright (2004).

Primary teeth, whether human or bovine, show significantly higher porosity and lower mineral content, leading to faster experimental responses and more pronounced effects when compared to permanent enamel. These differences were taken into account during experimental planning and procedure (406, 417).

2.1.2 Synthetic Hydroxyapatite

The synthesised HA was characterised using a wide range of analytical techniques presented in section 1.3. This enabled different experimental approaches to be used, allowing the appropriate manipulation of its physicochemical properties to resemble, as closely as possible, those of dental enamel. Further details on the properties of the synthetic HA used and the preparation method can be found in sections 2.2.2 and 2.2.3.

2.2 Methods

In order to meet the project's aims and objectives (Section 2.6), enamel and synthetic HA needed to be prepared to be used as substrates and properly treated to enable monitoring of potential changes in their physicochemical properties due to maturation. Permanent and primary bovine incisors were polished and ground into rectangular blocks. This way a flat surface, which is easier to be monitored and analysed, was acquired. The whole process is explained in detail in section 2.2.1.

The synthesised HA was pelleted in rectangular blocks, which were treated in order to acquire similar physical structure (density, porosity) and properties (hardness) to those of bovine enamel. In order to achieve that, an appropriately designed wet precipitation protocol was used, which allowed the synthesis of thermally stable HA and is described in section 2.2.2. The produced HA was then pelleted in rectangular blocks similar to enamel (Section 2.2.3).

Treatment of the bovine enamel blocks and synthetic pellets was performed using a pH-cycling protocol (Section 2.2.4). Such protocols can mimic the conditions inside the oral

environment under controlled experimental conditions and can be easily modified. By choosing the proper experimental conditions it is also possible to accelerate phenomena observed in the caries process, which could take significantly more time to develop in the mouth.

2.2.1 Dental Enamel Block Preparation

Enamel block preparation was performed using a Buehler Metaserv-2000 Grinder/Polisher equipped with Magnomet CSi paper disks (Buehler, USA) and an Isomet low speed saw (Buehler, USA) equipped with diamond wafering blades (Series 15LC, Buehler, USA). The primary and permanent bovine incisors used (Figure 2-2a, b) were provided by Modus Laboratories, Reading, UK. Prior to being used, the teeth were stored in a solution which contained 0.2 g l^{-1} of Thymol (Sigma-Aldrich, USA) and 9.0 g l^{-1} of NaCl (Fisher Scientific, UK). pH was kept at 7.00 using KOH (Sigma-Aldrich, USA) and was refreshed weekly.

Initially the palatal surface of the incisor was ground to create a flat surface (Figure 2-2c) and remove any remaining soft tissue. Next, the labial surface of the incisor was abraded and polished in order to remove the top 100 μm and expose the underlying enamel, which had not been subjected to PEM and the subsequent physicochemical modifications (27, 79). Grinding and polishing was performed sequentially using CSi paper with decreasing abrasivity (grade P800-P2500, Buehler, USA), which led to the creation of a flat surface with no visible grinding marks (Figure 2-2d). The tooth was then cut to form a rectangular block (Figure 2-2e, f), following the cervico-incisal axis, with the intention to study different enamel areas (cusp, cervical); since the enamel is known to be highly heterogeneous, anisotropic and asymmetrical along all its axes (418-420). At the same time, increased fracture toughness has been observed along the cervico-incisal axis (421, 422), which denotes that different enamel areas behave differently. As a result, by including different enamel areas these variations can be averaged and make the results comparable between samples. Finally, the produced enamel

blocks were painted using nail polish (Max Factor, No. 37, Procter & Gamble, USA), leaving a window of exposed enamel on the surface with dimensions of 2.5 x 3 mm^2.

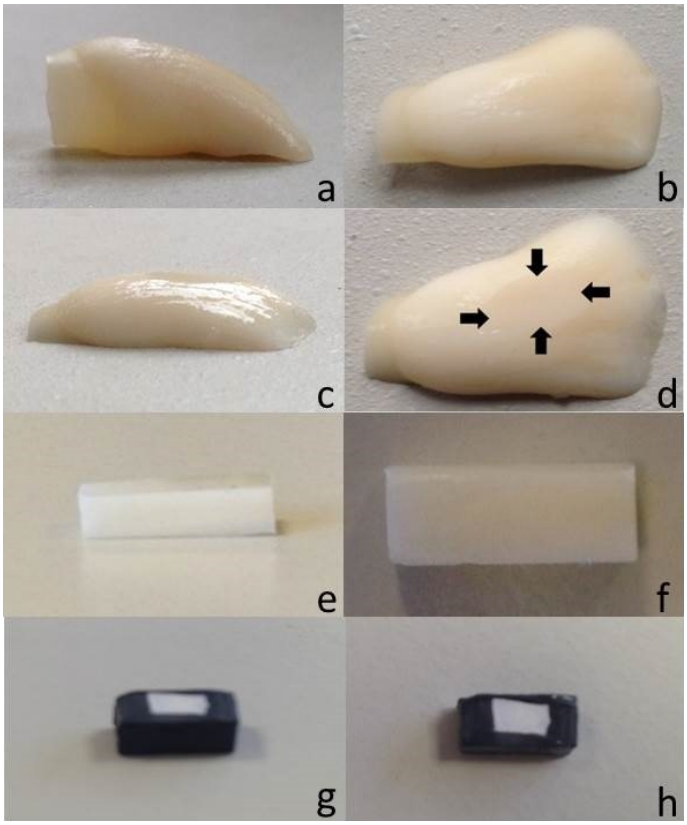

Figure 2-2: Bovine enamel block preparation from permanent bovine incisors. Initially the incisor was ground from underneath to remove any organic material and create a flat surface (a). Then a small window was created on the upper surface through abrasion and polishing (b-d). Finally, the incisor was cut so as to acquire a rectangular block (e, f), which was then painted with nail-polish (g, h) leaving a window of exposed enamel of a 2.5x3 mm^2 surface.

2.2.2 Pure Hydroxyapatite Synthesis

The HA used was synthesised using a wet precipitation method. The protocol used led to the precipitation of thermally stable HA powders and sustained no chemical degradations up to a temperature of 1200° C. Phosphate (1.0 M of $(NH_4)_2HPO_4$, Sigma-Aldrich, USA) was added dropwise inside a vigorous stirring Ca^{2+} solution (1.75 M of $Ca(NO_3)_2{\cdot}4H_2O$, Sigma-Aldrich, UK) at a constant rate of 150 ml h^{-1}. The pH of the reacting solutions was maintained around 10.5 using concentrated $(NH_4)OH$ (27% vol., Sigma-Aldrich, UK) at room temperature. Stoichiometric and thermally stable HA can be synthesised when pH values are above 9.0 (242, 423). The resultant solution was then heated and kept at 90°C under continuous stirring

for 24 hours. The gelatinous precipitate was then washed 3 times using deionised water (DW) to remove any remaining $(NH_4)OH$ (243). Half of the product was placed inside an oven and dried at 80ºC overnight, while the rest was freeze dried for 24 hours at 10.0 Pa and -55ºC, using an Edwards Super Modulyo Freeze Dryer, after being rapidly frozen using liquid nitrogen. The oven dried HA was ground to fine powder using a Retsch MM200 ball-mill for 30 minutes at a vibrating frequency of 25 Hz. The freeze dried material needed no milling because the acquired powder was already fine.

2.2.3 Pelleting of Hydroxyapatite

Synthetic HA pellets, similar to the enamel blocks, were produced by pelleting the HA powders and then sintering the pellets at various temperatures. Pellets were formed using a Z030 mechanical tester (Zwick/Roell, UK) operating parallel platens at a compression velocity of 20 μm s^{-1}, acquiring force-displacement data at a frequency of 100 Hz. Pellets were produced via uniaxial compaction using a 13.00 mm diameter Atlas evacuable pellet die (Specac, UK), compressing to a maximum load of 30 kN. An average amount of 0.40 g was used for the creation of each pellet. The pellets produced were circular with average diameter of 13.00 mm and average height of 1.827 mm. Some of the produced pellets were then sintered for 3 hours using a CWF-1200 (Carbolite, UK) oven. Sintering was performed starting from room temperature and increased using a step of 10ºC min^{-1}. Finally, the sintered material was left to cool down to room temperature. The process was performed for three different temperatures (500º C, 800º C, 1100º C). Similar to the enamel blocks (Section 2.2.2) the produced pellets were painted with nail polish leaving an exposed window of 2.5 x 3 mm^2.

2.2.4 pH-Cycling Models

pH-cycling models are *in vitro* experimental procedures involving sequential cycles of enamel exposure to remineralising and demineralising solutions (Figure 2-3) simulating low pH conditions during a cariogenic challenge and subsequent neutralisation, as well as the effect of F^-, hence the dynamics taking place during mineral changes and caries formation (405, 424). The advantages of such protocols are that they offer higher scientific control, reproducibility, sensitivity and have a simpler procedure when compared to other *in situ* and *in vivo* models (424) and can be used to study and understand the basic mechanisms of phenomena, which have been observed during such studies and are difficult to explain during the complex *in vivo* conditions.

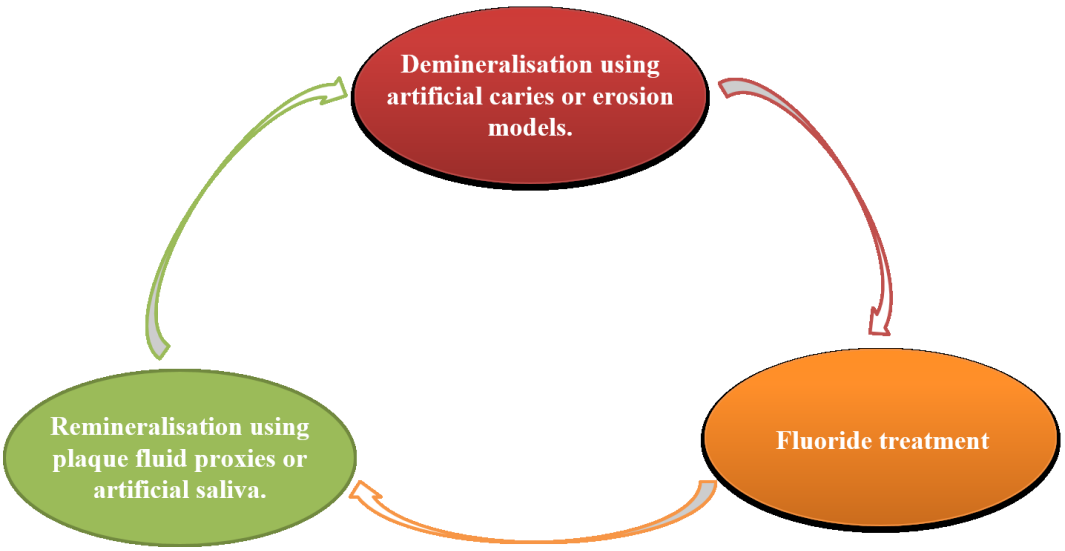

Figure 2-3: Schematic of the basic parts of a pH-cycling model.

On the other hand, several limitations also exist. As most *in vitro* models, they cannot completely replicate the complexity of the intraoral conditions or mimic the solid surface area vs. solution ratios or the exact saliva and plaque fluid composition (425). Another difference with *in vivo* conditions is that the substrates used are appropriately prepared and not in their original form, while the remineralisation, demineralisation and F^- treatment periods are completely distinct and there is no gradual transition between them as would normally happen (424).

In the long run, *in vitro* pH-cycling models help gather the data which will allow scientists to design proper *in situ* and *in vivo* experiments and clinical trials (405, 426-428). As a result, pH-cycling experiments are appropriate for monitoring the process of PEM, which was hypothesised to rely on sequential demineralisation and remineralisation cycles (104, 106, 321). To achieve this, a 3-step pH-cycling protocol was designed, which contained sequential cycles of demineralisation, remineralisation and F^- treatments to describe a full day inside the oral cavity. Demineralisation periods corresponded to pH drop below the critical pH area which is observed shortly after a meal containing fermentable carbohydrates in sufficient amounts and the following enamel softening and potential dissolution; while remineralisation periods correspond to the restitution of the pH to its resting values and the subsequent remineralisation through the saliva and the plaque fluid. The F-step simulates the tooth-brushing interval taking place twice a day (after waking up and before going to bed).

Simple pH-cycling experiments simulating the daily oral conditions contain three remineralisation and demineralisation and two F^- treatment periods (Figure 2-4), use artificial saliva (AS) to study the saliva and enamel interaction (405, 429) and as stated above no gradual transition between demineralisation and remineralisation periods exists (424). In order to create a pH-cycling model which would be appropriate to study PEM, the experimental conditions needed to be modified accordingly.

To begin with, AS was substituted with a plaque fluid proxy (PF) and milder acid conditions during the demineralisation period were used to simulate the plaque/ enamel interaction as the proposed (398) PEM model suggests. At the same time, an extra intermediate remineralisation period was incorporated, which followed each F^- treatment and contained slightly increased background F^- (BF) concentration (Figure 2-5). This period simulates the transition period between each F^- treatment and the main remineralisation period, during which elevated F^- retention by the plaque fluid takes place (430-432). In all cases the temperature was held at

37ºC using an incubator, which is close to the reported average temperature of the oral cavity (433, 434).

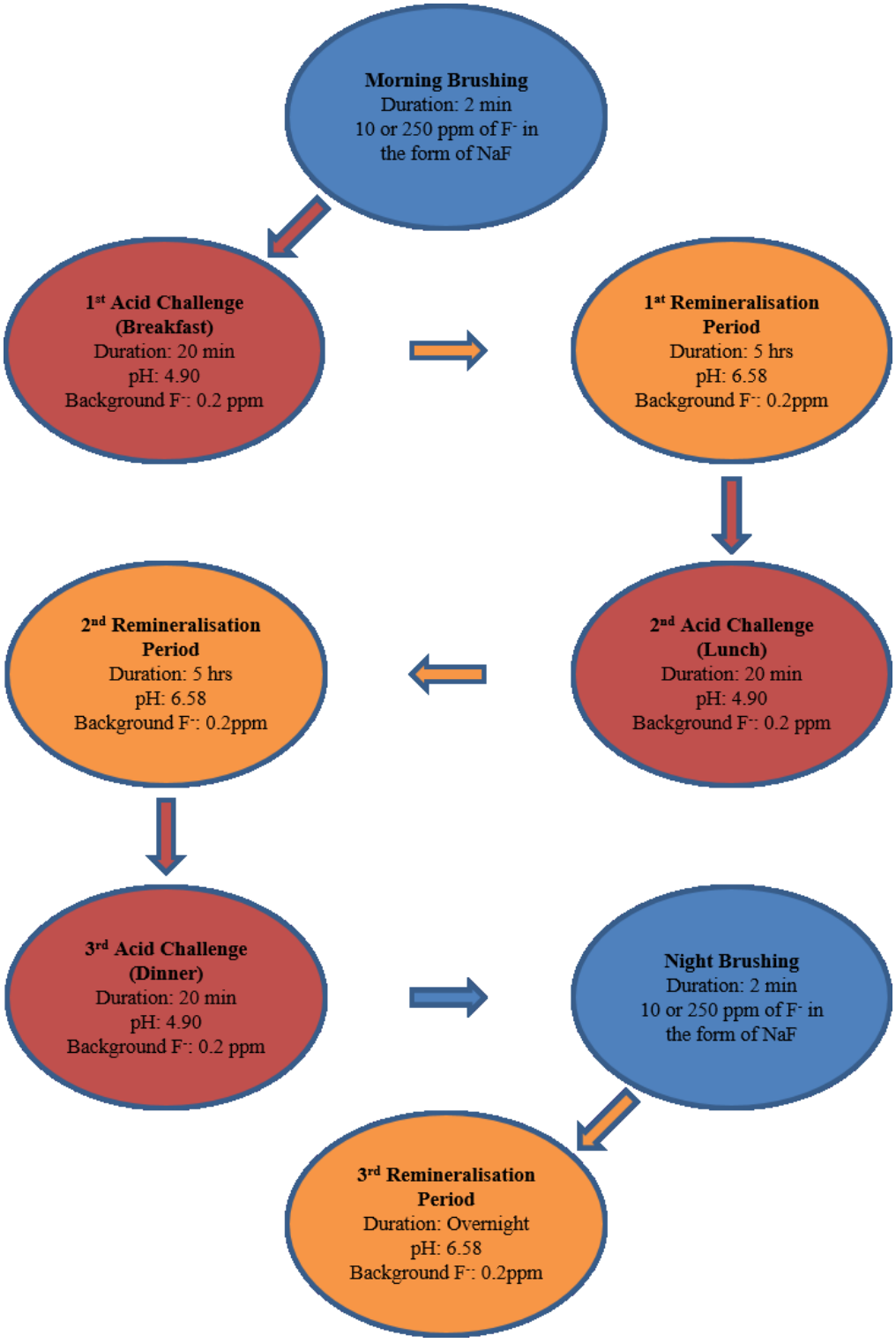

Figure 2-4: Flow chart of a simple pH cycling study, which simulates a whole day inside the oral cavity and is used to study the PF – enamel interaction.

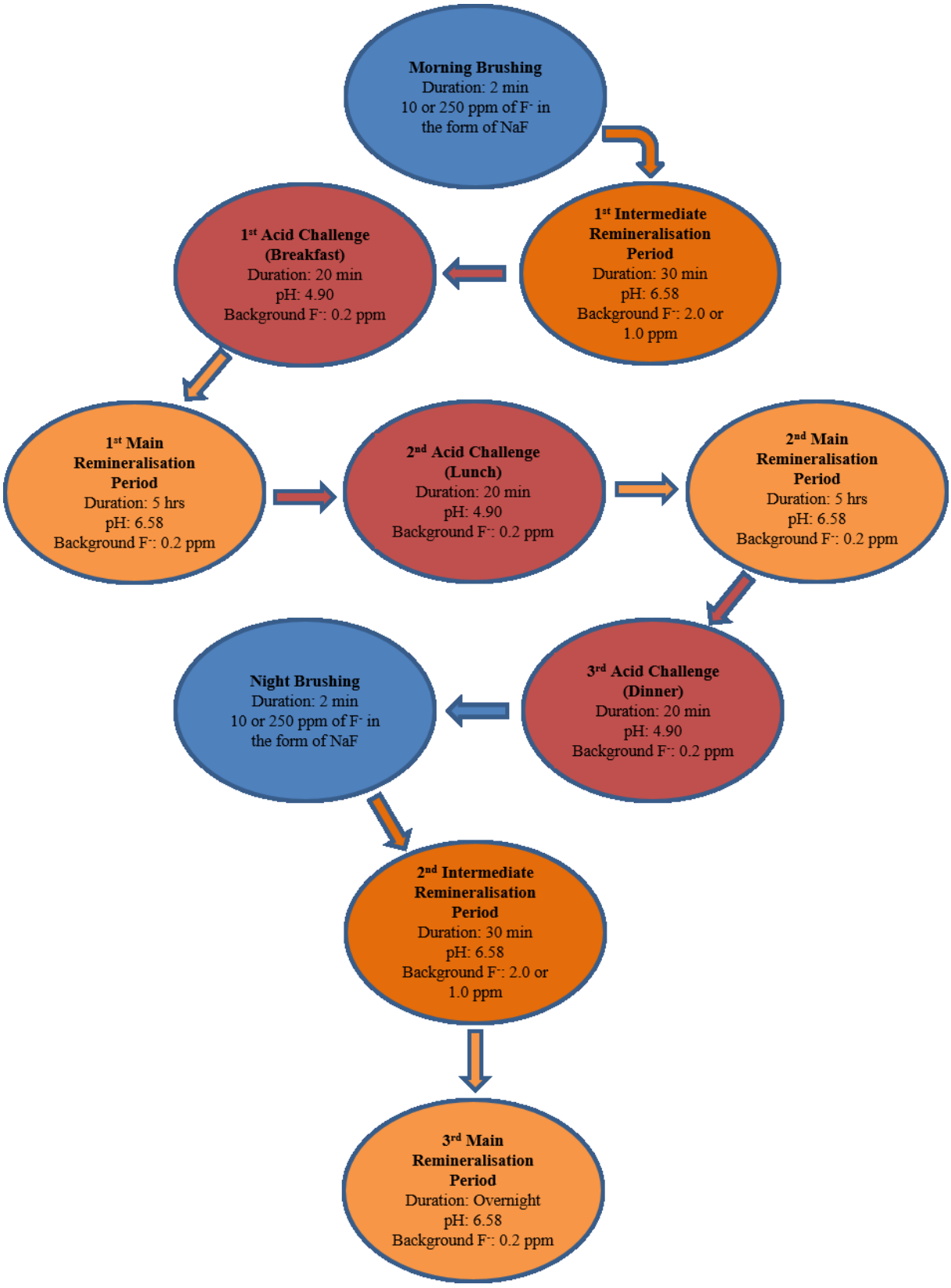

Figure 2-5: Flow chart of a modified pH cycling study, which simulates a whole day inside the oral cavity and can be used to study the PF – enamel interaction. The current model incorporates an extra remineralisation period, which follows the F^- treatment (tooth brushing) and is used to model the transition period during which increased F^- retention takes place. The modified model was used during the current experimental procedure.

Firstly, the demineralising solution consisted of 50 mM of acetic acid (Fisher Scientific, UK), 4.1 mM of $CaCl_2 \cdot 2H_2O$ (Fisher Scientific, UK), 8.0 mM of KH_2PO_4 (Sigma-Aldrich, USA) and 130 mM of KCl (Sigma-Aldrich, USA) (27, 414). In dental research, the correlation between the changes in plaque pH as a function of time following an acid challenge is being described using the Stephan curves (Figure 2-6) (435). Based on these, the pH of the demineralising solution was adjusted to 4.90 using KOH (Sigma-Aldrich, USA), which represents the pH value observed in the plaque of caries-risk children following a meal with sufficient fermentable carbohydrates (429, 436) and could also accelerate the whole process. For the same reason, the duration of the demineralisation challenge was 20 minutes, which, according to Stephan curves, is the average time the oral fluids are undersaturated with respect to tooth mineral (429, 436).

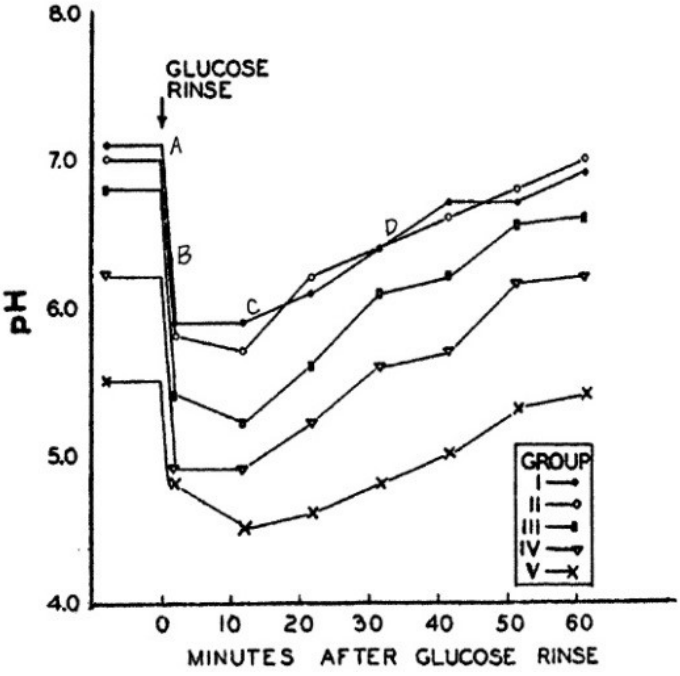

Figure 2-6: The original Stephan curve displaying the response of plaque pH of the labial surfaces of upper anterior teeth following glucose rinse for different caries groups. I. No caries; II. minimal caries activity; III. slight caries activity; IV. marked caries activity and V. extreme caries activity. Reprinted by permission from Sage Publications: Journal of Dental Research, from reference (435), copyright (1944).

Secondly, the remineralisation treatment consisted of a plaque fluid proxy which contained 20 mM HEPES (Sigma-Aldrich, USA), 30 mM of lactic acid (Sigma-Aldrich, USA), 5.5 mM of $CaCl_2 \cdot 2H_2O$ (Fisher Scientific, UK), 9.4 mM of KH_2PO_4 (Sigma-Aldrich, USA) and 63 mM of KCl (Sigma-Aldrich, USA) (437). The pH of the remineralising solution was adjusted to 6.58 using KOH (Sigma-Aldrich, USA) (438).

Finally, fluoride treatment took place by immersion in a solution which contained the desired F^- concentration in the form of NaF (Sigma-Aldrich, USA). The concentrations used were based on the 1:3 (dentifrice:diluent) dilution factor, of the minimum anti-caries effective F^- concentration (1000 ppm) used in dentifrices, usually employed during *in vitro* experiments (439-441), and the amount of plaque accumulated on the surface of the tooth. Accumulated plaque acts as a barrier and inhibits F^- from reaching the surface of the tooth (27, 442). This could happen in cases during which it is not easy to fully clean the plaque from the surface of the tooth (e.g. shortly after eruption, gum margin) (27, 432). On the other hand, when the enamel is easily accessible and can be properly cleaned, the amount of F^- reaching the surface of the enamel is considerably higher and is affected mainly by salivary dilution (443-445). As a result, it was decided to use two different F^- concentrations during the pH-cycling study of 10 ppm and 250 ppm, which correspond to the amount of F^- reaching the enamel during strong plaque accumulation and the concentration a tooth cleaned of plaque would be exposed to during brushing respectively.

Whenever needed, a background F^- concentration of 0.2 ppm, 1 ppm or 2 ppm was added inside the remineralising and demineralising solutions. The former value corresponds to the average resting F^- concentration present in the plaque and corresponds to F^-, which was adsorbed from drinking waters and other sources. The latter two values correspond to the temporary increased F^- plaque retention originating from the increased amount of F^-

administered during tooth brushing and is subsequently diluted from the oral fluids (430-432, 446).

2.2.5 Statistical Analysis

Unless stated otherwise, the statistical analysis and significant changes and correlations of the experimental parameters were performed using the Analysis of Variance (ANOVA). ANOVA is a statistical model, which is used to study and compare the means of different groups and denote whether statistical significance exists or not. It was decided to use ANOVA because, unlike t-tests, it allows comparison amongst more than two groups and provides useful correlations between all of the experimental parameters used (447). The statistical analysis of the current thesis was performed using SPSS Statistics 22 (IBM, USA).

2.3 Analytical Techniques

In order to monitor potential changes in the physicochemical properties of both the enamel blocks and the synthetic HA pellets several analytical techniques were used. The properties needed to be tested were chemical and structural identification of the used materials, phase identification and potential changes in chemical composition, morphology and hardness.

Chemical and structural identification and changes were monitored using X-ray diffractometry (XRD, Section 2.3.1), Fourier transform infrared spectrometry (FTIR, Section 2.3.2), the Brunauer, Emmett and Teller Surface Area Analysis (BET, Section 2.3.3), He-densitometry (Section 2.3.4) and Hg-porosimetry (Section 2.3.5). These techniques were chosen because they allow the full characterisation of a material including structural identification of present phases, crystallite dimensions, chemical substitutions, surface area, powder density and porosity.

Changes in chemical composition were estimated by analysing the solutions used during the pH-cycling experimental procedure. Using ion chromatography (IC, Section 2.3.6) and flame atomic absorption spectroscopy (FAAS, Section 2.3.7) it was possible to measure changes in the concentration of PO_4^{3-} and F^- and Ca^{2+} respectively. The specific instruments were used because they provided the necessary sensitivity required for each element.

Finally, changes in the physical properties of the tested materials were monitored using atomic force microscopy (AFM, Section 2.3.8) and micro-indentation (Section 2.3.9). The former allows the non-destructive imaging of the materials' surface down to the nano-level, while micro-indentation is used to measure the hardness of the blocks and pellets, a property which is directly correlated with PEM.

2.3.1 X-Ray Diffractometry (XRD)

XRD instruments are used in the structural identification of the phases present in a certain material and can also provide information on the crystal sizes of the respective materials. This can be achieved using Scherrer's equation and the (002) peak of the acquired diffractograms. Scherrer's equation is given by the formula: $D=\frac{K\lambda}{\beta cos\theta}$, where D is the crystal size, K is Scherrer's shape factor constant (0.9 for HA), λ is the wavelength used during the analysis, β is the full width at half maximum of the (002) peak and θ is the angle for which the maximum is observed (206, 239).

XRDs are usually formed from three different parts: a cathode ray tube in which X-rays are generated, a sample holder and the X-ray detector (Figure 2-7) (448). X-ray diffraction is based on Bragg's law: $n\lambda=2d\sin\theta$ (which is the correlation of the wavelength λ of the beam, the diffraction angle θ and the lattice spacing d, which is characteristic for each sample) and the constructive interference between the incident beams and the tested material (Figure 2-8)

(448, 449). Identification of materials is achieved through the comparison of the results with known reference patterns, which are enlisted in the database of the Joint Committee on Powder Diffraction Standards (JCPDS, Swarthmore, USA).

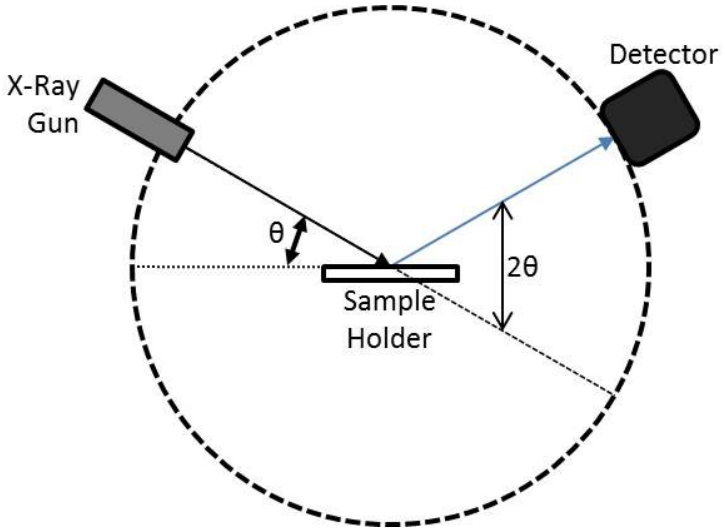

Figure 2-7: Schematic of the principle of operation of an X-ray diffractometer.

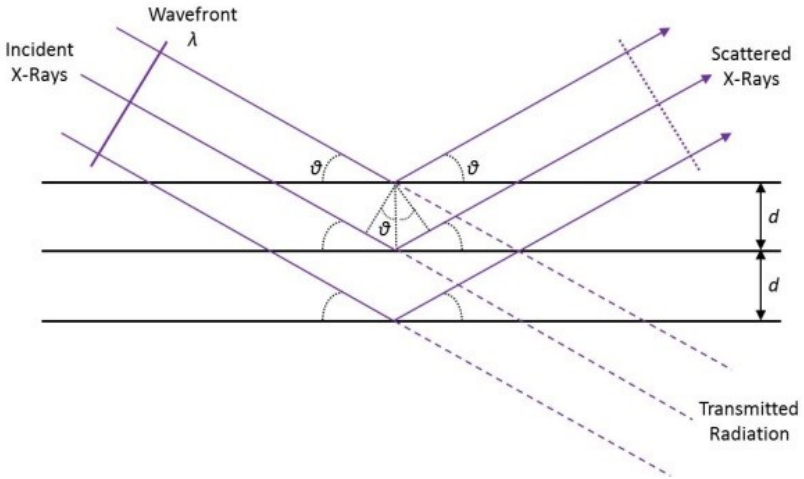

Figure 2-8: Simplified schematic of the diffraction geometry applied in XRD instruments.

The X-ray patterns produced during analysis is generated after the analysed material is bombarded by electrons beams, which are produced by heating a filament and accelerated by applying the appropriate voltage. The incoming electrons displace inner shell electrons leading to the production of diffractograms, which consist of several components corresponding to different emission lines. The most commonly used are K_α and K_β, with K_α consisting of two sub-components K_{α_1} and K_{α_2}. K_{α_1} has higher intensity and shorter wavelength than K_{α_2} and the wavelengths for each are characteristic of the material. In order for monochromatic radiation to be acquired several filters (foils or crystals) are used, while the final λ used is a weighted average of K_{α_1} and K_{α_2}. The produced X-rays are directed into the sample using appropriate optics. The sample and detector are rotated with respect to the direction of X-ray beam at an angle θ and 2θ respectively. The recorded signal is the result of the interference (constructive or destructive) of the inbound X-rays and is translated into counts per minute (448, 450).

During the current study the XRD patterns for the powdered enamel and the as-produced and calcined powders were collected with a D8 Advance powder diffractometer (Bruker, USA) using Cu-K_α radiation (λ=0.15408 nm). The 2θ range of the diffractograms collected was from 20^o up to 70^o, with a step of 0.02^o and a step time of 0.42 sec.

2.3.2 Fourier Transform Infrared Spectrometry (FTIR)

FTIR spectroscopy is a highly sensitive, fast, non-destructive technique and it is used for the identification of materials, the constituents of a mixture and the purity of a certain sample. A standard FTIR instrument (Figure 2-9) consists of the IR source, a collimator which regulates the intensity that will reach the sample, a Michelson interferometer, the sample holder a detector and a computer unit where Fast Fourier Transformation (FFT) takes place.

The analysis process (Figure 2-9) begins with the source producing an IR beam, which passes through an aperture and reaches a Michelson interferometer (MIF). The MIF consists of a beamsplitter (BS) where the beam is divided. The first part is directed towards a fixed flat mirror (M1), while the second part is directed towards a moving mirror (M2). By changing the distance of M2 from the BS an appropriate difference in the optical path of the two beams is created. The beams are then guided back to the BS where they interfere and compose a new beam, which is called an interferogram. Due to the differences in the optical path of the two beams, each point of the interferogram contains all the frequencies produced by the IR source. The beam then reaches the sample and is either transmitted through or reflected by it. As the beam passes through the sample it interacts with its molecules, which have the ability to absorb energy and excite to higher vibrational states. The energy absorbed is λ specific and is characteristic for each molecule. While the sample-specific frequencies are absorbed by the sample, the remaining beam is then measured by the detector and the missing frequencies are identified. The produced signal passes through a computer where the FFT takes place and the desired IR spectrum is displayed (451).

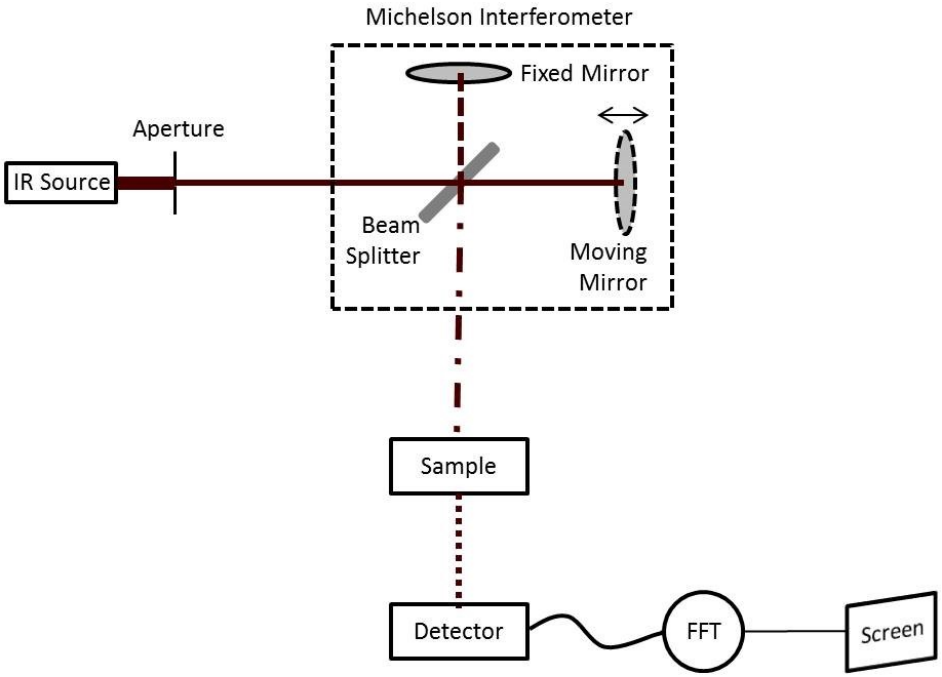

Figure 2-9: Schematic of the principle of operation of a FTIR. An IR source emits a beam which reaches a beamsplitter. The beam is then divided and half is directed towards a fixed flat mirror, while the rest is directed towards a moving flat mirror. By positioning the moving mirror accordingly the desired difference in the optical path of the two beams can be achieved. The beams then are again directed towards the beamsplitter where they interfere and the combined (Interferogram) is directed towards the sample. The beam is transmitted through the sample, where the sample-specific frequencies are absorbed from the sample. The remaining wave reaches the detector and then a computer unit where is subjected to a Fast Fourier Transformation providing the desired IR spectrum.

During the current study the FTIR spectra for powders and pellets were acquired using a Cary-670 FTIR Spectrometer (Agilent Technologies, USA) equipped with a mercury cadmium telluride detector. The spectra were obtained from 4000 up to 500 cm^{-1} by measuring the % transmittance, averaging a number of 64 scans and a resolution of 4 cm^{-1}.

2.3.3 Brunauer, Emmett & Teller Surface Area Analysis (BET)

BET instruments (Figure 2-10) are used to determine the specific surface area of powders, through the physical adsorption of a gas from the surface of the material. Gas adsorption is the result of weak van der Waals forces, which develop between the surface area of the material and the gas molecules (452-454).

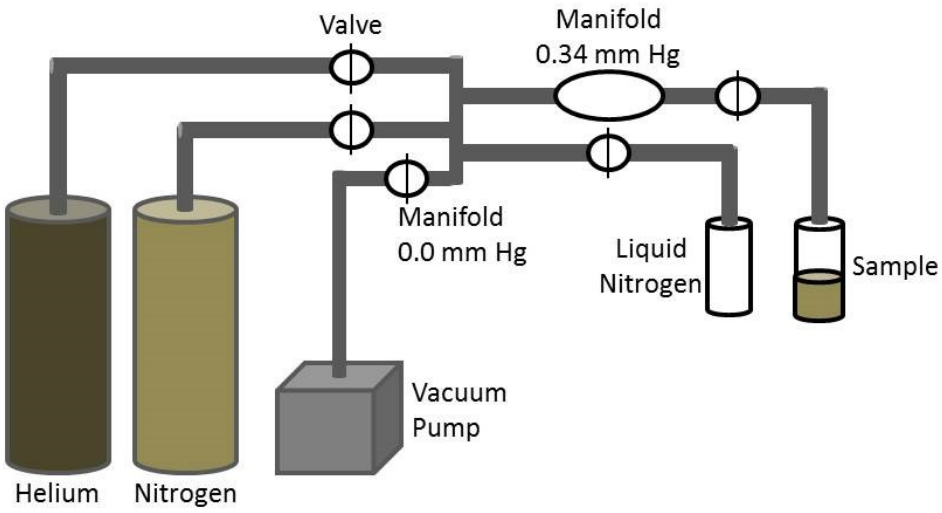

Figure 2-10: Simplified schematic of a BET instrument.

The first step in the process is to remove any gases and vapours that exist naturally on the surface of the sample to be measured (outgassing). If outgassing is not performed a "pseudo-area" may be measured which will lead to the acquisition of lower or variable surface area values. The time, pressure and temperature used during outgassing are highly significant, because they must not lead to any physicochemical alterations of the sample to be tested. Outgassing is usually achieved by initially applying a vacuum and then running a dry gas through the sample (e.g. nitrogen). After outgassing is completed, the sample is purged with a non-adsorbed gas (helium) which fills the dead volume. The sample is then immersed in liquid nitrogen so that the sample surface temperature reaches 77.4 K.

When equilibrium is reached, nitrogen is administered until the evacuated space above the sample is filled and the BET adsorption isotherm is calculated through the equation:

$$\frac{1}{\left[V_{\alpha}\left(\frac{P_0}{P}\text{-}1\right)\right]}=\frac{C\text{-}1}{V_m C}\times\frac{P}{P_0}+\frac{1}{V_m C}$$

Where P and P_0 are the partial vapour pressure in equilibrium with the surface at 77.4 K and the saturated pressure measured of the adsorbate gas respectively in Pa, V_{α} is the volume of the adsorbed gas at standard temperature and pressure (STP, 273.15 K, 1.013E^5 Pa) in ml, V_m is the volume of the gas adsorbed on the surface of the sample at STP in ml and C is a constant related to the thermodynamic relation of the adsorbate gas and the sample. The surface area S is then calculated through the equation: $S=\frac{V_m N\alpha}{22400\times m}$, where N is the Avogadro constant (6.022E^{23} mol^{-1}), α is the effective cross-sectional area of an adsorbate molecule (0.162 nm^2 for nitrogen) in m^2, m is the mass of test powder in gr, and 22400 is the volume occupied by 1 mole of the adsorbate gas at STP allowing for minor departures from the ideal in ml (453-455).

The BET method was used to measure the specific surface area of the enamel and the as-produced and sintered synthetic powders. All samples were outgassed for 3 hours at 200ºC prior to measuring the specific surface area using a SA-3100 Surface Area Analyser (Beckman-Coulter, USA).

2.3.4 Helium Pycnometry (HP)

HP is used to measure the volume and density of materials. The principle of operation is based on gas displacement, which is more accurate and reproducible than liquid pycnometers. A typical instrument comprises of a sample vessel (pycnometer), the sealing chamber, the gas insertion and extraction system and a secondary compartment used for volume measurement (Figure 2-11) (456).

Measurement begins by placing the sample into the pycnometer and sealing it into a chamber of known volume. The chamber is evacuated and then filled with He, which is then extracted into a secondary compartment. The difference in pressure during inserting and extracting the gas is used to calculate the volume of the sample. The density is then calculated by dividing the sample weight with the calculated volume. The working equation of an HP with sample tank of volume V_c and pressure before the sample is inserted P_1, sample volume V_s, gas tank volume V_r and equilibrated pressure P_2 is: $V_S = V_C + \frac{V_r}{1 + \frac{P_1}{P_2}}$ (456, 457).

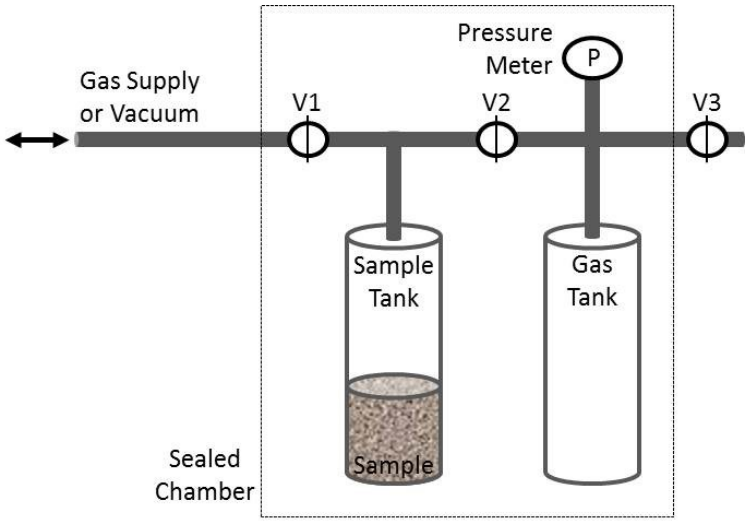

Figure 2-11: Principle of operation of a He densitometer. The sample is placed inside a pycnometer and entered into a sealed chamber. He is then inserted inside the chamber through valve V1 until equilibrium inside the chamber is reached. Valve V2 opens and the gas is extracted into the second chamber and equilibrium is reached again. The volume of the powder is measured by the difference in pressure during gas insertion and extraction. The density is calculated by dividing the sample mass with the calculated volume. Finally, the gas is allowed to escape into the atmosphere through valve V3.

True densities were determined using a Helium Pycnometer AccuPyc II 1340 (Micromeritics, UK) employing 20 measurements per sample. The sample chamber was allowed to equilibrate at 134 kPa for each measurement cycle.

2.3.5 Mercury Porosimetry (MP)

MPs are instruments which are used to measure the porosity of a material (empty vs. bulk space). This is achieved by measuring the amount of Hg which can penetrate the material. This way the sizes of the pores and any empty space present in the material in question can be determined. MP instruments (Figure 2-12) typically consist of a glass tube (penetrometer) where the sample is positioned, a pump which evacuates the penetrometer, a pump which fills the tube with Hg, a piston which applies pressure on the Hg and forces it to enter the sample and appropriate electronics which calculate the amount of Hg entering the sample the porosity and pore size distribution (458).

Measurement begins by loading the sample inside a penetrometer, inserting it inside the instrument and sealing it so that the evacuation process can start. A pump then empties the tube from any gases that may be present and then the whole tube is filled with Hg. A piston then comes down and applies pressure on the liquid, forcing it to fill potential pores and cavities inside the sample. By measuring how much the piston moved and the applied pressure the porosity and pore size can be determined (458).

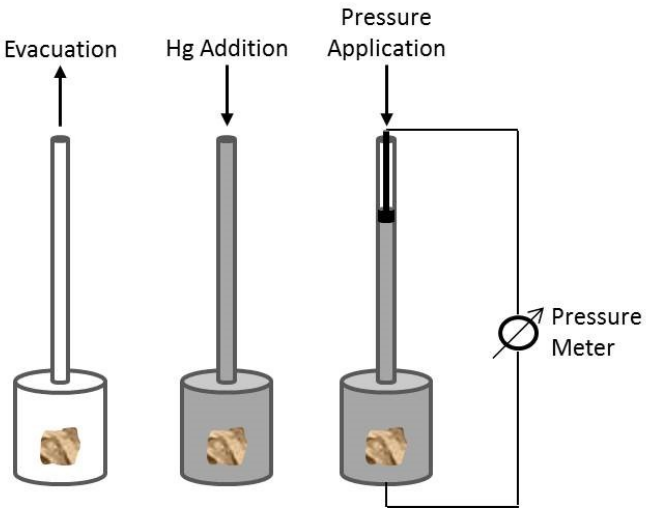

Figure 2-12: Simplified schematic of a MP instrument. The sample is places inside a penetrometer which is then evacuated using a pump. A second pump fills the tube with liquid Hg and then a pressure is applied in an attempt to force the mercury enter the pores and cavities present inside the sample.

During the project the samples were weighed and added to a glass penetrometer suitable for powder samples. The penetrometer was sealed and the sample analysed using an AutoPore IV mercury porosimeter (Micromeritics, UK) at pressures in the range 3 kPa – 207 MPa. Hg intrusion into the sample was analysed using the Washburn equation (459) in order to determine the pore diameter distribution: $D=-\frac{4\gamma}{P}cos\theta$, where D is pore diameter, P is the applied pressure, γ is the surface tension of Hg at 20°C, which is assumed to be 0.485 N m^{-1}, and θ is the contact angle between the Hg and the porous solid, which is assumed to be 130°.

2.3.6 Ion Chromatography (IC)

Ion chromatography is used for the chemical analysis of aqueous solutions and can be distinguished into anion and cation chromatography. Anion instruments can detect the concentration of species such as F^-, Cl^-, NO_3^-, NO_2^-, SO_4^{2-} and PO_4^{3-}, while cation instruments can detect species such as Li^+, Na^+, NH_4^+, K^+, Ca^{2+} and Mg^{2+}; with the range of detection being typically between 0.1 ppm and 100 ppm (460, 461). Typical IC instruments (Figure 2-13) contain a sample injection system, where the sample is mixed with a carrier fluid (eluent),

an adsorbing column, a detector and a suppressor which is used to reduce and enhance the conductance of the eluent and sample respectively (461).

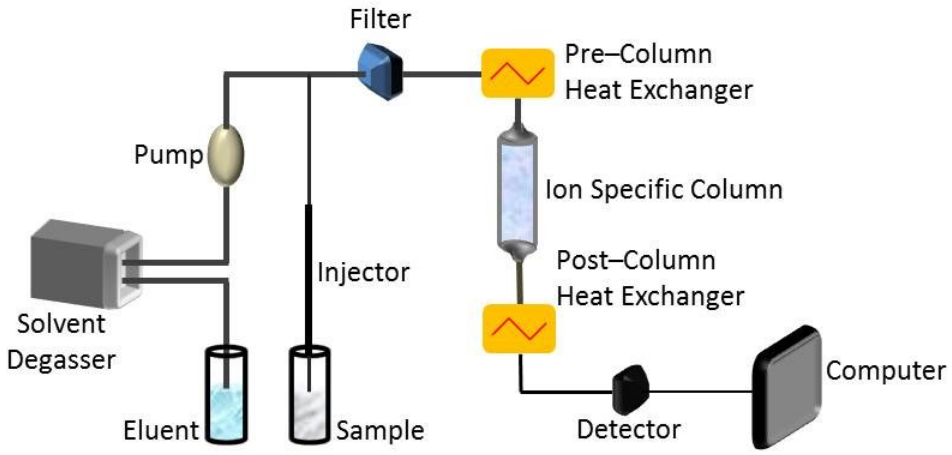

Figure 2-13: Schematic of a typical IC instrument. The sample enters the instrument mixed with the eluent. The resulting solution is heated by the pre-column heat exchanger and reaches the column, which is made of resin. As the solution passes through the column the forces which develop between the resin and the ions of the elements present in the solution are different. As a result, the various ions need different times to pass through the column and reach the detector. Depending on the time needed for each ion to reach the detector, characterisation of the elements takes place.

Analysis of the sample begins with the injection of the sample inside the eluent and the mixture is then directed towards a column (Figure 2-14) made of an adsorbing material (e.g. resin). The elements present in the sample are retained by the column while the eluent/sample mixture is moving through it. The force with which the various elements adhere onto the adsorbing material depends on their type and size, which leads the different ions moving through the column at different speeds. As a result, the elements are separated and reach the detector at different time intervals. The detector analyses each of the ions emerging from the column and translates the signal as a peak on a chromatograph (460, 461).

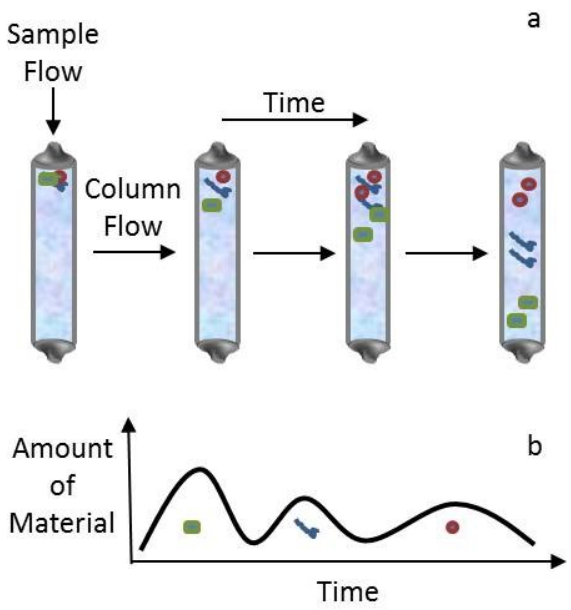

Figure 2-14: Schematic of the principle of operation of an IC column. (a) The sample enters the column from the top and as there is continuous eluent flow, different ions need different time to travel through the column and reach the detector. (b) As a result, the various ions are separated in different groups and are characterised depending on the time needed to pass through the column and reach the detector.

Solution F^- and PO_4^{3-} concentration changes were measured using an ICS-2000 Ion Chromatography system (Dionex, USA), equipped with an anion specific column. Changes in the chemical composition of the solutions were calculated by subtracting the final F^- and PO_4^{3-} concentrations from the initial. Thus, negative concentration values indicate release of material into the test solutions, and positive values indicate uptake from the test substrate. The use of blank samples and laboratory produced standards ensured correction of potential drifts and calibration of the instruments. In the case of the enamel blocks which were treated with the F-treatment, as described in section 1.2.4, the loosely bound fluoride deposited on the surface of the respective blocks in the form of CaF_2 was also measured. Since CaF_2 is KOH soluble, the blocks were immersed in 10 ml of 1 M KOH solution for 24 hours under gentle agitation and then removed and rinsed with DW for 5 minutes. The pH of the resulted solutions was brought to neutral using HCl (462, 463). The baseline was evaluated by applying the same treatment to 5 untreated enamel blocks, which were painted with nail polish as the treated blocks.

2.3.7 Atomic Absorption Spectroscopy (AAS)

AAS is a technique which is used for the chemical analysis of solutions. Depending on the method used (flame or graphite furnace) the sensitivity of the technique varies, with the latter detecting concentrations down to a few ppb (464-467). Measurement is based on the fact that each element can absorb and emit certain wavelengths (λ), which correspond to the energies needed to excite electrons to a higher level. AAS instruments (Figure 2-15) consist of a light source, a sample cell (flame or furnace) through which the sample is evaporated, a monochromator which is used to set the correct λ for each element to be studied, a detector and a computer to analyse the results (464, 465).

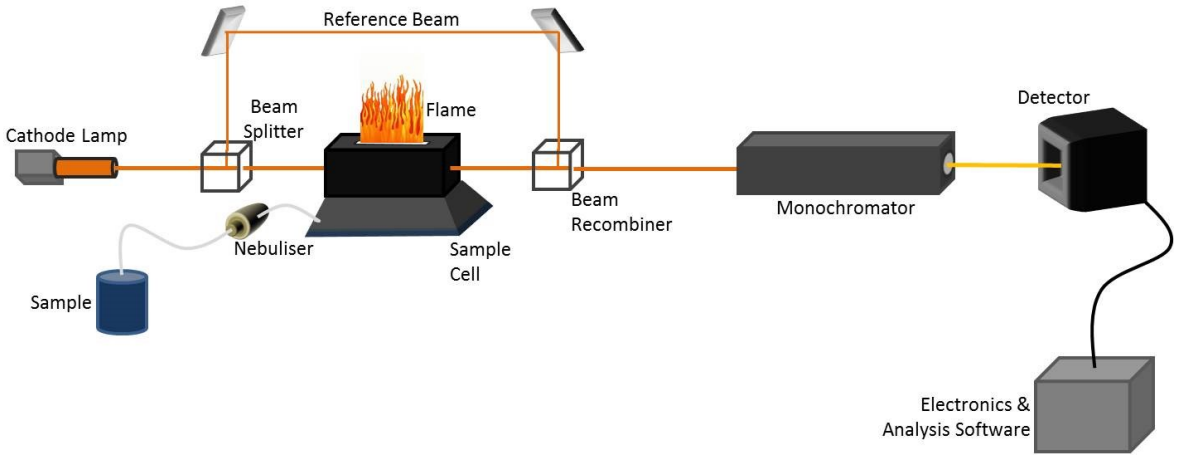

Figure 2-15: Schematic of a double beam AAS. A cathode lamp emits a light beam which is divided by a beam splitter. Most of the beam passes through the sample cell, while the rest acts as a reference beam so as to check there is no loss in sensitivity. The beam passing through the sample cell interacts with droplets created and vaporised using a nebuliser and a flame respectively. The atoms of the element to be tested absorb in a specific wavelength. The remaining beam is then recombined with the reference and directed towards a monochromator, where the desired λ is selected and allowed to reach a detector. Finally, the signal is analysed using appropriate electronics and software.

Analysis begins with the atomisation of the sample either through aspiration of the solution using a flame or through an electrothermal instrument, during which a drop of the solution is deposited into a graphite furnace and heated electrically. At the same time, light is produced by a cathode lamp containing atoms of the element to be analysed, which is divided using a beamsplitter. Most of it is directed towards the sample, while the rest acts as a reference and is used to verify the stability of the produced light spectrum. The two beams are recombined

after the sample and directed towards a monochromator where the desired λ is selected. The beam exits the monochromator and reaches a detector where the signal is measured and with appropriate electronics the result is analysed and displayed (465).

Changes in Ca^{2+} concentration between the initial and the post-treatment solutions were measured using an AAnalyst-300 flame atomic absorption spectrometer (PerkinElmer, USA) equipped with a Ca^{2+} lamp. A 5-point calibration was used and an average of 3 replicates for each sample was measured. As in the case of IC, changes in the chemical composition of the solutions were calculated by subtracting the final Ca^{2+} concentrations from the initial.

2.3.8 Atomic Force Microscopy (AFM)

AFM instruments are used to acquire high-resolution images and extract information (e.g. roughness, size) from various samples (solids, powders, liquids) down to the nanometre scale. AFMs (Figure 2.16) consist of a cantilever which scans the sample through a sharp probe attached to it, a XYZ scanner, a He-Ne LASER, a detector and a computer (468, 469). There are three main types of operating modes: contact mode (C-AFM), tapping mode (IC-AFM) and non-contact mode (NC-AFM). During C-AFM the probe is always in contact with the sample during scanning, while IC-AFM and NC-AFM are oscillating above the sample with the IC-AFM touching the sample periodically (469-471). The most sensitive of all the modes is NC-AFM through which atomic resolution images can be acquired (472).

Sample scanning is performed by a cantilever with a sharp probe attached to it. The cantilever is controlled by an XYZ scanner, which has the ability to perform highly precise movements (Figure 2-16). When the probe approaches the surface of the sample a force which follows Hooke's law develops between the two. As the probe moves, it deflects and stays at the same distance d from the surface of the sample by maintaining the deflecting forces (Van der Waals, electrostatic forces) acting between the sample and the probe tip constant (Figure 2-

17). Potential changes to the cantilever position due to respective changes in the sample morphology, are monitored with the use of a He-Ne LASER which is reflected from the surface of the cantilever and is directed towards a detector. As a result, any changes in the position of the cantilever are translated into respective changes on the position of the LASER onto the detector. The signal is then analysed and the XYZ scanner moves on the *z* axis to maintain the distance between the probe and the sample. This movement is transformed to sample morphology and thus an image is acquired (468, 470).

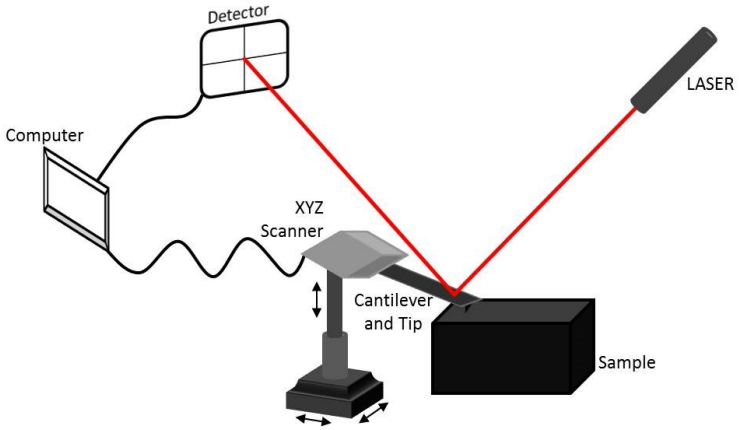

Figure 2-16: Schematic of the principle of operation of an AFM. The sample is scanned from a sharp probe attached to a cantilever, which is controlled by an XYZ scanner. The distance between the sample and the probe is maintained stable during the scanning process. Potential changes in the position of the cantilever are monitored through respective changes in the position of a LASER which is reflected on the top surface of the cantilever and is directed towards a detector. Any detected changes in the position of the LASER are analysed using appropriate software and transferred to the XYZ detector so as to reposition the cantilever. These z-axis movements are used to produce the topography of the sample.

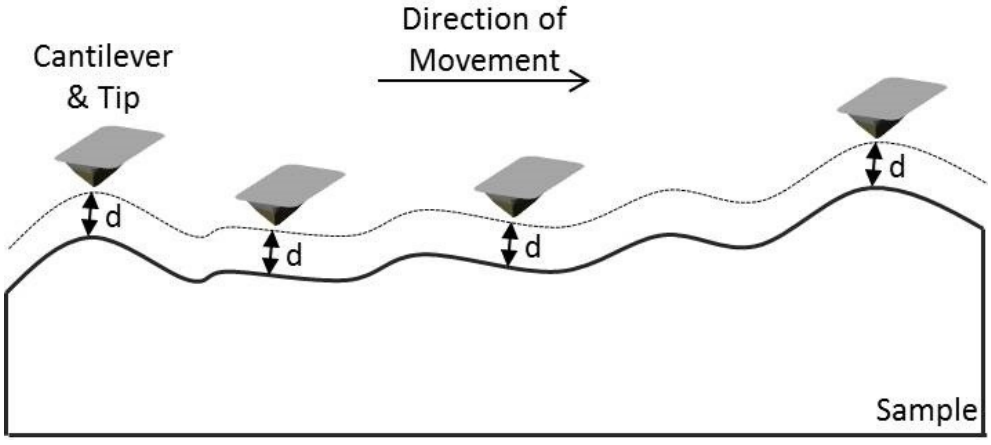

Figure 2-17: Schematic of the AFM tip scanning. The sample is scanned from a sharp probe attached to a cantilever, which is controlled by an XYZ scanner. The distance between the sample and the probe during scanning remains stable, by maintaining the deflecting forces applied between the sample and the tip constant.

Imaging of the as-produced powders, the pellets and the enamel blocks was performed in non-contact mode using a XE-100 Advanced Scanning Probe AFM (Park Systems, USA); equipped with PPP-NCHR Al coated silicone probe having a spring constant of 42 N m^{-1}. The scan frequency was 0.25 Hz; the set point was 0.45 and the gain 0.6%. In order to image the powders a small amount of each of the freeze and heat dried was diluted in absolute ethanol (1 mg of powder per 1 ml of absolute ethanol). Following a sonication for 5 minutes, an aliquot of each solution was deposited on separate glass slides and left to air dry (472).

2.3.9 Micro-Indentation (MI)

Micro-Indenters are instruments that can measure the hardness of a material, which may be described as its resistance to plastic deformation when a load (P) is applied for a certain amount of time (Figure 2-18). There are several methods to measure the hardness of the material depending on the geometry of the tip used to apply the load. One of the most common is Vickers, which uses a pyramidal shaped tip (Figure 2-18a). The hardness H of the material tested is calculated by dividing the applied load P with the area (Figure 2-18b) of the indent A: $H=\frac{P}{A}=\beta\frac{P}{d^2}$, where d is the diagonal of the indent and β is a constant which is characteristic of the indenters geometry (473-477).

The advantage of the Vickers method is that the true contact area can be calculated and used, while in other methods (e.g. Knoop) a projected area is calculated (474, 477, 478). Vickers hardness is used to measure the hardness of hard materials, but if the material is also brittle (e.g. ceramics) it is highly possible to crack it. Knoop, on the other hand, is being used for materials which are also brittle since it penetrates the sample almost half as deep as Vickers does, which also makes it more sensitive when measuring superficial softening (474, 475, 478). An indentation instrument (Figure 2-19) consists of an imaging and an indenting part.

The former is usually an optical microscope which is used to focus and scan through the sample, while the second consists of a dilatation part, a load transducer and an indenter tip.

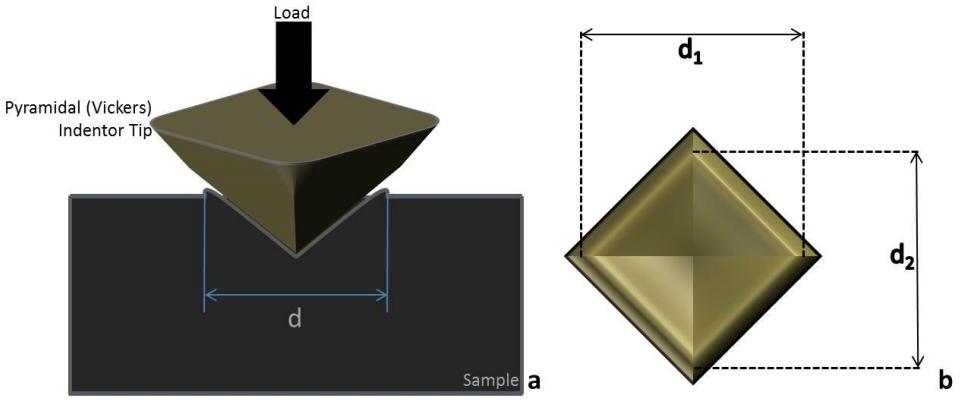

Figure 2-18: Schematic illustrating the principle of operation of a Vickers indenter. (a) A load (P) is applied on a pyramidal shaped tip, which results on a deformation on the tested material. The hardness (H) of the material is then calculated by dividing the applied load with the area (A) which is created during the tip penetration ($H=\frac{P}{A}$). (b) The deformation resulting during Vickers indentation is of pyramidal shape. In this case the true contact area can be calculated by measuring the d_1 and d_2 dimensions of the produced indentation.

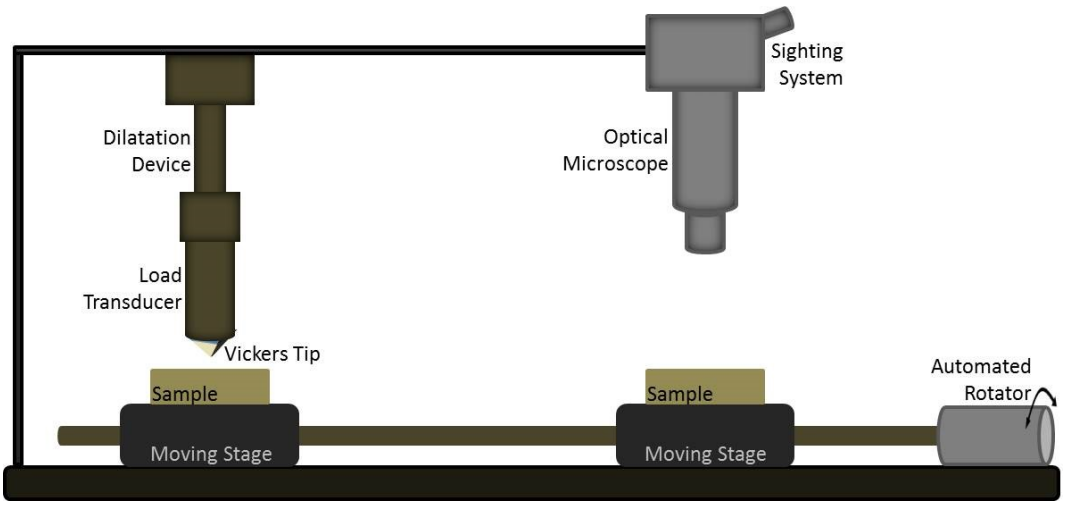

Figure 2-19: Simplified schematic of a MI instrument consisting of an imaging and an indention part. The imaging part consists of an optical microscope and a sighting system. It is used to focus on the sample and automatically calculate the initial indentor-sample distance. The indentation part consists of a dilatation device, which is used to move the load transducer and the indentor tip (Vickers). The rotator is used to precisely position the sample stage underneath the indentor.

Micro-Indentation of the bovine enamel blocks and the synthetic pellets was performed using a Duramin micro-indenter (Struers, DK) employing a Vickers indenter. Indentations were performed normal to the planar sample surface, each in a different unperturbed area, free of visible defects. Samples were indented using a maximum load of 1.961 N (0.2 VH) and a hold time of 20 seconds. Hardness measurements were acquired both prior to and after immersion inside the solutions.

Analytical results in this thesis are presented using the SI system of units; it was therefore decided to convert the acquired Vickers hardness to GPa. To do so, the original Vickers hardness unit of kgf mm^{-2} needed to be converted to the more commonly used SI hardness unit of GPa, which corresponds to 10^{-3} N mm^{-2}. This can be calculated by multiplying the Vickers hardness with the standard gravity g value of 9.80665 m s^{-2}. The resulting equation, which was used for all conversions is: Hardness (GPa) = 0.00980665 VH.

Page intentionally left blank

3. pH-Cycling Studies Using Permanent Bovine Enamel

This Chapter presents an investigation of the mechanism involved in PEM of enamel. It is an experimental study, designed around the exposure of bovine enamel (as a proxy for human enamel) to a number of artificial solutions, which simulate caries attack and subsequent neutralisation by saliva in the oral environment. The 1st sub-section describes the core series of experiments, during which an attempt to replicate the PEM process on freshly exposed surfaces of bovine enamel is presented. The 2nd sub-section describes an alternative approach, whereby experiments simulate the PEM process in pre-matured bovine enamel. In practice, the duration of the pH-cycling procedure was doubled and analysed the same way as the main study. Finally, the 3rd sub-section studies mixed fluoride treatments so as to simulate different states of plaque accumulation on the surface of the enamel. In all cases, extensive monitoring of the physicochemical properties of bovine enamel was performed.

3.1 pH-Cycling of Dental Enamel & Artificial Maturation

pH-cycling models were introduced and described in general terms in section 2.2.4. The idea behind these cycling experiments was to expose teeth to sequential cycles of F^- treatments, simulating demineralising and remineralising periods. Since the purpose of this study was to develop an understanding of the proposed mechanism (398) behind PEM, a range of complementary treatments were tested.

Commencing with a control treatment of deionised water (DW), different experimental variables were gradually employed so as to create a progressively more complex combination of experimental parameters. This way it was possible to separately monitor the effects of enamel exposure to remineralising solutions (PF), demineralising solutions (AC), F^- containing solutions and finally the effects of the appropriate background F^- concentration, which was added inside the solutions used each time. These treatments correspond to the effect of plaque fluid, the conditions existing shortly after a meal, tooth-brushing and the effect of retention phase F^- respectively. Each aforementioned variable was studied alone and in every possible combination with the rest. Thus, the combination of all separate results made it possible to understand the contribution of each variable on the PEM process. Each treatment contained 12 enamel blocks, 3 of which were randomly sampled and analysed every 5 days. The treatments are presented in Table 3-1.

ID, Solutions & Treatments	**pH Cycling Rounds**																
ID	**M1**	**M2**	**M3**	**M4**	**M5**	**M6**	**M7**	**M8**	**M9**	**M10**	**M11**	**M12**	**M13**	**M14**	**M15**	**M16**	**Duration**
Main Remineralisation Treatment	DW	DW	DW	DW	PF	PF	PF	PF	DW	DW	DW	DW	PF	PF	PF	PF	5 hrs/ treatment and overnight
Intermediate Remineralisation Treatment	N/A	N/A	N/A	DW	N/A	N/A	N/A	PF	N/A	N/A	N/A	DW	N/A	N/A	N/A	PF	30 min/ treatment
Demineralisation Challenge	DW	DW	DW	DW	DW	DW	DW	DW	AC	AC	AC	AC	AC	AC	AC	AC	20 min/ treatment
Background F Concentration	No	Yes	No	Yes	No	Yes	No	Yes	No	Yes	No	Yes	No	Yes	No	Yes	Same as the remineralising and demineralising solutions
Brushing F Concentration	No	No	Yes	Yes	No	No	Yes	Yes	No	No	Yes	Yes	No	No	Yes	Yes	2 min/ treatment

Table 3-1: Experimental conditions for the treatments studied. Several treatments were employed in order to test the effect of each experimental variable on the process of PEM. DW: Deionised Water, PF: Plaque Fluid Proxy, AC: Acid Challenge.

3.1.1 Chemical Analysis

Section 3.1.1 presents the chemical analysis of the solutions used for the treatments presented in table 3-1. Firstly, Ca^{2+} results are presented because it is the basis of both apatitic and secondary phases (e.g. OCP, TCP, DCPD) and CaF_2; and subsequently the link between PO_4^{3-} and F^- interaction. Secondly, PO_4^{3-} results are analysed as phosphate is present in all potential phases precipitated (HA, FA, fHA, TCP, OCP, DCPD). The section ends with the F^- results, which can be incorporated inside the crystal structure of apatites and/or is adsorbed on the surface of the pellets as loosely bound ionic F^- or deposited in the form of CaF_2. In all cases the results are presented as the difference from the baseline value (i.e. the concentration of the solutions prior to the treatment). This means that positive values denote adsorption of the element from the substrate, while negative results correspond to release to the solutions.

3.1.1.1 Calcium Results

This section describes the changes in the Ca^{2+} concentration within the demineralising and remineralising solutions used during the pH-cycling procedure. There are 3 different types of solutions presented. The 1st treatment contains the solutions used as proxies for the demineralisation challenge, the 2nd the solutions used during the 30 minute remineralisation period following F^- treatment (during which the background F^- concentration is elevated) and the 3rd presents the main remineralisation treatment. The pH of the remineralising and demineralising solutions used, as well as the fluoride concentrations used as background and during the F^- treatment are presented in Table 3-2 and explained in detail in section 2.2.4. Where present, the subscript in the ID number of the tested groups denotes the amount of F^- used during the 2 minute F^- treatment.

ID, Solutions & Treatments	pH Cycling Rounds											
ID	M5	M6	$M7_{10}$	$M8_{10}$	$M7_{250}$	$M8_{250}$	M13	M14	$M15_{10}$	$M16_{10}$	$M15_{250}$	$M16_{250}$
Remineralising Solution (pH)	6.58	6.58	6.58	6.58	6.58	6.58	6.58	6.58	6.58	6.58	6.58	6.58
Demineralising Solution (pH)	DW	DW	DW	DW	DW	DW	4.90	4.90	4.90	4.90	4.90	4.90
Background F^- Concentration (ppm)	0.0	0.2	0.0	0.2	0.0	0.2	0.0	0.2	0.0	0.2	0.0	0.2
Background F^- Concentration during the intermediate remineralisation period (ppm)	0.0	0.0	0.0	2.0	0.0	1.0	0.0	0.0	0.0	2.0	0.0	1.0
Brushing F^- Concentration (ppm)	0	0	10	10	250	250	0	0	10	10	250	250

Table 3-2: Experimental conditions for the groups studied during the main study. The groups presented were treated with a plaque fluid proxy. The subscript used in the group ID denotes the amount of F^- used during the tooth-brushing simulation.

To begin with, Figure 3-1 displays the changes in the Ca^{2+} concentration for the total remineralisation period, which correspond to the cumulative effect of the main and intermediate remineralisation treatments. The groups treated with PF and DW or AC only presented a positive peak on the 6^{th} (M5) and 11^{th} (M13) day respectively, which was followed by a plateau in slightly lower values. Addition of the F^- treatment ($M7_{10}$, $M7_{250}$) led to a peak which was slightly higher than before, especially in the case of $M7_{10}$; while addition of background F^- only (M6) led to a smoother curve with significantly lower Ca^{2+} values. On the other hand, the presence of F^- as background treatment ($M8_{10}$, $M8_{250}$, $M15_{10}$, $M15_{250}$, $M16_{10}$, $M16_{250}$) resulted in negative Ca^{2+} values during the first days of the experimental procedure, which was followed by a reverse in the trend observed from day 6 onwards and in most cases plateaus by day 16.

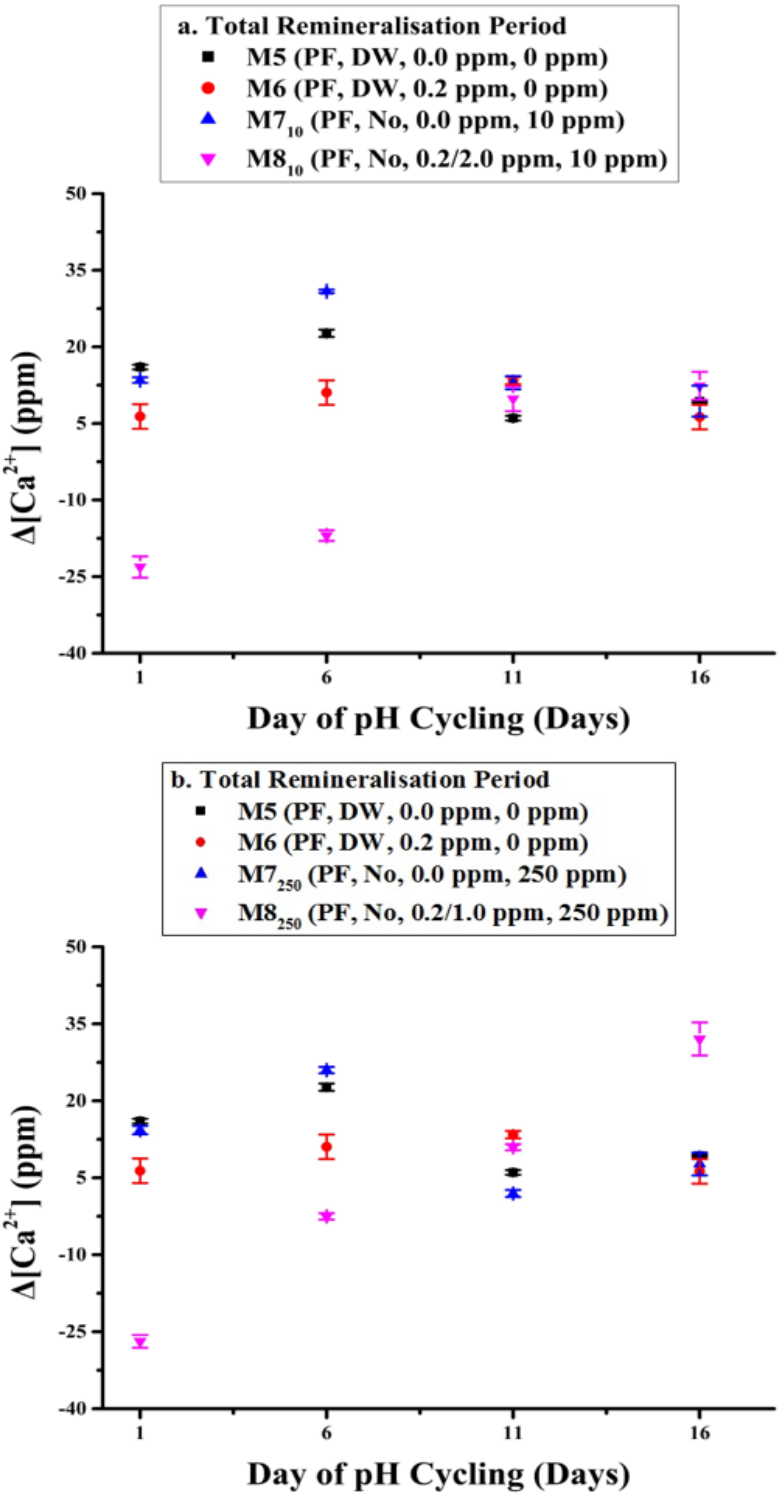

Figure 3-1: Changes in the concentration of Ca^{2+} during the total remineralisation period, which was calculated through the addition of the results of the intermediate and main remineralisation period. Comparisons are made between the groups which were treated with the plaque fluid proxy and no acid challenge, with or without background F^-, for the a. 10 ppm and b. 250 ppm treated groups; and the enamel blocks treated with both the PF and the AC again for the c. 10 ppm and d. 250 ppm. In all cases the respective groups (M5, M6 or M13, M14) which either had no F^- added or had only a background F^- of 0.2 ppm are also displayed.

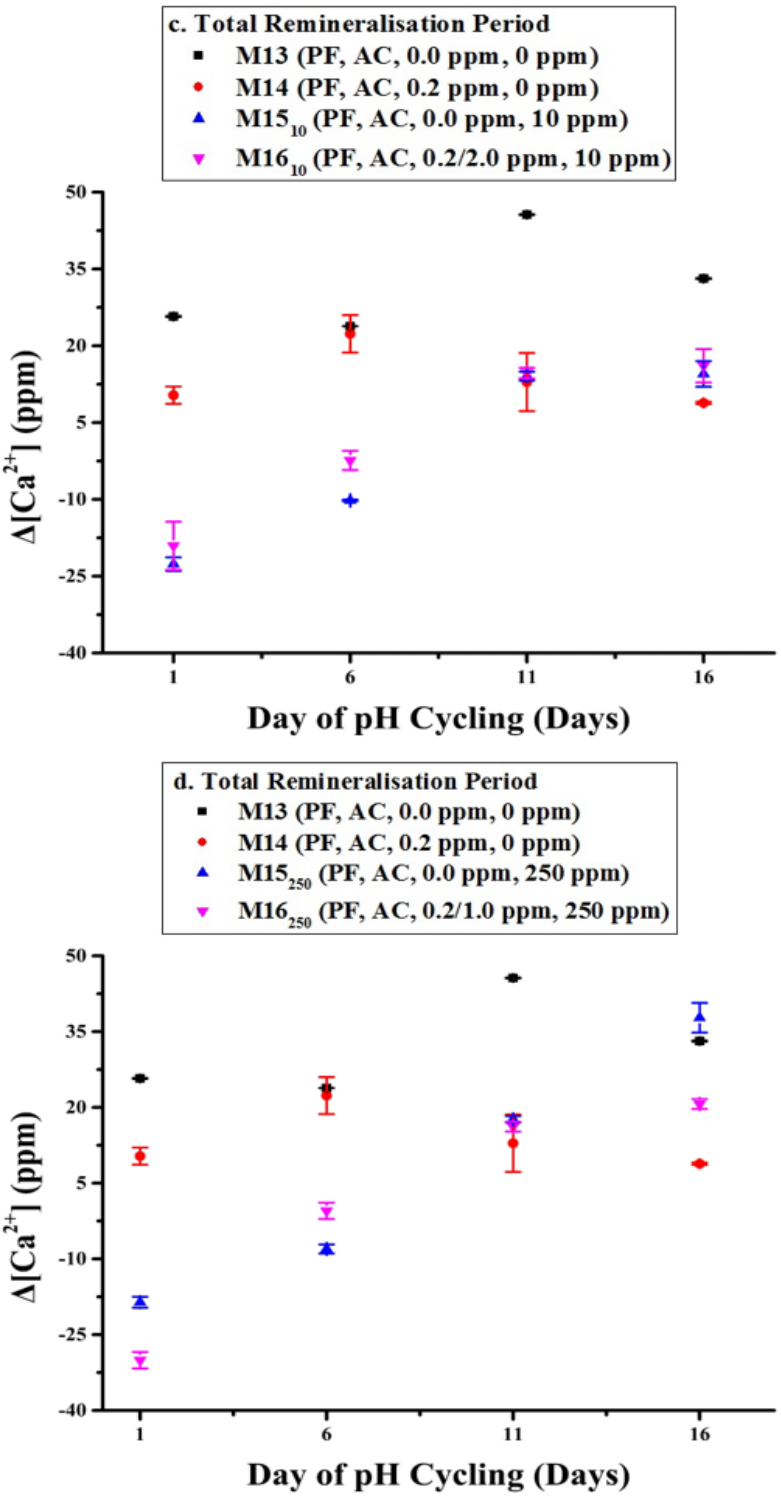

Figure 3-1 (Continued): Changes in the concentration of Ca^{2+} during the total remineralisation period, which was calculated through the addition of the results of the intermediate and main remineralisation period. Comparisons are made between the groups which were treated with the plaque fluid proxy and no acid challenge, with or without background F^-, for the a. 10 ppm and b. 250 ppm treated groups; and the enamel blocks treated with both the PF and the AC again for the c. 10 ppm and d. 250 ppm. In all cases the respective groups (M5, M6 or M13, M14) which either had no F^- added or had only a background F^- of 0.2 ppm are also displayed.

Figure 3-2 presents the Ca^{2+} results for the intermediate (Figures 3-2a, c) and main (Figures 3-2b, d) remineralisation periods separately. In both cases, groups $M7_{10}$ and $M7_{250}$ present similar behaviour with Ca^{2+} uptake, which peaked on day 6 and decreased slightly for the remaining experimental period. On the other hand, the remaining groups presented negative values during the first 6 days of the intermediate remineralisation period, which reversed into positive from day 11 onwards.

During the main remineralisation period an uptake of Ca^{2+} was generally observed for the whole duration of the experimental procedure. In the case of the groups treated with 10 ppm of F^- ($M8_{10}$, $M15_{10}$, $M16_{10}$) concentration was higher during the 1st day, reached a minimum on day 6 ($M15_{10}$, $M16_{10}$) or day 11 ($M8_{10}$) and then increased again. This behaviour was also observed for group $M16_{250}$, which was treated with 250 ppm of F^-. The behaviour of the remaining groups treated with 250 ppm of F^- ($M8_{250}$, $M15_{250}$) was similar to the intermediate remineralisation period, during which increased background F^- treatment was used, but returned to positive values from the 6th day onwards.

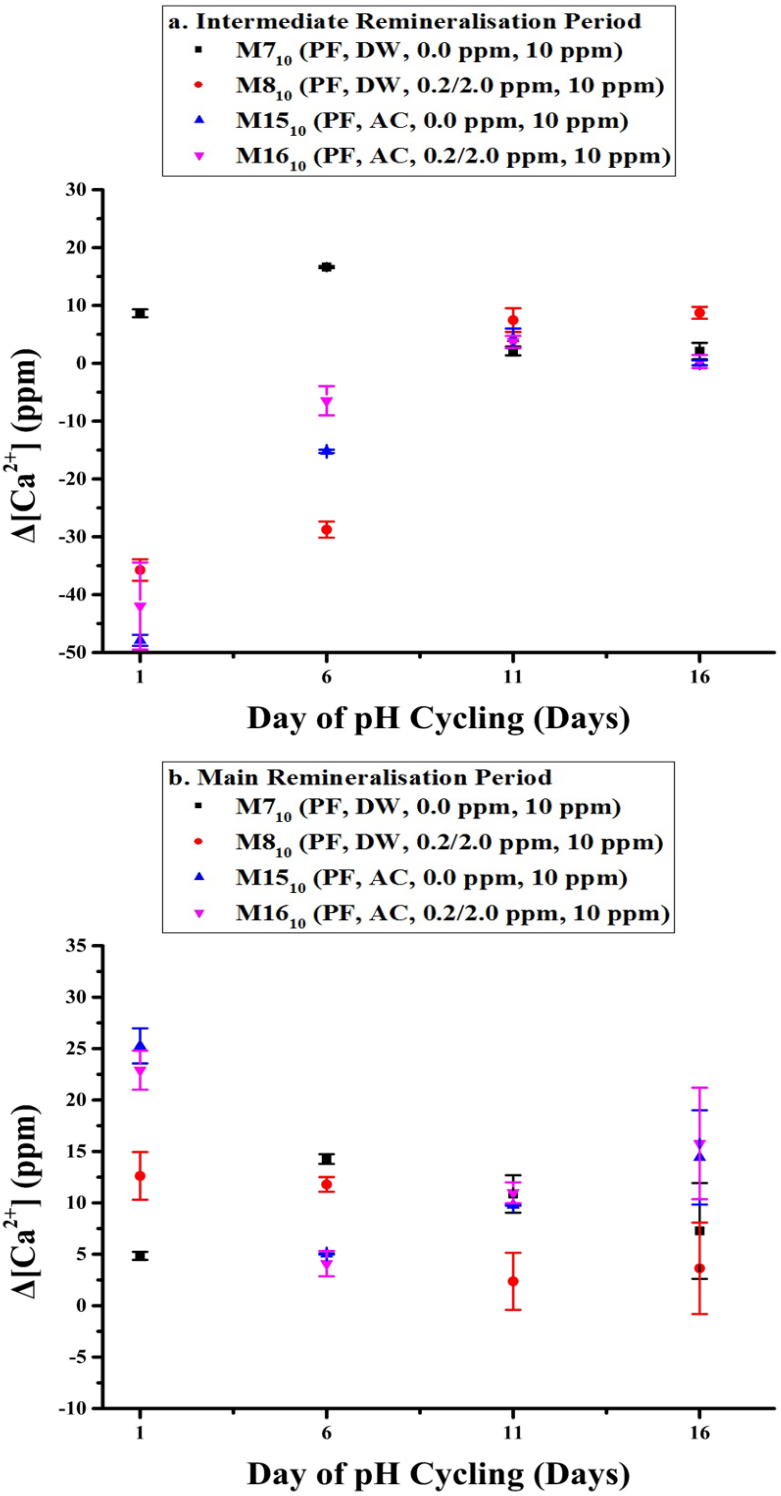

Figure 3-2: Changes in the concentration of Ca^{2+} during the intermediate (a, c) and main (b, d) remineralisation periods for the groups treated with PF and DW and PF and AC and 10 ppm (a. and b.) or 250 ppm (c. and d.) of F^-.

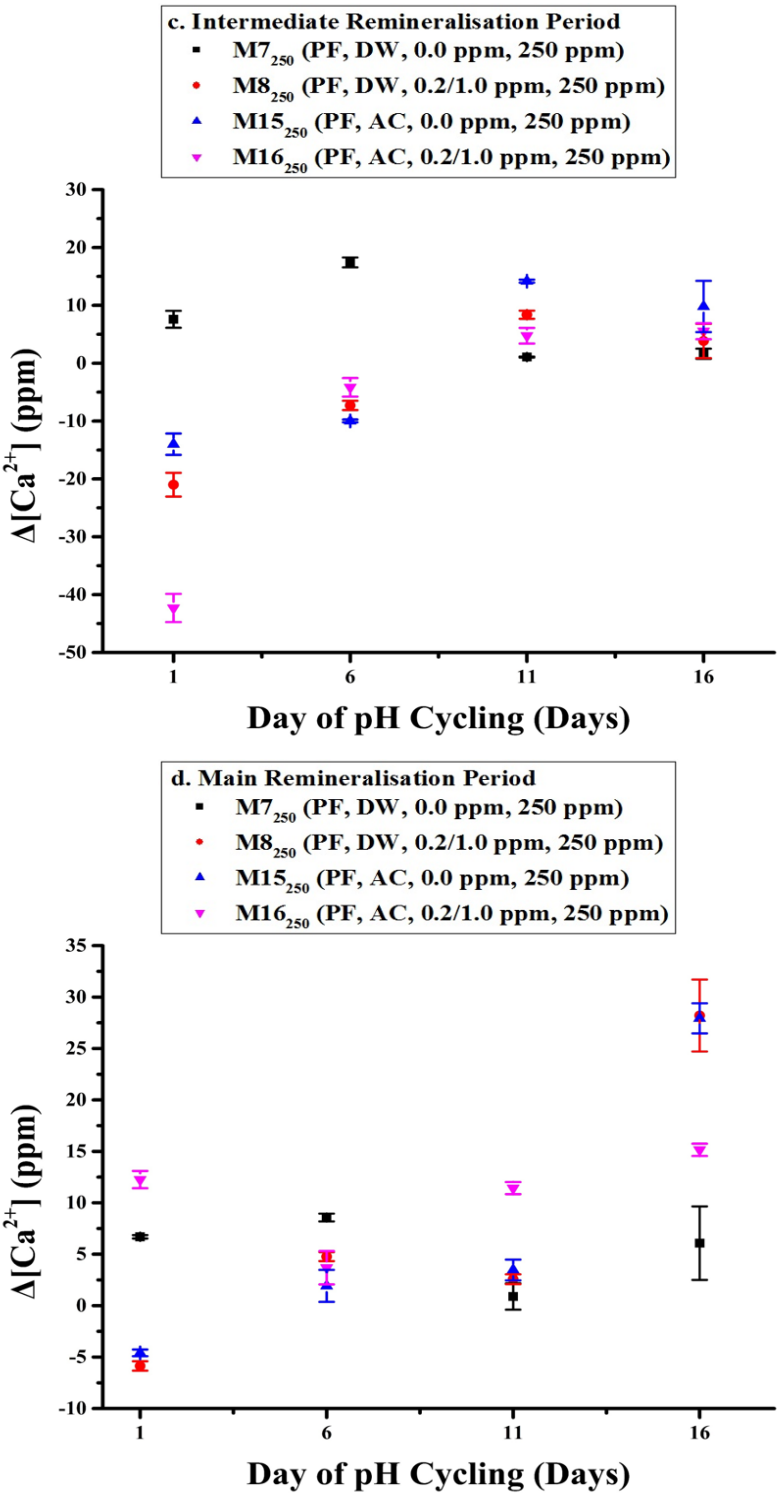

Figure 3-2 (Continued): Changes in the concentration of Ca^{2+} during the intermediate (a, c) and main (b, d) remineralisation periods for the groups treated with PF and DW and PF and AC and 10 ppm (a. and b.) or 250 ppm (c. and d.) of F^-.

Finally, Figure 3-3 presents the changes in the Ca^{2+} concentration with time for the demineralising solutions, without (Figure 3-3a, b) or with the use of PF (Figure 3-3c, d). The experimental conditions for each group are presented in Table 3-3. Unexpectedly, uptake of Ca^{2+} took place during the demineralisation challenge, which was stronger for the groups treated with PF (3-3c, d) and not DW as the remineralisation treatment and decreased with time. The decrease was faster for the groups treated with 10 ppm of F^-.

ID, Solutions & Treatments	**pH Cycling Rounds**											
ID	M9	M10	$M11_{10}$	$M12_{10}$	$M11_{250}$	$M12_{250}$	M13	M14	$M15_{10}$	$M16_{10}$	$M15_{250}$	$M16_{250}$
Remineralising Solution (pH)	DW	DW	DW	DW	DW	DW	6.58	6.58	6.58	6.58	6.58	6.58
Demineralising Solution (pH)	4.90	4.90	4.90	4.90	4.90	4.90	4.90	4.90	4.90	4.90	4.90	4.90
Background F Concentration (ppm)	0.0	0.2	0.0	0.2	0.0	0.2	0.0	0.2	0.0	0.2	0.0	0.2
Background F^- Concentration during the intermediate remineralisation period (ppm)	0.0	0.0	0.0	2.0	0.0	1.0	0.0	0.0	0.0	2.0	0.0	1.0
Brushing F Concentration (ppm)	0	0	10	10	250	250	0	0	10	10	250	250

Table 3-3: Experimental conditions for the groups studied during the main study. The groups presented were treated with the acid challenge and DW or PF. The subscript used in the group ID denotes the amount of F^- used during the tooth-brushing simulation.

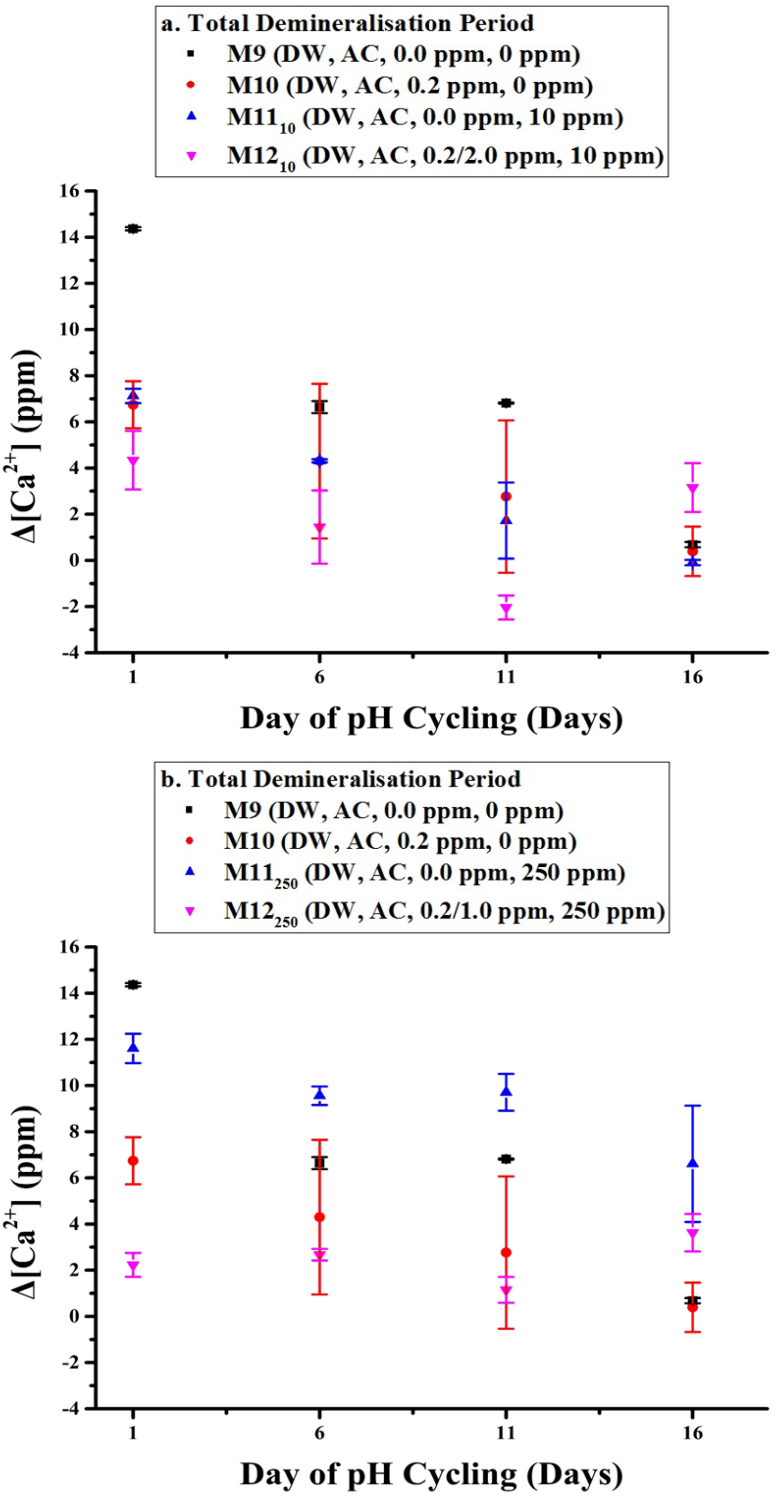

Figure 3-3: Comparison of Ca^{2+} change during the demineralisation challenge for the groups treated with AC and DW and a. 10 ppm or b. 250 ppm of F^- and with PF, AC and c. 10 ppm and d. 250 ppm of F^-.

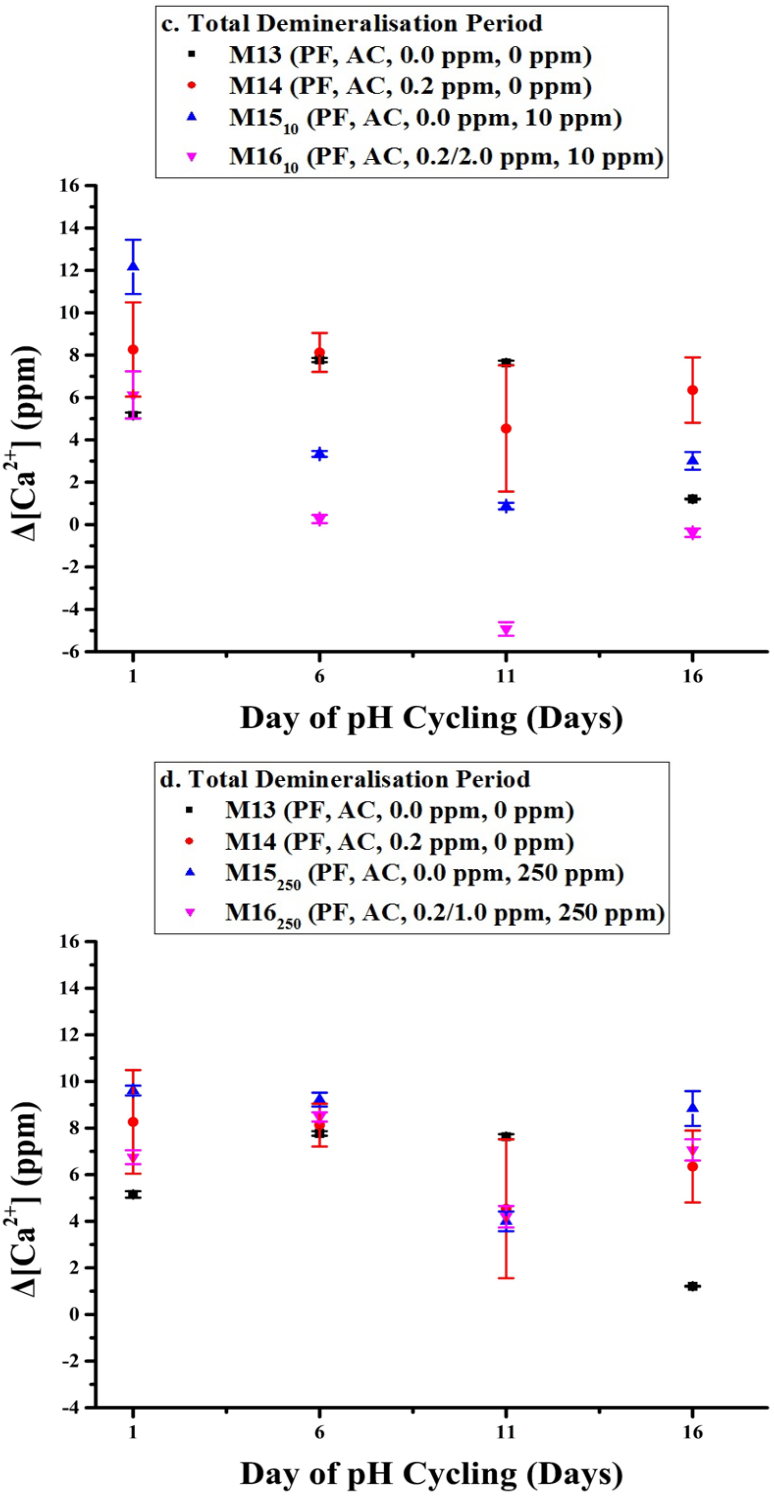

Figure 3-3 (Continued): Comparison of Ca^{2+} change during the demineralisation challenge for the groups treated with AC and DW and a. 10 ppm or b. 250 ppm of F^- and with PF, AC and c. 10 ppm and d. 250 ppm of F^-.

3.1.1.2 Phosphate & Fluoride Results

The second part of the chemical analysis describes the changes in the concentration of PO_4^{3-} and F^- in the solutions used during the pH-cycling. The analysis of F^- is broken into two parts: the analysis of the main solutions used during the pH-cycling and the analysis of the solutions produced after treating the pH-cycled enamel blocks with 1 M of KOH to remove the loosely bound F^- from the surface of the enamel as presented in section 2.3.1. The groups studied have been presented in tables 3-2 and 3-3.

Figure 3-4 presents the changes in the total PO_4^{3-} concentration with time for the groups treated with PF, without (Figures 3-4a, b) or with (Figures 3-4c, d) AC. The behaviour of the solutions differs depending whether DW or AC was used during the demineralisation period and resembles that of Ca^{2+}. Most of the groups treated with DW presented a similar trend with some PO_4^{3-} uptake, which decreased over time; with the exception of $M8_{10}$ and $M8_{250}$ for which PO_4^{3-} release was observed up to the 6th day, which was followed by a maximum on day 11 and a reverse towards positive values. On the other hand, the groups treated with AC presented higher phosphate uptake, which increased over time. With the exception of M14, which presented a relatively steady uptake and a maximum on day 6, the rest of the groups presented PO_4^{3-} release during the first 6 days, which was followed by a reverse into positive values and a continuously increasing uptake.

Figure 3-5 presents the phosphate changes during the intermediate (Figures 3-5a, c) and main (Figures 3-5b, d) remineralisation periods for the groups treated with 10 ppm (Figures 3-5a, b) and 250 ppm (Figures 3-5c, d) of F^-. During the first days of the intermediate remineralisation period, a strong increase in PO_4^{3-} took place, which decreased with time; with the exception of groups $M16_{10}$ and $M16_{250}$, which presented a minimum on day 6 and which was followed by

increasing uptake. During the main remineralisation period PO_4^{3-} release took place initially, which was followed by increasing uptake.

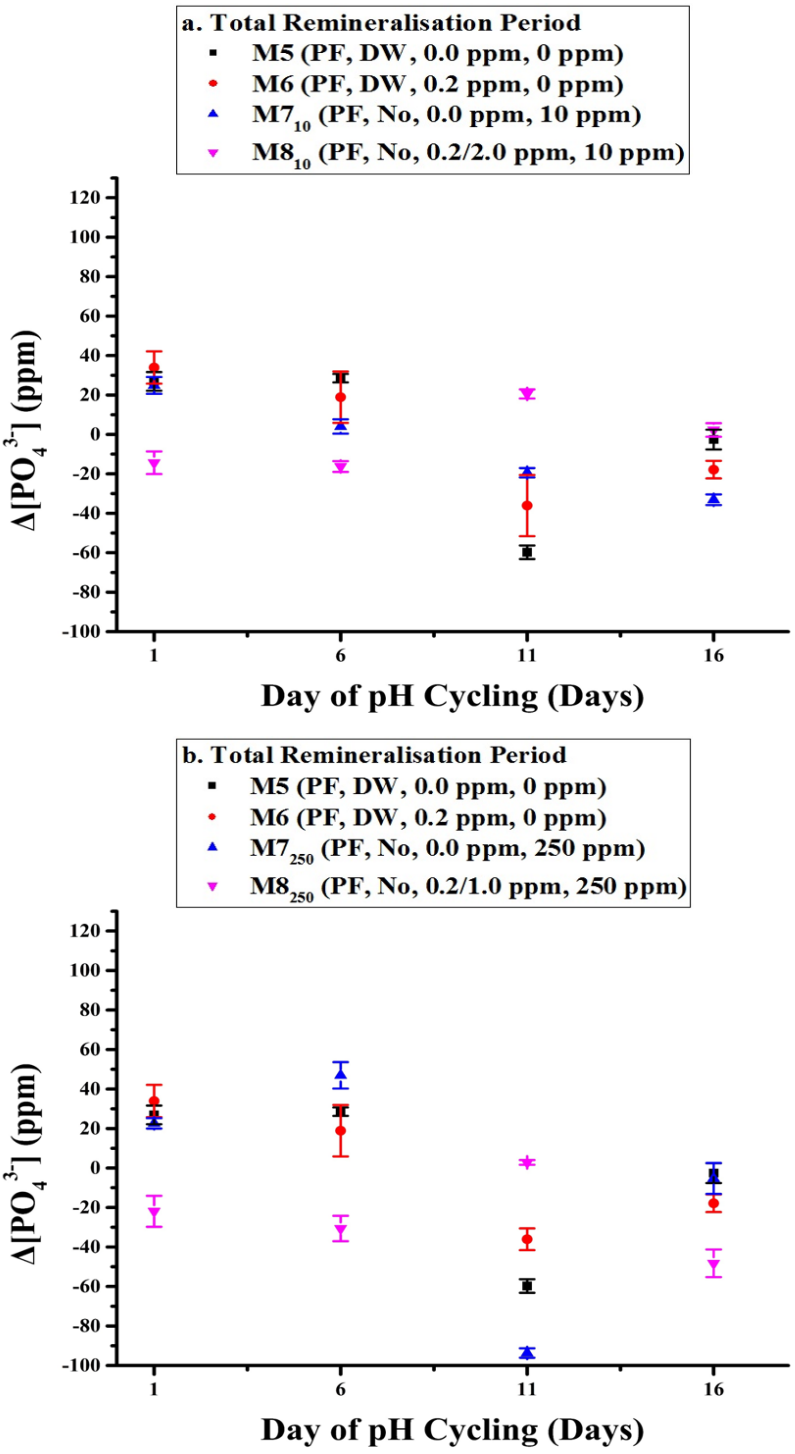

Figure 3-4: Changes in the concentration of PO_4^{3-} during the total remineralisation period. Comparisons are made between the groups which were treated with the plaque fluid proxy and no acid challenge, with or without background F^-, for the groups treated with a. 10 ppm and b. 250 ppm; and with both PF and AC using c. 10 ppm and d. 250 ppm. In all cases the respective groups (M5, M6 or M13, M14) which either had no F^- added or had only a background F^- of 0.2 ppm are also displayed.

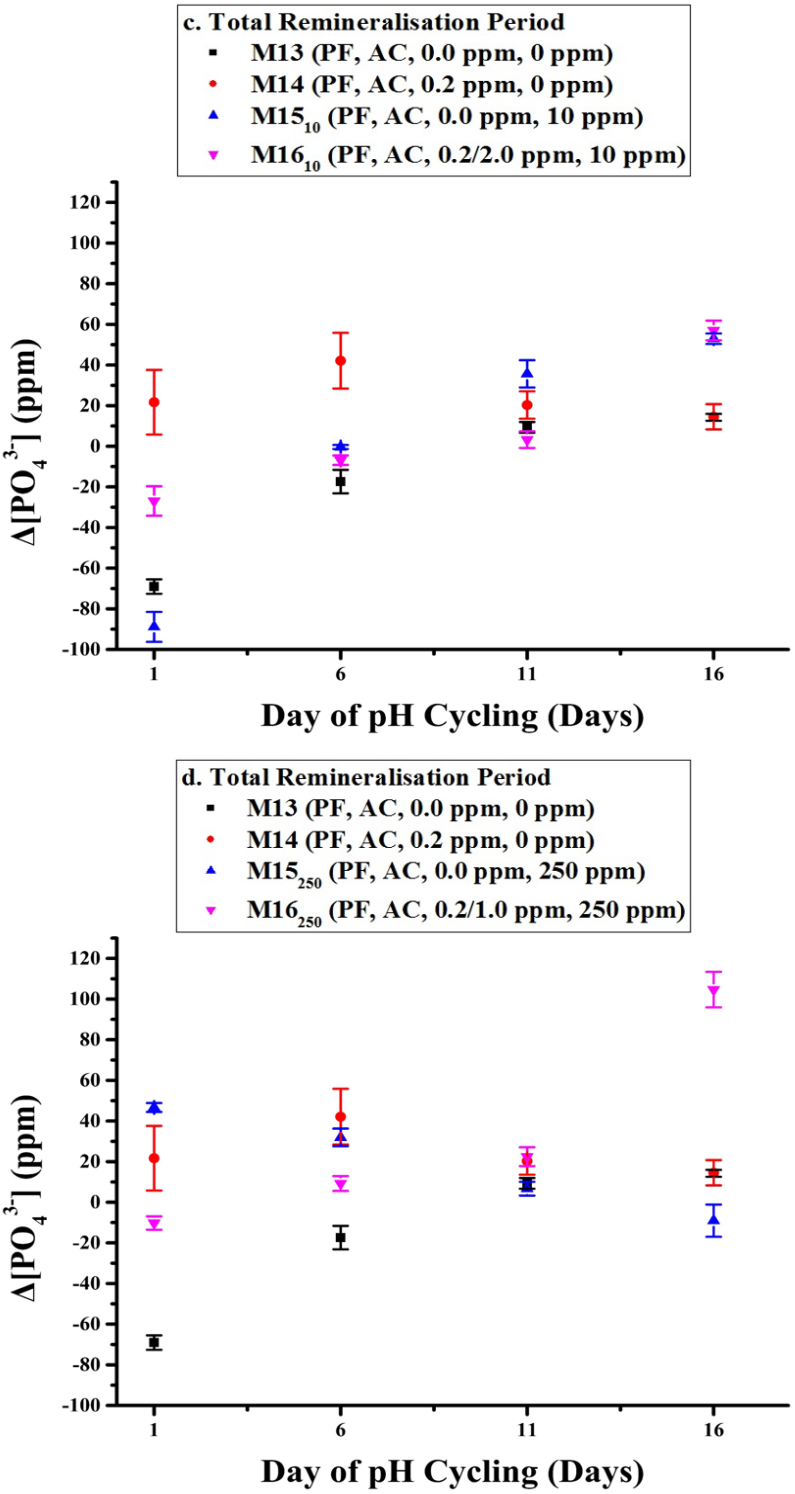

Figure 3-4 (Continued): Changes in the concentration of PO_4^{3-} during the total remineralisation period. Comparisons are made between the groups which were treated with the plaque fluid proxy and no acid challenge, with or without background F^-, for the groups treated with a. 10 ppm and b. 250 ppm; and with both PF and AC using c. 10 ppm and d. 250 ppm. In all cases the respective groups (M5, M6 or M13, M14) which either had no F^- added or had only a background F^- of 0.2 ppm are also displayed.

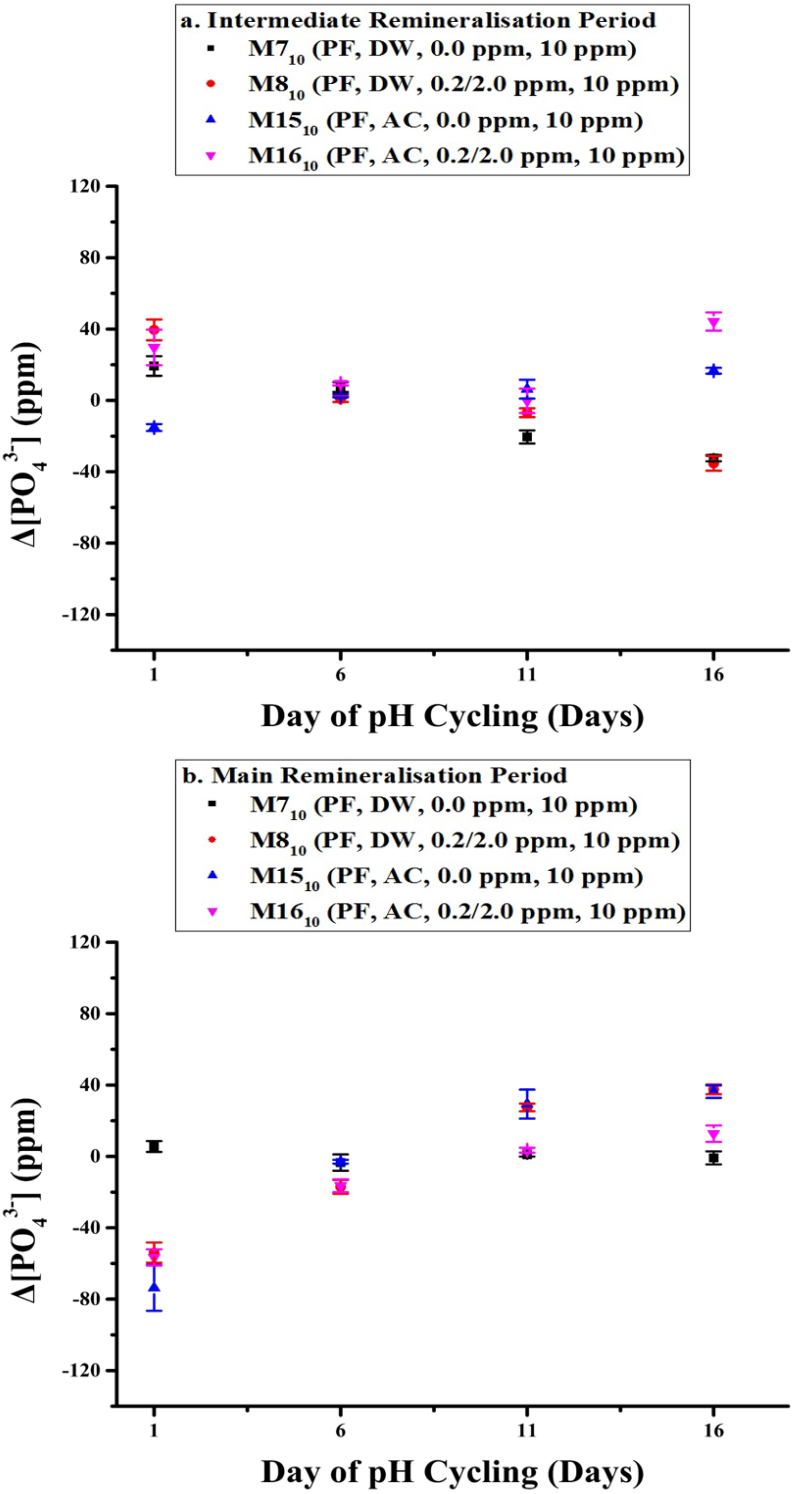

Figure 3-5: Comparison of PO_4^{3-} changes during the intermediate (a, c) and main (b, d) remineralisation periods for the groups treated with PF and DW and PF and AC and 10 ppm (a, b) or 250 ppm (c, d) of F^-.

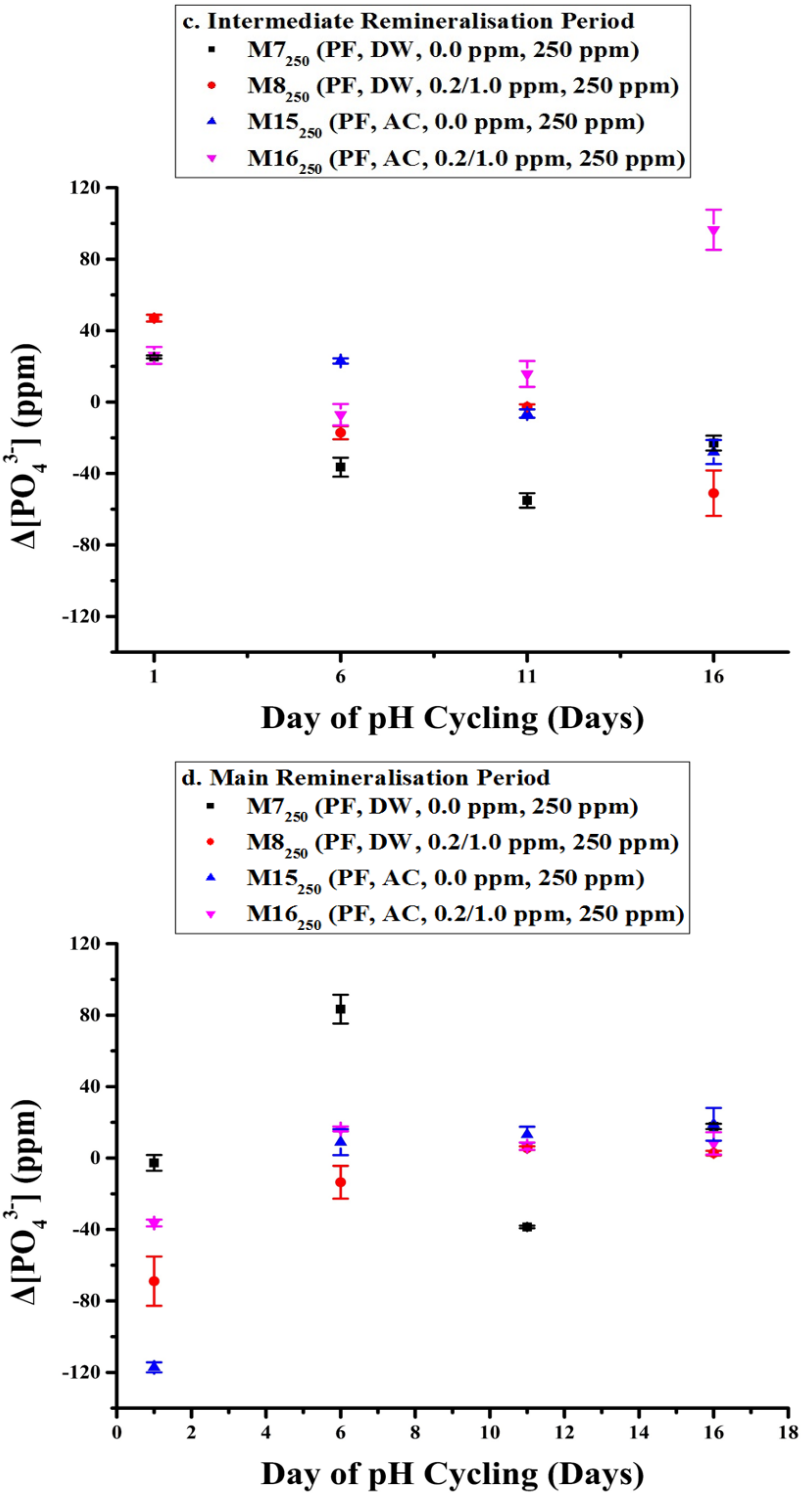

Figure 3-5 (Continued): Comparison of PO_4^{3-} changes during the intermediate (a, c) and main (b, d) remineralisation periods for the groups treated with PF and DW and PF and AC and 10 ppm (a, b) or 250 ppm (c, d) of F^-.

Figure 3-6 presents the PO_4^{3-} changes during the demineralisation period for the groups which were exposed to either DW (Figures 3-6a, b) or PF (Figures 3-6c, d) as a remineralisation treatment. With the exception of group M9, for which no F^- was used and presents strong dissolution, PO_4^{3-} uptake is generally observed. Groups that were treated with 10 ppm or 250 ppm of F^-, as well as group M10, for which background F^- of 0.2 ppm was present in the solutions, adsorb PO_4^{3-} with a steady rate. On the other hand, groups M13 (for which no F^- was used) and M14 (for which background F^- of 0.2 ppm was present in the solutions) show stronger uptake, which decreases over time.

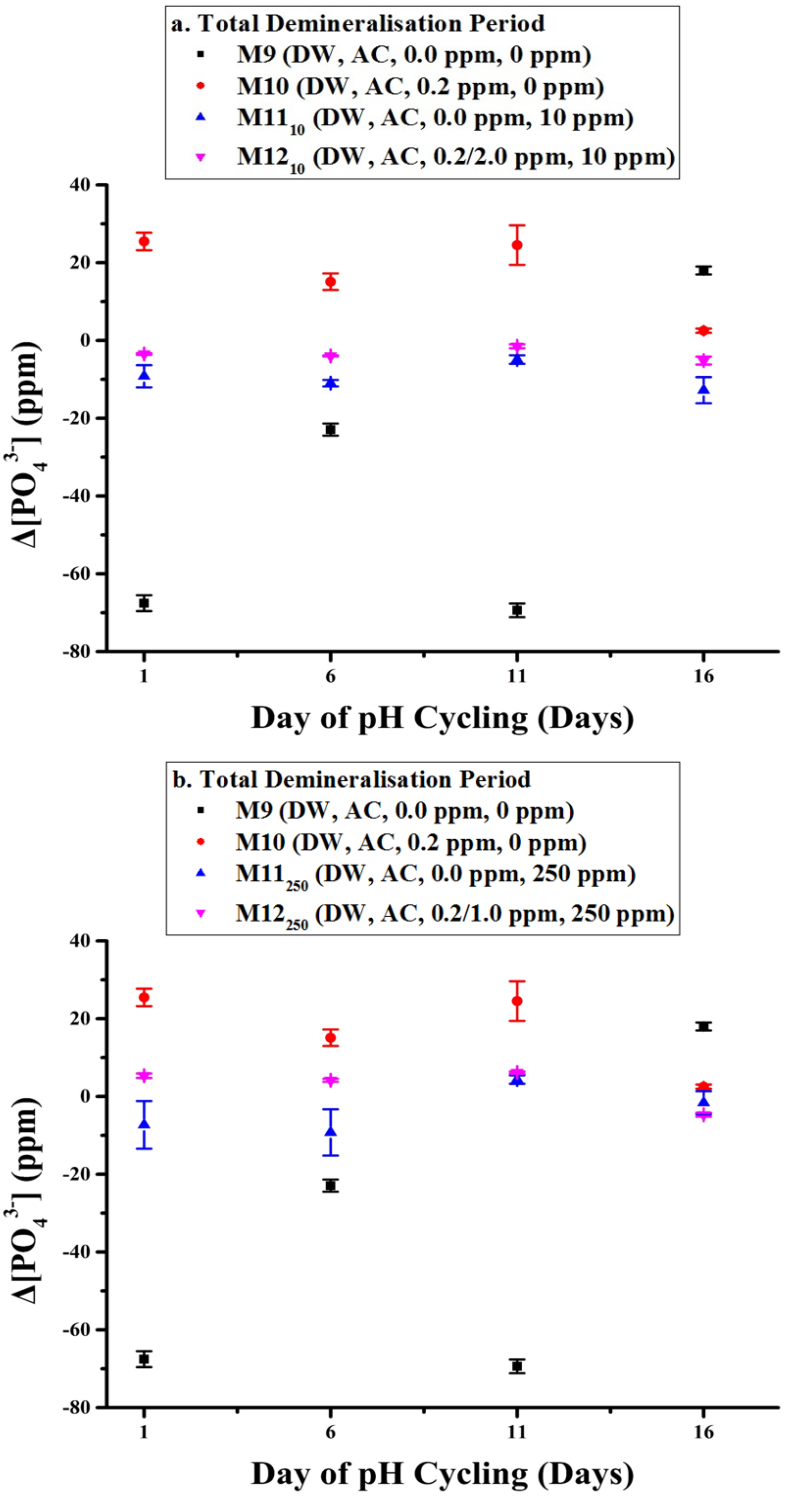

Figure 3-6: Comparison of PO_4^{3-} change during the demineralisation challenge for the groups treated with AC and DW and a. 10 ppm or b. 250 ppm of F^- and those treated with PF, AC and c. 10 ppm and d. 250 ppm of F^-.

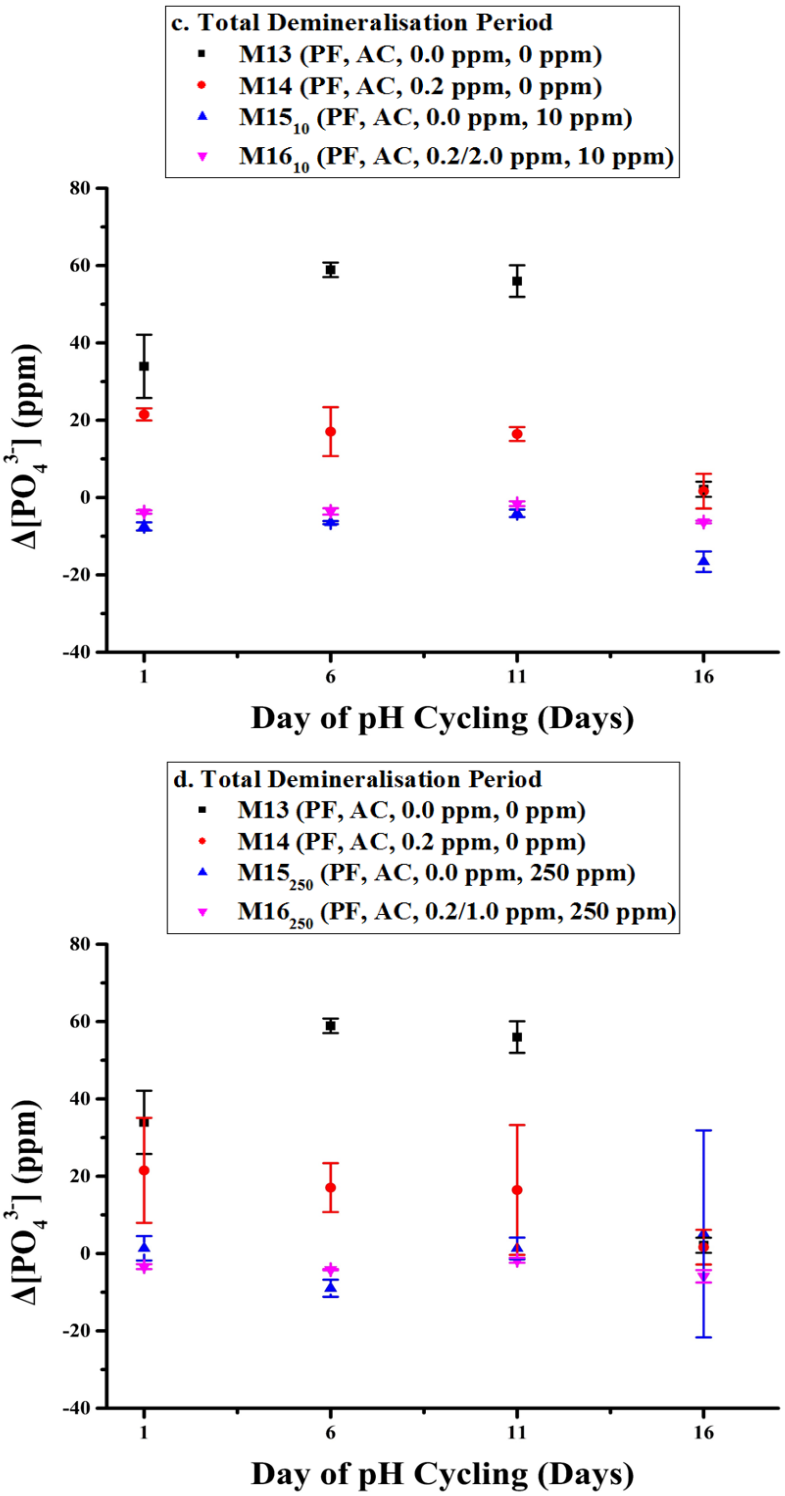

Figure 3-6 (Continued): Comparison of PO_4^{3-} change during the demineralisation challenge for the groups treated with AC and DW and a. 10 ppm or b. 250 ppm of F^- and those treated with PF, AC and c. 10 ppm and d. 250 ppm of F^-.

In addition to studying PO_4^{3-} concentration, Ion Chromatography was also used to measure fluorine in the solutions where F^- treatment was involved. The groups analysed are presented in Table 3-4 and the results in Figure 3-7.

ID, Solutions & Treatments	pH Cycling Rounds															
ID	$M3_{10}$	$M4_{10}$	$M3_{250}$	$M4_{250}$	$M7_{10}$	$M8_{10}$	$M7_{250}$	$M8_{250}$	$M11_{10}$	$M12_{10}$	$M11_{250}$	$M12_{250}$	$M15_{10}$	$M16_{10}$	$M15_{250}$	$M16_{250}$
Remineralising Solution pH	DW	DW	DW	DW	6.58	6.58	6.58	6.58	DW	DW	DW	DW	6.58	6.58	6.58	6.58
Demineralising Solution pH	DW	DW	DW	DW	DW	DW	DW	DW	4.90	4.90	4.90	4.90	4.90	4.90	4.90	4.90
Background F Concentration (ppm)	0.0	0.2	0.0	0.2	0.0	0.2	0.0	0.2	0.0	0.2	0.0	0.2	0.0	0.2	0.0	0.2
Background F- Concentration during the intermediate remineralisation period (ppm)	0.0	2.0	0.0	1.0	0.0	2.0	0.0	1.0	0.0	2.0	0.0	1.0	0.0	2.0	0.0	1.0
Brushing F Concentration (ppm)	10	10	250	250	10	10	250	250	10	10	250	250	10	10	250	250

Table 3-4: Experimental conditions for the groups treated with the F^- treatment during the main study. The groups presented are the groups which were treated either with 10 or 250 ppm of F^- in the form of NaF. The subscript used in the group ID denotes the amount of F^- used during the tooth-brushing simulation.

Figure 3-7 presents the F^- results for both the groups treated with 10 ppm (a) and 250 ppm (b) of F^-. A similar trend can be observed in all cases. There is an increase in the amount of F^- which either is incorporated into the enamel structure or is deposited on the surface of the enamel. The increase peaks on days 11 and 6 for the groups treated with 10 ppm and 250 ppm of F^- respectively and is followed by a gradual decrease, the rate of which depends on the experimental conditions.

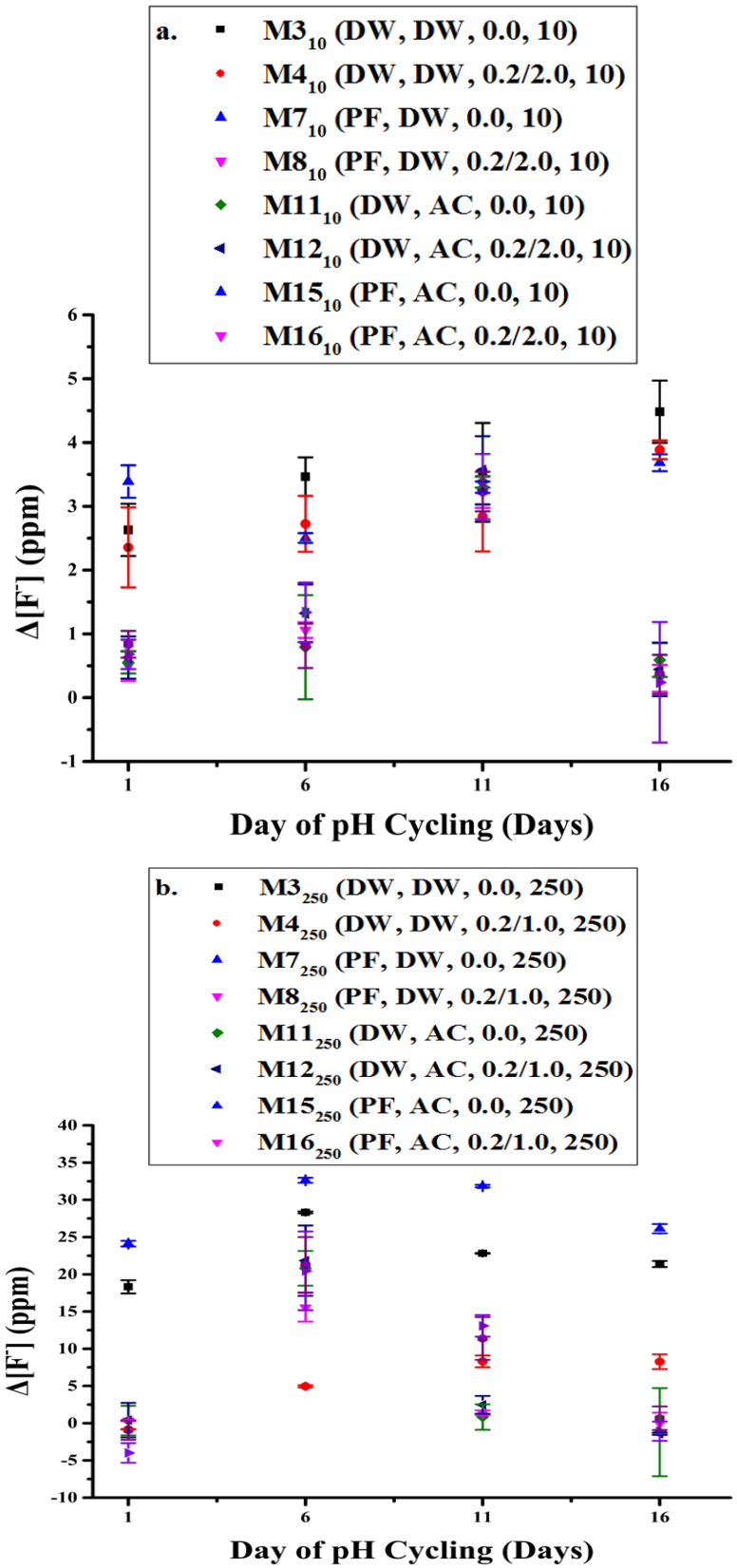

Figure 3-7: Comparison of F^- changes during the main study for the groups treated a. 10 ppm or b. 250 ppm of F^- in the form of NaF.

Finally, the last part of the chemical analysis was to calculate the amount of F^- which was loosely bound on the surface of the enamel blocks. This was achieved, as already stated, by treating the blocks with 1 M of KOH for 24 hours. The control values were calculated by treating with KOH 5 non pH-cycled blocks. The results are presented in Figure 3-8 in the form of $[F^-]$ per cm^2 and as can be seen the amount of loosely bound F^- is similar in all cases, with slightly higher values for the groups treated with 250 ppm of F^- and is in accordance with the results presented in the case of the main F^- treatment.

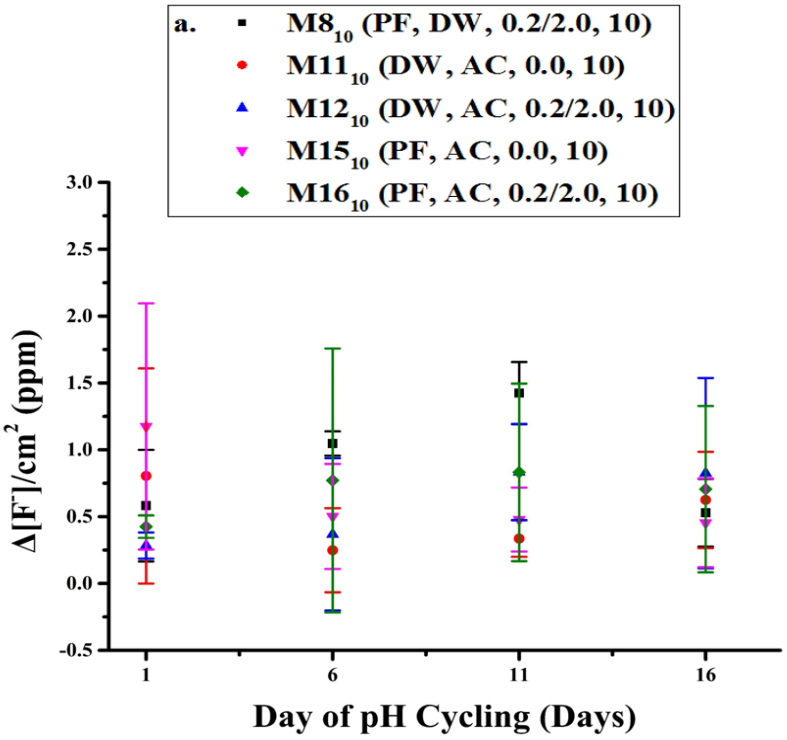

Figure 3-8: Comparison of the loosely bound F^- on the surface of the pH-cycled enamel blocks treated with a. 10 ppm and b. 250 ppm of F^-, which was extracted through the immersion of the blocks inside 1 M of KOH for 24 hours.

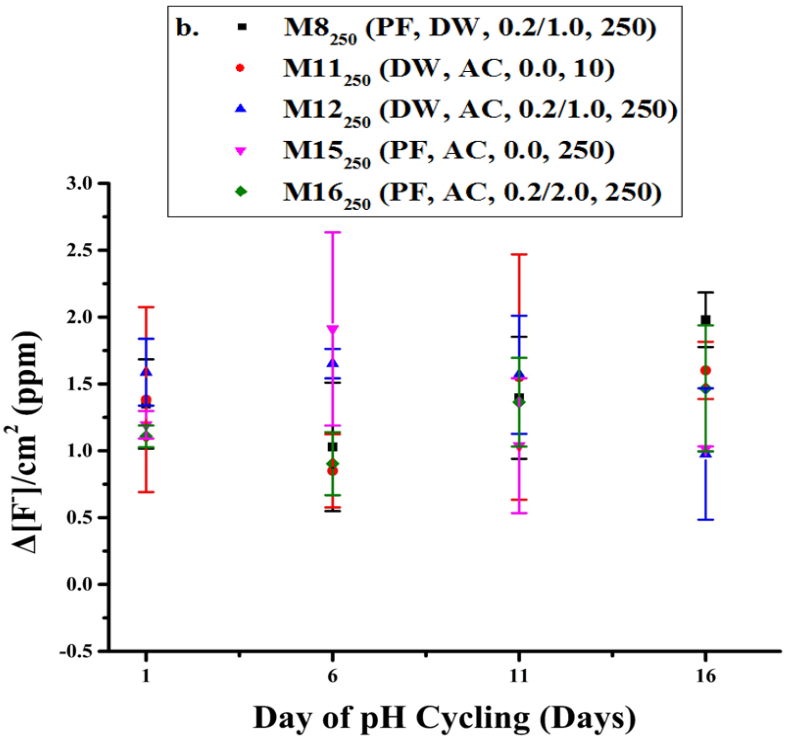

Figure 3-8 (Continued): Comparison of the loosely bound F^- on the surface of the pH-cycled enamel blocks treated with a. 10 ppm and b. 250 ppm of F^-, which was extracted through the immersion of the blocks inside 1 M of KOH for 24 hours.

3.1.2 Structural Analysis

Besides the chemical analysis, FTIR analysis was performed on the enamel blocks to identify potential changes due to the pH-cycling treatment and correlate them with the results presented in the previous section. Each graph depicts a single group and the changes in the respective FTIR spectra over time. The analysis was performed by identifying the most significant peaks present, the bond they represent and the material with which they are correlated by using appropriate reference books and peer-reviewed published articles. The absolute values of the positions, area and height of the peaks mentioned are presented in respective tables in the appendix. Due to the large volume of results, only the most characteristic are presented.

To begin with, analysis of the enamel blocks which were treated only with DW during the remineralisation and demineralisation challenges is presented in Figure 3-9. In general the groups treated with DW only (Figure 3-9a) or with the addition of background F^- (Figure 3-9b) present peaks which are typical of HA, while no significant changes can be observed in the spectra over time; with the exception of slight F^- accumulation, as the presence and increase in the intensity of the peak around 750 cm^{-1} corresponding to the F^- - OH^- substitution (479, 480), suggests.

In all cases peaks corresponding to the υ_4 PO_4^{3-} mode of apatite can be observed in the region between 540 cm^{-1} and 615 cm^{-1} (481-483); along with peaks around 1020 cm^{-1} (484-486), 1050 cm^{-1} (487, 488) and 1120 cm^{-1} (489, 490) which correspond to the υ_6 HPO_4^{2-} and υ_3 PO_4^{3-} modes respectively.

At the same time, the OH^- liberation mode around 630 cm^{-1} (479, 480, 491) is present, as well as peaks between 1900 cm^{-1} and 2200 cm^{-1} which correspond to HPO_4^{2-} (479, 492) and are characteristic of well crystalline HA. Several CO_3^{2-} peaks are also observed, such as the υ_2 mode at 700 cm^{-1}, the υ_4 around 830 cm^{-1} and 1370 cm^{-1} and the υ_1 around 1450 cm^{-1} and 1640 cm^{-1} (487, 493, 494). Of similar nature are the peaks which correspond to the C-O stretching mode and the carbonyl group (C=O) around 1730 cm^{-1} (487, 495, 496).

The addition of either 10 ppm ($M3_{10}$, $M4_{10}$, Figures 3-9c, d) or 250 ppm ($M3_{250}$, $M4_{250}$, Figures 3-9e, f) of F^- treatment during the pH-cycling affects the observed spectra. Fluoride incorporation is higher in this case, since the peak at 750 cm^{-1} is significantly stronger, especially when no BF was used ($M3_{10}$, $M3_{250}$). At the same time changes in the surface and number of the υ_4 PO_4^{3-} peaks between 540 cm^{-1} and 615 cm^{-1} also take place, which are more pronounced for the groups treated with 250 ppm of F^- ($M3_{250}$, $M4_{250}$). Some weak peaks,

which correspond to newly precipitated HA and can be traced around 1020 cm^{-1} (484-486), are also present for the groups treated with 10 ppm and appear towards the end of the experimental procedure for the groups treated with 250 ppm of F^-. Such peaks are observed below 540 cm^{-1} and around 1010 cm^{-1} and 1150 cm^{-1}, which correspond to free HPO_4^{2-} (481-483, 497) and υ_3 PO_4^{3-} (484, 498, 499) and denote the presence of OCP and/or TCP. Finally, slight decrease is also observed in the total intensity of the CO_3^{2-} related peaks especially in the case of groups $M3_{250}$ and $M4_{250}$ as the changes in the surface area of the respective peaks suggest.

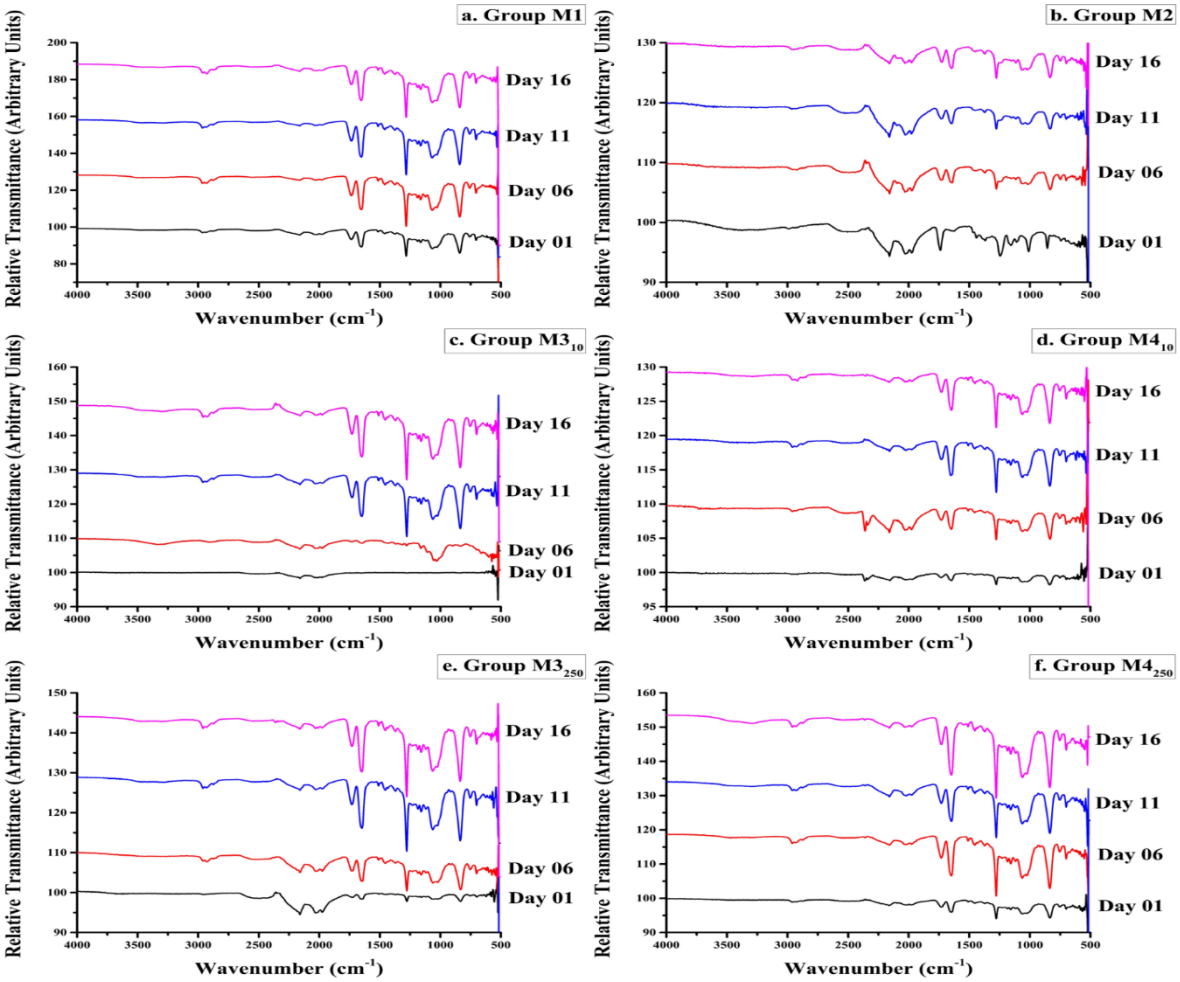

Figure 3-9: FTIR spectra of the enamel blocks treated a. only with DW (M1), b. with DW and a background [F^-] of 0.2 ppm (M2), c. with DW and F^- treatment of 10 ppm ($M3_{10}$), d. DW, F^- treatment of 10 ppm and background F^- of 0.2 ppm and 2 ppm ($M4_{10}$), e. DW and F^- treatment of 250 ppm ($M3_{250}$) and f. DW, F^- treatment of 250 ppm and background F^- of 0.2 ppm and 1 ppm ($M4_{250}$) for the duration of the pH-cycling experiment.

Figure 3-10 presents the groups which were treated with PF and DW as the acid challenge, with or without the presence of F^-. While no significant changes can be observed in the υ_4 PO_4^{3-} peaks (540-615 cm^{-1}) for the groups which were not treated with the F^- treatment (M5, M6), a decrease in their absolute number can be observed for the F^- treated groups along with a significant broadening of the remaining peaks. The decrease is higher for the groups treated with 250 ppm of F^- ($M7_{250}$, $M8_{250}$). At the same time, the intensity of the OH^- liberation mode (630 cm^{-1}) nearly doubles for groups M5 and M6 up to the 16^{th} day, while the exact opposite is true for the rest of the groups. The 750 cm^{-1} peak, which is correlated with F^- incorporation inside the enamel, can also be observed for the latter and gets stronger with time; especially for the 250 ppm treated groups and the groups for which no BF was used ($M7_{10}$, $M7_{250}$). This peak can also be observed for M6 (the solutions of which contained BF) although it is much weaker in this case.

In all cases the appearance of peaks which are correlated with OCP and/or TCP are observed. Such peaks are the υ_4 PO_4^{3-}, the HPO_4^{2-} and the υ_3 PO_4^{3-} peaks below 540 cm^{-1}, at 1010 cm^{-1} and 1150 cm^{-1} respectively. In the case of M5 and M6, where no F^- or only BF was used, a continuous increase in the intensity of the peaks below 540 cm^{-1} and at 1150 cm^{-1} can be observed. On the other hand, the groups which were treated with the F^- treatment as well present an increase in the intensity of the peaks which is followed by a decrease towards the end of the experimental procedure.

At the same time, significant increase in intensity of the peaks which are correlated with the presence of newly precipitated HA can be observed. In all cases significant increase along with a shift towards higher wavenumbers is observed for the υ_6 HPO_4^{2-} and υ_3 PO_4^{3-} at 1020 cm^{-1} and 1050 cm^{-1}, which is also in accordance with the increase in intensity of the HPO_4^{2-} peaks between 1900 cm^{-1} and 2200 cm^{-1}.

Finally, the CO_3^{2-} content of the enamel blocks also changes with time. The peaks observed are the υ_2 mode at 700 cm^{-1} and 850 cm^{-1}, the υ_4 around 830 cm^{-1} and 1370 cm^{-1} and the υ_1 around 1450 cm^{-1} and 1640 cm^{-1}. A redistribution of the carbonate content can be noted between the observed peaks throughout the experimental procedure, which is followed by either an increase or a decrease in the carbonate content. In general, CO_3^{2-} increase is observed in the cases where no or 250 ppm of F^- were used, while decrease was observed for the groups treated with 10 ppm of F^-.

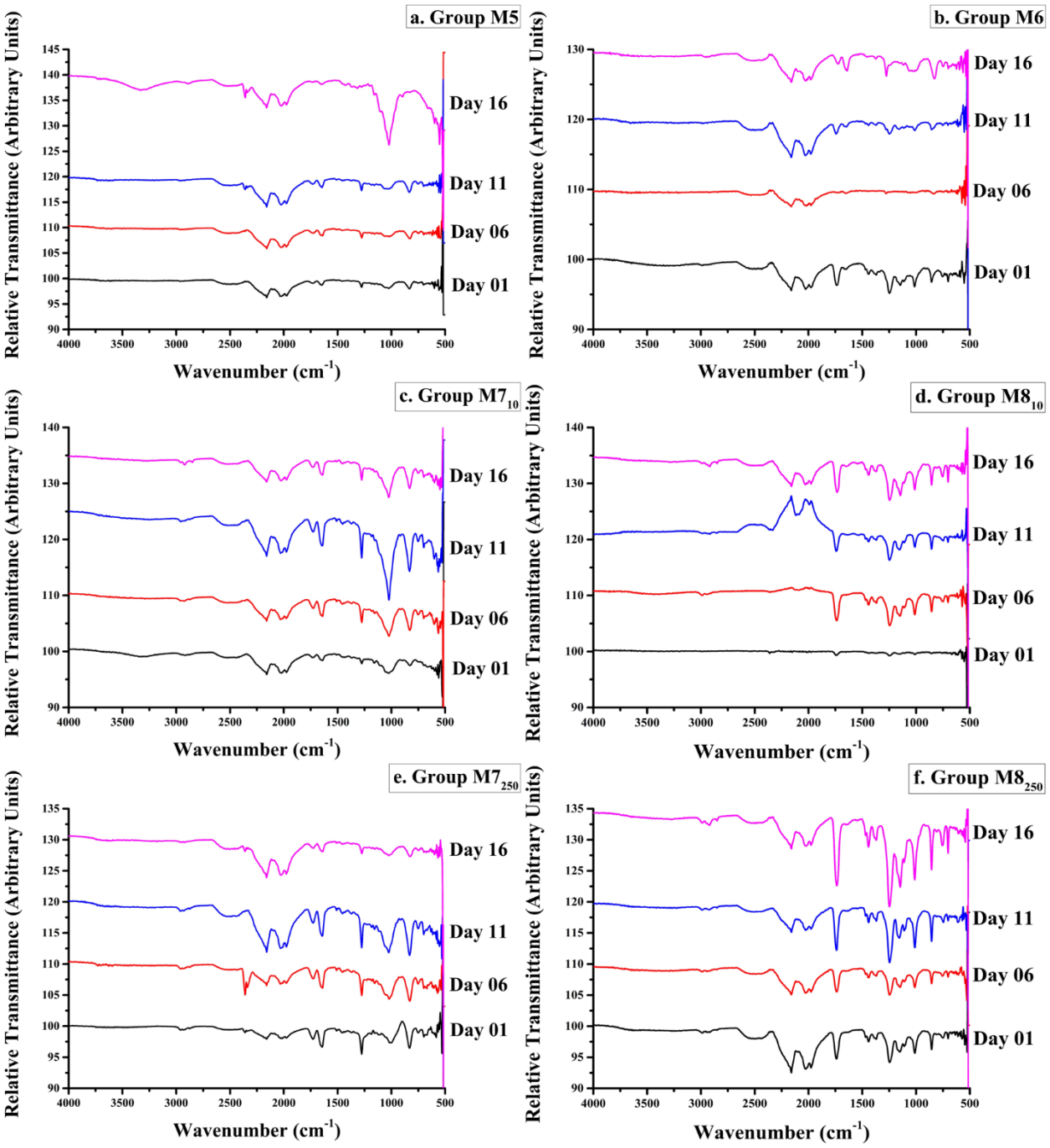

Figure 3-10: FTIR spectra of the enamel blocks treated a. only with PF and DW (M5), b. with PF, DW and a background [F^-] of 0.2 ppm (M6), c. with PF, DW and F^- treatment of 10 ppm ($M7_{10}$), d. PF, DW, F^- treatment of 10 ppm and background F^- of 0.2 ppm and 2 ppm ($M8_{10}$), e. PF, DW and F^- treatment of 250 ppm ($M7_{250}$) and f. PF, DW, F^- treatment of 250 ppm and background F^- of 0.2 ppm and 1 ppm ($M8_{250}$) for the duration of the pH cycling experiment.

The next set of results (Figure 3-11) contains the groups which were treated with DW and AC during the remineralisation and demineralisation treatments respectively. Group M9, for which no F^- was used, presents a strong decrease in the peaks which are correlated with HA like the υ_4 PO_4^{3-} between 540 cm^{-1} and 615 cm^{-1} and the HPO_4^{2-} between 1900 cm^{-1} and 2200 cm^{-1} and the OH^- liberation mode around 630 cm^{-1}. Similar decrease is also observed to the CO_3^{2-} peaks. By the end of the experimental procedure only the υ_2 CO_3^{2-} mode around 850 cm^{-1} is present and with decreased surface area. At the same time, some HA and OCP and/or TCP, DCPD precipitation takes place as the presence of weak bands at 1020 cm^{-1} and 1120 cm^{-1} and 1150 cm^{-1} respectively denote.

The introduction of F^- inside the experimental procedure leads to different results. To begin with, the incorporation of F^- inside the enamel is evident through the presence of the peak at 750 cm^{-1}, which is stronger the higher the amount of F^- administered is and when no BF was used. The reduction in the surface area of the aforementioned peaks is significantly lower when only BF was added inside the solutions (M10). The addition of the F^- treatment leads to redistribution and delayed reduction of the surface of the PO_4^{3-}, HPO_4^{2-} and CO_3^{2-} peaks, which is more pronounced when BF is also added ($M12_{10}$, $M12_{250}$). At the same time, the presence of secondary phases like OCP and/or TCP (below 540 cm^{-1}) can be observed. These peaks initially increase with time and are generally stronger than those observed previously although decrease of their respective surface areas takes place towards the end of the experimental procedure. This could be also correlated with the presence of peaks correlating to newly precipitated HA (e.g. 1020 cm^{-1}), which are traced mainly during the second half of the experimental procedure, which increase with time and shift towards higher wavenumbers.

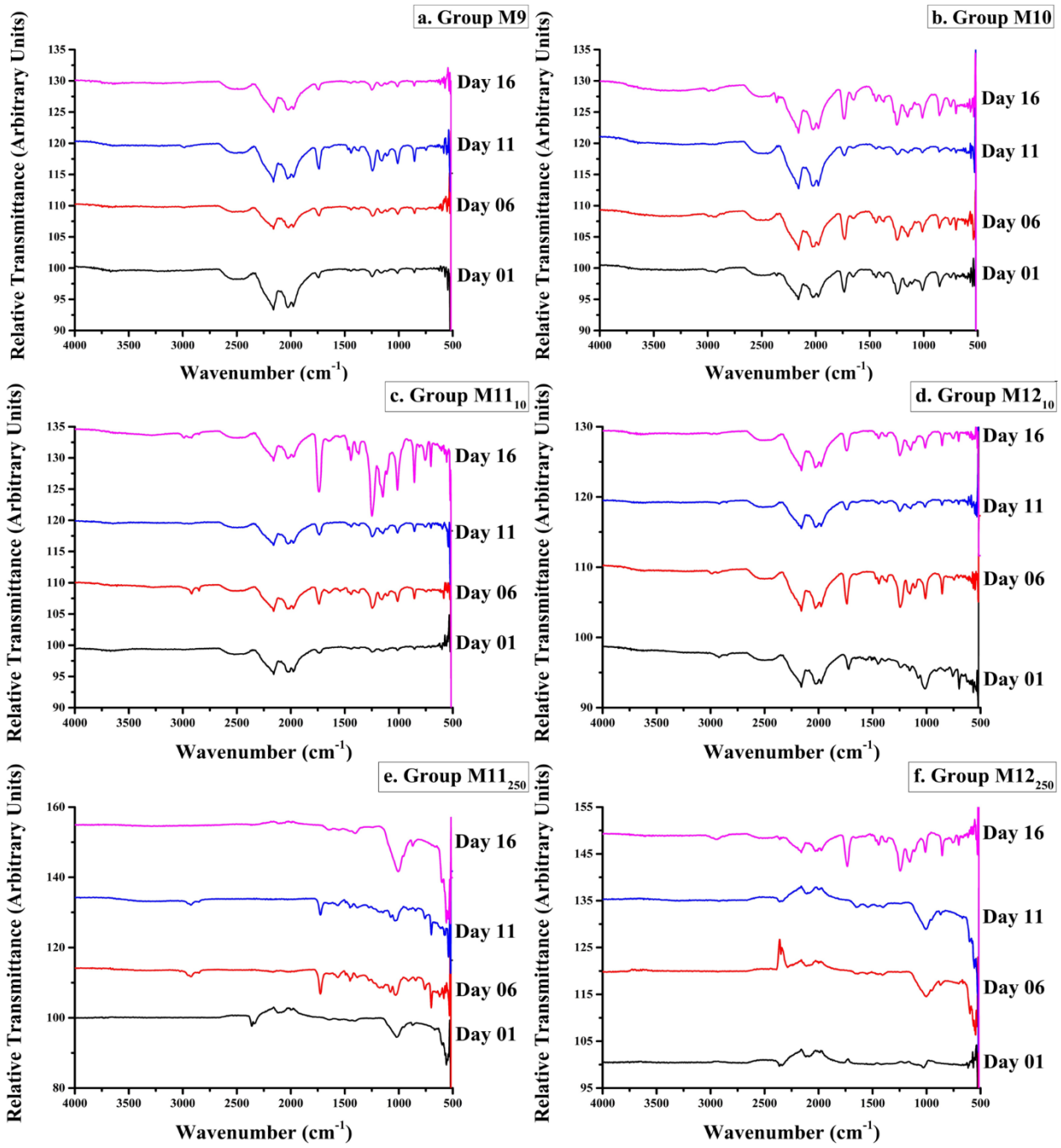

Figure 3-11: FTIR spectra of the enamel blocks treated a. only with DW and AC (M9), b. with DW, AC and a background [F^-] of 0.2 ppm (M10), c. with DW, AC and F^- treatment of 10 ppm ($M11_{10}$), d. DW, AC, F^- treatment of 10 ppm and background F^- of 0.2 ppm and 2 ppm ($M12_{10}$), e. DW, AC and F^- treatment of 250 ppm ($M11_{250}$) and f. DW, AC, F^- treatment of 250 ppm and background F^- of 0.2 ppm and 1 ppm ($M12_{250}$) for the duration of the pH cycling experiment.

Finally, figure 3-12 presents the groups treated with both PF and AC with or without F^- presence. Group 13, for which no F^- was used, presents several υ_4 PO_4^{3-} modes between 540 cm^{-1} and 615 cm^{-1}, which increase in intensity with time along with a shift in their respective positions; as well as the OH^- liberation mode around 630 cm^{-1}. Similar is the behaviour of the HPO_4^{2-} peaks between 1900 cm^{-1} and 2200 cm^{-1}, which correspond to well-crystalline HA. From day 6 onwards several peaks corresponding to the presence of phases like OCP and/or TCP can be observed. The HPO_4^{2-} peaks below 530 cm^{-1} initially increase and then decrease in surface area, while the υ_3 PO_4^{3-} modes at 1010 cm^{-1} and 1150 cm^{-1} continuously increase with time. In a similar manner, the υ_6 HPO_4^{2-} peak at 1020 cm^{-1} which is correlated to the presence of newly precipitated HA also increases with time and shifts towards higher wavenumbers. Several CO_3^{2-} peaks are initially observed especially in the region between 660 cm^{-1} and 900 cm^{-1} and are assigned to the υ_4, υ_2 and υ_1 CO_3^{2-} modes, as well as around 1440 cm^{-1} and 1465 cm^{-1} and correspond to υ_3 CO_3^{2-}. By the end of the pH-cycling procedure most of the peaks disappear except those at 856 cm^{-1} and 1440 cm^{-1}.

The addition of BF (M14) leads to similar results. Slight F^- accumulation takes place as the presence of a weak peak at 750 cm^{-1}, which corresponds to F^- vs. OH^- substitution inside the apatite lattice; while the OH^- liberation mode (620 cm^{-1}) shifts towards higher wavenumbers and increases in intensity. Several peaks corresponding to OCP and/or TCP are also present, like the HPO_4^{2-} modes below 540 cm^{-1} and the υ_3 PO_4^{3-} at 1010 cm^{-1} and 1150 cm^{-1}. These peaks initially increase in intensity and then decrease, while at the same time an increase in the intensity of the peaks corresponding to newly precipitated (e.g. 1120 cm^{-1}) HA is observed with a simultaneous shift towards higher wavenumbers.

At the same time, the peaks correlated with the presence of CO_3^{2-} decrease in surface area and number in a way similar to that observed in the case of the enamel blocks treated with PF and DW and 10 ppm of F^- ($M7_{10}$ and $M8_{10}$) as the remineralisation, demineralisation and F^- treatments respectively and DW and AC with or without the presence of F^- (M9, M10, $M11_{10}$, $M12_{10}$, $M11_{250}$, $M12_{250}$), which denotes decrease in carbonate content through the dissolution of the original enamel surface.

Besides the changes just mentioned, the groups which were treated with 10 ppm or 250 ppm of F^- present far higher fluoride accumulation as the intensity of the peak at 750 cm^{-1} suggests; while the OH^- liberation mode (630 cm^{-1}) disappears by the end of the experimental procedure. Additionally, a decrease in the absolute number with a respective broadening of the remaining peaks takes place for the υ_4 PO_4^{3-} modes between 540 cm^{-1} and 615 cm^{-1}. On the other hand, the intensity of the HPO_4^{2-} modes between 1900 cm^{-1} and 2200 cm^{-1} increases. Peaks corresponding to the presence of OCP and/or TCP are also traced below 530 cm^{-1} and at 1150 cm^{-1}. Initially these peaks increase in intensity, which is followed by rapid decrease on day 16. Similar is the behaviour of the carbonate peaks. The υ_4, υ_2 and υ_3 CO_3^{2-} modes at 700 cm^{-1}, 850 cm^{-1} and 1440 cm^{-1} respectively increase up to the 6^{th} day and then rapidly decrease. Opposite is the behaviour of the modes assigned to υ_6 HPO_4^{2-} and υ_3 PO_4^{3-} and correspond to newly precipitated HA at 1020 cm^{-1} and 1120 cm^{-1}. These peaks increase in surface area and shift towards higher wavenumbers as time progresses.

Finally, it must be noted that the aforementioned changes are more pronounced for the groups treated with no BF ($M15_{10}$, $M15_{250}$) and with 10 ppm of F^- ($M15_{10}$, $M16_{10}$) and more gradual for the groups treated with 250 ppm ($M15_{250}$, $M16_{250}$). The latter present also OH^- stretching peaks in the region between 3000 cm^{-1} and 4000 cm^{-1}. Such peaks are present from day 6

onwards at 3210 cm^{-1}, 3640 cm^{-1}, 3688 cm^{-1} and 3748 cm^{-1}. Most of the peaks either weaken significantly or disappear by day 16, although the latter shifts towards lower wavenumbers with significant increase in surface area.

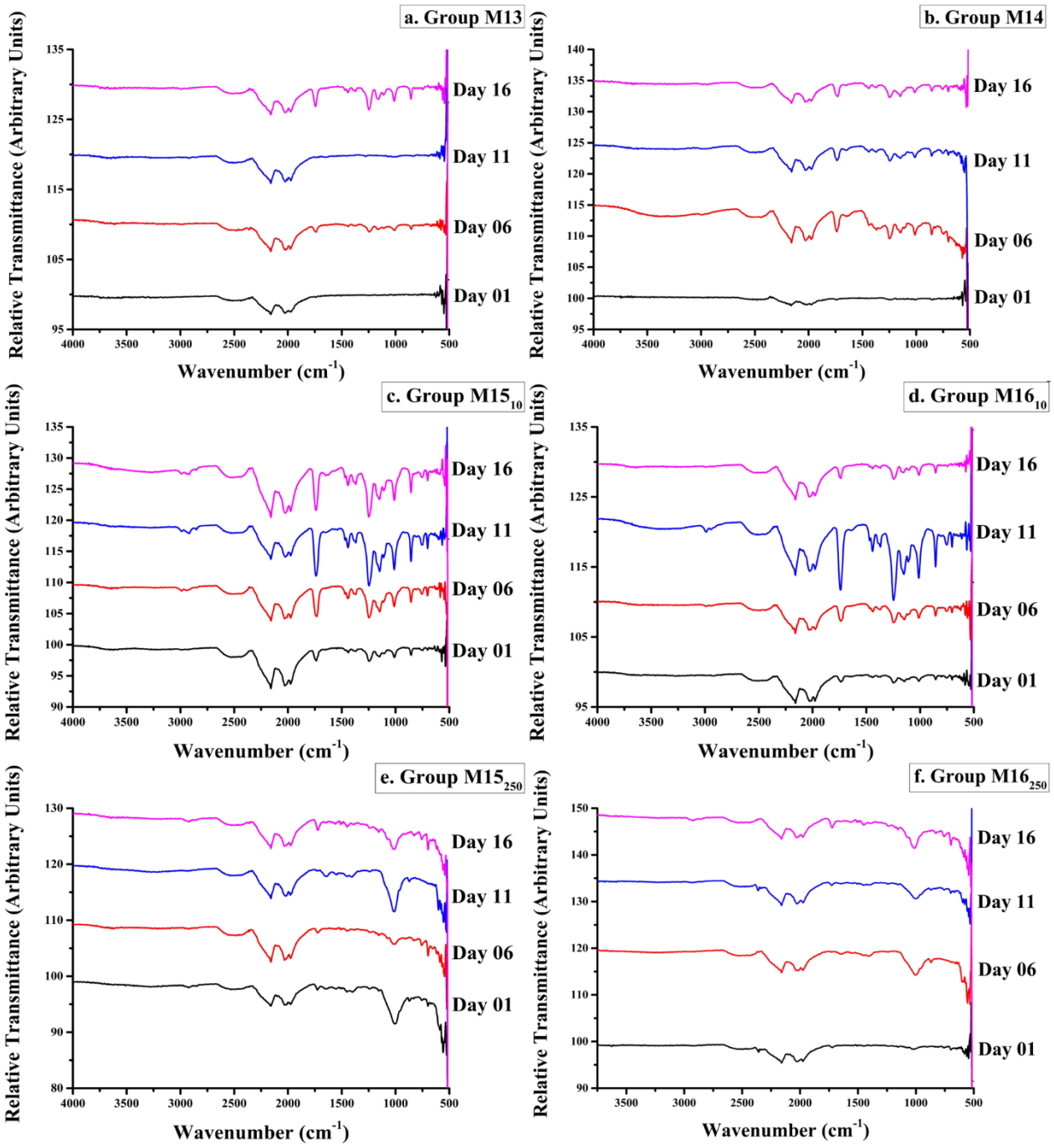

Figure 3-12: FTIR spectra of the enamel blocks treated a. only with PF and AC (M13), b. with PF, AC and a background [F^-] of 0.2 ppm (M14), c. with PF, AC and F^- treatment of 10 ppm ($M15_{10}$), d. PF, AC, F^- treatment of 10 ppm and background F^- of 0.2 ppm and 2 ppm ($M16_{10}$), e. PF, AC and F^- treatment of 250 ppm ($M15_{250}$) and f. PF, AC, F^- treatment of 250 ppm and background F^- of 0.2 ppm and 1 ppm ($M16_{250}$) for the duration of the pH cycling experiment.

3.1.3 Mechanical Properties & Morphology

The last part of the analysis was an investigation into the changes in the mechanical properties and the surface morphology of the enamel blocks. Potential hardness changes were measured using a Vickers' micro-indenter and the morphology was studied using AFM. Further details on the instruments and the analyses parameters can be found in sections 2.3.10 and 2.3.7 respectively. The results are presented below.

3.1.3.1 Micro-Hardness

The results of micro-hardness are presented in Figure 3-12. The results are divided according to the type of solution used during the remineralisation and demineralisation periods. Figures 3-13a, 3-13b, 3-13c and 3-13d contain the groups which were treated with DW only (M1-M4), PF and DW (M5-M8), DW and AC (M9-M12) and PF and AC (M13-M16) with or without the presence of F^- respectively. The results are presented below as the difference in the micro-hardness between the post-experimental and baseline hardness measurements.

The groups treated with DW only present relatively stable micro-hardness although some minor increase can be observed in the case of the groups treated with 10 ppm or 250 ppm of F^-. Significant increase in hardness is observed for both the groups treated with PF and DW (M4-M8) and PF and AC (M13-M16), which is higher for the groups which were treated with the F^- treatment; while those treated with BF only present values similar to those for which no fluoride was used. The hardness increase is also higher for the groups treated with PF and AC, than with PF alone. Finally, significant is the decrease in the surface hardness of the groups treated with DW and AC (M9-M12), which is higher when no F^- was used, followed by those which contained BF only, then those treated with 10 ppm and finally the groups treated with 250 ppm of F^-.

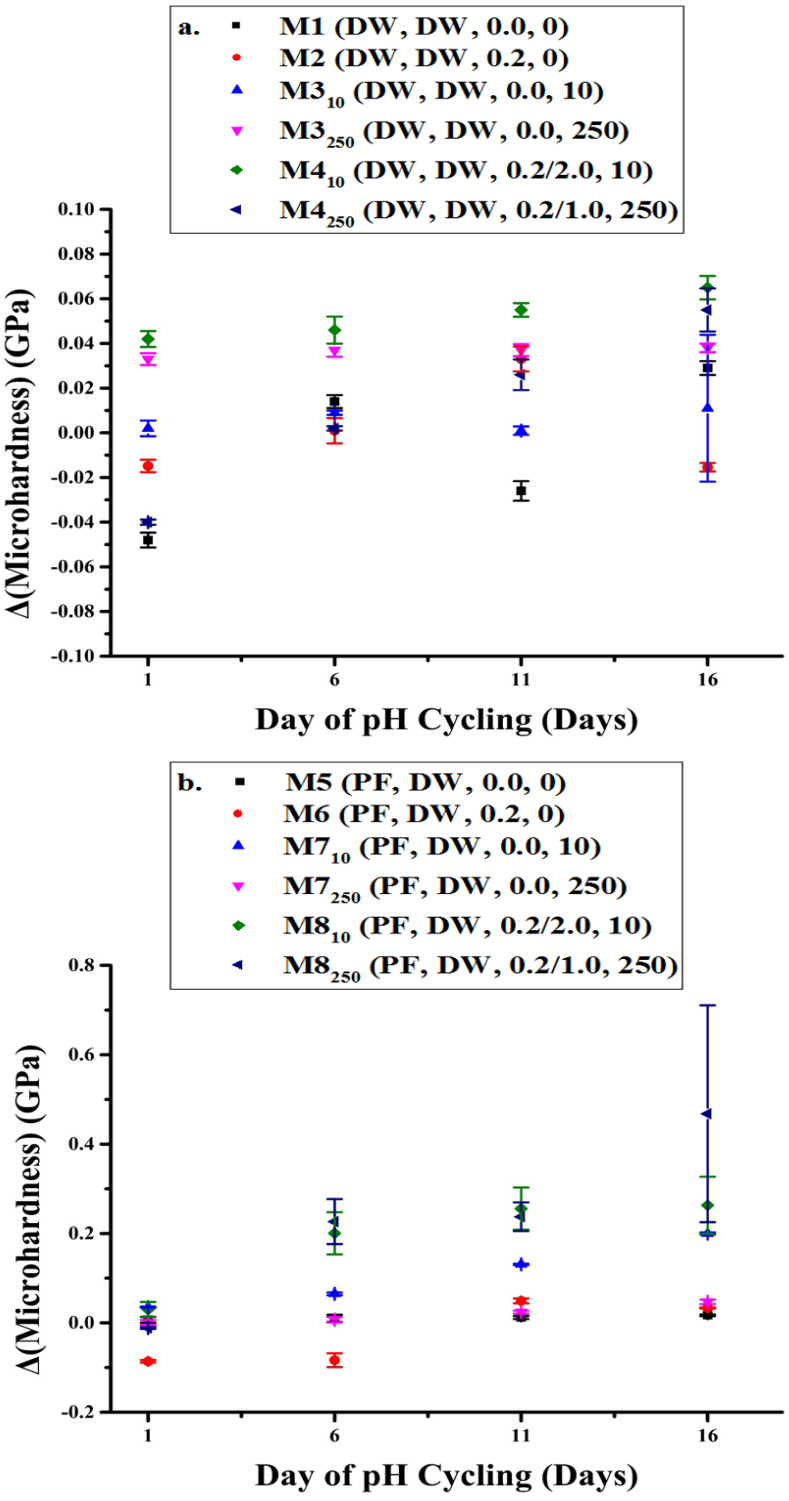

Figure 3-13: Changes in surface enamel hardness for the blocks treated a. only with DW and with or without F^- treatments (M1-M4), b. with PF, DW and with or without F^- treatments (M5-M8), c. with DW, AC and with or without F^- treatments (M9-M12) and d. PF, AC with or without F^- treatments (M13-M16).

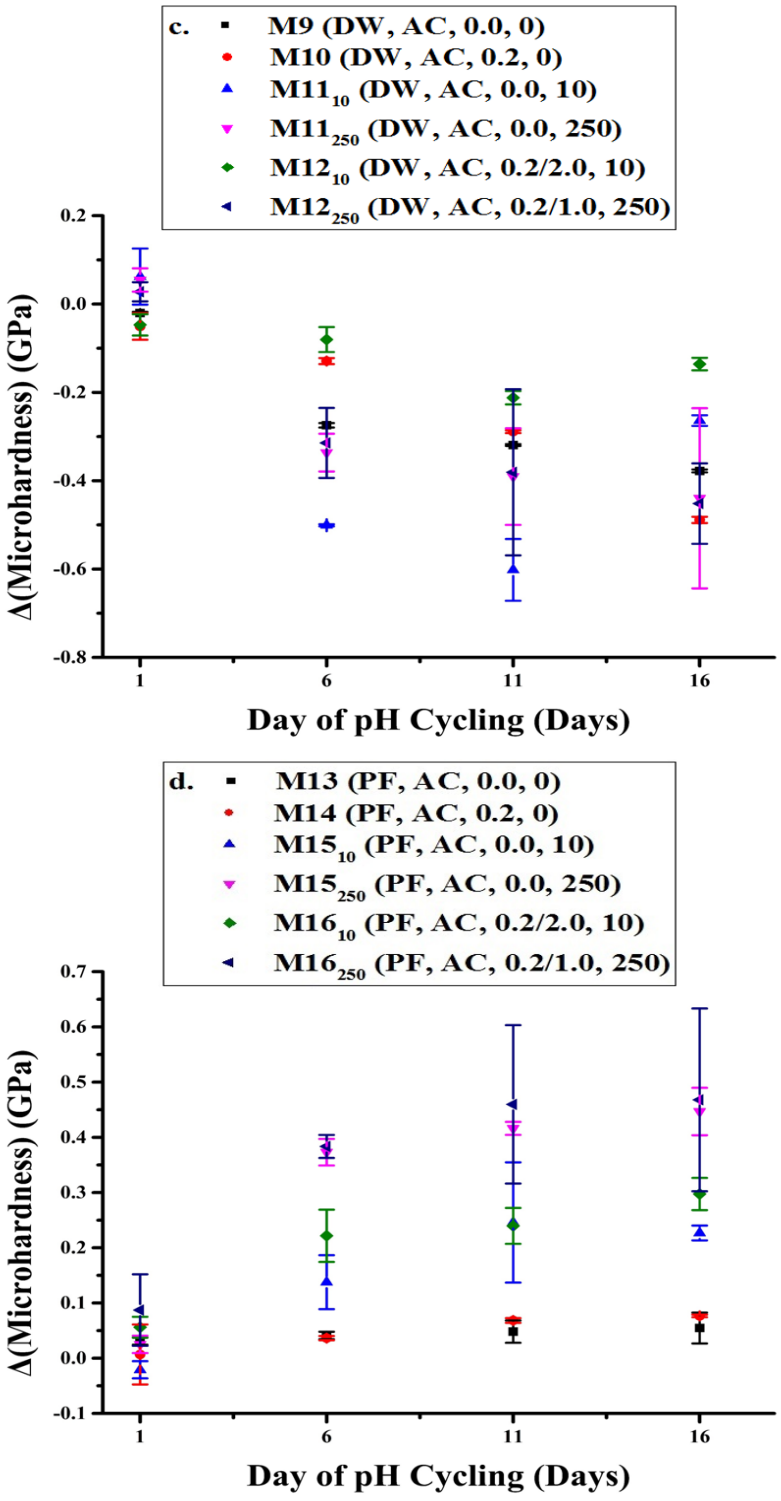

Figure 3-13 (Continued): Changes in surface enamel hardness for the blocks treated a. only with DW and with or without F^- treatments (M1-M4), b. with PF, DW and with or without F^- treatments (M5-M8), c. with DW, AC and with or without F^- treatments (M9-M12) and d. PF, AC with or without F^- treatments (M13-M16).

3.1.3.2 Surface Morphology

The last part of the analysis has to do with the changes on the morphology of the surface of the enamel blocks due to the pH-cycling procedure. Some characteristic results are presented below.

Figures 3-14 and 3-15 present the morphology of enamel blocks originating from groups $M8_{10}$ and $M8_{250}$, which were treated with PF and DW with the addition of BF and 10 ppm and 250 ppm of F^- respectively. The image on the right is the surface of the enamel shortly after its removal from the experimental solutions, while on the left the surface following the KOH treatment.

In both cases deposition of material can be observed which becomes stronger with time. Besides the loosely bound deposited material, which is removed by KOH, an effect on the surface of the enamel itself is apparent following comparison with the baseline image. The observations are in accordance with the chemical and structural analyses presented in sections 3.2.1 and 3.2.2, which suggest progressively stronger accumulation of Ca^{2+}, PO_4^{3-} and F^- and the precipitation of HA and other phases like OCP and/or TCP.

Figures 3-16 and 3-17 present blocks originating from groups $M12_{10}$ and $M12_{250}$ respectively and were treated with DW and AC with the addition of BF and with 10 ppm and 250 ppm of F^- respectively. Some KOH soluble material deposition is evident during the first half of the experimental procedure, which is followed by strong dissolution as the resemblance between the untreated and KOH treated images suggests, along with the gradual smoothening of the surfaces.

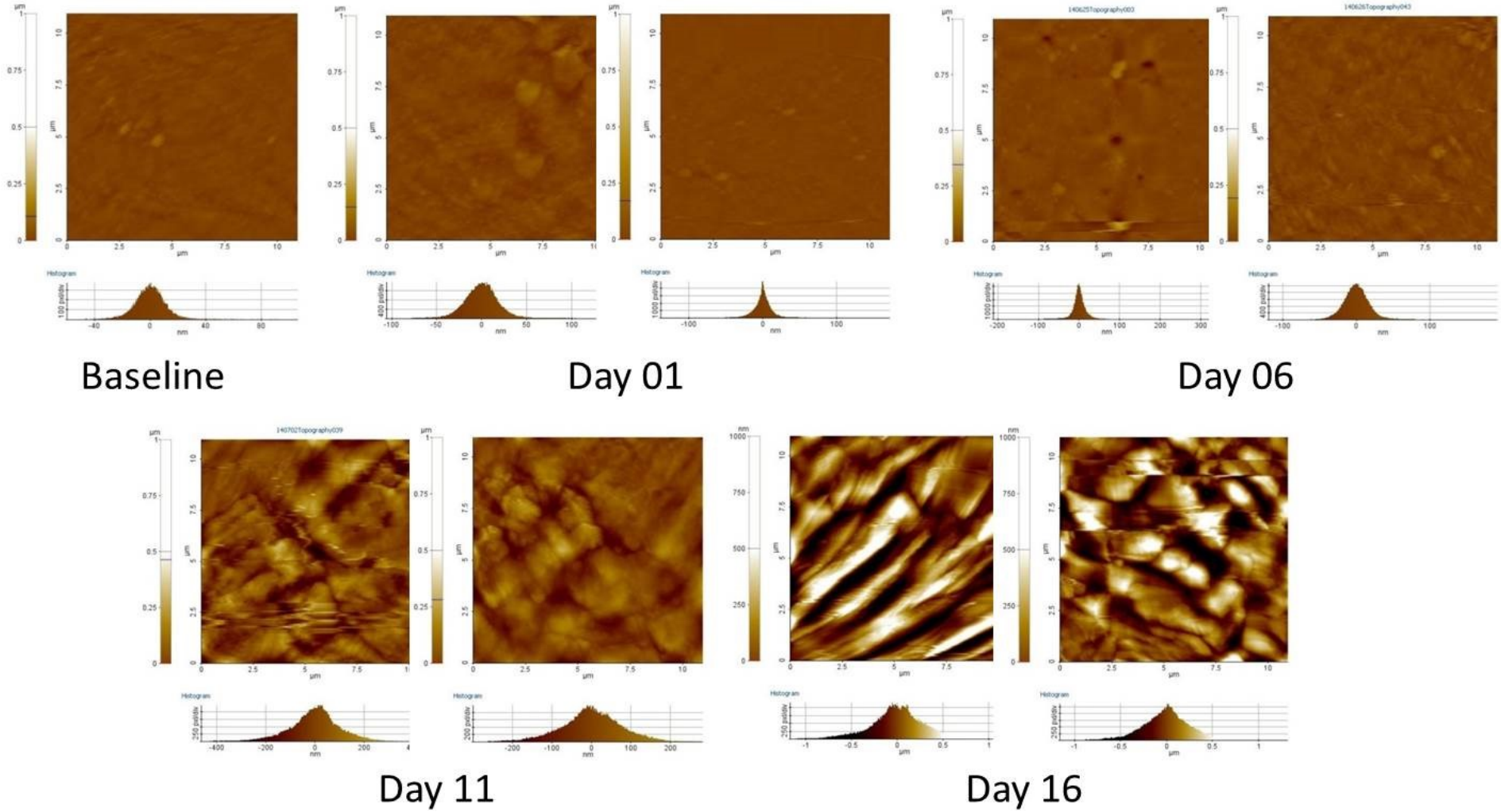

Figure 3-14: Changes in the morphology of the surface of the enamel blocks of Group $M8_{10}$ (PF, DW, 0.2/2.0, 10). In each case, the left picture corresponds to the surface of the enamel block as soon as it was removed from the solutions, while the on the right the same block following the 1 M KOH treatment to remove the loosely bound F^- is displayed.

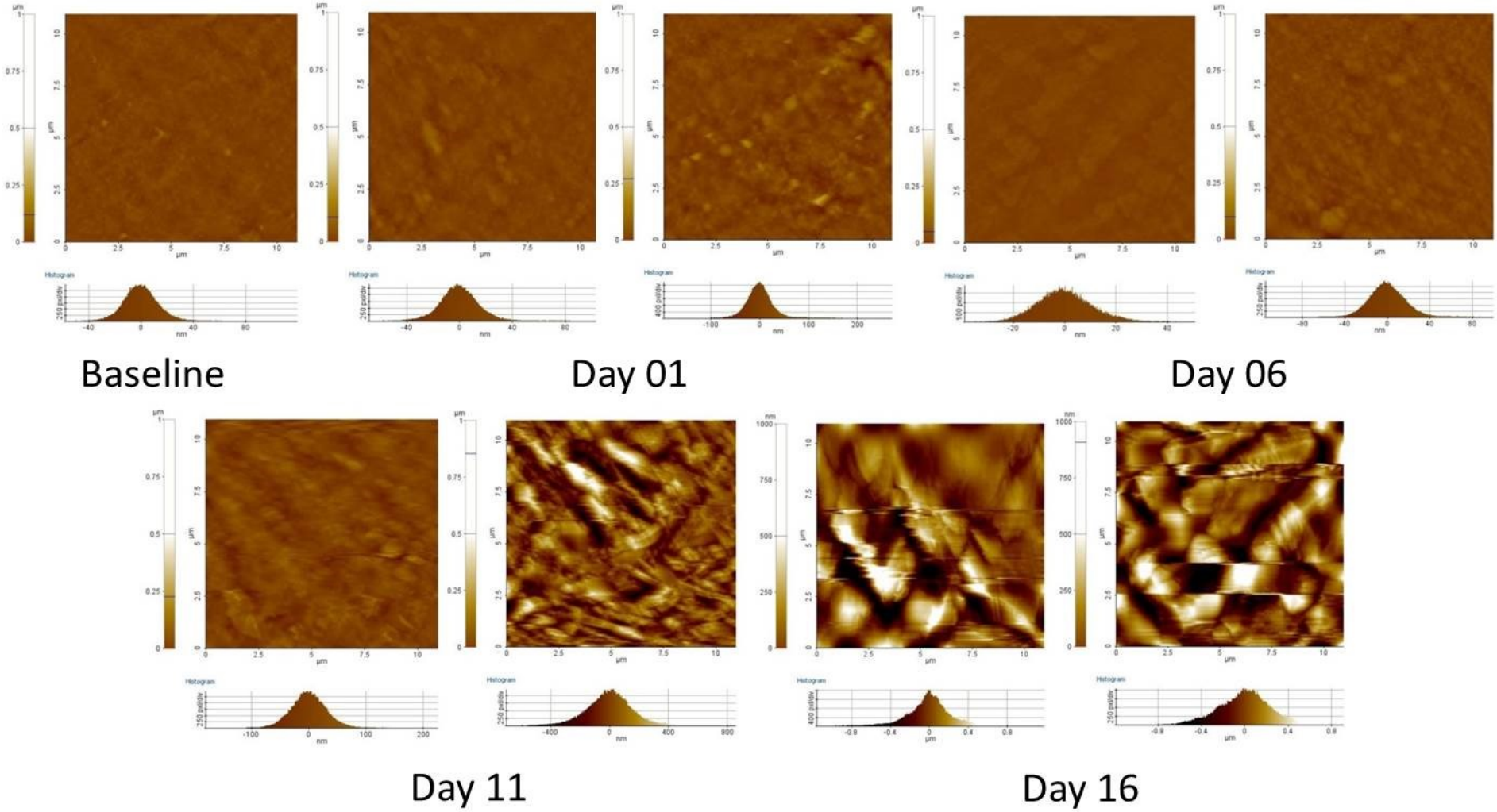

Figure 3-15: Changes in the morphology of the surface of the enamel blocks of Group $M8_{250}$ (PF, DW, 0.2/1.0, 250). In each case, the left picture corresponds to the surface of the enamel block as soon as it was removed from the solutions, while the on the right the same block following the 1 M KOH treatment to remove the loosely bound F^- is displayed.

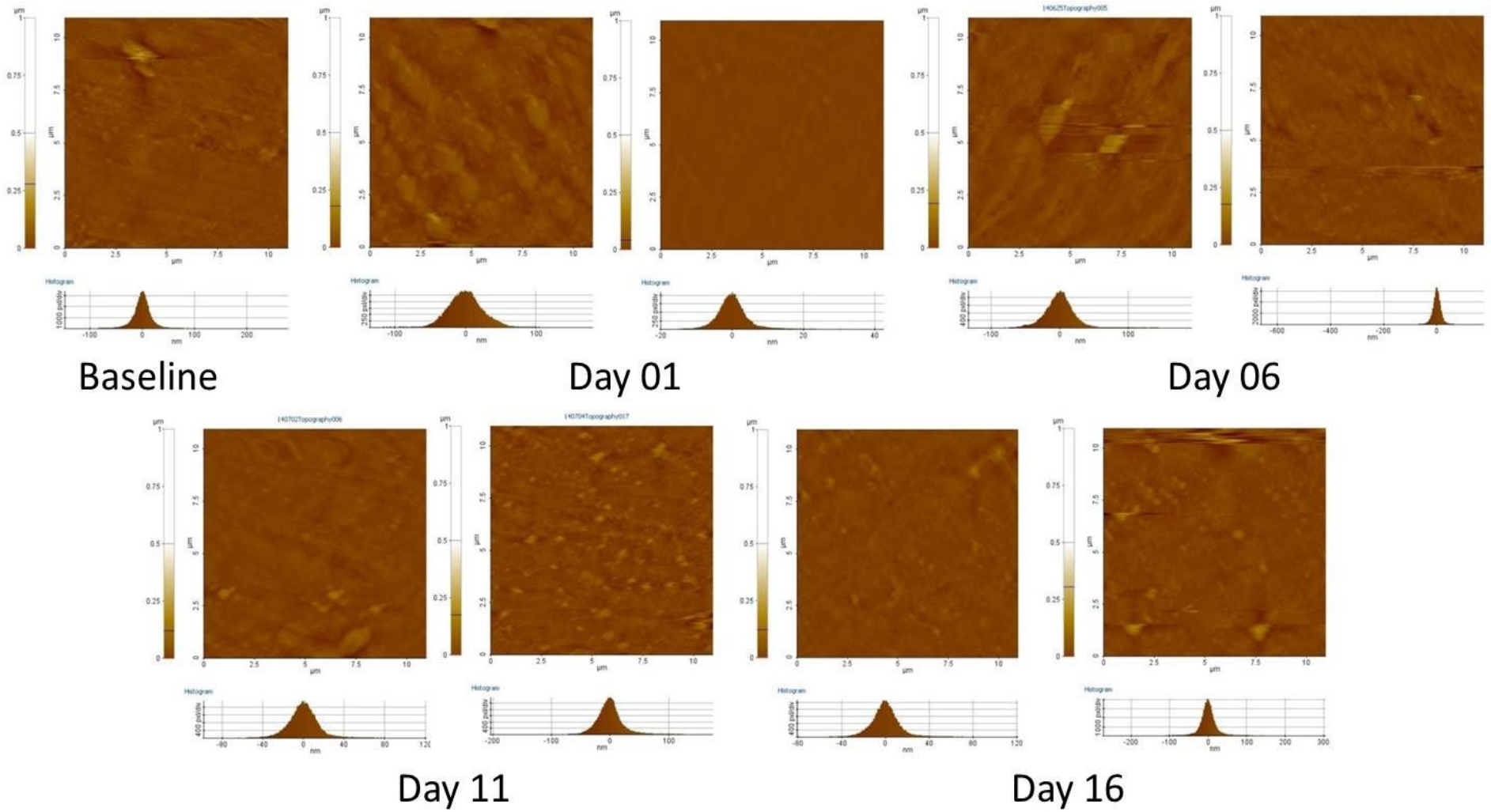

Figure 3-16: Changes in the morphology of the surfaces of the enamel blocks of Group $M12_{10}$ (DW, AC, 0.2/2.0, 10). In each case, the left picture corresponds to the surface of the enamel block as soon as it was removed from the solutions, while the on the right the same block following the 1 M KOH treatment to remove the loosely bound F^- is displayed.

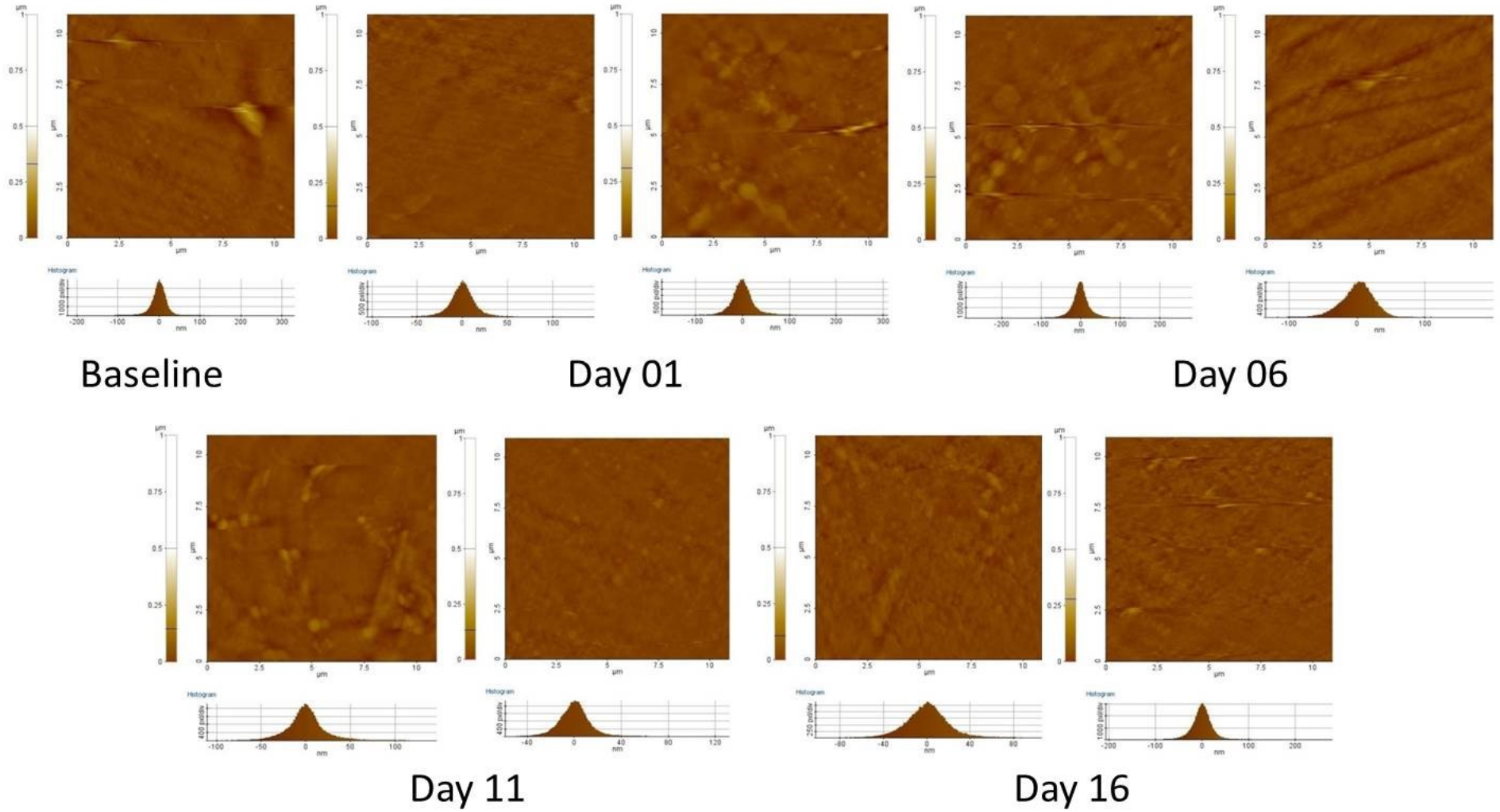

Figure 3-17: Changes in the morphology of the surface of the enamel blocks of Group $M12_{250}$ (DW, AC, 0.2/1.0, 250). In each case, the left picture corresponds to the surface of the enamel block as soon as it was removed from the solutions, while the on the right the same block following the 1 M KOH treatment to remove the loosely bound F^- is displayed.

Finally, images 3-18 and 3-19 present blocks treated with the full pH-cycling model for both the 10 and 250 ppm F^- treatment respectively. In both cases, it can be observed that there is strong deposition of material on the surface of the enamel blocks, which is KOH soluble. This is mainly CaF_2 as can be seen on Day 11 of the $M16_{250}$ group. The effect of the pH-cycling on the actual surface of the enamel blocks can also be observed. The anomalies on the surface of the enamel, especially on Day 16, suggest that enamel dissolution probably takes place which is then followed by precipitation of material which is firmly deposited on the surface creating an amorphous (non-prismatic layer). The observations are in accordance with the chemical analysis presented earlier and denote progressively stronger Ca^{2+}, PO_4^{3-} and F^- uptake; as well as with the structural analysis during which the F^- accumulation and the formation of HA and secondary phases like OCP and/or TCP takes place.

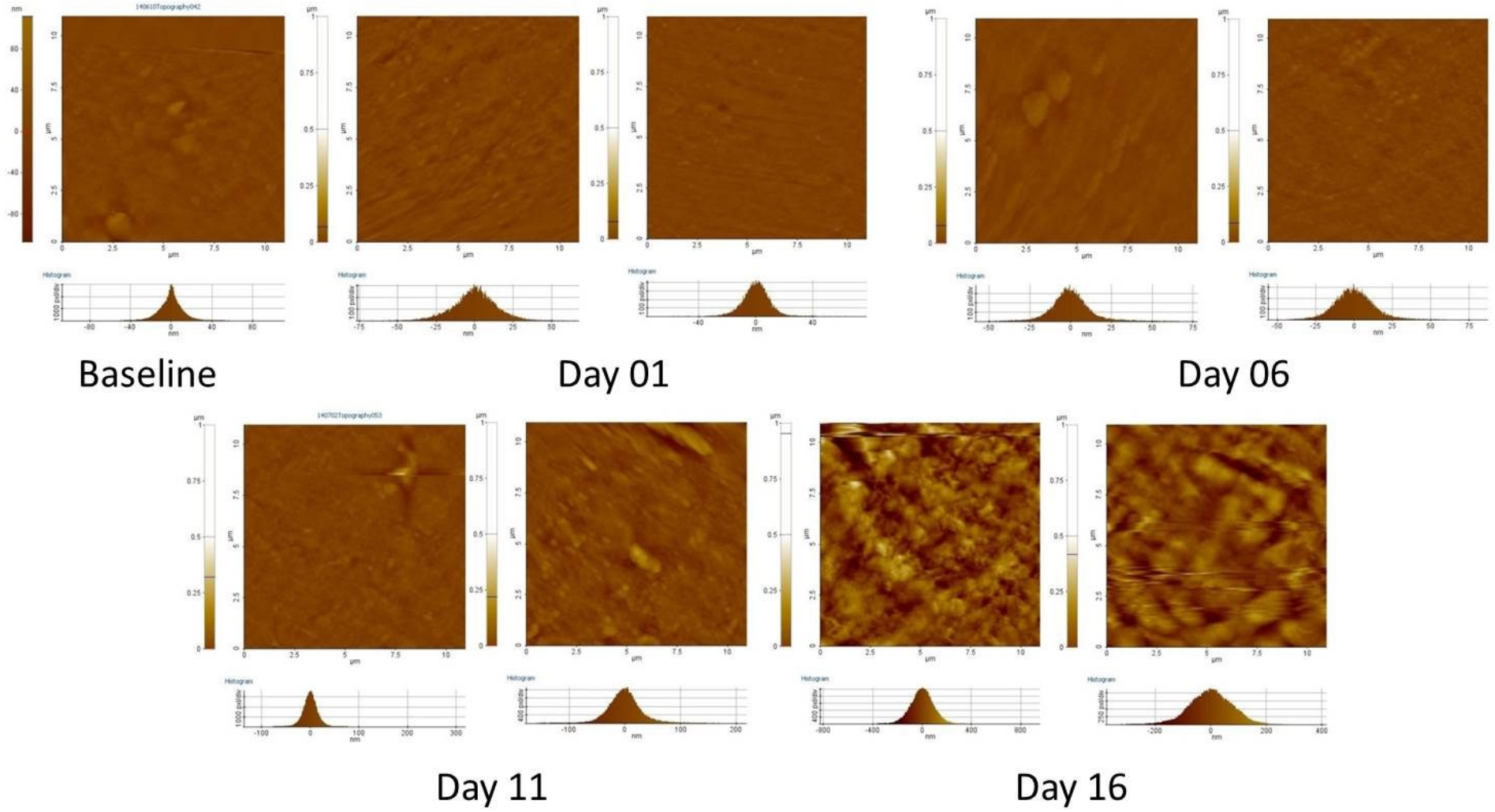

Figure 3-18: Changes in the morphology of the surface of the enamel blocks of Group $M16_{10}$ (PF, AC, 0.2/2.0, 10). In each case, the left picture corresponds to the surface of the enamel block as soon as it was removed from the solutions, while the on the right the same block following the 1 M KOH treatment to remove the loosely bound F^- is displayed.

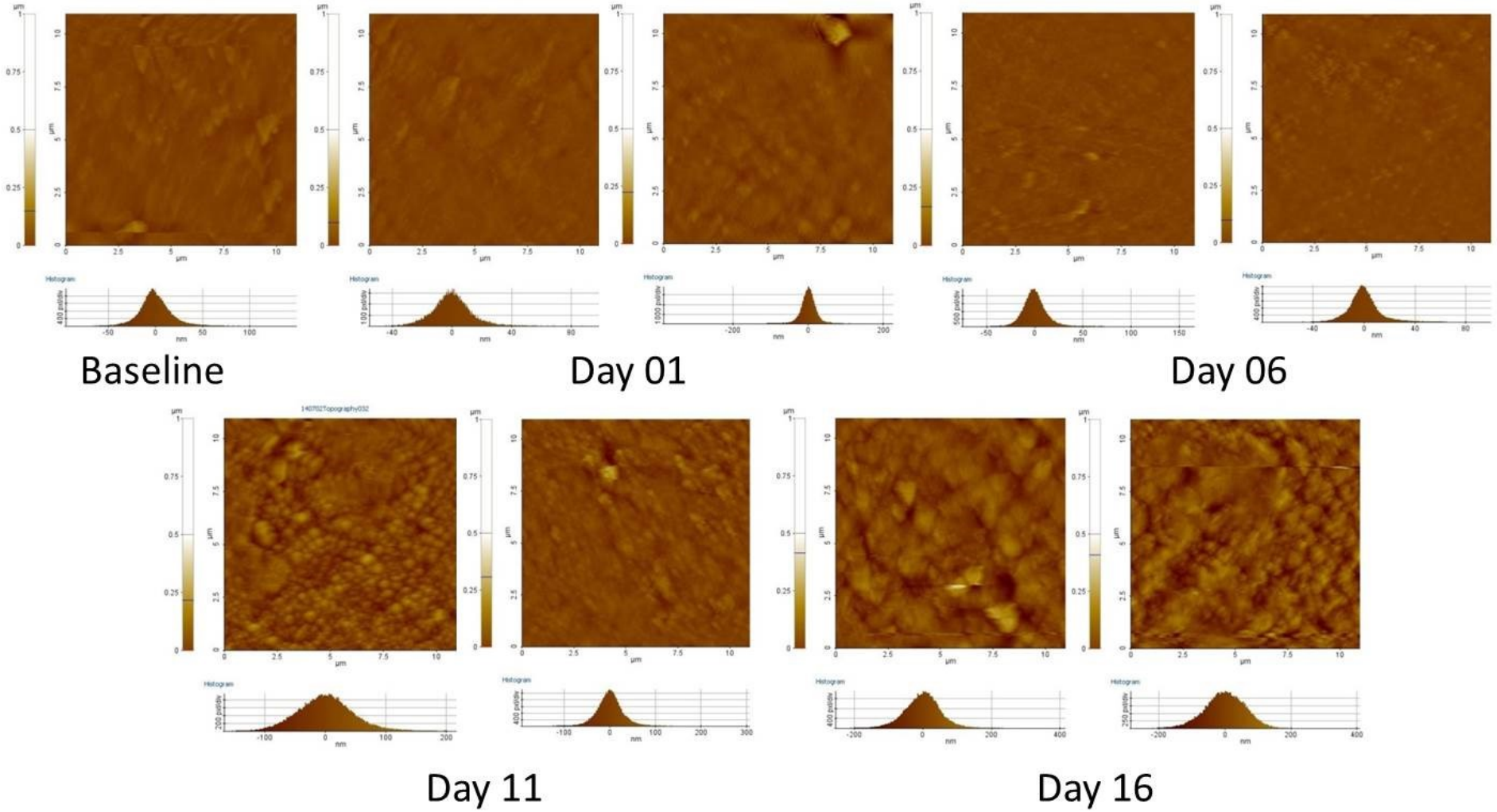

Figure 3-19: Changes in the morphology of the surface of the enamel blocks of Group $M16_{250}$ (PF, AC, 0.2/1.0, 250). In each case, the left picture corresponds to the surface of the enamel block as soon as it was removed from the solutions, while the on the right the same block following the 1 M KOH treatment to remove the loosely bound F^- is displayed.

3.1.4 Discussion

Section 3.1 presented a simulation of PEM of permanent bovine enamel and the proposed (398) mechanism governing the whole process. To monitor potential physicochemical changes taking place through the interaction of the surface of the enamel with the oral fluids, a pH-cycling model was employed which mimicked the oral environment and most significantly the dynamics taking place during mineral changes and caries formation (405, 424). The model contained sequential cycles of F^-, demineralising and remineralising periods; which correspond to the effect of tooth-brushing, plaque fluid and the acid conditions existing shortly after a meal with fermentable carbohydrates respectively (405, 429). To overcome the limitations of the pH-cycling models (405, 424, 425), the process was redesigned and an extra remineralisation step was added, which mimicked the transition from the "peak" concentrations observed in the plaque immediately after brushing and the low concentration (retention) phase observed during the rest of the day (430-432). The effect of retention phase F^- was studied through the addition of the appropriate amount of F^- within the remineralising and demineralising solutions (430-432).

Post-eruptive maturation is generally considered to be a long-term process (76, 104, 106, 107), the end of which is not precisely defined (88, 317, 318, 500) and generally considered to be of surface nature (86-88, 91). This is due to the morphological changes observed, in the form of a precipitated surface layer which is thicker, more acid resistant (87, 88, 323, 332), less porous (76, 91, 109) and harder (104, 105, 320) than the original enamel. These studies are in agreement with the results acquired during the present study, where a continuous increase in hardness with time (section 3.1.3.1), along with morphological changes of the surface of the pH-cycled enamel blocks (section 3.1.3.2) have been observed.

While the effects of PEM are widely accepted and studied (27) a clear mechanism to describe the process does not exist although a few have been proposed in the past (398, 501, 502). In fact, the processes of PEM and remineralisation were considered to be completely distinct (341, 503, 504) and that PEM was governed by the growth of the enamel crystallites, while remineralisation was the result of material deposited in the interprismatic space. At the same time, sequential remineralisation and demineralisation cycles resulted in mineral exchange of the enamel with the oral environment and led it to its initial condition through the re-deposition of the removed material (504).

Later on, it was proposed that PEM was the combination of acid demineralisation, which was followed by remineralisation through the uptake of Ca^{2+} and PO_4^{3-} following interaction with the oral fluids and could be significantly enhanced with the use of remineralising agents and especially F^- (51, 102, 398, 505-507). The reason behind the lack of a clear mechanism could be due to the fact that although the PEM period starts as soon as the tooth starts to erupt inside the oral cavity, the gums covering the tooth, the increased sensitivity and the accumulated plaque observed during this period make it hard to study the changes taking place during this period. At the same time, proper cleaning and fluoridation of the enamel is also hard (27, 398, 432), which in combination with the accumulated plaque make the enamel more caries prone (321, 322, 342). As a result, less F^- reaches the enamel although it has been proposed that PO_4^{3-} (346, 347) and F^- (348, 353) uptake is higher during this period and this is why sigificant decrease in caries susceptibility is also observed (508, 509).

The aforementioned reasons are why part of the enamel groups studied were treated with 10 ppm of fluoride; while the rest were treated with 250 ppm, which corresponds to the amount of F^- reaching the enamel surface during different states of plaque accumulation when toothpastes containing the minimum effective anti-caries concentration of 1000 ppm are being

used (441). The 250 ppm concentration used corresponds to the amount of F^- reaching the surface of a fully cleaned from the plaque tooth (443-445) when the 1:3 dentifrice dilution with the saliva (439-441) is taken into account and the 10 ppm is the estimated PF F^- concentration shortly after tooth-brushing (431).

One of the main and significant effects of PEM on enamel is hardness increase. Such an increase is observed during the experimental procedure for both F^- concentrations (Figure 3-13), which is correlated with Ca^{2+} uptake during the main remineralisation period (ANOVA, $p < 0.02$) and to the author's knowledge it is the first time that it is observed in sound enamel during *in vitro* experiments. At the same time, strong correlation between the Ca^{2+} and F^- uptake also exists ($p = 0.02$), as well as between Ca^{2+} and PO_4^{3-} uptake ($p < 0.05$) during the intermediate remineralisation period. The observed hardness increase is in agreement with previous studies monitoring the post-eruptive changes of human and bovine enamel and has been mainly attributed to the precipitation of more acid resistant phases like HA, fHA and FA on the surface of the enamel in the form of a prismless surface layer (see Figure 1-12) (104-107, 341, 510). These changes probably correspond to the observed changes in the surface morphology of the pH-cycled enamel blocks through AFM imaging (Section 3.2.3.2).

The chemical and structural changes which could result in subsequent hardness increase were monitored through FTIR (Section 3.1.2). HA presence is mainly denoted by the appearance and increase in intensity of the modes around 1020 cm^{-1} (484-486), 1050 cm^{-1} (487, 488) and 1120 cm^{-1} (489, 490), which correspond to the υ_3 PO_4^{3-} mode; and is observable for all groups which used PF during the remineralisation treatment. Weak peaks around 1020 cm^{-1} are also observed for the groups which were treated with DW and AC as the remineralisation and demineralisation challenges respectively. These peaks are correlated with newly precipitated

and poorly crystalline HA and their shift towards higher wavenumbers with time denotes material maturation and increase in crystallinity (484, 485).

This conclusion is further supported by the increase in intensity of the HPO_4^{2-} peaks between 1900 cm^{-1} and 2200 cm^{-1}, which correspond to HPO_4^{2-} and the presence of mature HA (492, 511) and the significant decrease in CO_3^{2-} content; which is expressed through the significant decrease of the total surface areas of the υ_4, υ_2 and υ_3 CO_3^{2-} modes observed around 700 cm^{-1}, 850 cm^{-1} and 1450 cm^{-1} respectively. Such changes are in accordance with older *in vitro* studies which either studied extracted human teeth or conducted *in vitro* carious attacks of varying ages and pointed out the loss of pre-existing enamel impurities during PEM (52, 78, 79) and especially carbonate the presence of which can reach up to 3% per volume inside the enamel (512).

While CO_3^{2-} decreases with time, incorporation of F^- inside the enamel structure takes place, which is expressed through the increase in the intensity of the peak around 750 cm^{-1} and corresponds to F^--OH^- substitution (479, 480). Fluoride incorporation has been also linked with the decrease in the number and intensity of the υ_3 PO_4^{3-} peaks between 540 cm^{-1} and 615 cm^{-1} (513) and the continuous decrease, and in some cases disappearance, of the OH^- liberation mode around 630 cm^{-1} (479, 491); changes which were also observed during the current experimental procedure.

Although the degree of F^- accumulation is correlated with the amount of F^- administration, the rate of the process is faster for the groups treated with 10 ppm of F^-. On the other hand, groups treated with 250 ppm of F^- present significantly higher amounts of loosely bound F^-, which is probably in the form of a CaF_2-like material (331-333, 514) as observations in AFM images suggest. This is in agreement with studies claiming that fluoride concentrations below

45 ppm promote its incorporation inside the enamel; while higher promote the deposition of CaF_2-like material, which acts as F^- reservoir and protects the enamel against acid attacks (514, 515).

At the same time, it has been also suggested that topical application of high F^- concentrations can promote the formation of fluoridated HA (516). Although CaF_2 is considered to be an important F^- reservoir (517), it is probably not directly implicated in the PEM process. CaF_2 is not found in PF (518), unless a Ca^{2+} containing pre-rinse is used prior to F^- administration (519). As a result, any potential effects on PEM originate from CaF_2 dissolution and F^- release in the saliva which is then transferred into the plaque and subsequently diffuses towards the surface of the enamel (517), from where it is passively adsorbed on the superficial enamel layers, but not in the deeper layers as modelling studies have pointed out (375).

Another important observation is the presence of peaks corresponding to acidic calcium phosphates like OCP and DCPD. The precipitation of such phases is favoured over HA under low-pH conditions (520, 521) and have been suggested to act as precursors of HA precipitation (295-297, 522) and enamel formation (301-305, 523). Such peaks are those below 540 cm^{-1} and around 1010 cm^{-1} and 1150 cm^{-1}, which correspond to free HPO_4^{2-} (481-483, 497) and υ_3 PO_4^{3-} (484, 498, 499) respectively.

The appearance of these peaks is accompanied by significant increase in intensity during the first half of the pH-cycling study, which is then followed by rapid decrease and probably signifies apatite formation through epitaxial growth (524, 525) and OCP hydrolysis (119, 271, 296, 526). This conclusion is also supported by the continuous intensity increase of the peaks correlated with the presence of newly precipitated HA and especially the υ_3 PO_4^{3-} around 1020 cm^{-1} (484-486), which peaks earlier when background F^- is present. As a result, it is possible

that during the proposed PEM mechanism (398), a gradual process occurs, involving the remineralisation of demineralised superficial enamel through the epitaxial growth of apatites and the incorporation of F^- through the plaque.

A similar process has been observed during HA crystal growth studies (228, 298, 527, 528); and is stimulated by the presence of F^-, which favours the formation of FA and fHA in neutral pH conditions (529). It has also been demonstrated in simulated enamel mineralisation studies during amelogenesis (310, 530, 531) and observed during dentine formation, during which OCP and HA were found to coexist in the central part and the edges of the same crystal respectively (532). According to Nelson and Barry (1989) the whole process is based on a stepwise mechanism during which the formed OCP crystal grows until a critical size is reached, after which apatite is formed through hydrolysis of the outer OCP crystal and embeds the OCP crystal in the centre of the HA crystal (533). In the case of enamel the presence of 1 or 2 ppm of F^- has been observed to lead to the presence of a mixed OCP and apatite and just apatite system respectively (531). These values correspond to the F^- concentrations used during the intermediate remineralisation period and further support the stepwise epitaxial and OCP hydrolysis HA growth model proposed to take place during PEM.

Finally, of high significance is the strong correlation ($p < 0.05$) observed between the increase in hardness and F^- uptake with the observed Ca^{2+} and PO_4^{3-} uptake during the demineralisation challenge for the groups treated with PF and AC. These results mean that some remineralisation takes place during the demineralisation challenge, most likely through the deposition of fHA and/or FA, and has been also observed for caries-like subsurface lesions treated under acid conditions (144, 534, 535).

Since this study used caries-free enamel blocks, the observed remineralisation could correspond to that of newly formed pre-cavitated caries-like lesions, which are formed on the upper enamel layers (27). This could take place through concurrent enamel dissolution and the deposition of either acidic calcium phosphate phases mentioned earlier, or fluoride containing apatites (536) the precipitation of which is also promoted under low-pH conditions when the plaque fluid is undersaturated with respect to enamel and at the same time supersaturated with respect to acidic calcium phosphates and FA and/or fHA (517).

The suggestion that during PEM a distinct acid resistant (87, 88, 323, 332) and less porous (76, 91, 109) surface layer is formed seems to oppose this hypothesis. The contradiction is overcome if the temporary softening and increase in porosity of the surface of the enamel is considered, which could allow further ionic diffusion resulting either in enamel remineralisation (144, 534, 535) or deposition of material in the interstices between the enamel prisms (91-93, 101, 102). Under neutral pH conditions though, surface enamel remineralisation may take place, which blocks the pores of surface enamel and hence the diffusion of Ca^{2+}, PO_4^{3-} and F^- in the deeper enamel layers (537, 538).

The conclusions of the current section support one of the proposed PEM mechanisms. PEM could take place through the dissolution of the underlying enamel under low-pH conditions and the creation of superficial sub-clinical caries-like lesions, which then remineralise through the crystal growth of HA or fHA or FA. This can take place in two ways. Firstly, following a hydrolysis process during which precipitation of acidic calcium phosphates (e.g. OCP) takes place which then hydrolyse into HA, fHA and/or FA through the enhancement of BF; and secondly, by direct precipitation of fHA and/or FA. Under neutral pH conditions surface mineralisation takes place where HA, fHA and/or FA is precipitated and deposited on the

surface of the enamel, blocking the existing pores and inhibiting any ionic diffusion towards the underlying enamel.

3.2 pH-Cycling of Pre-Matured Permanent Bovine Enamel

In order to assess the long-term effects of PEM two groups of enamel blocks were treated with the same pH-cycling model used in section 3.1, but the duration of the experimental procedure was extended to 32 days and two separate groups of enamel blocks were treated in order to preserve the samples used during the main pH-cycling study presented in section 3.1. This way it was possible to monitor potential changes in the physicochemical properties of enamel, after it being artificially matured during the first 16 days. This is why sampling and analysis started on the 17th day of the experimental procedure and was repeated every 5 days until the 32nd and final day. The experimental conditions were the same as those used for groups $M16_{10}$ and $M16_{250}$ presented earlier and are displayed in table 3-5. Analyses of the results were performed following the same philosophy as presented in section 3.1.

ID, Solutions & Treatments	**pH Cycling Rounds**		
ID	**$PR1_{10}$**	**$PR2_{250}$**	**Duration**
Remineralising Solution (pH)	6.58	6.58	Main remineralisation period: 5 hrs/ treatment and overnight Intermediate remineralisation period: 30 min/ treatment
Demineralising Solution (pH)	4.90	4.90	20 min/ treatment
Background F^- Concentration (ppm)	0.2	0.2	Same as Remineralising and Demineralising solutions
Background F- Concentration during the intermediate remineralisation period (ppm)	2.0	1.0	Same as the intermediate remineralisation period
Brushing F^- Concentration (ppm)	10.0	250.0	2 min/ treatment

Table 3-5: Experimental conditions for the groups studied during the extended pH-cycling study. The groups presented were treated with plaque fluid proxy, acid challenge and F^- treatment of 10 ppm or 250 ppm. The subscript used in the group ID denotes the amount of F^- used during the tooth-brushing simulation.

3.2.1 Chemical Analysis

Section 3.2.1 presents the chemical analysis of the solutions used for the treatments presented in table 3-5. Similarly, to section 3.1.1 the Ca^{2+} results are presented first and are followed by PO_4^{3-} and finally F^-. Again, the results are presented as the difference from the baseline (i.e. the respective concentration of the solutions prior to the treatment). This means that positive values denote adsorption of the respective element from the synthetic pellets, while negative results correspond to release inside the solutions.

3.2.1.1 Calcium Results

The first part of the chemical analysis describes the changes in Ca^{2+} concentration inside the solutions used during the remineralisation and demineralisation periods for the duration of the pH-cycling procedure for the pre-matured (17 first day treatment) bovine enamel. As before, 3 types of solutions have been analysed, two of which corresponded to the remineralisation and one to the demineralisation period. The remineralisation period is broken down into 2 sub-periods: the intermediate and the main remineralisation periods. The former lasted for 30 minutes after the F^- treatment and had elevated BF concentration and the latter the main remineralisation period, which took place between the demineralisation periods and the overnight treatment.

Figure 3-20 presents the changes in Ca^{2+} concentration with time during the total remineralisation period, which originates from the addition of the results of the main and intermediate remineralisation periods. For both groups continuous increase in the amount of Ca^{2+} accumulated was observed during the duration of the pH-cycling procedure, which is in accordance with the trend observed during the final days of the main study (Figure 3-1c, d). During the last days of the experimental procedure a plateau was reached.

The breakdown of the total remineralisation period into its core components (main vs. intermediate, Figure 3-21) demonstrates that in both cases the same pattern was followed, but the uptake is higher for the group treated with 10 ppm of F^- during the intermediate period, while it was similar during the main remineralisation period. Figure 3-22 presents the results obtained during the demineralisation period. A release of Ca^{2+} was observed which plateaued during the second half of the experimental procedure and was similar to the amount of Ca^{2+} obtained during the intermediate remineralisation period.

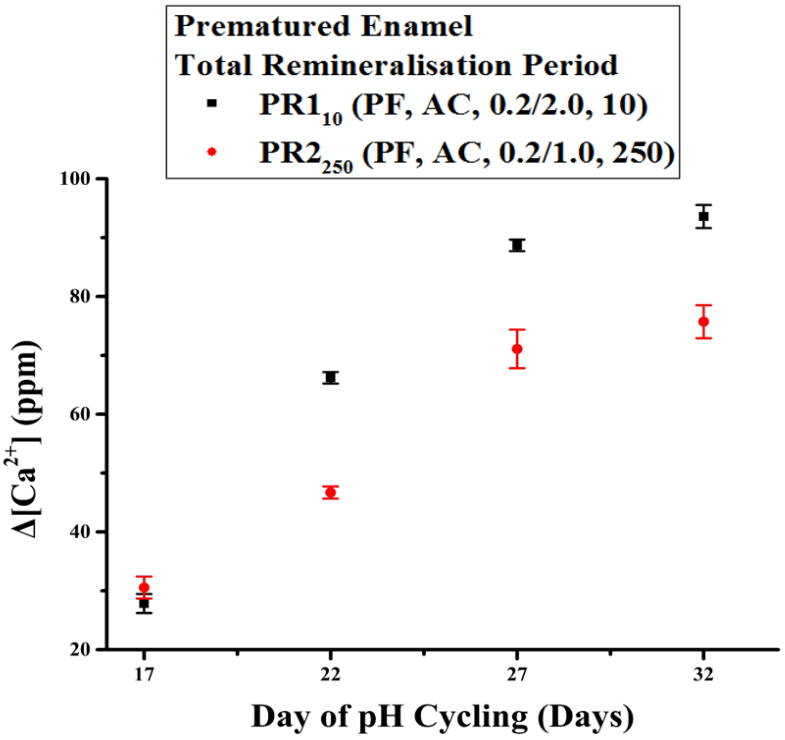

Figure 3-20: Changes in the concentration of Ca^{2+} during the total remineralisation period for the groups treated with 10 ppm of F^- ($PR1_{10}$) and 250 ppm of F^- ($PR2_{250}$) for the pre-matured bovine enamel.

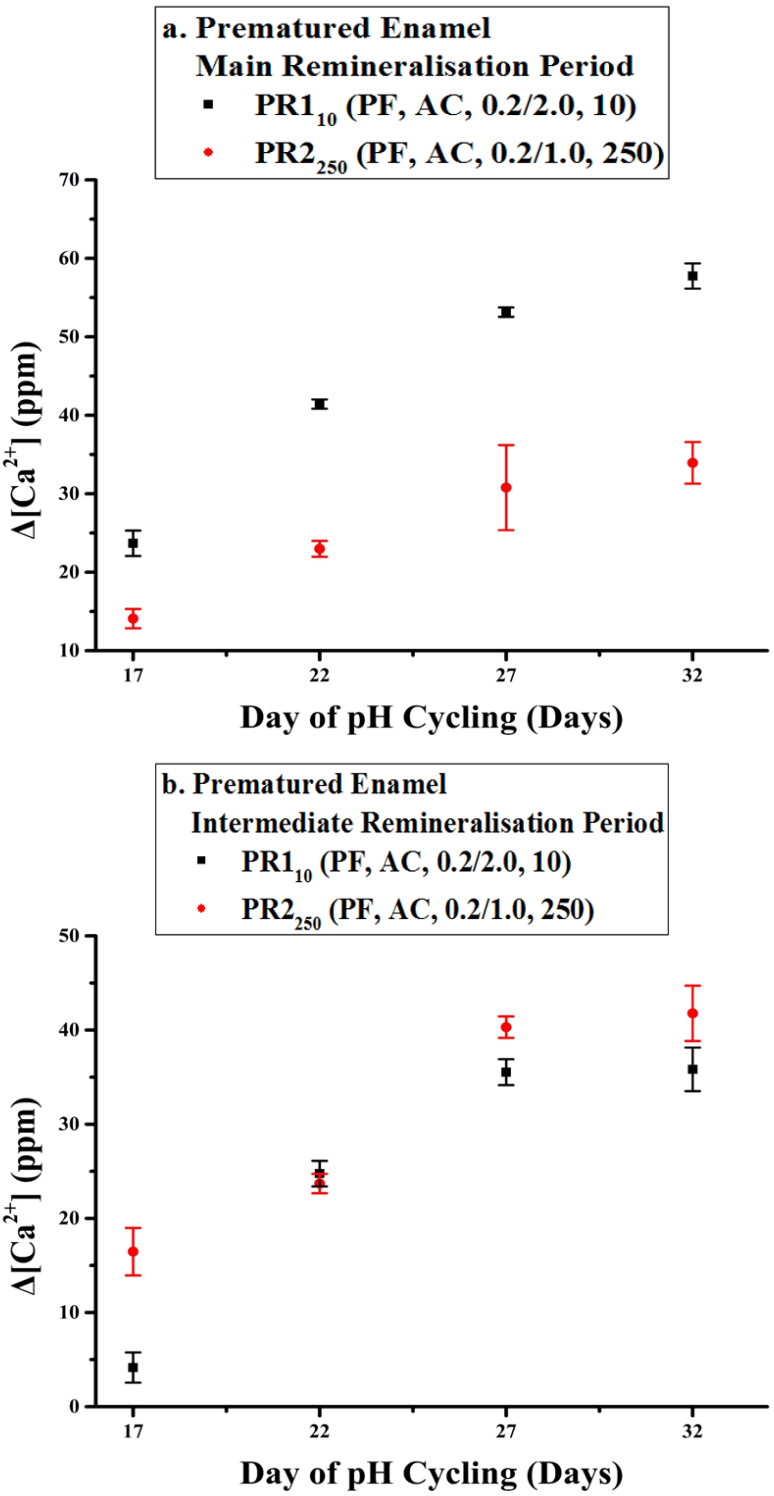

Figure 3-21: Changes in the concentration of Ca^{2+} during the a. main and b. intermediate remineralisation period for the groups treated with 10 ppm of F^- ($PR1_{10}$) and 250 ppm of F^- ($PR2_{250}$) for the pre-matured bovine enamel.

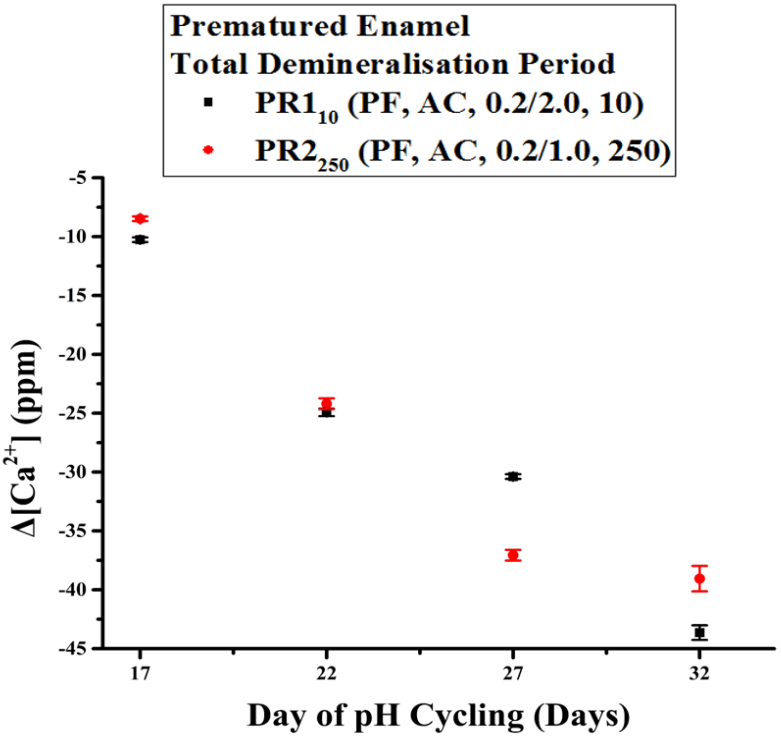

Figure 3-22: Changes in the concentration of Ca^{2+} during the demineralisation period for the groups treated with 10 ppm of F^- ($PR1_{10}$) and 250 ppm of F^- ($PR2_{250}$) for the pre-matured bovine enamel.

3.2.1.2 Phosphate & Fluoride Results

The analyses for the changes in PO_4^{3-} and F^- concentrations are presented below. Figure 3-23 presents the PO_4^{3-} results for the main remineralisation period, which demonstrates continuous increase in the total amount of phosphate accumulated up to day 22 and 27 for the groups treated with 10 ppm and 250 ppm of F^- respectively. In both cases, a significant reduction was observed on day 32, while the accumulation is higher for the 10 ppm treated group. Figure 3-24 demonstrates that the behaviour was similar for both remineralisation sub-periods although the peak is on day 22 and day 27 for the intermediate and main remineralisation periods respectively. Interestingly enough, uptake of PO_4^{3-} was also observed during the demineralisation period (Figure 3-25).

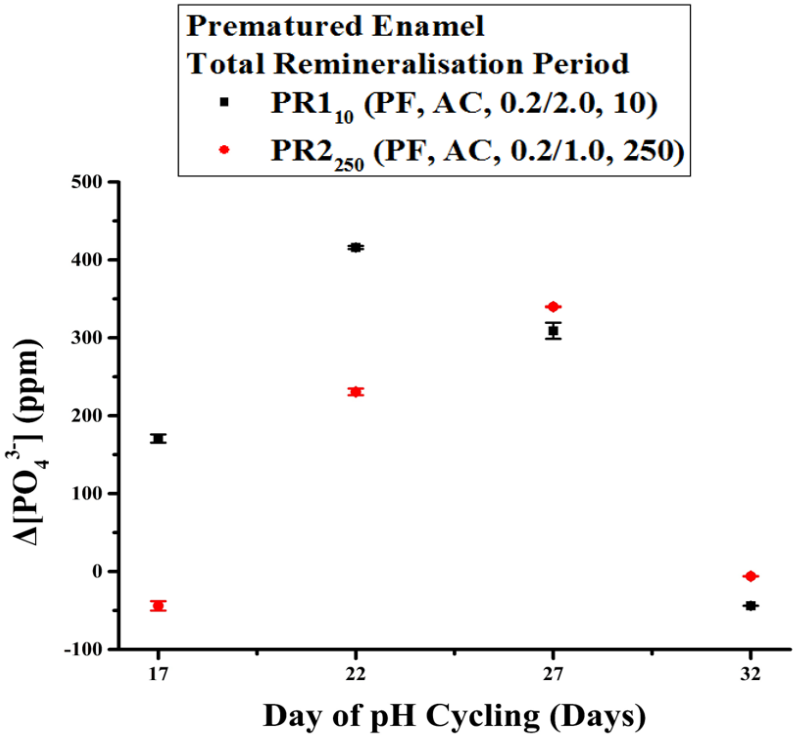

Figure 3-23: Changes in the concentration of PO_4^{3-} during the total remineralisation period for the groups treated with 10 ppm of F^- ($PR1_{10}$) and 250 ppm of F^- ($PR2_{250}$) for the pre-matured bovine enamel.

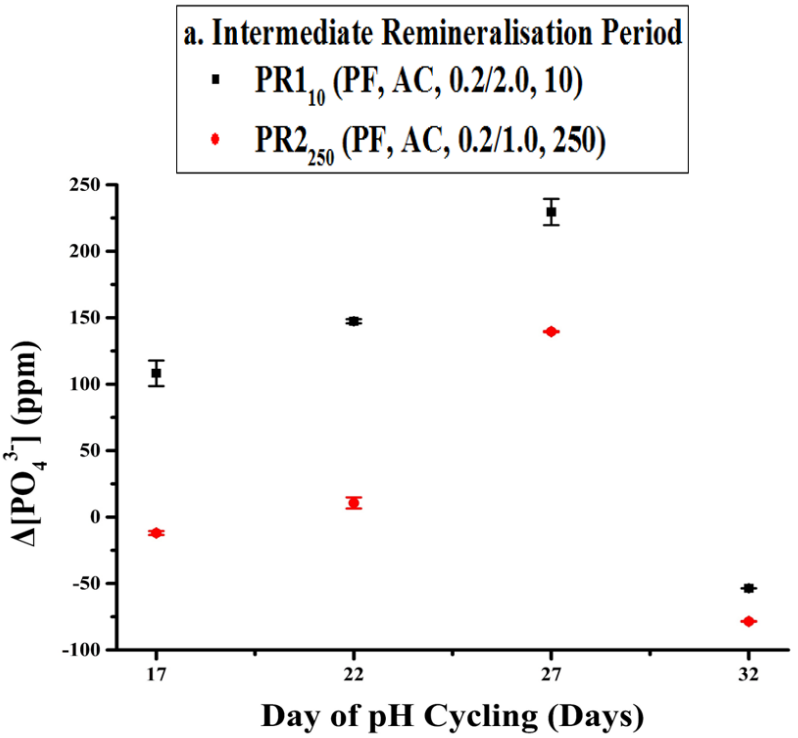

Figure 3-24: Changes in the concentration of PO_4^{3-} during the a. main and b. intermediate remineralisation period for the groups treated with 10 ppm of F^- ($PR1_{10}$) and 250 ppm of F^- ($PR2_{250}$) for the pre-matured bovine enamel.

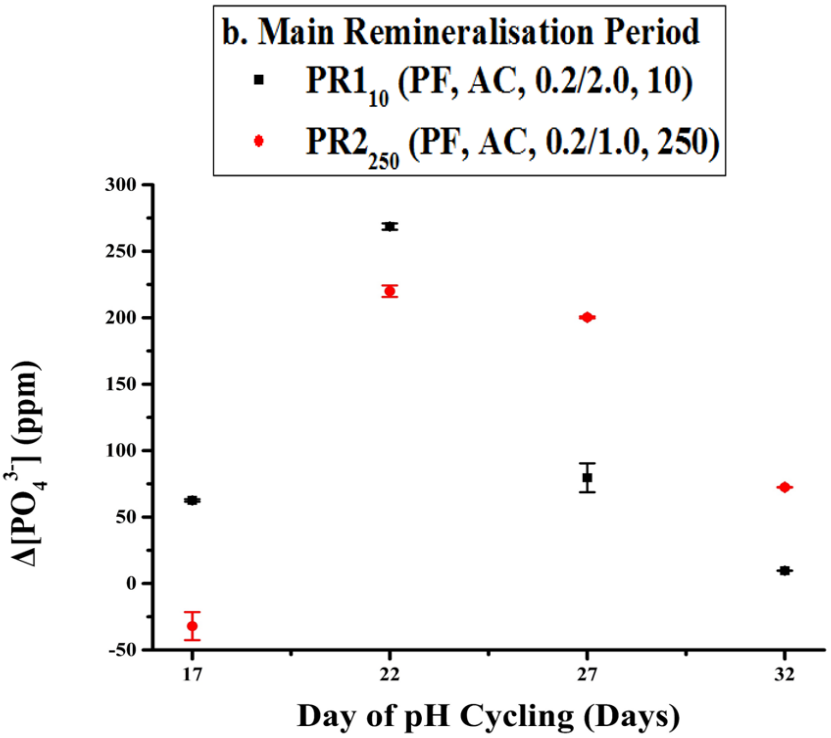

Figure 3-24 (Continued): Changes in the concentration of PO_4^{3-} during the a. main and b. intermediate remineralisation period for the groups treated with 10 ppm of F^- ($PR1_{10}$) and 250 ppm of F^- ($PR2_{250}$) for the pre-matured bovine enamel.

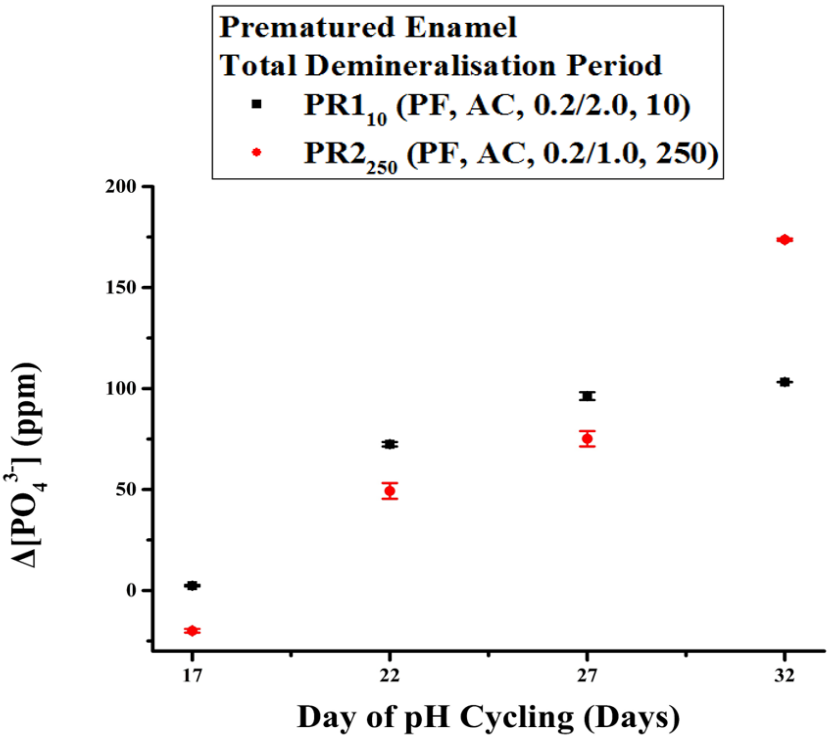

Figure 3-25: Changes in the concentration of PO_4^{3-} during the demineralisation period for the groups treated with 10 ppm of F^- ($PR1_{10}$) and 250 ppm of F^- ($PR2_{250}$) for the pre-matured bovine enamel.

Finally, figure 3-26 presents the changes in the amount of F^- during the pH-cycling procedure. In both cases F^- release took place. The group treated with 250 ppm of F^- presented significantly higher release, which peaked on day 22 and then gradually reversed into positive values. Similar is the behaviour of the group treated with 10 ppm of fluoride, although much lower release is observed. In this case, F^- uptake can be also observed on the last day of the pH-cycling.

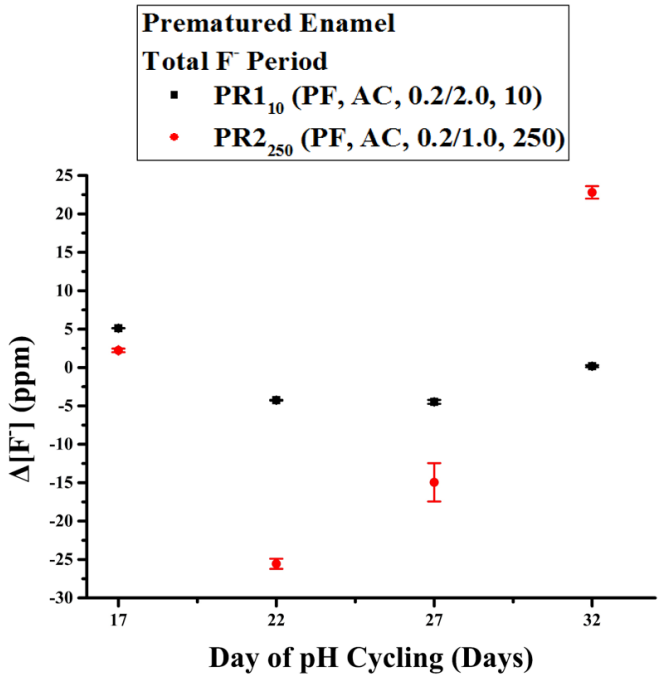

Figure 3-26: Changes in the concentration of F^- during the demineralisation period for the groups treated with 10 ppm of F^- ($PR1_{10}$) and 250 ppm of F^- ($PR2_{250}$) for the pre-matured bovine enamel.

3.2.2 Structural Analysis

FTIR analysis (Figure 3-27) shows that in both cases peaks which are attributed to the υ_4 PO_4^{3-} mode between 540 cm^{-1} and 615 cm^{-1} are present, the number of which is stable throughout the experimental procedure; while gradual decrease in intensity is observed for the group treated with 10 ppm of F^-. At the same time, the OH^- liberation mode (630 cm^{-1}) increases in intensity for both groups, with a simultaneous shift towards higher wavenumbers. The increase is higher in the case of $PR1_{10}$, while the opposite is true for the F^--OH^- peak around 750 cm^{-1}. Noticeable increase is also observed in the intensity of the 1020 cm^{-1} peak, which corresponds to υ_6 HPO_4^{2-} and is correlated with the precipitation of poorly crystalline HA; as well as the peaks between 1900 cm^{-1} and 2200 cm^{-1}, which are attributed to HPO_4^{2-} and well-crystalline HA.

Peaks corresponding to secondary phases like OCP and/or TCP are traced below 540 cm^{-1}, which significantly decrease in intensity by the end of the pH-cycling procedure. Finally, similar are the findings for the υ_2, υ_4 and υ_1 CO_3^{2-} peaks at 700 cm^{-1}, 830 cm^{-1} and 1370 cm^{-1} and 1450 cm^{-1} and 1640 cm^{-1}, which continuously decrease in intensity and have nearly disappeared by day 32, especially in the case of $PR1_{10}$.

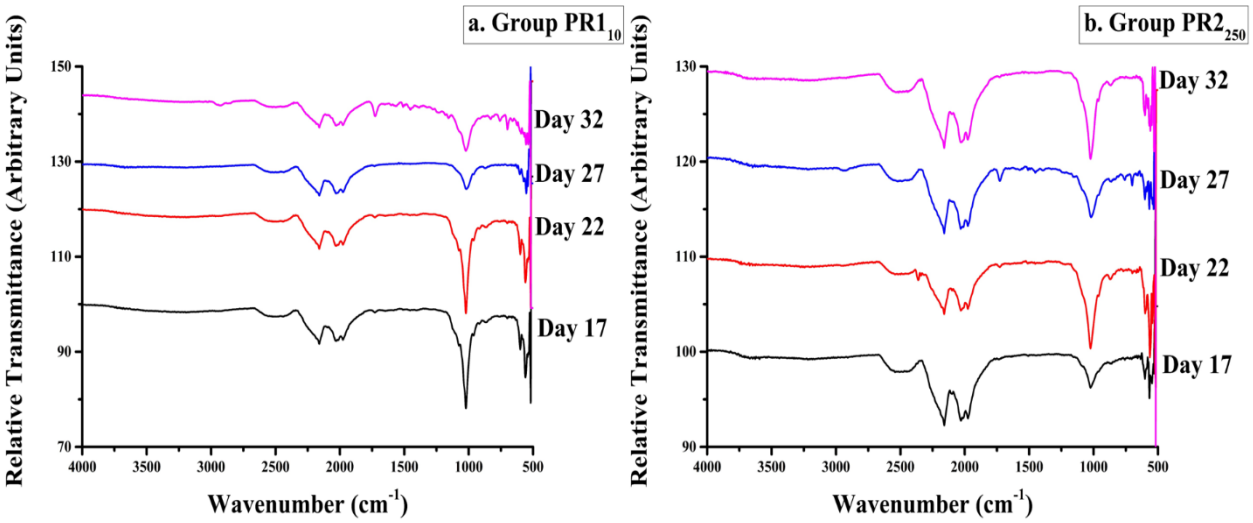

Figure 3-27: FTIR spectra of the pre-matured enamel blocks treated with a. 10 ppm of F^- and b. 250 ppm of F^-.

3.2.3 Mechanical Properties & Morphology

The last part of the analysis presents the changes observed in the micro-hardness and surface morphology of the treated groups. Similar to section 3.1.3.1, micro-hardness results are presented as the difference from the baseline, while sequential images of the surface of the enamel blocks are presented in the case of surface morphology. Further details on the instruments and the analyses parameters can be found in sections 2.3.10 and 2.3.7 respectively.

3.2.3.1 Micro-Hardness Results

The hardness results are presented in figure 3-28. As can be seen there were no major changes in hardness throughout the duration of the extended pH-cycling when compared to the results of the main study (i.e. from day 16), although some slight increase in hardness was still observed, which cannot be attributed to experimental error. Although the blocks measured were not the same as in section 3.1, analysis showed that the changes up to the 16th day of the pH-cycling was similar to that observed during the main pH-cycling study.

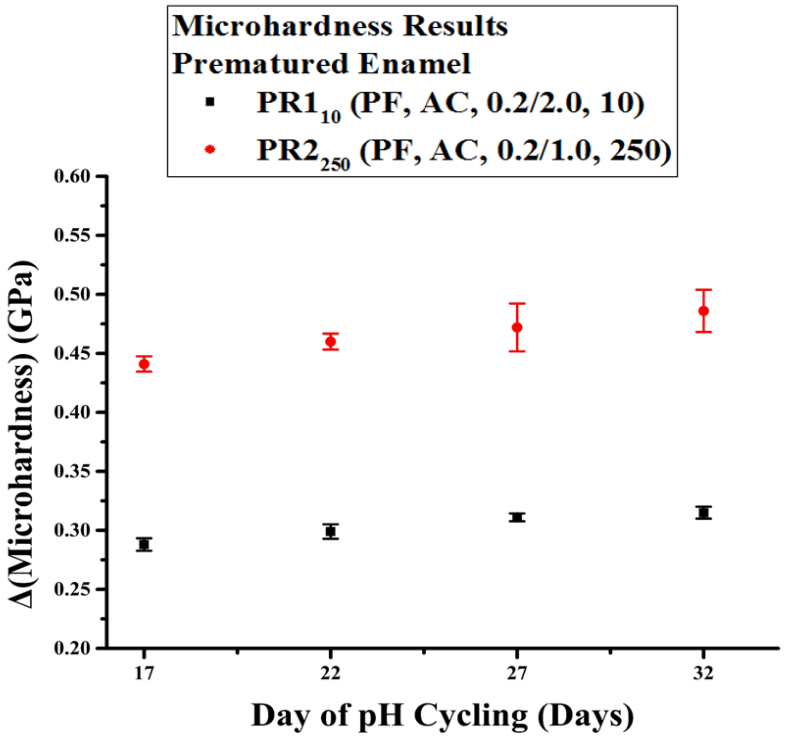

Figure 3-28: Changes in surface enamel hardness for the pre-matured enamel blocks.

3.2.3.2 Surface Morphology

Finally, changes on the surface morphology of the enamel blocks were monitored using AFM. The images are presented in figures 3-29 and 3-30 for groups $PR1_{10}$ and $PR2_{250}$ respectively. In both cases, strong deposition of material was observed, especially for the group treated with 250 ppm of F^-. The results are supported by the chemical and structural analysis presented in sections 3.2.1 and 3.2.2 and are also in accordance with the surface morphology of the respective groups, which were studied in section 3.1 and presented in section 3.1.3.2 (Figures 3-18, 3-19).

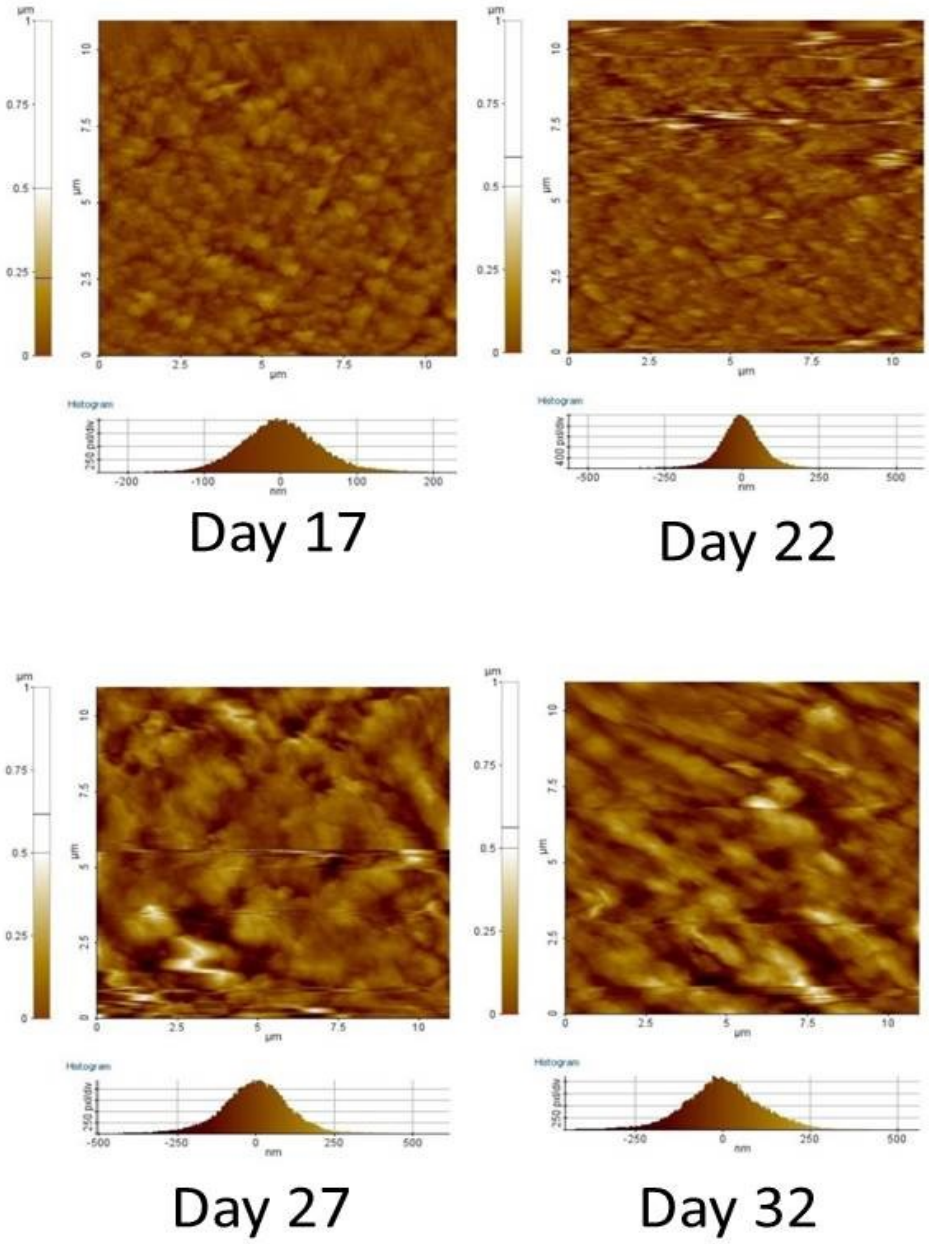

Figure 3-29: Changes in the morphology of the surface of the enamel blocks of Group $PR1_{10}$.

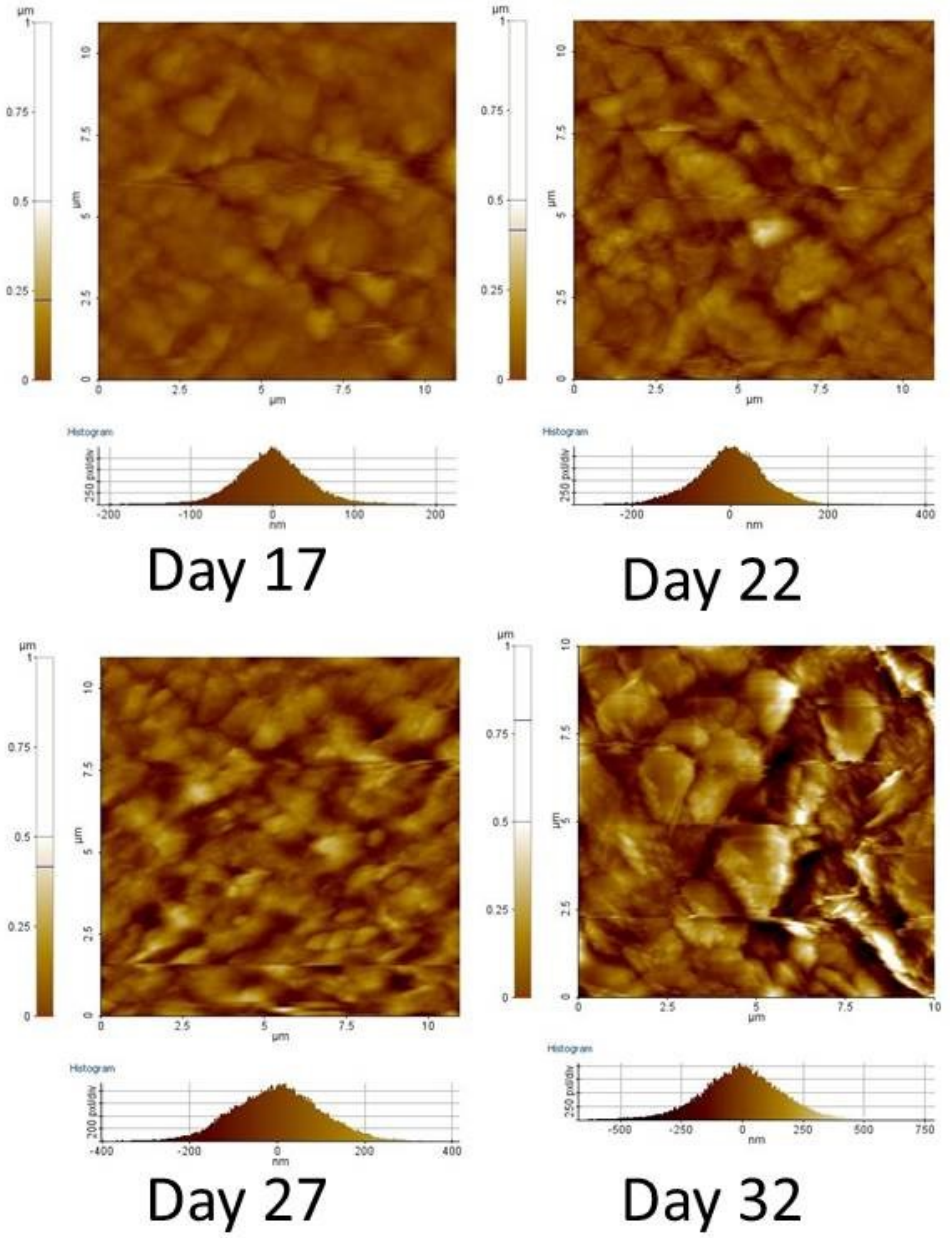

Figure 3-30: Changes in the morphology of the surface of the enamel blocks of Group $PR2_{250}$.

3.2.4 Discussion

PEM is generally considered a continuous process (76, 104, 106, 107), the end of which is not precisely defined. As a result, several proposals have been made regarding its duration, ranging from a few months to lifelong (88, 317, 318, 500). In order to assess longer-term effects and their potential influence in PEM, a group of enamel blocks was treated for 32 instead of 16 days. Sampling started on the 17th day of the experimental procedure and was repeated every 5 days until day 32.

Although the results are generally similar to those presented in section 3.1, the rate of the observed changes has slowed down. While strong Ca^{2+} and PO_4^{3-} accumulation is observed, the rate of hardness increase is lower and is correlated ($p < 0.02$) with Ca^{2+} uptake during the total remineralisation period. Calcium uptake is similar for both treatments during the intermediate remineralisation period, but at the same time significantly higher during that of the 10 ppm treated group. The observation that below 45 ppm, and low pH experimental conditions, F^- incorporation in the enamel is promoted over CaF_2 deposition, as proposed by Mohammed et al. (2013), support the current observations that less CaF_2 may have been deposited on the surface of the enamel blocks, which allowed further interaction with the simulated oral environment. This conclusion is also supported by the PO_4^{3-} results, which present maxima on day 22 and 27 of the pH-cycling for the group treated with 10 ppm and 250 ppm respectively which are followed by rapid decrease.

On the other hand, Ca^{2+} was released during the demineralisation challenges, the amount of which increases with time; but is similar to that accumulated during the intermediate remineralisation period. As a result, the net change in mineral content between the intermediate remineralisation and demineralisation period is close to zero, which suggests that the release is mainly of surface origin either through surface or CaF_2 dissolution. It could also

mean that the upper layers of the underlying enamel have become significantly more acid resistant and further ionic diffusion is limited. Further Ca^{2+} accumulation takes place during the main remineralisation period, along with the increased F^- uptake probably signifies the precipitation of CaF_2-like material, which is deposited on the surface of the enamel blocks. One possible explanation is the finite adsorbing capacity of HA to adsorb F^-, which decreases with time (352, 534). As adsorption continues, a plateau would be reached after which incorporation of extra material inside the enamel would stop (539, 540).

The above conclusions are also supported by the structural and surface morphology results. The υ_3 PO_4^{3-} and υ_6 HPO_4^{2-} modes around 1020 cm^{-1} (484-486), 1050 cm^{-1} (487, 488) and 1120 cm^{-1} (489, 490) which correspond to newly precipitated and maturing HA are stronger than those observed in section 3.1. At the same time, the CO_3^{2-} peaks have significantly decreased or disappeared, while the F^- peak around 750 cm^{-1} (479, 480) is always present and does not significantly increase. Finally, AFM images show strong surface changes in surface morphology of the enamel blocks, for both groups.

The conclusion of section 3.2 is that the *in vitro* results suggest that the extension of simulated PEM will lead to saturation of enamel, which significantly decreases its absorbing capacities and slows down the PEM process. During this time the upper layers of the underlying enamel have become significantly more mineralised and the changes observed are mainly of surface nature. At the same time, a state of equilibrium is also reached between the mineral lost and gained through the interaction of the enamel with the surrounding environment. In the end, the main interaction is through CaF_2 formation and dissolution.

3.3 Mixed Fluoride pH-Cycling of Permanent Bovine Enamel & Artificial Maturation

The last part of Chapter 3 describes a mixed-F^- pH-cycling model. The purpose of this study was to simulate different degrees of plaque accumulation on the same tooth, which affects the amount of F^- reaching the surface of the enamel, and to identify the effects on the proposed (398) PEM mechanism. Shortly after eruption, the gums may be tender, which makes it harder to clean the newly erupted enamel and results in more plaque accumulation on the enamel. With time, brushing of the enamel becomes easier, which results either in a clean enamel surface or less plaque present on the surface of the tooth and higher degree of fluoridation. So far it has been observed that dosages of 10 ppm and 250 ppm promote F^- incorporation inside the enamel and deposition of material in the form mainly of CaF_2 respectively. This is why a group of enamel blocks was treated with 10 ppm of fluoride and 250 ppm for days 1-6 and 7-16 respectively, while the rest of the experimental conditions were the same to those used for groups $M16_{10}$, $M16_{250}$ during the main and $PR1_{10}$ and $PR2_{250}$ during the pre-matured enamel study. The experimental parameters are summarised in Table 3-6.

ID, Solutions & Treatments	**pH Cycling Rounds**	
ID	**PMix**	**Duration**
Remineralising Solution (pH)	6.58	Main remineralisation period:5 hrs/ treatment and overnight Intermediate remineralisation period: 30 min/ treatment
Demineralising Solution (pH)	4.90	20 min/ treatment
Days 1 – 6		
Background F^- Concentration (ppm)	0.2	Same as remineralisation and demineralisation periods and overnight
Background F- Concentration during the intermediate remineralisation period (ppm)	2.0	Same as intermediate remineralisation period
Brushing F^- Concentration (ppm)	10.0	2 min/ treatment
Days 7 – 16		
Background F^- Concentration (ppm)	0.2	Same as remineralisation and demineralisation periods and overnight
Background F^- Concentration during the intermediate remineralisation period (ppm)	1.0	Same as intermediate remineralisation period
Brushing F^- Concentration (ppm)	250	2 min/ treatment

Table 3-6: Experimental conditions for the groups studied during the mixed-F^- pH-cycling study. The groups presented were treated with plaque fluid proxy, acid challenge and F^- treatment of 10 ppm for the first 6 and 250 ppm for the remaining days of the study

3.3.1 Chemical Analysis

Chemical analysis is presented following the order used during the previous sections. Firstly, the Ca^{2+} results are presented since it is the element which is present in the enamel and all of the potential secondary precipitated phases (OCP, TCP, FA, fHA, CaF_2). Secondly, PO_4^{3-} is presented as an integral part of the calcium phosphates (OCP, TCP, FA, fHA) and is followed by F^- which is the last to be either deposited or incorporated on the surface and inside the enamel as FA, fHA and CaF_2 respectively. The results are presented as the difference from the baseline, which is the concentration of the respective element inside the solutions before their use in the pH-cycling procedure.

3.3.1.1 Calcium Results

Figures 3-31 and 3-32 display the changes in Ca^{2+} concentration with time for the total and main vs. intermediate remineralisation periods respectively. Results showed that during the first days of the pH cycling decrease in the total amount of calcium acquired by the enamel blocks took place. This is in agreement with the results of the main study. The difference is that on the 16^{th} day a plateau was observed on the main study, while an apparent increase was observed in this case. Comparison of the intermediate vs. main remineralisation period showed that the two studies followed the same trend. In this case though, the intermediate study presented higher accumulation values when compared to the main study. Finally, figure 3-33 presented the results during the demineralisation period, which showed a significant decrease on the amount of the dissolved enamel with time.

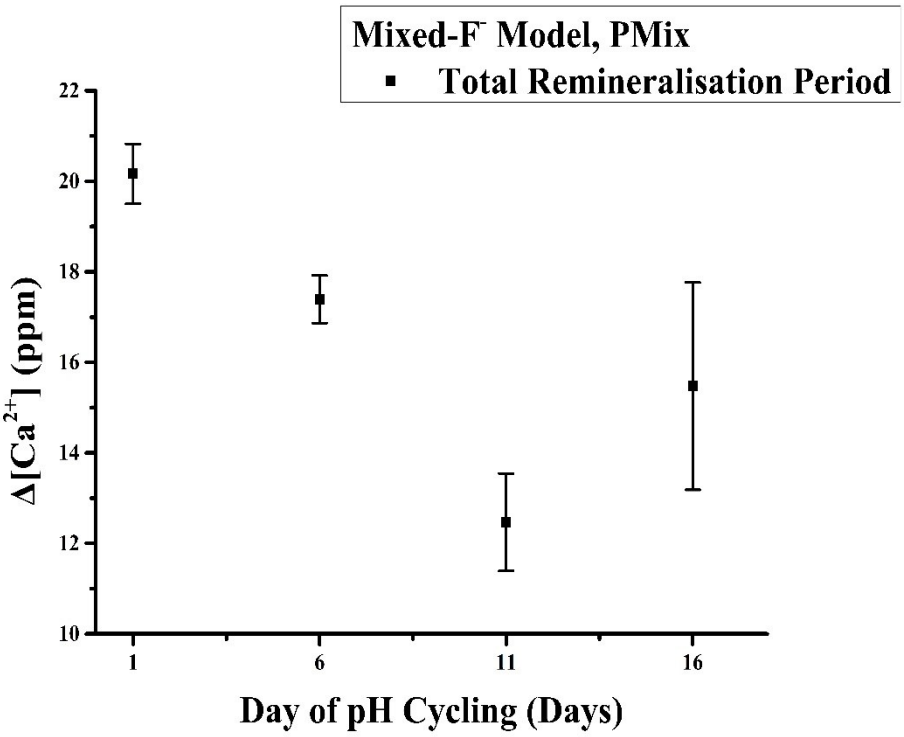

Figure 3-31: Changes in the Ca^{2+} for the mixed-F^- pH-cycling model.

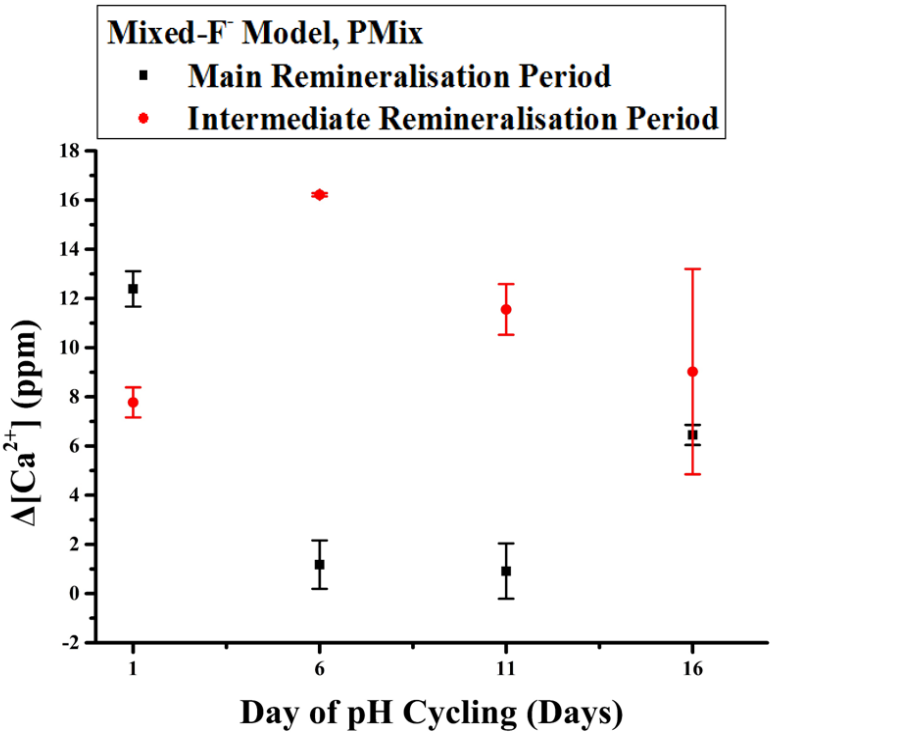

Figure 3-32: Changes in the Ca^{2+} for the mixed-F^- pH-cycling model and for the main and intermediate remineralisation periods.

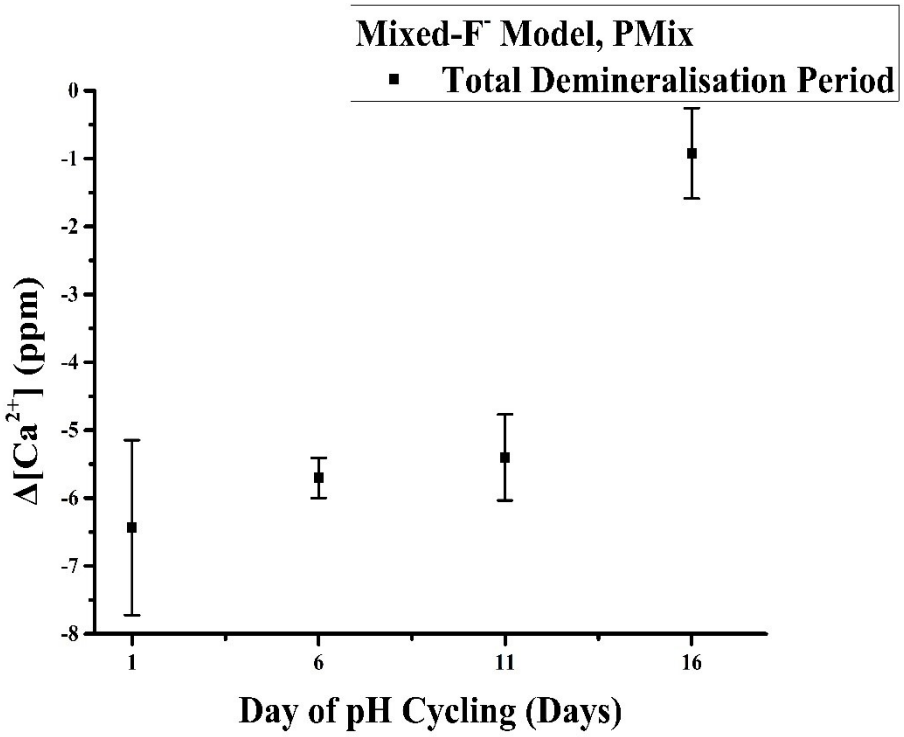

Figure 3-33: Changes in the Ca^{2+} for the mixed-F^- pH-cycling model and for the total demineralisation period.

3.3.1.2 Phosphate & Fluoride Results

Figures 3-34 and 3-35 present the results for the phosphate changes of the current group during the total and main vs. intermediate remineralisation periods respectively. The results follow the trend observed during the main study, of continuous uptake followed by decrease on the last day. The main difference in this case was observed in the demineralisation (Figure 3-36) solutions. While in the first 11 days the behaviour was similar, reversal with significant amount of phosphate moving towards the enamel took place on day 16; which is also in agreement with those of calcium for the current study.

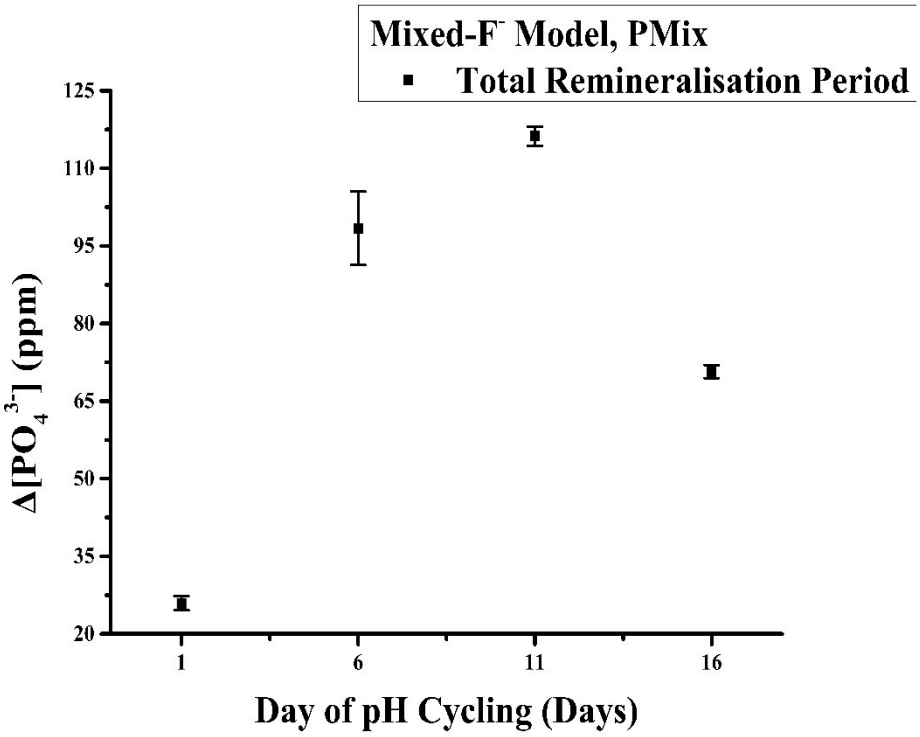

Figure 3-34: Changes in the PO_4^{3-} concentration for the mixed-F⁻ pH-cycling model.

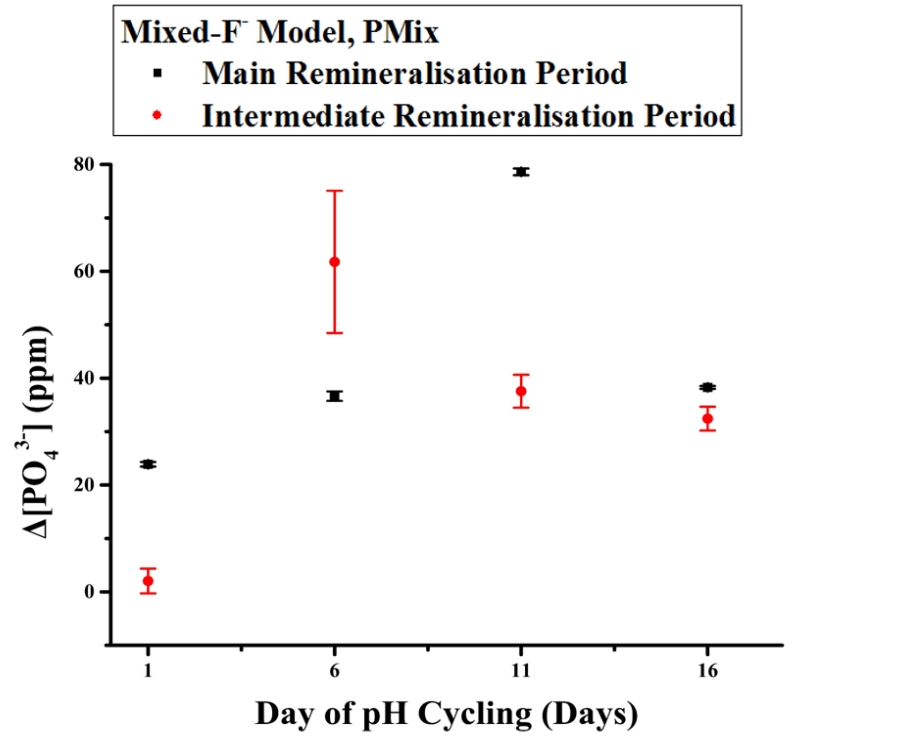

Figure 3-35: Changes in the PO_4^{3-} concentration for the mixed-F⁻ pH-cycling model and for the main and intermediate remineralisation periods.

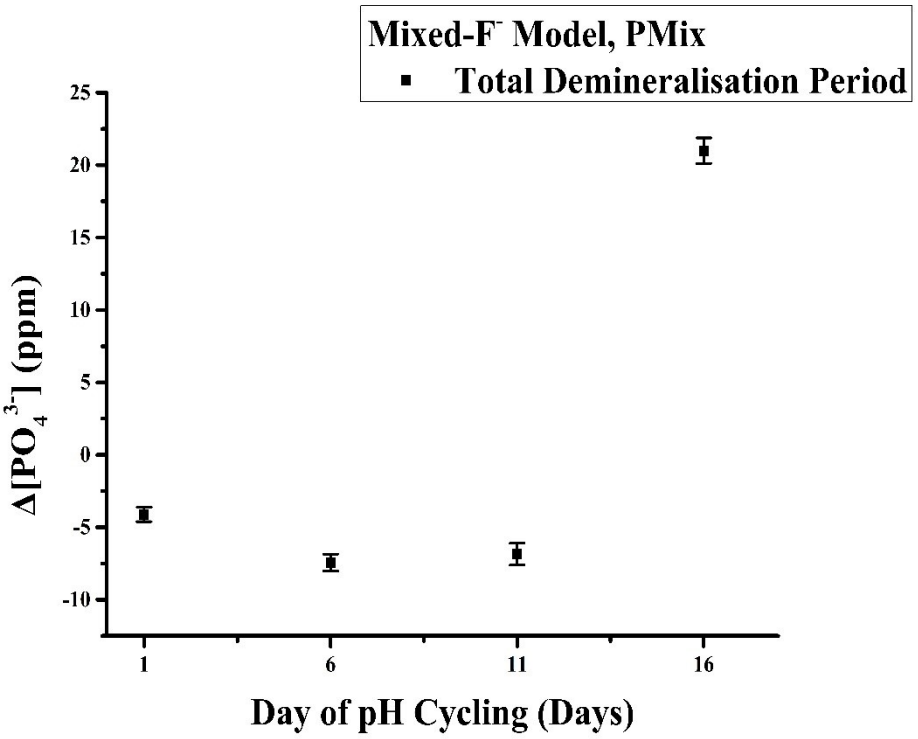

Figure 3-36: Changes in the PO_4^{3-} for the mixed-F^- pH-cycling model and for the total demineralisation period.

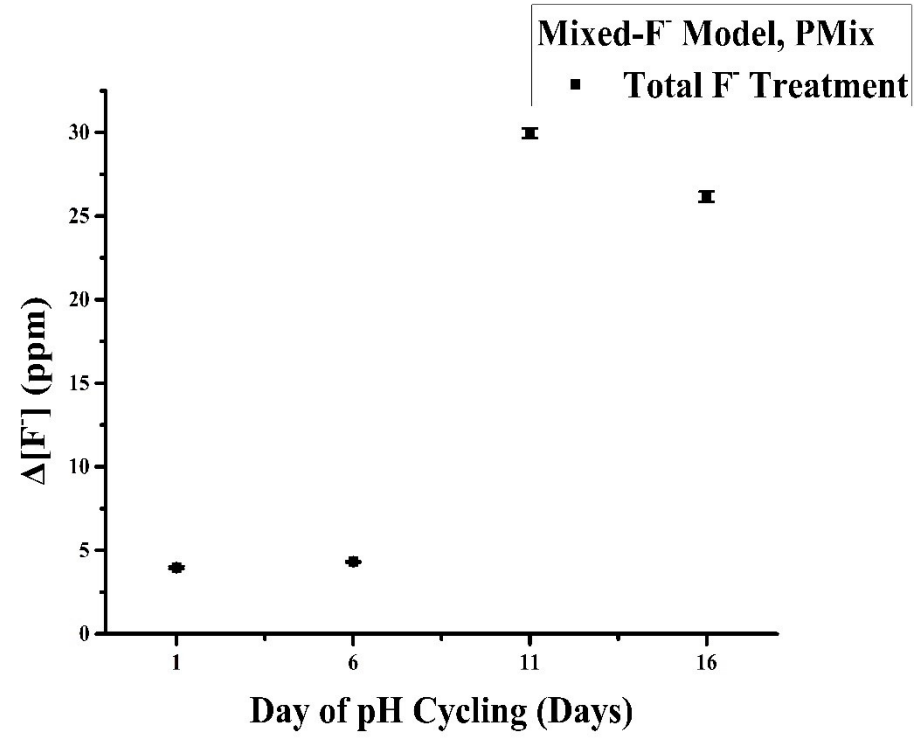

Figure 3-37: Changes in F^- concentration for the mixed-F^- pH-cycling model.

3.3.2 Structural Analysis

The FTIR results of the current group are in agreement with those observed during the main study. In all cases peaks corresponding to the υ_4 PO_4^{3-} mode of apatite can be observed, which weaken and redistribute with time. At the same time, significant increase in the peak correlated to F^--OH^- substitution at 750 cm^{-1} can be observed; along with an initial strong increase, which is followed by strong decrease in intensity of the OCP and/or TCP correlated peaks below 540 cm^{-1} (free HPO_4^{2-}) and 1150 cm^{-1} (υ_3 PO_4^{3-}). On the other hand, continuous increase in the intensity of the peaks correlated with newly precipitated HA (υ_6 HPO_4^{2-}: 1020 cm^{-1}, 1050 cm^{-1} and υ_3 PO_4^{3-}: 1120 cm^{-1}) takes place, which with time shift towards higher wavenumbers. The changes are also accompanied by continuous decrease in the surface area of the modes assigned to CO_3^{2-} content although in this case the decrease is slower when compared to the main study.

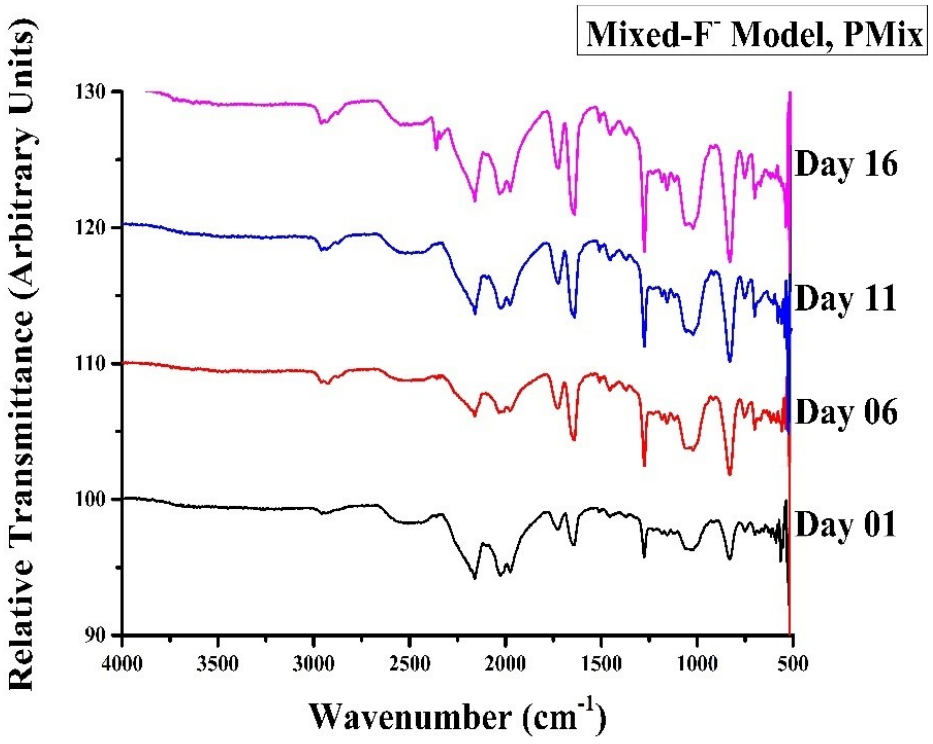

Figure 3-38: FTIR spectra of the mixed-F^- model treated enamel blocks.

3.3.3 Mechanical Properties & Morphology

The last part of the analysis of this study and Chapter presents the changes in the micro-hardness and surface morphology of the group treated with the mixed-F^- model. Similar to the previous sections, micro-hardness results are presented as the difference from the baseline, while sequential images of the surface of the enamel blocks are presented in the case of surface morphology. Further details on the instruments and the analyses parameters can be found in sections 2.3.10 and 2.3.7 respectively.

3.3.3.1 Micro-Hardness Results

The hardness of the enamel blocks used during the mixed-F^- pH cycling study increased in a way similar to that of the main study. During the first 6 days of the experimental procedure, when the blocks were treated with 10 ppm of F^-, the increase was similar to that observed for group $M16_{10}$ of the main study, which were also treated with 10 ppm of F^-. For the remaining days of the experimental procedure (days 7 to 16) the blocks which were treated with 250 ppm of F^-, showed further increase the rate of which, however, was slower than that observed in the case of the corresponding time period of group $M16_{250}$ of the main study.

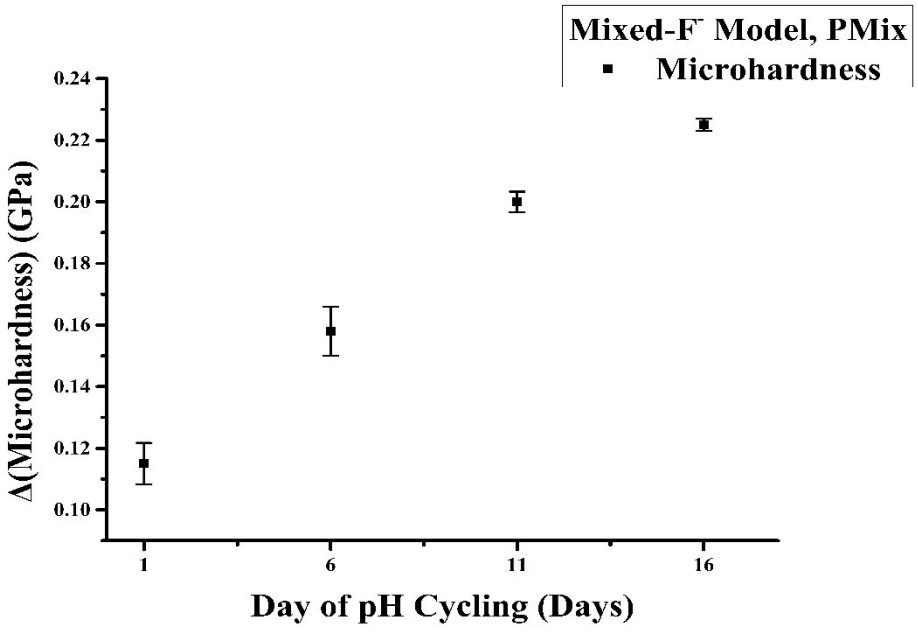

Figure 3-39: Changes in surface enamel hardness for the mixed-F^- model enamel blocks.

3.3.3.2 Surface Morphology

The changes in surface morphology are presented as imaged with AFM. Up to day 6 the changes were similar to those observed for the respective group of the main study ($M16_{10}$). From day 11 onwards strong deposition of material was observed, which was probably due to the 250 ppm F^- treatment which promoted the deposition of material on the surface of the enamel and not fluoride incorporation. This is also evident from the CaF_2 like layer which could be observed on day 16.

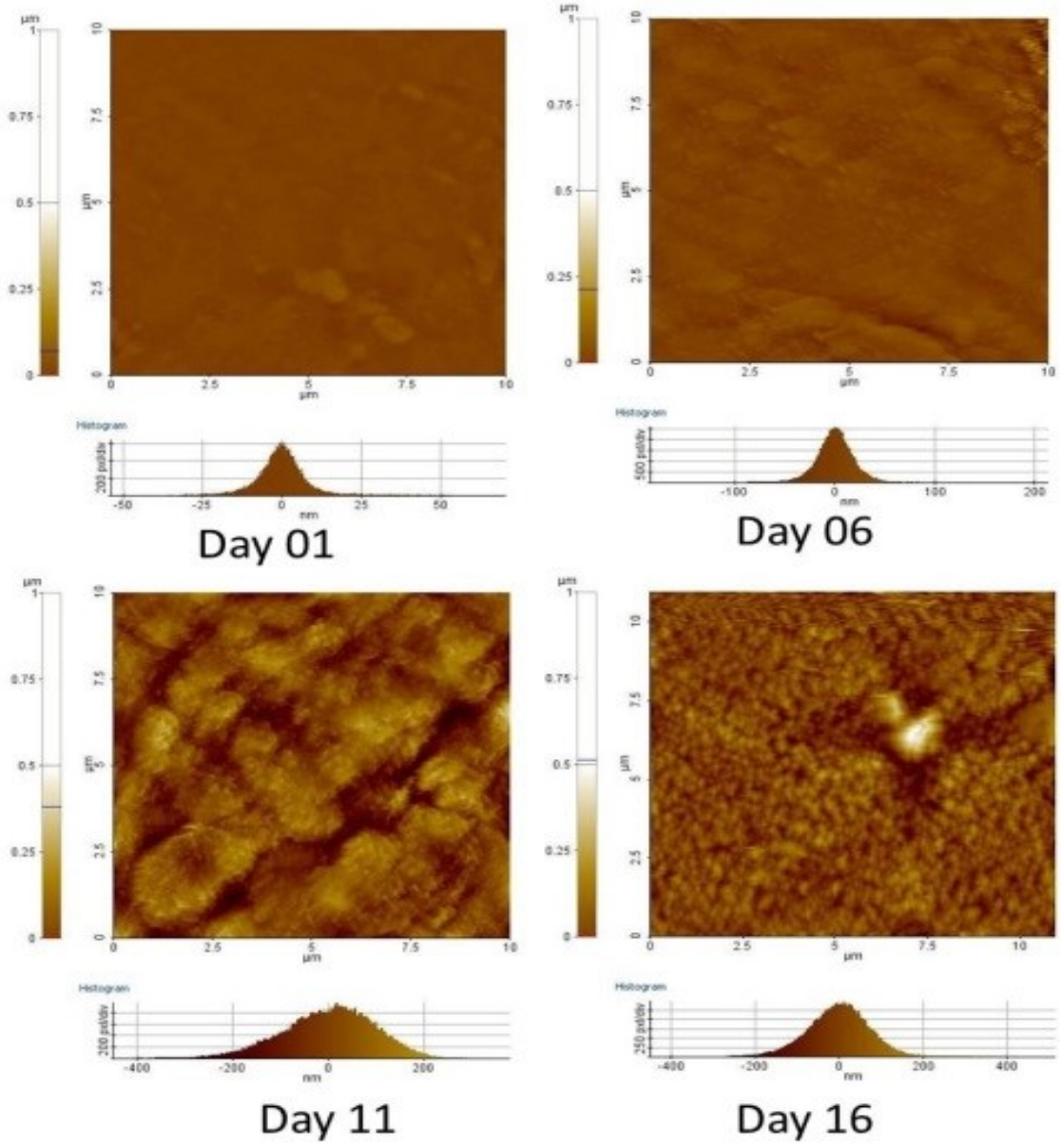

Figure 3-40: Changes in the morphology of the surface of the enamel blocks treated with the mixed-F^- model.

3.3.4 Discussion

As stated in section 3.1.4 plaque accumulation can occur as soon as the tooth starts to erupt inside the oral cavity from the gums covering the tooth, and the increased sensitivity and the accumulated plaque observed during this period can make it hard to properly clean the enamel. If plaque is not removed during tooth-brushing, the result is decreased exposure to high concentrations of F^- during brushing (27, 398, 432). As the post-eruptive age increases, the enamel surface may become easier to clean and hence be exposed to higher concentrations of F^- during tooth-brushing. In order to simulate these two scenarios, a mixed-F^- pH-cycling model was employed, where the enamel blocks used were treated with peak F^- concentrations of 10 ppm during the first 6 and 250 ppm for the remaining days of the experimental procedure.

Morphologically two distinct periods can be observed (Figure 3-40). During the first 6 days some surface changes are observed, which are followed by strong material deposition for the remainder of the experimental period. Significant correlation exists between the main remineralisation period and hardness increase for both Ca^{2+} and PO_4^{3-} ($p < 0.03$), which in this case increases with a slower rate when compared to the respective groups of the main study (section 3.1.3.1). The most significant finding though is that significant correlation exists ($p < 0.01$) between all four experimental parameters (Ca^{2+}, PO_4^{3-}, F^-, hardness). Chemical analysis of the demineralising solutions demonstrates a rapid decrease in enamel dissolution; while strong Ca^{2+} and PO_4^{3-} uptake is observed during the remineralisation period. The uptake is stronger for the intermediate remineralisation period during the first 6 days, while the opposite takes place following the switch to the 250 ppm F^- treatment. Finally, F^- results are nearly identical with the results of the main study for groups $M16_{10}$ (Days 1 and 6) and $M16_{250}$ (Days 11 and 16).

The FTIR results are in agreement with those observed during the main study (Section 3.1.2). Strong fluoride accumulation is observed through the increase in the surface area of the F^--OH^- peak around 750 cm^{-1}, which is faster during the first 6 days of the experimental procedure and is correlated with weakening and redistribution of the υ_4 PO_4^{3-} modes between 540 cm^{-1} and 615 cm^{-1} over time. Initially an increase is also observed for the OCP/TCP related peaks below 540 cm^{-1} (free HPO_4^{2-}) and 1150 cm^{-1} (υ_3 PO_4^{3-}), which is followed by strong decrease, with simultaneous increase in the intensity of the peaks correlated with newly precipitated HA (υ_3 PO_4^{3-}: 1020 cm^{-1}, 1050 cm^{-1} and υ_6 HPO_4^{2-}: 1120 cm^{-1}) and suggests the hydrolysis of the OCP/TCP phases (119, 271, 296, 526). The latter peaks also shift towards higher wavenumbers, which denotes mineral maturation (484, 485). These changes are also accompanied by continuous decrease in the surface area of the modes assigned to CO_3^{2-} content although in this case the decrease is slower than that of the main study.

3.4 Conclusions

Chapter 3 presents a study of a proposed mechanism governing the process of PEM and its effects on the physicochemical properties of permanent bovine enamel. To achieve this, a pH-cycling protocol was designed replicating the plaque/enamel interaction and the oral conditions taking place during PEM. The results support the proposed PEM model, indicating that the mechanism may involve a stepwise process of crystal growth of HA, fHA and FA and the remineralisation of superficial sub-clinical caries-like lesions, which are created through acid challenges under low-pH conditions and is significantly stimulated by F^- presence. Remineralisation takes place through the deposition of either pure or fluoridated apatites (HA, FA, fHA) and/or acidic calcium phosphates (e.g. OCP). The latter subsequently hydrolyse into HA with the help of background F^-. Under neutral pH conditions the changes are mainly limited to the surface of the enamel with precipitated material blocking the enamel pores and

inhibiting further ionic diffusion. The rate of the process is affected by the amount of plaque accumulated on the surface of the enamel inhibiting large quantities of F^- reaching its surface (demonstrated by the use of 10 ppm of F^- during the F^- treatment). As the surface of the tooth gets cleaner (demonstrated by the use of 250 ppm of F^- during the F^- treatment), more F^- reaches the surface of the enamel and the deposition of CaF_2 is promoted over structural incorporation. While CaF_2 has little, if any, protective effect on a clean enamel surface, as caries attack take place when plaque is present, if it were deposited on a clean surface shortly after brushing, which was subsequently overgrown, then some protective effect should exist through release of fluoride into the plaque-fluid at the interface with the enamel. Further, it acts as F^- reservoir providing the saliva with fluoride, which is subsequently transferred in the plaque. As post-eruptive age increases saturation of the enamel, with respect to F^-, may take place and its ability to adsorb F^- and other mineralising agents decreased or inhibited.

Page intentionally left blank

4. pH Cycling Studies Using Primary Bovine Enamel

Chapter 4 studies the effects of the proposed PEM model (398) in primary teeth through the pH-cycling of primary bovine incisors. Data regarding PEM of primary enamel are limited (187, 327, 541) and have dealt with post-eruptive changes of metal elements present in primary enamel (187) and the comparison of the effects of carious attacks on newly erupted permanent and older primary human teeth (327, 541). In all cases results suggested that PEM takes place in primary enamel. A recent study by Lucchese et al. (2012) found no significant changes in primary enamel porosity and permeability with post-eruptive age, which indirectly suggests that PEM has no or minimal effect on its properties (542). Primary enamel is in general thinner (27, 543, 544), more porous and less mineralised (27, 545-547) and presents different trace element concentration (27, 548-550) and higher CO_3^{2-} (27, 551, 552) and organic content (27, 553) than permanent enamel. As a result, primary teeth are found to have lower hardness values (510, 554) and chemical degradation (e.g. caries progression, erosion) can take place at much faster rate (417, 555).

In order to test the effects of PEM on primary enamel, the same pH-cycling model used in Chapter 3, and presented in detail in section 2.2.4, has been applied to enamel blocks originating from primary bovine incisors. Due to the physicochemical differences of primary and permanent enamel, presented in short in the previous paragraph, a modification of the duration of the experimental procedure was needed. Generally it has been stated that in order to generate comparable experimental results between permanent and primary enamel, either the modification of the chemical experimental parameters (e.g. increase background F^- concentration of the remineralising and demineralising solutions) (405, 556) or the reduction of the duration of the pH-cycling experimental procedure is needed (405, 557). Due to the limited amount of bovine primary incisors available, it was decided to reduce the duration of

the experimental procedure to 10 days and maintain the rest of the experimental parameters intact and sampling was performed every 3 days instead of five.

4.1 pH-Cycling of Primary Enamel Bovine Blocks

For continuation and comparability purposes and to test the interaction of the primary bovine enamel blocks with PF the same experimental pH-cycling procedure as in Chapter 3 has been applied. As described in detail in section 2.2.4, the remineralisation treatment consisted of a PF proxy (pH: 6.58) and the demineralisation challenge was an AC (pH: 4.90). The F^- treatment consisted of 10 ppm ($p1_{10}$), 250 ppm ($p2_{250}$) and 10 ppm for the first 4 days and 250 ppm for the remaining 6 days of the experimental procedure (pMix) in the form of NaF. In total 3 groups were created, each containing 12 primary enamel blocks, the experimental conditions of which are presented in Table 4-1 and are similar to the full pH-cycling model used in Chapter 3 (groups $M16_{10}$, $M16_{250}$, $PR1_{10}$, $PR2_{250}$ and PMix).

ID, Solutions & Treatments	**pH Cycling Rounds**			
ID	**$p1_{10}$**	**$p2_{250}$**	**pMix**	**Duration**
Remineralising Solution (pH)	6.58	6.58	6.58	Main Remineralisation Period: 5 hrs/ treatment and overnight Intermediate Remineralisation Period: 30 mon/ treatment
Demineralising Solution (pH)	4.90	4.90	4.90	20 min/ treatment
Days 1-4				
Background F^- Concentration (ppm)	0.2	0.2	0.2	Same as remineralisation and demineralisation periods and overnight
Background F^- Concentration during the intermediate remineralisation period (ppm)	2.0	1.0	2.0	Same as intermediate remineralisation period
Brushing F^- Concentration (ppm)	10.0	250.0	10.0	2 min/ treatment
Days 5-10				
Brushing F^- Concentration (ppm)	0.2	0.2	0.2	Same as remineralisation and demineralisation periods and overnight
Background F^- Concentration during the intermediate remineralisation period (ppm)	2.0	1.0	1.0	Same as intermediate remineralisation period
Brushing F^- Concentration (ppm)	10.0	250.0	250.0	2 min/ treatment

Table 4-1: Experimental conditions for the groups containing primary bovine enamel blocks. The groups presented were treated with plaque fluid proxy, acid challenge and F^- treatment of 10 ppm for the first 6 and 250 ppm for the remaining days of the study.

4.1.1 Chemical Analysis

This section presents the chemical analysis of the solutions used during the pH-cycling procedure, following the order used in Chapter 3. Firstly, Ca^{2+} is described, being the common element in all the calcium phosphates (HA, FA, fHA, OCP, TCP) and CaF_2. Next, PO_4^{3-} is presented which is present inside all the calcium phosphates (HA, FA, fHA, OCP, TCP) and finally F^-, which can be traced inside FA, fHA and CaF_2. In all cases the results are presented as the difference from the baseline (i.e. the respective concentration of the solutions prior to the treatment). This means that positive values denote uptake of the respective element by the enamel blocks, while negative results correspond to release in the solutions.

4.1.1.1 Calcium Results

Figure 4-1 presents the changes in Ca^{2+} concentration during the total remineralisation period. It represents the cumulative effect of the values of the 30-minute remineralisation period after the F^- treatment and the main period between the demineralisation periods and the overnight treatment. Figure 4-2 presents the two remineralisation periods separately. As can be seen from the images a constant increase in Ca^{2+} uptake takes place for the entire duration of the pH-cycling process.

During the total remineralisation period (Fig. 4-1) some Ca^{2+} release was observed on day 1, as indicated by the negative values, which was followed by a reverse in positive values (uptake) and continuous increase. The increase was nearly double than that observed in the case of permanent enamel (Section 3.1.1.1). Another difference was that for primary enamel constant increase is observed, while a plateau is reached for permanent enamel. Similar conclusions may be reached if a breaking down of the remineralisation period into its core components is performed (Fig. 4-2). The main remineralisation period has a similar behaviour

in both cases. On the other hand, Ca^{2+} accumulation is continuously increasing in this case while a plateau is observed for permanent enamel.

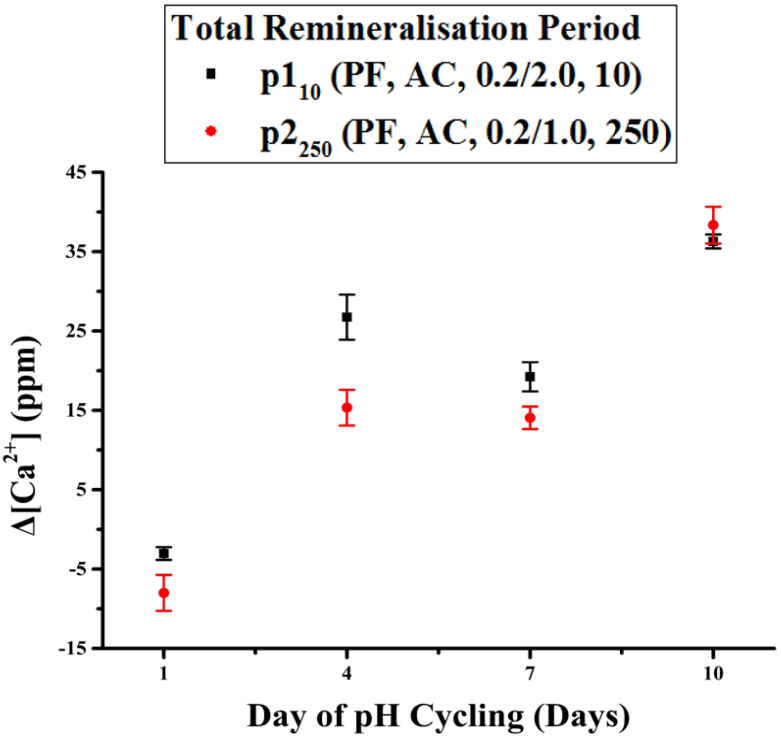

Figure 4-1: Changes in the concentration of Ca^{2+} during the total (main + intermediate) remineralisation period for the primary enamel bovine blocks ($p1_{10}$ and $p2_{250}$).

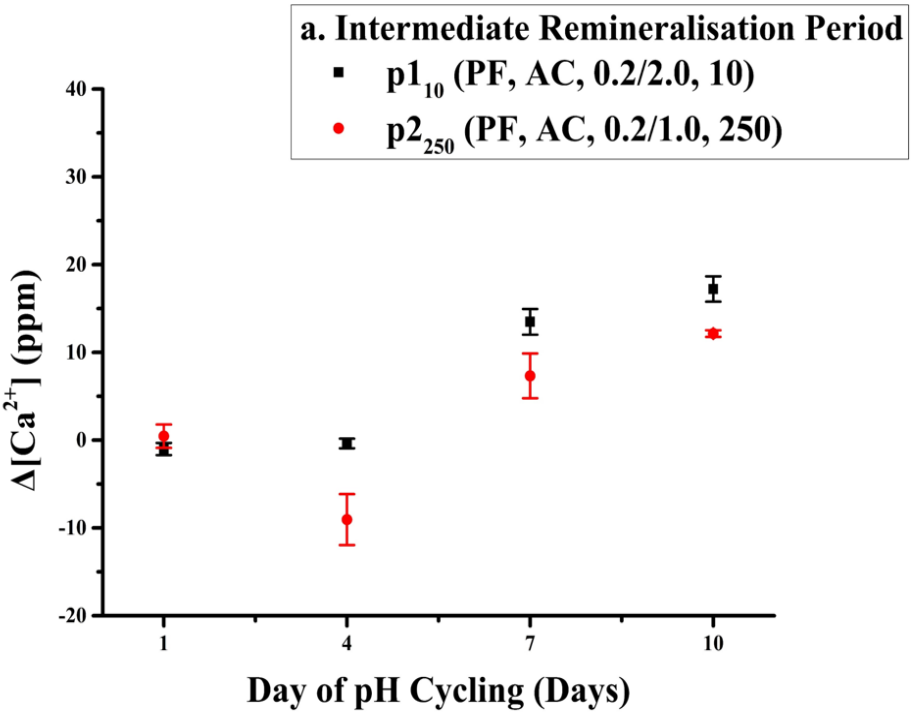

Figure 4-2: Changes in the concentration of Ca^{2+} of the a. intermediate and b. main remineralisation period.

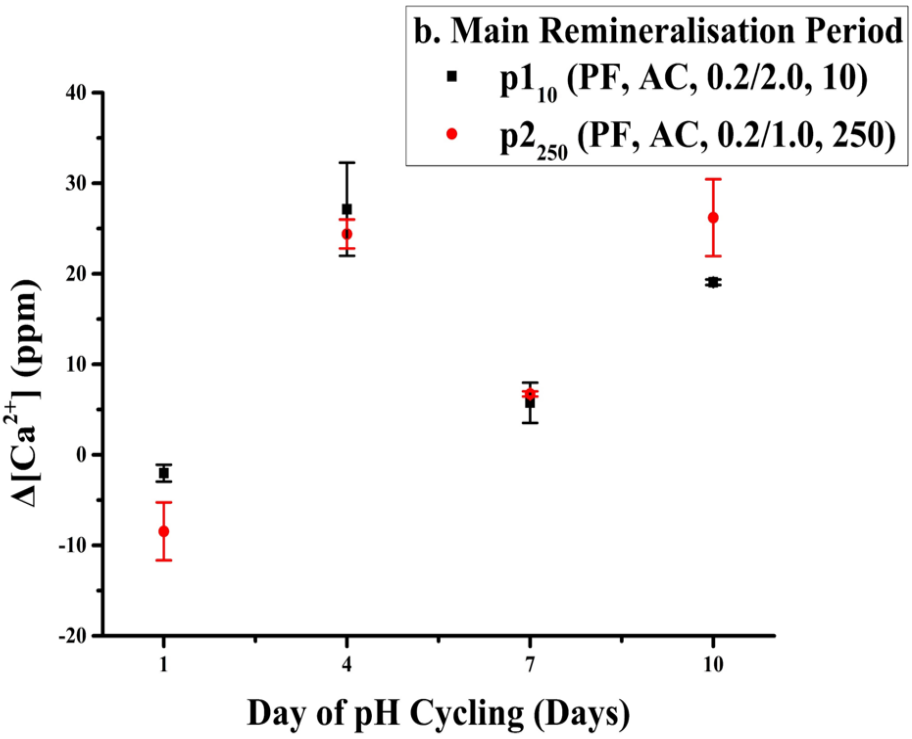

Figure 4-2 (Continued): Changes in the concentration of Ca^{2+} of the a. intermediate and b. main remineralisation period.

As far as the demineralisation period (Figure 4-3) is concerned, the behaviour of primary enamel is somewhat different. In both $p1_{10}$ and $p2_{250}$ a significant release of Ca^{2+} is observed, which suggests strong enamel dissolution. The decrease is more pronounced for the groups treated with 250 ppm of F^-, which supports the hypothesis that lower F^- administration favours its faster incorporation inside the enamel structure (515) and was also observed in Chapter 3, although in the long run the blocks treated with 250 ppm catch up. This decrease slows down and plateaus around day 7, after which a reversal in the trend is observed. This probably suggests the precipitation of a more acid resistant material, which can be interpreted as a sign of enamel maturation. If the pH-cycling period was extended, a reversal to positive values may be possible.

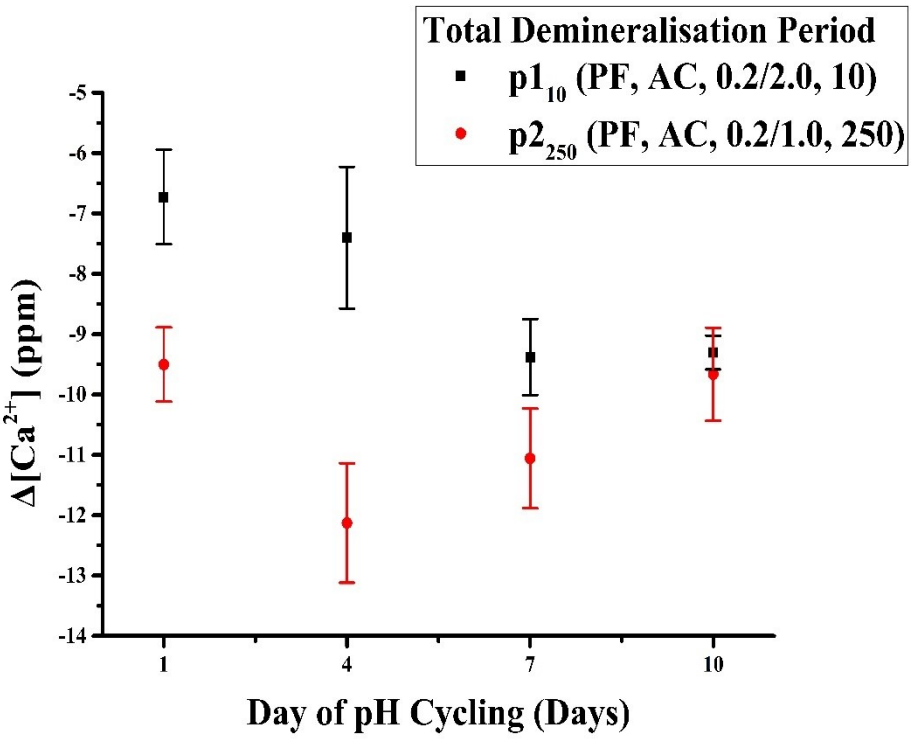

Figure 4-3: Changes in the concentration of Ca^{2+} during the total demineralisation period.

4.1.1.2 Phosphate & Fluoride Results

Figures 4-4 and 4-5 present the changes in phosphate concentration with time for the remineralising solutions. During the total remineralisation period (Figure 4-4), an initial release of material is observed, which decreases with time and levels around 0 for $p1_{10}$, while it has a continuous trend towards positive values for $p2_{250}$. The trend is similar for both intermediate (Fig. 4-5a) and main (Fig. 4-5b) remineralisation periods, although increasingly strong PO_4^{3-} uptake can be observed for both cases during the main remineralisation period. The results are similar to those observed during the main study (Section 3.1.1.2), but the values are a lot lower.

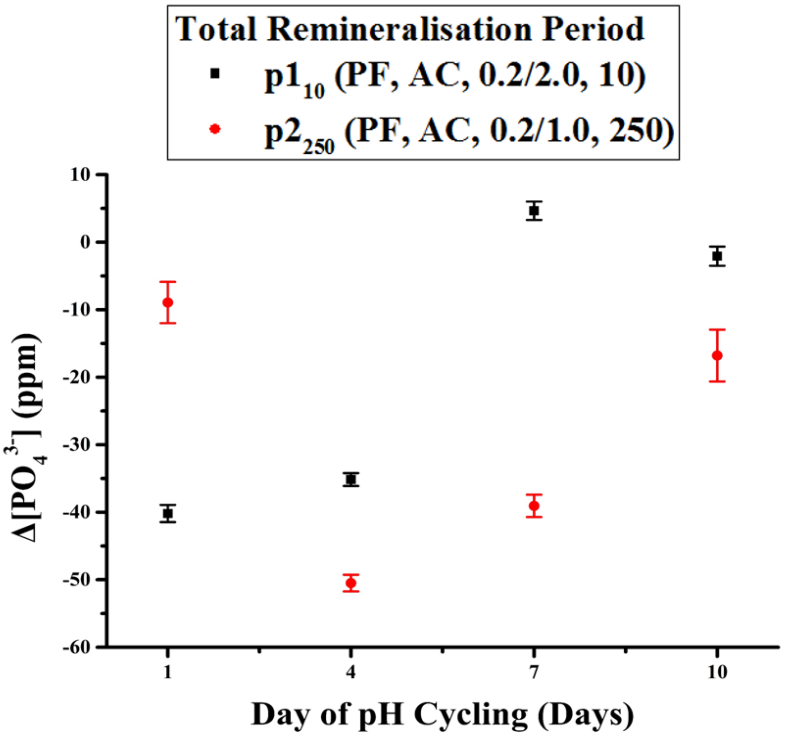

Figure 4-4: Changes in the concentration of PO_4^{3-} during the total remineralisation period for the primary enamel bovine blocks ($p1_{10}$ and $p2_{250}$).

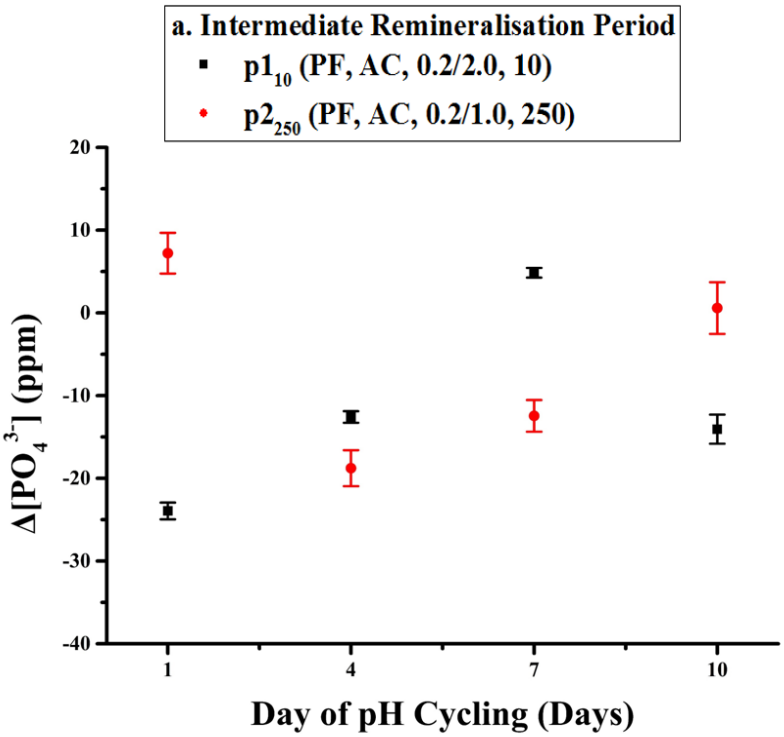

Figure 4-5: Changes in the concentration of PO_4^{3-} for the a. intermediate and b. main remineralisation period.

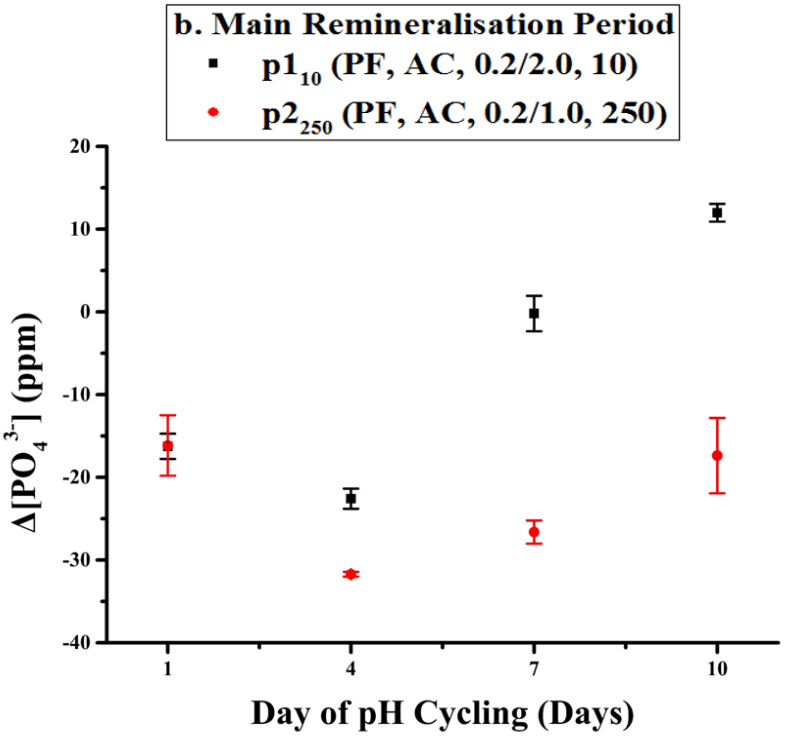

Figure 4-5 (Continued): Changes in the concentration of PO_4^{3-} for the a. intermediate and b. main remineralisation period.

The demineralisation results (Figure 4-6) are also similar to those of the main study. In both cases, uptake of PO_4^{3-} takes place with a relatively constant rate. In the case of the primary blocks, the uptake is much stronger than in the case of permanent enamel. The uptake is also stronger for the groups treated with 250 ppm of F^-.

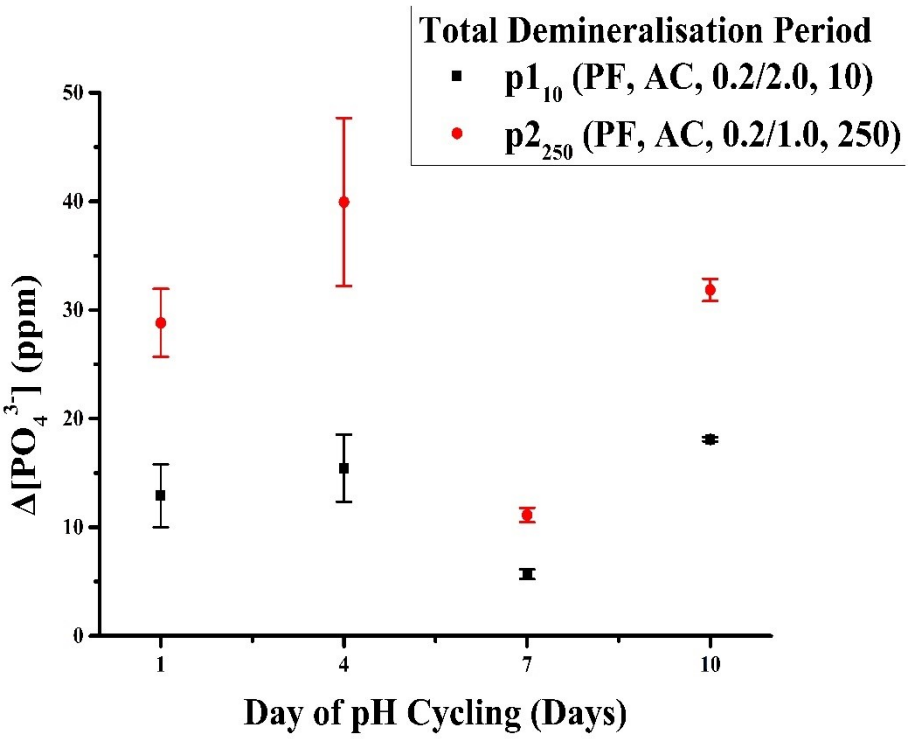

Figure 4-6: Changes in the concentration of PO_4^{3-} during the total demineralisation period.

Finally, the fluoride results denote F^- uptake for the duration of the pH-cycling procedure. The uptake is much stronger for group $p2_{250}$, which may suggest that in this case CaF_2 deposition is favoured over structural incorporation. On the other hand, a relatively stable, with much lower values, uptake can be observed for $p1_{10}$. In this case, structural incorporation is more likely.

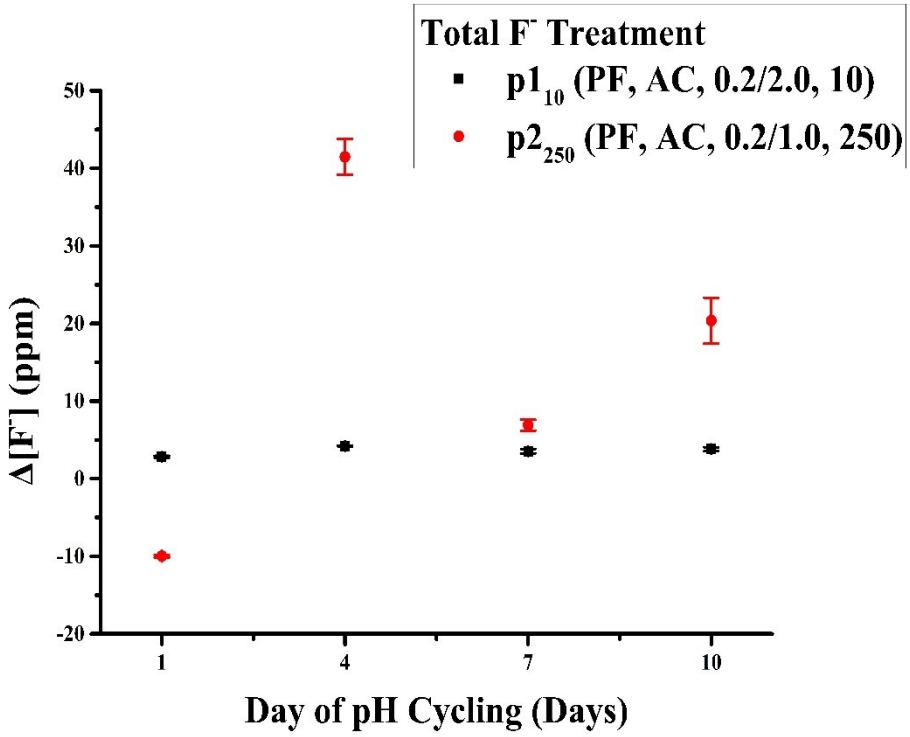

Figure 4-7: Changes in the F^- concentration of the solutions used during the tooth-brushing simulation.

4.1.2 Structural Analysis

The FTIR results for groups $p1_{10}$ and $p2_{250}$ are presented in Figure 4-8. During the first day the blocks from both groups present 4 peaks between 540 cm^{-1} and 615 cm^{-1} which correspond to the υ_4 PO_4^{3-} vibrational mode of apatite (481-483). During the pH-cycling the number of these peaks drops to half for $p1_{10}$ and to 3 for $p2_{250}$ with a simultaneous shift of position and broadening of their respective surface (e.g. for $p1_{10}$: from 541 cm^{-1} and 11.879 cm^2 to 547 cm^{-1} and 31.520 cm^2; and to 569 cm^{-1} and 0.683 cm^2 to 574 cm^{-1} and 11.405 cm^2). At the same time the OH^- modes around 630 cm^{-1} and 3665 cm^{-1} (479, 480, 491) continuously decrease and disappear by the end of the 10^{th} day for $p1_{10}$ and drops by 50% for $p2_{250}$; while in both cases the F^--OH^- peak around 750 cm^{-1} (479, 480) nearly triples in surface and shifts towards higher wavenumber values. Finally, the peaks between 1900 and 2200 cm^{-1}, which are attributed to HPO_4^{2-} and well-crystallised HA (479, 492), increase both in

numbers and area. With time, the presence of well crystallised HA around 1060 cm^{-1} which corresponds to the υ_6 stretching vibration of HPO_4^{2-} (487, 488) can also be observed.

The υ_4, υ_2, and υ_1 CO_3^{2-} peaks between 660 cm^{-1} and 900 cm^{-1} (487, 493, 494), decrease in number (3 to 2 for $p1_{10}$ and 2 to 1 for $p2_{250}$) and increase in total surface area (58.2% and 70.9% respectively). Similarly an increase in the surface of the υ_3 CO_3^{2-} and carbonyl peaks (C=O) around 1450 cm^{-1} and 1730 cm^{-1} (487, 495, 496) can also be observed, which is more significant for $p1_{10}$.

Significant is the presence of peaks correlated to the presence of secondary phases and newly precipitated material. The presence of peaks correlated to crystalline acid phosphates and more precisely OCP (free HPO_4^{2-}, 520-540 cm^{-1} (481-483, 497)) can be observed since day 1 of the pH cycling. These peaks increase both in numbers and areas during the early days of the procedure and then decrease in surface. Significant are also the peaks which are correlated to the υ_3 PO_4^{3-} mode of newly precipitated HA around 1110 cm^{-1} and 1150 cm^{-1} (484, 498, 499). These peaks initially increase in surface with time and then decrease in total surface with a simultaneous shift towards 1120 cm^{-1} and 1160 cm^{-1} respectively. Similarly the υ_6 HPO_4^{2-} mode around 1020 cm^{-1} is correlated with poorly crystallised mix of HA, OCP and TCP (484-486) and is also present, after day 1, and significantly increases with time especially in the case of the blocks treated with 10 ppm of F^- (>> 100 %). It must be also noted, that in the case of primary blocks peaks correlated with organic material can be also observed in the region 2490 cm^{-1} to 2570 cm^{-1}, which decrease with time; this also applies to the presence of H_2O (2990 cm^{-1}-3550 cm^{-1}) (558).

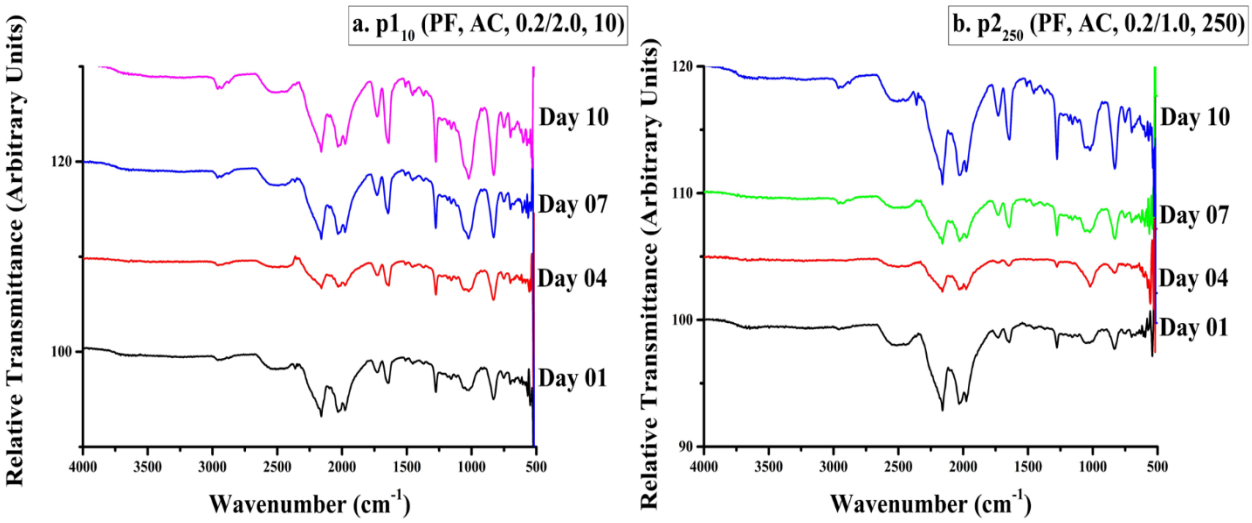

Figure 4-8: FTIR spectra of pH-cycled primary enamel blocks treated with a. 10 ppm of F^- and b. 250 ppm of F^-.

4.1.3 Mechanical Properties & Morphology

The last part of the analysis involves changes in the mechanical properties and the surface morphology of the primary enamel blocks. Hardness was measured using Vickers' micro-indenter and the morphology was studied using AFM. Further details on the instruments and the analyses parameters can be found in sections 2.3.10 and 2.3.7 respectively. The results are presented below.

4.1.3.1 Micro-Hardness

The hardness of primary enamel blocks, as measured with micro-indentation, increases with time as can be seen in Figure 4-9. The increase is really slow, when compared to permanent enamel, and accelerates after day 7. The increase is slightly bigger for the groups treated with 250 ppm of F^-, which is consistent with higher uptake of F^- in the $p02_{250}$ experiments.

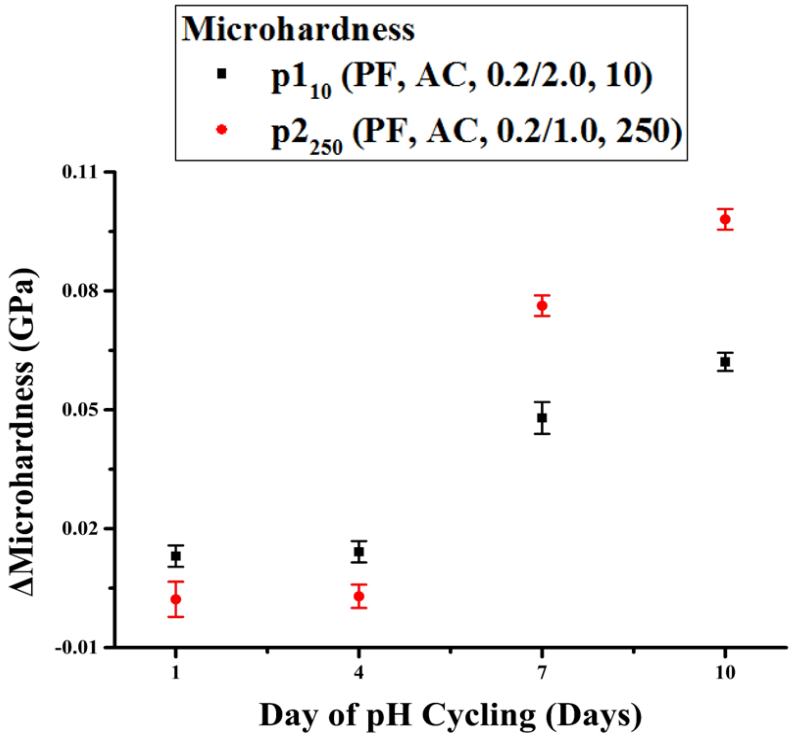

Figure 4-9: Changes in hardness as a function of time in the primary enamel treated blocks.

4.1.3.2 Surface Morphology

Figures 4-10 and 4-11 present the changes in surface morphology of primary enamel blocks for $p1_{10}$ and $p2_{250}$ respectively. In both cases deposition of material which may indicate rapid precipitation of a secondary phase such as CaF_2 is observed on day 1 and is stronger in the case of $p2_{250}$. Further deposition of material appears to takes place with time. The nature of the deposited material resembles that which can be seen on the last day of the pH-cycling of pre-matured enamel treated with 250 ppm of F^-.

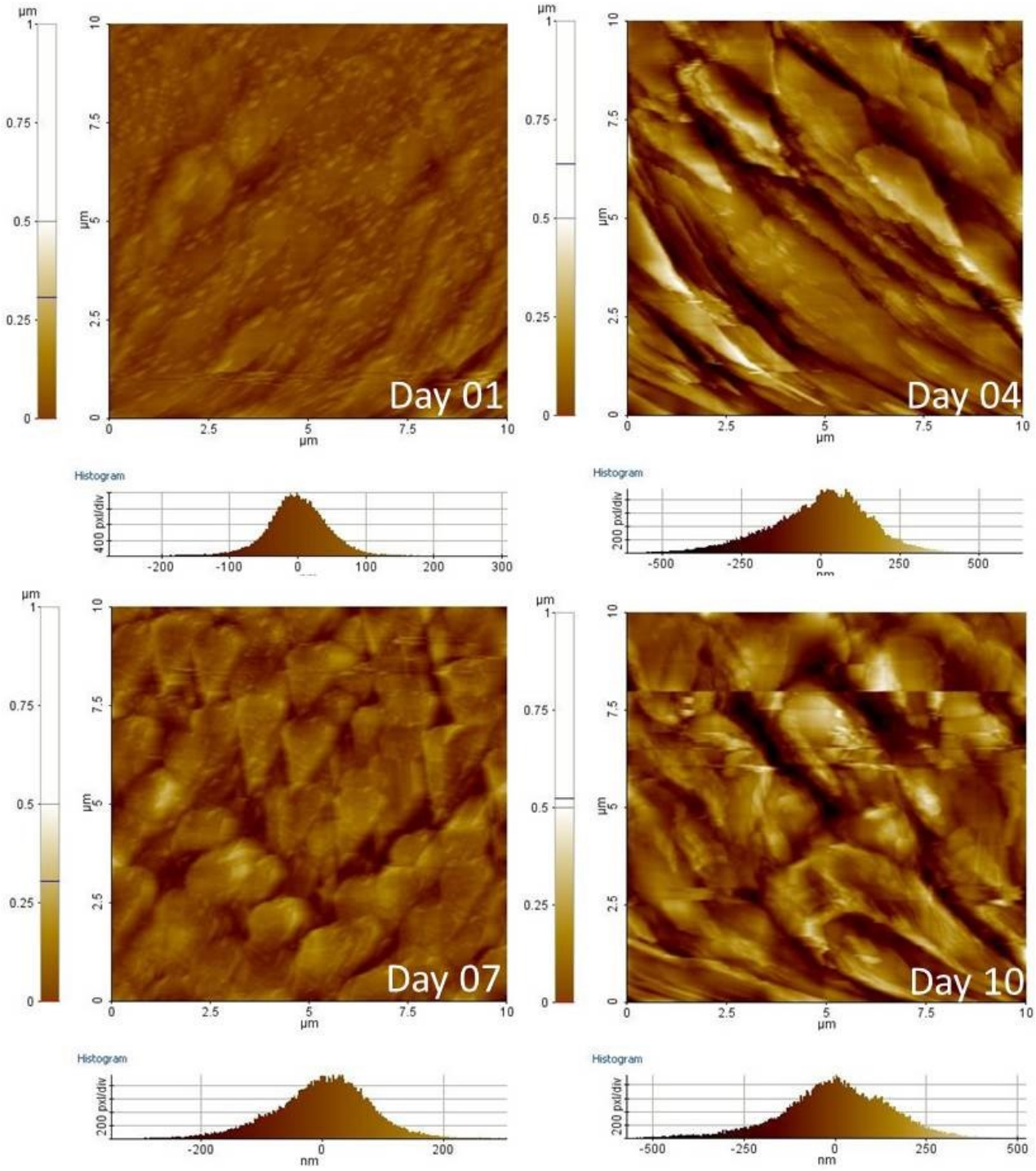

Figure 4-10: Changes in the surface morphology of primary enamel blocks (group $p01_{10}$) treated with the full pH-cycling model and with F^- concentration of 10 ppm.

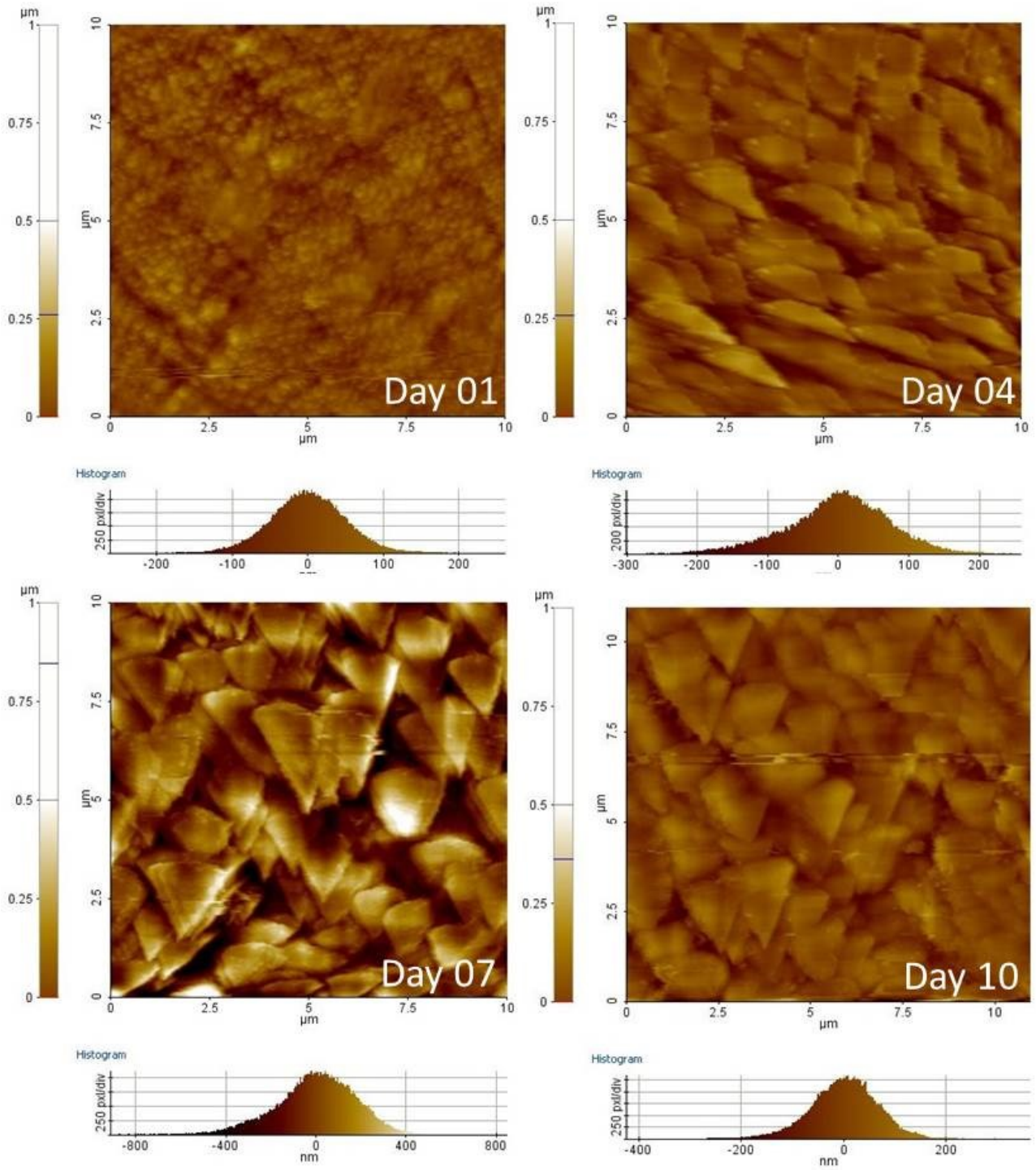

Figure 4-11: Changes in the surface morphology of primary enamel blocks (group $p02_{250}$) treated with the full pH-cycling model and with F^- concentration of 250 ppm.

4.1.4 Discussion

The results of the current study provide insights on the proposed PEM mechanism (398), and also suggest that primary is more reactive than permanent enamel. The latter is supported by the chemical analysis of the solutions and agrees with other studies analysing the nature of primary enamel (417, 555). Both Ca^{2+} (Figures 4-1, 4-2) and F^- (Figure 4-7) results suggest that continuously increasing accumulation of these ions takes place for both $p1_{10}$ and $p2_{250}$; although the rate of uptake of F^- is much slower for $p1_{10}$. As mentioned in Chapter 3, the 10 ppm and 250 ppm treatments promote F^- incorporation and CaF_2 deposition respectively (515). This is probably the case for primary enamel as well. Strong correlation exists ($p < 0.001$) between F^- uptake and hardness for $p1_{10}$, while $p2_{250}$ is correlated with phosphate changes during the intermediate remineralisation period ($p < 0.03$). At the same time, strong correlation exists between Ca^{2+}, PO_4^{3-} and F^- for the total remineralisation period for both groups ($p1_{10}$: $p < 0.05$; $p2_{250}$: $p < 0.02$). On the other hand, if the total remineralisation period is broken down to main and intermediate phases significant correlation exists only for the intermediate ($p < 0.05$) and main ($p < 0.02$) remineralisation periods for groups $p1_{10}$ and $p2_{250}$ respectively; which suggests that treatment with 250 ppm of F^- corresponds to long-term, while 10 ppm correspond to more rapid changes.

Chemical analysis (Section 4.1.1) also denotes the differences in behaviour between primary and permanent enamel. While in this case continuous Ca^{2+} uptake is observed (figures 4-1, 4-2), in the case of permanent enamel (figures 3-1, 3-2) a plateau is reached by the end of the pH-cycling procedure, which is more obvious for the main and total remineralisation periods. On the other hand, the behaviour of F^- (figure 3-7) is similar for the case of $p1_{10}$ and permanent enamel treated with 10 ppm of F^-. While permanent groups treated with 250 ppm seem to get saturated by the end of the pH-cycling procedure, which reduces enamel's capacity to adsorb extra F^- and other mineralising agents (414, 534, 539, 540), this is not the

case for primary enamel. Fluoride uptake and incorporation inside the enamel is indicated through the decrease in intensity of the OH^- peaks around 630 cm^{-1} and 3665 cm^{-1} and the respective increase of the F^--OH^- mode around 750 cm^{-1}, which suggests OH^- substitution by F^- and the formation of FA or fHA (479, 480).

Different from those of permanent enamel are the PO_4^{3-} results, which suggest dissolution of material during the early days of the remineralisation periods (Figures 4-4, 4-5), followed by a reversal during the second half of the pH-cycling procedure. At the same time, continuous accumulation during the demineralisation period is observed (Figure 4-6). These results are similar to those of permanent enamel (Figures 3-4, 3-5, 3-6) and probably suggest the precipitation of secondary phases like OCP, DCPD and/or TCP, which are favoured under low-pH conditions (520, 521) as the strong correlation ($p < 0.001$) between the Ca^{2+} and PO_4^{3-} during the demineralisation period suggests. This idea is also supported by the presence of HPO_4^{2-} peaks (520 cm^{-1}-540 cm^{-1}) linked to the presence of OCP and/or TCP (481-483). These peaks initially increase and then decrease in surface and number, which suggests precipitation of secondary phases and then transformation into initially poorly crystalline HA (45, 313) same as in the case of permanent enamel. This is further supported by the presence of the PO_4^{3-} mode around 1020 cm^{-1} which is correlated with poorly crystallised mixture of HA, OCP and TCP (485, 486) and the υ_3 PO_4^{3-} peaks around 1110 cm^{-1} and 1150 cm^{-1} respectively, which are correlated with newly precipitated HA and shift slightly with time towards higher values; an indication of mineral maturation (484, 498, 499, 559). The transformation probably takes place through the same mechanism of epitaxial growth (524, 525) and hydrolysis of the acidic calcium phosphates into apatite (119, 271, 296, 526), which is enhanced by the presence of BF (310, 530, 531) and was described in detail in section 3.1.4.

It must be also noted, that due to the nature of primary enamel the precipitation of material leads to more pronounced changes in the CO_3^{2-} content of the enamel. Although some of the carbonate peaks decrease or disappear with time and the total CO_3^{2-} content decreases, as FTIR results suggest, some peaks increase in surface probably due to carbonate redistribution. For example, the υ_4, υ_2, and υ_1 CO_3^{2-} peaks between 660 cm^{-1} and 900 cm^{-1} (487) and the υ_3 CO_3^{2-} and carbonyl peaks around 1450 cm^{-1} and 1730 cm^{-1} (487) respectively, decrease in number and the remaining peaks increase in total surface. All of the above also result in the decrease of organic material as the changes in the peaks between 2490 cm^{-1} and 2570 cm^{-1} suggest, and also of hydration, as seen by the peaks linked to H_2O (2990 cm^{-1}-3550 cm^{-1}) (558).

As a conclusion, it can be said that the results suggest that primary enamel undergoes PEM following the same mechanism as permanent enamel, which is through the remineralisation of demineralised enamel, probably in the form of pre-cavitated caries lesions and the direct precipitation or epitaxial growth of apatitic phases (HA, fHA, FA) following OCP hydrolysis as proposed in Chapter 3. In this case though, and due to the nature of primary enamel (increased porosity, higher content of natural impurities), the process is much slower. Similarly to permanent enamel, low F^- treatment leads mainly to F^- incorporation inside the enamel, while higher leads to CaF_2 deposition on its surface (515). This is why the most significant periods are the demineralisation and intermediate for group $p1_{10}$, when the surface enamel is softened, more reactive and further ionic diffusion takes place towards the upper layers of the underlying enamel, which results either in enamel remineralisation (144, 534, 535) or material deposition in the interstices between the enamel prisms (91-93, 101, 102). On the other hand, for $p2_{250}$ the main remineralisation phase is more significant, where the excess in F^- content provides the necessary driving force for the long-term transformation of the

already present and newly precipitated HA, which is formed on the surface of the enamel under neutral pH conditions, into FA and/or fHA (516).

4.2 Mixed-F^- pH-Cycling Model of Primary Enamel Bovine Blocks

The last part of this Chapter studies the effects of different degrees of plaque accumulation using a mixed-F^- pH-cycling model. As in Chapter 3, the purpose of this study was to simulate different states of plaque accumulation on the same tooth, which affects the amount of F^- reaching the surface of the enamel, and to identify the effects on the proposed (398) PEM mechanism. The experimental conditions are similar to section 3.3, a group of enamel blocks was treated with 10 ppm of fluoride and 250 ppm for days 1-4 and 5-10 respectively. The rest of the experimental conditions were the same to those used in Chapter 3 and Section 4.1. The experimental parameters are summarised in Table 4-2.

ID, Solutions & Treatments	**pH Cycling Rounds**	
ID	**pMix**	**Duration**
Remineralising Solution (pH)	6.58	Main Remineralisation Period: 5 hrs/ treatment and overnight Intermediate Remineralisation Period: 30 min/ treatment
Demineralising Solution (pH)	4.90	20 min/ treatment
Days 1 – 4		
Background F^- Concentration (ppm)	0.2	Same as remineralisation and demineralisation periods and overnight
Background F^- Concentration during the intermediate remineralisation period (ppm)	2.0	Same as intermediate remineralisation period
Brushing F^- Concentration (ppm)	10.0	2 min/ treatment
Days 5 – 10		
Background F^- Concentration (ppm)	0.2	Same as remineralisation and demineralisation periods and overnight
Background F^- Concentration during the intermediate remineralisation period (ppm)	1.0	Same as intermediate remineralisation period
Brushing F^- Concentration (ppm)	250	2 min/ treatment

Table 4-2: Experimental conditions for the groups studied during the mixed-F^- pH-cycling study. The group presented was treated with plaque fluid proxy, acid challenge and F^- treatment of 10 ppm for the first 4 and 250 ppm for the remaining days of the study.

4.2.1 Chemical Analysis

Chemical analysis is presented following the order used during the previous sections. Firstly, the Ca^{2+} results are presented. Secondly, PO_4^{3-} and is followed by F^-. It should be noted that the results are presented as the difference from the baseline, which is the concentration of the respective element inside the solutions before their use in the pH-cycling procedure.

4.2.1.1 Calcium Results

The changes in Ca^{2+} concentration with time, for the mixed-F^- pH-cycling procedure and during the total remineralisation period (Figure 4-12), follow the same behaviour as the main pH-cycling procedure presented above. The trend is similar when a breakdown of the remineralisation period in its core components is performed (Figure 4-13). Strong uptake can be observed on day 4 of the pH-cycling. For the remaining days, a continuous increase can be observed, but the values are lower in absolute numbers. Some differences between the main and the mixed-F^- model can be observed during the demineralisation period (Figure 4-14). An initial continuous drop can be observed, which reaches a minimum on day 4 and is followed by significantly decreased release, the rate of which seems to decrease slowly from then on. The difference between groups $p2_{250}$ and pMix for days 7-10 (when both groups were treated with 250 ppm of F^-), is that the decrease is more rapid and resembles more the values of $p1_{10}$.

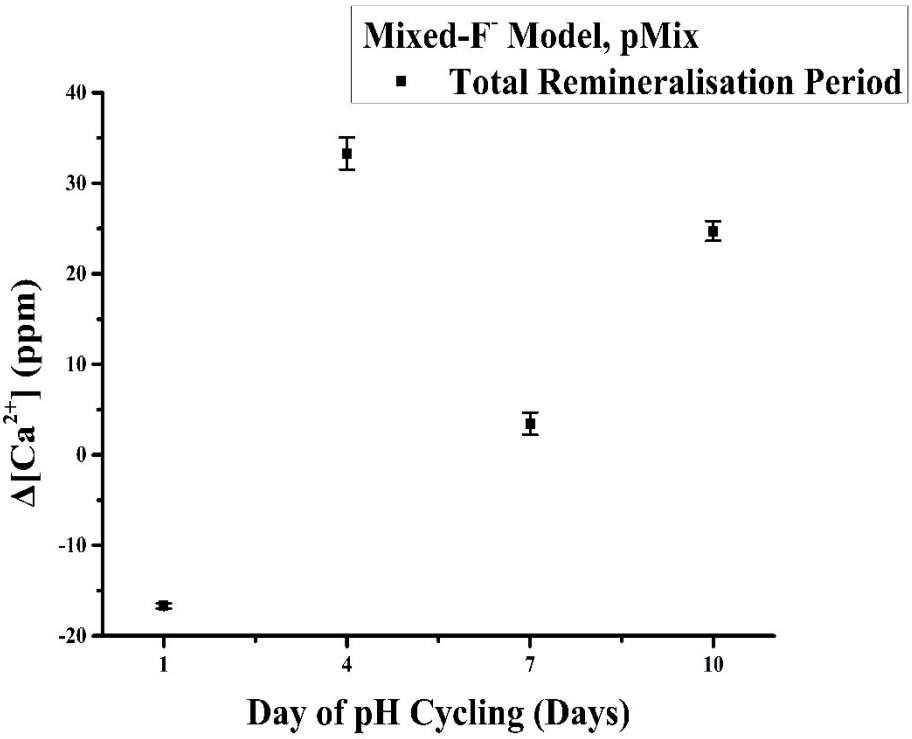

Figure 4-12: Changes in the concentration of Ca^{2+} during the total (main+intermediate) remineralisation period for the primary enamel bovine blocks treated with the mixed-F^- pH-cycling model.

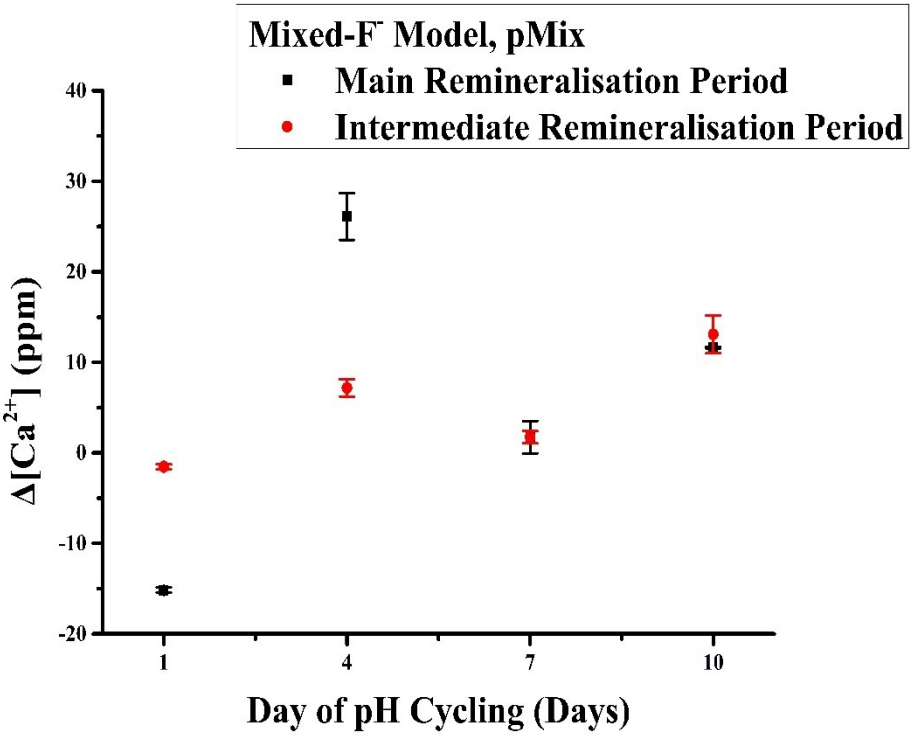

Figure 4-13: Changes in the concentration of Ca^{2+} during the main and intermediate remineralisation periods for the primary enamel bovine blocks treated with the mixed-F^- pH-cycling model.

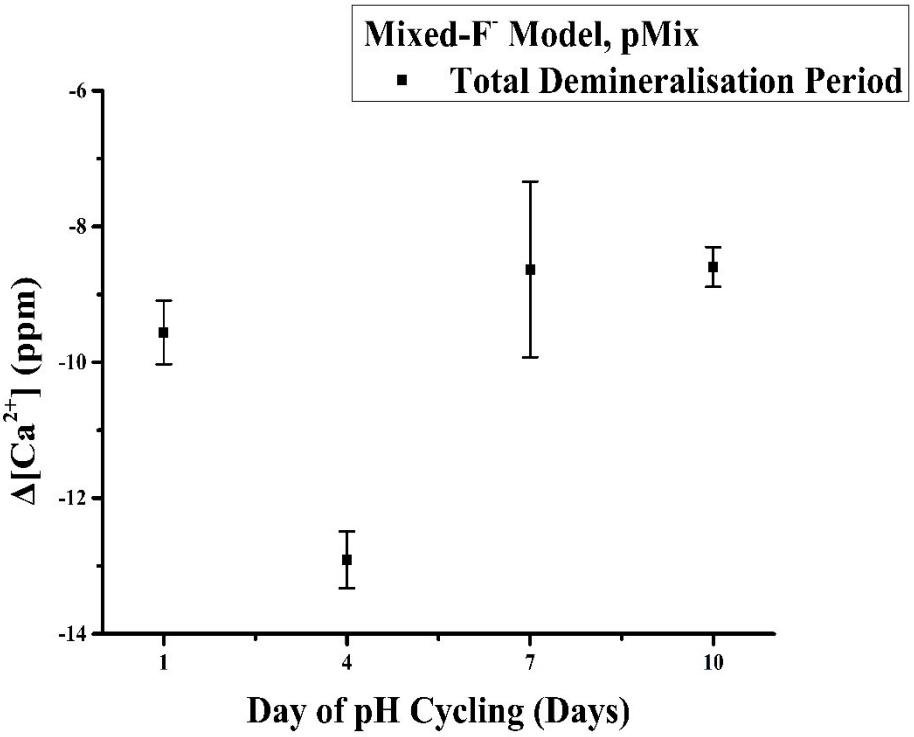

Figure 4-14: Changes in the concentration of Ca^{2+} during the total demineralisation period for the primary enamel bovine blocks treated with the mixed-F^- pH-cycling model.

4.2.1.2 Phosphate & Fluoride Results

The phosphate results also resemble those acquired during the main pH-cycling study with primary blocks. For the remineralisation treatment, initial release of PO_4^{3-} inside the solutions is observed, which is followed by uptake especially during the main remineralisation period. The behaviour follows that observed in group $p1_{10}$, but with higher (from day 7 onward) values which correspond to those observed for group $p2_{250}$. This is true for both the total (Figure 4-15) remineralisation period and its components main and intermediate phases (Figure 4-16). As far as the demineralising solutions are concerned (Figure 4-16), continuous uptake of PO_4^{3-} is observed. In this case the trend observed is a mixture of $p1_{10}$ and $p2_{250}$. Finally, continuous F^- uptake is also observed for the duration of the pH-cycling procedure (Figure 4-17). While during the first 4 days the trend is similar to group $p1_{10}$, for the remaining days the trend and values observed resemble those observed from day 4 to 7 of group $p2_{250}$.

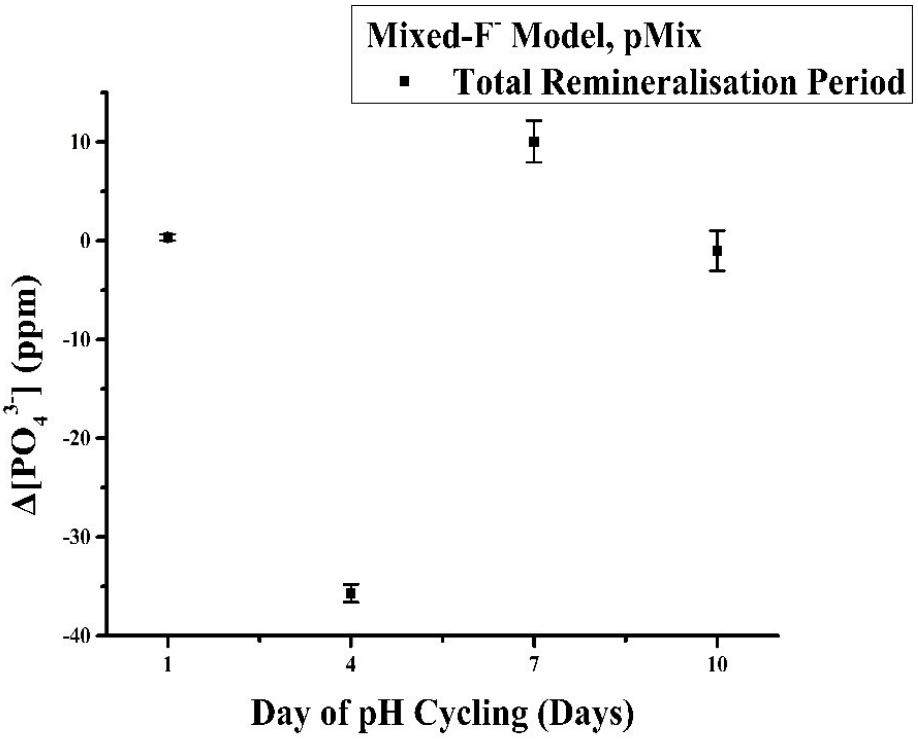

Figure 4-15: Changes in the concentration of PO_4^{3-} during the total (main+intermediate) remineralisation period for the primary enamel bovine blocks treated with the mixed-F^- pH-cycling model.

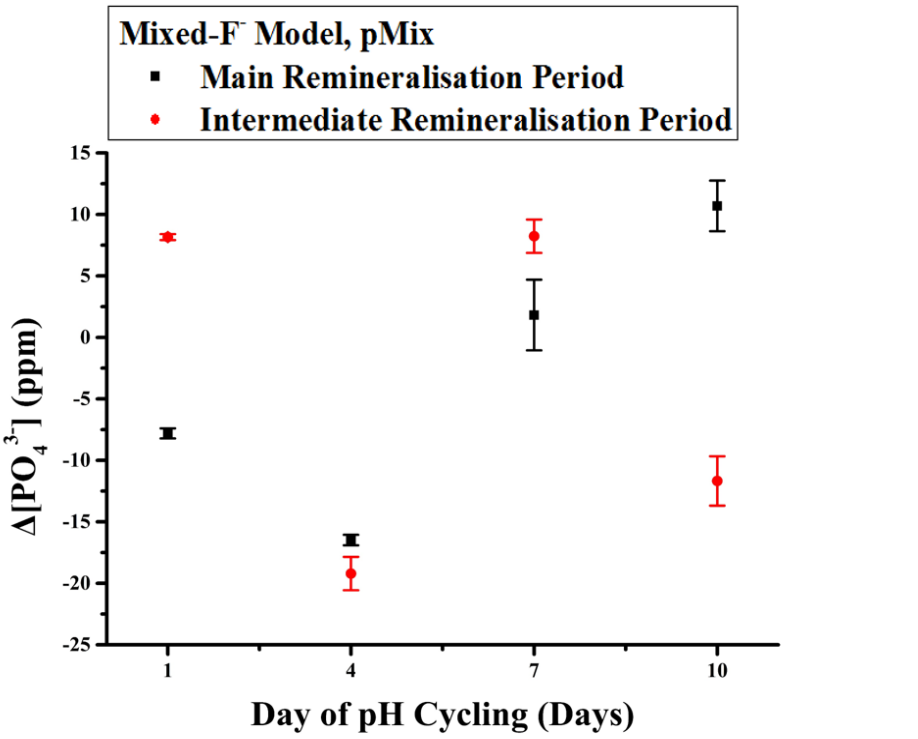

Figure 4-16: Changes in the concentration of PO_4^{3-} during the main and intermediate remineralisation periods for the primary enamel bovine blocks treated with the mixed-F^- pH-cycling model.

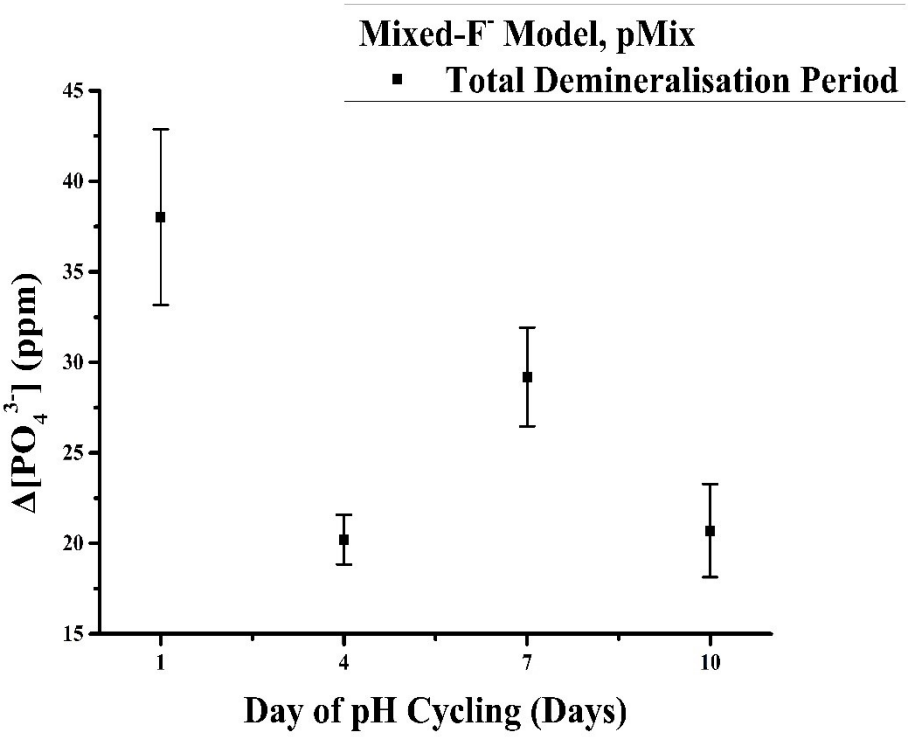

Figure 4-17: Changes in the concentration of PO_4^{3-} during the total demineralisation period for the primary enamel bovine blocks treated with the mixed-F^- pH-cycling model.

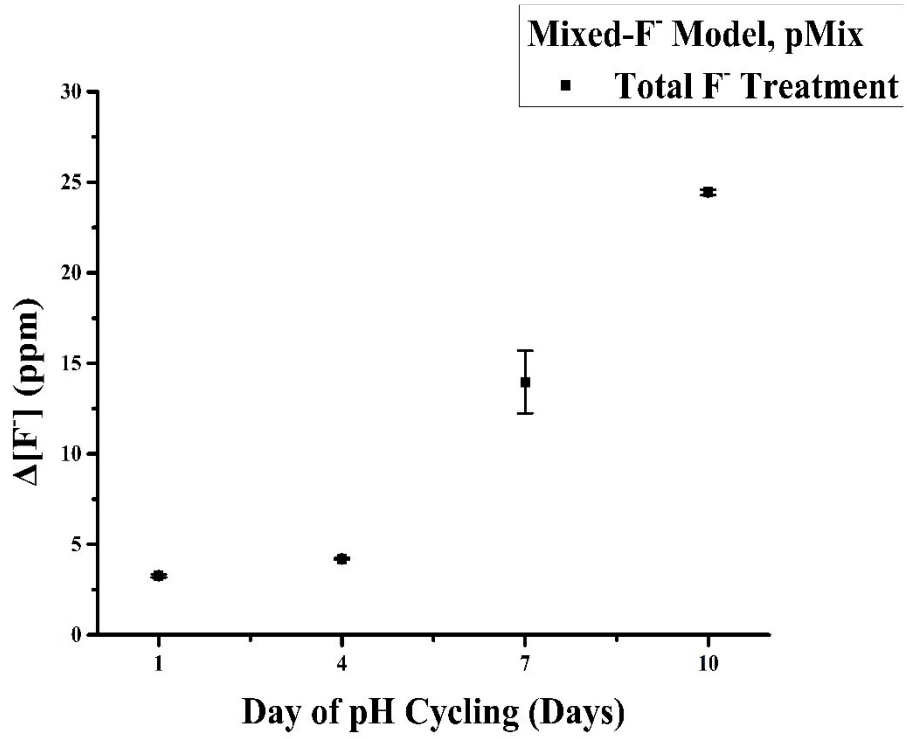

Figure 4-18: Changes in the concentration of F^- for the primary enamel bovine blocks treated with the mixed-F^- pH-cycling model.

4.2.2 Structural Analysis

The FTIR results for group pMix are presented in Figure 4-18. On day 1, 3 peaks between 540 cm^{-1} and 615 cm^{-1}, which correspond to the υ_4 PO_4^{3-} vibrational mode of HA (481-483) can be observed. These peaks drop to 2 by the end of the pH-cycling procedure with simultaneous shift of position and a decrease of about 50% of their total area. At the same time, the OH^- modes around 630 cm^{-1} (479, 480, 491) (surface: 3.339 cm^2) and 3665 cm^{-1} (surface: 1.103 cm^2) continuously decrease and disappear by the end of day 10.

At the same time, the F^--OH^- peak around 750 cm^{-1} (479, 480) increases in intensity (from 0.268 cm^2 to 27.993 cm^2); while the peaks between 1900 cm^{-1} and 2200 cm^{-1}, which are attributed to HPO_4^{2-} and well crystallised HA (479, 492), significantly increase both in numbers and area. With time, the presence of well crystalline HA around 1060 cm^{-1} which corresponds to the υ_3 PO_4^{3-} stretching vibration (487, 488) can also be observed with increasing intensity (0 to 15.401 cm^2).

As far as carbonate is concerned, the υ_4, υ_2, and υ_1 CO_3^{2-} peaks between 660 and 900 cm^{-1} (487, 493, 494) decrease in number and increase in total surface (from 33.264 cm^2 to 249.522 cm^2). Similarly an increase in the surface of the υ_3 CO_3^{2-} and carbonyl peaks (C=O) around 1450 cm^{-1} and 1730 cm^{-1} (487, 495, 496) can also be observed, which is more significant for 1450 cm^{-1} peak.

Noticeable presence of peaks corresponding to secondary phases, like acidic calcium phosphates, and newly precipitated HA was also observed. In this case, the presence of peaks correlated to crystalline acid phosphates and more precisely OCP (free HPO_4^{2-}, 520 cm^{-1}-540 cm^{-1}) (481-483, 497)) can be observed from day 1 and decrease in surface by the end of the pH-cycling (from 96.100 cm^2 to 12.722 cm^2). Significant is the peak correlated to the υ_3 PO_4^{3-} mode of newly precipitated HA around 1150 cm^{-1} (484, 498, 499), which increases in surface (~81.7%) with time with a simultaneous shift towards 1160 cm^{-1} (from 1149.597 cm^{-1} to 1156.914 cm^{-1}). Similarly the υ_3 PO_4^{3-} mode around 1020 cm^{-1} (484-486), which is correlated with a poorly crystallised mix of HA, OCP and TCP, is also present after day 1, and significantly increases with time, peaking on day 7 (36.921 cm^2) and then dropping slightly (32.377 cm^2). It must be also noted, that in the case of primary blocks peaks correlated with organic material can be also observed in the region 2490 cm^{-1} to 2570 cm^{-1} (558), which decrease with time.

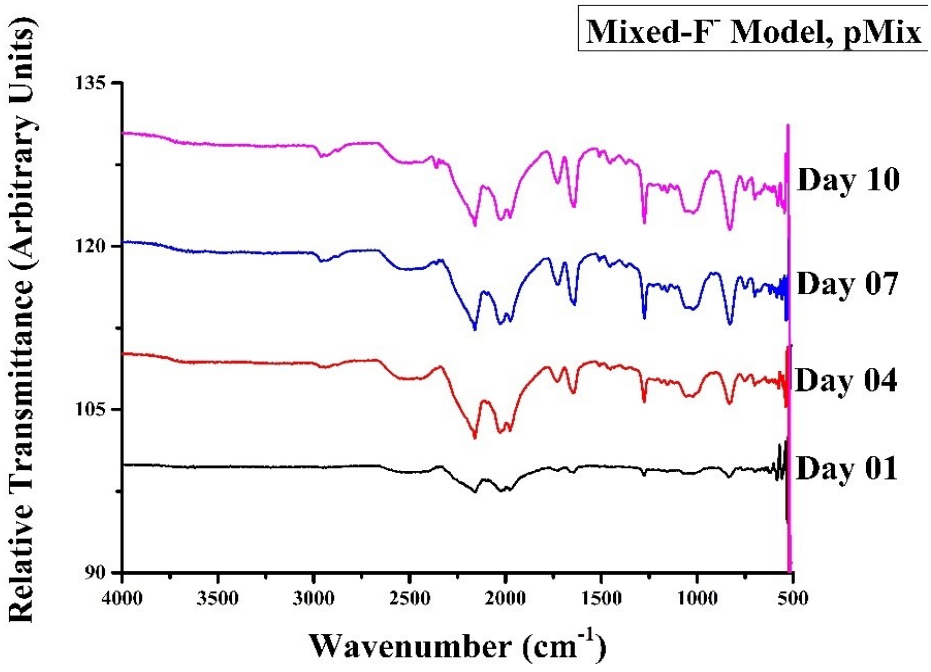

Figure 4-19: FTIR spectra of pH-cycled primary enamel blocks treated using the mixed-F^- pH-cycling model.

4.2.3 Mechanical Properties & Morphology

The last part of the analysis describes changes in the mechanical properties and surface morphology. Hardness changes were measured using a Vickers' micro-indenter and morphology was studied using AFM. Further details on the instruments and the analyses parameters can be found in sections 2.3.10 and 2.3.7 respectively. The results are presented below.

4.2.3.1 Micro-Hardness

The hardness results of pMix are consistent with those of the standard pH-cycling study. A continuous increase in hardness is observed especially after day 4, same as in the previous section. The increase is really slow compared to permanent enamel.

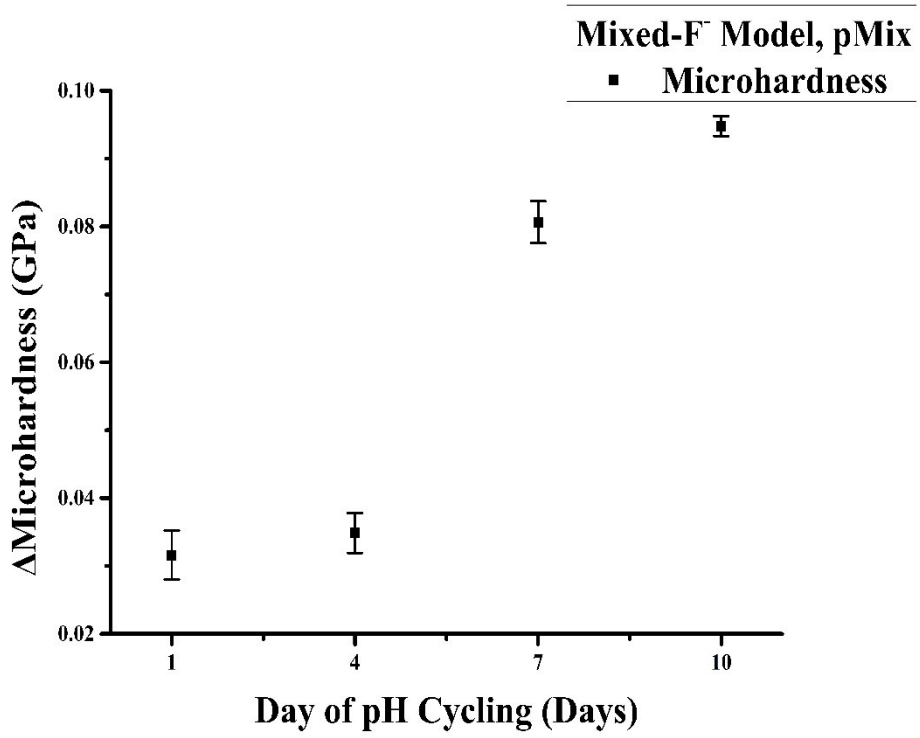

Figure 4-20: Changes in the hardness of the primary enamel treated with the mixed-F⁻ model.

4.2.3.2 Surface Morphology

Finally, AFM imaging of the surfaces of the treated primary enamel blocks are presented in figure 4-21. Similarly to $p1_{10}$ and $p2_{250}$, strong deposition of material can be observed from day 4 onwards. This deposition becomes more intense as the experimental procedure progresses. These images are in agreement with the chemical analysis, which suggests mainly deposition of CaF_2-like on the surface of the blocks, which becomes stronger over time.

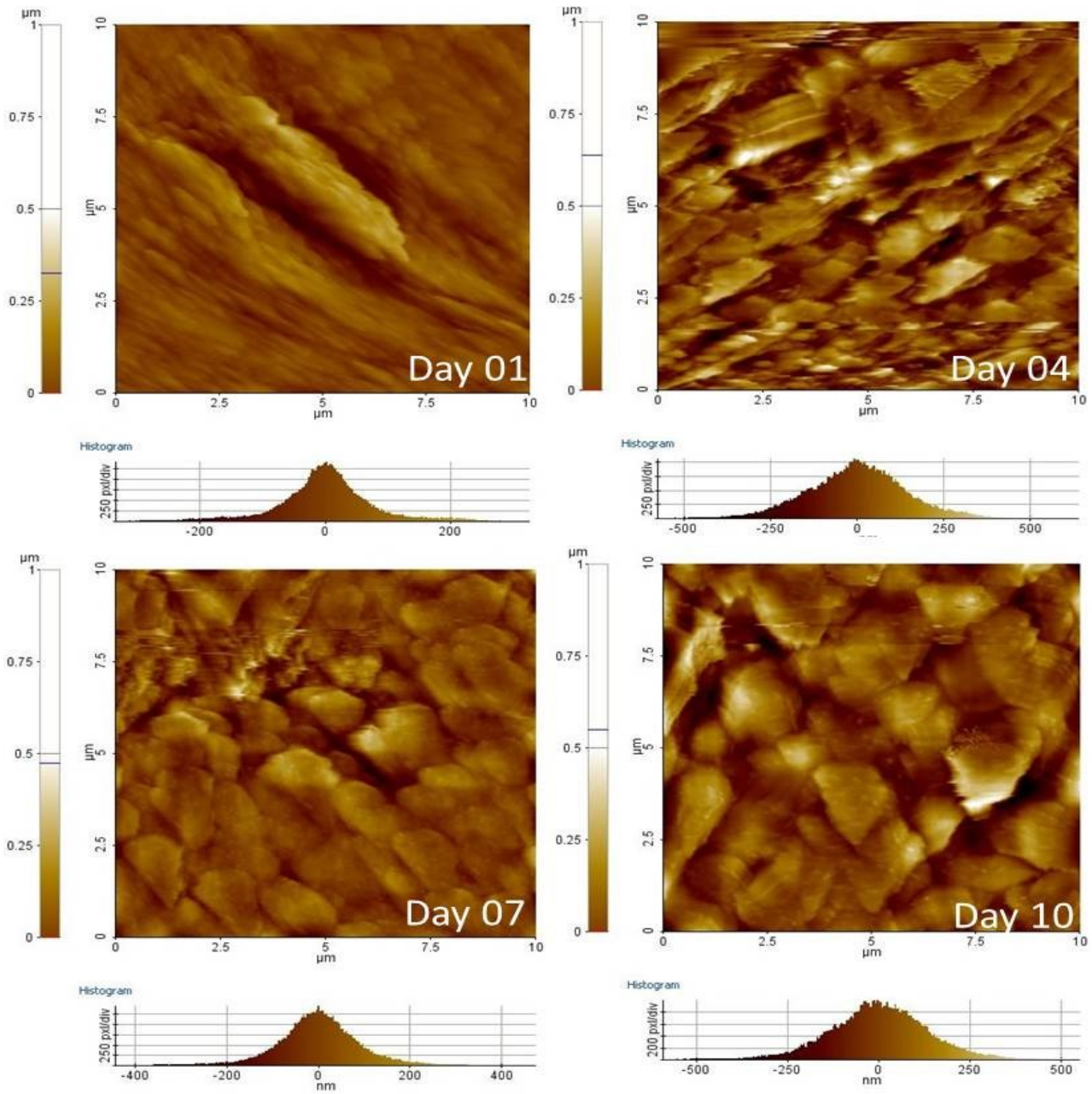

Figure 4-21: Changes in the surface morphology of primary enamel blocks treated with the mixed-F^- pH-cycling model.

4.2.4 Discussion

The results of the mixed-F^- pH-cycling model using primary enamel are similar to those using the standard pH-cycling protocol. Both Ca^{2+} (4-12, 4-13) and PO_4^{3-} (4-15, 4-16) changes follow the same trend as in section 4.1, with increasing accumulation of both with time. Calcium uptake peaks again on day 4 when the total remineralisation period is taken into account, then drops on day 11 and increases again on day 16. The phosphate trend mirrors that of Ca^{2+}. Initially, PO_4^{3-} release in the solutions peaks on day 4 and then the trend reverses and accumulation is observed. These results are different than those for the respective group of permanent enamel. In this case strong Ca^{2+} uptake is observed which decreases with time (Figure 3-31, 3-32). Another difference is that the most significant remineralisation period is the main for primary (Figure 4-13) and the intermediate for permanent (Figure 3-32) enamel. This can be attributed to the higher porosity and permeability of the former, which allows more intense and longer ionic diffusion (27, 545-547). On the other hand, for permanent enamel the temporary softening and increase in permeability (144, 534, 535) is more important. As far as the demineralisation period is concerned, increase in Ca^{2+} release is observed (Figure 4-14) up to day 4. After that day, the amount of Ca^{2+} released decreases, which seems to plateau by day 10. The decrease in this case is much faster than in the case of the standard pH-cycling model, which is probably the result of the increased F^- used.

The trend of the PO_4^{3-} results is similar to that of Ca^{2+}. Primary enamel presents strong PO_4^{3-} accumulation during the demineralisation period (Figure 4-17); while release is observed for the 1st half of the remineralisation period, which is followed by accumulation (Figure 4-16). Permanent enamel presents the opposite trend. Strong accumulation is observed during the remineralisation period (Figures 3-34, 3-35) while strong release is observed up to day 11, followed by accumulation on day 16 (Figure 3-36). This could be attributed to the primary

enamel containing more impurities (e.g. CO_3^{2-}) (27, 548-553), which result in a more distorted lattice and may lead to faster dissolution than permanent enamel.

It must be also noted that F^- behaves differently in this case (Figure 4-17), due to the switch from 10 ppm to 250 ppm of fluoride treatment. The first half resembles the behaviour of $p1_{10}$, while the 2nd that of $p2_{250}$. This is probably the reason why no significant correlations were observed between Ca^{2+}, PO_4^{3-} and F^- for the remineralisation period, while it is strongly correlated with Ca^{2+} ($p < 0.05$) and PO_4^{3-} ($p < 0.05$) during the demineralisation period. As stated in section 4.1.4 the most significant periods for $p1_{10}$ and $p2_{250}$ are the intermediate and main remineralisation periods respectively. In the case of the mixed-F^- pH-cycling model, the change in F^- administration leads to increase in the significance of the demineralisation period, but at the same time reduces the significance of the other two. This is also likely to have an effect on the hardness, which correlates with both Ca^{2+} ($p < 0.001$) and PO_4^{3-} ($p < 0.001$) during the demineralisation period. Highly significant correlation was also calculated between Ca^{2+} and PO_4^{3-} ($p < 0.0001$) for the same period.

These conclusions are also supported by the FTIR data (Figure 4-18), which follow those of the main pH-cycling study of primary enamel and the equivalent permanent experimental results (section 3.3.2). Similar changes to the standard model for the peaks between 540 cm^{-1} and 610 cm^{-1}, which correspond to the υ_4 PO_4^{3-} vibrational mode (481-483), are observed with decrease in number, shift in position and decrease of the total area. As already stated, these changes are correlated with F^- uptake. This is highlighted by the decrease in the OH^- modes around 630 cm^{-1} and 3665 cm^{-1} and the increase in the intensity of the F^--OH^- peak around 750 cm^{-1} (479, 480).

Precursor HA phases were also observed since the beginning of the pH-cycling procedure, indicated by the free HPO_4^{2-} modes existing below 540 cm^{-1} (481-483). These peaks decrease with time, while the υ_3 PO_4^{3-} around 1150 cm^{-1} increases and shifts towards 1160 cm^{-1} suggesting mineral maturation (484, 498, 499, 559). These results suggest the formation of OCP, DCPD and/or TCP, which are then hydrolysed (119, 271, 296, 526) into apatites (479, 480). Same as before the PO_4^{3-} mode around 1020 cm^{-1} (485, 486) is correlated with poorly crystallised mix of HA, OCP and TCP and its presence significantly increases with time up to day 7. The precipitation of new material is also indicated by the changes in the CO_3^{2-} peaks between 660 cm^{-1} and 900 cm^{-1} (υ_4, υ_2, and υ_1) and the υ_3 CO_3^{2-} and carbonyl (C=O) peaks around 1450 cm^{-1} and 1730 cm^{-1} (487) respectively. Finally in this instance as well, a decrease is observed in the peaks correlated with the presence of organic material between 2490 cm^{-1} and 2570 cm^{-1} (558).

4.3 Conclusions

Chapter 4 studied the effects of the proposed PEM mechanism on primary enamel. The results suggest that although the same broad principles proposed in Chapter 3 apply, the process is much slower when compared to permanent enamel. Due to its nature, primary enamel presents generally stronger dissolution than permanent enamel, which is followed by a reversal of the process and precipitation of material. Although material precipitation becomes stronger over time, the process is much slower than in the case of permanent enamel as hardness results also suggest.

The material which is precipitated is again a combination of precursor (e.g. OCP) and apatitic (poorly crystalline HA, fHA, FA) phases, which either transforms or matures with time towards more crystalline HA, fHA and FA. Precipitation of the precursor phases takes place mainly during the demineralisation period, which is found to be highly significant for the whole process. Depending on the amount administered during each treatment, faster or slower F^- incorporation takes place. Low F^- dosage favours structural incorporation, which makes the intermediate remineralisation phase as significant as the demineralisation period, due to the fairly increased background F^- concentration, which enhances OCP transformation in apatite.

On the other hand, higher F^- administration favours the precipitation and subsequent deposition of CaF_2 on the surface of the enamel. As a result, F^- incorporation inside the enamel is slower, which favours the incorporation primarily of acidic phosphates, their hydrolysis into HA and its subsequent transformation into fHA and/or FA, possibly with the help of F^- provided by the deposited CaF_2. Since this is a longer-term process, the main remineralisation period becomes more significant.

5. Development of Enamel Proxies & Comparison with Permanent Bovine Enamel

The chemical and structural similarities between biogenic apatite and synthetic HA (560, 561), in combination with the ease the latter can be produced (section 1.4.3) and the need to substitute the former in many common medical and dental procedures has led to extensive research aiming to develop synthetic HA as bone or dental enamel substitute (155, 193, 214, 562-564). Over time, several techniques have been used to produce biomimetic HA (section 1.4.3), but in all cases the product lacked some or all of the necessary mechanical properties to make it functional (367-369). Sintering techniques can theoretically improve some of the properties in question like density, flexural strength and hardness. On the other hand, it is also highly likely that they could lead to chemical deterioration due to HA transformation into other phases like β-TCP or CaO (370-372). Other proposed approaches to improve material properties include composites (565-568), dopants (569-571) and microstructural control (572-574). In all cases, though, the resulting material was classified as a poor analogue to natural biogenic HA.

For dental enamel in particular, reproducing its mechanical properties is really important, since it is the hardest tissue in the human body (29, 30). Recently, some studies have suggested that it is possible to synthesise thermally stable HA, which can be pelleted and sintered improving its mechanical properties (206, 242-244, 396). Out of the methods identified in the literature, the most promising for the present study were considered to be those where synthesis of nano-sized HA involved wet-precipitation techniques and freeze-drying of the precipitant (243, 244). This Chapter investigates the potential use of such techniques in the development of a material that could be potentially used as enamel substitute. Following the synthesis and processing of HA complete physicochemical characterisation takes place and comparison with the respective properties of enamel. Finally,

a simulation of the three elements used during the pH-cycling model using static solutions has been applied to both synthetic material and natural to compare the behaviour between the two.

5.1 Preparation & Characterisation of Thermally Stable HA

5.1.1 Preparation Techniques

The wet-precipitation technique used during HA synthesis is explained in detail in section 2.2.2. In short a solution of 1.0 M of $(NH_4)_2HPO_4$ was added dropwise to a solution of 1.75 M of $Ca(NO_3)_2 \cdot 4H_2O$ at a constant rate of 150 ml/h and at room temperature. The pH of the resulting solution was maintained in the region of 10.5 using $(NH_4)OH$. The produced solution was then heated at 90ºC and matured at this temperature under continuous stirring for 24 hours (242, 243). Half of the produced material was heat dried overnight at 80ºC in an oven, while the rest was freeze dried for 48 hours, after being rapidly frozen using liquid nitrogen.

The oven dried hydroxyapatite (HD-HA) was ground to fine powder using a ball-mill for 30 minutes at a vibrating frequency of 25 Hz; while the freeze dried powder (FD-HA) needed no milling because the acquired powder was already fine. Out of the produced powders pellets were created using a mechanical press and a maximum load of 30 kN. Some of the produced pellets were then sintered for 3 hours using 3 different temperatures (500ºC, 800ºC and 1100ºC). Finally, the produced pellets were then painted with nail polish leaving an exposed window of 2.5 x 3 mm^2, in preparation for chemical testing.

The produced synthetic powders and pellets along with enamel powder and blocks (prepared as described in section 2.2.1) were then characterised and compared.

5.1.2 Hydroxyapatite Powder Characterisation

5.1.2.1 Size & Morphology Characterisation

The difference in the way the synthesised HA was dried led to powders with different properties. This was also obvious by the direct production of FD-HA as fine powder; the oven dried material needed milling to become so. Figure 5-1 presents AFM images of the heat and freeze dried powders and powdered enamel. The figures show that both powdered enamel and FD-HA are in a finer form when compared to the oven dried material, which presents large aggregates. This is also supported by size measurements performed through the AFM images. The size distribution of the enamel, FD-HA and HD-HA powders are presented in figure 5-2. Enamel and FD-HA present similar sizes, while HD-HA presents significantly higher values due to the large amount of aggregates present. At the same time, FD-HA has a taller and narrower Gaussian distribution when compared to the other two. This is explained by the direct production of FD-HA in fine form and needed no milling as the other two did. This is also depicted in the significant standard deviations of enamel and HD-HA when the average particle size was calculated; which is 301±222 nm and 425±148 nm respectively, as measured through the AFM images. The size range for enamel is 86-1268 nm, while it is from 121 nm to 1120 nm for the HD-HA. The freeze dried powder, on the other hand, has an average particle size of 206±95 nm and a range of 78-781 nm. It is also worth noting that the freeze dried HA presents its maximum particle size at the same order with enamel (130 nm-160 nm).

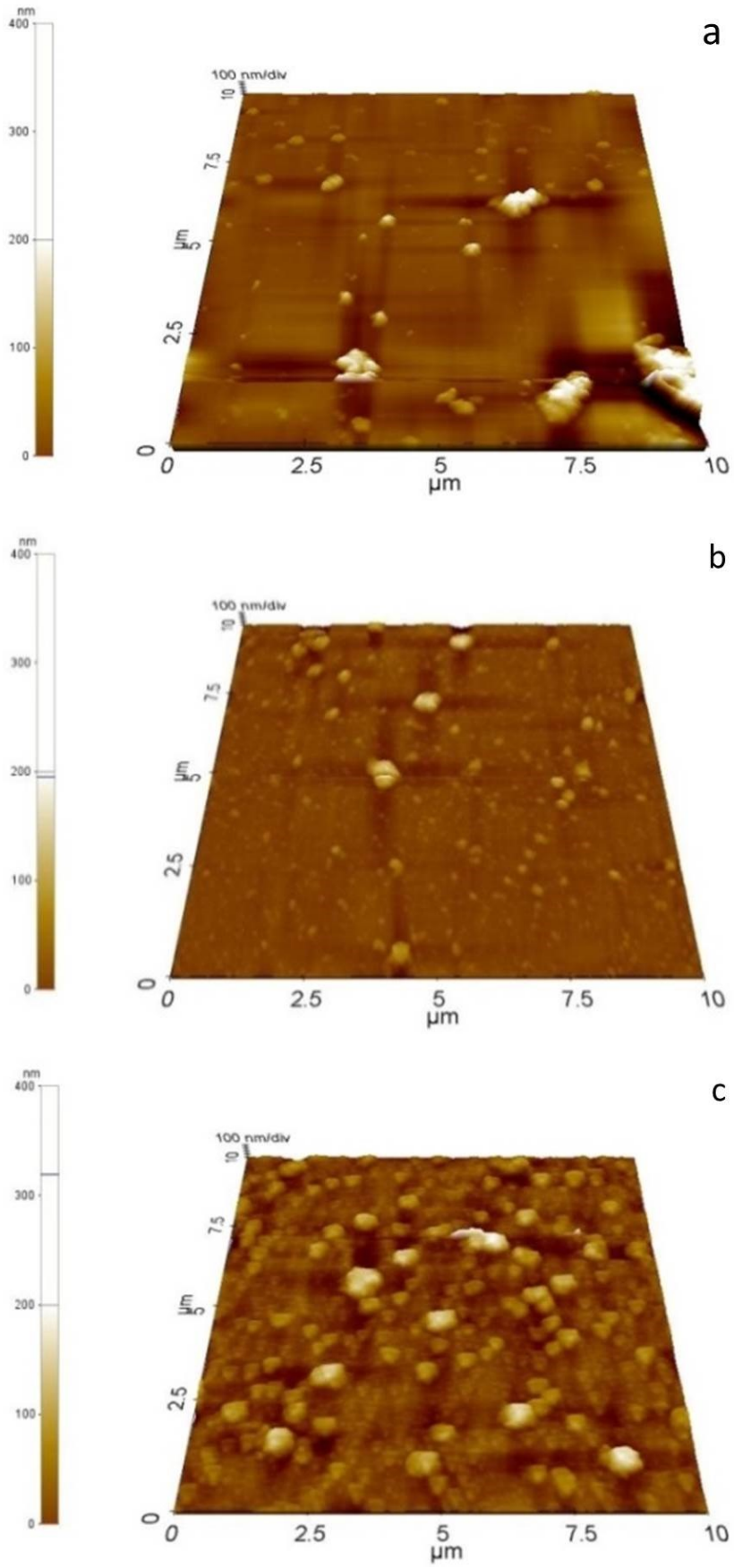

Figure 5-1: AFM images of a. powdered bovine enamel, b. freeze and c. oven dried HA.

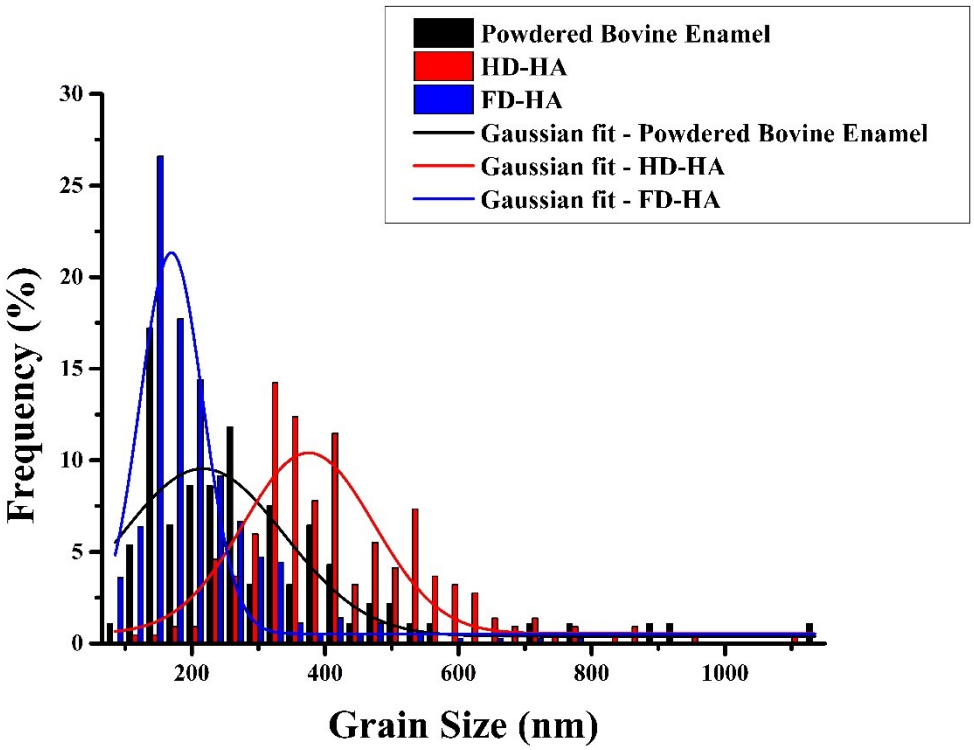

Figure 5-2: Size distribution of the bovine enamel (black), oven dried HA (red) and freeze dried HA (blue) powders, as measured through the AFM images.

5.1.2.2 Structural Characterisation

Structural characterisation of powdered bovine enamel and the as-produced and calcined at 500ºC, 800ºC and 1100ºC synthetic HD-HA and FD-HA powders was performed using FTIR and XRD. Details on the methodologies and the analysis parameters used can be found in sections 2.3.1 and 2.3.2 of Chapter 2 respectively.

Figure 5-3 and table A-1 in the Appendix present the FTIR spectra and associated peaks respectively for powdered enamel, FD-HA and HD-HA. All 3 materials present peaks which are associated with HA such as the υ_4 PO_4^{3-} modes in the region 540-610 cm^{-1} (481-483), which are also in similar positions especially in the case of enamel and FD-HA. Peaks associated with the υ_1 PO_4^{3-} mode around 960 cm^{-1} (575-577), which are related to poorly crystalline HA can be observed in the case of enamel and FD-HA and are similar in area. A similar peak can be also observed around 1030 cm^{-1} and corresponds to υ_3 PO_4^{3-} (575-577) for all 3 materials. In this case a shift in the peak position exists, which is correlated to mineral

maturation. For enamel, it is located at 1025 cm^{-1}, while for FD-HA and HD-HA is located at 1028 cm^{-1} and 1032 cm^{-1} respectively, which suggests more crystalline material. The more mature HD-HA can be attributed to the heating process used to dry it. Enamel also presents the υ_4 CO_3^{2-} peaks around 872 cm^{-1} (207, 578, 579) and the υ_3 peaks around 1414 cm^{-1} and 1452 cm^{-1} (487, 493, 494). A similar υ_3 CO_3^{2-} peak can be observed for FD-HA around 1419 cm^{-1} (487, 493, 494), which probably originates from the adsorption of dissolved CO_2 present in the waters used during the HA synthesis. In the case of HD-HA any similar peak has disappeared due to the heat drying process. FD-HA also presents peaks at 627 cm^{-1} and 3743 cm^{-1}, which are attributed to OH^- (479, 480) and verify the presence of HA. Finally, the peaks observed for FD-HA and HD-HA between 2200 cm^{-1} and 2400 cm^{-1} are attributed to ambient CO_2 (370, 580, 581) present during the FTIR measurements.

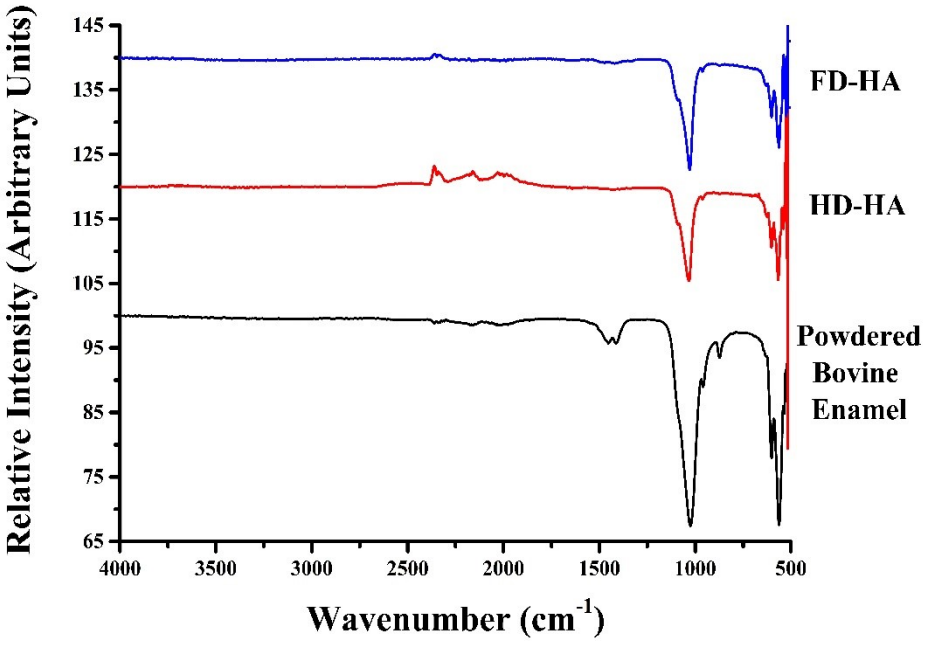

Figure 5-3: FTIR Spectra of powdered bovine enamel (black), HD-HA (red) and FD-HA (blue) powders.

Analyses of the XRD patterns of powdered enamel and the as-produced and calcined at 500ºC, 800ºC and 1100ºC HD-HA (Figure 5-4) and FD-HA (Figure 5-5) were performed using the JCPDS card No. 01-076-0694. Results show that in all cases the characteristic pattern of HA can be observed without any secondary phases due to structural transformation (370-372). It is notable that the as-produced and calcined at 500ºC diffractograms are poorly resolved and of low intensity, which is consistent with the low crystallinity of the materials. This is also evident by the broad patterns which correspond to the peaks found at (211) and (002); and signify that the crystallites are really small in size and present significant atomic oscillations (220). The crystal sizes, calculated using Scherrer's formula (Section 2.3.1), of enamel and the as-produced and sintered at 500ºC HD-HA and FD-HA powders have crystal sizes which range from 37.8 - 40.9 nm, while those sintered at 800ºC and 1100ºC have crystal sizes between 52.0-55.5 nm and 84.5-89.0 nm respectively.

Calcination up to 1100ºC does not seem to have an effect on the phases present in the material; although an increase in crystallinity is observed, which is expressed through the increase in intensity and narrowing of the XRD peaks. The above are also supported by the calculated crystal sizes, with increasing calcination temperature which was calculated using Scherrer's equation (Section 2.3.1) (206, 239) and can be seen in table 5-1. At the same time, underlying peaks which could not be observed at lower temperatures become visible (e.g. (112), (300)). In both cases, it seems that the HA which is closer to enamel is the HA calcined at 500ºC.

Type of Powder	Crystal Size (nm)
Bovine Enamel	37.8
Heat Dried HA	39.4
Heat Dried HA, Calcined at 500ºC	40.5
Heat Dried HA, Calcined at 800ºC	52.3
Heat Dried HA, Calcined at 1100ºC	84.7
Freeze Dried HA	38.0
Freeze Dried HA, Calcined at 500ºC	39.0
Freeze Dried HA, Calcined at 800ºC	55.3
Freeze Dried HA, Calcined at 1100ºC	89.9

Table 5-1: Calculated crystal sizes of the powdered bovine enamel and the as-produced and calcined heat and freeze dried synthetic powders. Calculation was performed using Scherrer's formula.

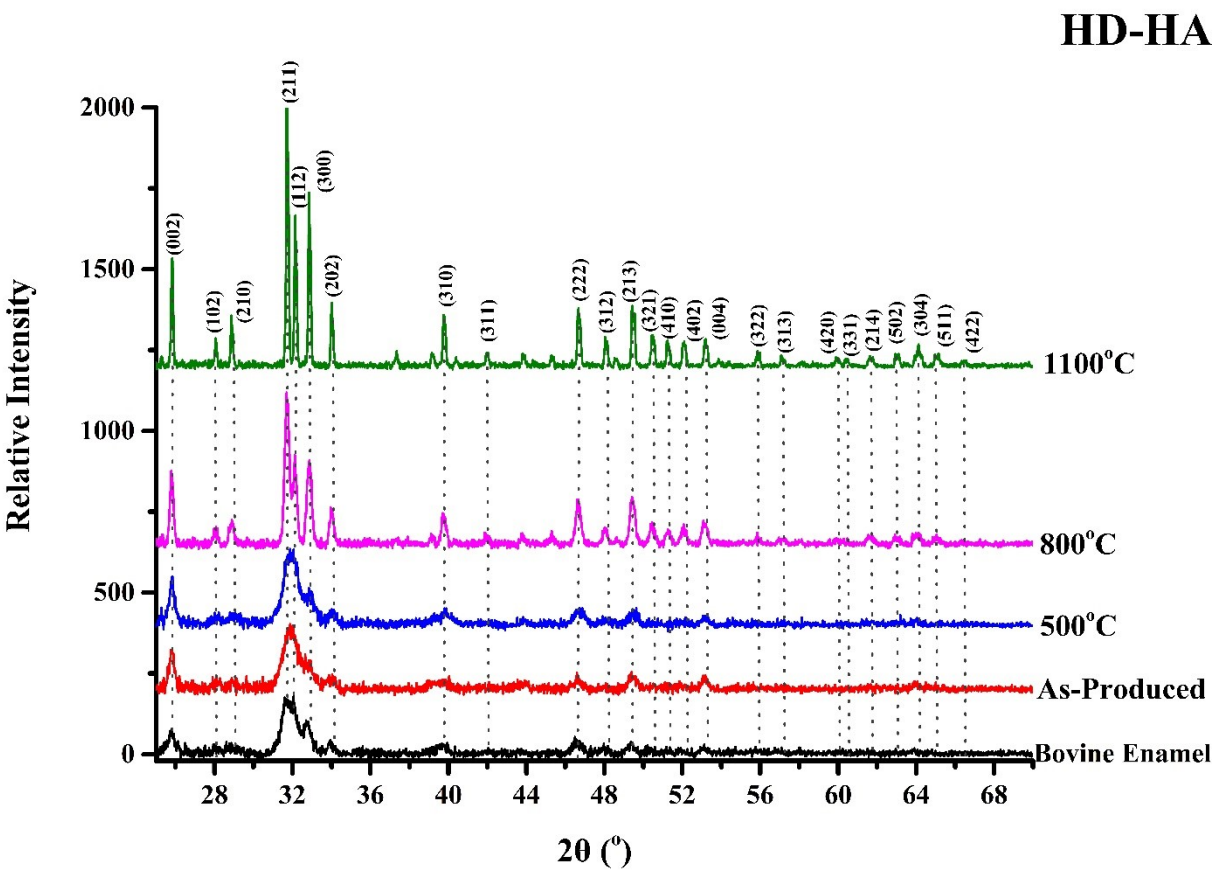

Figure 5-4: XRD patterns and peak assignment of bovine enamel compared to the as-produced and calcined at 3 different temperatures (500ºC, 800ºC and 1100ºC) heat dried HA.

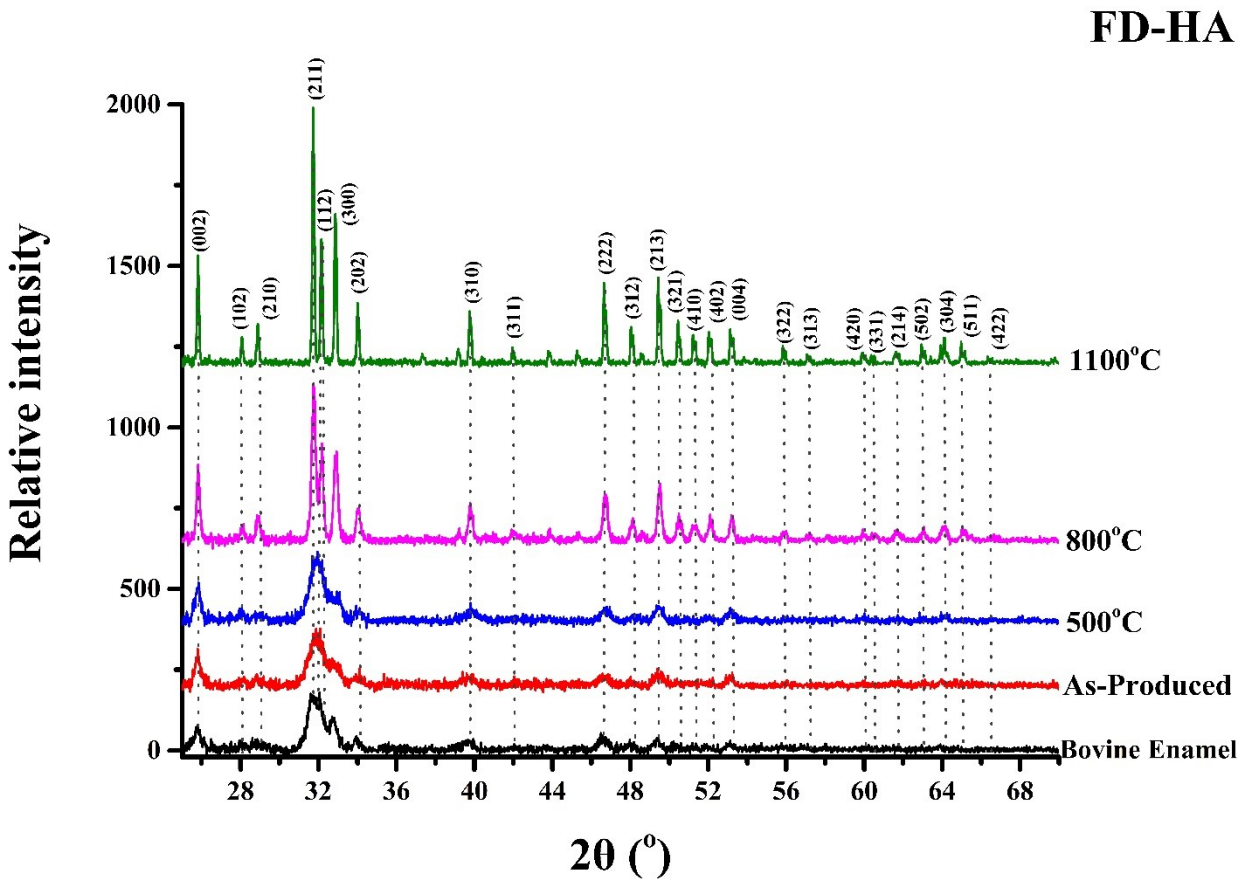

Figure 5-5: XRD patterns and peak assignment of powdered bovine enamel compared to the as-produced and calcined at 3 different temperatures (500°C, 800°C and 1100°C) FD-HA.

5.1.2.3 Powder Density & Surface area

The surface area and density of the powdered enamel and the synthesised and calcined HA powders was measured using the BET and He-densitometry methods respectively. Both methods are described fully in sections 2.3.3 and 2.3.4 of Chapter 2. Densitometry results (Table 5-2) show that HA density increases with increasing calcination temperature. As can be seen the increase in density is significant above 800°C. The significant increase also points out to a the lack of secondary phases inside the HA due to structural transformation, since in this case the result would be lower (206, 582, 583). It is also worth noting that the experimental values closer to that reported for HA (206, 218, 583, 584) are those for the powders sintered at 800°C, while that of enamel is much lower. This is likely to be because

biogenic apatite contains several impurities (e.g. CO_3^{2-}, Zn^{2+}, Sr^{2+}) (78, 79) and potentially other phases like TCP and/or OCP (99, 100, 153, 154).

Material	Powder Density (g cm^{-3})	Standard Deviation (g cm^{-3})
HA (Theoretical)	3.160	N/A
Bovine Enamel	2.960	0.002
Heat Dried HA	2.787	0.003
Heat Dried HA, Calcined at 500ºC	2.968	0.002
Heat Dried HA, Calcined at 800ºC	3.154	0.004
Heat Dried HA, Calcined at 1100ºC	3.252	0.002
Freeze Dried HA	2.736	0.003
Freeze Dried HA, Calcined at 500ºC	2.751	0.005
Freeze Dried HA, Calcined at 800ºC	3.216	0.005
Freeze Dried HA, Calcined at 1100ºC	3.244	0.002

Table 5-2: Density measurements of the powdered bovine enamel and the as-produced and calcined heat and freeze dried synthetic powders.

As far as surface area is concerned (Table 5-3), the wet-precipitation method and subsequent maturation used during synthesis leads to a material which has a high surface area and is in general highly reactive (585). Increasing the calcination temperature leads to significant reduction of the surface area, which is in agreement with previous studies (241, 372). The value closer to that measured for powdered enamel through BET (8.1±0.8 m^2g^{-1}) is the value of HA powders calcined at 800ºC.

Material	Surface Area (m^2 g^{-1})	Standard Deviation (m^2 g^{-1})
Bovine Enamel	8.1	0.8
Heat Dried HA	153.4	4.9
Heat Dried HA, Calcined at 500ºC	112.2	0.2
Heat Dried HA, Calcined at 800ºC	12.9	0.1
Heat Dried HA, Calcined at 1100ºC	0.7	0.1
Freeze Dried HA	172.7	6.7
Freeze Dried HA, Calcined at 500ºC	121.2	4.2
Freeze Dried HA, Calcined at 800ºC	6.3	0.2
Freeze Dried HA, Calcined at 1100ºC	1.9	0.1

Table 5-3: Surface area measurements of the powdered bovine enamel and the as-produced and calcined heat and freeze dried synthetic powders.

5.1.3 Discussion

The first part of Chapter 5 describes the synthesis of thermally stable HA powders. In order to do so, a wet-precipitation method was used which was followed by a 24 hour maturation period of the product. Finally, the resultant precipitant was either heat or freeze dried in order to acquire the powders for characterisation and comparison with powdered enamel. The resulting powders seem to have similar characteristics. The size distribution of the produced powders (Figure 5-2) lies within a similar range, but FD-HA presents a narrower distribution. This is because the freeze drying process leads to the production of fine powder, while enamel and HD-HA need milling. Comparison of the resultant powders led to the conclusion that the average size of FD-HA and powdered enamel are closer, while HD-HA presents significantly higher values due to the aggregates present following the milling process. Strong similarity is also observed for the density of the produced powders (Table 5-2). The measured densities of enamel, HD-HA and FD-HA are 2.960 g cm^{-3}, 2.787 g cm^{-3} and 2.736 g cm^{-3} respectively; while the theoretical value for pure HA is 3.160 g cm^{-3} (582, 586). On the other hand, significant differences exist between the surface areas of the produced materials and that of enamel. Both HD-HA and FD-HA present significantly high surface area values (153.4 ± 4.9 m^2 g^{-1} and 172.7 ± 6.7 m^2 g^{-1} respectively) while enamel is a lot lower (8.1 ± 0.8 m^2 g^{-1}).

As far as the thermal stability of the produced material is concerned, the XRD patterns (Figures 5-4, 5-5) do not significantly change when the powders were calcined at 500ºC for 3 hours. Calcination at 800ºC and 1100ºC leads to a significantly more crystalline material, with significantly higher crystallite sizes which were calculated using the (002) peak of the XRD patterns (Figures 5-4, 5-5). As the sintering temperature increases so do the crystal sizes of synthetic powders, which become more than double in size (from 39.4 nm to 84.7 nm and from 38.0 nm to 89.9 nm for HD-HA and FD-HA respectively), which denotes better crystallinity (206, 239). The as-produced and sintered at 500ºC HD-HAs have larger crystals

than the respective FD-HA and enamel powders. On the other hand, the as-produced FD-HA has similar crystal size to powdered enamel and the FD-HAs sintered at 800ºC and 1100ºC have crystal sizes greater than the respective HD-HAs. This is probably due to the drying process used for HD-HAs.

At the same time, no transformation of material into either TCP or CaO can be observed through XRD up to 1100ºC; this could be an indication of structural stability and close to a stoichiometric Ca/P ratio, since a ratio between 1.5 and 1.67 could have led to dissociation into either α-TCP (242) or more commonly β-TCP (243, 244). For greater Ca/P ratios between 1.67 and 2 the thermally unstable material would form CaO, P_2O_5 and possibly $Ca_4(PO_4)_2O$ (245-247). While no other phase is observed with increasing temperature, significant reduction of the surface area and densification of the produced material is observed. The wet-precipitation method used during synthesis led to high surface area powders regardless of the drying method used (Table 5-3). Calcination of the powders led to decreased surface area values, especially for the powders calcined at 800ºC and 1100ºC. The values measured for the powders calcined at 800ºC led to surface areas similar to those measured for bovine enamel (8.1 $m^2 g^{-1}$); with FD-HA (6.3 $m^2 g^{-1}$) being closer to the enamel than HD-HA (12.9 $m^2 g^{-1}$). These results are in agreement with other studies and are attributed to particle densification and coalescence (241, 587). This is also supported by the densification of the particles measured with increasing calcination temperature (Table 5-2). The measured densities of powdered enamel and the HD-HA and FD-HA powders calcined at 800ºC are 2.960 g cm^{-3}, 3.154 g cm^{-3} and 3.216 g cm^{-3} respectively, while the theoretical density of HA is 3.160 g cm^{-3}. This could suggest that the enamel and the powders calcined at 800ºC could behave similarly.

Comparison of the FTIR spectra (Figure 5-3) and XRD patterns (Figures 5-4, 5-5) for powdered enamel and the as-produced HA powders suggest that a lot similarities exist. In all cases a poorly crystalline material can be observed with low dimension crystallites as the broad and short (211) and (002) peaks suggest (220). At the same time, the FTIR results (Figure 5-3, Table 5-1) show that all 3 powders present similar peaks, which are characteristic for HA; like the υ_4 PO_4^{3-} asymmetric bending vibration (540-610 cm^{-1}), the υ_1 PO_4^{3-} symmetric stretching (~960 cm^{-1}) and the υ_3 PO_4^{3-} asymmetric stretching (1020-1030 cm^{-1}) (575-577).

At the same time, several differences are observed because, contrary to the synthesised powders, enamel is a Ca-deficient, non-stoichiometric HA (29, 32, 37, 578). The 3 cm^{-1} shift observed between the υ_1 PO_4^{3-} peaks between the enamel and FD-HA is characteristic for biogenic apatites (146) and is similar with the shift observed for the υ_3 peak from 1025 cm^{-1} for enamel to 1028 cm^{-1} for FD-HA and finally to 1032 cm^{-1} for HD-HA which denotes significantly increased crystallinity and maturation of mineral (485, 486).

Another difference between enamel and the synthetic materials is the presence of CO_3^{2-}, which is also characteristic for biogenic apatites and is the most significant impurity; reaching up to 3% per volume (512). Such peaks are the out of plane bending mode around 872 cm^{-1} which is also used to characterise Ca-deficient and non-stoichiometric apatites (207, 578, 579) and the asymmetric stretching modes observed between 1400 cm^{-1} and 1500 cm^{-1} (577, 588); which also present significantly high areas (Appendix, Table A-1). Such peaks may be absent from the synthetic HAs, since no CO_3^{2-} was intentionally added in the solutions during synthesis. In practice this is true for the HD-HA, which was heat-dried; but a small peak can be observed in the case of FD-HA around 1419 cm^{-1}. This peak probably originates by dissolved ambient CO_2, which was inside the waters used during the HA synthesis and got

incorporated in the apatite structure. The freeze-drying process used in the case of FD-HA allowed CO_3^{2-} to remain inside the apatite structure and not to be released as in the case of HD-HA.

The next part describes the HA pelleting and sintering at various temperatures and the characterisation of those pellets.

5.2 Pelleting & Sintering of Hydroxyapatite

5.2.1 Preparation Techniques

Pelleting of the synthesised powders was performed using a mechanical press as described in section 2.2.3. For each pellet an average mass of (0.400±0.001) g was used. The resulting pellets were circular discs with an average diameter of (13.005±0.019) mm and an average height of (1.827±0.041) mm. The pelleting process pointed out differences between the HD-HA and the FD-HA due to differences in particle size. As can be seen in figure 5-6 there is a delay in the time the pelleting force starts to be applied in the case of the HD-HA; which is due to the large aggregates present. When the powder is placed inside the dye for pelleting, air is trapped between the particles; which needs to be removed so that the pelleting can be formed. As the force starts to increase the air escapes and the empty space is gradually compacting. As soon as the air is completely removed, collapsing of the initial structure commences and the pellet is formed.

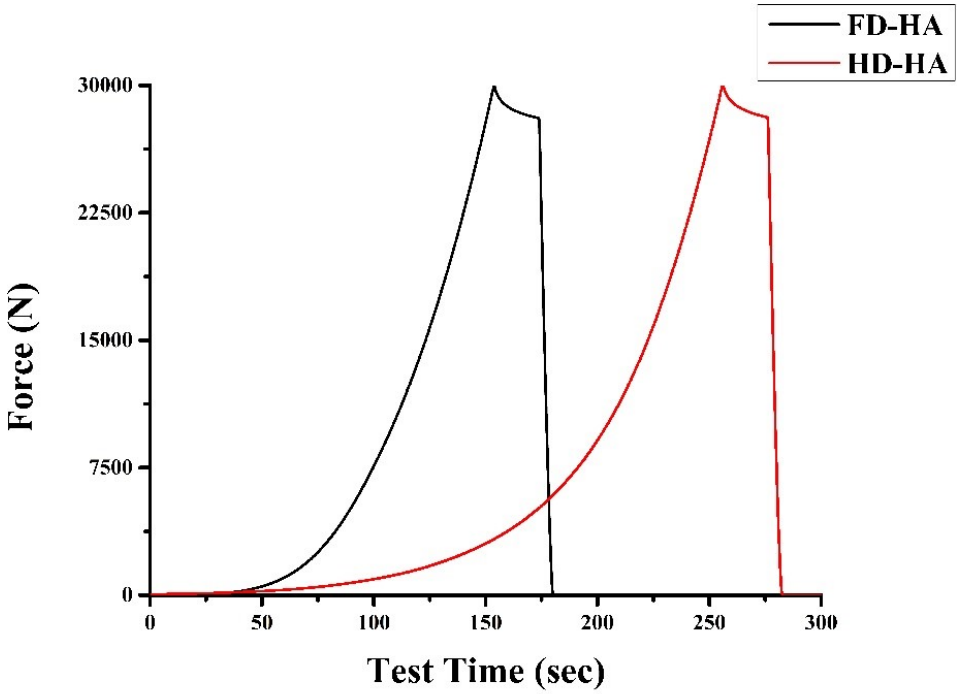

Figure 5-6: Force application during the pelleting process vs. test time.

Some of the produced pellets were then sintered to improve their stability and mechanical properties. Sintering of the pellets took place following the same procedure used during powder calcination. In short, the pellets were placed inside an oven and the temperature rose with a steady rate of 10°C min^{-1} up to the sintering temperature (500°C, 800°C or 1100°C). The pellets remained in the sintering temperatures for 3 hours and then allowed to cool down slowly to room temperature. The produced pellets were then characterised using FTIR, He-densitometry, Hg-porosimetry and Microindentation. The principles of application and analyses parameters are presented in Chapter 2, sections 2.3.2, 2.3.4, 2.3.5 and 2.3.10 respectively.

5.2.2 Hydroxyapatite Pellets Characterisation

5.2.2.1 Structural Characterisation

Figure 5-7 presents the spectra and tables A-2, A-3 and A-4 in the Appendix present the significant peaks of bovine enamel, HD-HA and FD-HA respectively. Results show that there are a lot of similarities between the acquired spectra. In all cases, several peaks which are characteristic of HA presence can be observed. Such peaks include the asymmetric bending vibrations of the υ_4 PO_4^{3-} mode (540-615 cm^{-1}) (575-577), which are in general strong and increase in intensity for the more crystalline synthetic material and especially for the pellets sintered at 800ºC; although decrease is observed for the pellets sintered at 1100ºC. Peaks corresponding to the symmetric (950-1000 cm^{-1}) and asymmetric (1000-1200 cm^{-1}) stretching of υ_1 and υ_3 PO_4^{3-} modes respectively (575-577) can also be observed, which are shifted in position and change in surface depending on the degree of crystallinity of the material. Some HPO_4^{2-} modes between 1900 cm^{-1} and 2200 cm^{-1} which correspond to well crystallised HA are also observed, which are a lot weaker as the crystallinity of material is reduced. Finally, lattice water (589, 590) can also be observed in some cases, for both the enamel and the synthetic pellets, which is removed as the sintering temperature increases.

As far as carbonate is concerned, the enamel presents several bands like the out of plane bending υ_4 CO_3^{2-} mode around 872 cm^{-1} (207, 578, 579), the υ_3 CO_3^{2-} asymmetric stretching mode between 1400 cm^{-1} and 1500 cm^{-1} (577, 588) and two CO_2 peaks between 2300 cm^{-1} and 2400 cm^{-1}. Some of these peaks, although much weaker, can also be observed in the case of the synthetic pellets, even in the case of those sintered at 500ºC. Both the as-produced HD-HA and FD-HA present a peak around 872 cm^{-1}; while FD-HA presents an extra peak around 1418 cm^{-1}. Some of the peaks are present in the case of the pellets sintered at 500ºC, but no carbonate can be observed in the cases of the pellets sintered at 800ºC and 1100ºC.

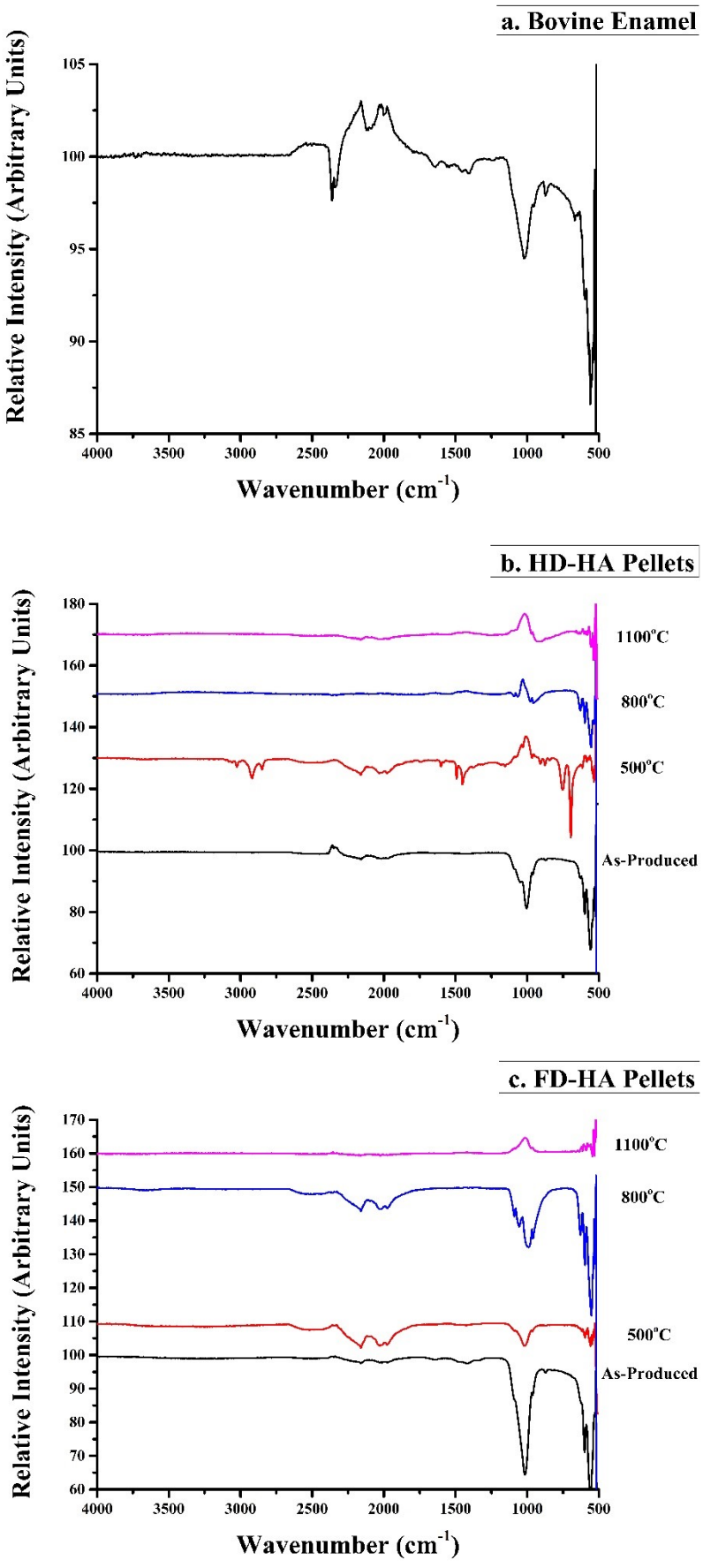

Figure 5-7: FTIR Spectra of a. bovine enamel block and as-produced and sintered b. HD-HA and c. FD-HA synthetic HA pellets.

5.2.2.2 Density & Porosity of the synthetic pellets

The changes in density and porosity of the heat and freeze dried synthetic HA pellets as a function of sintering temperature are presented in Table 5-4 and figure 5-8. The density of the HA pellets increases with increasing sintering temperature, reaching its maximum value at 1100ºC. The values of HD-HA and FD-HA are in general similar; although HD-HA presents slightly higher values, which is probably due to the post-synthesis drying procedure and the presence of aggregates following the milling procedure used to acquire the fine powder used for pellets. The values closer to those calculated for enamel are those of the HA sintered at 500ºC and 800ºC for HD-HA and FD-HA respectively. The calculated density of bovine enamel blocks is (3.027±0.008) g cm^{-3}, while it is (3.112±0.003) g cm^{-3} and (3.008±0.002) g cm^{-3} for HD-HA and FD-HA respectively.

The behaviour of porosity is different than that of density. The as-produced HD-HA pellets present higher porosity than the FD-HA do, which is probably due to the larger particle size and the aggregates present inside the powder used for pelleting. The calculated values of 27.9±0.9 and 25.2±1.0, measured as % empty space, are significantly higher than that calculated for the enamel blocks of (8.9±1.5)% empty space. The difference in this case is that initially an increase in porosity of 38.9% and 33.9% is observed for the pellets sintered at 500ºC, which is followed by fast decrease in the cases of the 800ºC and 1100ºC sintered pellets. This may be because the sintering process at 500ºC leads to a rearrangement of the powder without a collapse in its structure; and most significantly to removal of trapped air and/or water, which results in an initial increase of the available voids. As the temperature rises at 800ºC and 1100ºC a collapsing of the structure also takes place which results in the observed porosity decrease. In all cases significant correlation exists ($p < 0.05$) both between sintering temperature with density and porosity, as well as density vs. porosity.

Material	Density ($g\ cm^{-3}$)	Standard Deviation ($g\ cm^{-3}$)	Porosity (% empty space)	Standard Deviation (% empty space)
Bovine Enamel	3.027	0.008	8.9	1.5
Heat Dried HA	2.808	0.003	27.9	0.9
Heat Dried HA, Sintered at 500°C	2.999	0.002	38.8	4.1
Heat Dried HA, Sintered at 800°C	3.112	0.003	25.5	4.0
Heat Dried HA, Sintered at 1100°C	3.187	0.005	8.9	2.9
Freeze Dried HA	2.770	0.005	25.2	1.0
Freeze Dried HA, Sintered at 500°C	2.991	0.002	33.7	1.0
Freeze Dried HA, Sintered at 800°C	3.008	0.002	23.2	1.4
Freeze Dried HA, Sintered at 1100°C	3.145	0.004	10.7	2.6

Table 5-4: Changes in density and porosity of synthetic heat and freeze dried HA pellets with sintering temperature and comparison with bovine enamel blocks.

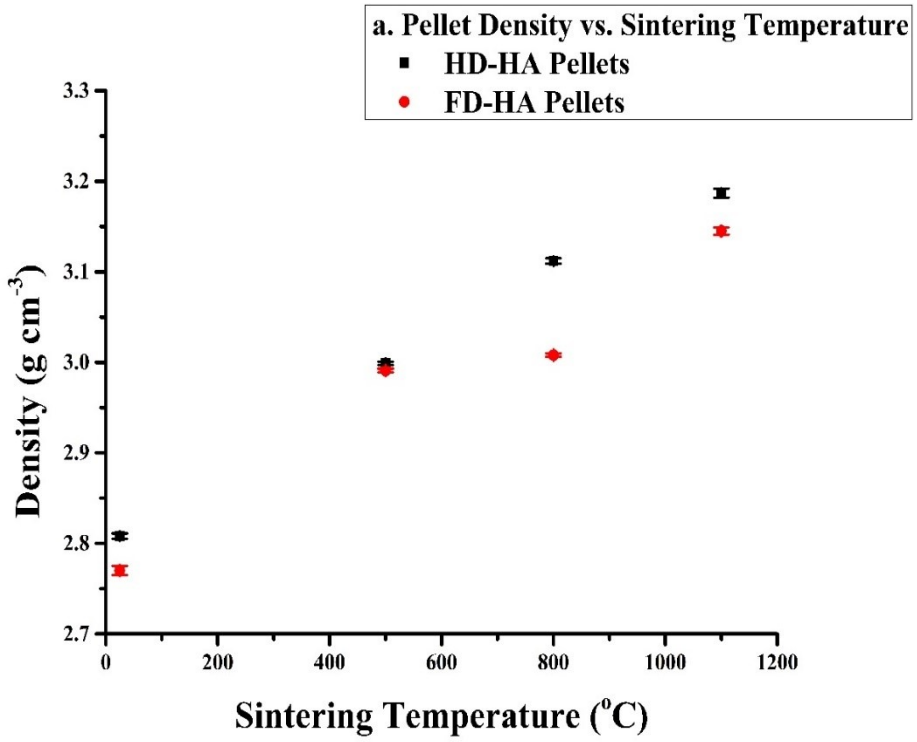

Figure 5-8: Changes in a. density and b. porosity of synthetic heat and freeze dried HA pellets as a function of the sintering temperature.

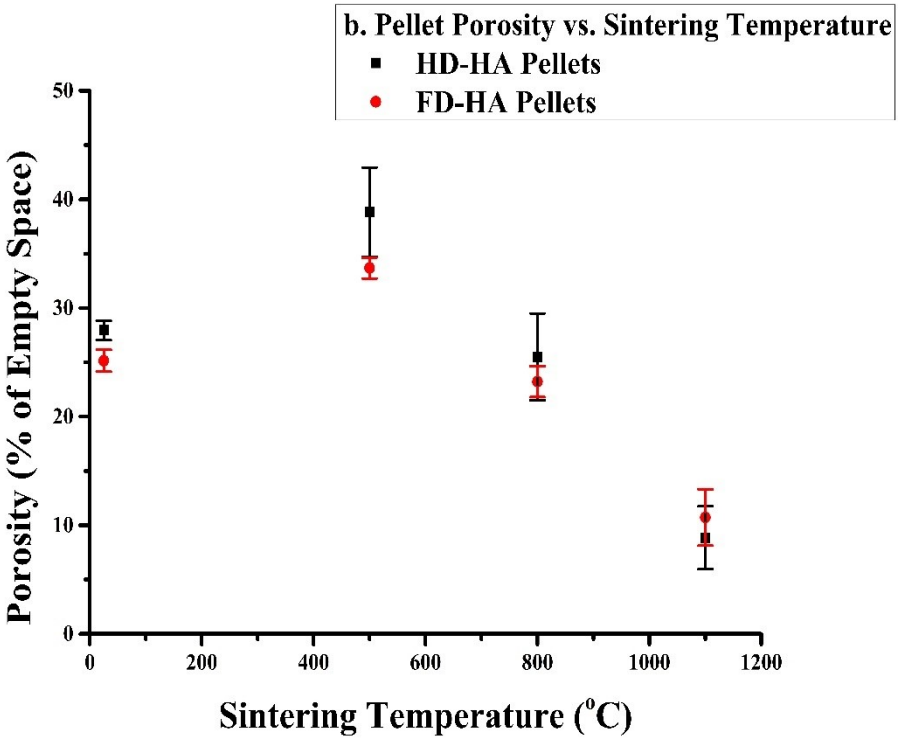

Figure 5-8 (Continued): Changes in a. density and b. porosity of synthetic heat and freeze dried HA pellets as a function of the sintering temperature.

5.2.2.3 Hardness of the synthetic pellets

The hardness of the synthetic pellets increases with increasing sintering temperature (Table 5-5, Figure 5-9). The hardness of the as-produced and sintered at 500ºC pellets (both HD-HA and FD-HA) is a lot lower than that reported for enamel (3.43 GPa). As the sintering temperature increases, there is a rapid increase in the hardness of the pellets. The hardness measured at 800ºC is similar to that of enamel and is (3.65±0.59) GPa and (3.63±0.86) GPa for HD-HA and FD-HA pellets respectively. The pellets sintered at 1100ºC present a far higher hardness, which is to be expected due to higher density and lower porosity observed in this case.

Material	Hardness (GPa)	Standard Deviation (GPa)
Bovine Enamel (Average Reported Value)	3.43	N/A
Heat Dried HA	1.27	0.13
Heat Dried HA, Sintered at 500°C	1.78	0.34
Heat Dried HA, Sintered at 800°C	3.65	0.59
Heat Dried HA, Sintered at 1100°C	5.86	0.65
Freeze Dried HA	1.13	0.20
Freeze Dried HA, Sintered at 500°C	1.48	0.47
Freeze Dried HA, Sintered at 800°C	3.63	0.86
Freeze Dried HA, Sintered at 1100°C	5.83	0.49

Table 5-5: Changes in the hardness of the as-produced and sintered HA pellets for both the heat and freeze dried material.

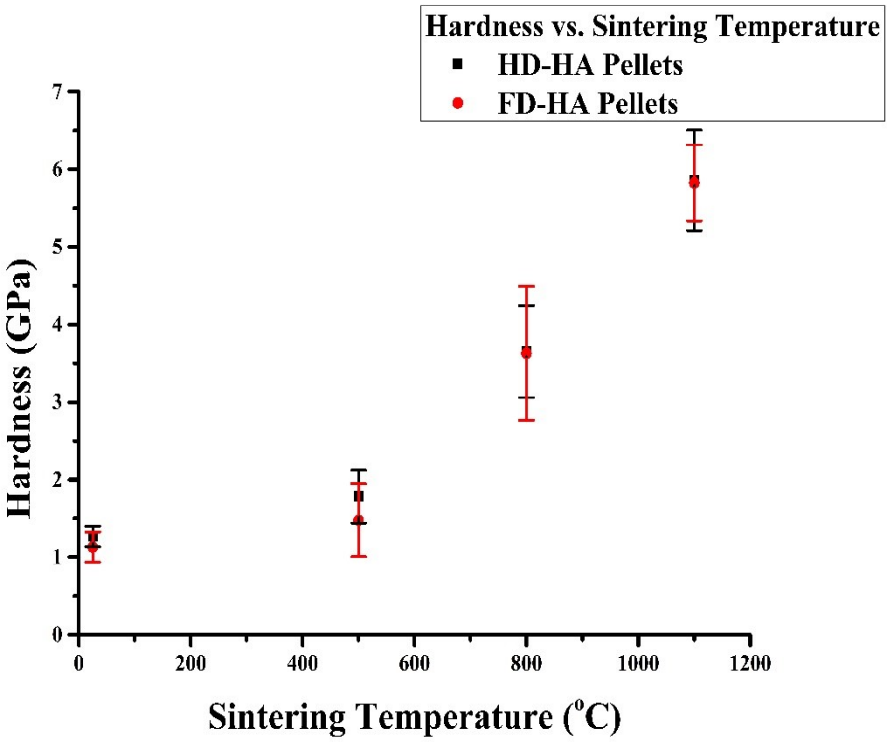

Figure 5-9: Changes in the hardness of the as-produced and sintered synthetic HA pellets.

5.2.2.4 Surface Morphology

Figures 5-10 and 5-11 present AFM images of the surfaces of the as-produced (Figures 5-10a, 5-11a) and the pellets sintered at 500°C (Figures 5-10b, 5-11b), 800°C (Figures 5-10c, 5-11c) and 1100°C (Figures 5-10d, 5-11d) HD-HA and FD-HA pellets. Images suggest that the surface of the pellets becomes smoother as the sintering temperature increase, which also suggests the more crystalline and ceramic nature of the sintered material.

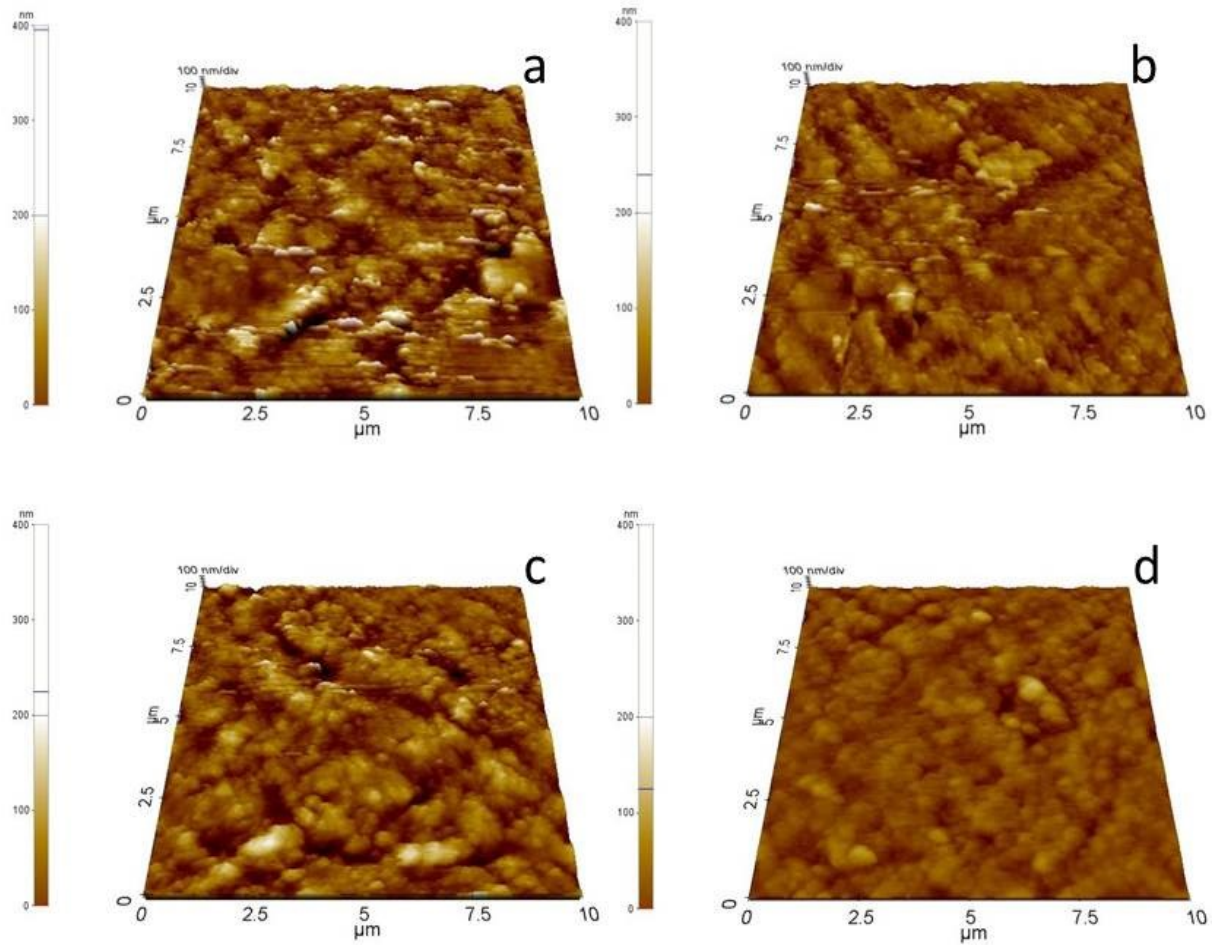

Figure 5-10: Surface morphology of the a. as-produced and sintered at b. 500°C, c. 800°C and d. 1100°C HD-HA synthetic pellets.

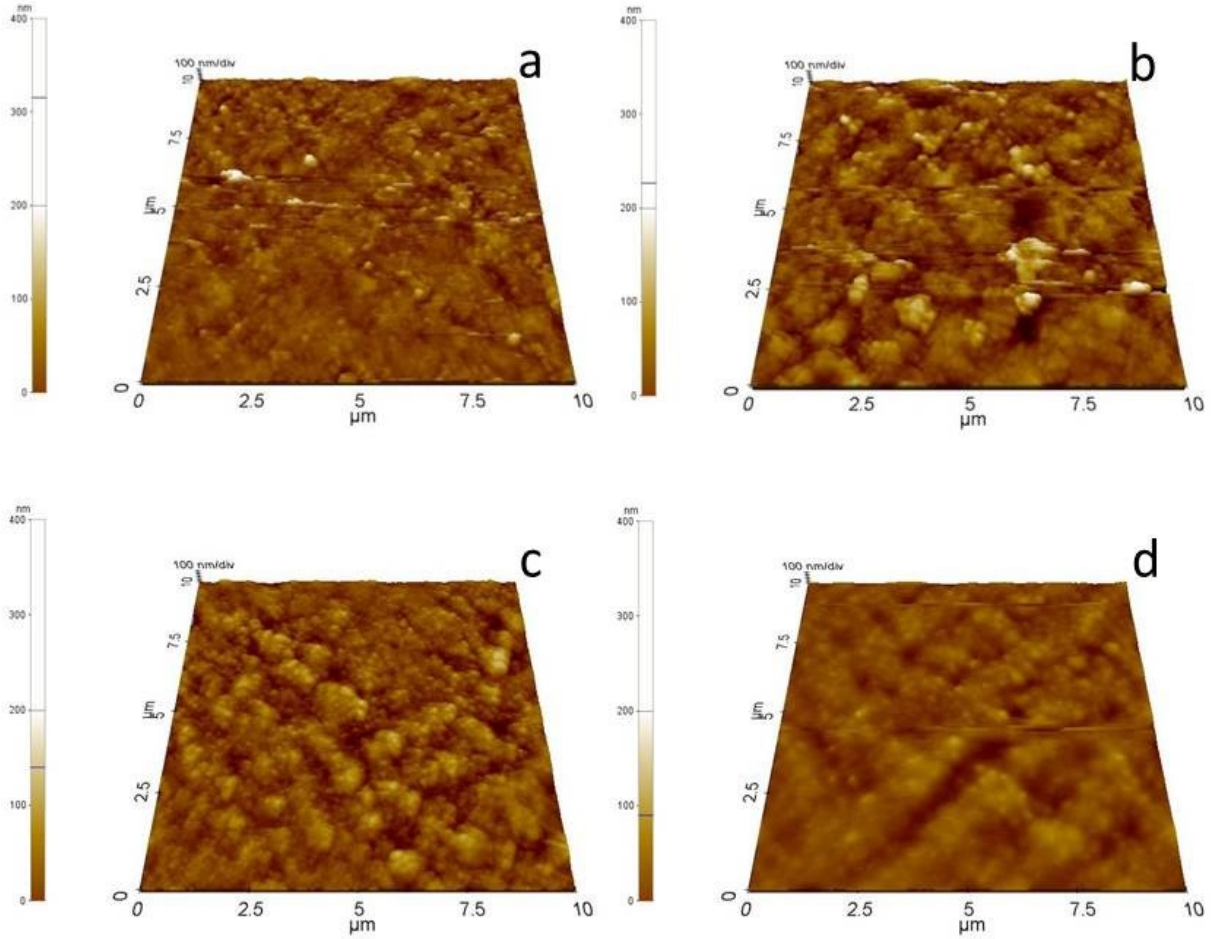

Figure 5-11: Surface morphology of the a. as-produced and sintered at b. 500ºC, c. 800ºC and d. 1100ºC FD-HA synthetic pellets.

5.2.3 Discussion

The current section described the production of HA synthetic pellets, some of which were sintered using different temperatures (500ºC, 800ºC and 1100ºC). The as-produced pellets present FTIR spectra which are similar to those of enamel, although they have lower density and significantly higher porosity than the enamel blocks studied. In all 3 materials (bovine enamel, HD-HA, FD-HA) peaks which are characteristic of HA can be observed like the asymmetric bending vibrations of the υ_4 PO_4^{3-} mode (540-615 cm^{-1}) (575-577). These peaks are more intense in the case of the synthetic material, which is purer than the biogenic apatite of the enamel. At the same time, both the as-produced HD-HA and FD-HA are poorly crystalline as the XRD patterns in section 5.1.2.3 suggest and this is depicted in the asymmetric stretching of the υ_3 PO_4^{3-} mode which can be traced around 1004 cm^{-1} (484, 591,

592) and 1046 cm^{-1} (390, 593) for HD-HA and 1015 cm^{-1} (484-486) for FD-HA; the position of which is indicative of newly precipitated and immature material (484, 485, 498). A similar peak is observed around 1020 cm^{-1} for enamel. Some weak peaks of well crystalline material can be also observed in all cases in the region of 1900 cm^{-1} and 2200 cm^{-1} which corresponds to HPO_4^{2-} (479, 492).

Carbonate can also be traced in all 3 materials. The out of plane bending υ_4 CO_3^{2-} mode around 872 cm^{-1} (207, 578, 579) is observed in all cases, while the asymmetric stretching mode between 1400 cm^{-1} and 1500 cm^{-1} (577, 588) can be observed only in the case of the enamel and FD-HA. Some peaks attributed to molecular CO_2 can also be observed between 2200 cm^{-1} and 2400 cm^{-1} (370, 580, 581). Comparison of the peaks shows that they are much weaker in the case of the synthetic materials. In their case their presence can be explained by CO_2 which was dissolved in the waters used to synthesise the powders or got trapped during the pelleting process.

Sintering of the pellets leads to a shift of the peaks corresponding to poorly crystalline material towards higher values, with a respective change in their surface areas which denotes material of higher crystallinity (484, 485) and becomes stronger as the temperature increases (239, 594, 595). Another indication of increased crystallinity with increasing temperature can be observed through the presence of the symmetric stretching of the υ_1 PO_4^{3-} peaks in the region of 950 cm^{-1} to 1000 cm^{-1}. These peaks can be observed for the pellets sintered at 500ºC and have been found to decrease as the crystallinity of the material increases and the carbonate content decreases (488, 596), which is the case as the sintering temperature increases (Tables 5-5, 5-6). It is interesting to note the pellets sintered at 800ºC and 1100ºC present some carbonate peaks, which probably originate from the interaction of the surface of the pellets with CO_2 present inside the oven during the sintering process.

The increase in the sintering temperature has also an effect in the morphology, density and porosity of the produced pellets. The density increases significantly as a function of temperature and reaches 100% and 99.5% of the theoretical density of HA (3.160 g cm^{-3}) for HD-HA and FD-HA respectively at 1100ºC; while it is close to that observed for enamel (3.027 g cm^{-3}) for the HD-HA and FD-HA pellets sintered at 500ºC and 800ºC respectively. In general the densities of HD-HA are higher than those of FD-HA, which denotes that oven drying of the HA has an extra effect on its properties and is consistent with previous studies (372, 583, 597, 598). Porosity, on the other hand, increases in the case of the pellets sintered at 500ºC, which is followed by significant decrease for higher temperatures. This can be explained by the observation that, for temperatures around 500ºC, the HA particles come together and form larger agglomerates, which is accompanied by light densification and no pore size reduction (599-602); while the increase observed can be attributed to trapped air and water which escapes the pellets leading to more space being available and can be also affected by the presence of moisture and/or CO_2 in the atmosphere which have been found to delay the sintering process (603, 604). The decrease observed in the case of the pellets sintered at 800ºC and 1100ºC is thus attributed to the subsequent pore size decrease, grain increase and significant densification observed for higher temperatures (599, 605-607). The results are also supported by the morphology of the surface of the produced pellets, which becomes smoother with increasing temperature. This also suggests the significant densification of the material with increasing temperature.

These results are also depicted into the micro-hardness measurements. As can be seen in figure 5-9 a continuous increase takes place as the sintering temperature increases, which is far more rapid in the cases of the pellets sintered at 800ºC and 1100ºC. At 500ºC the increase in hardness is not so significant, which could be attributed to the fact that although some densification may take place, this is not accompanied by a respective decrease in porosity as

in the case of the pellets sintered at higher temperatures (583). The final hardness values at 1100ºC (~5.8 GPa) are consistent with previous studies and any variations are attributed to the different methods used during HA preparation and treatment (243, 370, 608). This is also supported by the significant correlation for both HD-HA and FD-HA between porosity and hardness ($p < 0.01$) and between density and porosity ($p < 0.05$). As a final note it must be pointed out that the hardness of the pellets sintered at 800ºC is similar to the value reported for enamel of 3.432 GPa (609, 610).

The next and final part of this Chapter is to compare the behaviour of the produced HA pellets in various solutions and compare it with the respective behaviour of enamel blocks.

5.3 Evaluation of the Behaviour of Synthetic Hydroxyapatite Pellets & Comparison with Permanent Bovine Enamel

5.3.1 Aqueous Experiments

The final section of Chapter 5 studied the behaviour of the synthetic pellets when placed inside various solutions and how they compare to the respective behaviour of enamel. In order to do so, several groups, each of which contained 3 samples, of bovine enamel blocks and as-produced and sintered HA pellets were placed for 5 days inside solutions which are similar to those used during the pH-cycling studies. These solutions were: (a) remineralising solution (pH: 6.58) to simulate plaque fluid, (b) demineralising solution to simulate acid challenge (pH: 4.9) and (c) 250 ppm of F^- treatment in the form of NaF to simulate tooth-brushing. These treatments were described in more detail in section 2.2.4. In the end of the 5-day period analysis similar to that performed during the pH-cycling experiments took place and the results are presented below.

5.3.2 Chemical Analysis of the Solutions

For continuity, the chemical analyses are presented following the same order used in Chapters 3 and 4. Calcium results are presented first as the element present in all existing and potentially precipitated phases; and are followed by PO_4^{3-} and F^-, which are present into all the phosphate phases and FA, fHA and CaF_2 respectively.

5.3.2.1 Calcium Results

Figures 5-10 and 5-11 present the changes in Ca^{2+} concentration of the remineralising and demineralising solutions used during the simulation of the three elements of the pH-cycling study. During the remineralisation treatment, the behaviour of HD-HA (Figure 5-12, red) and FD-HA (Figure 5-12, blue) follow a different trend. While increase of the material accumulated is observed for FD-HA with increasing sintering temperature, HD-HA presents a maximum for the pellets sintered at 800ºC and a decrease for those treated at 1100ºC. The most important observation is that the pellets simulating best the behaviour of bovine enamel during remineralisation are the FD-HA pellets sintered at 800ºC.

As far as the demineralisation challenge is concerned (Figure 5-13), a constant decrease in the amount of Ca^{2+} released inside the solutions can be observed, which is similar for both HD-HA and FD-HA. At 800ºC the amount of Ca^{2+} released is significantly higher than that of enamel. In this case it seems that the pellets closer in behaviour with enamel are the FD-HA sintered at 1100ºC.

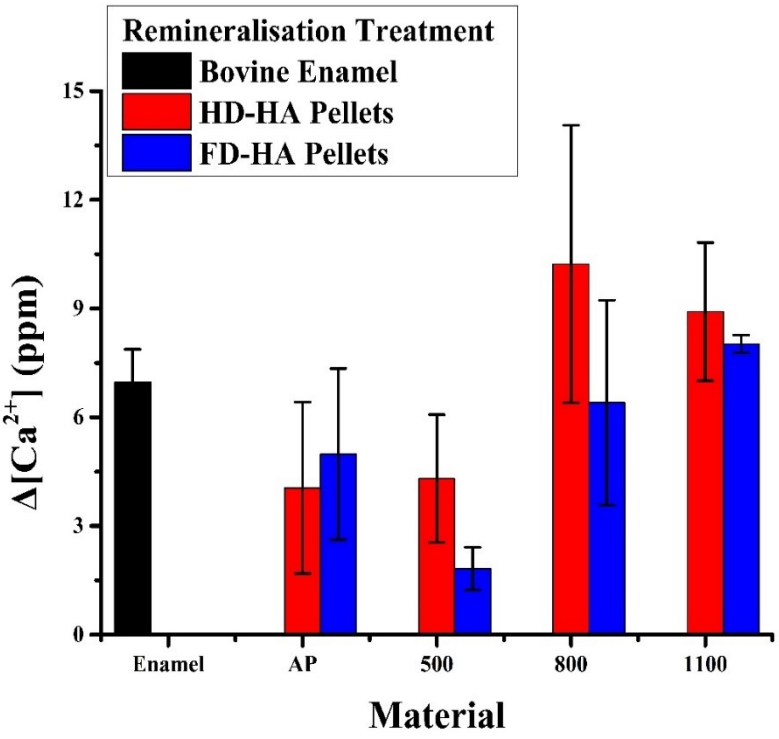

Figure 5-12: Changes in the Ca^{2+} concentration in the remineralising solutions used during the simulation of the three elements of the pH-cycling study.

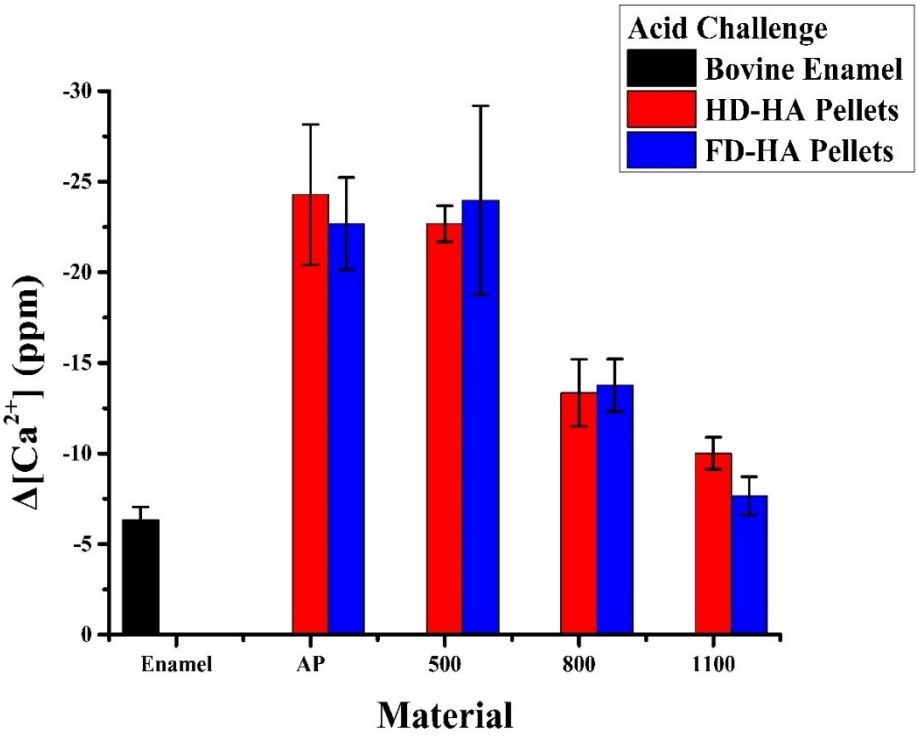

Figure 5-13: Changes in the Ca^{2+} concentration in the demineralising solutions used during the simulation of the three elements of the pH-cycling study.

5.3.2.2 Phosphate & Fluoride Results

The PO_4^{3-} results for the simulation of the three elements of the pH-cycling study are presented in figures 5-14 and 5-15 for the remineralisation and demineralisation treatments respectively. The behaviour of both the HD-HA and FD-HA pellets is similar, with decreasing PO_4^{3-} accumulation with increasing sintering temperature; although a slight increase is observed for both pellets sintered at 500ºC. The accumulation is always significantly higher for the FD-HA pellets when compared to the HD-HA. Same as in the case of the Ca^{2+} results, the FD-HA pellets sintered at 800ºC simulate best the behaviour of enamel. Another interesting finding is that no significant changes can be observed between the as-produced and sintered at 500ºC and 800ºC HD-HA pellets.

In the case of the demineralising solutions (Figure 5-15) accumulation of material is observed for both HD-HA and FD-HA, which decreases with increasing sintering temperature. Similar to the remineralising solutions the FD-HA values are significantly higher than those observed for HD-HA. The enamel value in this case lies between the values observed for the HD-HA and FD-HA pellets sintered at 800ºC, although the FD-HA pellets sintered at 800ºC are closer to the enamel blocks.

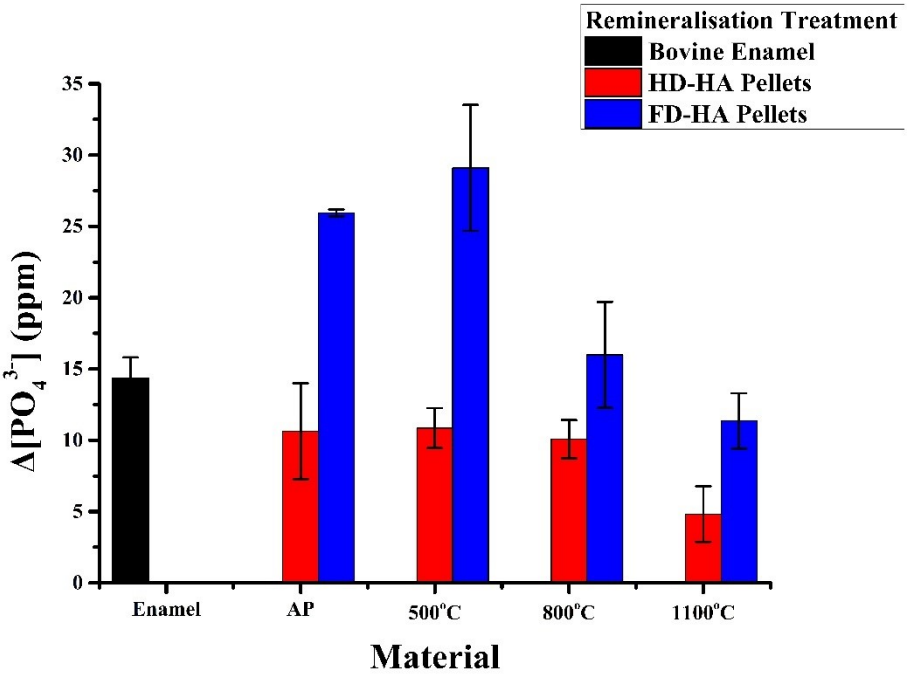

Figure 5-14: Changes in the PO_4^{3-} concentration in the remineralising solutions used during the simulation of the three elements of the pH-cycling study.

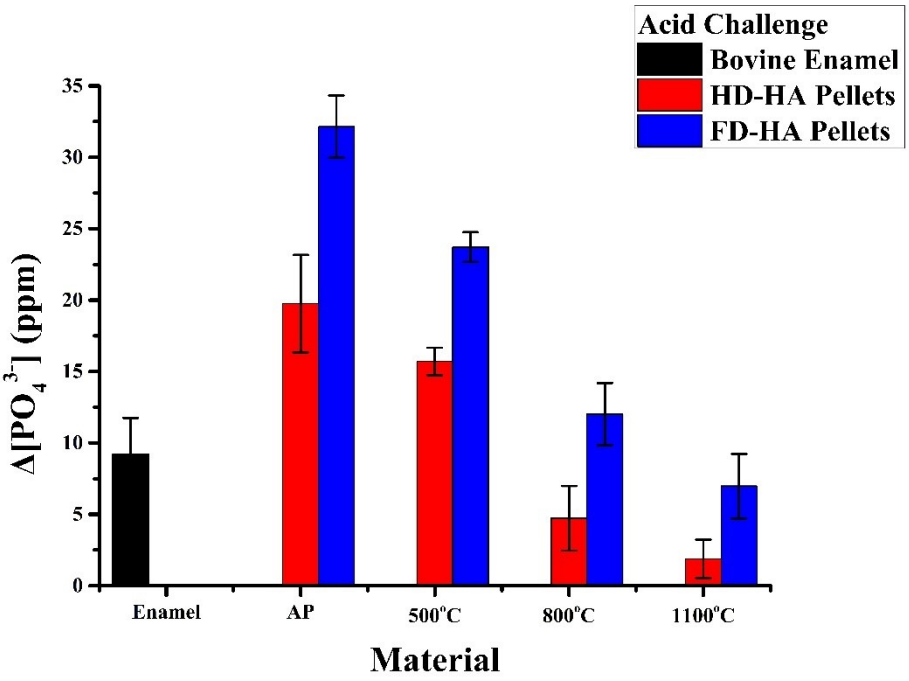

Figure 5-15: Changes in the PO_4^{3-} concentration in the demineralising solutions used during the simulation of the three elements of the pH-cycling study.

Finally, the F^- results (Figure 5-16) follow the same trend as PO_4^{3-} in the case of the demineralising solutions. In this case, no significant differences can be observed between the respective HD-HA and FD-HA pellets. The values closer to those observed for bovine enamel are those sintered at 800ºC, although the FD-HA pellets are slightly closer.

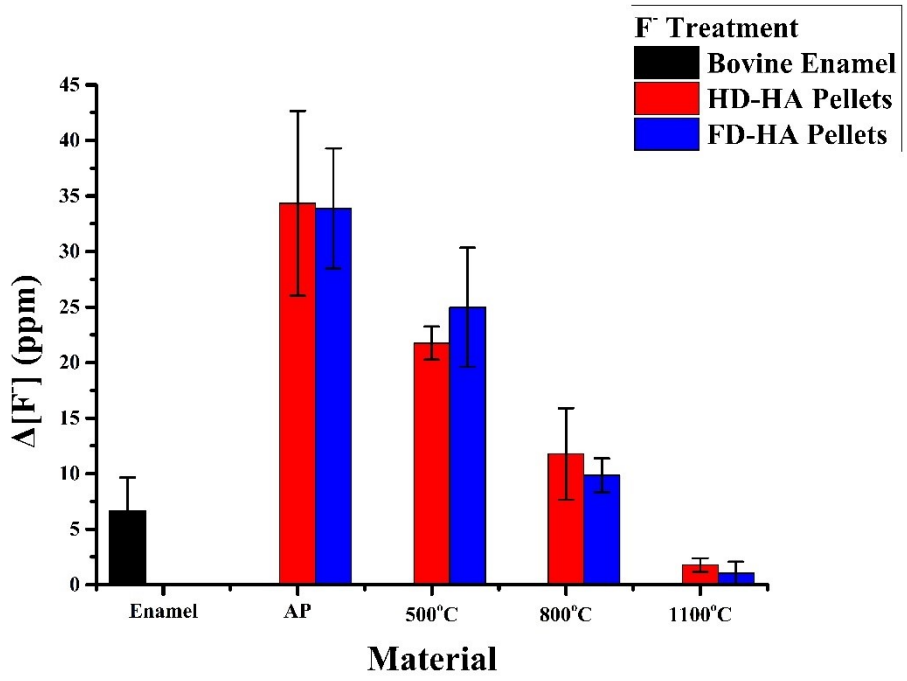

Figure 5-16: Changes in the F^- concentration in the solutions used during the simulation of the three elements of the pH-cycling study.

5.3.3 Structural Analysis

Figures 5-17 and 5-18 present the FTIR spectra of bovine enamel blocks vs. the as-produced and sintered HD-HA and FD-HA following the 5 day immersion in the remineralising (Figures 5-17a and 5-18a), demineralising (Figures 5-17b and 5-18b) and F^- treatment solutions (Figures 5-17c and 5-18c). In all cases peaks which correspond to the υ_4 PO_4^{3-} mode can be observed in the region between 540 cm^{-1} and 610 cm^{-1}. The peaks in the case of the synthetic blocks are more in number and larger in area. In the case of the F^- treated groups a decrease in the number and broadening in area can be observed, which is consistent with F^- accumulation.

Peaks which correspond to υ_3 PO_4^{3-} mode of newly precipitated poorly crystalline HA are observed (1020 cm^{-1}, 1060 cm^{-1}, 1120 cm^{-1}), as well as PO_2 peaks (1180 cm^{-1}, 1275 cm^{-1}). The position and area of these peaks varies depending on the material and the sintering conditions. For the remineralising and demineralising solutions the FD-HA pellets sintered at 800ºC present similar values to the enamel; while there is a shift in position towards lower values for the as-produced and sintered at 500ºC pellets and towards higher values for those sintered at 1100ºC. In the case of the F^- treated pellets the surface area of the enamel is similar to the as-produced and sintered at 500ºC pellets, while those of the pellets sintered at 800ºC and 1100ºC present far lower values. In all cases, peaks corresponding to HPO_4^{2-} (1900–2200 cm^{-1}) of well crystalline HA are present, but are significantly weaker in the case of enamel.

As far as the CO_3^{2-} is concerned, several peaks can be observed in the case of enamel; like the υ_4 CO_3^{2-} peak around 670 cm^{-1} and 830 cm^{-1}, the υ_2 mode around 700 cm^{-1} and the υ_4 and υ_3 around 1370 cm^{-1} and 1450 cm^{-1} and 1640 cm^{-1} respectively. Carbonate peaks are in general weaker in HAs than the enamel, but stronger incorporation can be observed for the as-produced and sintered at 500ºC pellets. In some cases, the incorporation is higher than the enamel itself; while in almost all cases the pellets sintered at 800ºC and 1100ºC present lower incorporation. It must be noted that the total surface area of the CO_3^{2-} peaks of the FD-HA pellets sintered at 800ºC is similar to that of enamel. For example, the surface areas of the υ_4 mode around 1370 cm^{-1} is 21.034 cm^2 and 21.061 cm^2 for the enamel and FD-HA respectively, while of similar nature are the results of the rest of the peaks. In all cases though, a shift is observed in the position of the peaks between the enamel and the synthetic pellets.

Finally, peaks corresponding to secondary phases can also be observed in the case of the remineralising solutions. Peaks in the region below 540 cm^{-1} which correspond to free HPO_4^{2-} and are linked to the presence of TCP or OCP can be observed in all cases. Peak areas in the case of the remineralising solution are similar for the enamel and the FD-HA pellets sintered at 800ºC, but in general the area of the peaks of the synthetic pellets are significantly lower than those of the enamel. In the case of the treatment with 250 ppm of F^- an extra peak correlated with OH^- substitution from F^- can be traced, which is higher in the case of the enamel.

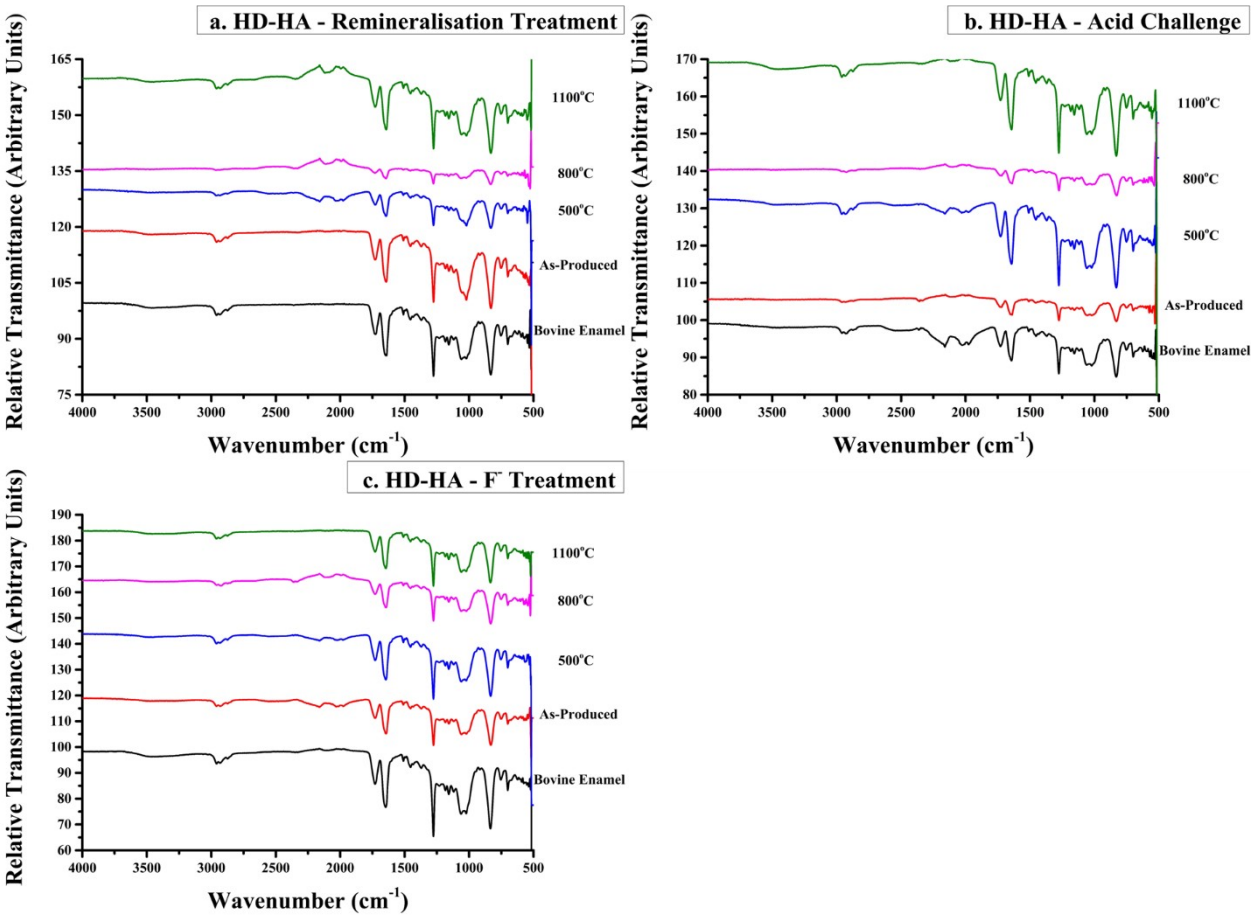

Figure 5-17: FTIR spectra for bovine enamel blocks and as-produced and sintered HD-HA pellets following immersion for 5 days in a. Remineralisation, b. Demineralisation and c. F^- containing solutions.

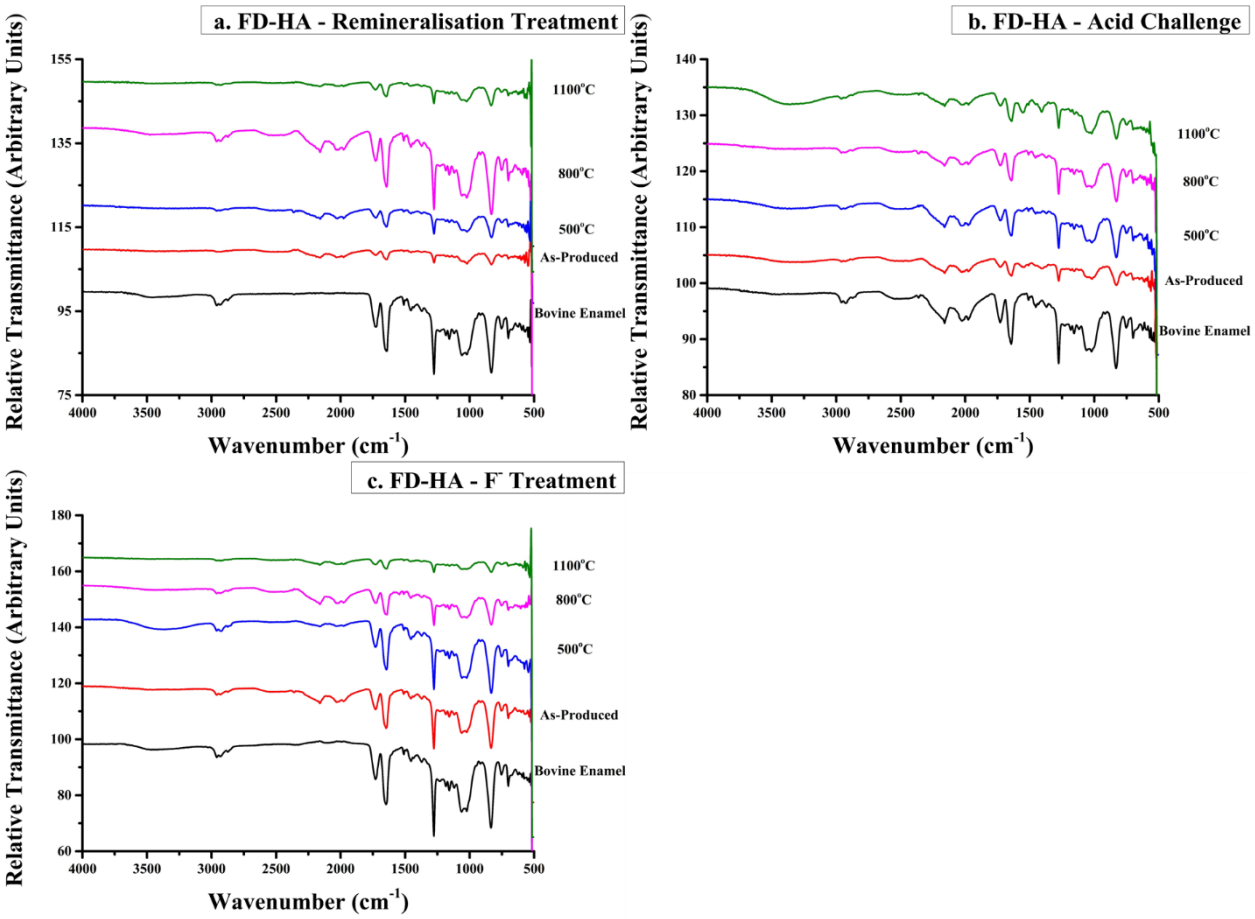

Figure 5-18: FTIR spectra for bovine enamel blocks and as-produced and sintered FD-HA pellets following immersion for 5 days in a. Remineralisation, b. Demineralisation and c. F^- containing solutions.

5.3.4 Hardness Measurements

Figure 5-19 presents the changes observed in the hardness of the enamel blocks and the synthetic pellets following the 5 day immersion in the solutions described above. In general the changes in the hardness of the synthetic pellets are similar; although HD-HA is more soluble as is suggested in the case of the demineralising solutions (Figure 5-19b). In the case of the remineralisation treatment (Figure 5-19a) an increase in hardness is observed in all cases, which is more significant for the blocks sintered at 500°C and decreases as the sintering temperature increases. Both the HD-HA and FD-HA pellets sintered at 800°C seem to have hardness which is closest to that observed for the enamel blocks. Similar are the results for the blocks and pellets treated with 250 ppm of F^- (Figure 5-19c). In this case though, no

significant differences seem to exist between the as-produced and the pellets sintered at 500ºC and 800ºC; while the increase in hardness is much lower for the pellets sintered at 1100ºC.

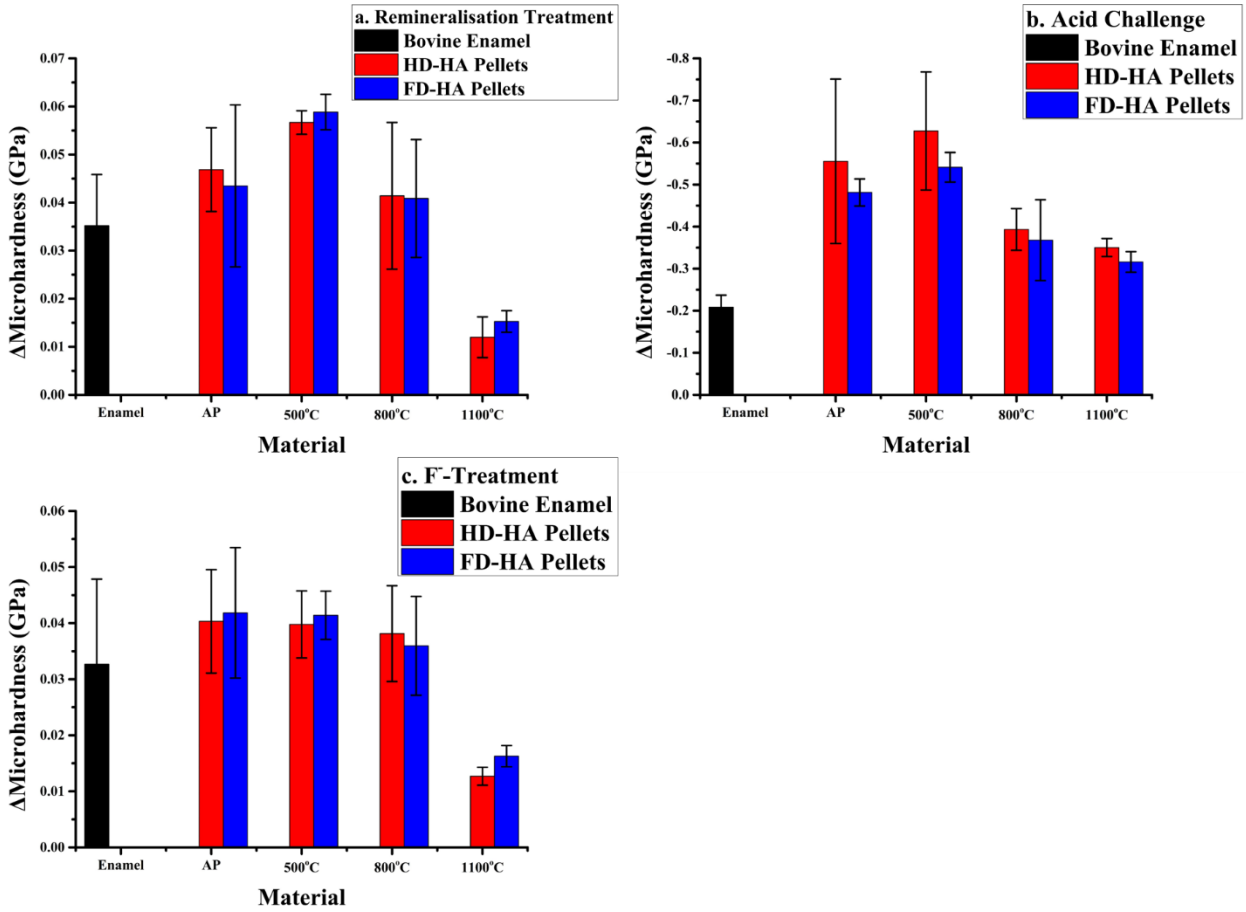

Figure 5-19: Hardness change for the bovine enamel blocks and the as-produced and sintered HD-HA and FD-HA pellets following immersion for 5 days in a. Remineralisation, b. Demineralisation and c. F^- containing solutions.

5.3.5 Changes in Surface Morphology

Figures 5-20, 5-21 and 5-22 present the changes in surface morphology of bovine enamel blocks and the as-produced and sintered HD-HA synthetic pellets, following the 5 day immersion inside a plaque fluid proxy (pH: 6.58), a demineralisation challenge (pH: 4.90) and a 250 ppm F^- treatment respectively. During the remineralisation treatment (Figures 5-20, 5-23) deposition of material can be observed in all cases, which becomes stronger for the synthetic pellets (Figure 5-20, 5-23, b-e) the higher the sintering temperature is. In this case, the surface resembling more closely that of enamel (Figure 5-20a, 23a) is the surface of the pellet sintered at 500ºC (Figure 5-20c) and 800ºC (Figure 5-23d) for the HD-HA and FD-HA pellets respectively.

In a similar manner, etching of the surface is observed during the demineralisation challenge (Figure 5-21). The etching is stronger for the enamel blocks (Figure 5-21a, 5-24a) and the as-produced (Figure 5-21b) and sintered at 500ºC (Figure 5-21c) for the HD-HA and at 800ºC (Figure 5-24d) and 1100ºC (Figure 5-24e) for the FD-HA the synthetic pellets, as significant flattening of the surface can be observed. For the HD-HA pellets higher sintering temperatures (Figure 5-21d, e) lead to some etching which is not as strong as in the previous cases; while no significant effect can be observed for the as-produced (Figure 5-24b) and the pellets sintered at 500ºC (Figure 5-24c) for the FD-HA.

In the case of the blocks and pellets treated with 250 ppm of F^- (Figure 5-22, 5-25), deposition of material in the form of CaF_2 can be observed in some cases. For the enamel blocks (Figure 5-22a, 5-25a) strong deposition exists, as the characteristic blob-like features suggest. Some deposition of CaF_2 can be also observed in the case of the as-produced (Figure 5-22b) and sintered at 500ºC (Figure 5-22c) for the HD-HA pellets and those sintered at 500ºC (Figure 5-25c) and 800ºC (Figure 5-25d) for the FD-HA. The strongest deposition for each case can be observed for the pellets sintered at 500ºC and 800ºC respectively. Nearly no deposition can be

observed for the pellets sintered at 800ºC (Figure 5-22d) for HD-HA and the as-produced (Figure 5-25b) and sintered at 1100ºC (Figure 5-25e) for FD-HA. It is interesting to note that strong surface changes can be observed in the case of the blocks sintered at 1100ºC (Figure 5-22e).

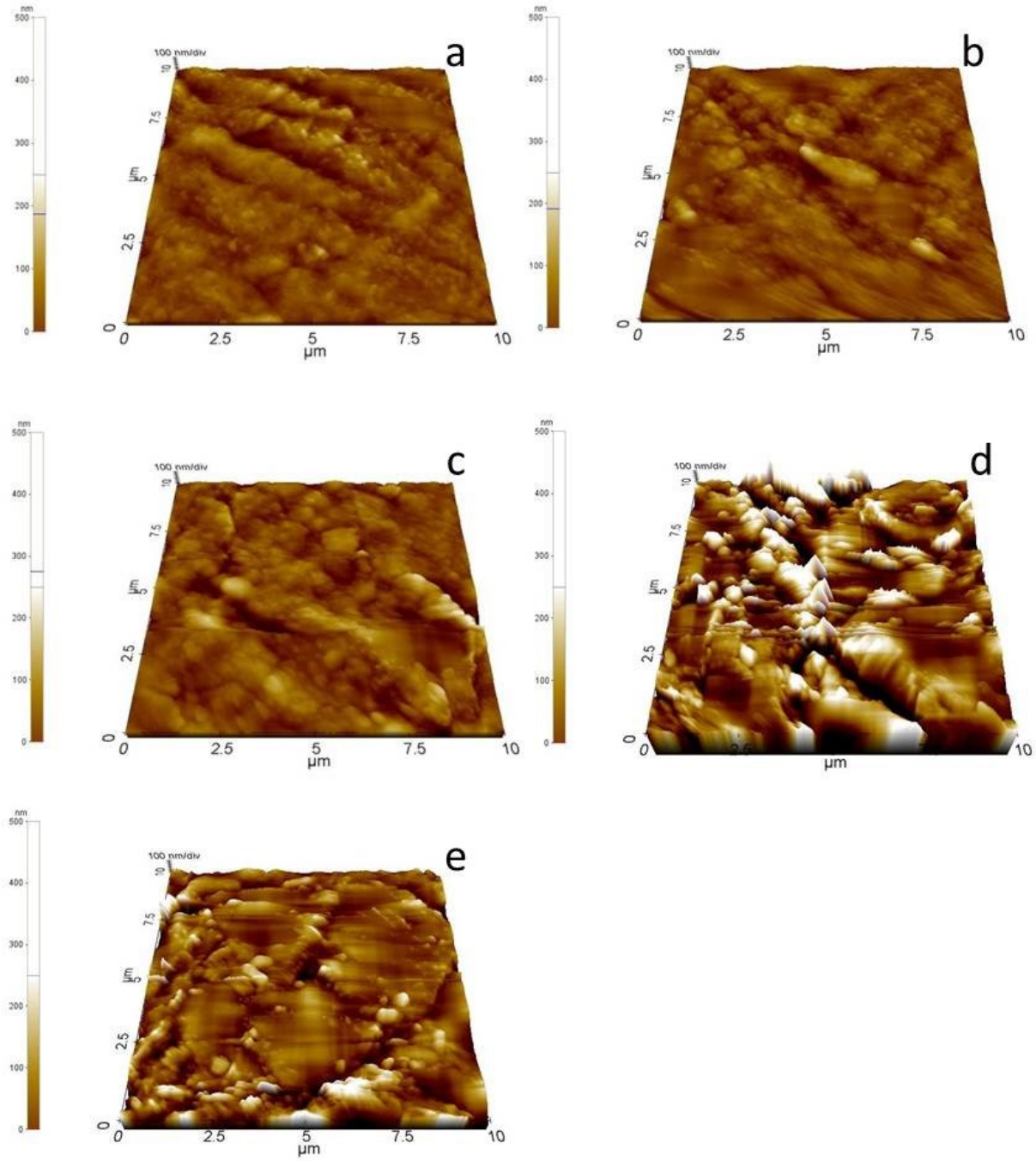

Figure 5-20: Changes in the surface morphology of the a. bovine enamel blocks and the b. as-produced and sintered at c. 500ºC, d. 800ºC and e. 1100ºC HD-HA synthetic pellets, following a 5 day immersion inside a plaque fluid proxy (pH: 6.58).

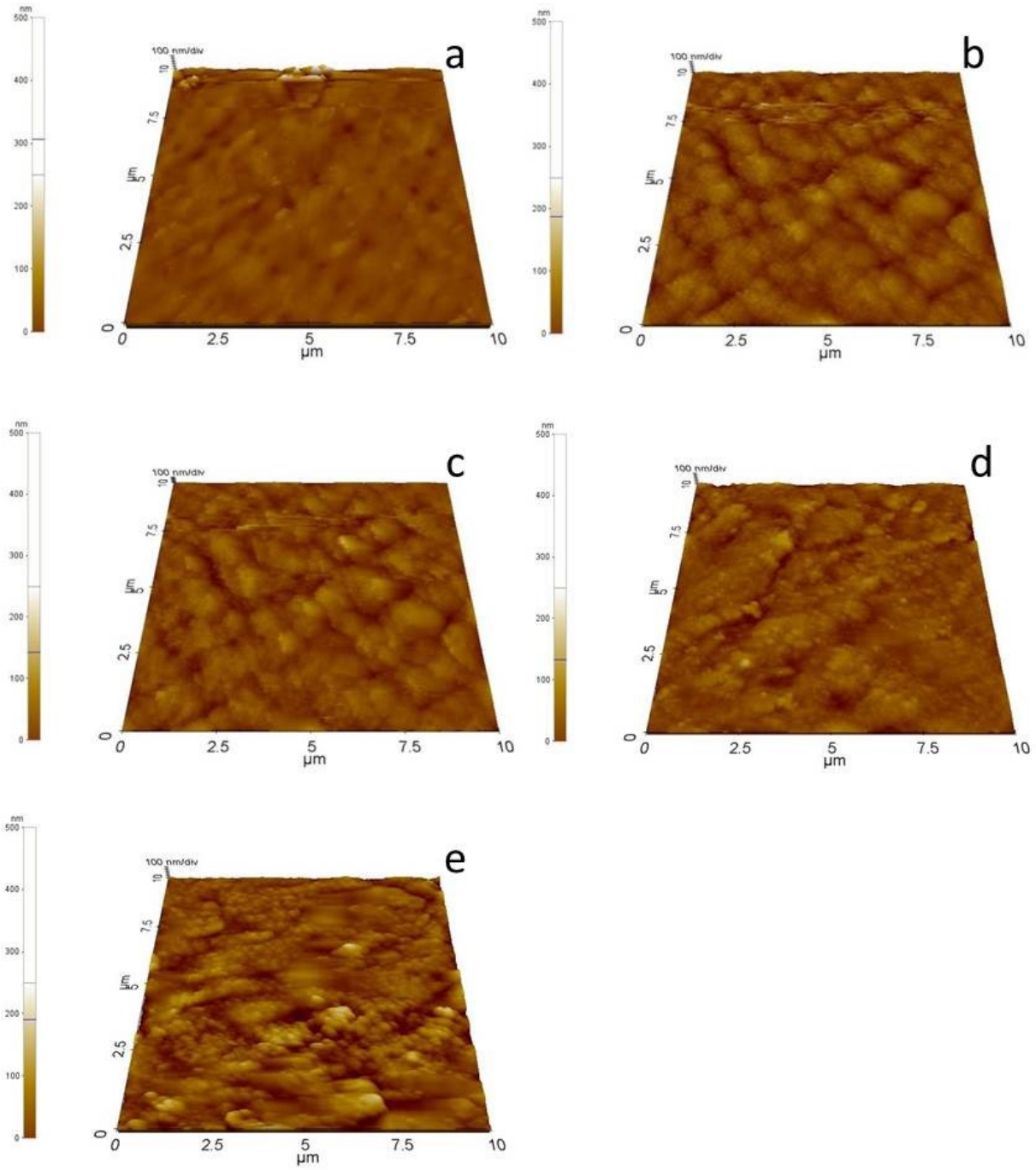

Figure 5-21: Changes in the surface morphology of the a. bovine enamel blocks and the b. as-produced and sintered at c. 500°C, d. 800°C and e. 1100°C HD-HA synthetic pellets, following a 5 day immersion inside an acid challenge solution (pH: 4.9).

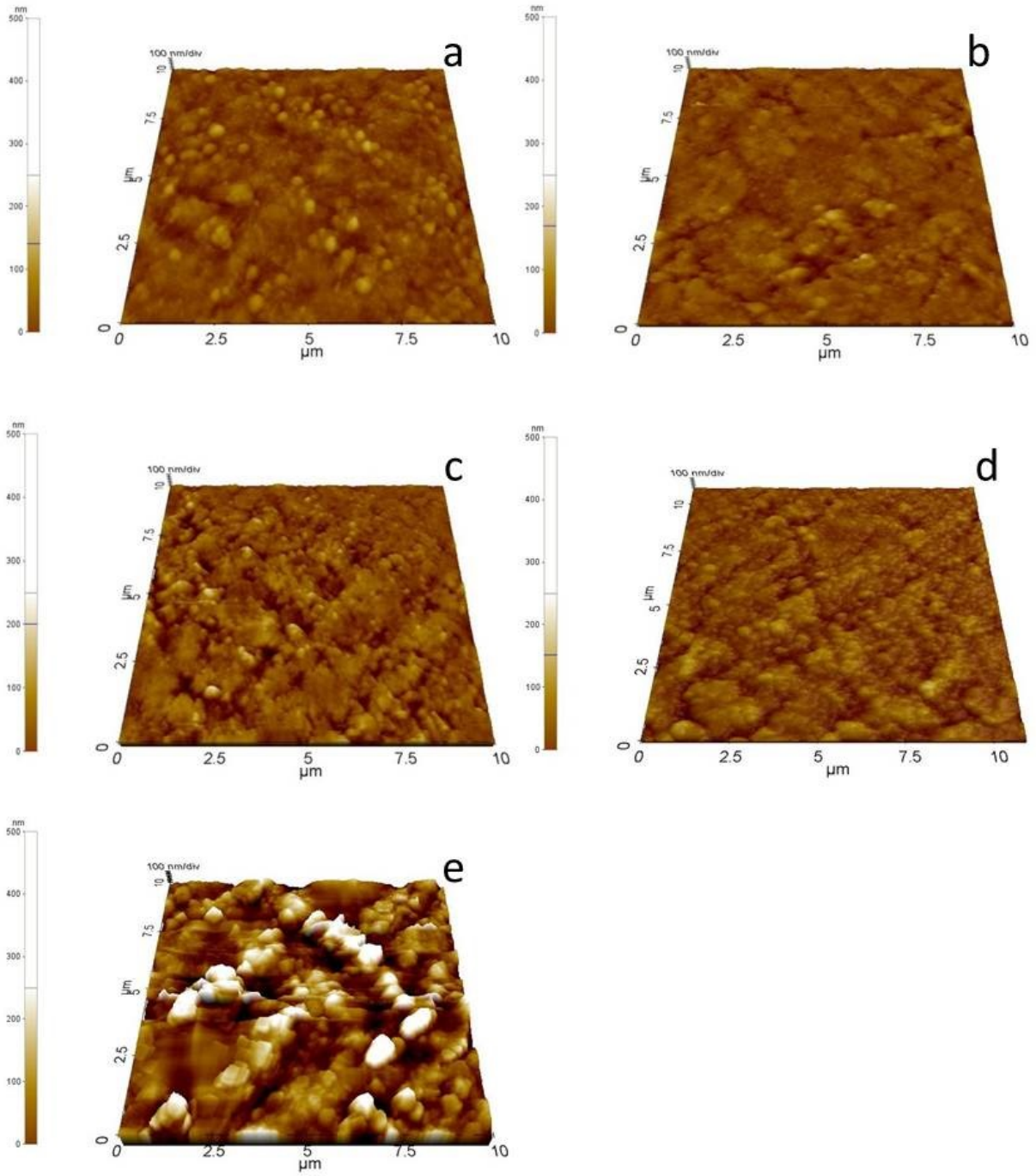

Figure 5-22: Changes in the surface morphology of the a. bovine enamel blocks and the b. as-produced and sintered at c. 500°C, d. 800°C and e. 1100°C HD-HA synthetic pellets, following a 5 day immersion inside a 250 ppm F^- containing solution.

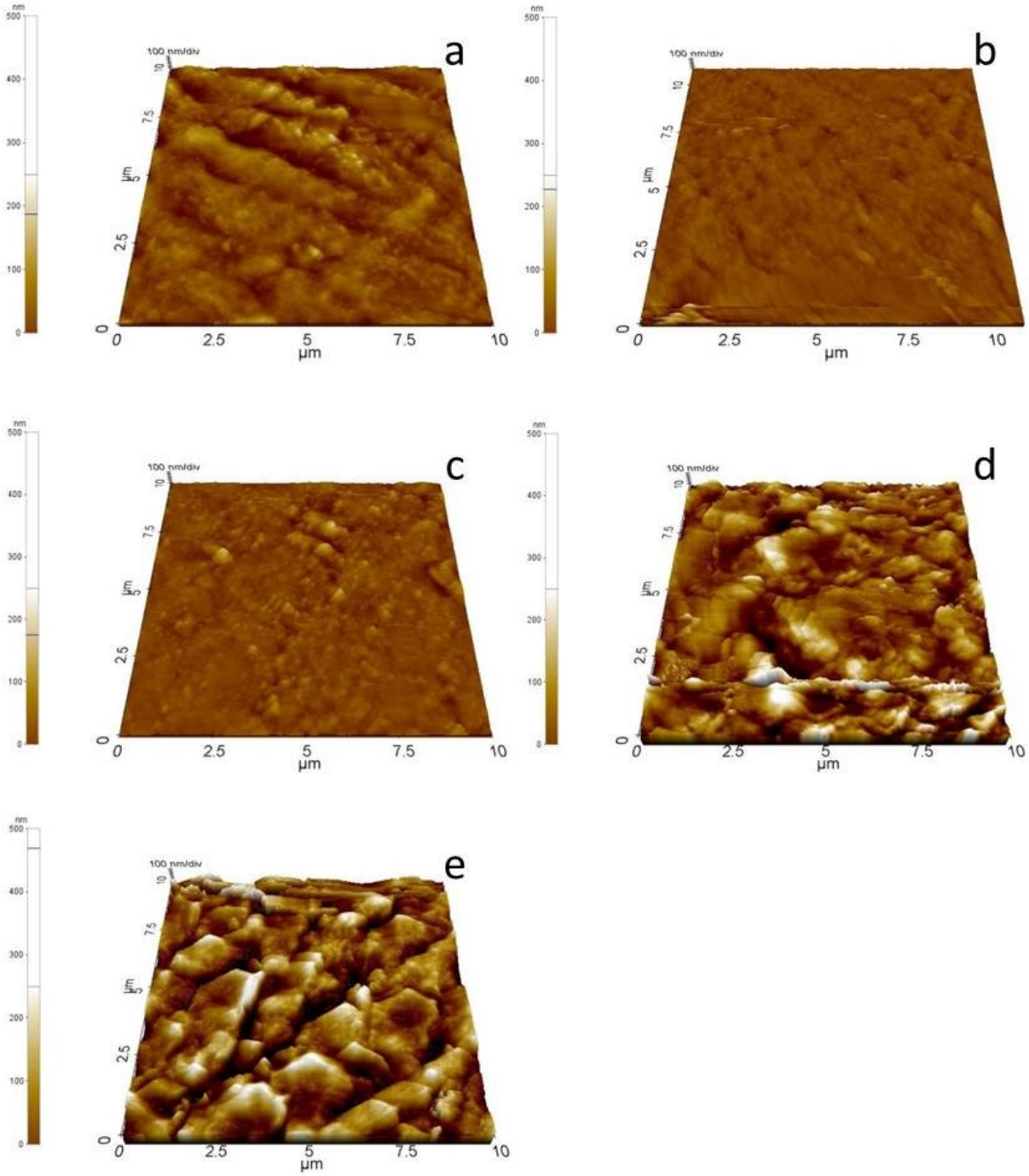

Figure 5-23: Changes in the surface morphology of the a. bovine enamel blocks and the b. as-produced and sintered at c. 500ºC, d. 800ºC and e. 1100ºC FD-HA synthetic pellets, following a 5 day immersion inside a plaque fluid proxy (pH: 6.58)

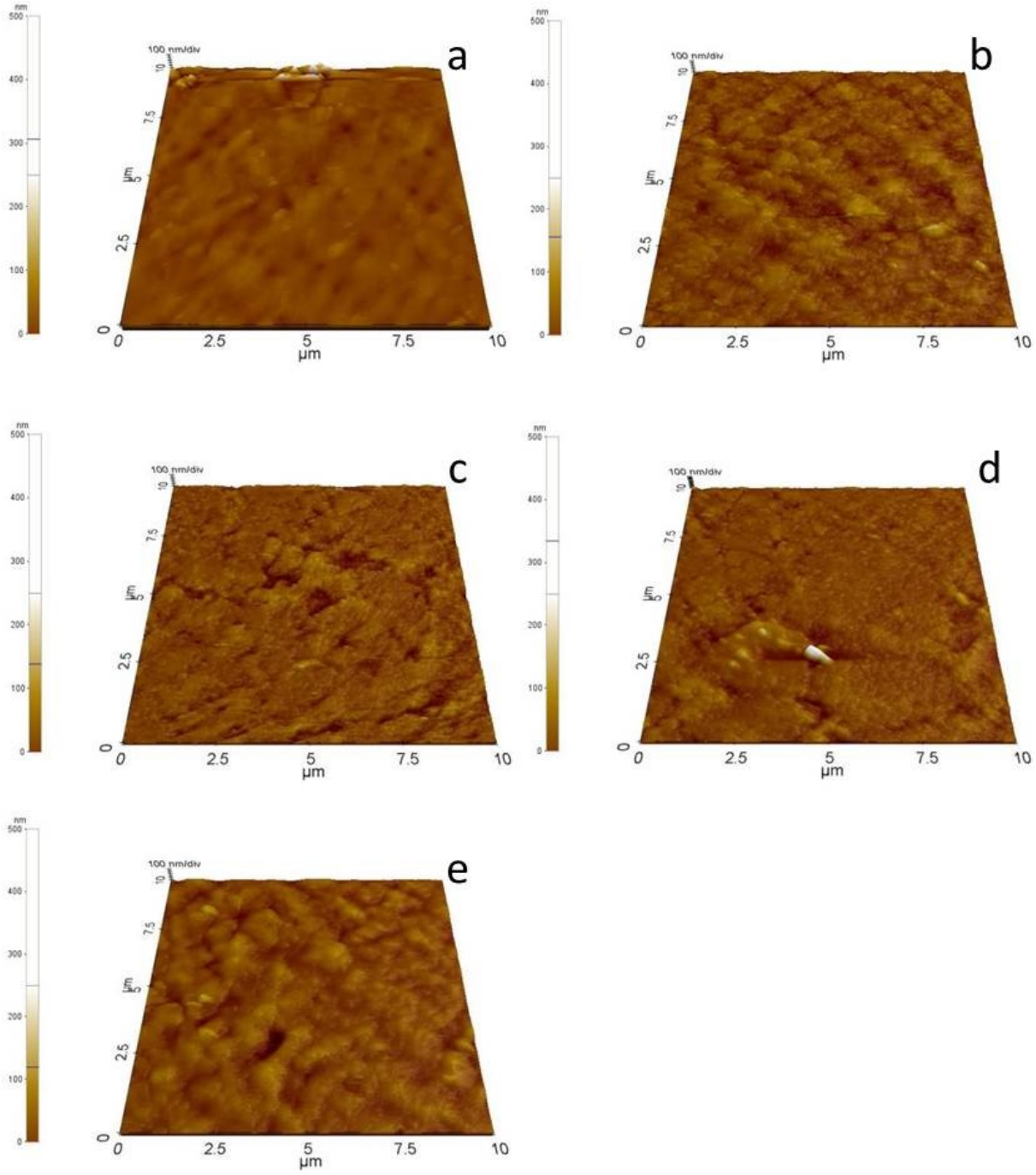

Figure 5-24: Changes in the surface morphology of the a. bovine enamel blocks and the b. as-produced and sintered at c. 500ºC, d. 800ºC and e. 1100ºC FD-HA synthetic pellets, following a 5 day immersion inside an acid challenge solution (pH: 4.9).

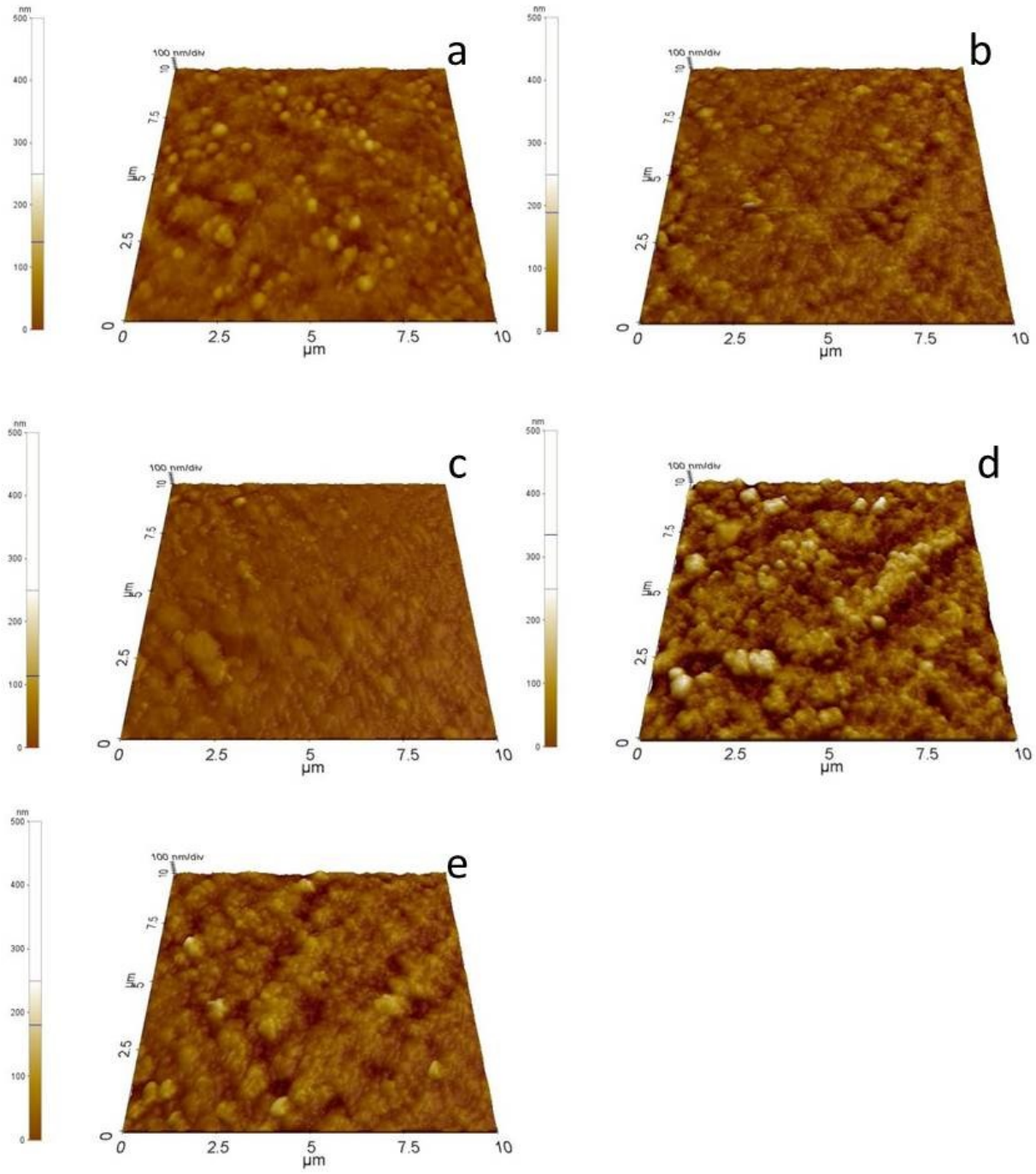

Figure 5-25: Changes in the surface morphology of the a. bovine enamel blocks and the b. as-produced and sintered at c. 500ºC, d. 800ºC and e. 1100ºC FD-HA synthetic pellets, following a 5 day immersion inside a 250 ppm F^- containing solution.

5.3.6 Discussion

The last part of Chapter 5 describes the evaluation of the behaviour of the produced HA pellets, when immersed in different types of solutions. The solutions used were a remineralisation treatment in the form of a plaque fluid proxy (pH: 6.58), a demineralisation challenge (pH: 4.90) and finally a 250 ppm F^- treatment. The HD-HA and FD-HA pellets present a shift in their behaviour, which is probably due to the heat treatment the HD-HA sustained during the drying process. The differences observed on the properties of the produced powders also lead to a difference in material distribution during the pelleting process; with subsequent effects on the sintering and significant improvement of their properties (584, 611), as the results below also suggest.

Morphologically, deposition of material is observed for the enamel blocks in the case of the remineralisation and F^- treatment, and the synthetic pellets as the smoothing of the surface observed in the AFM images suggests. The deposited material could be either apatitic (HA, FA, fHA) or precursor phases (OCP, TCP) and as CaF_2, depending on the treatment used each time. The deposition becomes stronger as the sintering temperature increases, which is supported by the changes observed in the case of the Ca^{2+} present inside the solutions used; but not from the PO_4^{3-} and F^- results especially in the case of the FD-HA pellets. This is probably due to the significantly increased porosity observed for the as-produced (~26%) and sintered at 500ºC (~36%) pellets, which allows material infusion towards the lower HA layers and to the minimal sintering observed on the surface as the images of the original surfaces suggest. On the other hand, the pellets sintered at 800ºC may also present high porosity (~24%), but sintering effects on the surface (as images suggest) decrease the ability of the precipitated material to infuse inside the pellets. In the case of the pellets sintered at 1100ºC, where the strongest deposition can be observed, a combination of significant porosity decrease (~9%) and increased sintering of the material on the surface leads to the increased

deposition observed, although chemical analysis suggests that these are the pellets on which the lowest amount of Ca^{2+}, PO_4^{3-} and F^- is deposited. As a result, the slight increase in hardness is probably mainly due to a decrease in porosity (227, 583, 612) for the as-produced and the pellets sintered at 500ºC and to surface material deposition and interaction for the rest. In general, the synthetic pellets present similar changes in hardness, which is higher than that observed for enamel; although both the HD-HA and FD-HA pellets sintered at 800ºC are behaving closer to enamel.

As the Ca^{2+} results also suggest, decrease in solubility is observed during the demineralisation challenge as the sintering temperature increases, which is also indicative of the more ceramic nature of the pellets sintered at 800ºC and 1100ºC; and is in agreement with similar studies (612-614). It is also worthwhile noting that no significant differences can be observed in the amount of Ca^{2+} released between the as-produced and the pellets sintered at 500ºC. This result also supports the hypothesis that up to 500ºC, no significant sintering effects can be observed, while the increase in porosity also leads to increased solubility (227, 583, 612). On the other hand, phases other than HA may be precipitated and diffused or deposited on the pellets as the phosphate results suggest. Such phases could be either TCP or OCP, which are known to precipitate under low pH conditions (520, 521); and could subsequently transform into apatitic forms (615, 616).

Comparison between the FTIR spectra of the treated bovine blocks and the synthetic pellets suggests strong similarities between the two and especially for the FD-HA. Besides the characteristic HA peaks, peaks which correspond to newly formed, non-stoichiometric and poorly crystalline HA can be observed around 1020 cm^{-1} (484-486), 1060 cm^{-1} (487, 488) and 1150 cm^{-1} (498) and correspond to the υ_3 PO_4^{3-} asymmetric stretching mode. These peaks present a shift towards higher or lower wavenumbers depending on the degree of crystallinity

of the material, with a respective change in their surface area (485, 498). These peaks are in similar positions for the enamel blocks and the FD-HA pellets sintered at 800ºC and have comparable surfaces. The rest of the pellets present either lower or higher values depending on the crystallinity of the material and the heating treatment sustained. The presence of these peaks has been correlated with the presence of precursor phases (OCP) and has been also suggested that if no precursor phase existed during precipitation the resulting HA would be stoichiometric and of high crystallinity (616). Such peaks are present in most cases, especially in the region below 540 cm^{-1} which corresponds to either υ_4 PO_4^{3-} or free HPO_4^{2-}, and are correlated with OCP presence (481-483, 497). Taking into account that the synthesised HA is stoichiometric (as shown in section 5.1) and that it presents higher crystallinity than the enamel, as the XRD and FTIR results of section 5.1.2 suggest, it can be proposed that enamel and the FD-HA pellets sintered at 800ºC are the closest pair in behaviour.

The results of the carbonate content show that although no significant changes in concentration were observed in the non-treated, this is not the case for the treated pellets. The extra content is probably due to the dissolved CO_2 present in the solutions used during the study and got incorporated during material dissolution and precipitation (617, 618). The peaks traced are the υ_4 CO_3^{2-} mode around 830 cm^{-1} and 1370 cm^{-1}, the υ_2 around 700 cm^{-1} and the υ_1 around 1450 cm^{-1} and 1640 cm^{-1}; while the υ_4 CO_3^{2-} at 670 cm^{-1} (487, 493, 494) is only traced for enamel and FD-HA pellets sintered at 800ºC. In this case, the surfaces of the modes observed are similar for the enamel blocks and the 800ºC FD-HA pellets; while it is significantly lower for the more crystalline and in some cases larger for the less crystalline pellets.

Finally, the blocks and pellets immersed inside the 250 ppm of F^- solutions present a strong peak around 750 cm^{-1}, which is characteristic of OH^- vs. F^- substitution (479, 480). This is also supported by a reduction in the number of the υ_4 PO_4^{3-} peaks in the region between 540 cm^{-1} and 615 cm^{-1} with a subsequent broadening of the remaining peaks, which is attributed to F^- incorporation inside the enamel (492, 511). As far as the surfaces of the peaks around 750 cm^{-1} are concerned, the low crystallinity pellets (as-produced, sintered at 500ºC) present areas similar to those of enamel (~80 cm^2), while the rest present slightly lower areas (~55 cm^2). This is consistent with the F^- results from the chemical analysis of the solutions used during the study and show that the amount of F^- accumulated decreases with increasing sintering temperature.

5.4 Conclusions

Chapter 5 studied the synthesis of thermally stable HA, which was similar to enamel. The produced material could be pelleted and treated so that its mechanical properties simulate those of enamel. The wet-precipitation method and drying methods (oven and freeze drying) used led to the production of powders with slightly different characteristics, but similar in particle size and structure with powdered bovine enamel; and at the same time lower densities and far higher surface areas. Calcination of the synthesised powders up to 1100ºC did not lead to any dissociation into secondary phases like TCP or CaO, which was also supported by the densification observed to the levels of pure and well crystallised HA; while significant drop in surface area was only observed for calcination temperatures over 800ºC.

Pelleting of the heated and freeze dried powders produced, led to pellets with lower density and far higher porosity than enamel blocks, but similar in structure as FTIR suggested; the freeze dried material behaves like enamel more than the heat dried HA, probably due to the drying method used. Sintering of the pellets led to gradual densification, with the pellets sintered at 800ºC being closest to the enamel. On the other hand, porosity remains significantly higher than enamel up to the sintering temperature of 800ºC; while rapid decrease is observed at 1100ºC. As far as the mechanical properties are concerned, significant improvement was observed with increasing temperature. The pellets sintered at 800ºC were those closer to the average hardness of enamel, although a bit higher in absolute values.

Finally, in order to test the behaviour of the synthesised materials vs. bovine enamel, a simulation of the three elements used during the pH-cycling studies of Chapters 3 and 4 using static solutions was used. As-produced, sintered pellets and enamel blocks were immersed for 5 days inside the solutions used during the pH-cycling studies (plaque fluid proxy, acid challenge and F^- treatment). Chemical analysis of the solutions used, structural analysis and hardness measurements led to the conclusion that the pellets with behaviour closest to that of the enamel were the FD-HA sintered at 800ºC. In general, it was also concluded that the drying process has a significant result in the overall properties of HA; since the behaviour exhibited by the aforementioned material, is exhibited in the case of the heat dried material sintered at 500ºC but with inferior mechanical properties. As a result, it was decided that the pellets to be used as enamel proxies and tested through a normal pH-cycling procedure would be the freeze dried pellets sintered at 800ºC.

Page intentionally left blank

6. pH-Cycling Experiments Using Synthetic Hydroxyapatite Pellets

Chapter 6 describes the pH-cycling experiments with sintered synthetic HA pellets. As stated in the previous Chapter, the pellets chosen were those freeze dried and sintered at 800ºC. The selection was based on the observation that these pellets had physicochemical properties closest to those of enamel. The purpose of this Chapter is to demonstrate that the synthetic HA pellets represent good proxies for dental enamel. For this reason, the pellets were subjected to the same treatment as the primary and permanent enamel blocks of Chapters 3 and 4 as follows: three groups consisting of 12 synthetic pellets were formed, which were painted with nail polish leaving a window of 2.5 x 3 mm^2 of exposed surface. Sampling was performed by randomly picking 3 blocks every 5 days (1^{st}, 6^{th}, 11^{th} and 16^{th} day) and analysing both the pellets and the solutions used. The groups formed were subjected to sequential remineralisation and demineralisation challenges and F^- treatments. While the remineralisation and demineralisation challenges were the same for all three groups, three separate F^- treatments were used. Groups FD_{10} and FD_{250} were treated with 10 ppm and 250 ppm of F^- respectively to simulate different degrees of plaque accumulation on the surface of the tooth (as Section 3.1), while FD_{Mix} was treated with 10 ppm of F^- until day 6 and with 250 ppm of F^- from then onwards, which simulates different degrees of plaque accumulation on the same tooth (as Section 3.3).

A summary of the experimental conditions used in each case can be found in Table 6-1 and the physicochemical analysis is presented in sections 6.1 to 6.3, followed by the discussion section (6.4). Analysis was performed the same way as in the case of the enamel blocks in Chapters 3 and 4. Results presentation begins with the chemical analysis of the solutions used during the experimental procedure, which provide quantitative information on the chemical changes taking place in the solution in contact with the surface of the HA pellets. These are followed by the structural changes in the pellets (6.2), which add both quantitative and

qualitative information. Finally the resulting variations on the mechanical (6.3.1) and morphological (6.3.2) properties of the pellets are presented, which act as a verification of the observations based on the chemical analysis.

ID, Solutions & Treatments	pH Cycling Rounds				
ID	**FD_{10}**	**FD_{250}**	**FD_{Mix}**		**Duration**
pH Remineralising Solution	6.58	6.58	6.58		Main Remineralisation Period: 5 hrs/ treatment and overnight Intermediate Remineralisation Period: 30 min/ treatment
pH of Demineralising Solution	4.90	4.90	4.90		20 min/ treatment
Background F^- Concentration (ppm)	0.2	0.2	Days 1-6 0.2	Days 7-16 0.2	Same as Main Remineralisation Period
Background F^- Concentration during the intermediate remineralisation period (ppm)	2.0	1.0	2.0	1.0	Same as intermediate remineralisation period
F^- Treatment Concentration (ppm)	10	250	Days 1-6 10	Days 7-16 250	2 min/ treatment

Table 6-1: Experimental conditions used during the pH-cycling study using the freeze dried synthetic pellets, sintered at 800°C.

6.1 Chemical Analysis

Section 6.1 presents the analytical results from the treatments shown in table 6-1. Firstly the Ca^{2+} results will be presented, followed by PO_4^{3-} and lastly the F^- measurements. In all cases the results are presented as the difference from the baseline (i.e. the concentration of the respective solutions prior to the treatment). This means that positive values denote uptake of the respective element from the synthetic pellets, while negative results correspond to release into the solutions. Calcium results are presented first, since Ca^{2+} is present in both apatitic phases and CaF_2. Then the PO_4^{3-} results follow, as phosphate is present in all potential phases precipitated (HA, FA, fHA, TCP, OCP) except CaF_2. The section ends with the F^- results, which can either precipitate as fHA or FA and stabilise apatite, as CaF_2 and act as a reservoir for F^-, or adsorb on the surface of the pellets as adsorbed F^-.

6.1.1 Calcium Results

Figures 6-1 and 6-2 present the changes in Ca^{2+} concentration for the solutions used during the remineralisation periods for all three groups, the experimental conditions of which were presented in Table 6-1. Each day, the total remineralisation period is the sum of two components:

- The Intermediate remineralisation period, which represents the elevated peak F^- concentrations shortly after the F^- treatment and lasts for 30 minutes. During this time, slightly elevated BF concentration is observed (430-432), the magnitude of which depends on the fluoride concentration used during the F^- treatment.
- The main remineralisation period, is the remaining remineralisation time between the acid challenges and overnight and lasts for 5 hours between the AC and 12 hours during the overnight period.

The changes in Ca^{2+} concentration are similar for all 3 groups. During the total remineralisation period (Figure 6-1), release of Ca^{2+} inside the solutions is observed for groups FD_{10} and FD_{Mix}, which were treated with 10 ppm of F^-; while no significant release or uptake is observed for the pellets treated with 250 ppm of F^- (FD_{250}). On day 6, no significant Ca^{2+} uptake or release is observed in any of the treatments. This is followed by strong uptake for the remaining days. The uptake in all cases peaks on day 11 and is stronger for the pellets treated with the mixed-F^- model (FD_{Mix}), while it is similar for the pellets treated with 10 ppm and 250 ppm of F^-. On day 16 the uptake is similar in all cases.

Figure 6-2 presents the breakdown of the total remineralisation period in its core components, namely intermediate (Figure 6-2a) and main (Figure 6-2b) remineralisation periods. During the Intermediate period release of Ca^{2+} is observed until day 6 for all groups, which is followed by strong Ca^{2+} adsorption which peaks on day 11. The observed uptake corresponds to about 50% of the total Ca^{2+} accumulated during the pH-cycling procedure as comparison between Figures 6-1 and 6-2a suggests. The remaining 50% comes from the adsorption observed during the main remineralisation period for the same time frame. In this case though, Ca^{2+} uptake is also observed during the first 6 days of the experimental procedure.

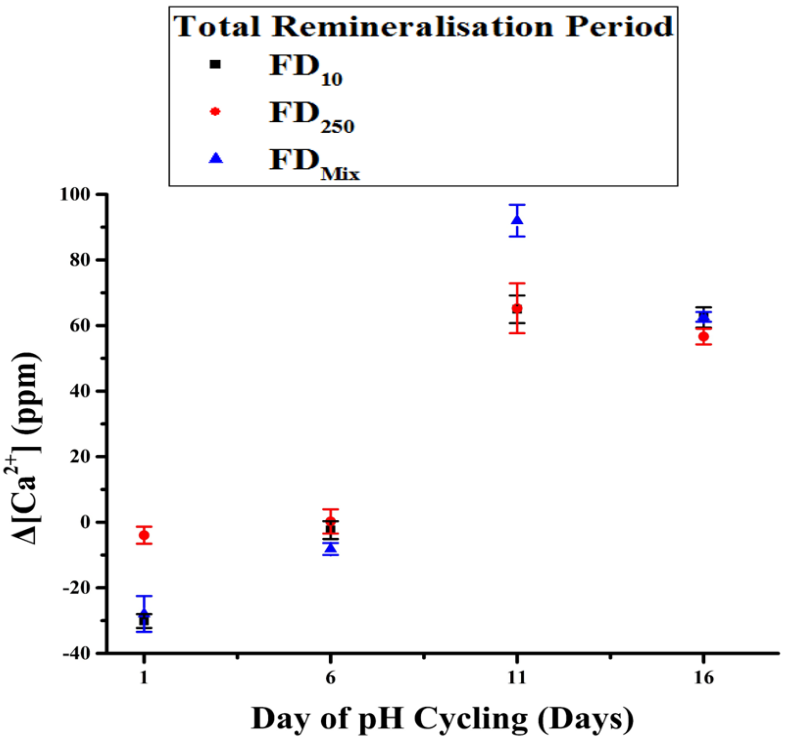

Figure 6-1: Changes in the concentration of Ca^{2+} during the total (main+intermediate) remineralisation period for the synthetic pellets treated with the 10 ppm (black square), 250 ppm (red circle) and the mixed-F^- (blue triangle) fluoride treatments.

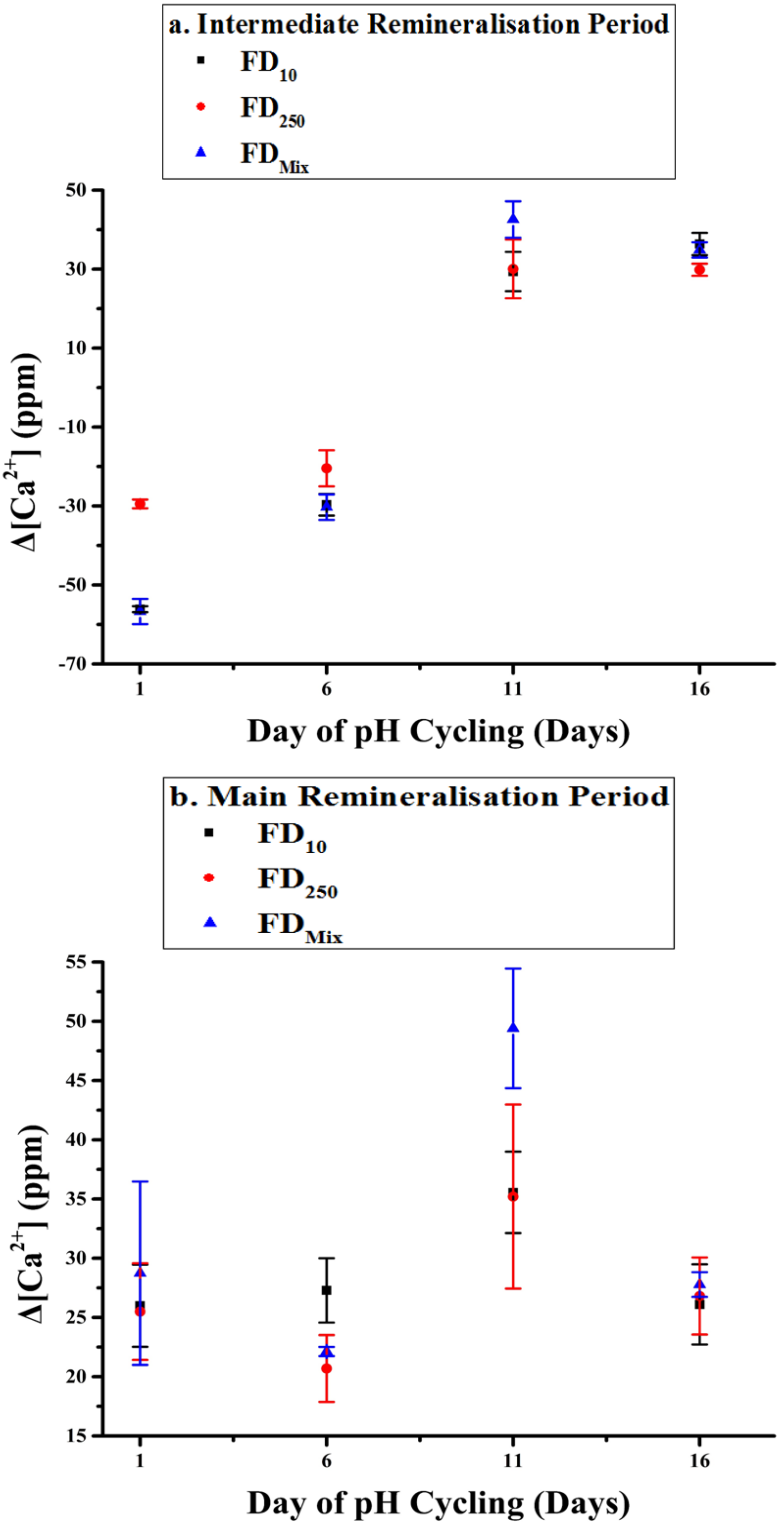

Figure 6-2: Changes in the concentration of Ca^{2+} during the a. main and b. intermediate remineralisation period for the synthetic pellets treated with the 10 ppm (black square), 250 ppm (red circle) and the mixed-F^- (blue triangle) fluoride treatments.

Finally, the demineralisation Ca^{2+} results are presented in Figure 6-3. In all cases Ca^{2+} release is observed, which peaks on day 11 and decreases significantly on day 16. The release is stronger for the pellets treated with 10 ppm of F^-, which are followed by the mixed-F^- treated pellets; although on day 16 the latter present stronger release than those treated with 10 ppm of F^-. Finally, the pellets treated with 250 ppm of F^- present lower Ca^{2+} release in all cases.

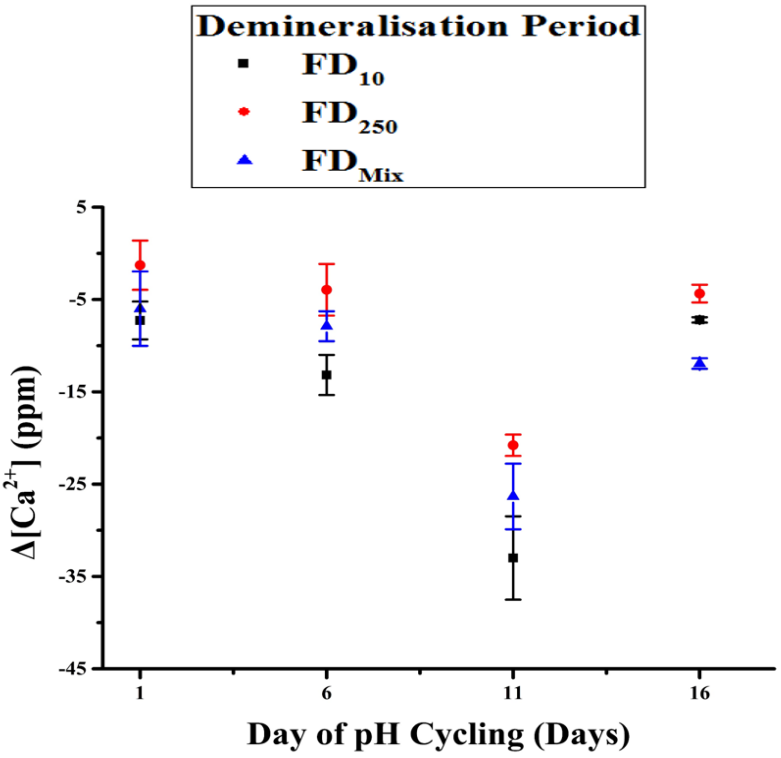

Figure 6-3: Changes in the concentration of Ca^{2+} during the Demineralisation period for the synthetic pellets treated with the 10 ppm (black square), 250 ppm (red circle) and the mixed-F^- (blue triangle) fluoride treatments.

6.1.2 Phosphate & Fluoride Results

The phosphate results of the Total remineralisation period (Figure 6-4) denote that strong uptake into the pellets takes place during the 1st day of the pH-cycling procedure, which then decreases and seems to plateau around 5 ppm of PO_4^{3-}. In the case of the pellets treated with 250 ppm of F^- a negative peak can be observed on day 11, which corresponds to a similar peak observed in the case of Ca^{2+}. A negative peak can be also observed for the pellets treated with the mixed-F^- treatment, but on day 16. If the remineralisation periods are examined separately, it is observed that PO_4^{3-} release is observed during the intermediate remineralisation period (Figure 6-5a), which decreases over time; while phosphate uptake takes place mainly during the main remineralisation period (Figure 6-5b). During the same period a negative peak, for the FD_{250} pellets, can also be observed.

As far as the demineralisation period is concerned (Figure 6-6), after an initial release (which is stronger for the FD_{10} and FD_{Mix} pellets) phosphate uptake can be observed. The uptake is highest on day 6 for the pellets treated with 250 ppm of F^- and on day 11 for the pellets treated with 10 ppm and the mixed-F^- treatment. The pellets treated with the mixed-F^- treatment present also the highest uptake, which is nearly double as that of the pellets treated with 10 ppm of F^-. In all cases a decrease in uptake can be observed on day 16, which is more significant for groups FD_{10} and FD_{Mix}.

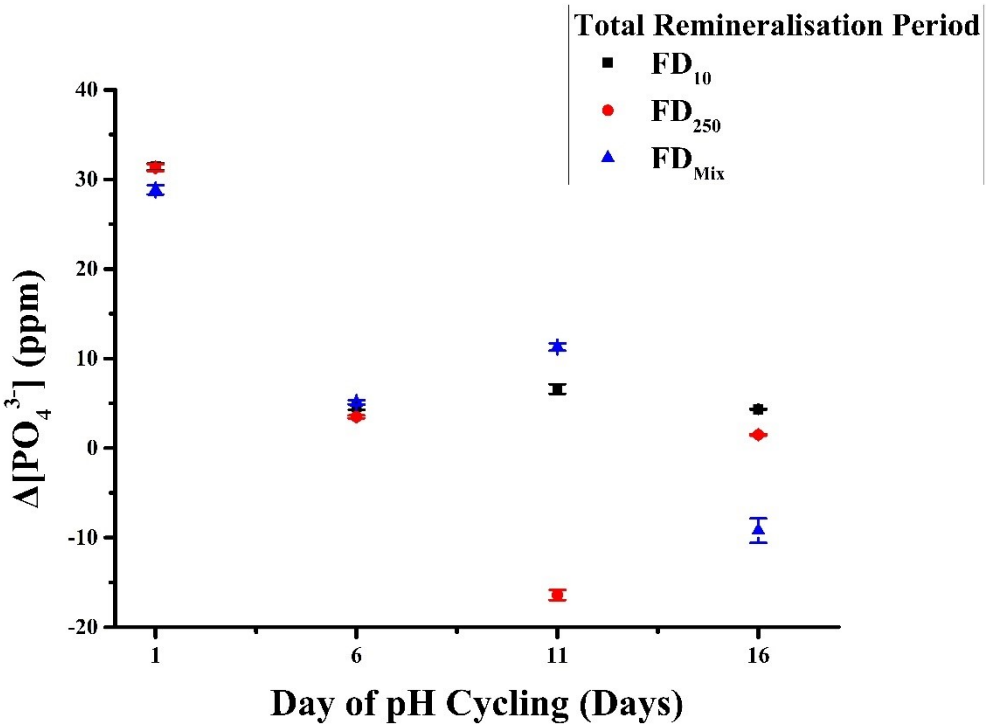

Figure 6-4: Changes in the concentration of PO_4^{3-} during the Total (Main + Intermediate) remineralisation period for the synthetic pellets treated with the 10 ppm (black square), 250 ppm (red circle) and the mixed-F^- (blue triangle) fluoride treatments.

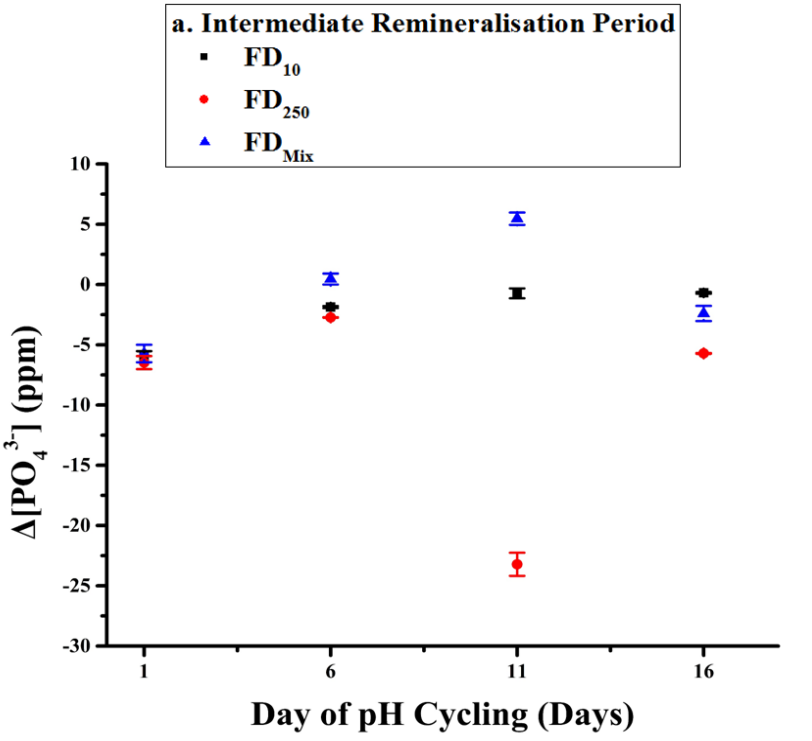

Figure 6-5: Changes in the concentration of PO_4^{3-} during the a. Intermediate and b. Main remineralisation periods for the synthetic pellets treated with the 10 ppm (black square), 250 ppm (red circle) and the mixed-F^- (blue triangle) fluoride treatments.

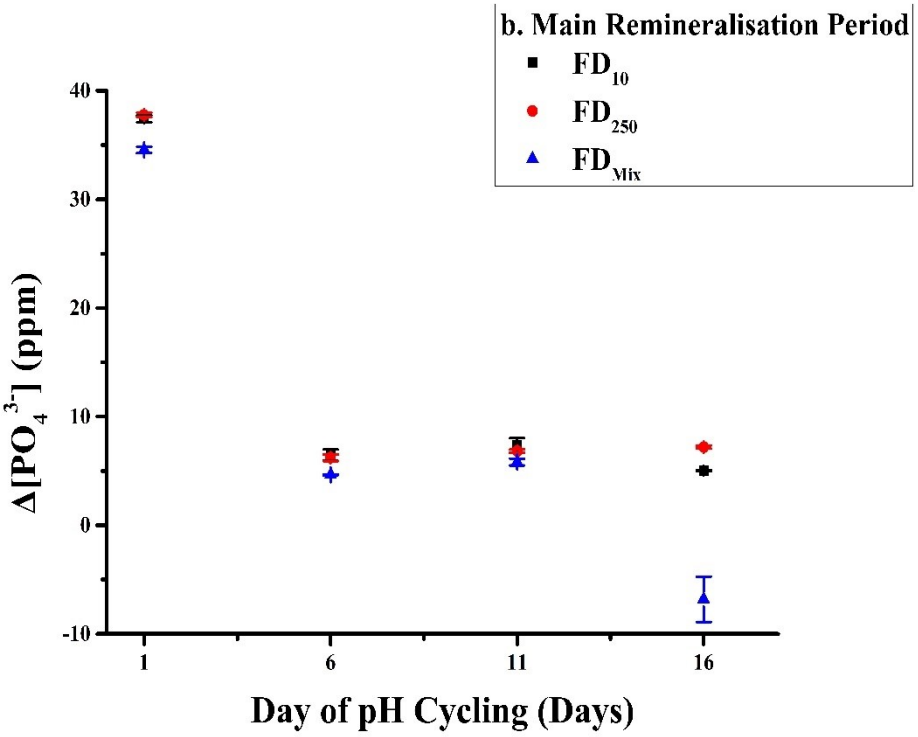

Figure 6-5 (Continued): Changes in the concentration of PO_4^{3-} during the a. Intermediate and b. Main remineralisation periods for the synthetic pellets treated with the 10 ppm (black square), 250 ppm (red circle) and the mixed-F^- (blue triangle) fluoride treatments.

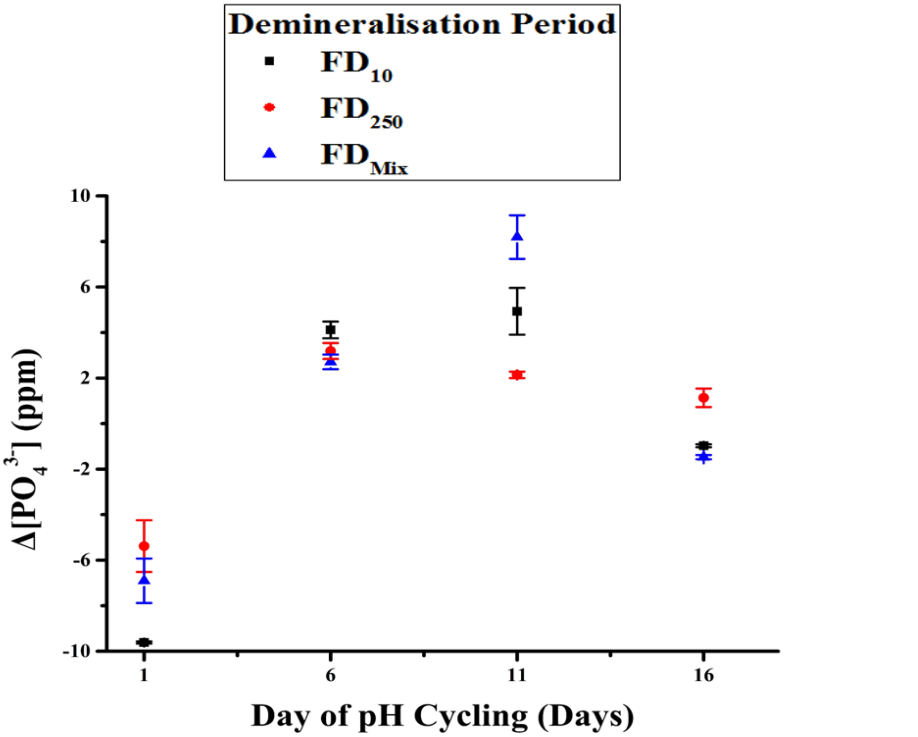

Figure 6-6: Changes in the concentration of PO_4^{3-} during the Demineralisation period for the synthetic pellets treated with the 10 ppm (black square), 250 ppm (red circle) and the mixed-F^- (blue triangle) fluoride treatments.

Finally, F^- results (Figure 6-7) show a constant uptake by the pellets, which increases and peaks on day 6 for the FD_{10} and on day 11 for the FD_{250} and FD_{Mix} pellets, which is strongest for the pellets treated with the mixed-F^- model. After the observed peak a decrease in uptake is observed, which is rapid in the case of the FD_{250} and FD_{Mix} pellets; while a plateau seems to be reached around 0 for the FD_{10} pellets. This result could suggest that saturation of the pellets (in terms of F^-) has taken place, after which no more uptake is possible.

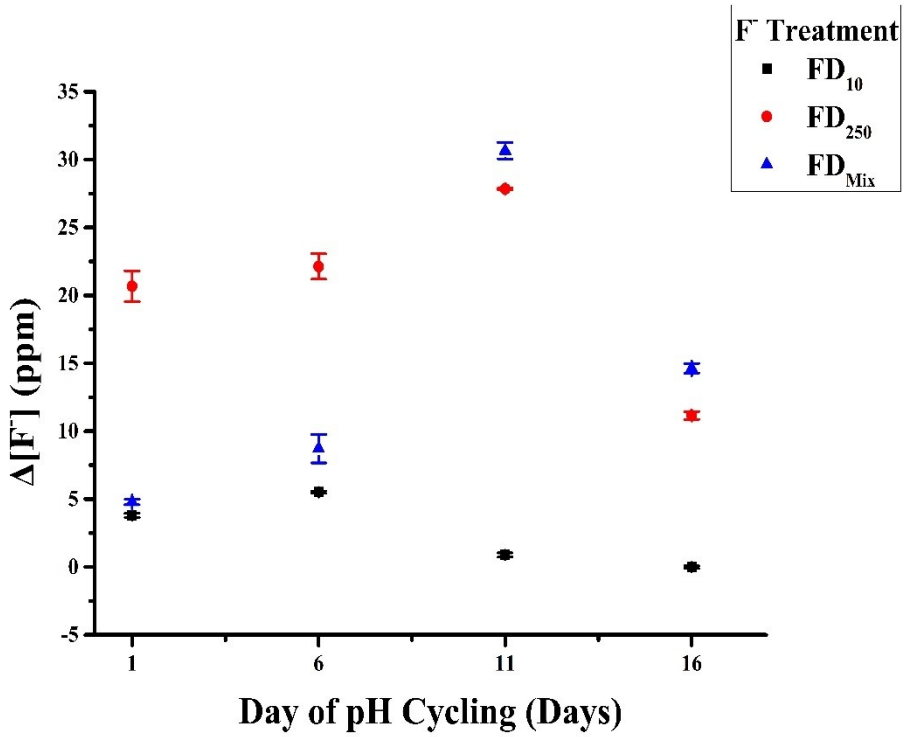

Figure 6-7: Changes in the concentration of F^- during the total tooth brushing simulation period for the synthetic pellets treated with the 10 ppm (black square), 250 ppm (red circle) and the mixed-F^- (blue triangle) fluoride treatments.

6.2 Structural Analysis

The FTIR spectra of the pH-cycled synthetic pellets are presented on figure 6-8. On day 1, three peaks of the υ_4 PO_4^{3-} asymmetric bending vibration mode are observed in the region between 540 cm^{-1} and 615 cm^{-1} (481-483), as well as the OH^- liberation mode around 630 cm^{-1} (479, 480, 491); which have similar surface areas and are indicative of HA presence. At the same time, a number of peaks corresponding to the asymmetric stretching of υ_3 PO_4^{3-} (1000-1200 cm^{-1}) (484-488, 498) are observed; with the surface area of the FD_{250} pellets being significantly higher.

On the other hand, the HPO_4^{2-} peaks between 1900 cm^{-1} and 2200 cm^{-1}, which are characteristic of well crystallised HA (479, 492) are present in all spectra and are stronger in the case of the FD_{10} and FD_{Mix} pellets. A single peak corresponding to free HPO_4^{2-} and indicating the presence of TCP or OCP can also be observed in all cases below 530 cm^{-1} (481-483, 497). Incorporation of F^- is suggested by the presence of a weak peak around 750 cm^{-1} and is characteristic of the OH^- vs. F^- substitution (479, 480).

In terms of CO_3^{2-} the υ_2 and υ_4 peaks around 700 cm^{-1} and 830 cm^{-1} can be observed in all cases; which are similar in size. The pellets treated with 10 ppm and 250 ppm of F^- present υ_3 peaks around 1370 cm^{-1}, 1450 cm^{-1} and 1640 cm^{-1} (487, 493, 494), while those treated with the mixed-F^- model present only the peak around 1640 cm^{-1}. The strongest peak is observed for the FD_{10} and FD_{250} pellets around 1640 cm^{-1} and is followed by that around 1370 cm^{-1} in the case of the FD_{10} pellets and the peak around 1450 cm^{-1} for the FD_{250} pellets. Finally, weak ambient CO_2 peaks around 2400 cm^{-1} (370, 580, 581) are present for FD_{10} and FD_{250}.

As time progresses, a decrease in the number of the υ_4 PO_4^{3-} (540-615 cm^{-1}) peaks is observed for the pellets treated with 10 ppm and 250 ppm of F^-, with a simultaneous broadening of the remaining peaks. In the end a single peak remains, which is also correlated with the increasing intensity of the OH^- - F^- peaks around 750 cm^{-1} and the disappearance of the OH^- peak around 630 cm^{-1}. In the case of the pellets treated with the mixed-F^- model a decrease in the area of the υ_4 PO_4^{3-} (540-615 cm^{-1}) peaks is observed, but no decrease in absolute number exists. On the other hand, significant increase is observed in the surface area of the F^--OH^-, in accordance with the switch from 10 ppm to 250 ppm of F^- treatment. On day 16 the presence of the OH^- peaks around 630 cm^{-1} and 3750 cm^{-1} are also visible, which signify the precipitation of HA.

In all cases, the peaks located between 1000 cm^{-1} and 1200 cm^{-1} and correspond to the υ_3 PO_4^{3-} mode significantly increase; with a simultaneous shift towards higher wavenumber values. The increase is stronger for the peak located around 1020 cm^{-1} especially in the case of the FD_{250} pellets and is followed by the FD_{Mix} and finally the FD_{10} pellets. The area of the peaks treated with 250 ppm of F^- is twice the size of the peaks observed for the FD_{10} and FD_{Mix} pellets. The opposite behaviour can be observed for the peaks which correspond to the presence of TCP or OCP (< 540 cm^{-1}). After an initial increase, both in number and area, which is observed during the first days of the pH cycling, a significant drop in surface is observed by the end of day 16 especially in the case of FD_{10} and FD_{Mix} pellets. At the same time, significant increase is observed in the area of the peaks observed between 1900 cm^{-1} and 2200 cm^{-1}, which correspond to the presence of crystalline HA.

The changes observed in the peaks corresponding to CO_3^{2-} presence are mixed. In all cases a redistribution of CO_3^{2-} seems to take place as the decrease in the area of the peak around 700 cm^{-1} with a simultaneous increase in the area of the 830 cm^{-1} peak suggests. A similar trend is observed in the case of the υ_3 peaks around 1370 cm^{-1}, 1450 cm^{-1} and 1640 cm^{-1} for the pellets treated with 10 ppm and 250 ppm of F^-. The peaks around 1370 cm^{-1} and 1450 cm^{-1} decrease with time, while the peak around 1640 cm^{-1} becomes stronger. A similar increase is observed in the case of the FD_{Mix} pellets. In this case, the υ_3 peaks around 1450 cm^{-1} and 1730 cm^{-1}, which were not present on day 1, can be observed from day 6 onwards but are weak and their intensities remain stable. A slight increase can also be observed in the case of the CO_2 peaks, which become stronger and double in number.

The results are also consistent with those acquired during the chemical analysis of the solutions used. The peaks in the region between 1000 cm^{-1} and 1200 cm^{-1} are correlated to newly precipitated and poorly crystalline HA, as the Ca^{2+} and PO_4^{3-} results during the mineralisation period indicate. On the other hand, the peaks corresponding to the presence of OCP and TCP may also be correlated to the observed PO_4^{3-} uptake during the demineralisation period. Finally, the changes in carbonate content may be explained by the presence of dissolved CO_2 inside the solutions used during the pH-cycling and the exchange of material observed between the pellets and the solutions, which probably led to CO_3^{2-} incorporation inside the pellets.

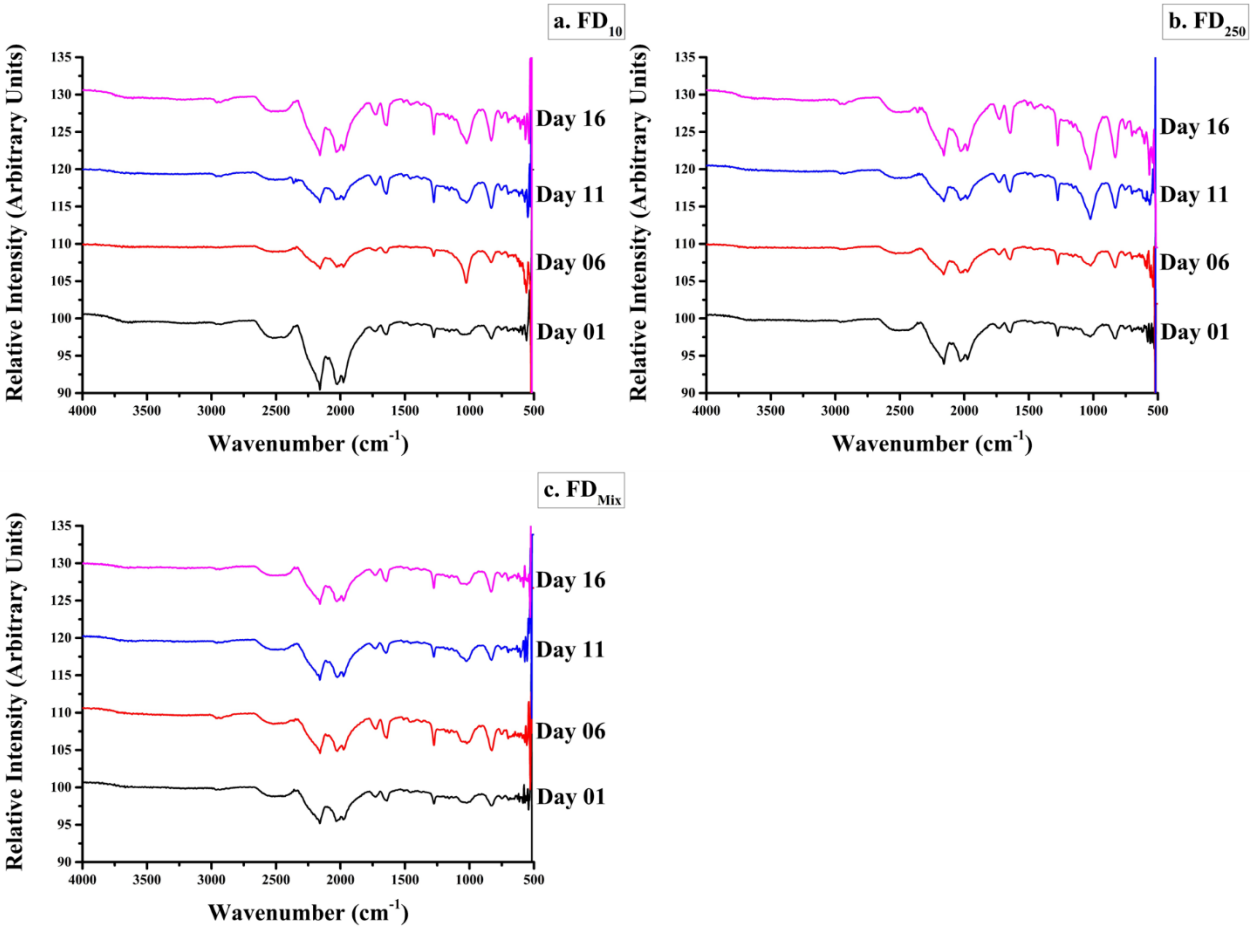

Figure 6-8: FTIR spectra of the pH-cycled freeze dried pellets which were treated with a. 10 ppm, b. 250 ppm and c. the mixed-F^- model.

6.3 Mechanical Properties & Morphology

Section 6.3 provides information on the hardness and morphology of the treated synthetic pellets, which will be interpreted alongside the chemical and structural analysis of sections 6.1 and 6.2 respectively. Initially the hardness results are presented (Section 6.3.1), which quantify the changes observed in the mechanical properties of the pellets and are directly correlated to the chemical changes presented in the previous sections. The results are presented in the same format as the chemical results, i.e. as the difference from the baseline measurements. Positive values correspond to increased hardness, while the opposite is true for negative ones. The analysis part of this Chapter finishes with a sequence of AFM images (Section 6.3.2), providing qualitative information of the changes taking place on the surface of the HA pellets during the pH-cycling procedure.

6.3.1 Micro-Hardness Measurements

Figure 6-9 presents the changes in the micro-hardness of the FD_{10}, FD_{250} and FD_{Mix} synthetic pellets with time. During the first 6 days of the pH-cycling process the hardness of all groups increases in a similar manner, while as time progresses the increase in the hardness of the FD_{Mix} and FD_{250} pellets appears to be more significant. In the cases of FD_{10} and FD_{250} pellets, an apparent plateau is reached around the 16th day; which is not so clear in the case of FD_{Mix} and can be attributed to the switch in the amount of F^- administered during the fluoride treatment. This is also in accordance with the phosphate results, during which the negative peak observed in the case of FD_{250} on day 11 can be observed on day 16 for the FD_{Mix} pellets.

The observed increase in hardness is probably due to the formation of more crystalline HA and/or fHA and FA, as mentioned in the previous section and is indicated by the shift in the position of the FTIR peaks especially around 1020 cm^{-1}, which is correlated with the maturation and better crystallisation of newly precipitated mineral.

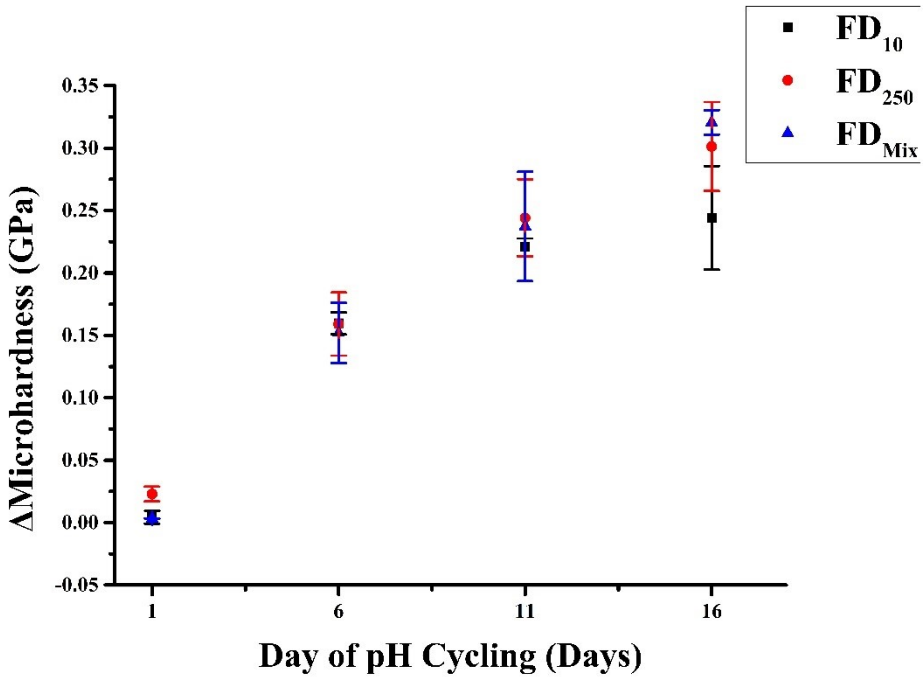

Figure 6-9: Changes in the hardness of the pH-cycled synthetic pellets, which were treated with 10 ppm (black square), 250 ppm (red circle) ppm of F^- and the mixed-F^- model (blue triangle).

6.3.2 Surface Morphology

The above results can also be observed through the changes in the surface morphology of the pH-cycled pellets (Figures 6-10, 6-11 and 6-12). The accumulation of material during the pH cycling process is evident especially during day 6 for all groups (Figures 6-10b, 6-11b and 6-12b) and day 11 especially for the FD_{10} and FD_{250} pellets (Figures 6-10c and 6-11c) as the significant increase in height (expressed through respective changes in the colour map) of the surface suggests. The increased roughness indicates reactivity between the surface of the pellets and the solutions and the partial dissolution and reprecipitation of the surface material as both the remineralisation and demineralisation chemical analyses also suggest. The deposition seems to be stronger in the case of the FD_{250} pellets, as the image especially during day 6 (Figure 6-11b) indicates. On day 16 (Figures 6-10d, 6-11d and 6-12d) a smoother and more mineralised surface seems to have formed, which probably indicates the formation of a more acid-resistant layer of apatitic nature. The observation that in the case of the FD_{Mix} pellets the surface is somewhat rougher than before is probably consistent with a delay in the artificial maturation process. This conclusion is also supported by the decrease in the amount of Ca^{2+} released during the demineralisation challenge and that a plateau is observed in the amount of Ca^{2+} and PO_4^{3-} accumulated during the total remineralisation treatment and the significant decrease in the amount of F^- accumulated.

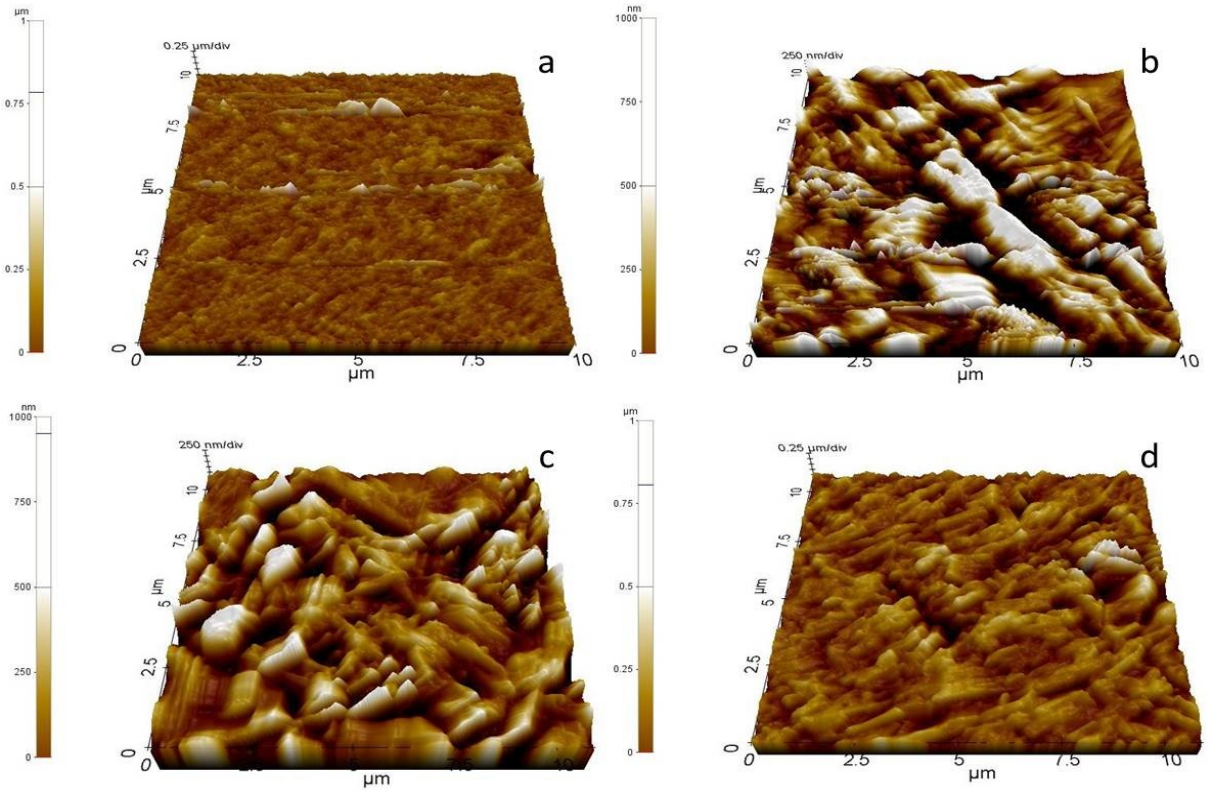

Figure 6-10: Changes in the surface morphology of the freeze dried synthetic pellets during the pH-cycling process, which were treated with 10 ppm of F^-. The images correspond to the a. 1st, b. 6th, c. 11th and d. 16th day of pH-cycling.

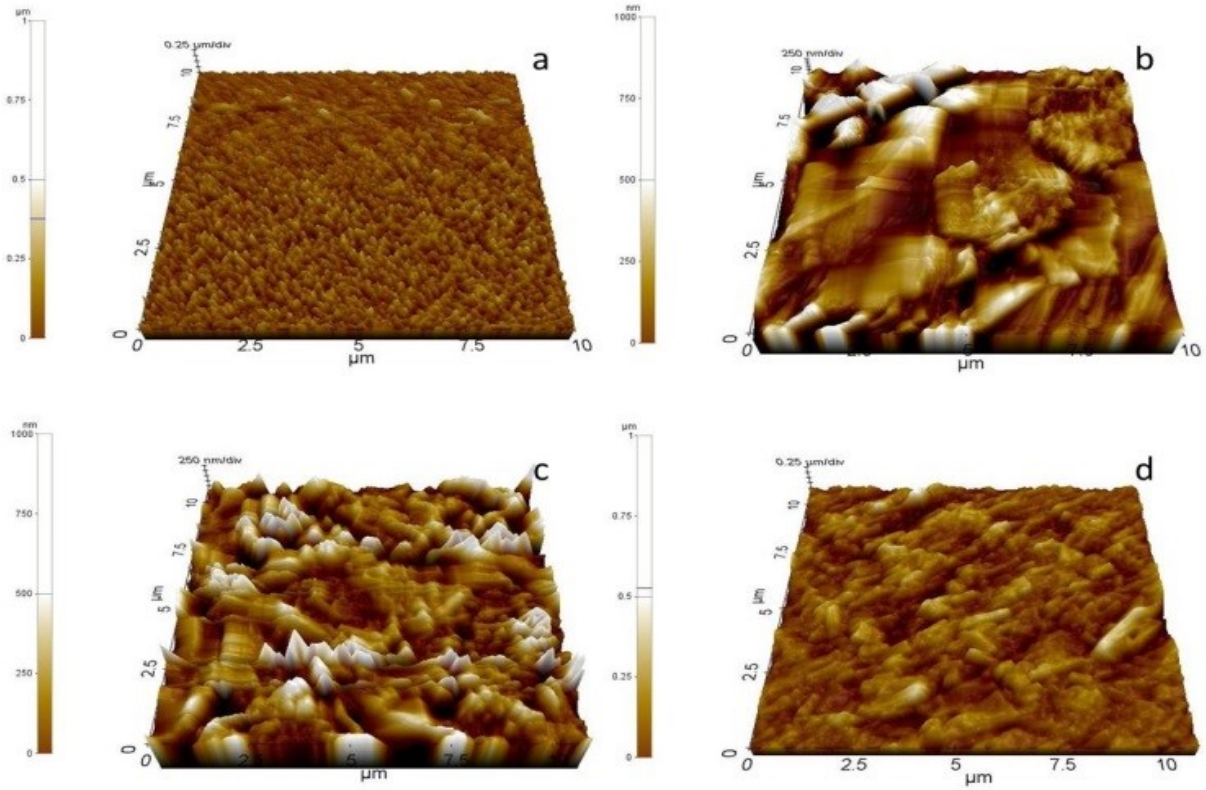

Figure 6-11: Changes in the surface morphology of the freeze dried synthetic pellets during the pH-cycling process, which were treated with 250 ppm of F^-. The images correspond to the a. 1st, b. 6th, c. 11th and d. 16th day of pH-cycling.

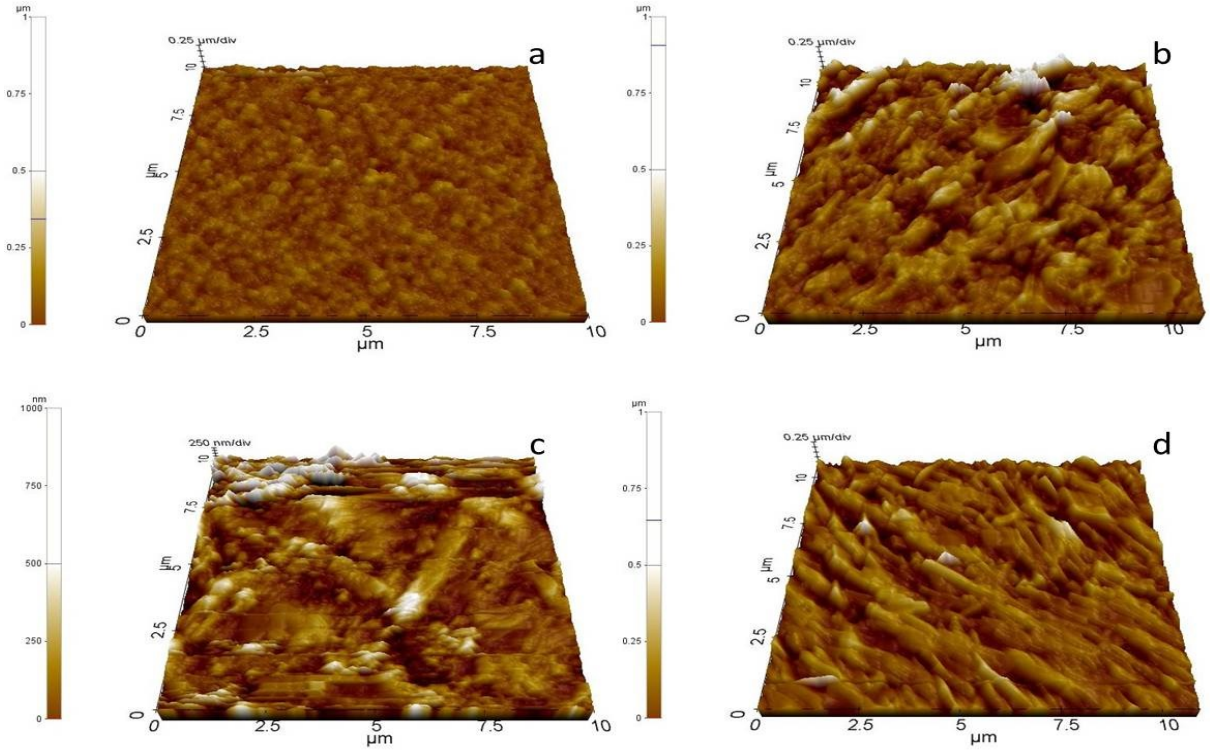

Figure 6-12: Changes in the surface morphology of the freeze dried synthetic pellets during the pH-cycling process, which were treated with the mixed-F^- pH-cycling model. The images correspond to the a. 1st, b. 6th, c. 11th and d. 16th day of pH-cycling.

6.4 Discussion

The results presented during Chapter 6 indicate that the behaviour of the freeze dried synthetic HA pellets is similar to that of enamel blocks which were treated with the same pH-cycling protocol. Chemical analysis of the remineralising solutions, during the combined period of main and intermediate remineralisation periods (Figure 6-1), shows that some demineralisation takes place, especially for the pellets treated with 10 ppm of F^- and the mixed-F^- model (in the form of NaF), which is followed by remineralisation and Ca^{2+} and PO_4^{3-} accumulation (Figures 6-1, 6-4). In all cases, some dissolution of the pellets can be observed during the intermediate remineralisation period, as both the Ca^{2+} (Figure 6-2a) and PO_4^{3-} (Figure 6-5a) results indicate. HA dissolution takes place through the interaction of the surface of the pellets with the solutions used, which may be enhanced by the increased porosity the synthetic pellets present (619).

The dissolution is more intense in the case of the pellets treated with 10 ppm of F^- (FD_{10}, FD_{Mix}), while it is almost half for the FD_{250} (~ 55 ppm for FD_{10} and FD_{Mix} vs. ~ 30 ppm for FD_{250}) and may be attributed to differences in the amount of F^- used during the preceding treatment. This conclusion is in agreement with the results obtained for enamel since, as stated in Chapters 3 and 4, fluoride treatment with 250 ppm of F^- favours CaF_2 deposition on the surface of the enamel (514, 515), which could act to some extent as a protective layer on the surface of the pellets, blocking their pores and inhibiting enamel dissolution, and as F^- reservoir, providing the solution with F^- and thus having a protective against dissolution.

On the other hand, administration of 10 ppm of F^- favours a dissolution and reprecipitation mechanism resulting in F^- incorporation inside the HA structure, which is more important during the proposed mechanism (398) of PEM. A similar observation has been also made by Featherstone et al. (1990), who saw an exponential correlation between increasing F^- concentration and inhibition in the demineralisation of carbonated HA synthetic pellets and dental enamel (620).

The longer the pellets are left inside the remineralising solutions, the more their behaviour changes and remineralisation takes place as the results of the main remineralisation period indicate (Figures 6-2b, 6-5b) and is expressed through strong Ca^{2+} and PO_4^{3-} adsorption. With increasing time in the cycling regime, stronger uptake is observed in both the intermediate (Figures 6-2a, 6-5a) and main (Figures 6-2b, 6-5b) remineralisation periods, which peaks on day 11 and is in total more intense in the case of FD_{Mix} (~ 95 ppm) and similar for FD_{10} and FD_{250} (~ 65 ppm).

This behaviour is different from that observed in the case of the enamel blocks (sections 3.3.1 and 3.3.2). In the case of the enamel the switch in F^- treatment concentration, leads to some increase in the amount of Ca^{2+} and PO_4^{3-} accumulated, but a smooth continuity in the process

similar to the simple model is observed. On the other hand, the switch in the amount of F^- used for the pellets leads to what can be described as a delay in the whole process. Although Ca^{2+} results present a similar behaviour, the PO_4^{3-} results present a delay when compared to the pellets treated with 250 ppm of F^-. The minimum observed on day 11 for the intermediate remineralisation period in their case, is now visible on day 16. This is probably due to the different nature and structure of the enamel and the pure HA (399, 403-405) and more specifically the significantly higher porosity, which means that more material is needed to fill the empty space.

As far as the demineralisation period (Figures 6-3, 6-6) is concerned, dissolution of the HA pellets is observed in all cases as the Ca^{2+} results indicate. The dissolution is strongest for the FD_{10} and weakest for the FD_{250} treatments, peaks on day 11, and can be attributed to the higher amount of F^- used and the protective CaF_2 layer which potentially forms on their surface. This is further supported by the results of FD_{Mix} (following the switch to the 250 ppm F^- treatment), which are between those of FD_{10} and FD_{250} and also suggests the deposition of CaF_2 on the surface of the pellets. The observation that it is lower than that of the pellets treated with 250 ppm of F^- can be attributed to surface changes which happened during the 10 ppm F^- treatment period, during which incorporation of F^- is favoured in the HA structure.

On the other hand, the PO_4^{3-} results indicate strong dissolution on day 1; which is followed by accumulation on days 6 and 11 and decreases on day 16. The apparent inconsistencies between calcium and phosphate may indicate that, as in the case of enamel, concurrent precipitation of material could also take place during the demineralisation period in the form of e.g. OCP or DCPD, which have a different Ca/P ratio and are known to form under low pH conditions (520, 521). These phases have also been traced in the FTIR spectra of the treated pellets (Figure 6-8); as the increasing surface of free HPO_4^{2-} modes between 520 cm^{-1} and

540 cm^{-1} (481-483) suggest and can further explain the PO_4^{3-} uptake observed during the chemical analysis of the demineralising solutions used.

Fluoride results (Figure 6-7) show that both groups present F^- accumulation, which is far higher in the case of the FD_{250} and from day 11 onwards the FD_{Mix} pellets. Fluoride uptake peaks on day 6 and day 11 for FD_{10} and FD_{250} and FD_{Mix} respectively, after which a drop in accumulation takes place. These results suggest that saturation of the pellets, in terms of F^-, takes place after which their ability to structurally incorporate material reduces significantly and has been demonstrated to take place in both enamel (414, 534, 539, 540) and synthetic HA (621). This is probably the reason why, by day 16, the amount of F^- accumulated by the FD_{10} pellets reduced to zero, while a significant decrease is also observed in the case of the FD_{250} and FD_{Mix} pellets. The difference in the amount of F^- adsorbed, between the two groups, can be explained by the different route with which F^- is incorporated as in the case of enamel. For the pellets treated with 250 ppm of F^- CaF_2 deposition was likely favoured (FD_{250}, FD_{Mix}), while structural incorporation is favoured in the case of the pellets treated with 10 ppm of F^- (FD_{10}) (515).

Fluoride incorporation for all groups is demonstrated by the increase in the F^--OH^- FTIR peak around 750 cm^{-1} (479, 480), although the rate of the process is faster in the case of the FD_{10} pellets as it peaks on day 6 (Figure 6-7). The delay for FD_{250} pellets (peak observed on day 11) can be explained by the strong presence of CaF_2, which blocks apatite dissolution through the formation of a protective layer on the surface of the pellets (514, 622); and the blocking of the surface pores of the HA pellets, which inhibits ionic diffusion. As a result, the surface HA reacts mainly with the deposited CaF_2, which results in slower material dissolution and reprecipitation with F^- incorporation. This conclusion becomes clearer through the changes in the F^--OH^- peak of the FD_{Mix} pellets around 750 cm^{-1}. In their case the rate of increase in

surface area of the peak is stronger while they are treated with 10 ppm of F^- and slows down when the treatment switches to 250 ppm.

In terms of artificial maturation the FTIR (Figure 6-8) and hardness (Figure 6-9) results suggest that it does take place in synthetic pellets and follows a mechanism similar to that proposed (398) for enamel (Chapter 3). The mechanism is based on sequential dissolution and reprecipitation cycles, which lead to HA, fHA and FA precipitation either directly or through epitaxial growth with OCP acting as the precursor, which then hydrolyses in more stable apatites (615, 616) and material which is precipitated and fills the pores of the pellets. At the same time, CO_3^{2-} and F^- are incorporated in the apatite lattice as the υ_2, υ_3 and υ_4 CO_3^{2-} modes around 700 cm^{-1}, 1450 cm^{-1} and 1640 cm^{-1} and 830 cm^{-1} (487, 493, 494) respectively and the F^--OH^- peaks around 750 cm^{-1} (479, 480) suggest. The carbonate probably originates from dissolved CO_2 in the waters used during the pH-cycling study (617, 618), while the incorporation of F^- in the crystal lattice of synthetic HA through pH-cycling has been extensively used as a method for FA and fHA synthesis (623, 624).

The precipitation of precursor phases can be monitored through the FTIR spectra in the region below 540 cm^{-1}, which correspond to free HPO_4^{2-} and are characteristic of the presence of OCP or TCP (481-483). These peaks are either absent or really weak on day 1 and present a noticeable increase in intensity and surface area (> 100%) on day 6. The surface area of the HPO_4^{2-} peaks corresponding to the FD_{10} pellets is significantly higher than that of the FD_{250}, which also points to a higher rate of HA reactivity and structural incorporation when less F^- is administered. In both cases the peaks become weaker with time, which suggests either dissolution of the material or hydrolysis in HA. The suggestion that the precursor phases are transformed to HA is supported by the behaviour of the υ_3 PO_4^{3-} asymmetric stretching mode

peaks (1000-1200 cm^{-1}). These peaks are located around 1020 cm^{-1} (484-486), 1050 cm^{-1} (487, 488) and 1150 cm^{-1} (498) and correspond to the υ_3 PO_4^{3-} asymmetric stretching mode. During the duration of the pH-cycling procedure, the peak around 1020 cm^{-1} is the dominant and in all cases increases in surface area and shifts towards higher wavenumbers. The surface area of the peak around 1020 cm^{-1} reaches a maximum on day 11 for all groups and corresponds to the decrease observed for the precursor phases. On day 16 a decrease in surface area is observed, which suggests higher mineral maturation.

The results also show that the most mineralised pellets are those treated with the mixed-F^- pH-cycling model (FD_{Mix}) as the stronger intensity of the OH^- liberation and stretching modes around 630 cm^{-1} and 3750 cm^{-1}, which correspond to HA presence suggest. At the same time, the 1020 cm^{-1} peak shifts from non-existent to 1022 cm^{-1} on day 6 and finally to 1025 cm^{-1} for FD_{10}, from 1021 cm^{-1} to 1024 cm^{-1} for FD_{250} and from non-existent to 1024 cm^{-1} for FD_{Mix}. These results are in agreement with earlier observations by Rey et al. (1991) and Paschalis et al. (1997), who saw that as HA matures and becomes more mineralised, these peaks shift towards higher wavenumbers and decrease in surface area (485, 498).

In this case, the most important period during the artificial maturation process is the intermediate remineralisation period as the correlation (FD_{10}: $p = 0.001$, FD_{250}: $p = 0.007$, FD_{Mix}: $p = 0.004$) between all the experimental parameters (Ca^{2+}, PO_4^{3-}, F^-, hardness) suggests. More specifically, strong correlation exists between the Ca^{2+} changes during the intermediate remineralisation period and hardness increase for all groups ($p < 0.001$). A similar correlation ($p < 0.002$) exists with the PO_4^{3-} changes during the demineralisation period for the FD_{10} and FD_{Mix} pellets, while the longer-term nature of the FD_{250} is mirrored through the correlation ($p < 0.001$) with PO_4^{3-} changes of both the demineralisation and the

main remineralisation period. In all cases, fluoride incorporation inside the HA structure and deposition of CaF_2-like material seems to take place during the main remineralisation period (FD_{10}: $p = 0.03$, FD_{250}: $p = 0.002$, FD_{Mix}: $p = 0.04$). Finally, the potential effects of artificial maturation can be observed, for all groups, through the strong correlation of the decrease in Ca^{2+} release during the demineralisation period with hardness increase ($p < 0.05$) and F^- accumulation ($p < 0.03$).

A comparison of the results of Chapter 6 with those of bovine enamel shows that the synthetic freeze dried pellets, which were sintered at 800ºC, can be artificially matured using the same pH-cycling protocol used during the artificial PEM of dental enamel. While the behaviour between the two materials is similar, the process is more intense and faster in the case of the synthetic pellets.

Another significant factor, which can explain the differences in behaviour between the natural enamel blocks and the synthetic pellets, is the higher porosity of the synthetic pellets, even after sintering at 800ºC as presented in section 5.2.2.2. This results to higher chemical transport of material, precipitated in the surrounding environment, which fills the intra-pellet empty space making the pellets denser and harder; in a way similar to precipitated material filling the inter-prismatic space of enamel during PEM (91, 101, 102, 325, 504) and is supported from the comparison of the chemical analysis results of sections 3.1 and 6.1. Another supporting factor are the FTIR spectra (sections 3.1.2 and 6.2), where the changes observed, during the pH-cycling procedure, are similar but a lot more intense in the case of the synthetic material. Finally, the slightly higher increase in hardness observed for the synthetic pellets can be attributed to a combination of the precipitation of more stable material of apatitic nature and the densification taking place following the chemical transport of material in the pore spaces and the resulting reduced porosity and has been also observed in studies regarding enamel (91, 101, 102, 325, 504).

6.5 Conclusions

Chapter 6 presented the results of the pH-cycling of synthetic HA pellets freeze dried and sintered at 800ºC, and the potential effects of artificial maturation on their physicochemical properties. The results show that the pellets can be artificially matured and the observed changes are similar to those of enamel described in Chapter 3 (hardness increase, solubility decrease). As expected, due to the differences in the physicochemical properties and physical structure of the two materials, several differences exist, which result in faster maturation rate of the synthetic material, but the trends are similar in both cases.

At the same time, the intermediate remineralisation period (shortly after F^- treatment) seems to be the most active and significant period of the process; and is strongly correlated with hardness increase and in some cases (FD_{10}) F^- accumulation. This also points out the significance of the amount of F^- reaching the surface of the pellet/enamel. In terms of PEM it is more preferable for the maturing mineral to sustain some demineralisation, which will be accompanied by slower F^- incorporation into the apatite lattice; than administrating high dosages of F^-, which favours CaF_2 formation and deposition. The presence of a thin plaque layer could be desirable in this case as it will "protect" the lesion from the high F^- concentration and CaF_2. In this context, the presence of CaF_2 could act as a reservoir, which would provide the necessary F^- needed to remineralise the formed subclinical carious lesions.

Although the synthetic pellets produced seem to be a good analogue for dental enamel, further work is needed in order to improve their intrinsic physical and chemical similarity to natural enamel, and subsequent behaviour during *in vitro* demineralisation and remineralisation studies. In all cases though, the current pellets can be used as useful and importantly,

relatively homogeneous analogue for dental enamel, to assist in strategies to design *in vitro* and *in situ* studies for PEM using enamel.

Page intentionally left blank

7. Summary & Concluding Remarks

This Chapter presents the research conclusions derived during the experimental procedure (Section 7.1), the contributions to knowledge and the gaps filled (Section 7.2) and future work and recommendations on how to further improve the experimental process (Section 7.3). Before doing that, the work presented in the previous 4 research Chapters will be briefly reviewed.

Chapters 3 and 4 of this thesis addressed the lack of *in vitro* models to simulate PEM, and presented data to support a proposed PEM model (398). The work described the effects of maturation on the physicochemical properties of dental biogenic apatites (bovine, as proxies for human enamel). The motivation for this study was primarily the lack of a complete model to describe the entire PEM process, despite substantial literature on the post-eruptive physicochemical changes of dental enamel. Additionally, most of the relevant literature can be traced back to the 50s, 60s and early 70s when analytical techniques were not as advanced as currently and in some cases unavailable. Finally, the work considered here was considered topical, as PEM is a process that directly affects the presence of pathological enamel conditions and most importantly dental caries (1-3). Recent studies appear to show an end of caries decline (17, 18) and indeed reversal (18, 19) due to modern lifestyles. This implies that current caries fighting strategies have stopped being as effective as they once were. As a result, new caries preventing approaches and clinical techniques are needed, which will lead to better strategies for caries prevention rather than treatment. A thorough understanding of PEM has the potential to achieve this. If the mechanism governing the process is described fully, it will be possible for dental and materials scientists to intervene and introduce new treatments that could enhance and accelerate PEM thus significantly reducing caries susceptibility at a younger age.

In order to test potential mechanisms behind PEM, appropriate *in vitro* experimental techniques are needed. This is why the current study took advantage of already existing pH-cycling models and their perceived advantages, which include high control on experimental variables, reproducibility, sensitivity, a simpler design, compared to other *in situ* and *in vivo* models (424), the ability to mimic, simply but realistically, the oral environment, and most importantly, the ability to replicate the dynamic nature of mineral changes and caries formation (405, 424). For these reasons, an experimental model was developed, which aimed to simulate the PF/enamel interaction, on which the proposed PEM model is based (398), and not the saliva/enamel interaction usually studied through pH-cycling. This was achieved using a PF proxy, instead of artificial saliva, and appropriately adjusting the durations of the experimental periods to match those taking place during PF/enamel interaction. At the same time, to make the model more realistic, an extra remineralisation period was added containing slightly elevated amount of BF, with the purpose to simulate the transition from the "peak" concentrations observed in the plaque immediately after brushing and the low concentration (retention) phase observed during the rest of the day (430-432). The experimental procedure was then applied on bovine enamel and the PEM model proposed by Fejerskov et al. (1994) was tested.

Chapters 5 and 6 addressed the lack of synthetic enamel proxies with similar physicochemical properties to bovine enamel, which may successfully mimic enamel behaviour and may be used to study potential PEM models. More specifically, the experimental study addressed the issue of inferior mechanical properties by most synthetic materials (367-369) and the failure of experimental approaches, such as sintering, to improve properties such as density, flexural strength and hardness due to both physical and limitations of the derived materials (370-372). Properties such as solubility and hardness have been observed to be inter-correlated (320, 408,

503) and may influence directly PEM and thus their monitoring was necessary during the study of the proposed PEM model.

To meet the project objectives, adaptation of recent studies demonstrating the synthesis of thermally stable HA (206, 242-244, 396, 397) was performed. It was thus possible to produce a material for which no structural deterioration could be observed for temperatures up to 1200ºC and could be pelleted and thermally treated leading to pellets with mechanical properties which compared favourably to those of bovine enamel. Following the production of wide range enamel-like pellets, with slightly different mechanical properties, their behaviour was evaluated and those which most closely resembled that of enamel were artificially matured using the same pH-cycling model applied in the case of bovine enamel.

7.1 Research Conclusions

The findings of Chapters 3 and 4 support the proposed PEM model (398) by demonstrating that it is possible to artificially mature sound enamel blocks and increase their hardness. Such hardness increase may also take place *in vivo*, through the remineralisation of the surface layers of enamel, by the deposition of Ca^{2+}, PO_4^{3-} and F^- originating from the oral fluids and dental treatments. The deposition may take place via two separate mechanisms:

1. Under low pH, softening of the enamel surface is followed by a porosity increase leading to the concurrent dissolution of superficial enamel and the deposition of kinetically favoured non-apatitic phases (e.g. OCP) or less soluble apatitic phases (FA, fHA). As a result it would be possible to remineralise newly formed pre-cavitated caries-like lesions through the precipitation and deposition of acidic calcium phosphates (e.g. OCP, DCPD) (520, 521)) and F^- containing apatites (536), and introduce additional strength by filling the interstices between enamel prisms. This proposal is supported by the chemical and

structural analysis of the present thesis and is in agreement with earlier *in vitro* PEM and remineralisation studies (91-93, 101, 102, 144, 534, 535).

2. Under neutral pH-conditions the surface of the enamel hardens by remineralisation and deposition of material, which blocks the surface pores and inhibits any further dissolution and ionic diffusion towards the underlying enamel. At the same time, a more acid resistant layer is formed as suggested by the gradual decrease of Ca^{2+} and PO_4^{3-} release during the demineralisation period suggests. Precipitation of both HA and fluoridated HA is possible, at the pH of the remineralising fluid (6.58), which is supersaturated with respect to both enamel and FA (536). These conditions also favour the hydrolysis of the precipitated acidic calcium phosphates (e.g. OCP) and transformation to apatites; as the reductions of the FTIR peaks corresponding to the presence of acidic calcium phosphates and the simultaneous increase of those corresponding to newly formed and poorly crystalline HA suggest. With time, decrease of the newly formed poorly crystalline HA takes place with subsequent increase of those correlated with highly crystalline HA and fHA as FTIR data suggest. The observed changes translate in mineral maturation, the kinetics of which may be translated into the formation of stronger enamel (228, 298, 527, 528).

In both cases, F^- seems to play a significant role in the whole process. The amount of F^- reaching the surface is "regulated" by the degree of plaque accumulation (517). When the degree of accumulation is high, lower amounts of F^- can diffuse through it and F^- incorporation into the enamel structure is favoured; while when no or a thin plaque layer exists the excess F^- present favours the deposition of a CaF_2 layer (514, 515). In every case though, F^- stimulates the formation of apatites either directly or through the hydrolysis of precursor phases (531).

In the present work, stronger F^- adsorption was observed for the enamel blocks treated with 10 ppm of F^-, as FTIR data suggest, which corresponds to strong plaque accumulation and stronger inhibition of F^- diffusion through the plaque. Such conditions may be observed shortly after eruption and may explain studies by Sognnaes and Shaw (1952) and Sognnaes et al. (1955) where it was observed that fluoride absorption can be up to 20 times higher shortly after eruption (346, 347); and *in vivo* caries studies by Aasenden et al. (1972) who found that fluoride is more effective during the early post-eruptive period (348).

For higher F^- concentrations, the presence of such a CaF_2 layer was validated during the experimental procedure both chemically and morphologically. Treatment of the pH-cycled enamel blocks with KOH led to the dissolution of the loosely bound F^- (in the form of CaF_2), the concentration of which was found to be similar for the blocks treated with the same F^- concentrations. Since CaF_2 is not incorporated in the apatite structure, it is not directly correlated with PEM. Calcium fluoride has more of a protective role against acid attacks, while at the same time acts as a reservoir of F^- in saliva, which is transferred into the plaque and diffused on the surface of the enamel (517).

Finally, chemical analysis suggests that with time the enamel gets saturated and its ability to absorb F^- and other mineralising agents reduces which slows down the maturation rate and is expressed through the plateau observed in the F^- diagrams towards the end of the pH-cycling. In the end, a state of equilibrium is reached between the enamel and the oral environment, leaving the formation of CaF_2 as the main interaction route. These observations are also in agreement with studies concerning the decreasing adsorbing abilities of enamel with increasing post-eruptive age (144, 534, 539, 540).

The conclusion of the first part of the thesis is that the produced results support the PEM model proposed by Fejerskov et al. (1994). This conclusion opposes early *in vitro* and *in vivo*

studies (503, 504) claiming that the processes of PEM maturation and remineralisation were totally distinct and that the former was correlated solely with crystallographic growth, while the latter corresponded to material filling the interprismatic space. On the other hand, it is in accordance with later studies suggesting a similar mechanism behind the whole process after analysing the changes in the physicochemical properties of extracted human teeth of varying post-eruptive ages (104, 106, 321). At the same time, the results suggest that the reduced F^- concentrations reaching the enamel due to plaque presence are more efficacious than the increased peak concentrations reaching the enamel when the plaque has been thoroughly cleaned, which has been also proposed by Robinson (2012) for the interaction of F^- with caries lesions (442). As a result, it is concluded that the presence of a thin plaque layer, with the appropriate caveats, may be desirable during PEM as it will enhance the process.

Chapters 5 and 6 describe studies designed to evaluate various preparation techniques to optimise HA pellets as enamel proxies, which have similar physicochemical properties and behaviour to that of enamel. Previous studies (47, 367), so far, could not replicate both the mechanical properties and chemical/mineralogical properties of biogenic apatite, lacking in all cases some or all of the necessary qualities to simulate enamel (47, 367, 565, 625). Sintering techniques, which in theory could improve properties like density, flexural strength and hardness, also led to chemical deterioration due to HA decomposition into other phases like β-TCP or CaO (370-372). Lately, HA synthesis using high pH (> 9.0) has led to thermally stable powders (242, 423) and could potentially be used to overcome the above issues. At the same time the drying method (oven or freeze drying) of the synthesised powders has also an effect on their properties.

In this thesis, the use of a wet precipitation method and freeze drying of the produced material led to powders similar in particle size, but with differences in physical structure (density, surface area) with powdered enamel. Although the precipitated powders presented initially

lower densities and far higher surface areas, heat treatment for 3 hours at 800ºC overcame these potential concerns without any chemical dissociation into secondary phases, such as TCP and CaO.

Pelleting of the as-produced powders and sintering at 800ºC led to pellets with mechanical properties and physical structure (density, surface area) similar to that of enamel, as the FTIR, densitometry and hardness results showed. The only condition which was not met was the porosity of the produced pellets, which was significantly higher than that of enamel. The similarity in the behaviours of the produced HA pellets and enamel was verified using static solutions, which simulated the three elements of the pH-cycling model used during this thesis (Section 5.3). By immersing sintered pellets and bovine enamel blocks for 5 days inside the solutions used during the enamel pH-cycling studies (plaque fluid proxy, acid challenge and F^- treatment) it has been demonstrated, through chemical analyses of the solutions used, structural analyses and hardness measurements, that the pellets with behaviour closest to that of bovine enamel are the freeze dried sintered at 800ºC. The effect of the drying process (freeze drying vs. oven drying) was also demonstrated since the pellets created by oven dried HA and similar behaviour to that of enamel were those sintered at 500ºC, but with inferior mechanical properties. As a result, it was concluded that the pellets to be used as enamel proxies and tested through a normal pH-cycling procedure would be the freeze dried pellets sintered at 800ºC.

Artificial maturation of the chosen pellets, using the same pH-cycling model as in the case of enamel, led to the conclusion that it is possible to artificially mature them in a way similar to that of enamel. This is expressed through the increase in the hardness of the treated pellets and the decrease in HA dissolution observed during the demineralisation period. These results suggest the precipitation of a more acid resistant material and further densification through

reduction in the porosity of the pellets. The increased Ca^{2+} and PO_4^{3-} uptake, which is observed compared to bovine enamel, is attributed to the higher porosity of the synthetic pellets and the stronger diffusion of Ca^{2+}, PO_4^{3-} and F^-; since the surface area of the powders and the enamel are similar. The significant reduction of F^- uptake towards the end of the experimental procedure also suggests that saturation of the pellets also takes place in a way similar to that on enamel.

The mechanism behind the whole process also seems to be similar to that of enamel, as the presence of acidic calcium phosphates and F^- uptake was observed through FTIR. At the same time, the changes in the PO_4^{3-} peaks suggest that crystal growth takes place in this case as well. With time, more crystalline materials forms with the simultaneous reduction of the acidic calcium phosphate peaks and those correlated with poorly crystalline HA.

The conclusion of the second part of the present thesis is that the produced synthetic HA pellets, which were freeze dried and sintered at 800ºC, can be a good substitute for enamel, although more work is needed to further refine preparation techniques of HA for use as an analogue for enamel. As the results of this study stand, the main difference between biogenic apatites and the artificial substitute produced here is that the former are mainly Ca-deficient (32, 34) and contain several impurities (e.g. trace elements, CO_3^{2-}) (78, 79), whereas the latter were pure and close to stoichiometry; which also explains their thermal stability (243-247). As a result, their behaviour was similar, but not identical to that of enamel. It would, however, be intriguing to investigate how they might perform *in vivo*.

7.2 Contributions to Knowledge

Prior to this thesis, most of the reported data regarding PEM were mainly traced during the 50s, 60s and early 70s and is some cases during the 80s when remineralisation became a research interest. However, these studies did not provide a model, which fully described the PEM process. At the same time, the mechanism of action of topical F^- administration through water fluoridation, toothpastes and oral solutions had not been fully understood. Since then most of the PEM data are incidental and are mainly used for the evaluation of caries detection techniques (e.g. enamel electrical resistivity) and subsequent treatment.

The aims of this thesis were to simulate the process of PEM using an appropriate experimental protocol and to develop synthetic enamel proxies, which could replicate the physicochemical properties of enamel and mimic its behaviour. A simple pH-cycling was developed, which simulated the PF/enamel interaction and the PEM process. This model was then used to test the PEM model proposed by Fejerskov et al. (1994) and the results support the proposed PEM mechanism. At the same time, the changes of the physicochemical properties of dental enamel were monitored and further understanding of the combined role of the distinct demineralisation, remineralisation and topical F^- administration was achieved. The conclusions reached can be used as a guide for both basic and clinical research and help identify new methods and dental products, which will help reverse the recently observed decrease in caries decline and its effects on the everyday life of people.

The present thesis also demonstrated that it is possible to synthesise a material, which has similar physicochemical properties and behaviour to those of enamel. This was achieved through the adaptation of various experimental techniques used during HA synthesis, which allowed the appropriate treatment of the produced material and could overcome the limitations regarding the simultaneous replication of the chemical and mechanical properties of biogenic apatites. It has been also demonstrated that it is possible to produce synthetic

proxies, which behave similarly to enamel. Such proxies can be used as enamel substitutes and help design more accurate and detailed clinical studies, as they offer greater reliability and reproducibility in composition, while being readily available when needed. Finally, by replicating the physicochemical enamel properties it will also be possible to create new biocompatible fillings and dental implants without the biological contamination risks of current substitutes.

7.3 Future Work & Recommendations

The work presented in this thesis has not exhausted the parameters affecting the PEM process. Future studies, on both primary and permanent enamel, should focus on the role of metal ions which are either present in the enamel structure or are adsorbed during post-eruptive life. Several metals such as Sr^{2+}, Zn^{2+} and Sn^{2+} have been proposed to enhance enamel remineralisation and to decrease its solubility, while others like Mg^{2+}, Pb^{2+} and Cd^{2+} seem to have to opposite effect. Some elements have also been proposed to enhance F^- adsorption (e.g. Sr^{2+}), while others enhance remineralisation through more complex bonding (e.g. F^--Al^{3+}-PO_4^{3-}). Decoding the potential role of each element, may allow dental and material scientists to create new processes and oral products, which will allow the intervention in the PEM process and subsequent acceleration and enhancement. *In vitro* studies employing pre-treated enamel and lesion creation should also be performed, as they will provide valuable evidence regarding cariogenic challenges. At the same time, *in vitro* studies should act as the base for detailed *in situ* studies designed to investigate the effects of PEM using a more realistic system. Such studies can assist not only in pointing out the differences between the behaviour of primary and permanent enamel, but also in testing the efficacy of newly designed oral products. In the long run, the *in vitro* and *in situ* results need to be validated through carefully planned clinical studies. This will open the door for the production of novel techniques and

products, which will help to chemically enhance and accelerate the PEM process and promote caries prevention.

As far as the synthetic materials are concerned, studies should focus in the creation of techniques which will lead to even better enamel proxies. Similarly to bovine enamel, studies should try to replicate the complex composition of biogenic apatites by doping the synthesised powders with the most significant elements, which affect the physicochemical properties of enamel. Doping for each element should be performed not only as stand-alone, but also through co-doping of two or more trace elements. In the long run, it should also be attempted to replicate the gradients in concentrations observed for each element as a function of the depth from the surface of the enamel. Such studies will allow more detailed *in vitro* modelling of the behaviour of enamel, which will also lead to more detailed and targeted *in situ* and *in vivo* clinical studies. Finally, novel synthesis techniques should be used, which employ the simultaneous precipitation and detailed deposition of the produced powders in a way which will resemble the hierarchical structure of enamel. This will result in synthetic HA pellets with the properties and behaviour of enamel, while it will make possible the production of more biocompatible dental materials, which will minimise potential contamination risks.

Page intentionally left blank

Appendix I

Appendix I presents the analytical FTIR data of the enamel blocks and synthetic FD-HA pellets, which were analysed during this thesis. The data can be found in full in the micro SD card attached at the end of this volume. Here the data of group $M16_{10}$, the experimental conditions of which can be found in Table A-1, are presented (Tables A-2 to A-5) as an example.

Solutions & Treatments	Experimental Conditions
pH Remineralising Solution	6.58
pH of Demineralising Solution	4.90
Background F^- Concentration (ppm) (Main/ Intermediate Periods)	0.2/ 2.0
F^- Treatment Concentration (ppm)	10

Table A-1: Experimental conditions used during the pH-cycling study for the Group $M16_{10}$, which was treated with PF during the remineralising, AC during the demineralising period, 10 ppm of F^- and added BF of either 0.2 ppm or 1.0 ppm during the main and intermediate remineralisation periods respectively.

Day of pH-cycling	Assignment	Peak (cm^{-1})	Area (cm^2)	Height (cm)
1	$\upsilon_4\ PO_4^{3-}$	548	6.095	0.578
		581	20.993	1.854
		605	7.558	0.831
		620	1.591	0.779
	OH^-	632	3.469	0.360
	$\upsilon_2\ CO_3^{2-}$	702	5.570	0.556
	F - OH	751	0.906	0.051
	$\upsilon_4\ CO_3^{2-}$	856	8.174	0.574
	$\upsilon_3\ PO_4^{3-}$	1011	22.484	0.686
		1109	0.405	0.057
		1145	5.542	0.304
	$\upsilon_3\ CO_3^{2-}$	1441	3.593	0.212
	C=O Stretching	1736	28.391	0.840
	HPO_4^{2-}	1977	2.809	0.865
		2014	2.379	0.190
		2159	15.817	0.905
		2175	10.921	0.097

Table A-2: FTIR results of Group $M16_{10}$ following the 1st day of the pH-cycling process.

Day of pH-cycling	Assignment	Peak (cm^{-1})	Area (cm^2)	Height (cm)
6	$\upsilon_4\ PO_4^{3-}$	533	208.190	15.088
		549	5.314	1.540
		560	11.828	1.836
		580	17.222	1.899
	OH^-	632	2.276	0.483
	$\upsilon_2\ CO_3^{2-}$	703	11.471	0.878
	F - OH	756	15.178	0.586
	$\upsilon_4\ CO_3^{2-}$	856	23.510	1.302
	$\upsilon_3\ PO_4^{3-}$	1011	48.491	1.434
		1113	5.314	0.257
		1148	25.735	0.861
	$\upsilon_3\ CO_3^{2-}$	1371	11.770	0.454
		1439	10.908	0.593
	C=O Stretching	1736	92.261	2.157
	HPO_4^{2-}	1976	8.438	0.687
		2021	2.127	0.143
		2160	16.657	1.061
		2181	22.886	0.327

Table A-3: FTIR results of Group $M16_{10}$ following the 6th day of the pH-cycling process.

Day of pH-cycling	Assignment	Peak (cm^{-1})	Area (cm^2)	Height (cm)
11	HPO_4^{2-}	531	62.268	8.675
	$\upsilon_4\ PO_4^{3-}$	566	17.658	2.839
		588	6.586	0.756
	$\upsilon_2\ CO_3^{2-}$	703	23.255	2.020
	F - OH	750	42.250	1.591
	$\upsilon_4\ CO_3^{2-}$	856	85.296	4.829
	$\upsilon_3\ PO_4^{3-}$	1012	186.303	5.605
		1110	25.021	1.263
		1151	94.464	2.871
	$\upsilon_4\ CO_3^{2-}$	1370	328.272	8.053
		1442	48.751	1.831
	C=O Stretching	1741	37.895	2.103
	HPO_4^{2-}	1976	360.986	8.785
		2027	3.108	1.241
		2159	336.867	4.386
	OH^- (OCP)	2433	2.324	0.019
	C-H Stretching	2947	8.144	0.275
		2990	17.383	0.661

Table A-4: FTIR results of Group $M16_{10}$ following the 11th day of the pH-cycling process.

Day of pH-cycling	Assignment	Peak (cm^{-1})	Area (cm^2)	Height (cm)
16	HPO_4^{2-}	531	29.307	4.781
	$\upsilon_4\ PO_4^{3-}$	554	6.945	0.928
		575	14.357	1.993
	F - OH	755	50.004	0.286
	$\upsilon_4\ CO_3^{2-}$	856	19.071	1.160
	$\upsilon_3\ PO_4^{3-}$	1011	41.679	1.384
		1105	7.370	0.365
		1157	22.454	0.737
	$\upsilon_3\ CO_3^{2-}$	1441	6.413	0.388
	C=O Stretching	1738	56.927	1.688
	HPO_4^{2-}	1976	1.935	0.864
		2032	38.513	1.220
		2159	229.012	2.947

Table A-5: FTIR results of Group $M16_{10}$ following the 16th day of the pH-cycling process.

Page intentionally left blank

List of References

1. Fanning RJ, Shaw JH, Sognnaes RF. Salivary contribution to enamel maturation and caries resistance. The Journal of the American Dental Association. 1954;49(6):668-71.
2. Hicks J, Garcia-Godoy F, Flaitz C. Biological factors in dental caries enamel structure and the caries process in the dynamic process of demineralization and remineralization (part 2). Journal of Clinical Pediatric Dentistry. 2004;28(2):119-24.
3. Hicks J, Garcia-Godoy F, Flaitz C. Biological factors in dental caries: role of remineralization and fluoride in the dynamic process of demineralization and remineralization (part 3). Journal of Clinical Pediatric Dentistry. 2004;28(3):203-14.
4. Hollister M, Weintraub J. The association of oral status with systemic health, quality of life, and economic productivity. Journal of Dental Education. 1993;57(12):901-12.
5. McGrath C, Bedi R. The association between dental anxiety and oral health-related quality of life in Britain. Community Dentistry and Oral Epidemiology. 2004;32(1):67-72.
6. Wong RMS, Ng SKS, Corbet EF, Keung Leung W. Non-surgical periodontal therapy improves oral health-related quality of life. Journal of Clinical Periodontology. 2012;39(1):53-61.
7. Jankauskiene B, Narbutaite J. Changes in oral health-related quality of life among children following dental treatment under general anaesthesia. A systematic review. Stomatologija. 2010;12(2):60-4.
8. McGrath C, Broder H, Wilson-Genderson M. Assessing the impact of oral health on the life quality of children: implications for research and practice. Community Dentistry and Oral Epidemiology. 2004;32(2):81-5.
9. Sheiham A. Dental caries affects body weight, growth and quality of life in pre-school children. Br Dent J. 2006;201(10):625-6.
10. Listl S, Galloway J, Mossey PA, Marcenes W. Global Economic Impact of Dental Diseases. Journal of Dental Research. 2015.
11. Petersen PE, Bourgeois D, Ogawa H, Estupinan-Day S, Ndiaye C. The global burden of oral diseases and risks to oral health. Bulletin of the World Health Organization. 2005;83:661-9.
12. Widström E, Eaton KA. Oral healthcare systems in the extended European union. Oral health & preventive dentistry. 2003;2(3):155-94.
13. Kathmandu RY. The burden of restorative dental treatment for children in Third World countries. International dental journal. 2002;52(1):1-9.
14. McDonagh MS, Whiting PF, Wilson PM, Sutton AJ, Chestnutt I, Cooper J, et al. Systematic review of water fluoridation. BMJ. 2000;321(7265):855-9.
15. Mejàre I, Lingström P, Petersson LG, Holm AK, Twetman S, Källestål C, et al. Caries-preventive effect of fissure sealants: a systematic review. Acta Odontologica Scandinavica. 2003;61(6):321-30.
16. Twetman S, Axelsson S, Dahlgren H, Holm AK, Källestål C, Lagerlöf F, et al. Caries-preventive effect of fluoride toothpaste: a systematic review. Acta Odontologica Scandinavica. 2003;61(6):347-55.
17. Dye BA, Tan S, Smith V, Lewis B, Barker L, Thornton-Evans G, et al. Trends in oral health status: United States, 1988-1994 and 1999-2004. Vital and health statistics Series 11, Data from the national health survey. 2007(248):1-92.
18. Bagramian RA, Garcia-Godoy F, Volpe AR. The global increase in dental caries. A pending public health crisis. Am J Dent. 2009;22(1):3-8.
19. Selwitz RH, Ismail AI, Pitts NB. Dental caries. The Lancet. 2007;369(9555):51-9.
20. Ruben J, Arends J, Christoffersen J. The Effect of Window Width on the Demineralization of Human Dentine and Enamel. Caries research. 1999;33(3):214-9.
21. Arends J, Dijkman GEHM, Dijkman AG. Review of Fluoride Release and Secondary Caries Reduction by Fluoridating Composites. Advances in Dental Research. 1995;9(4):367-76.
22. Lynch RJM, ten Cate JM. The Effect of Adjacent Dentine Blocks on the Demineralisation and Remineralisation of Enamel in vitro. Caries research. 2006;40(1):38-42.
23. Scheid RC. Woelfel's dental anatomy. Lippincott Williams & Wilkins; 2012.
24. Nanda RS. Eruption of human teeth. American Journal of Orthodontics. 1960;46(5):363-78.

25. Psoter W, Morse D, Pendrys D, Zhang H, Mayne S. Median ages of eruption of the primary teeth in white and Hispanic children from Arizona. Pediatric dentistry. 2003;25(3):257-61.
26. Nanci A. Physiologic tooth movement: eruption and shedding. Ten Cate's oral histology—development, structure, and function 7th ed St Louis, MO, USA: Mosby. 2007:268-89.
27. Lynch RJM. The primary and mixed dentition, post-eruptive enamel maturation and dental caries: a review. International dental journal. 2013;63:3-13.
28. Olze A, van Niekerk P, Ishikawa T, Zhu BL, Schulz R, Maeda H, et al. Comparative study on the effect of ethnicity on wisdom tooth eruption. Int J Legal Med. 2007;121(6):445-8.
29. Shore RC, Robinson C, Kirkham J, Brookes SJ. Structure of mature enamel. Dental Enamel: Formation to Destruction, 1st ed CRC Press, London1995. p. 151-66.
30. Robinson C, Brookes SJ, Bonass WA, Shore RC, Kirkham J. Enamel maturation. Ciba Foundation symposium. 1997;205:156-70; discussion 70-4.
31. Dorozhkin S. Nanodimensional and Nanocrystalline Apatites and Other Calcium Orthophosphates in Biomedical Engineering, Biology and Medicine. Materials. 2009;2(4):1975-2045.
32. Dorozhkin SV. Nanosized and nanocrystalline calcium orthophosphates. Acta Biomaterialia. 2010;6(3):715-34.
33. Stepnick RJ, Nakata TM, Zipkin I. The effects of age and fluoride exposure on fluoride, citrate and carbonate content of human cementum. Journal of periodontology. 1975;46(1):45-50.
34. Robinson C, Kirkham J, Shore R. Dental enamel: formation to destruction: CRC; 1995.
35. Pasteris JD, Wopenka B, Valsami-Jones E. Bone and Tooth Mineralization: Why Apatite? Elements. 2008;4(2):97-104.
36. Hannig M, Hannig C. Nanomaterials in preventive dentistry. Nat Nano. 2010;5(8):565-9.
37. Cui F-Z, Ge J. New observations of the hierarchical structure of human enamel, from nanoscale to microscale. Journal of Tissue Engineering and Regenerative Medicine. 2007;1(3):185-91.
38. Sarikaya M, Tamerler C, Jen AKY, Schulten K, Baneyx F. Molecular biomimetics: nanotechnology through biology. Nat Mater. 2003;2(9):577-85.
39. Kirkham J, Brookes SJ, Shore RC, Wood SR, Smith DA, Zhang J, et al. Physico-chemical properties of crystal surfaces in matrix–mineral interactions during mammalian biomineralisation. Current Opinion in Colloid & Interface Science. 2002;7(1–2):124-32.
40. Daculsi G, Menanteau J, Kerebel LM, Mitre D. Length and shape of enamel crystals. Calcif Tissue Int. 1984;36(1):550-5.
41. He LH, Swain MV. Enamel—A "metallic-like" deformable biocomposite. Journal of Dentistry. 2007;35(5):431-7.
42. Anderson P, Elliott JC. Rates of Mineral Loss in Human Enamel during in vitro Demineralization Perpendicular and Parallel to the Natural Surface. Caries research. 2000;34(1):33-40.
43. Daculsi G, LeGeros RZ, Mitre D. Crystal dissolution of biological and ceramic apatites. Calcif Tissue Int. 1989;45(2):95-103.
44. Nanci A. Ten Cate's Oral Histology: Development, Structure, and Function. 8th ed: Elsevier Health Sciences; 2008.
45. Simmer JP, Fincham AG. Molecular Mechanisms of Dental Enamel Formation. Critical Reviews in Oral Biology & Medicine. 1995;6(2):84-108.
46. Margolis HC, Beniash E, Fowler CE. Role of Macromolecular Assembly of Enamel Matrix Proteins in Enamel Formation. Journal of Dental Research. 2006;85(9):775-93.
47. He LH, Swain MV. Understanding the mechanical behaviour of human enamel from its structural and compositional characteristics. Journal of the Mechanical Behavior of Biomedical Materials. 2008;1(1):18-29.
48. Sakae T, Hirai G. Calcification and Crystallization in Bovine Enamel. Journal of Dental Research. 1982;61(1):57-9.
49. Smith CE. Cellular and Chemical Events During Enamel Maturation. Critical Reviews in Oral Biology & Medicine. 1998;9(2):128-61.
50. Dirks OB. Posteruptive Changes in Dental Enamel. Journal of Dental Research. 1966;45(3):503-11.
51. Briner W, Francis M, Widder J. Factors affecting the rate of post-eruptive maturation of dental enamel. Calc Tis Res. 1971;7(1):249-56.

52. Driessens FCM, Heijligers HJM, Borggreven JMPM, Wöltgens JHM. Posteruptive Maturation of Tooth Enamel Studied with the Electron Microprobe. Caries research. 1985;19(5):390-5.
53. Simmer J, Hu J. Dental enamel formation and its impact on clinical dentistry. Journal of Dental Education. 2001;65(9):896-905.
54. Thesleff I, Åberg T. Tooth Morphogenesis and the Differentiation of Ameloblasts. Ciba Foundation Symposium 205 - Dental Enamel: John Wiley & Sons, Ltd.; 2007. p. 3-17.
55. Arsenault AL, Robinson B. The dentino-enamel junction: A structural and microanalytical study of early mineralization. Calcif Tissue Int. 1989;45(2):111-21.
56. Katchburian E, Holt SJ. Studies on the Development of Ameloblasts: I. Fine Structure. Journal of Cell Science. 1972;11(2):415-47.
57. Boyde A. The development of enamel structure. Proceedings of the Royal Society of Medicine. 1967;60(9):923-8.
58. Kallenbach E. The fine structure of tomes' process of rat incisor ameloblasts and its relationship to the elaboration of enamel. Tissue and Cell. 1973;5(3):501-24.
59. Eastoe JE. Organic Matrix of Tooth Enamel. Nature. 1960;187(4735):411-2.
60. Paine ML, Krebsbach PH, Chen LS, Paine CT, Yamada Y, Deutsch D, et al. Protein-to-Protein Interactions: Criteria Defining the Assembly of the Enamel Organic Matrix. Journal of Dental Research. 1998;77(3):496-502.
61. Fincham AG, Moradian-Oldak J, Simmer JP. The Structural Biology of the Developing Dental Enamel Matrix. Journal of Structural Biology. 1999;126(3):270-99.
62. Robinson C, Brookes SJ, Shore RC, Kirkham J. The developing enamel matrix: nature and function. European Journal of Oral Sciences. 1998;106(S1):282-91.
63. Paine ML, Snead ML. Protein Interactions During Assembly of the Enamel Organic Extracellular Matrix. Journal of Bone and Mineral Research. 1997;12(2):221-7.
64. Ronnholm E. The amelogenesis of human teeth as revealed by electron mircoscopy I. The fine structure of the ameloblasts. J Ultrastruct Res. 1962;6:229-48.
65. Ronnholm E. The amelogenesis of human teeth as revealed by electron microscopy: II. The development of the enamel crystallites. Journal of Ultrastructure Research. 1962;6(3–4):249-303.
66. Travis DF, Glimcher MJ. The Structure and Organization of, and the Relationship Between the Organic Matrix and the Inorganic Crystals of Embryonic Bovine Enamel. The Journal of Cell Biology. 1964;23(3):447-97.
67. White SN, Luo W, Paine ML, Fong H, Sarikaya M, Snead ML. Biological Organization of Hydroxyapatite Crystallites into a Fibrous Continuum Toughens and Controls Anisotropy in Human Enamel. Journal of Dental Research. 2001;80(1):321-6.
68. Skobe Z. Enamel rod formation in the monkey observed by scanning electron microscopy. The Anatomical Record. 1977;187(3):329-33.
69. Shore RC, Robinson C, Kirkham J, Brookes SJ. Structure of developing enamel. Dental Enamel Formation to Destruction: CRC Press New York; 1995. p. 135-50.
70. Robinson C, Briggs HD, Atkinson PJ, Weatherell JA. Chemical changes during formation and maturation of human deciduous enamel. Archives of Oral Biology. 1981;26(12):1027-33.
71. Josephsen K, Takano Y, Frische S, Praetorius J, Nielsen S, Aoba T, et al. Ion transporters in secretory and cyclically modulating ameloblasts: a new hypothesis for cellular control of preeruptive enamel maturation. American Journal Of Physiology - Cell Physiology. 2010;299(6):C1299-C307.
72. Kirkham J, Robinson C, Weatherell JA, Richards A, Fejerskov O, Josephsen K. Maturation in Developing Permanent Porcine Enamel. Journal of Dental Research. 1988;67(9):1156-60.
73. Boyde A, Reith E. Cyclical uptake pattern of tetracycline in post-secretory maturation phase enamel demonstrated in rooted teeth. Calcif Tissue Int. 1983;35(1):762-6.
74. Robinson C. Enamel maturation: a brief background with implications for some enamel dysplasias. Frontiers in Physiology. 2014;5:388.
75. Sasaki S, Takagi T, Suzuki M. Cyclical changes in pH in bovine developing enamel as sequential bands. Archives of Oral Biology. 1991;36(3):227-31.
76. Kotsanos N, Darling AI. Influence of Posteruptive Age of Enamel on Its Susceptibility to Artificial Caries. Caries research. 1991;25(4):241-50.
77. Brudevold F, Tehrani A, Bakhos Y. Intraoral Mineralization of Abraded Dental Enamel. Journal of Dental Research. 1982;61(3):456-9.

78. Arnold WH, Gaengler P. Quantitative analysis of the calcium and phosphorus content of developing and permanent human teeth. Annals of Anatomy - Anatomischer Anzeiger. 2007;189(2):183-90.
79. Gaengler P, Norén JG, Hoyer I, Bjarnason S, Kraft U, Odelius H, et al. Reactivity of young and old human enamel to demineralization. European Journal of Oral Sciences. 1993;101(6):345-9.
80. Moreno EC, Kresak M, Zahradnik RT. Fluoridated Hydroxyapatite Solubility and Caries Formation. Nature. 1974;247(5435):64-5.
81. Ten Cate JM, Arends J. Remineralization of Artificial Enamel Lesions *in vitro*. Caries research. 1977;11(5):277-86.
82. Crombie F, Cochrane N, Manton D, Palamara J, Reynolds E. Mineralisation of developmentally hypomineralised human enamel in vitro. Caries research. 2012;47(3):259-63.
83. Lynch RJM, Churchley D, Butler A, Kearns S, Thomas GV, Badrock TC, et al. Effects of Zinc and Fluoride on the Remineralisation of Artificial Carious Lesions under Simulated Plaque Fluid Conditions. Caries research. 2011;45(3):313-22.
84. Norén JG, Lodding A, Odelius H, Linde A. Secondary Ion Mass Spectrometry of Human Deciduous Enamel. Caries research. 1983;17(6):496-502.
85. Norén JG, Odelius H, Rosander B, Linde A. SIMS Analysis of Deciduous Enamel from Normal Full-Term Infants, Low Birth Weight Infants and from Infants with Congenital Hypothyroidism. Caries research. 1984;18(3):242-9.
86. Fosdick L. Some theoretical aspects of dental caries control with dentifrices and mouth-washes. J Soc cosmetic Chem. 1959;10:283-91.
87. Yonan T, Fosdick LS. The Degree of Etching as a Function of the Age of the Teeth. Journal of Dental Research. 1964;43(4):629.
88. Yonan T, Nicolau J, Fosdick LS. The Posteruptive Maturation of Teeth II. Normal Posteruptive Maturation of Hamster Teeth. Journal of Dental Research. 1966;45(6):1701-5.
89. Palamara J, Phakey PP, Rachinger WA, Orams HJ. Electron microscopy of surface enamel of human unerupted and erupted teeth. Archives of Oral Biology. 1980;25(11):715-25.
90. Ripa LW, Gwinnett AJ, Buonocore MG. The "prismless" outer layer of deciduous and permanent enamel. Archives of Oral Biology. 1966;11(1):41-8.
91. Silverstone LM, Johnson NW. The Effect on Sound Human Enamel of Exposure to Calcifying Fluids *in vitro*. Caries research. 1971;5(4):323-42.
92. Gwinnett AJ. The ultrastructure of the "prismless" enamel of deciduous teeth. Archives of Oral Biology. 1966;11(11):1109-15.
93. Gwinnett AJ. The ultrastructure of the "prismless" enamel of permanent human teeth. Archives of Oral Biology. 1967;12(3):381-7.
94. Brudevold F, Aasenden R, Bakhos Y. A Preliminary Study of Posteruptive Maturation of Teeth in situ. Caries research. 1982;16(3):243-8.
95. Imanishi H, Nishino M. Post eruptive maturation of immature young permanent enamel. Journal of the International Association of Dentistry for Children. 1983;14(2):49-54.
96. Tüfekçi E, Almy DM, Carter JM, Moon PC, Lindauer SJ. Bonding properties of newly erupted and mature premolars. American Journal of Orthodontics and Dentofacial Orthopedics. 2007;131(6):753-8.
97. Joyston-Bechal S, Duckworth R, Braden M. Diffusion of radioactive ions into human dental enamel. Archives of Oral Biology. 1971;16(4):375-84.
98. Sasaki T, Debari K, Higashi S. Energy-dispersive X-ray microanalysis and scanning electron microscopy of developing and mature cat enamel. Archives of Oral Biology. 1984;29(6):431-6.
99. Wöltgens JHM, Bervoets TJM, Witjes F, Driessens FCM. Changes in the composition of the enamel of human premolar teeth shortly after eruption. Archives of Oral Biology. 1981;26(9):717-9.
100. Wöltgens JHM, Bervoets TJM, Witjes F, Driessens FCM. Effect of post-eruptive age on Ca and P loss from human enamel during demineralization in vitro. Archives of Oral Biology. 1981;26(9):721-5.
101. Arends J, Jongebloed WL, Schuthof J. Crystallite Diameters of Enamel near the Anatomical Surface. Caries research. 1983;17(2):97-105.
102. Tarbet WJ, Fosdick LS. Permeability of human dental enamel to acriflavine and potassium fluoride. Archives of Oral Biology. 1971;16(8):951-61.

103. Von der Fehr F. Maturation and remineralization of enamel. Adv Fluorine Res. 1965;3:83-95.
104. Cardoso CAB, Magalhães AC, Rios D, Lima JEO. Cross-Sectional Hardness of Enamel from Human Teeth at Different Posteruptive Ages. Caries research. 2009;43(6):491-4.
105. Fonseca RB, Haiter-Neto F, Carlo HL, Soares CJ, Sinhoreti MAC, Puppin-Rontani RM, et al. Radiodensity and hardness of enamel and dentin of human and bovine teeth, varying bovine teeth age. Archives of Oral Biology. 2008;53(11):1023-9.
106. Palti DG, Machado MAdAM, Silva SMBd, Abdo RCC, Lima JEdO. Evaluation of superficial microhardness in dental enamel with different eruptive ages. Brazilian Oral Research. 2008;22:311-5.
107. Park S, Wang D, Zhang D, Romberg E, Arola D. Mechanical properties of human enamel as a function of age and location in the tooth. Journal of Materials Science: Materials in Medicine. 2008;19(6):2317-24.
108. Fearnhead R, Kawasaki K, Inoue K. Comments on the porosity of human tooth enamel. Journal of dental research. 1982:1524-31.
109. Bertacci A, Chersoni S, Davidson CL, Prati C. In vivo enamel fluid movement. European Journal of Oral Sciences. 2007;115(3):169-73.
110. Weerheijm KL, Jälevik B, Alaluusua S. Molar–Incisor Hypomineralisation. Caries research. 2001;35(5):390-1.
111. Takahashi K, Cunha Correia AdS, Cunha RF. Molar Incisor Hypomineralization. Journal of Clinical Pediatric Dentistry. 2009;33(3):193-8.
112. Bajwa NK, Jingarwar MM, Pathak A. Molar Incisor Hypomineralization. International Journal of Experimental Dental Science. 2014;3(1):37-40.
113. Crombie FA, Manton DJ, Palamara JEA, Zalizniak I, Cochrane NJ, Reynolds EC. Characterisation of developmentally hypomineralised human enamel. Journal of Dentistry. 2013;41(7):611-8.
114. Beentjes V, Weerheijm K, Groen H. Factors involved in the aetiology of molar-incisor hypomineralisation (MIH). European Journal of Paediatric Dentistry. 2002;3:9-13.
115. Jälevik B, Odelius H, Dietz W, Norén J. Secondary ion mass spectrometry and X-ray microanalysis of hypomineralized enamel in human permanent first molars. Archives of Oral Biology. 2001;46(3):239-47.
116. Thylstrup A, Fejerskov O. Clinical appearance of dental fluorosis in permanent teeth in relation to histologic changes. Community Dentistry and Oral Epidemiology. 1978;6(6):315-28.
117. Osujp OO, Leake JL, Chipman ML, Nikiforuk G, Locker D, Levine N. Risk Factors for Dental Fluorosis in a Fluoridated Community. Journal of Dental Research. 1988;67(12):1488-92.
118. Fejerskov O, Manji F, Baelum V. The Nature and Mechanisms of Dental Fluorosis in Man. Journal of Dental Research. 1990;69(Suppl 2):692-700.
119. Aoba T, Fejerskov O. Dental Fluorosis: Chemistry and Biology. Critical Reviews in Oral Biology & Medicine. 2002;13(2):155-70.
120. Levy SM. An update on fluorides and fluorosis. Journal (Canadian Dental Association). 2003;69(5):286-91.
121. Weyant RJ, Tracy SL, Anselmo T, Beltrán-Aguilar ED, Donly KJ, Frese WA, et al. Topical fluoride for caries prevention. The Journal of the American Dental Association. 2013;144(11):1279-91.
122. Mascarenhas AK. Risk factors for dental fluorosis: a review of the recent literature. Pediatric dentistry. 2000;22(4):269-77.
123. Theuns HM, van Dijk JWE, Driessens FCM, Groeneveld A. The Influence of the Composition of Demineralizing Buffers on the Surface Layers of Artificial Carious Lesions. Caries research. 1984;18(6):509-18.
124. LeGeros RZ, Silverstone LM, Daculsi G, Kerebel LM. In vitro Caries-like Lesion Formation in F-containing Tooth Enamel. Journal of Dental Research. 1983;62(2):138-44.
125. Silverstone LM. The Histopathology of Enamel Lesions Produced *in vitro* in Teeth Previously Exposed to Calcifying Fluids. Caries research. 1970;4(1):31-48.
126. Widenheim J, Petersson LG, Koch G. Fluorine concentration in primary tooth enamel in 6-year-olds after 3 years of daily intake of fluoride-containing tablets (Fludent). Swed Dent J. 1984;8(4):203-7.

127. Vieira A, Hancock R, Limeback H, Schwartz M, Grynpas M. How Does Fluoride Concentration in the Tooth Affect Apatite Crystal Size? Journal of Dental Research. 2003;82(11):909-13.
128. Newbrun E. Systemic Benefits of Fluoride and Fluoridation. Journal of Public Health Dentistry. 2004;64:35-9.
129. Leverett DH. Appropriate Uses of Systemic Fluoride: Considerations for the ′90s. Journal of Public Health Dentistry. 1991;51(1):42-7.
130. Tóth Z, Gintner Z, Bánóczy J. The effect of ingested fluoride administered in salt, milk, and tablets on salivary and urinary fluoride concentrations. Fluoride. 2005;38(3):199.
131. Bottenberg P, Cleymaet R, De Muynck C, Remon JP, Coomans D, Slop D. Comparison of salivary fluoride concentrations after administration of a bioadhesive slow-release tablet and a conventional fluoride tablet. Journal of Pharmacy and Pharmacology. 1992;44(8):684-6.
132. Lussi A, Schlueter N, Rakhmatullina E, Ganss C. Dental Erosion – An Overview with Emphasis on Chemical and Histopathological Aspects. Caries research. 2011;45(Suppl. 1):2-12.
133. Zero DT. Etiology of dental erosion – extrinsic factors. European Journal of Oral Sciences. 1996;104(2):162-77.
134. Scheutzel P. Etiology of dental erosion – intrinsic factors. European Journal of Oral Sciences. 1996;104(2):178-90.
135. Almeida E Silva JS, Baratieri LN, Araujo E, Widmer N. Dental Erosion: Understanding This Pervasive Condition. Journal of Esthetic and Restorative Dentistry. 2011;23(4):205-16.
136. Lussi A, Hellwig E, Ganss C, Jaeggi T. Dental Erosion. Operative Dentistry. 2009;34(3):251-62.
137. Benjamin RM. Oral Health: The Silent Epidemic. Public Health Reports. 2010;125(2):158-9.
138. Filoche S, Wong L, Sissons CH. Oral Biofilms: Emerging Concepts in Microbial Ecology. Journal of Dental Research. 2010;89(1):8-18.
139. Higham SM, Edgar WM. Human dental plaque pH, and the organic acid and free amino acid profiles in plaque fluid, after sucrose rinsing. Archives of Oral Biology. 1989;34(5):329-34.
140. Geddes DAM. Acids Produced by Human Dental Plaque Metabolism *in situ*. Caries research. 1975;9(2):98-109.
141. Bishara SE, Ostby AW. White Spot Lesions: Formation, Prevention, and Treatment. Seminars in Orthodontics. 2008;14(3):174-82.
142. Ten Cate JM. Contemporary perspective on the use of fluoride products in caries prevention. Br Dent J. 2013;214(4):161-7.
143. Torres CRG, Borges AB, Torres LMS, Gomes IS, de Oliveira RS. Effect of caries infiltration technique and fluoride therapy on the colour masking of white spot lesions. Journal of Dentistry. 2011;39(3):202-7.
144. Lynch RJM, Mony U, ten Cate JM. The Effect of Fluoride at Plaque Fluid Concentrations on Enamel De- and Remineralisation at Low pH. Caries research. 2006;40(6):522-9.
145. Dorozhkin SV. Calcium orthophosphates: Occurrence, properties, biomineralization, pathological calcification and biomimetic applications. Biomatter. 2011;1(2):121-64.
146. Pasteris JD, Wopenka B, Freeman JJ, Rogers K, Valsami-Jones E, van der Houwen JAM, et al. Lack of OH in nanocrystalline apatite as a function of degree of atomic order: implications for bone and biomaterials. Biomaterials. 2004;25(2):229-38.
147. Valsami-Jones E. Nucleation and growth of nano-apatite: Insights into bone formation. Geochimica et Cosmochimica Acta Supplement. 2003;67:507.
148. Hughes JM, Rakovan J. The Crystal Structure of Apatite, $Ca_5(PO_4)_3(F,OH,Cl)$. Reviews in Mineralogy and Geochemistry. 2002;48(1):1-12.
149. Pan Y, Fleet ME. Compositions of the Apatite-Group Minerals: Substitution Mechanisms and Controlling Factors. Reviews in Mineralogy and Geochemistry. 2002;48(1):13-49.
150. Skinner HCW. Biominerals. Mineralogical Magazine. 2005;69(5):621-41.
151. Wang L, Nancollas GH. Calcium Orthophosphates: Crystallization and Dissolution. Chemical Reviews. 2008;108(11):4628-69.
152. Dorozhkin S. Calcium Orthophosphates in Nature, Biology and Medicine. Materials. 2009;2(2):399-498.

153. Driessens FCM. The mineral in bone, dentin and tooth enamel. Bulletin des Sociétés Chimiques Belges. 1980;89(8):663-89.
154. Wöltgens JHM, Vingerling PA, Witjes F. Chemical evidence of two separate apatite phases in human enamel. Archives of Oral Biology. 1980;25(6):435-6.
155. Dorozhkin S. Calcium Orthophosphate-Based Bioceramics. Materials. 2013;6(9):3840.
156. Gower LB. Biomimetic Model Systems for Investigating the Amorphous Precursor Pathway and Its Role in Biomineralization. Chemical Reviews. 2008;108(11):4551-627.
157. Beniash E, Metzler RA, Lam RSK, Gilbert PUPA. Transient amorphous calcium phosphate in forming enamel. Journal of Structural Biology. 2009;166(2):133-43.
158. Olszta MJ, Odom DJ, Douglas EP, Gower LB. A New Paradigm for Biomineral Formation: Mineralization via an Amorphous Liquid-Phase Precursor. Connective Tissue Research. 2003;44(1):326-34.
159. Mahamid J, Sharir A, Addadi L, Weiner S. Amorphous calcium phosphate is a major component of the forming fin bones of zebrafish: Indications for an amorphous precursor phase. Proceedings of the National Academy of Sciences. 2008;105(35):12748-53.
160. Dorozhkin SV. Amorphous calcium (ortho)phosphates. Acta Biomaterialia. 2010;6(12):4457-75.
161. Kanzaki N, Treboux G, Onuma K, Tsutsumi S, Ito A. Calcium phosphate clusters. Biomaterials. 2001;22(21):2921-9.
162. Brès EF, Moebus G, Kleebe HJ, Pourroy G, Werkmann J, Ehret G. High resolution electron microscopy study of amorphous calcium phosphate. Journal of Crystal Growth. 1993;129(1–2):149-62.
163. Cuisinier FJG, Voegel JC, Yacaman J, Frank RM. Structure of initial crystals formed during human amelogenesis. Journal of Crystal Growth. 1992;116(3–4):314-8.
164. Combes C, Rey C. Amorphous calcium phosphates: Synthesis, properties and uses in biomaterials. Acta Biomaterialia. 2010;6(9):3362-78.
165. Boskey AL, Posner AS. Conversion of amorphous calcium phosphate to microcrystalline hydroxyapatite. A pH-dependent, solution-mediated, solid-solid conversion. The Journal of Physical Chemistry. 1973;77(19):2313-7.
166. Li Y, Weng W. In vitro synthesis and characterization of amorphous calcium phosphates with various Ca/P atomic ratios. Journal of Materials Science: Materials in Medicine. 2007;18(12):2303-8.
167. Harries JE, Hukins DWL, Holt C, Hasnain SS. Conversion of amorphous calcium phosphate into hydroxyapatite investigated by EXAFS spectroscopy. Journal of Crystal Growth. 1987;84(4):563-70.
168. Blumenthal NC, Posner AS, Holmes JM. Effect of preparation conditions on the properties and transformation of amorphous calcium phosphate. Materials Research Bulletin. 1972;7(11):1181-9.
169. Eanes ED, Posner AS. Intermediate phases in the basic solution preparation of alkaline earth phosphates. Calc Tis Res. 1968;2(1):38-48.
170. Li YB, Weng WJ, Cheng K, Du PY, Shen G, Han GR. Complexes of Ca(II) with polymers as precursors for preparation of amorphous calcium phosphate. Materials Science and Technology. 2004;20(9):1075-8.
171. Liu S, Weng W, Li Z, Pan L, Cheng K, Song C, et al. Effect of PEG amount in amorphous calcium phosphate on its crystallized products. Journal of Materials Science: Materials in Medicine. 2009;20(1):359-63.
172. Rodrigues A, Lebugle A. Influence of ethanol in the precipitation medium on the composition, structure and reactivity of tricalcium phosphate. Colloids and Surfaces A: Physicochemical and Engineering Aspects. 1998;145(1–3):191-204.
173. Yu T, Ye J, Wang Y. Synthesis and property of a novel calcium phosphate cement. Journal of Biomedical Materials Research Part B: Applied Biomaterials. 2009;90B(2):745-51.
174. Gbureck U, Grolms O, Barralet JE, Grover LM, Thull R. Mechanical activation and cement formation of β-tricalcium phosphate. Biomaterials. 2003;24(23):4123-31.
175. Vaidya SN, Sugandhi V. Pressure induced amorphization in calcium phosphates. Journal of Materials Science. 1999;34(15):3769-78.
176. Weng J, Liu X-G, Li X-D, Zhang X-D. Intrinsic factors of apatite influencing its amorphization during plasma-spray coating. Biomaterials. 1995;16(1):39-44.

177. Gross KA, Berndt CC, Herman H. Amorphous phase formation in plasma-sprayed hydroxyapatite coatings. Journal of Biomedical Materials Research. 1998;39(3):407-14.
178. Maciejewski M, Brunner TJ, Loher SF, Stark WJ, Baiker A. Phase transitions in amorphous calcium phosphates with different Ca/P ratios. Thermochimica Acta. 2008;468(1–2):75-80.
179. Glimcher MJ. Bone: Nature of the Calcium Phosphate Crystals and Cellular, Structural, and Physical Chemical Mechanisms in Their Formation. Reviews in Mineralogy and Geochemistry. 2006;64(1):223-82.
180. Shen P, Cai F, Nowicki A, Vincent J, Reynolds EC. Remineralization of Enamel Subsurface Lesions by Sugar-free Chewing Gum Containing Casein Phosphopeptide-Amorphous Calcium Phosphate. Journal of Dental Research. 2001;80(12):2066-70.
181. Walker G, Cai F, Shen P, Reynolds C, Ward B, Fone C, et al. Increased remineralization of tooth enamel by milk containing added casein phosphopeptide-amorphous calcium phosphate. Journal of Dairy Research. 2006;73(01):74-8.
182. Termine JD, Posner AS. Amorphous/crystalline interrelationships in bone mineral. Calc Tis Res. 1967;1(1):8-23.
183. Tannenbaum P, Schraer H, Posner A. Crystalline changes in avian bone related to the reproductive cycle. Calc Tis Res. 1974;14(1):83-6.
184. Posner AS, Betts F. Synthetic amorphous calcium phosphate and its relation to bone mineral structure. Accounts of Chemical Research. 1975;8(8):273-81.
185. Cross KJ, Huq NL, Palamara JE, Perich JW, Reynolds EC. Physicochemical Characterization of Casein Phosphopeptide-Amorphous Calcium Phosphate Nanocomplexes. Journal of Biological Chemistry. 2005;280(15):15362-9.
186. Robinson C, Weatherell JA, Hallsworth AS. Distribution of Magnesium in Mature Human Enamel. Caries research. 1981;15(1):70-7.
187. Sabel N, Klinberg G, Nietzsche S, Robertson A, Odelius H, Norén JG. Analysis of some elements in primary enamel during postnatal mineralization. Swed Dent J. 2009;33(2):85-95.
188. Dorozhkin SV. Self-setting calcium orthophosphate formulations. Journal of functional biomaterials. 2013;4(4):209-311.
189. Reynolds EC, Cai F, Cochrane NJ, Shen P, Walker GD, Morgan MV, et al. Fluoride and Casein Phosphopeptide-Amorphous Calcium Phosphate. Journal of Dental Research. 2008;87(4):344-8.
190. Iijima Y, Cai F, Shen P, Walker G, Reynolds C, Reynolds EC. Acid Resistance of Enamel Subsurface Lesions Remineralized by a Sugar-Free Chewing Gum Containing Casein Phosphopeptide-Amorphous Calcium Phosphate. Caries research. 2004;38(6):551-6.
191. Reynolds EC. Anticariogenic complexes of amorphous calcium phosphate stabilized by casein phosphopeptides: A review. Special Care in Dentistry. 1998;18(1):8-16.
192. Bohner M. Physical and chemical aspects of calcium phosphates used in spinal surgery. Eur Spine J. 2001;10(2):S114-S21.
193. Dorozhkin SV. Amorphous calcium orthophosphates: nature, chemistry and biomedical applications. Int J Mater Chem. 2012;2:19-46.
194. Carrodeguas RG, De Aza S. α-Tricalcium phosphate: Synthesis, properties and biomedical applications. Acta Biomaterialia. 2011;7(10):3536-46.
195. Li X, Ito A, Sogo Y, Wang X, LeGeros RZ. Solubility of Mg-containing β-tricalcium phosphate at 25 °C. Acta Biomaterialia. 2009;5(1):508-17.
196. Kitamura M, Ohtsuki C, Iwasaki H, Ogata S-i, Tanihara M, Miyazaki T. The controlled resorption of porous α-tricalcium phosphate using a hydroxypropylcellulose coating. Journal of Materials Science: Materials in Medicine. 2004;15(10):1153-8.
197. Camire C, Jegou S-JS, Hansen S, McCarthy I, Lidgren L. Hydration characteristics of alpha-tricalcium phosphates: Comparison of preparation routes. Journal of applied biomaterials & biomechanics: JABB. 2004;3(2):106-11.
198. Jokic B, Jankovic-Castvan I, Veljovic D, Bucevac D, Obradovic-Djuricic K, Petrovic R, et al. Synthesis and settings behavior of α-TCP from calcium deficient hyroxyapatite obtained by hydrothermal method. Journal of optoelectronics and advanced materials. 2007;9(6):1904-10.

199. Bohner M, Brunner TJ, Doebelin N, Tang R, Stark WJ. Effect of thermal treatments on the reactivity of nanosized tricalcium phosphate powders. Journal of Materials Chemistry. 2008;18(37):4460-7.
200. Cicek G, Aksoy E, Durucan C, Hasirci N. Alpha-tricalcium phosphate (α-TCP): solid state synthesis from different calcium precursors and the hydraulic reactivity. Journal of Materials Science: Materials in Medicine. 2011;22(4):809-17.
201. Ayers R, Nielsen-Preiss S, Ferguson V, Gotolli G, Moore JJ, Kleebe H-J. Osteoblast-like cell mineralization induced by multiphasic calcium phosphate ceramic. Materials Science and Engineering: C. 2006;26(8):1333-7.
202. Burkes D, Moore J, Ayers R. Method for producing calcium phosphate powders using an auto-ignition combustion synthesis reaction. US2008/0112874 A. 2008;1.
203. Sayer M, Stratilatov AD, Reid J, Calderin L, Stott MJ, Yin X, et al. Structure and composition of silicon-stabilized tricalcium phosphate. Biomaterials. 2003;24(3):369-82.
204. Reid JW, Tuck L, Sayer M, Fargo K, Hendry JA. Synthesis and characterization of single-phase silicon-substituted α-tricalcium phosphate. Biomaterials. 2006;27(15):2916-25.
205. Mirtchi AA, Lemaitre J, Terao N. Calcium phosphate cements: study of the β-tricalcium phosphate — monocalcium phosphate system. Biomaterials. 1989;10(7):475-80.
206. Mostafa NY. Characterization, thermal stability and sintering of hydroxyapatite powders prepared by different routes. Materials Chemistry and Physics. 2005;94(2–3):333-41.
207. Raynaud S, Champion E, Bernache-Assollant D, Thomas P. Calcium phosphate apatites with variable Ca/P atomic ratio I. Synthesis, characterisation and thermal stability of powders. Biomaterials. 2002;23(4):1065-72.
208. Meejoo S, Maneeprakorn W, Winotai P. Phase and thermal stability of nanocrystalline hydroxyapatite prepared via microwave heating. Thermochimica Acta. 2006;447(1):115-20.
209. Tao J, Jiang W, Zhai H, Pan H, Xu X, Tang R. Structural Components and Anisotropic Dissolution Behaviors in One Hexagonal Single Crystal of β-Tricalcium Phosphate. Crystal Growth & Design. 2008;8(7):2227-34.
210. Tao J, Pan H, Zhai H, Wang J, Li L, Wu J, et al. Controls of tricalcium phosphate single-crystal formation from its amorphous precursor by interfacial energy. Crystal Growth and Design. 2009;9(7):3154-60.
211. Zijderveld SA, Zerbo IR, Van Den Bergh J, Schulten E, ten Bruggenkate CM. Maxillary sinus floor augmentation using a beta-tricalcium phosphate (Cerasorb) alone compared to autogenous bone grafts. The International journal of oral & maxillofacial implants. 2004;20(3):432-40.
212. Szabo G, Huys L, Coulthard P, Maiorana C, Garagiola U, Barabás J, et al. A prospective multicenter randomized clinical trial of autogenous bone versus beta-tricalcium phosphate graft alone for bilateral sinus elevation: histologic and histomorphometric evaluation. The International journal of oral & maxillofacial implants. 2004;20(3):371-81.
213. Urist MR, Lietze A, Dawson E. [beta]-tricalcium Phosphate Delivery System for Bone Morphogenetic Protein. Clinical Orthopaedics and Related Research. 1984;187:277-80.
214. Dorozhkin S. Calcium orthophosphates in dentistry. Journal of Materials Science: Materials in Medicine. 2013;24(6):1335-63.
215. Chapuy MC, Pamphile R, Paris E, Kempf C, Schlichting M, Arnaud S, et al. Combined Calcium and Vitamin D3 Supplementation in Elderly Women: Confirmation of Reversal of Secondary Hyperparathyroidism and Hip Fracture Risk: The Decalyos II Study. Osteoporos Int. 2002;13(3):257-64.
216. Satoh S, Tabata K, Izume K, Takeuchi T, Watanabe T. Effect of Dietary Tricalcium Phosphate on Availability of Zinc to Rainbow Trout. Nippon Suisan Gakkaishi. 1987;53(7):1199-205.
217. Xiao X, Wang W, Liu D, Zhang H, Gao P, Geng L, et al. The promotion of angiogenesis induced by three-dimensional porous beta-tricalcium phosphate scaffold with different interconnection sizes via activation of PI3K/Akt pathways. Scientific Reports. 2015;5:9409.
218. Lim GK, Wang J, Ng SC, Chew CH, Gan LM. Processing of hydroxyapatite via microemulsion and emulsion routes. Biomaterials. 1997;18(21):1433-9.
219. Evis Z. Reactions in hydroxylapatite–zirconia composites. Ceramics International. 2007;33(6):987-91.

220. Mobasherpour I, Heshajin MS, Kazemzadeh A, Zakeri M. Synthesis of nanocrystalline hydroxyapatite by using precipitation method. Journal of Alloys and Compounds. 2007;430(1–2):330-3.
221. Xu JL, Khor KA, Dong ZL, Gu YW, Kumar R, Cheang P. Preparation and characterization of nano-sized hydroxyapatite powders produced in a radio frequency (rf) thermal plasma. Materials Science and Engineering: A. 2004;374(1–2):101-8.
222. Luo P, Nieh TG. Synthesis of ultrafine hydroxyapatite particles by a spray dry method. Materials Science and Engineering: C. 1995;3(2):75-8.
223. Kuriakose TA, Kalkura SN, Palanichamy M, Arivuoli D, Dierks K, Bocelli G, et al. Synthesis of stoichiometric nano crystalline hydroxyapatite by ethanol-based sol–gel technique at low temperature. Journal of Crystal Growth. 2004;263(1–4):517-23.
224. Fathi MH, Hanifi A. Evaluation and characterization of nanostructure hydroxyapatite powder prepared by simple sol–gel method. Materials Letters. 2007;61(18):3978-83.
225. Han Y, Li S, Wang X, Chen X. Synthesis and sintering of nanocrystalline hydroxyapatite powders by citric acid sol–gel combustion method. Materials Research Bulletin. 2004;39(1):25-32.
226. Rhee S-H. Synthesis of hydroxyapatite via mechanochemical treatment. Biomaterials. 2002;23(4):1147-52.
227. Pramanik S, Agarwal AK, Rai KN, Garg A. Development of high strength hydroxyapatite by solid-state-sintering process. Ceramics International. 2007;33(3):419-26.
228. Shih W-J, Chen Y-F, Wang M-C, Hon M-H. Crystal growth and morphology of the nano-sized hydroxyapatite powders synthesized from $CaHPO_4{\cdot}2H_2O$ and $CaCO_3$ by hydrolysis method. Journal of Crystal Growth. 2004;270(1–2):211-8.
229. Sarig S, Kahana F. Rapid formation of nanocrystalline apatite. Journal of Crystal Growth. 2002;237–239, Part 1(0):55-9.
230. Li X, Huang J, Edirisinghe MJ. Novel patterning of nano-bioceramics: template-assisted electrohydrodynamic atomization spraying2008 2008-02-06 00:00:00. 253-7 p.
231. Li X, Koller G, Huang J, Di Silvio L, Renton T, Esat M, et al. A novel jet-based nano-hydroxyapatite patterning technique for osteoblast guidance. Journal of The Royal Society Interface. 2010;7(42):189-97.
232. Zhu K, Yanagisawa K, Shimanouchi R, Onda A, Kajiyoshi K, Qiu J. Synthesis and crystallographic study of Pb–Sr hydroxyapatite solid solutions by high temperature mixing method under hydrothermal conditions. Materials Research Bulletin. 2009;44(6):1392-6.
233. Elliott JC, Mackie PE, Young RA. Monoclinic Hydroxyapatite. Science. 1973;180(4090):1055-7.
234. Dorozhkin S. Calcium Orthophosphates: Occurrence, Properties and Major Applications. Bioceram Dev Appl. 2014;4(081):2.
235. Guo X, Wang W, Wu G, Zhang J, Mao C, Deng Y, et al. Controlled synthesis of hydroxyapatite crystals templated by novel surfactants and their enhanced bioactivity. New Journal of Chemistry. 2011;35(3):663-71.
236. Li H, Huang W, Zhang Y, Zhong M. Biomimetic synthesis of enamel-like hydroxyapatite on self-assembled monolayers. Materials Science and Engineering: C. 2007;27(4):756-61.
237. Rangavittal N, Landa-Cánovas AR, González-Calbet JM, Vallet-Regí M. Structural study and stability of hydroxyapatite and β-tricalcium phosphate: Two important bioceramics. Journal of Biomedical Materials Research. 2000;51(4):660-8.
238. Mathew M, Takagi S. Structures of biological minerals in dental research. Journal of Research-National Institute of Standards And Technology. 2001;106(6):1035-44.
239. Pang YX, Bao X. Influence of temperature, ripening time and calcination on the morphology and crystallinity of hydroxyapatite nanoparticles. Journal of the European Ceramic Society. 2003;23(10):1697-704.
240. Patel N, Gibson IR, Ke S, Best SM, Bonfield W. Calcining influence on the powder properties of hydroxyapatite. Journal of Materials Science: Materials in Medicine. 2001;12(2):181-8.
241. Haberko K, Bućko MM, Brzezińska-Miecznik J, Haberko M, Mozgawa W, Panz T, et al. Natural hydroxyapatite—its behaviour during heat treatment. Journal of the European Ceramic Society. 2006;26(4–5):537-42.

242. Kweh SWK, Khor KA, Cheang P. The production and characterization of hydroxyapatite (HA) powders. Journal of Materials Processing Technology. 1999;89–90(0):373-7.
243. Lu H, Qu Z, Zhou Y. Preparation and mechanical properties of dense polycrystalline hydroxyapatite through freeze-drying. Journal of Materials Science: Materials in Medicine. 1998;9(10):583-7.
244. Phillips MJ, Darr JA, Luklinska ZB, Rehman I. Synthesis and characterization of nano-biomaterials with potential osteological applications. Journal of Materials Science: Materials in Medicine. 2003;14(10):875-82.
245. Raynaud S, Champion E, Bernache-Assollant D, Laval J-P. Determination of Calcium/Phosphorus Atomic Ratio of Calcium Phosphate Apatites Using X-ray Diffractometry. Journal of the American Ceramic Society. 2001;84(2):359-66.
246. Heimann RB. Classic and advanced ceramics: from fundamentals to applications: John Wiley & Sons; 2010.
247. Gross KA, Berndt CC. Thermal processing of hydroxyapatite for coating production. Journal of Biomedical Materials Research. 1998;39(4):580-7.
248. Porter AE, Patel N, Skepper JN, Best SM, Bonfield W. Effect of sintered silicate-substituted hydroxyapatite on remodelling processes at the bone–implant interface. Biomaterials. 2004;25(16):3303-14.
249. Hing KA, Best SM, Tanner KE, Bonfield W, Revell PA. Mediation of bone ingrowth in porous hydroxyapatite bone graft substitutes. Journal of Biomedical Materials Research Part A. 2004;68A(1):187-200.
250. Ripamonti U, Roden LC, Renton LF. Osteoinductive hydroxyapatite-coated titanium implants. Biomaterials. 2012;33(15):3813-23.
251. Jung U-W, Hwang J-W, Choi D-Y, Hu K-S, Kwon M-K, Choi S-H, et al. Surface characteristics of a novel hydroxyapatite-coated dental implant. J Periodontal Implant Sci. 2012;42(2):59-63.
252. Knabe C, Klar F, Fitzner R, Radlanski RJ, Gross U. In vitro investigation of titanium and hydroxyapatite dental implant surfaces using a rat bone marrow stromal cell culture system. Biomaterials. 2002;23(15):3235-45.
253. Knabe C, Howlett CR, Klar F, Zreiqat H. The effect of different titanium and hydroxyapatite-coated dental implant surfaces on phenotypic expression of human bone-derived cells. Journal of Biomedical Materials Research Part A. 2004;71A(1):98-107.
254. Jimbo R, Coelho PG, Bryington M, Baldassarri M, Tovar N, Currie F, et al. Nano Hydroxyapatite-coated Implants Improve Bone Nanomechanical Properties. Journal of Dental Research. 2012;91(12):1172-7.
255. Straub DA. Calcium Supplementation in Clinical Practice: A Review of Forms, Doses, and Indications. Nutrition in Clinical Practice. 2007;22(3):286-96.
256. Tschoppe P, Zandim DL, Martus P, Kielbassa AM. Enamel and dentine remineralization by nano-hydroxyapatite toothpastes. Journal of Dentistry. 2011;39(6):430-7.
257. Jeong S, Jang S, Kim KN, Kwon H, Park YD, Kim B. Remineralization potential of new toothpaste containing nano-hydroxyapatite. Key Engineering Materials. 2006;309:537-40.
258. Niwa M, Sato T, Li W, Aoki H, Aoki H, Daisaku T. Polishing and whitening properties of toothpaste containing hydroxyapatite. Journal of Materials Science: Materials in Medicine. 2001;12(3):277-81.
259. Guo C, Liu H, Katayama I. Effect of hydroxyapatite toothpaste on vital tooth color. Journal of Dental Research. 2002;81:1964.
260. Kim S-H, Park J-B, Lee C-W, Koo K-T, Kim T-I, Seol Y-J, et al. The clinical effects of a hydroxyapatite containing toothpaste for dentine hypersensitivity. J Korean Acad Periodontol. 2009;39(1):87-94.
261. Kang S-J, Kwon Y-H, Park J-B, Herr Y, Chung J-H. The effects of hydroxyapatite toothpaste on tooth hypersensitivity. J Korean Acad Periodontol. 2009;39(1):9-16.
262. Kawasaki T, Kobayashi W, Ikeda K, Takahashi S, Monma H. High-performance liquid chromatography using spherical aggregates of hydroxyapatite micro-crystals as adsorbent. European Journal of Biochemistry. 1986;157(2):291-5.

263. Pinto G, Caira S, Mamone G, Ferranti P, Addeo F, Picariello G. Fractionation of complex lipid mixtures by hydroxyapatite chromatography for lipidomic purposes. Journal of Chromatography A. 2014;1360(0):82-92.
264. Hilbrig F, Freitag R. Isolation and purification of recombinant proteins, antibodies and plasmid DNA with hydroxyapatite chromatography. Biotechnology Journal. 2012;7(1):90-102.
265. Palazzo B, Iafisco M, Laforgia M, Margiotta N, Natile G, Bianchi CL, et al. Biomimetic Hydroxyapatite–Drug Nanocrystals as Potential Bone Substitutes with Antitumor Drug Delivery Properties. Advanced Functional Materials. 2007;17(13):2180-8.
266. Kim H-W, Knowles JC, Kim H-E. Hydroxyapatite/poly(ε-caprolactone) composite coatings on hydroxyapatite porous bone scaffold for drug delivery. Biomaterials. 2004;25(7–8):1279-87.
267. Ye F, Guo H, Zhang H, He X. Polymeric micelle-templated synthesis of hydroxyapatite hollow nanoparticles for a drug delivery system. Acta Biomaterialia. 2010;6(6):2212-8.
268. Wilson RM, Elliott JC, Dowker SEP, Rodriguez-Lorenzo LM. Rietveld refinements and spectroscopic studies of the structure of Ca-deficient apatite. Biomaterials. 2005;26(11):1317-27.
269. Mayer I, Jacobsohn O, Niazov T, Werckmann J, Iliescu M, Richard-Plouet M, et al. Manganese in Precipitated Hydroxyapatites. European Journal of Inorganic Chemistry. 2003;2003(7):1445-51.
270. Hutchens SA, Benson RS, Evans BR, O'Neill HM, Rawn CJ. Biomimetic synthesis of calcium-deficient hydroxyapatite in a natural hydrogel. Biomaterials. 2006;27(26):4661-70.
271. Durucan C, Brown PW. α-Tricalcium phosphate hydrolysis to hydroxyapatite at and near physiological temperature. Journal of Materials Science: Materials in Medicine. 2000;11(6):365-71.
272. LeGeros RZ. Calcium phosphates in oral biology and medicine. Monographs in oral science. 1990;15:1-201.
273. Rey C, Combes C, Drouet C, Sfihi H. Chemical diversity of apatites. Advances in Science and Technology. 2006;49:27-36.
274. Kasten P, Luginbühl R, van Griensven M, Barkhausen T, Krettek C, Bohner M, et al. Comparison of human bone marrow stromal cells seeded on calcium-deficient hydroxyapatite, β-tricalcium phosphate and demineralized bone matrix. Biomaterials. 2003;24(15):2593-603.
275. Kasten P, Vogel J, Luginbühl R, Niemeyer P, Tonak M, Lorenz H, et al. Ectopic bone formation associated with mesenchymal stem cells in a resorbable calcium deficient hydroxyapatite carrier. Biomaterials. 2005;26(29):5879-89.
276. Liu T-Y, Chen S-Y, Liu D-M, Liou S-C. On the study of BSA-loaded calcium-deficient hydroxyapatite nano-carriers for controlled drug delivery. Journal of Controlled Release. 2005;107(1):112-21.
277. Rodríguez-Lorenzo LM, Hart JN, Gross KA. Influence of fluorine in the synthesis of apatites. Synthesis of solid solutions of hydroxy-fluorapatite. Biomaterials. 2003;24(21):3777-85.
278. Wei M, Evans JH, Bostrom T, Grøndahl L. Synthesis and characterization of hydroxyapatite, fluoride-substituted hydroxyapatite and fluorapatite. Journal of Materials Science: Materials in Medicine. 2003;14(4):311-20.
279. Nikčević I, Jokanović V, Mitrić M, Nedić Z, Makovec D, Uskoković D. Mechanochemical synthesis of nanostructured fluorapatite/fluorhydroxyapatite and carbonated fluorapatite/fluorhydroxyapatite. Journal of Solid State Chemistry. 2004;177(7):2565-74.
280. Eslami H, Solati-Hashjin M, Tahriri M. The comparison of powder characteristics and physicochemical, mechanical and biological properties between nanostructure ceramics of hydroxyapatite and fluoridated hydroxyapatite. Materials Science and Engineering: C. 2009;29(4):1387-98.
281. Jha LJ, Best SM, Knowles JC, Rehman I, Santos JD, Bonfield W. Preparation and characterization of fluoride-substituted apatites. Journal of Materials Science: Materials in Medicine. 1997;8(4):185-91.
282. Wang Y, Zhang S, Zeng X, Ma LL, Weng W, Yan W, et al. Osteoblastic cell response on fluoridated hydroxyapatite coatings. Acta Biomaterialia. 2007;3(2):191-7.
283. Van der Lugt W, Knottnerus DIM, Young RA. NMR Determination of Fluorine Position in Mineral Hydroxyapatite. Caries research. 1970;4(1):89-95.
284. Kay MI, Young R, Posner A. Crystal structure of hydroxyapatite. 1964.

285. Young RA, Elliott JC. Atomic-scale bases for several properties of apatites. Archives of Oral Biology. 1966;11(7):699-707.
286. McIvor M. Acute Fluoride Toxicity. Drug-Safety. 1990;5(2):79-85.
287. Jantová S, Theiszová M, Letašiová S, Birošová L, Palou TM. In vitro effects of fluor-hydroxyapatite, fluorapatite and hydroxyapatite on colony formation, DNA damage and mutagenicity. Mutation Research/Genetic Toxicology and Environmental Mutagenesis. 2008;652(2):139-44.
288. Maguire A. ADA clinical recommendations on topical fluoride for caries prevention. Evid-based Dent. 2014;15(2):38-9.
289. Marinho VCC. Cochrane fluoride reviews: an overview of the evidence on caries prevention with fluoride treatments. Faculty Dental Journal. 2014;5(2):78-83.
290. Clark MB, Slayton RL. Fluoride Use in Caries Prevention in the Primary Care Setting. Pediatrics. 2014;134(3):626-33.
291. Rugg-Gunn AJ, Do L. Effectiveness of water fluoridation in caries prevention. Community Dentistry and Oral Epidemiology. 2012;40:55-64.
292. Jowsey J, Johnson WJ, Taves DR, Kelly PJ. Effects of dialysate calcium and fluoride on bone disease during regular hemodialysis. The Journal of Laboratory and Clinical Medicine. 1972;79(2):204-14.
293. Bibby JK, Bubb NL, Wood DJ, Mummery PM. Fluorapatite-mullite glass sputter coated Ti_6Al_4V for biomedical applications. Journal of Materials Science: Materials in Medicine. 2005;16(5):379-85.
294. Razavi M, Fathi MH, Meratian M. Fabrication and characterization of magnesium–fluorapatite nanocomposite for biomedical applications. Materials Characterization. 2010;61(12):1363-70.
295. Graham S, Brown PW. Reactions of octacalcium phosphate to form hydroxyapatite. Journal of Crystal Growth. 1996;165(1–2):106-15.
296. Brown WE, Eidelman N, Tomazic B. Octacalcium Phosphate as a Precursor in Biomineral Formation. Advances in Dental Research. 1987;1(2):306-13.
297. Suzuki O, Kamakura S, Katagiri T, Nakamura M, Zhao B, Honda Y, et al. Bone formation enhanced by implanted octacalcium phosphate involving conversion into Ca-deficient hydroxyapatite. Biomaterials. 2006;27(13):2671-81.
298. Arellano-Jiménez MJ, García-García R, Reyes-Gasga J. Synthesis and hydrolysis of octacalcium phosphate and its characterization by electron microscopy and X-ray diffraction. Journal of Physics and Chemistry of Solids. 2009;70(2):390-5.
299. LeGeros R. Preparation of octacalcium phosphate (OCP): A direct fast method. Calcif Tissue Int. 1985;37(2):194-7.
300. Boanini E, Gazzano M, Rubini K, Bigi A. Collapsed Octacalcium Phosphate Stabilized by Ionic Substitutions. Crystal Growth & Design. 2010;10(8):3612-7.
301. Brown WE, Smith JP, Lehr JR, Frazier AW. Octacalcium Phosphate and Hydroxyapatite: Crystallographic and Chemical Relations between Octacalcium Phosphate and Hydroxyapatite. Nature. 1962;196(4859):1050-5.
302. Brown WE. Crystal Growth of Bone Mineral. Clinical Orthopaedics and Related Research. 1966;44:205-20.
303. Iijima M, Tohda H, Suzuki H, Yanagisawa T, Moriwaki Y. Effects of F- on apatite-octacalcium phosphate intergrowth and crystal morphology in a model system of tooth enamel formation. Calcif Tissue Int. 1992;50(4):357-61.
304. Kamakura S, Sasano Y, Homma H, Suzuki O, Kagayama M, Motegi K. Implantation of Octacalcium Phosphate (OCP) in Rat Skull Defects Enhances Bone Repair. Journal of Dental Research. 1999;78(11):1682-7.
305. Suzuki O. Biological Role of Synthetic Octacalcium Phosphate in Bone Formation and Mineralization. Journal of Oral Biosciences. 2010;52(1):6-14.
306. Kamakura S, Sasano Y, Shimizu T, Hatori K, Suzuki O, Kagayama M, et al. Implanted octacalcium phosphate is more resorbable than β-tricalcium phosphate and hydroxyapatite. Journal of Biomedical Materials Research. 2002;59(1):29-34.
307. LeGeros RZ. Properties of Osteoconductive Biomaterials: Calcium Phosphates. Clinical Orthopaedics and Related Research. 2002;395:81-98.

308. Habibovic P, de Groot K. Osteoinductive biomaterials—properties and relevance in bone repair. Journal of Tissue Engineering and Regenerative Medicine. 2007;1(1):25-32.
309. Shelton RM, Liu Y, Cooper PR, Gbureck U, German MJ, Barralet JE. Bone marrow cell gene expression and tissue construct assembly using octacalcium phosphate microscaffolds. Biomaterials. 2006;27(14):2874-81.
310. Aoba T. The Effect of Fluoride On Apatite Structure and Growth. Critical Reviews in Oral Biology & Medicine. 1997;8(2):136-53.
311. Fan Y, Sun Z, Moradian-Oldak J. Controlled remineralization of enamel in the presence of amelogenin and fluoride. Biomaterials. 2009;30(4):478-83.
312. Fan Y, Sun Z, Moradian-Oldak J. Effect of Fluoride on the Morphology of Calcium Phosphate Crystals Grown on Acid-Etched Human Enamel. Caries research. 2009;43(2):132-6.
313. Siew C, Gruninger SE, Chow LC, Brown WE. Procedure for the study of acidic calcium phosphate precursor phases in enamel mineral formation. Calcif Tissue Int. 1992;50(2):144-8.
314. Johnsson MS-A, Nancollas GH. The Role of Brushite and Octacalcium Phosphate in Apatite Formation. Critical Reviews in Oral Biology & Medicine. 1992;3(1):61-82.
315. Ferreira A, Oliveira C, Rocha F. The different phases in the precipitation of dicalcium phosphate dihydrate. Journal of Crystal Growth. 2003;252(4):599-611.
316. Sivakumar GR, Girija EK, Narayana Kalkura S, Subramanian C. Crystallization and Characterization of Calcium Phosphates: Brushite and Monetite. Crystal Research and Technology. 1998;33(2):197-205.
317. Kataoka S, Sakuma S, Wang J, Yoshihara A, Miyazaki H. Changes in Electrical Resistance of Sound Fissure Enamel in First Molars for 66 Months from Eruption. Caries research. 2007;41(2):161-4.
318. Schulte A, Gente M, Pieper K. Posteruptive Changes of Electrical Resistance Values in Fissure Enamel of Premolars. Caries research. 1999;33(3):242-7.
319. Flim GJ, Arends J. Diffusion of ^{45}Ca in bovine enamel. Calc Tis Res. 1977;24(1):59-64.
320. Wei SHY, Koulourides T. Electron Microprobe and Microhardness Studies of Enamel Remineralization. Journal of Dental Research. 1972;51(2):648-51.
321. He B, Huang S, Zhang C, Jing J, Hao Y, Xiao L, et al. Mineral densities and elemental content in different layers of healthy human enamel with varying teeth age. Archives of Oral Biology. 2011;56(10):997-1004.
322. Carvalho JC, Ekstrand KR, Thylstrup A. Dental Plaque and Caries on Occlusal Surfaces of First Permanent Molars in Relation to Stage of Eruption. Journal of Dental Research. 1989;68(5):773-9.
323. Wöltgens J, Bervoets T, de Blieck-Hogervorst J, Driessens F. Remineralization in human premolars of different posteruptive age. Journal de biologie buccale. 1983;11(1):35-40.
324. Attin T, Kielbassa AM, Schwanenberg M, Hellwig E. Effect of fluoride treatment on remineralization of bleached enamel. Journal of Oral Rehabilitation. 1997;24(4):282-6.
325. Johansson B. Remineralization of slightly etched enamel. Journal of dental research. 1965;44(1):64-70.
326. Brudevold F, Gardner DE, Smith FA. The Distribution of Fluoride in Human Enamel. Journal of Dental Research. 1956;35(3):420-9.
327. Gruythuysen R, van der Linden L, Wöltgens J, Geraets W. Differences between primary and permanent teeth in posteruptive age dependency of radiological changes in enamel during the development of approximal caries. Journal de biologie buccale. 1992;20(1):59-62.
328. Huang A, Nakagaki H, Tsuboi S, Ji H, Ohno N, Chen R, et al. Fluoride profiles of perikymata in enamel surfaces of human premolars. Archives of Oral Biology. 1998;43(9):669-77.
329. Aasenden R. Fluoride concentrations in the surface tooth enamel of young men and women. Archives of Oral Biology. 1974;19(8):697-701.
330. Aasenden R. Post-eruptive changes in the fluoride concentrations of human tooth surface enamel. Archives of Oral Biology. 1975;20(5–6):359-63.
331. Jeng Y-R, Lin T-T, Wong T-Y, Chang H-J, Shieh D-B. Nano-mechanical Properties of Fluoride-treated Enamel Surfaces. Journal of Dental Research. 2008;87(4):381-5.
332. Gerth HUV, Dammaschke T, Schäfer E, Züchner H. A three layer structure model of fluoridated enamel containing CaF_2, $Ca(OH)_2$ and FAp. Dental Materials. 2007;23(12):1521-8.

333. Christoffersen J, Christoffersen MR, Arends J, Leonardsen ES. Formation of Phosphate-Containing Calcium Fluoride at the Expense of Enamel, Hydroxyapatite and Fluorapatite. Caries research. 1995;29(3):223-30.
334. Daculsi G, Kerebel B. High-resolution electron microscope study of human enamel crystallites: Size, shape, and growth. Journal of Ultrastructure Research. 1978;65(2):163-72.
335. LeGeros RZ, Piliero JA, Pentel L. Comparative Properties of Deciduous and Permanent (Young and Old) Human Enamel. Gerodontology. 1983;2(1):1-8.
336. Brudevold F. A Study of the Phosphate Solubility of the Human Enamel Surface. Journal of Dental Research. 1948;27(3):320-9.
337. Sperber GH, Buonocore MG. Enamel surface in white spot formation. J Dent Res. 1963;42:724-31.
338. Mumford JM. Resistivity of human enamel and dentine. Archives of Oral Biology. 1967;12(7):925-7.
339. Hoppenbrouwers PMM, Scholberg HPF, Borggreven JMPM. Measurement of the Permeability of Dental Enamel and its Variation with Depth using an Electrochemical Method. Journal of Dental Research. 1986;65(2):154-7.
340. EL-Faramawy NA, Rühm W. Additional Criteria for EPR Dosimetry using Tooth Enamel. Radiation Research. 2007;167(2):244-50.
341. Stiefel A, Binus W. Maturation of enamel and tooth eruption. Deutsche Stomatologie (Berlin, Germany: 1990). 1990;41(9):337-40.
342. Demirci M, Tuncer S, Yuceokur AA. Prevalence of caries on individual tooth surfaces and its distribution by age and gender in university clinic patients. European journal of dentistry. 2010;4(3):270.
343. Härkänen T, Larmas MA, Virtanen JI, Arjas E. Applying Modern Survival Analysis Methods to Longitudinal Dental Caries Studies. Journal of Dental Research. 2002;81(2):144-8.
344. Steinman RR, Hewes CG, Woods RW. Histochemical Analysis of Lesions in Incipient Dental Caries. Journal of Dental Research. 1959;38(3):592-605.
345. Wynn W, Haldi J. Dental Caries in the Albino Rat on High Sucrose Diets Containing Different Amounts of Aluminum. The Journal of Nutrition. 1954;54(2):285-90.
346. Sognnaes RF, Shaw JH. Salivary and Pulpal Contributions to the Radiophosphorus Uptake in Enamel and Dentin. The Journal of the American Dental Association. 1952;44(5):489-505.
347. Sognnaes RF, Shaw JH, Bogoroch R. Radiotracer Studies on Bone, Cementum, Dentin and Enamel of Rhesus Monkeys1955 1955-01-31 00:00:00. 408-20 p.
348. Aasenden R, DePaola PF, Brudevold F. Effects of daily rinsing and ingestion of fluoride solutions upon dental caries and enamel fluoride. Archives of Oral Biology. 1972;17(12):1705-14.
349. Fitzgerald R, Larson R. Age and caries susceptibility in gnotobiotic rats. Helvetica odontologica acta. 1967;11(1):49-52.
350. Saunders M, Weidmann SM. Uptake and retention of fluoride by teeth of dogs of different ages. Archives of Oral Biology. 1969;14(4):365-72.
351. von der Fehr FR, Löe H, Theilade E. Experimental Caries in Man. Caries research. 1970;4(2):131-48.
352. Weaver R. The inhibition of dental caries by fluorine. Proceedings of the Royal Society of Medicine. 1948;41(5):284.
353. Brudevold F, Gron P, McCann H. Physico-Chemical Aspects of the Enamel-Saliva System. Advances in fluorine research and dental caries prevention. 1964;21:63-78.
354. Little MF, Steadman LT. Chemical and physical properties of altered and sound enamel—IV: Trace element composition. Archives of Oral Biology. 1966;11(3):273-8.
355. Ludwig TG, Adkins BL, Losee FL. Relationship of concentrations of eleven elements in public water supplies to caries prevalence in American schoolchildren*. Australian Dental Journal. 1970;15(2):126-32.
356. Shearer TR, Britton JL, DeSart DJ, Johnson JR. Influence of Cadmium on Caries and the Cariostatic Properties of Fluoride in Rats. Archives of Environmental Health: An International Journal. 1980;35(3):176-80.
357. Hallsworth AS, Robinson C, Weatherell JA. Mineral and Magnesium Distribution within the Approximal Carious Lesion of Dental Enamel. Caries research. 1972;6(2):156-68.

358. Lammers PC, Borggreven JMPM, Driessens FCM, van ’t Hof MA. Acid-Susceptibility of Lesions in Bovine Enamel after Remineralization in the Presence of Fluoride and/or Carbonate. Caries research. 1992;26(1):1-7.
359. Bhussry BR. Chemical and Physical Studies of Enamel From Human Teeth: 1. Specific Gravity and Nitrogen Content of Enamel From Different Surfaces. Journal of Dental Research. 1958;37(5):832-6.
360. Fang M, Lei K, Kilgore L. Effects of Zinc Deficiency on Dental Caries in Rats1'2'3. J Nutr. 1980;110:1032-6.
361. Curzon MEJ, Adkins BL, Bibby BG, Losee FL. Combined Effect of Trace Elements and Fluorine on Caries. Journal of Dental Research. 1970;49(3):526-8.
362. Curzon MEJ, Spector PC, Iker HP. An association between strontium in drinking water supplies and low caries prevalence in man. Archives of Oral Biology. 1978;23(4):317-21.
363. Gedalia I, Anaise J, Laufer E. Effect of Prenatal, Preeruptive, and Posteruptive Strontium Administration on Dental Caries in Hamster Molars. Journal of Dental Research. 1975;54(6):1240.
364. Mohammed NR, Mneimne M, Hill RG, Al-Jawad M, Lynch RJM, Anderson P. Physical chemical effects of zinc on in vitro enamel demineralization. Journal of Dentistry. 2014;42(9):1096-104.
365. Yamagishi K, Onuma K, Suzuki T, Okada F, Tagami J, Otsuki M, et al. Materials chemistry: A synthetic enamel for rapid tooth repair. Nature. 2005;433(7028):819.
366. Palmer LC, Newcomb CJ, Kaltz SR, Spoerke ED, Stupp SI. Biomimetic Systems for Hydroxyapatite Mineralization Inspired By Bone and Enamel. Chemical Reviews. 2008;108(11):4754-83.
367. Martin RI, Brown PW. Mechanical properties of hydroxyapatite formed at physiological temperature. Journal of Materials Science: Materials in Medicine. 1995;6(3):138-43.
368. Tsui YC, Doyle C, Clyne TW. Plasma sprayed hydroxyapatite coatings on titanium substrates Part 1: Mechanical properties and residual stress levels. Biomaterials. 1998;19(22):2015-29.
369. Suchanek W, Yoshimura M. Processing and properties of hydroxyapatite-based biomaterials for use as hard tissue replacement implants. Journal of Materials Research. 1998;13(01):94-117.
370. Wang P, Chaki TK. Sintering behaviour and mechanical properties of hydroxyapatite and dicalcium phosphate. Journal of Materials Science: Materials in Medicine. 1993;4(2):150-8.
371. Ruys AJ, Wei M, Sorrell CC, Dickson MR, Brandwood A, Milthorpe BK. Sintering effects on the strength of hydroxyapatite. Biomaterials. 1995;16(5):409-15.
372. Kothapalli C, Wei M, Vasiliev A, Shaw MT. Influence of temperature and concentration on the sintering behavior and mechanical properties of hydroxyapatite. Acta Materialia. 2004;52(19):5655-63.
373. Li L, Pan H, Tao J, Xu X, Mao C, Gu X, et al. Repair of enamel by using hydroxyapatite nanoparticles as the building blocks. Journal of Materials Chemistry. 2008;18(34):4079-84.
374. Hench LL. Bioceramics: From Concept to Clinic. Journal of the American Ceramic Society. 1991;74(7):1487-510.
375. de Leeuw NH. Resisting the Onset of Hydroxyapatite Dissolution through the Incorporation of Fluoride. The Journal of Physical Chemistry B. 2004;108(6):1809-11.
376. Roveri N, Battistella E, Bianchi CL, Foltran I, Foresti E, Iafisco M, et al. Surface enamel remineralization: biomimetic apatite nanocrystals and fluoride ions different effects. J Nanomaterials. 2009;2009:1-9.
377. Roveri N, Battistella E, Foltran I, Foresti E, Iafisco M, Lelli M, et al. Synthetic biomimetic carbonate-hydroxyapatite nanocrystals for enamel remineralization. Advanced Materials Research. 2008;47:821-4.
378. Besinis A, De Peralta T, Tredwin CJ, Handy RD. Review of Nanomaterials in Dentistry: Interactions with the Oral Microenvironment, Clinical Applications, Hazards, and Benefits. ACS Nano. 2015;9(3):2255-89.
379. Najibfard K, Ramalingam K, Chedjieu I, Amaechi B. Remineralization of early caries by a nano-hydroxyapatite dentifrice. Journal of Clinical Dentistry. 2011;22(5):139.

380. Orsini G, Procaccini M, Manzoli L, Giuliodori F, Lorenzini A, Putignano A. A double-blind randomized-controlled trial comparing the desensitizing efficacy of a new dentifrice containing carbonate/hydroxyapatite nanocrystals and a sodium fluoride/potassium nitrate dentifrice. Journal of Clinical Periodontology. 2010;37(6):510-7.
381. Habibovic P, Barrère F, Van Blitterswijk CA, de Groot K, Layrolle P. Biomimetic Hydroxyapatite Coating on Metal Implants. Journal of the American Ceramic Society. 2002;85(3):517-22.
382. Xie R, Feng Z, Li S, Xu B. EDTA-Assisted Self-Assembly of Fluoride-Substituted Hydroxyapatite Coating on Enamel Substrate. Crystal Growth & Design. 2011;11(12):5206-14.
383. Gestrelius S, Andersson C, Johansson A-C, Persson E, Brodin A, Rydhag L, et al. Formulation of enamel matrix derivative for surface coating. Journal of Clinical Periodontology. 1997;24(9):678-84.
384. Lacefield WR. Hydroxyapatite Coatings. Annals of the New York Academy of Sciences. 1988;523(1):72-80.
385. Johnson AL. Synthetic enamel coating process. Google Patents; 1969.
386. Legeros RZ, Sakae T, Bautista C, Retino M, Legeros JP. Magnesium and Carbonate in Enamel and Synthetic Apatites. Advances in Dental Research. 1996;10(2):225-31.
387. Young RA, Bartlett ML, Spooner S, Mackie PE, Bonel G. Reversible high temperature exchange of carbonate and hydroxyl ions in tooth enamel and synthetic hydroxyapatite. J Biol Phys. 1981;9(1):1-26.
388. Featherstone JDB, Mayer I, Driessens FCM, Verbeeck RMH, Heijligers HJM. Synthetic apatites containing Na, Mg, and CO_3 and their comparison with tooth enamel mineral. Calcif Tissue Int. 1983;35(1):169-71.
389. Leventouri T. Synthetic and biological hydroxyapatites: Crystal structure questions. Biomaterials. 2006;27(18):3339-42.
390. Penel G, Leroy G, Rey C, Bres E. MicroRaman Spectral Study of the PO_4 and CO_3 Vibrational Modes in Synthetic and Biological Apatites. Calcif Tissue Int. 1998;63(6):475-81.
391. Aoba T, Moreno EC, Shimoda S. Competitive adsorption of magnesium and calcium ions onto synthetic and biological apatites. Calcif Tissue Int. 1992;51(2):143-50.
392. Nelson D, Featherstone J. Preparation, analysis, and characterization of carbonated apatites. Calcif Tissue Int. 1981;34:S69-81.
393. Nelson D, Williamson B. Low-temperature laser Raman spectroscopy of synthetic carbonated apatites and dental enamel. Australian Journal of Chemistry. 1982;35(4):715-27.
394. Chen H, Clarkson BH, Sun K, Mansfield JF. Self-assembly of synthetic hydroxyapatite nanorods into an enamel prism-like structure. Journal of Colloid and Interface Science. 2005;288(1):97-103.
395. Simmelink JW, Abrigo SC. Crystal Morphology and Decalcification Patterns Compared in Rat and Human Enamel and Synthetic Hydroxyapatite. Advances in Dental Research. 1989;3(2):241-8.
396. Zhang S, Gonsalves KE. Preparation and characterization of thermally stable nanohydroxyapatite. Journal of Materials Science: Materials in Medicine. 1997;8(1):25-8.
397. Lazić S, Zec S, Miljević N, Milonjić S. The effect of temperature on the properties of hydroxyapatite precipitated from calcium hydroxide and phosphoric acid. Thermochimica Acta. 2001;374(1):13-22.
398. Fejerskov O, Larsen MJ, Richards A, Baelum V. Dental Tissue Effects of Fluoride. Advances in Dental Research. 1994;8(1):15-31.
399. Yassen GH, Platt JA, Hara AT. Bovine teeth as substitute for human teeth in dental research: a review of literature. Journal of Oral Science. 2011;53(3):273-82.
400. Edmunds DH, Whittaker DK, Green RM. Suitability of Human, Bovine, Equine, and Ovine Tooth Enamel for Studies of Artificial Bacterial Carious Lesions. Caries research. 1988;22(6):327-36.
401. Featherstone JDB, Mellberg JR. Relative Rates of Progress of Artificial Carious Lesions in Bovine, Ovine and Human Enamel. Caries research. 1981;15(1):109-14.
402. Reis AF, Giannini M, Kavaguchi A, Soares CJ, Line S. Comparison of microtensile bond strength to enamel and dentin of human, bovine, and porcine teeth. The journal of adhesive dentistry. 2003;6(2):117-21.

403. Mellberg J. Hard-tissue substrates for evaluation of cariogenic and anti-cariogenic activity in situ. Journal of dental research. 1992;71:913-9.
404. Ogaard B, Rølla G. Intra-oral models: comparison of in situ substrates. Journal of dental research. 1992;71:920-3.
405. Buzalaf MAR, Hannas AR, Magalhães AC, Rios D, Honório HM, Delbem ACB. pH-cycling models for in vitro evaluation of the efficacy of fluoridated dentifrices for caries control: strengths and limitations. Journal of Applied Oral Science. 2010;18:316-34.
406. Fonseca RB, Haiter-Neto F, Fernandes-Neto AJ, Barbosa GAS, Soares CJ. Radiodensity of enamel and dentin of human, bovine and swine teeth. Archives of Oral Biology. 2004;49(11):919-22.
407. Reeh ES, Douglas WH, Levine MJ. Lubrication of human and bovine enamel compared in an artificial mouth. Archives of Oral Biology. 1995;40(11):1063-72.
408. Feagin F, Koulourides T, Pigman W. The characterization of enamel surface demineralization, remineralization, and associated hardness changes in human and bovine material. Archives of Oral Biology. 1969;14(12):1407-17.
409. Davidson CL, Boom G, Arends J. Calcium Distribution in Human and Bovine Surface Enamel. Caries research. 1973;7(4):349-59.
410. Gwinnett AJ, Buonocore MG, Sheykholeslam Z. Effect of fluoride on etched human and bovine tooth enamel surfaces as demonstrated by scanning electron microscopy. Archives of Oral Biology. 1972;17(2):271-8.
411. Sydney-Zax M, Mayer I, Deutsch D. Carbonate Content in Developing Human and Bovine Enamel. Journal of Dental Research. 1991;70(5):913-6.
412. Sano H, Ciucchi B, Matthews WG, Pashley DH. Tensile Properties of Mineralized and Demineralized Human and Bovine Dentin. Journal of Dental Research. 1994;73(6):1205-11.
413. Soares CJ, Barbosa LM, Santana FR, Soares PBF, Mota ASd, Silva GRd. Fracture strength of composite fixed partial denture using bovine teeth as a substitute for human teeth with or without fiber-reinforcement. Brazilian Dental Journal. 2010;21:235-40.
414. Lynch RJM, ten Cate JM. The Effect of Lesion Characteristics at Baseline on Subsequent De- and Remineralisation Behaviour. Caries research. 2006;40(6):530-5.
415. Lippert F, Butler A, Lynch RJM. Characteristics of Methylcellulose Acid Gel Lesions Created in Human and Bovine Enamel. Caries research. 2013;47(1):50-5.
416. Zero DT. In Situ Caries Models. Advances in Dental Research. 1995;9(3):214-30.
417. Whittaker DK. Structural variations in the surface zone of human tooth enamel observed by scanning electron microscopy. Archives of Oral Biology. 1982;27(5):383-92.
418. Scheider I, Xiao T, Yilmaz E, Schneider GA, Huber N, Bargmann S. Damage modeling of small-scale experiments on dental enamel with hierarchical microstructure. Acta Biomaterialia. 2015;15:244-53.
419. Cheng Z-j, Wang X-m, Ge J, Yan J-x, Ji N, Tian Ll, et al. The mechanical anisotropy on a longitudinal section of human enamel studied by nanoindentation. Journal of Materials Science: Materials in Medicine. 2010;21(6):1811-6.
420. DarendelİLer S, DarendelİLer H, KinoĞLu T. Analysis of a central maxillary incisor by using a three-dimensional finite element method. Journal of Oral Rehabilitation. 1992;19(4):371-83.
421. Hassan R, Caputo AA, Bunshah RF. Fracture Toughness of Human Enamel. Journal of Dental Research. 1981;60(4):820-7.
422. Palamara JEA, Palamara D, Messer HH, Tyas MJ. Tooth morphology and characteristics of non-carious cervical lesions. Journal of Dentistry. 2006;34(3):185-94.
423. Salma K, Berzina-Cimdina L, Borodajenko N. Calcium phosphate bioceramics prepared from wet chemically precipitated powders. Processing and Application of Ceramics. 2010;4(1):45-51.
424. White DJ. The Application of in Vitro Models to Research on Demineralization and Remineralization of the Teeth. Advances in Dental Research. 1995;9(3):175-93.
425. White D. The comparative sensitivity of intra-oral, in vitro, and animal models in the'profile'evaluation of topical fluorides. Journal of dental research. 1992;71:884-94.
426. Ten Cate JM. In vitro Studies on the Effects of Fluoride on De- and Remineralization. Journal of Dental Research. 1990;69(Suppl 2):614-9.
427. Shellis RP, Ganss C, Ren Y, Zero DT, Lussi A. Methodology and Models in Erosion Research: Discussion and Conclusions. Caries research. 2011;45(Suppl. 1):69-77.

428. Roberts AJ. Role of Models in Assessing New Agents for Caries Prevention—Non-Fluoride Systems. Advances in Dental Research. 1995;9(3):304-11.
429. Robinson C, Kirkham J, Baverstock AC, Shore RC. A flexible and rapid pH cycling procedure for investigations into the remineralisation and demineralisation behaviour of human enamel. Caries research. 1992;26(1):14-7.
430. Saunders F, Bosma M, Buch R, Kollar C, Martinez-Mier E, Zero D, editors. Evaluation of Plaque Fluid Fluoride Retention after Dentifrice Application. IADR Abstract; 2007.
431. Newby E, Bosma M, Yadav M. Evaluation of plaque fluid fluoride retention after dentifrice application. Caries research. 2009;43:208.
432. Creeth J, Zero D, Mau M, Bosma ML, Butler A. The effect of dentifrice quantity and toothbrushing behaviour on oral delivery and retention of fluoride in vivo. International dental journal. 2013;63(Suppl 2):14-24.
433. Airoldi G, Riva G, Vanelli M, Filippi d V, Garattini G. Oral environment temperature changes induced by cold/hot liquid intake. American Journal of Orthodontics and Dentofacial Orthopedics. 1997;112(1):58-63.
434. Longman CM, Pearson GJ. Variations in tooth, surface temperature in the oral cavity during fluid intake. Biomaterials. 1987;8(5):411-4.
435. Stephan RM. Intra-Oral Hydrogen-Ion Concentrations Associated With Dental Caries Activity. Journal of Dental Research. 1944;23(4):257-66.
436. Dong YM, Pearce EIF, Yue L, Larsen MJ, Gao XJ, Wang JD. Plaque pH and Associated Parameters in Relation to Caries. Caries research. 1999;33(6):428-36.
437. Lippert F, Butler A, Lynch RJM. Enamel Demineralization and Remineralization under Plaque Fluid-Like Conditions: A Quantitative Light-Induced Fluorescence Study. Caries research. 2011;45(2):155-61.
438. Gao XJ, Fan Y, Kent RL, Van Houte J, Margolis HC. Association of Caries Activity with the Composition of Dental Plaque Fluid. Journal of Dental Research. 2001;80(9):1834-9.
439. Philpotts CJ, Weader E, Joiner A. The measurement in vitro of enamel and dentine wear by toothpastes of different abrasivity. International dental journal. 2005;55(S3):183-7.
440. Vicentini BC, Braga SRM, Sobral MAP. The measurement in vitro of dentine abrasion by toothpastes. International dental journal. 2007;57(5):314-8.
441. Hellwig E, Altenburger M, Attin T, Lussi A, Buchalla W. Remineralization of initial carious lesions in deciduous enamel after application of dentifrices of different fluoride concentrations. Clin Oral Invest. 2010;14(3):265-9.
442. Robinson C. Fluoride and the caries lesion: interactions and mechanism of action. European Archives of Paediatric Dentistry. 2012;10(3):136-40.
443. Manly RS, Schickner FA. Factors Influencing Tests on the Abrasion of Dentin by Brushing with Dentifrices. Journal of Dental Research. 1944;23(1):59-72.
444. Franzò D, Philpotts CJ, Cox TF, Joiner A. The effect of toothpaste concentration on enamel and dentine wear in vitro. Journal of Dentistry. 2010;38(12):974-9.
445. Duke S, Forward G. The conditions occurring in vivo when brushing with toothpastes. British dental journal. 1982;152(2):52.
446. Lynch RJM, Navada R, Walia R. Low-levels of fluoride in plaque and saliva and their effects on the demineralisation and remineralisation of enamel; role of fluoride toothpastes. International dental journal. 2004;54(S5):304-9.
447. Tabachnick BG, Fidell LS. Experimental designs using ANOVA: Thomson/Brooks/Cole; 2007.
448. Langford JI, Daniel L. Powder diffraction. Reports on Progress in Physics. 1996;59(2):131.
449. Birkholz M. Principles of X-ray Diffraction. Thin Film Analysis by X-Ray Scattering: Wiley-VCH Verlag GmbH & Co. KGaA; 2006. p. 1-40.
450. Culity B, Stock S. Elements of X-ray Diffraction. 2nd, Addition-Wesley, MA, London. 1978.
451. Markovich RJ, Pidgeon C. Introduction to Fourier Transform Infrared Spectroscopy and Applications in the Pharmaceutical Sciences. Pharmaceutical Research. 1991;8(6):663-75.
452. Rouquerol J, Rouquerol F, Llewellyn P, Maurin G, Sing KS. Adsorption by powders and porous solids: principles, methodology and applications: Academic press; 2013.

453. Brunauer S, Emmett PH, Teller E. Adsorption of Gases in Multimolecular Layers. Journal of the American Chemical Society. 1938;60(2):309-19.
454. Brunauer S, Deming LS, Deming WE, Teller E. On a Theory of the van der Waals Adsorption of Gases. Journal of the American Chemical Society. 1940;62(7):1723-32.
455. Patil SP, Modi SR, Bansal AK. Generation of 1:1 Carbamazepine:Nicotinamide cocrystals by spray drying. European Journal of Pharmaceutical Sciences. 2014;62:251-7.
456. Tamari S. Optimum design of the constant-volume gas pycnometer for determining the volume of solid particles. Measurement Science and Technology. 2004;15(3):549.
457. Lowell S, Shields JE, Thomas MA, Thommes M. Characterization of porous solids and powders: surface area, pore size and density: Springer Science & Business Media; 2012.
458. Abell AB, Willis KL, Lange DA. Mercury Intrusion Porosimetry and Image Analysis of Cement-Based Materials. Journal of Colloid and Interface Science. 1999;211(1):39-44.
459. Washburn EW. Note on a Method of Determining the Distribution of Pore Sizes in a Porous Material. Proceedings of the National Academy of Sciences of the United States of America. 1921;7(4):115-6.
460. Haddad PR. Ion chromatography. Handbook on Metals in Clinical and Analytical Chemistry. 1994:135.
461. Weis J. Ion chromatography: John Wiley & Sons; 2008.
462. Caslavska V, Moreno EC, Brudevold F. Determination of the calcium fluoride formed from in vitro exposure of human enamel to fluoride solutions. Archives of Oral Biology. 1975;20(5–6):333-9.
463. Cruz R, Ögaard B, Rölla G. Uptake of KOH-soluble and KOH-insoluble fluoride in sound human enamel after topical application of a fluoride varnish (Duraphat) or a neutral 2% NaF solution in vitro. European Journal of Oral Sciences. 1992;100(3):154-8.
464. Robinson JW. Atomic Absorption Spectroscopy. Analytical Chemistry. 1960;32(8):17A-29A.
465. Welz B, Sperling M. Atomic absorption spectrometry: John Wiley & Sons; 2008.
466. L'Vov BV. Recent advances in absolute analysis by graphite furnace atomicabsorption spectrometry. Spectrochimica Acta Part B: Atomic Spectroscopy. 1990;45(7):633-55.
467. L'Vov BV. Graphite furnace atomic absorption spectrometry-on the way to absolute analysis. Journal of Analytical Atomic Spectrometry. 1988;3(1):9-12.
468. Binnig G, Quate CF, Gerber C. Atomic Force Microscope. Physical Review Letters. 1986;56(9):930-3.
469. Geisse NA. AFM and combined optical techniques. Materials Today. 2009;12(7–8):40-5.
470. Meyer E. Atomic force microscopy. Progress in Surface Science. 1992;41(1):3-49.
471. Blanchard RC. Atomic Force Microscopy. The Chemical Educator. 1996;1(5):1-8.
472. Siperko LM, Landis WJ. Atomic scale imaging of hydroxyapatite and brushite in air by force microscopy. Applied Physics Letters. 1992;61(21):2610-2.
473. Oliver WC, Pharr GM. An improved technique for determining hardness and elastic modulus using load and displacement sensing indentation experiments. Journal of Materials Research. 1992;7(06):1564-83.
474. Sakharova NA, Fernandes JV, Antunes JM, Oliveira MC. Comparison between Berkovich, Vickers and conical indentation tests: A three-dimensional numerical simulation study. International Journal of Solids and Structures. 2009;46(5):1095-104.
475. Clinton DJ, Morrell R. Hardness testing of ceramic materials. Materials Chemistry and Physics. 1987;17(5):461-73.
476. Gong J, Wang J, Guan Z. A comparison between Knoop and Vickers hardness of silicon nitride ceramics. Materials Letters. 2002;56(6):941-4.
477. Chicot D, Mercier D, Roudet F, Silva K, Staia MH, Lesage J. Comparison of instrumented Knoop and Vickers hardness measurements on various soft materials and hard ceramics. Journal of the European Ceramic Society. 2007;27(4):1905-11.
478. Marshall DB. Controlled Flaws in Ceramics: A Comparison of Knoop and Vickers Indentation. Journal of the American Ceramic Society. 1983;66(2):127-31.
479. Freund F, Knobel RM. Distribution of fluorine in hydroxyapatite studied by infrared spectroscopy. Journal of the Chemical Society, Dalton Transactions. 1977(11):1136-40.
480. Vasconcellos LA, dos Santos LA. Calcium phosphate cement scaffolds with PLGA fibers. Materials Science and Engineering: C. 2013;33(3):1032-40.

481. Bouhaouss A, Bensaoud A, Laghzizil A, Ferhat M. Effect of chemical treatments on the ionic conductivity of carbonate apatite. International Journal of Inorganic Materials. 2001;3(6):437-41.
482. Domínguez MI, Carpena J, Borschnek D, Centeno MA, Odriozola JA, Rose J. Apatite and Portland/apatite composite cements obtained using a hydrothermal method for retaining heavy metals. Journal of Hazardous Materials. 2008;150(1):99-108.
483. Rey C, Shimizu M, Collins B, Glimcher M. Resolution-enhanced fourier transform infrared spectroscopy study of the environment of phosphate ions in the early deposits of a solid phase of calcium-phosphate in bone and enamel, and their evolution with age. I: Investigations in the υ_4 PO_4 domain. Calcif Tissue Int. 1990;46(6):384-94.
484. Gadaleta SJ, Paschalis EP, Betts F, Mendelsohn R, Boskey AL. Fourier transform infrared spectroscopy of the solution-mediated conversion of amorphous calcium phosphate to hydroxyapatite: New correlations between X-ray diffraction and infrared data. Calcif Tissue Int. 1996;58(1):9-16.
485. Paschalis EP, Betts F, DiCarlo E, Mendelsohn R, Boskey AL. FTIR Microspectroscopic Analysis of Normal Human Cortical and Trabecular Bone. Calcif Tissue Int. 1997;61(6):480-6.
486. Xie J, Riley C, Kumar M, Chittur K. FTIR/ATR study of protein adsorption and brushite transformation to hydroxyapatite. Biomaterials. 2002;23(17):3609-16.
487. Antonakos A, Liarokapis E, Leventouri T. Micro-Raman and FTIR studies of synthetic and natural apatites. Biomaterials. 2007;28(19):3043-54.
488. Pleshko N, Boskey A, Mendelsohn R. Novel infrared spectroscopic method for the determination of crystallinity of hydroxyapatite minerals. Biophysical Journal. 1991;60(4):786-93.
489. Murugan R, Ramakrishna S. Aqueous mediated synthesis of bioresorbable nanocrystalline hydroxyapatite. Journal of Crystal Growth. 2005;274(1–2):209-13.
490. Kim B-H, Jeong J-H, Jeon Y-S, Jeon K-O, Hwang K-S. Hydroxyapatite layers prepared by sol–gel assisted electrostatic spray deposition. Ceramics International. 2007;33(1):119-22.
491. Rapacz-Kmita A, Paluszkiewicz C, Ślósarczyk A, Paszkiewicz Z. FTIR and XRD investigations on the thermal stability of hydroxyapatite during hot pressing and pressureless sintering processes. Journal of Molecular Structure. 2005;744–747:653-6.
492. Gibson IR, Rehman I, Best SM, Bonfield* W. Characterization of the transformation from calcium-deficient apatite to β-tricalcium phosphate. Journal of Materials Science: Materials in Medicine. 2000;11(12):799-804.
493. Rehman I, Bonfield W. Characterization of hydroxyapatite and carbonated apatite by photo acoustic FTIR spectroscopy. Journal of Materials Science: Materials in Medicine. 1997;8(1):1-4.
494. Ren F, Ding Y, Leng Y. Infrared spectroscopic characterization of carbonated apatite: A combined experimental and computational study. Journal of Biomedical Materials Research Part A. 2014;102(2):496-505.
495. Wahab R, Ansari SG, Kim YS, Mohanty TR, Hwang IH, Shin H-S. Immobilization of DNA on nano-hydroxyapatite and their interaction with carbon nanotubes. Synthetic Metals. 2009;159(3–4):238-45.
496. Kim H-W, Knowles JC, Kim H-E. Hydroxyapatite porous scaffold engineered with biological polymer hybrid coating for antibiotic Vancomycin release. Journal of Materials Science: Materials in Medicine. 2005;16(3):189-95.
497. Ouizat S, Barroug A, Legrouri A, Rey C. Adsorption of bovine serum albumin on poorly crystalline apatite: influence of maturation. Materials Research Bulletin. 1999;34(14–15):2279-89.
498. Rey C, Shimizu M, Collins B, Glimcher MJ. Resolution-enhanced fourier transform infrared spectroscopy study of the environment of phosphate ion in the early deposits of a solid phase of calcium phosphate in bone and enamel and their evolution with age: 2. Investigations in the υ_3 PO_4 domain. Calcif Tissue Int. 1991;49(6):383-8.
499. Gandolfi MG, Taddei P, Tinti A, De Stefano Dorigo E, Prati C. Alpha-TCP improves the apatite-formation ability of calcium-silicate hydraulic cement soaked in phosphate solutions. Materials Science and Engineering: C. 2011;31(7):1412-22.
500. Ten Bosch JJ, Fennis-le Y, Verdonschot EH. Time-dependent Decrease and Seasonal Variation of the Porosity of Recently Erupted Sound Dental Enamel in vivo. Journal of Dental Research. 2000;79(8):1556-9.
501. Dalderup LM. Comparison between Initial Caries Attack and Immaturity of Dental Tissues in the Rat. Journal of Dental Research. 1962;41(6):1476.

502. Ten Cate JM, Duijsters PPE. Alternating Demineralization and Remineralization of Artificial Enamel Lesions. Caries research. 1982;16(3):201-10.
503. Koulourides T. Dynamics of tooth surface-oral fluid equilibrium. Adv Oral Biol. 1966;2:149-71.
504. Lenz H, Newsely H. Discussion on maturation and remineralization of the enamel. Advances in Fluorine Research and Dental Caries Prevention. 1965;21:95-8.
505. Etty EJ, Henneberke M, Gruythuysen RJ, Wöltgens JHM. Influence of Oral Hygiene on Early Enamel Caries. Caries research. 1994;28(2):132-6.
506. Kolmakow S, Honkala E, Kuzmina E, Borovsky E, Vasina S, Smirnova T, et al. Surface-specific effect of a mineralizing agent on the permanent teeth and on periodontal status. The Journal of clinical pediatric dentistry. 1990;15(2):113-9.
507. Wöltgens J, Etty E, Geraets W. Posteruptive age dependency of cariogenic changes in enamel of permanent teeth of children. Journal de biologie buccale. 1990;18(1):49-53.
508. Carlos JP, Gittelsohn AM. Longitudinal studies of the natural history of caries—II. Archives of Oral Biology. 1965;10(5):739-51.
509. Jackson D, Burch PRJ. Dental caries: Distribution, by age-group, between homologous (right-left) mesial and distal surfaces of human permanent maxillary incisors. Archives of Oral Biology. 1970;15(11):1059-67.
510. Mahoney E, Holt A, Swain M, Kilpatrick N. The hardness and modulus of elasticity of primary molar teeth:an ultra-micro-indentation study. Journal of Dentistry. 2000;28(8):589-94.
511. Dahm S, Risnes S. A Comparative Infrared Spectroscopic Study of Hydroxide and Carbonate Absorption Bands in Spectra of Shark Enameloid, Shark Dentin, and a Geological Apatite. Calcif Tissue Int. 1999;65(6):459-65.
512. Weatherell JA, Robinson C, Hiller CR. Distribution of carbonate in thin sections of dental enamel. Caries research. 1968;2(1):1-9.
513. Penel G, Leroy G, Rey C, Sombret B, Huvenne JP, Bres E. Infrared and Raman microspectrometry study of fluor-fluor-hydroxy and hydroxy-apatite powders. Journal of Materials Science: Materials in Medicine. 1997;8(5):271-6.
514. Ten Cate JM. Review on fluoride, with special emphasis on calcium fluoride mechanisms in caries prevention. European Journal of Oral Sciences. 1997;105(5):461-5.
515. Mohammed NR, Kent NW, Lynch RJM, Karpukhina N, Hill R, Anderson P. Effects of Fluoride on in vitro Enamel Demineralization Analyzed by ^{19}F MAS-NMR. Caries research. 2013;47(5):421-8.
516. Yanagisawa T, Takuma S, Tohda H, Fejerskov O, Fearnhead RW. High Resolution Electron Microscopy of Enamel Crystals in Cases of Human Dental Fluorosis. Journal of Electron Microscopy. 1989;38(6):441-8.
517. Vogel GL. Oral fluoride reservoirs and the prevention of dental caries. Monogr Oral Sci. 2011;22:146-57.
518. Vogel GL, Tenuta LMA, Schumacher GE, Chow LC. No Calcium-Fluoride-Like Deposits Detected in Plaque Shortly after a Sodium Fluoride Mouthrinse. Caries research. 2010;44(2):108-15.
519. Vogel GL, Tenuta LMA, Schumacher GE, Chow LC. A Calcium Prerinse Required to Form Calcium Fluoride in Plaque from a Sodium Fluoride Rinse. Caries research. 2014;48(2):174-8.
520. Zhang H, Wang Y, Yan Y, Li S. Precipitation of biocompatible hydroxyapatite whiskers from moderately acid solution. Ceramics International. 2003;29(4):413-8.
521. Viswanath B, Ravishankar N. Controlled synthesis of plate-shaped hydroxyapatite and implications for the morphology of the apatite phase in bone. Biomaterials. 2008;29(36):4855-63.
522. Liu X, Lin K, Qian R, Chen L, Zhuo S, Chang J. Growth of Highly Oriented Hydroxyapatite Arrays Tuned by Quercetin. Chemistry – A European Journal. 2012;18(18):5519-23.
523. Ten Huisen KS, Brown PW. Formation of calcium-deficient hydroxyapatite from α-tricalcium phosphate. Biomaterials. 1998;19(23):2209-17.
524. Iijima M, Tohda H, Moriwaki Y. Growth and structure of lamellar mixed crystals of octacalcium phosphate and apatite in a model system of enamel formation. Journal of Crystal Growth. 1992;116(3):319-26.

525. Miake Y, Shimoda S, Fukae M, Aoba T. Epitaxial overgrowth of apatite crystals on the thin-ribbon precursor at early stages of porcine enamel mineralization. Calcif Tissue Int. 1993;53(4):249-56.
526. Almirall A, Larrecq G, Delgado JA, Martínez S, Planell JA, Ginebra MP. Fabrication of low temperature macroporous hydroxyapatite scaffolds by foaming and hydrolysis of an α-TCP paste. Biomaterials. 2004;25(17):3671-80.
527. Hohl H, Koutsoukos PG, Nancollas GH. The crystallization of hydroxyapatite and dicalcium phosphate dihydrate; representation of growth curves. Journal of Crystal Growth. 1982;57(2):325-35.
528. Nancollas GH, Tomazic B. Growth of calcium phosphate on hydroxyapatite crystals. Effect of supersaturation and ionic medium. The Journal of Physical Chemistry. 1974;78(22):2218-25.
529. Shiwaku Y, Anada T, Yamazaki H, Honda Y, Morimoto S, Sasaki K, et al. Structural, morphological and surface characteristics of two types of octacalcium phosphate-derived fluoride-containing apatitic calcium phosphates. Acta Biomaterialia. 2012;8(12):4417-25.
530. Mura-Galelli M, Narusawa H, Shimada T, Iijima M, Aoba T. Effects of fluoride on precipitation and hydrolysis of octacalcium phosphate in an experimental-model simulating enamel mineralization during amelogenesis. Cells and Materials. 1992;2(3):221-30.
531. Iijima M, Moradian-Oldak J. Control of apatite crystal growth in a fluoride containing amelogenin-rich matrix. Biomaterials. 2005;26(13):1595-603.
532. Bodier-Houlle P, Steuer P, Voegel J-C, Cuisinier FJG. First Experimental Evidence for Human Dentine Crystal Formation Involving Conversion of Octacalcium Phosphate to Hydroxyapatite. Acta Crystallographica Section D. 1998;54(6 Part 2):1377-81.
533. Nelson DGA, Barry JC. High resolution electron microscopy of nonstoichiometric apatite crystals. The Anatomical Record. 1989;224(2):265-76.
534. Lynch R, Mony U, ten Cate J. De-and remineralisation of enamel lesions at low pH under simulated plaque-fluid conditions. Caries research. 2004;38:399-400.
535. Yamazaki H, Margolis HC. Enhanced Enamel Remineralization under Acidic Conditions in vitro. Journal of Dental Research. 2008;87(6):569-74.
536. Lynch RJM, Smith SR. Remineralization Agents – New and Effective or Just Marketing Hype? Advances in Dental Research. 2012;24(2):63-7.
537. Larsen MJ, Fejerkov OLE. Chemical and structural challenges in remineralization of dental enamel lesions. European Journal of Oral Sciences. 1989;97(4):285-96.
538. Ten Cate J, Featherstone J. Physicochemical aspects of fluoride-enamel interactions. Fluoride in dentistry Copenhagen: Munksgaard. 1996:252-72.
539. Adler P, Straub J, Popovics M. Intravital uptake of fluorides by the teeth under various conditions. Journal of dental research. 1950;29(4):549-55.
540. Retief DH, Bradley EL, Holbrook M, Switzer P. Enamel Fluoride Uptake, Distribution and Retention from Topical Fluoride Agents. Caries research. 1983;17(1):44-51.
541. Gruythuysen R, van der Linden L, Wöltgens J, Geraets W. Approximal caries in children. Nederlands tijdschrift voor tandheelkunde. 1991;98(1):38-40.
542. Lucchese A, Bertacci A, Chersoni S, Portelli M. Primary enamel permeability: a SEM evaluation in vivo. European journal of paediatric dentistry: official journal of European Academy of Paediatric Dentistry. 2012;13(3):231-5.
543. Mortimer KV. The Relationship of Deciduous Enamel Structure to Dental Disease. Caries research. 1970;4(3):206-23.
544. Grine FE. Enamel thickness of deciduous and permanent molars in modern Homo sapiens. American Journal of Physical Anthropology. 2005;126(1):14-31.
545. Lindén LÅ, Björkman S, Hattab F. The diffusion in vitro of fluoride and chlorhexidine in the enamel of human deciduous and permanent teeth. Archives of Oral Biology. 1986;31(1):33-7.
546. Shellis RP. Relationship between human enamel structure and the formation of caries-like lesions in vitro. Archives of Oral Biology. 1984;29(12):975-81.
547. Wang LJ, Tang R, Bonstein T, Bush P, Nancollas GH. Enamel Demineralization in Primary and Permanent Teeth. Journal of Dental Research. 2006;85(4):359-63.
548. Apap M. [Mineral components of enamel and post-eruptive maturation]. L'Information dentaire. 1982;64(9):789-805.

549. Vrbič V, Štupar J, Byrne AR. Trace Element Content of Primary and Permanent Tooth Enamel (Short Communication). Caries research. 1987;21(1):37-9.
550. Shashikiran N, Subba Reddy V, Hiremath M. Estimation of trace elements in sound and carious enamel of primary and permanent teeth by atomic absorption spectrophotometry: An *in vitro* study2007 October 1, 2007. 157-62 p.
551. Cutress TW. A method for sampling and analysing thin layers of enamel for carbonate, fluoride and other inorganic components. Archives of Oral Biology. 1972;17(1):225-9.
552. Sønju Clasen AB, Ruyter IE. Quantitative Determination of Type A and Type B Carbonate in Human Deciduous and Permanent Enamel by Means of Fourier Transform Infrared Spectrometry. Advances in Dental Research. 1997;11(4):523-7.
553. Naujoks R, Schade H, Zelinka F. Chemical Composition of Different Areas of the Enamel of Deciduous and Permanent Teeth (The content of Ca, P, CO_2, Na and N_2). Caries research. 1967;1(2):137-43.
554. Lussi A, Kohler N, Zero D, Schaffner M, Megert B. A comparison of the erosive potential of different beverages in primary and permanent teeth using an in vitro model. European Journal of Oral Sciences. 2000;108(2):110-4.
555. Bonar LC, Shimizu M, Roberts JE, Griffin RG, Glimcher MJ. Structural and composition studies on the mineral of newly formed dental enamel: A chemical, X-ray diffraction, and ^{31}p and proton nuclear magnetic resonance study. Journal of Bone and Mineral Research. 1991;6(11):1167-76.
556. Thaveesangpanich P, Itthagarun A, King NM, Wefel JS. The effects of child formula toothpastes on enamel caries using two in vitro pH-cycling models. International dental journal. 2005;55(4):217-23.
557. Thaveesangpanich P, Itthagarun A, King NM, Wefel JS, Tay FR. In vitro model for evaluating the effect of child formula toothpastes on artificial caries in primary dentition enamel. American journal of dentistry. 2005;18(3):212-6.
558. Bachmann L, Diebolder R, Hibst R, Zezell DM. Infrared Absorption Bands of Enamel and Dentin Tissues from Human and Bovine Teeth. Applied Spectroscopy Reviews. 2003;38(1):1-14.
559. Rey C, Lian J, Grynpas M, Shapiro F, Zylberberg L, Glimcher MJ. Non-Apatitic Environments in Bone Mineral: FT-IR Detection, Biological Properties and Changes in Several Disease States. Connective Tissue Research. 1989;21(1-4):267-73.
560. Blumenthal NC, Betts F, Posner AS. Formation and structure of Ca-deficient hydroxyapatite. Calcif Tissue Int. 1981;33(1):111-7.
561. Young RA. Biological Apatite vs Hydroxyapatite at the Atomic Level. Clinical Orthopaedics and Related Research. 1975;113:249-62.
562. Ong JL, Chan DCN. Hydroxyapatite and Their Use As Coatings in Dental Implants: A Review. 2000;28(5&6):667-707.
563. Sun L, Berndt CC, Gross KA, Kucuk A. Material fundamentals and clinical performance of plasma-sprayed hydroxyapatite coatings: A review. Journal of Biomedical Materials Research. 2001;58(5):570-92.
564. Schmitz JP, Hollinger JO, Milam SB. Reconstruction of bone using calcium phosphate bone cements: A critical review. Journal of Oral and Maxillofacial Surgery. 1999;57(9):1122-6.
565. Labella R, Braden M, Deb S. Novel hydroxyapatite-based dental composites. Biomaterials. 1994;15(15):1197-200.
566. Li J, Liao H, Hermansson L. Sintering of partially-stabilized zirconia and partially-stabilized zirconia—hydroxyapatite composites by hot isostatic pressing and pressureless sintering. Biomaterials. 1996;17(18):1787-90.
567. Rizzi SC, Heath DJ, Coombes AGA, Bock N, Textor M, Downes S. Biodegradable polymer/hydroxyapatite composites: Surface analysis and initial attachment of human osteoblasts. Journal of Biomedical Materials Research. 2001;55(4):475-86.
568. Georgiou G, Knowles JC. Glass reinforced hydroxyapatite for hard tissue surgery—Part 1: mechanical properties. Biomaterials. 2001;22(20):2811-5.
569. Sato M, Sambito MA, Aslani A, Kalkhoran NM, Slamovich EB, Webster TJ. Increased osteoblast functions on undoped and yttrium-doped nanocrystalline hydroxyapatite coatings on titanium. Biomaterials. 2006;27(11):2358-69.

570. Thian ES, Huang J, Best SM, Barber ZH, Bonfield W. Novel silicon-doped hydroxyapatite (Si-HA) for biomedical coatings: An in vitro study using acellular simulated body fluid. Journal of Biomedical Materials Research Part B: Applied Biomaterials. 2006;76B(2):326-33.
571. Fielding GA, Roy M, Bandyopadhyay A, Bose S. Antibacterial and biological characteristics of silver containing and strontium doped plasma sprayed hydroxyapatite coatings. Acta Biomaterialia. 2012;8(8):3144-52.
572. Arita IH, Castano VM, Wilkinson DS. Synthesis and processing of hydroxyapatite ceramic tapes with controlled porosity. Journal of Materials Science: Materials in Medicine. 1995;6(1):19-23.
573. Fu Q, Rahaman MN, Dogan F, Bal BS. Freeze casting of porous hydroxyapatite scaffolds. I. Processing and general microstructure. Journal of Biomedical Materials Research Part B: Applied Biomaterials. 2008;86B(1):125-35.
574. Ahn ES, Gleason NJ, Nakahira A, Ying JY. Nanostructure Processing of Hydroxyapatite-based Bioceramics. Nano Letters. 2001;1(3):149-53.
575. Balamurugan A, Balossier G, Kannan S, Rajeswari S. Elaboration of sol–gel derived apatite films on surgical grade stainless steel for biomedical applications. Materials Letters. 2006;60(17–18):2288-93.
576. Chapman AC, Thirlwell LE. Spectra of phosphorus compounds—I the infra-red spectra of orthophosphates. Spectrochimica Acta. 1964;20(6):937-47.
577. Trommer RM, Santos LA, Bergmann CP. Alternative technique for hydroxyapatite coatings. Surface and Coatings Technology. 2007;201(24):9587-93.
578. Elliott J. Structure, crystal chemistry and density of enamel apatites. Dental enamel. 1997;205:54-72.
579. Kwon S-H, Jun Y-K, Hong S-H, Kim H-E. Synthesis and dissolution behavior of β-TCP and HA/β-TCP composite powders. Journal of the European Ceramic Society. 2003;23(7):1039-45.
580. Zyman ZZ, Rokhmistrov DV, Glushko VI, Ivanov IG. Thermal impurity reactions and structural changes in slightly carbonated hydroxyapatite. Journal of Materials Science: Materials in Medicine. 2009;20(7):1389-99.
581. Dowker SEP, Elliott JC. Infrared study of trapped carbon dioxide in thermally treated apatites. Journal of Solid State Chemistry. 1983;47(2):164-73.
582. Gu YW, Loh NH, Khor KA, Tor SB, Cheang P. Spark plasma sintering of hydroxyapatite powders. Biomaterials. 2002;23(1):37-43.
583. Muralithran G, Ramesh S. The effects of sintering temperature on the properties of hydroxyapatite. Ceramics International. 2000;26(2):221-30.
584. Ramesh S, Tan CY, Bhaduri SB, Teng WD, Sopyan I. Densification behaviour of nanocrystalline hydroxyapatite bioceramics. Journal of Materials Processing Technology. 2008;206(1–3):221-30.
585. Uota M, Arakawa H, Kitamura N, Yoshimura T, Tanaka J, Kijima T. Synthesis of High Surface Area Hydroxyapatite Nanoparticles by Mixed Surfactant-Mediated Approach. Langmuir. 2005;21(10):4724-8.
586. Champion E, Gautier S, Bernache-Assollant D. Characterization of hot pressed Al_2O_3-platelet reinforced hydroxyapatite composites. Journal of Materials Science: Materials in Medicine. 1996;7(2):125-30.
587. Bailliez S, Nzihou A. The kinetics of surface area reduction during isothermal sintering of hydroxyapatite adsorbent. Chemical Engineering Journal. 2004;98(1–2):141-52.
588. Berzina-Cimdina L, Borodajenko N. Research of calcium phosphates using Fourier transform infrared spectroscopy: INTECH Open Access Publisher; 2012.
589. Chaudhry AA, Haque S, Kellici S, Boldrin P, Rehman I, Khalid FA, et al. Instant nano-hydroxyapatite: a continuous and rapid hydrothermal synthesis. Chemical Communications. 2006(21):2286-8.
590. Wang Y, Chen J, Wei K, Zhang S, Wang X. Surfactant-assisted synthesis of hydroxyapatite particles. Materials Letters. 2006;60(27):3227-31.
591. Bai X, More K, Rouleau CM, Rabiei A. Functionally graded hydroxyapatite coatings doped with antibacterial components. Acta Biomaterialia. 2010;6(6):2264-73.
592. Sowa MG, Mantsch HH. FT-IR Step-Scan Photoacoustic Phase Analysis and Depth Profiling of Calcified Tissue. Appl Spectrosc. 1994;48(3):316-9.

593. Silva CC, Pinheiro AG, Miranda MAR, Góes JC, Sombra ASB. Structural properties of hydroxyapatite obtained by mechanosynthesis. Solid State Sciences. 2003;5(4):553-8.
594. Li-yun C, Chuan-bo Z, Jian-feng H. Influence of temperature, [Ca^{2+}], Ca/P ratio and ultrasonic power on the crystallinity and morphology of hydroxyapatite nanoparticles prepared with a novel ultrasonic precipitation method. Materials Letters. 2005;59(14–15):1902-6.
595. Panda RN, Hsieh MF, Chung RJ, Chin TS. FTIR, XRD, SEM and solid state NMR investigations of carbonate-containing hydroxyapatite nano-particles synthesized by hydroxide-gel technique. Journal of Physics and Chemistry of Solids. 2003;64(2):193-9.
596. Awonusi A, Morris M, Tecklenburg MJ. Carbonate Assignment and Calibration in the Raman Spectrum of Apatite. Calcif Tissue Int. 2007;81(1):46-52.
597. Cuneyt Tas A, Korkusuz F, Timucin M, Akkas N. An investigation of the chemical synthesis and high-temperature sintering behaviour of calcium hydroxyapatite (HA) and tricalcium phosphate (TCP) bioceramics. Journal of Materials Science: Materials in Medicine. 1997;8(2):91-6.
598. Prokopiev O, Sevostianov I. Dependence of the mechanical properties of sintered hydroxyapatite on the sintering temperature. Materials Science and Engineering: A. 2006;431(1–2):218-27.
599. Champion E. Sintering of calcium phosphate bioceramics. Acta Biomaterialia. 2013;9(4):5855-75.
600. Raynaud S, Champion E, Bernache-Assollant D. Calcium phosphate apatites with variable Ca/P atomic ratio II. Calcination and sintering. Biomaterials. 2002;23(4):1073-80.
601. Rootare HM, Craig RG. Characterization of the compaction and sintering of hydroxyapatite powders by mercury porosimetry. Powder Technology. 1974;9(4):199-211.
602. Bernache-Assollant D, Ababou A, Champion E, Heughebaert M. Sintering of calcium phosphate hydroxyapatite $Ca_{10}(PO_4)_6(OH)_2$ I. Calcination and particle growth. Journal of the European Ceramic Society. 2003;23(2):229-41.
603. Tagai H, Aoki H, Hastings G, Williams D. Preparation of synthetic hydroxyapatite and sintering of apatite ceramics: Mechanical properties of biomaterials. Chapter. 1987;39:213.
604. Lafon JP, Champion E, Bernache-Assollant D. Processing of AB-type carbonated hydroxyapatite $Ca_{10-x}(PO_4)_{6-x}(CO_3)_x(OH)_{2-x-2y}(CO3)_y$ ceramics with controlled composition. Journal of the European Ceramic Society. 2008;28(1):139-47.
605. Landi E, Tampieri A, Celotti G, Sprio S. Densification behaviour and mechanisms of synthetic hydroxyapatites. Journal of the European Ceramic Society. 2000;20(14–15):2377-87.
606. Putlayev V, Veresov A, Pulkin M, Soin A, Kuznetsov V. Silicon-substituted hydroxyapatite ceramics (Si-HAp): densification and grain growth through the prism of sintering theories. Materialwissenschaft und Werkstofftechnik. 2006;37(6):416-21.
607. Rootare HM, Craig RG. Charecterization of hydroxyapatite powders and compacts at room temprature and after sintering at 1200°C. Journal of Oral Rehabilitation. 1978;5(3):293-307.
608. Hoepfner TP, Case ED. The influence of the microstructure on the hardness of sintered hydroxyapatite. Ceramics International. 2003;29(6):699-706.
609. Habelitz S, Marshall Jr GW, Balooch M, Marshall SJ. Nanoindentation and storage of teeth. Journal of Biomechanics. 2002;35(7):995-8.
610. Willems G, Celis JP, Lambrechts P, Braem M, Vanherle G. Hardness and young's modulus determined by nanoindentation technique of filler particles of dental restorative materials compared with human enamel. Journal of Biomedical Materials Research. 1993;27(6):747-55.
611. Wang J, Shaw LL. Nanocrystalline hydroxyapatite with simultaneous enhancements in hardness and toughness. Biomaterials. 2009;30(34):6565-72.
612. Gross KA, Rodríguez-Lorenzo LM. Sintered hydroxyfluorapatites. Part II: Mechanical properties of solid solutions determined by microindentation. Biomaterials. 2004;25(7–8):1385-94.
613. Bezzi G, Celotti G, Landi E, La Torretta TMG, Sopyan I, Tampieri A. A novel sol–gel technique for hydroxyapatite preparation. Materials Chemistry and Physics. 2003;78(3):816-24.
614. Gross KA, Rodríguez-Lorenzo LM. Sintered hydroxyfluorapatites. Part I: Sintering ability of precipitated solid solution powders. Biomaterials. 2004;25(7–8):1375-84.
615. Meyer JL, Eanes ED. A thermodynamic analysis of the amorphous to crystalline calcium phosphate transformation. Calc Tis Res. 1978;25(1):59-68.

616. Tung MS, Brown WE. An intermediate state in hydrolysis of amorphous calcium phosphate. Calcif Tissue Int. 1983;35(1):783-90.
617. Hua Cheng Z, Yasukawa A, Kandori K, Ishikawa T. FTIR Study on incorporation of CO_2 into calcium hydroxyapatite. Journal of the Chemical Society, Faraday Transactions. 1998;94(10):1501-5.
618. Sachlos E, Gotora D, Czernuszka JT. Collagen scaffolds reinforced with biomimetic composite nano-sized carbonate-substituted hydroxyapatite crystals and shaped by rapid prototyping to contain internal microchannels. Tissue engineering. 2006;12(9):2479-87.
619. Elliott JC, Bollet-Quivogne FRG, Anderson P, Dowker SEP, Wilson RM, Davis GR. Acidic demineralization of apatites studied by scanning X-ray microradiography and microtomography. Mineralogical Magazine. 2005;69(5):643-52.
620. Featherstone JDB, Glena R, Shariati M, Shields CP. Dependence of in vitro Demineralization of Apatite and Remineralization of Dental Enamel on Fluoride Concentration. Journal of Dental Research. 1990;69(2 suppl):620-5.
621. Dybowska A, Manning DAC, Collins MJ, Wess T, Woodgate S, Valsami-Jones E. An evaluation of the reactivity of synthetic and natural apatites in the presence of aqueous metals. Science of The Total Environment. 2009;407(8):2953-65.
622. Tenuta LMA, Cerezetti RV, Del Bel Cury AA, Tabchoury CPM, Cury JA. Fluoride Release from CaF_2 and Enamel Demineralization. Journal of Dental Research. 2008;87(11):1032-6.
623. Eslami H, Solati-Hashjin M, Tahriri M. Synthesis and characterization of nanocrystalline fluorinated hydroxyapatite powder by modified wet-chemical process. J Ceram Process Res. 2008;9:224-9.
624. Azami M, Jalilifiroozinezhad S, Mozafari M, editors. Calcium fluoride/hydroxyfluorapatite nanocrystals as novel biphasic solid solution for tooth tissue engineering and regenerative dentistry. Key Engineering Materials; 2012: Trans Tech Publ.
625. Arcís RW, López-Macipe A, Toledano M, Osorio E, Rodríguez-Clemente R, Murtra J, et al. Mechanical properties of visible light-cured resins reinforced with hydroxyapatite for dental restoration. Dental Materials. 2002;18(1):49-57.

Table of Contents

Appendix I

Appendix I presents the analytical FTIR data of the enamel blocks and synthetic FD-HA pellets, which were treated during pH-cycling procedure. Each group contains 5 tables, the first of which corresponds to the experimental conditions used during the pH cycling. The remaining tables correspond to either the 1st, 6th, 11th and 16th day of the pH-cycling for permanent enamel (Chapter 3, Sections 3.1.2, 3.2.2 and 3.3.2) and synthetic FD-HA pellets (Chapter 6, Section 6.2); or to the 1st, 4th, 7th and 10th day of the pH-cycling for primary enamel (Chapter 4, Sections 4.1.2, 4.2.2).

3. pH-Cycling Studies Using Natural Mature Bovine Enamel

Permanent Bovine Enamel

Group M1

Solutions & Treatments	Experimental Conditions
Remineralising Solution (pH)	DW
Demineralising Solution (pH)	DW
Background F^- Concentration (ppm) (Main/ Intermediate Periods)	N/A
F^- Treatment Concentration (ppm)	N/A

Table A-1: Experimental conditions used during the pH-cycling study for the Group M1. Group M1 was treated with DW only.

Day of pH-cycling	Assignment	Peak (cm^{-1})	Area (cm^2)	Height (cm)
1	υ_4 PO_4^{3-}	545	7.168	1.771
		565	9.064	1.637
		579	7.782	1.259
		618	10.481	0.779
	υ_2 CO_3^{2-}	701	31.508	2.524
	υ_4 CO_3^{2-}	836	428.441	10.599
	υ_3 PO_4^{3-}	1025	38.414	0.937
		1052	71.700	2.491
		1119	8.765	0.644
		1159	19.185	1.489
	C=O Stretching	1184	11.077	0.927
	υ_4 CO_3^{2-}	1372	15.693	0.785
	υ_3 CO_3^{2-}	1454	17.980	0.907
		1648	321.791	8.543
	C=O Stretching	1731	174.429	4.576
	HPO_4^{2-}	1976	15.546	0.512
		2159	17.027	0.868
	C-H Stretching	2875	6.792	0.335
		2933	7.174	0.334

Table A-2: FTIR results of Group M1 following the 1st day of the pH-cycling process.

Day of pH-cycling	Assignment	Peak (cm^{-1})	Area (cm^2)	Height (cm)
6	υ_4 PO_4^{3-}	539	62.847	9.026
		622	8.282	0.737
	υ_2 CO_3^{2-}	701	48.035	3.902
	υ_4 CO_3^{2-}	836	746.187	18.481
	υ_3 PO_4^{3-}	1024	65.526	1.811
		1063	131.340	4.489
		1119	17.366	1.287
		1158	34.806	2.692
	C=O Stretching	1184	19.608	1.693
	PO_2	1277	345.924	19.304
	υ_4 CO_3^{2-}	1371	28.713	1.454
	υ_3 CO_3^{2-}	1454	36.365	1.834
	υ_4 CO_3^{2-}	1509	12.847	1.447
	υ_3 CO_3^{2-}	1648	608.457	16.301
	C=O Stretching	1731	351.195	8.948
	HPO_4^{2-}	1976	9.014	0.464
		2027	6.785	0.365
		2158	10.171	0.562
	C-H Stretching	2929	22.386	0.976
		2959	16.638	1.204

Table A-3: FTIR results of Group M1 following the 6th day of the pH-cycling process.

Day of pH-cycling	Assignment	Peak (cm^{-1})	Area (cm^2)	Height (cm)
11	υ_4 PO_4^{3-}	537	72.448	10.800
		543	11.853	2.294
	υ_2 CO_3^{2-}	701	104.092	5.307
	υ_4 CO_3^{2-}	836	794.548	19.708
	υ_3 PO_4^{3-}	1024	53.344	1.482
		1063	145.642	4.906
		1119	16.644	1.267
		1158	36.128	2.814
	C=O Stretching	1184	21.341	1.883
	PO_2	1278	365.358	20.789
	υ_4 CO_3^{2-}	1371	31.069	1.582
	υ_3 CO_3^{2-}	1454	35.049	1.801
	υ_4 CO_3^{2-}	1510	15.139	1.546
	υ_3 CO_3^{2-}	1648	650.147	17.319
	C=O Stretching	1730	346.298	8.916
	HPO_4^{2-}	1976	16.183	0.534
		2159	103.375	1.483
	C-H Stretching	2933	14.215	0.642
		2960	16.748	1.199

Table A-4: FTIR results of Group M1 following the 11th day of the pH-cycling process.

Day of pH-cycling	Assignment	Peak (cm^{-1})	Area (cm^2)	Height (cm)
16	υ_4 PO_4^{3-}	538	26.912	3.068
		565	26.446	2.420
	υ_2 CO_3^{2-}	701	48.205	3.989
	υ_4 CO_3^{2-}	836	768.396	19.058
	υ_3 PO_4^{3-}	1025	61.675	1.772
		1062	87.004	3.195
		1119	14.080	1.045
		1158	32.715	2.531
	C=O Stretching	1184	18.545	1.536
	PO_2	1278	364.270	20.258
	υ_4 CO_3^{2-}	1371	29.270	1.473
	υ_3 CO_3^{2-}	1455	34.420	1.760
	υ_4 CO_3^{2-}	1510	13.733	1.416
	υ_3 CO_3^{2-}	1648	630.736	16.827
	C=O Stretching	1731	329.281	8.414
	HPO_4^{2-}	1977	21.407	0.635
		2160	14.050	0.760
		2219	13.124	0.147
	OH^- (OCP)	2417	3.455	0.027
	C-H Stretching	2926	32.189	1.431
		2959	15.515	1.099

Table A-5: FTIR results of Group M1 following the 16th day of the pH-cycling process.

Group M2

Solutions & Treatments	Experimental Conditions
Remineralising Solution (pH)	DW
Demineralising Solution (pH)	DW
Background F^- Concentration (ppm) (Main/ Intermediate Periods)	0.2
F^- Treatment Concentration (ppm)	N/A

Table A-6: Experimental conditions used during the pH-cycling study for the Group M2. Group M2 was treated with DW and added BF of 0.2 ppm.

Day of pH-cycling	Assignment	Peak (cm^{-1})	Area (cm^2)	Height (cm)
1	υ_4 PO_4^{3-}	560	7.990	1.513
		659	5.142	0.314
	F^- - OH^-	744	7.484	0.527
	υ_4 CO_3^{2-}	856	37.262	2.330
	υ_3 PO_4^{3-}	1011	98.175	2.894
		1109	15.291	0.705
		1156	37.533	1.335
	υ_4 CO_3^{2-}	1369	17.020	0.646
	υ_3 CO_3^{2-}	1440	10.672	0.730
	C=O Stretching	1738	119.383	3.663
	HPO_4^{2-}	1975	7.662	0.856
		2159	22.722	1.230
		2178	17.051	0.154

Table A-7: FTIR results of Group M2 following the 1st day of the pH-cycling process.

Day of pH-cycling	Assignment	Peak (cm^{-1})	Area (cm^2)	Height (cm)
6	υ_4 PO_4^{3-}	545	13.885	2.722
		556	7.615	2.110
		569	13.965	2.196
		614	4.656	0.454
	υ_2 CO_3^{2-}	700	8.161	0.727
	F^- - OH^-	747	14.501	0.818
	υ_4 CO_3^{2-}	833	108.220	2.715
	υ_3 PO_4^{3-}	1017	29.039	0.582
		1061	5.022	0.228
		1118	4.797	0.340
	PO_2	1276	19.065	1.651
	υ_4 CO_3^{2-}	1371	10.827	0.524
	υ_3 CO_3^{2-}	1450	4.369	0.158
		1642	87.907	2.308
	C=O Stretching	1728	69.731	1.827
	HPO_4^{2-}	1974	24.030	0.832
		2030	5.682	0.428
		2095	3.410	0.277
		2159	18.705	1.054
		2179	1.706	0.185
	C-H Stretching	2412	13.853	0.251

Table A-8: FTIR results of Group M2 following the 6th day of the pH-cycling process.

Day of pH-cycling	Assignment	Peak (cm^{-1})	Area (cm^2)	Height (cm)
11	HPO_4^{2-}	535	35.452	5.604
	υ_4 PO_4^{3-}	544	3.684	0.475
		596	7.019	0.862
	OH^-	628	0.129	0.060
	υ_2 CO_3^{2-}	700	7.005	0.640
	F^- - OH^-	749	15.800	0.700
	υ_4 CO_3^{2-}	835	117.337	2.741
	υ_3 PO_4^{3-}	1020	2.594	0.217
		1060	15.632	0.571
	PO_2	1277	27.336	1.853
	υ_4 CO_3^{2-}	1373	10.152	0.495
	υ_3 CO_3^{2-}	1646	89.813	2.402
	C=O Stretching	1730	60.670	1.574
	HPO_4^{2-}	1977	19.154	0.798
		2028	31.271	1.046
		2098	4.752	0.319
		2160	237.823	2.981
	C-H Stretching	2428	10.049	0.152
		2559	4.294	0.057

Table A-9: FTIR results of Group M2 following the 11th day of the pH-cycling process.

Day of pH-cycling	Assignment	Peak (cm^{-1})	Area (cm^2)	Height (cm)
16	HPO_4^{2-}	518	136.164	42.935
		534	64.767	6.243
	$\upsilon_4\ PO_4^{3-}$	554	7.318	1.514
		587	4.840	0.706
		607	4.375	0.471
	OH^-	627	0.777	0.137
	$\upsilon_2\ CO_3^{2-}$	699	11.778	0.899
	F^- - OH^-	749	15.688	0.816
	$\upsilon_4\ CO_3^{2-}$	834	156.605	3.806
	$\upsilon_3\ PO_4^{3-}$	1061	24.893	0.901
		1117	7.277	0.484
	PO_2	1276	56.100	3.185
	$\upsilon_4\ CO_3^{2-}$	1372	12.897	0.628
	$\upsilon_3\ CO_3^{2-}$	1453	7.351	0.272
		1646	126.933	3.196
	C=O Stretching	1727	82.409	2.236
	HPO_4^{2-}	1977	9.861	0.445
		2031	6.229	0.388
		2159	15.228	0.736
		2219	12.263	0.126
	C-H Stretching	2424	0.726	0.109

Table A-10: FTIR results of Group M2 following the 16th day of the pH-cycling process.

Group M3$_{10}$

Solutions & Treatments	Experimental Conditions
Remineralising Solution (pH)	DW
Demineralising Solution (pH)	DW
Background F^- Concentration (ppm) (Main/ Intermediate Periods)	N/A
F^- Treatment Concentration (ppm)	10

Table A-11: Experimental conditions used during the pH-cycling study for the Group M3$_{10}$. Group M3$_{10}$ was treated with DW and F^- treatment of 10 ppm.

Day of pH-cycling	Assignment	Peak (cm^{-1})	Area (cm^2)	Height (cm)
1	υ_4 PO_4^{3-}	544	78.090	13.432
		559	8.207	1.939
		573	6.453	1.342
		588	1.828	0.353
		607	3.922	0.537
	OH^-	633	2.583	0.338
	PO_2	1276	1.078	0.089
	HPO_4^{2-}	1960	0.256	0.024
		1976	1.353	0.196
		2023	1.319	0.142
		2159	9.922	0.571
		2182	0.909	0.104

Table A-12: FTIR results of Group M3$_{10}$ following the 1st day of the pH-cycling process.

Day of pH-cycling	Assignment	Peak (cm^{-1})	Area (cm^2)	Height (cm)
6	HPO_4^{2-}	521	26.969	8.281
		537	12.108	1.601
	$\upsilon_4\ PO_4^{3-}$	545	0.374	0.288
		557	8.916	1.357
		574	12.239	2.257
		598	8.326	0.756
	$\upsilon_4\ CO_3^{2-}$	660	9.275	0.581
	$\upsilon_1\ CO_3^{2-}$	897	5.317	0.391
	$\upsilon_3\ PO_4^{3-}$	1030	54.347	0.986
		1054	13.910	0.856
		1107	13.203	0.758
		1160	18.825	1.059
	PO_2	1278	8.911	0.603
	$\upsilon_4\ CO_3^{2-}$	1369	4.877	0.270
	$\upsilon_3\ CO_3^{2-}$	1430	17.995	0.433
		1642	2.857	0.015
	C=O Stretching	1734	5.583	0.257
	HPO_4^{2-}	1976	14.072	0.565
		2034	4.387	0.287
		2099	1.019	0.122
		2161	19.693	0.815
		2190	0.167	0.042
	CO_2	2348	1.688	0.214
	$\upsilon_3\ CO_3^{2-}$	2393	1.902	0.071
	OH^- (OCP)	2430	0.158	0.031
	C-H Stretching	2862	0.760	0.073
		2916	0.762	0.091
	OH^-	3451	0.629	0.065

Table A-13: FTIR results of Group $M3_{10}$ following the 6^{th} day of the pH-cycling process.

Day of pH-cycling	Assignment	Peak (cm^{-1})	Area (cm^2)	Height (cm)
11	HPO_4^{2-}	517	2.480	0.910
		532	91.068	10.466
	$\upsilon_4\ PO_4^{3-}$	548	5.835	1.090
		574	11.004	1.956
		594	4.442	0.565
		618	4.784	0.603
	$\upsilon_2\ CO_3^{2-}$	700	21.987	1.882
	F^- - OH^-	753	30.195	1.369
	$\upsilon_4\ CO_3^{2-}$	834	351.403	8.347
	$\upsilon_3\ PO_4^{3-}$	915	2.227	0.232
		1023	48.564	1.069
		1059	48.404	1.686
		1119	5.723	0.385
		1157	13.599	1.061
	C=O Stretching	1184	6.556	0.601
	PO_2	1277	148.518	7.695
	$\upsilon_4\ CO_3^{2-}$	1372	12.418	0.626
	$\upsilon_3\ CO_3^{2-}$	1454	12.964	0.715
		1510	5.467	0.571
		1646	253.000	6.592
	C=O Stretching	1729	117.646	3.174
	HPO_4^{2-}	1976	3.888	0.666
		2009	1.174	0.127
		2024	4.906	0.274
		2159	55.339	1.668
	CO_2	2360	5.103	0.367
	C-H Stretching	2573	0.616	0.066
		2873	4.310	0.243
		2932	4.717	0.220
		2961	4.959	0.356
	OH^-	3661	1.556	0.136

Table A-14: FTIR results of Group $M3_{10}$ following the 11th day of the pH-cycling process.

Day of pH-cycling	Assignment	Peak (cm^{-1})	Area (cm^2)	Height (cm)
16	HPO_4^{2-}	530	29.265	6.449
	$\upsilon_4\ PO_4^{3-}$	551	11.954	2.332
		565	9.951	2.027
		577	8.150	1.186
		619	12.603	0.961
	$\upsilon_4\ CO_3^{2-}$	679	2.739	0.161
	$\upsilon_2\ CO_3^{2-}$	701	39.711	3.289
	F^- - OH^-	754	46.564	2.226
	$\upsilon_4\ CO_3^{2-}$	836	572.529	14.351
	$\upsilon_3\ PO_4^{3-}$	916	4.111	0.394
		1025	40.434	1.058
		1062	105.205	3.505
		1119	12.248	0.878
		1158	26.223	2.025
	C=O Stretching	1184	14.742	1.274
	PO_2	1277	260.493	14.791
	$\upsilon_4\ CO_3^{2-}$	1371	22.355	1.110
	$\upsilon_3\ CO_3^{2-}$	1454	26.092	1.345
		1510	9.895	1.144
		1549	4.259	0.257
		1648	470.204	12.472
	C=O Stretching	1730	236.950	6.188
	HPO_4^{2-}	1975	14.469	0.616
		2160	12.156	0.601
		2225	19.287	0.097
	OH^- (OCP)	2410	13.465	0.246
	C-H Stretching	2875	4.648	0.387
		2926	1.669	0.054
		2959	10.873	0.793

Table A-15: FTIR results of Group $M3_{10}$ following the 16th day of the pH-cycling process.

Group M3$_{250}$

Solutions & Treatments	Experimental Conditions
Remineralising Solution (pH)	DW
Demineralising Solution (pH)	DW
Background F^- Concentration (ppm) (Main/ Intermediate Periods)	N/A
F^- Treatment Concentration (ppm)	250

Table A-16: Experimental conditions used during the pH-cycling study for the Group M3$_{250}$. Group M3$_{250}$ was treated with DW and F^- treatment of 250 ppm.

Day of pH-cycling	Assignment	Peak (cm^{-1})	Area (cm^2)	Height (cm)
1	HPO_4^{2-}	524	75.753	13.010
		537	6.415	1.650
	$\upsilon_4\ PO_4^{3-}$	554	30.686	3.116
		577	10.361	1.431
		595	2.126	0.380
		621	5.033	0.584
	$\upsilon_2\ CO_3^{2-}$	698	9.616	0.534
	$F^- - OH^-$	754	4.893	0.283
	$\upsilon_4\ CO_3^{2-}$	832	64.890	1.704
	$\upsilon_3\ PO_4^{3-}$	1067	2.620	0.171
		1116	1.506	0.105
		1157	2.491	0.227
	C=O Stretching	1181	1.702	0.136
	PO_2	1276	26.536	1.444
	$\upsilon_4\ CO_3^{2-}$	1369	2.120	0.126
	$\upsilon_3\ CO_3^{2-}$	1457	0.329	0.006
		1640	3.835	0.378
		1655	3.100	0.194
	C=O Stretching	1726	2.676	0.149
	HPO_4^{2-}	1976	25.963	0.921
		2028	45.166	1.250
		2160	252.535	3.147
	CO_2	2349	1.662	0.246
	OH^- (OCP)	2431	0.004	0.005

Table A-17: FTIR results of Group M3$_{250}$ following the 1st day of the pH-cycling process.

Day of pH-cycling	Assignment	Peak (cm^{-1})	Area (cm^2)	Height (cm)
6	HPO_4^{2-}	525	60.647	10.550
	υ_4 PO_4^{3-}	544	4.196	1.142
		574	6.752	1.299
		598	11.282	1.056
		618	4.806	0.818
	υ_2 CO_3^{2-}	700	21.630	1.606
	F^- - OH^-	753	28.016	1.293
	υ_4 CO_3^{2-}	833	279.760	6.489
	υ_3 PO_4^{3-}	1022	26.636	0.682
		1060	36.532	1.262
		1119	4.734	0.393
		1158	11.865	0.870
	C=O Stretching	1183	5.717	0.495
	PO_2	1276	106.849	5.749
	υ_4 CO_3^{2-}	1371	10.829	0.524
	υ_3 CO_3^{2-}	1455	14.524	0.702
		1509	5.537	0.566
		1647	9.306	0.539
	C=O Stretching	1727	111.916	2.969
	HPO_4^{2-}	1975	6.661	0.609
		2022	31.996	0.873
		2159	19.821	1.024
	OH^- (OCP)	2432	0.023	0.003
	C-H Stretching	2874	8.502	0.271
		2928	12.647	0.533
		2957	7.400	0.363

Table A-18: FTIR results of Group $M3_{250}$ following the 6th day of the pH-cycling process.

Day of pH-cycling	Assignment	Peak (cm^{-1})	Area (cm^2)	Height (cm)
11	HPO_4^{2-}	521	36.722	9.577
	υ_4 PO_4^{3-}	559	49.011	4.588
		576	13.314	1.920
	OH^-	634	7.690	0.698
	υ_2 CO_3^{2-}	701	73.928	3.299
	F^- - OH^-	753	37.091	1.958
	υ_4 CO_3^{2-}	836	517.586	12.767
	υ_3 PO_4^{3-}	1062	87.906	2.988
		1119	11.087	0.799
		1158	22.017	1.704
	C=O Stretching	1184	12.685	1.071
	PO_2	1277	234.963	13.066
	υ_4 CO_3^{2-}	1371	19.098	0.964
	υ_3 CO_3^{2-}	1454	21.460	1.070
		1648	412.306	10.921
	C=O Stretching	1731	195.404	5.260
	HPO_4^{2-}	2160	37.572	1.151
		2219	6.626	0.025
	υ_3 CO_3^{2-}	2425	0.651	0.086
	C-H Stretching	2932	10.948	0.470
		2960	13.968	0.792

Table A-19: FTIR results of Group $M3_{250}$ following the 11^{th} day of the pH-cycling process.

Day of pH-cycling	Assignment	Peak (cm^{-1})	Area (cm^2)	Height (cm)
16	HPO_4^{2-}	532	37.465	5.869
	$\upsilon_4\ PO_4^{3-}$	543	4.688	1.454
		562	11.237	1.165
		579	10.775	1.685
		624	2.899	0.431
	$\upsilon_2\ CO_3^{2-}$	701	76.925	3.415
	F^- - OH^-	754	43.135	2.055
	$\upsilon_4\ CO_3^{2-}$	836	534.858	13.301
	$\upsilon_3\ PO_4^{3-}$	917	3.674	0.362
		1025	44.190	1.118
		1063	93.364	3.165
		1119	11.003	0.818
		1158	23.401	1.800
	C=O Stretching	1184	12.719	1.114
	PO_2	1278	25.282	14.347
	$\upsilon_4\ CO_3^{2-}$	1371	20.158	1.042
	$\upsilon_3\ CO_3^{2-}$	1454	21.708	1.137
		1510	9.687	0.988
		1648	456.709	11.918
	C=O Stretching	1730	220.350	5.707
	HPO_4^{2-}	1975	16.918	0.591
		2031	6.311	0.440
		2160	7.961	0.501
	CO_2	2361	7.148	0.508
	C-H Stretching	2932	9.926	0.456
		2960	11.237	0.773

Table A-20: FTIR results of Group $M3_{250}$ following the 16th day of the pH-cycling process.

Group M4$_{10}$

Solutions & Treatments	Experimental Conditions
Remineralising Solution (pH)	DW
Demineralising Solution (pH)	DW
Background F^- Concentration (ppm) (Main/ Intermediate Periods)	0.2/ 2.0
F^- Treatment Concentration (ppm)	10

Table A-21: Experimental conditions used during the pH-cycling study for the Group M4$_{10}$. Group M4$_{10}$ was treated with DW, F^- treatment of 10 ppm and BF of 0.2 ppm and 2.0 ppm for the main and intermediate remineralising periods respectively.

Day of pH-cycling	Assignment	Peak (cm^{-1})	Area (cm^2)	Height (cm)
1	HPO_4^{2-}	538	8.283	1.525
	υ_4 PO_4^{3-}	553	11.328	1.874
		568	6.576	1.214
		585	4.701	0.824
	F^- - OH^-	752	4.508	0.310
	υ_4 CO_3^{2-}	837	51.084	1.359
	υ_3 PO_4^{3-}	1059	4.224	0.125
	PO_2	1277	20.977	1.160
	υ_3 CO_3^{2-}	1650	30.120	0.935
	C=O Stretching	1731	17.447	0.520
	HPO_4^{2-}	1973	1.029	0.108
		2157	4.549	0.249
	CO_2	2339	5.558	0.293
		2362	9.790	0.592

Table A-22: FTIR results of Group M4$_{10}$ following the 1st day of the pH-cycling process.

Day of pH-cycling	Assignment	Peak (cm^{-1})	Area (cm^2)	Height (cm)
6	HPO_4^{2-}	523	68.639	14.145
		535	28.931	5.315
	$\upsilon_4\ PO_4^{3-}$	560	29.238	3.094
		586	11.407	1.178
		621	6.154	0.706
	$\upsilon_4\ CO_3^{2-}$	670	2.036	0.349
	$\upsilon_2\ CO_3^{2-}$	700	10.909	0.883
	F^- - OH^-	754	11.516	0.648
	$\upsilon_4\ CO_3^{2-}$	833	157.674	3.785
	$\upsilon_3\ PO_4^{3-}$	1023	22.340	0.589
		1062	19.633	0.709
		1120	2.804	0.211
		1158	5.788	0.462
	C=O Stretching	1184	3.594	0.297
	PO_2	1277	58.851	3.315
	$\upsilon_4\ CO_3^{2-}$	1371	4.860	0.234
	$\upsilon_3\ CO_3^{2-}$	1455	4.962	0.309
		1509	3.325	0.302
		1650	101.269	2.809
	C=O Stretching	1731	49.900	1.453
	HPO_4^{2-}	1976	-3.969	0.593
		2022	2.060	0.092
		2159	15.191	0.860
		2177	4.126	0.075
	CO_2	2341	14.877	0.698
		2361	28.959	1.834
	C-H Stretching	2877	1.829	0.127
		2960	3.507	0.210

Table A-23: FTIR results of Group $M4_{10}$ following the 6th day of the pH-cycling process.

Day of pH-cycling	Assignment	Peak (cm^{-1})	Area (cm^2)	Height (cm)
11	υ_4 PO_4^{3-}	546	2.006	0.550
		619	13.207	1.278
	υ_2 CO_3^{2-}	700	13.897	1.224
	F^- - OH^-	754	17.711	0.872
	υ_4 CO_3^{2-}	836	221.860	5.401
	υ_3 PO_4^{3-}	1023	20.439	0.563
		1063	35.881	1.239
		1158	9.255	0.734
	PO_2	1277	94.879	5.328
	υ_4 CO_3^{2-}	1371	7.912	0.394
	υ_3 CO_3^{2-}	1456	8.271	0.443
	C=O Stretching	1728	86.207	2.219
	HPO_4^{2-}	2159	7.400	0.451

Table A-24: FTIR results of Group $M4_{10}$ following the 11th day of the pH-cycling process.

Day of pH-cycling	Assignment	Peak (cm^{-1})	Area (cm^2)	Height (cm)
16	HPO_4^{2-}	549	47.598	3.726
	υ_4 PO_4^{3-}	568	6.405	1.182
		586	1.006	0.322
		613	7.177	0.946
	υ_2 CO_3^{2-}	700	18.867	1.468
	F^- - OH^-	754	18.216	0.883
	υ_4 CO_3^{2-}	836	229.584	5.765
	υ_3 PO_4^{3-}	1024	22.593	0.600
		1064	37.770	1.352
		1118	5.097	0.354
		1158	9.585	0.714
	C=O Stretching	1183	5.955	0.490
	PO_2	1278	100.967	5.613
	υ_4 CO_3^{2-}	1372	8.514	0.418
	υ_3 CO_3^{2-}	1454	10.009	0.551
		1646	172.618	4.619
	C=O Stretching	1730	79.734	2.240
	HPO_4^{2-}	1976	0.096	0.021
		2161	5.471	0.277
	C-H Stretching	2919	6.997	0.384
		2955	5.205	0.224

Table A-25: FTIR results of Group $M4_{10}$ following the 16th day of the pH-cycling process.

Group M4$_{250}$

Solutions & Treatments	Experimental Conditions
Remineralising Solution (pH)	DW
Demineralising Solution (pH)	DW
Background F^- Concentration (ppm) (Main/ Intermediate Periods)	0.2/ 1.0
F^- Treatment Concentration (ppm)	250

Table A-26: Experimental conditions used during the pH-cycling study for the Group M4$_{250}$. Group M4$_{250}$ was treated with DW, F^- treatment of 250 ppm and BF of 0.2 ppm and 1.0 ppm for the main and intermediate remineralising periods respectively.

Day of pH-cycling	Assignment	Peak (cm^{-1})	Area (cm^2)	Height (cm)
1	HPO_4^{2-}	518	25.095	45.227
	υ_4 PO_4^{3-}	549	18.898	2.145
		567	9.630	1.147
		581	6.190	0.939
	υ_2 CO_3^{2-}	701	10.226	0.903
	F^- - OH^-	754	13.857	0.710
	υ_4 CO_3^{2-}	835	167.896	3.992
	υ_3 PO_4^{3-}	1023	17.717	0.431
		1059	24.250	0.763
		1120	3.523	0.289
		1158	7.296	0.558
	C=O Stretching	1184	3.696	0.324
	PO_2	1277	66.909	3.763
	υ_4 CO_3^{2-}	1371	6.241	0.319
	υ_3 CO_3^{2-}	1456	6.796	0.353
		1647	-11.226	0.250
	C=O Stretching	1732	65.387	1.726
	HPO_4^{2-}	2034	2.303	0.149
		2162	12.029	0.504
		2253	3.147	0.071
	C-H Stretching	2932	2.175	0.127
		2960	5.459	0.296

Table A-27: FTIR results of Group M4$_{250}$ following the 1st day of the pH-cycling process.

Day of pH-cycling	Assignment	Peak (cm^{-1})	Area (cm^2)	Height (cm)
6	$\upsilon_4\ PO_4^{3-}$	552	12.341	1.885
		572	4.003	0.768
		592	5.795	0.908
	$\upsilon_4\ CO_3^{2-}$	674	5.374	0.398
	$\upsilon_2\ CO_3^{2-}$	700	34.852	2.841
	F^- - OH^-	754	36.741	1.932
	$\upsilon_4\ CO_3^{2-}$	836	509.050	12.691
	$\upsilon_3\ PO_4^{3-}$	917	4.050	0.374
		1024	50.500	1.309
		1062	83.727	2.877
		1119	10.927	0.813
		1158	21.718	1.666
	C=O Stretching	1184	12.985	1.101
	PO_2	1278	225.772	12.610
	$\upsilon_4\ CO_3^{2-}$	1363	17.921	0.949
	$\upsilon_3\ CO_3^{2-}$	1419	2.974	0.316
		1447	22.240	1.158
		1504	9.281	0.899
		1604	392.976	10.538
	C=O Stretching	1712	206.309	5.528
	HPO_4^{2-}	1960	8.705	0.486
		2138	36.501	1.153
		2208	5.084	0.074
	CO_2	2352	3.748	0.325
	C-H Stretching	2848	7.907	0.406
		2910	9.830	0.424
		2954	9.658	0.718

Table A-28: FTIR results of Group $M4_{250}$ following the 6th day of the pH-cycling process.

Day of pH-cycling	Assignment	Peak (cm^{-1})	Area (cm^2)	Height (cm)
11	HPO_4^{2-}	523	131.332	16.215
	$\upsilon_4\ PO_4^{3-}$	548	18.234	2.768
		571	10.890	1.321
	OH^-	625	9.191	0.968
	$\upsilon_2\ CO_3^{2-}$	701	28.806	2.507
	F^- - OH^-	754	41.104	1.880
	$\upsilon_4\ CO_3^{2-}$	835	475.474	11.687
	$\upsilon_3\ PO_4^{3-}$	1023	49.731	1.268
		1062	78.066	2.726
		1119	9.945	0.697
		1158	19.104	1.482
	C=O Stretching	1184	11.172	0.952
	PO_2	1277	196.360	10.993
	$\upsilon_4\ CO_3^{2-}$	1372	17.152	0.885
	$\upsilon_3\ CO_3^{2-}$	1454	20.241	1.092
		1510	8.277	0.795
		1646	355.100	9.623
	C=O Stretching	1731	172.304	4.635
	HPO_4^{2-}	1975	19.015	0.722
		2022	12.930	0.376
		2159	17.197	0.885
		2207	9.321	0.112
	C-H Stretching	2932	11.682	0.423

Table A-29: FTIR results of Group $M4_{250}$ following the 11^{th} day of the pH-cycling process.

Day of pH-cycling	Assignment	Peak (cm^{-1})	Area (cm^2)	Height (cm)
16	HPO_4^{2-}	524	56.009	10.487
	$\upsilon_4\ PO_4^{3-}$	546	8.517	1.637
		555	3.645	0.933
		571	9.930	1.417
		623	7.644	0.811
	$\upsilon_4\ CO_3^{2-}$	676	6.952	0.417
	$\upsilon_2\ CO_3^{2-}$	700	34.465	3.127
	F^- - OH^-	754	49.246	2.507
	$\upsilon_4\ CO_3^{2-}$	836	669.601	16.487
	$\upsilon_3\ PO_4^{3-}$	917	5.663	0.522
		1024	31.119	1.403
		1061	111.842	3.750
		1118	13.575	0.970
		1158	26.282	2.051
	C=O Stretching	1184	14.047	1.244
	PO_2	1278	301.006	16.847
	$\upsilon_4\ CO_3^{2-}$	1371	25.471	1.254
	$\upsilon_3\ CO_3^{2-}$	1434	2.765	0.338
		1454	26.514	1.453
		1510	9.321	1.012
		1547	8.802	0.437
		1648	559.601	14.548
	C=O Stretching	1731	231.685	6.222
	HPO_4^{2-}	1977	8.591	0.466
		2017	1.868	0.144
		2032	5.245	0.344
		2160	19.496	0.869
	$\upsilon_3\ CO_3^{2-}$	2364	4.685	0.412
	C-H Stretching	2875	7.868	0.461
		2933	12.895	0.537
		2960	11.404	0.772
	OH^-	3236	0.907	0.038

Table A-30: FTIR results of Group $M4_{250}$ following the 16th day of the pH-cycling process.

Group M5

Solutions & Treatments	Experimental Conditions
Remineralising Solution (pH)	PF (6.58)
Demineralising Solution (pH)	DW
Background F^- Concentration (ppm) (Main/ Intermediate Periods)	N/A
F^- Treatment Concentration (ppm)	N/A

Table A-31: Experimental conditions used during the pH-cycling study for the Group M5. Group M5 was treated with PF during the remineralising period and DW as the acid challenge.

Day of pH-cycling	Assignment	Peak (cm^{-1})	Area (cm^2)	Height (cm)
1	HPO_4^{2-}	529	84.334	13.965
	$\upsilon_4\ PO_4^{3-}$	541	3.331	0.897
		557	6.582	1.194
		577	5.687	0.628
		601	8.425	1.219
	$\upsilon_4\ CO_3^{2-}$	833	51.459	1.373
	$\upsilon_3\ PO_4^{3-}$	1025	13.674	0.357
		1051	3.219	0.107
	PO_2	1277	18.134	0.997
	$\upsilon_3\ CO_3^{2-}$	1650	4.592	0.203
	HPO_4^{2-}	1975	19.944	0.697
		2159	14.917	0.842
		2179	2.411	0.152
		2218	9.091	0.170
	OH^- (OCP)	2432	1.138	0.040
	C-H Stretching	2559	1.173	0.074

Table A-32: FTIR results of Group M5 following the 1st day of the pH-cycling process.

Day of pH-cycling	Assignment	Peak (cm^{-1})	Area (cm^2)	Height (cm)
6	HPO_4^{2-}	529	92.287	8.463
	$\upsilon_4\ PO_4^{3-}$	542	7.505	1.129
		551	6.042	1.083
		566	12.218	2.147
		580	4.920	1.047
		600	4.521	0.505
		619	5.623	0.851
	$\upsilon_2\ CO_3^{2-}$	700	4.160	0.435
	$\upsilon_4\ CO_3^{2-}$	827	56.110	1.410
	$\upsilon_3\ PO_4^{3-}$	1056	3.573	0.108
	PO_2	1275	21.406	1.171
	$\upsilon_4\ CO_3^{2-}$	1368	2.009	0.099
	$\upsilon_3\ CO_3^{2-}$	1457	5.494	0.230
	C=O Stretching	1733	0.939	0.026
	HPO_4^{2-}	1977	8.248	0.778
		2023	14.104	0.410
		2159	66.842	1.689
	C-H Stretching	2570	3.890	0.084

Table A-33: FTIR results of Group M5 following the 6th day of the pH-cycling process.

Day of pH-cycling	Assignment	Peak (cm^{-1})	Area (cm^2)	Height (cm)
11	HPO_4^{2-}	528	75.996	10.795
	$\upsilon_4\ PO_4^{3-}$	541	23.679	3.715
		558	13.332	2.850
		575	4.853	0.887
		609	3.029	0.550
	OH^-	632	3.148	0.501
	$\upsilon_2\ CO_3^{2-}$	700	6.263	0.515
	$\upsilon_4\ CO_3^{2-}$	833	83.419	2.135
	$\upsilon_3\ PO_4^{3-}$	1021	8.667	0.211
		1063	4.108	0.164
		1160	2.862	0.220
	PO_2	1277	31.333	1.650
	$\upsilon_4\ CO_3^{2-}$	1371	2.315	0.147
	$\upsilon_3\ CO_3^{2-}$	1455	3.092	0.213
		1645	46.241	1.428
	C=O Stretching	1731	22.586	0.698
	HPO_4^{2-}	1976	10.541	0.859
		2024	47.454	1.255
		2159	24.893	1.311
		2179	5.915	0.114
	CO_2	2341	2.473	0.329
		2360	13.808	0.870
	OH^- (OCP)	2445	1.745	0.100

Table A-34: FTIR results of Group M5 following the 11th day of the pH-cycling process.

Day of pH-cycling	Assignment	Peak (cm^{-1})	Area (cm^2)	Height (cm)
16	HPO_4^{2-}	518	127.641	22.216
	υ_4 PO_4^{3-}	552	38.453	4.282
		600	16.784	1.465
	υ_4 CO_3^{2-}	828	2.011	0.117
	υ_1 CO_3^{2-}	897	11.052	0.599
	υ_3 PO_4^{3-}	1022	472.869	8.031
		1104	13.271	0.594
		1160	12.073	0.814
	PO_2	1277	3.594	0.266
	υ_4 CO_3^{2-}	1368	6.713	0.366
	υ_3 CO_3^{2-}	1428	4.872	0.263
		1651	24.841	0.630
	HPO_4^{2-}	1976	30.857	1.040
		2023	12.454	0.391
		2160	29.866	1.421
	υ_3 CO_3^{2-}	2339	11.406	0.662
	CO_2	2359	27.090	1.877
	C-H Stretching	2883	1.088	0.050
	OH^-	3729	3.970	0.237

Table A-35: FTIR results of Group M5 following the 16th day of the pH-cycling process.

Group M6

Solutions & Treatments	Experimental Conditions
Remineralising Solution (pH)	PF (6.58)
Demineralising Solution (pH)	DW
Background F^- Concentration (ppm) (Main/ Intermediate Periods)	0.2
F^- Treatment Concentration (ppm)	N/A

Table A-36: Experimental conditions used during the pH-cycling study for the Group M6. Group M6 was treated with PF during the remineralising period , DW as the acid challenge and added 0.2 ppm of F^- as BF.

Day of pH-cycling	Assignment	Peak (cm^{-1})	Area (cm^2)	Height (cm)
1	υ_4 PO_4^{3-}	543	13.556	1.108
		552	19.795	1.996
		589	12.745	1.372
	υ_2 CO_3^{2-}	701	12.439	1.123
	υ_4 CO_3^{2-}	856	50.561	1.871
	υ_3 PO_4^{3-}	1013	50.369	1.745
		1147	23.496	0.900
	υ_4 CO_3^{2-}	1370	14.035	0.556
	υ_3 CO_3^{2-}	1442	12.191	0.656
	C=O Stretching	1738	107.713	2.768
	HPO_4^{2-}	1976	26.503	0.812
		2027	31.903	0.991
		2160	44.892	1.535
		2240	3.509	0.035
	C-H Stretching	2428	4.048	0.122

Table A-37: FTIR results of Group M6 following the 1st day of the pH-cycling process.

Day of pH-cycling	Assignment	Peak (cm^{-1})	Area (cm^2)	Height (cm)
6	HPO_4^{2-}	517	3.741	3.626
		531	43.926	7.406
	$\upsilon_4\ PO_4^{3-}$	543	30.573	4.817
		558	12.816	2.144
		573	14.970	2.376
		600	2.786	0.528
		614	2.477	0.601
	$\upsilon_2\ CO_3^{2-}$	704	1.597	0.194
	$\upsilon_4\ CO_3^{2-}$	833	1.086	0.064
	$\upsilon_1\ PO_4^{3-}$	917	1.798	0.176
	$\upsilon_3\ PO_4^{3-}$	995	0.747	0.080
	PO_2	1277	4.183	0.284
	$\upsilon_3\ CO_3^{2-}$	1541	1.292	0.132
		1652	5.672	0.228
	C=O Stretching	1731	1.025	0.080
	HPO_4^{2-}	1976	8.256	0.412
		2031	2.505	0.128
		2067	1.206	0.118
		2099	1.421	0.138
		2159	13.414	0.598
		2219	1.361	0.115
		2245	3.702	0.125
	$\upsilon_3\ CO_3^{2-}$	2392	1.392	0.065
	C-H Stretching	2416	0.892	0.085
	OH^-	3557	1.112	0.122

Table A-38: FTIR results of Group M6 following the 6th day of the pH-cycling process.

Day of pH-cycling	Assignment	Peak (cm^{-1})	Area (cm^2)	Height (cm)
11	HPO_4^{2-}	531	151.708	15.421
	$\upsilon_4\ PO_4^{3-}$	552	28.023	3.787
	F^- - OH^-	753	12.502	0.630
	$\upsilon_4\ CO_3^{2-}$	855	31.909	0.991
	$\upsilon_3\ PO_4^{3-}$	1011	13.785	0.646
		1157	11.675	0.433
	$\upsilon_2\ CO_3^{2-}$	1371	8.685	0.353
	C=O Stretching	1744	48.036	1.379
	HPO_4^{2-}	1978	24.356	0.912
		2160	247.991	2.977

Table A-39: FTIR results of Group M6 following the 11th day of the pH-cycling process.

Day of pH-cycling	Assignment	Peak (cm^{-1})	Area (cm^2)	Height (cm)
16	HPO_4^{2-}	518	217.997	72.128
		531	11.736	3.170
	$\upsilon_4\ PO_4^{3-}$	563	5.294	1.199
		596	12.576	1.382
	OH^-	632	6.405	0.800
	$F^- - OH^-$	749	14.666	0.740
	$\upsilon_4\ CO_3^{2-}$	829	114.741	2.703
	$\upsilon_3\ PO_4^{3-}$	1062	5.242	0.254
	PO_2	1275	36.820	1.969
	$\upsilon_4\ CO_3^{2-}$	1373	6.386	0.369
	$\upsilon_3\ CO_3^{2-}$	1640	75.326	2.064
	C=O Stretching	1724	37.486	1.068
	HPO_4^{2-}	1978	20.538	0.712
		2158	21.047	1.035
		2226	10.370	0.108
	C-H Stretching	2407	3.915	0.133

Table A-40: FTIR results of Group M6 following the 16th day of the pH-cycling process.

Group M7$_{10}$

Solutions & Treatments	Experimental Conditions
Remineralising Solution (pH)	PF (6.58)
Demineralising Solution (pH)	DW
Background F^- Concentration (ppm) (Main/ Intermediate Periods)	N/A
F^- Treatment Concentration (ppm)	10

Table A-41: Experimental conditions used during the pH-cycling study for the Group M7$_{10}$. Group M7$_{10}$ was treated with PF during the remineralising period, DW as the acid challenge and 10 ppm of F^-.

Day of pH-cycling	Assignment	Peak (cm^{-1})	Area (cm^2)	Height (cm)
1	HPO_4^{2-}	518	1.968	53.768
	$\upsilon_4\ PO_4^{3-}$	560	19.693	2.687
		575	12.858	1.636
		599	5.771	0.596
	$\upsilon_4\ CO_3^{2-}$	664	1.662	0.096
	$\upsilon_2\ CO_3^{2-}$	696	3.887	0.256
	$F^- - OH^-$	745	2.909	0.151
	$\upsilon_4\ CO_3^{2-}$	828	39.895	1.001
	$\upsilon_3\ PO_4^{3-}$	1026	35.398	0.528
		1159	8.534	0.492
	PO_2	1276	14.955	0.867
	$\upsilon_3\ CO_3^{2-}$	1452	3.723	0.166
		1641	30.950	0.954
	C=O Stretching	1735	17.306	0.524
	HPO_4^{2-}	1976	17.436	0.735
		2022	8.975	0.259
		2159	14.705	0.840

Table A-42: FTIR results of Group M7$_{10}$ following the 1st day of the pH-cycling process.

Day of pH-cycling	Assignment	Peak (cm^{-1})	Area (cm^2)	Height (cm)
6	HPO_4^{2-}	536	350.648	0.709
	$\upsilon_4\ PO_4^{3-}$	548	13.060	2.010
		568	14.769	1.361
		600	6.162	0.756
		611	3.155	0.452
	OH^-	628	3.201	0.454
	$\upsilon_2\ CO_3^{2-}$	699	3.655	0.563
	F^- - OH^-	753	13.088	0.661
	$\upsilon_4\ CO_3^{2-}$	831	154.755	3.629
	$\upsilon_3\ PO_4^{3-}$	1025	233.944	4.311
		1104	5.707	0.226
		1155	3.852	0.292
	PO_2	1276	47.475	2.492
	$\upsilon_4\ CO_3^{2-}$	1372	4.245	0.206
	$\upsilon_3\ CO_3^{2-}$	1454	7.759	0.345
		1510	1.916	0.211
		1640	91.755	2.425
	C=O Stretching	1733	37.531	1.050
	HPO_4^{2-}	1974	2.998	0.745
		2024	39.202	1.012
		2160	14.690	0.773
	C-H Stretching	2851	4.328	0.322
		2920	13.479	0.590
		2959	3.057	0.208

Table A-43: FTIR results of Group $M7_{10}$ following the 6^{th} day of the pH-cycling process.

Day of pH-cycling	Assignment	Peak (cm^{-1})	Area (cm^2)	Height (cm)
11	HPO_4^{2-}	518	103.113	29.032
	$\upsilon_4\ PO_4^{3-}$	533	6.022	1.231
		542	4.494	1.275
		562	16.641	1.846
		603	23.648	1.416
	$\upsilon_4\ CO_3^{2-}$	671	1.661	0.108
	$\upsilon_2\ CO_3^{2-}$	700	5.607	0.680
	$F^- - OH^-$	752	17.146	0.814
	$\upsilon_4\ CO_3^{2-}$	829	165.641	3.742
	$\upsilon_3\ PO_4^{3-}$	1023	355.658	4.634
		1156	4.855	0.390
		1183	2.338	0.214
	PO_2	1276	47.502	2.674
	$\upsilon_4\ CO_3^{2-}$	1371	4.723	0.252
	$\upsilon_3\ CO_3^{2-}$	1456	6.421	0.337
		1510	2.338	0.303
		1640	16.555	0.609
	C=O Stretching	1726	46.556	1.321
	HPO_4^{2-}	1977	6.746	0.684
		2032	2.436	0.055
		2095	0.268	0.054
		2160	14.744	0.869
		2177	1.999	0.126

Table A-44: FTIR results of Group $M7_{10}$ following the 11th day of the pH-cycling process.

Day of pH-cycling	Assignment	Peak (cm^{-1})	Area (cm^2)	Height (cm)
16	HPO_4^{2-}	530	69.220	9.327
	$\upsilon_4\ PO_4^{3-}$	552	17.037	1.895
		564	9.534	2.090
		574	5.512	1.147
		602	25.604	1.736
	$\upsilon_2\ CO_3^{2-}$	700	14.786	1.436
	F^- - OH^-	752	28.943	1.327
	$\upsilon_4\ CO_3^{2-}$	831	285.745	6.662
	$\upsilon_3\ PO_4^{3-}$	1023	774.304	11.268
		1154	3.977	0.323
		1184	3.630	0.352
	PO_2	1276	91.027	4.980
	$\upsilon_4\ CO_3^{2-}$	1371	7.399	0.393
	$\upsilon_3\ CO_3^{2-}$	1453	8.965	0.503
		1509	4.217	0.412
		1645	177.551	4.464
	C=O Stretching	1728	70.487	1.950
	HPO_4^{2-}	1976	6.974	1.172
		2030	58.840	1.672
		2160	315.149	4.128
	C-H Stretching	2877	2.845	0.141
		2957	3.800	0.233
	OH^-	3500	0.031	0.015

Table A-45: FTIR results of Group $M7_{10}$ following the 16^{th} day of the pH-cycling process.

Group M7$_{250}$

Solutions & Treatments	Experimental Conditions
Remineralising Solution (pH)	PF (6.58)
Demineralising Solution (pH)	DW
Background F^- Concentration (ppm) (Main/ Intermediate Periods)	N/A
F^- Treatment Concentration (ppm)	250

Table A-46: Experimental conditions used during the pH-cycling study for the Group M7$_{250}$. Group M7$_{250}$ was treated with PF during the remineralising period, DW as the acid challenge and 250 ppm of F^-.

Day of pH-cycling	Assignment	Peak (cm^{-1})	Area (cm^2)	Height (cm)
1	υ_4 PO_4^{3-}	550	8.989	2.054
		566	19.004	1.967
	F^- - OH^-	749	7.196	0.387
	υ_4 CO_3^{2-}	829	1.620	0.041
	υ_3 PO_4^{3-}	1023	20.967	0.450
	PO_2	1275	23.670	1.180
	υ_3 CO_3^{2-}	1638	49.154	1.368
	C=O Stretching	1726	23.780	0.693
	HPO_4^{2-}	1977	19.441	1.048
		2025	2.782	0.128
		2160	83.170	2.451
	CO_2	2362	9.821	0.679
	C-H Stretching	2550	9.929	0.064

Table A-47: FTIR results of Group M7$_{250}$ following the 1st day of the pH-cycling process.

Day of pH-cycling	Assignment	Peak (cm^{-1})	Area (cm^2)	Height (cm)
6	HPO_4^{2-}	530	66.659	10.498
	υ_4 PO_4^{3-}	583	13.278	1.395
	F^- - OH^-	751	12.476	0.622
	υ_4 CO_3^{2-}	831	158.293	3.700
	υ_3 PO_4^{3-}	1002	23.318	0.331
	PO_2	1276	92.499	3.459
	υ_4 CO_3^{2-}	1644	100.238	2.763
	υ_3 CO_3^{2-}	1730	57.911	1.514
	HPO_4^{2-}	1978	8.048	0.288

Table A-48: FTIR results of Group M7$_{250}$ following the 6th day of the pH-cycling process.

Day of pH-cycling	Assignment	Peak (cm^{-1})	Area (cm^2)	Height (cm)
11	HPO_4^{2-}	539	22.078	2.964
	$\upsilon_4\ PO_4^{3-}$	561	4.735	0.666
		570	3.327	0.734
		580	2.790	0.616
		606	4.453	0.463
		619	2.779	0.491
	$\upsilon_4\ CO_3^{2-}$	670	2.604	0.449
	$\upsilon_2\ CO_3^{2-}$	699	7.217	0.729
	F^- - OH^-	753	19.954	0.941
	$\upsilon_4\ CO_3^{2-}$	829	170.330	3.825
	$\upsilon_3\ PO_4^{3-}$	1000	1.019	0.080
		1021	59.608	1.294
		1052	8.641	0.230
		1156	6.553	0.512
		1183	2.791	0.286
	PO_2	1276	60.137	3.027
	$\upsilon_4\ CO_3^{2-}$	1369	5.835	0.272
	$\upsilon_3\ CO_3^{2-}$	1432	1.301	0.106
		1455	7.115	0.389
		1509	3.870	0.390
		1640	109.596	3.042
	C=O Stretching	1727	55.313	1.526
	HPO_4^{2-}	1977	15.093	0.565
		2012	1.746	0.192
		2033	4.393	0.336
		2160	11.130	0.685
		2173	1.450	0.078
		2212	1.666	0.163
	CO_2	2340	22.207	1.072
		2360	40.173	2.658
	C-H Stretching	2875	1.887	0.145
		2932	1.398	0.115
		2957	4.707	0.217
	OH^-	3731	3.394	0.259

Table A-49: FTIR results of Group $M7_{250}$ following the 11th day of the pH-cycling process.

Day of pH-cycling	Assignment	Peak (cm^{-1})	Area (cm^2)	Height (cm)
16	HPO_4^{2-}	531	28.418	6.130
	υ_4 PO_4^{3-}	568	6.986	1.384
		581	8.300	1.371
	υ_2 CO_3^{2-}	700	21.557	1.508
	F^- - OH^-	752	26.608	1.202
	υ_4 CO_3^{2-}	831	250.230	5.712
	υ_3 PO_4^{3-}	1025	283.215	4.324
		1157	8.015	0.627
	PO_2	1276	78.813	4.368
	υ_4 CO_3^{2-}	1371	7.455	0.377
	υ_3 CO_3^{2-}	1454	9.047	0.459
		1643	164.714	4.238
	C=O Stretching	1729	73.930	2.004
	HPO_4^{2-}	1976	16.668	1.072
		2030	10.819	0.624
		2159	29.657	1.650
	OH^- (OCP)	2441	5.436	0.118
	C-H Stretching	2562	4.781	0.012

Table A-50: FTIR results of Group $M7_{250}$ following the 16^{th} day of the pH-cycling process.

Group M8$_{10}$

Solutions & Treatments	Experimental Conditions
Remineralising Solution (pH)	PF (6.58)
Demineralising Solution (pH)	DW
Background F^- Concentration (ppm) (Main/ Intermediate Periods)	0.2/ 2.0
F^- Treatment Concentration (ppm)	10

Table A-51: Experimental conditions used during the pH-cycling study for the Group M8$_{10}$. Group M8$_{10}$ was treated with PF during the remineralising period, DW as the acid challenge, 10 ppm of F^- and 0.2 and 2.0 ppm of F^- during the main and intermediate remineralisation period respectively.

Day of pH-cycling	Assignment	Peak (cm^{-1})	Area (cm^2)	Height (cm)
1	HPO_4^{2-}	528	88.623	16.672
	υ_4 PO_4^{3-}	539	6.540	1.592
		553	5.311	1.195
		574	7.971	1.387
		612	4.468	0.444
	OH^-	630	2.060	0.329
	υ_4 CO_3^{2-}	668	2.735	0.309
	υ_3 PO_4^{3-}	1010	5.191	0.292
		1152	1.277	0.068
	PO_2	1247	18.779	0.539
	C=O Stretching	1743	22.706	0.682
	HPO_4^{2-}	2161	2.942	0.266

Table A-52: FTIR results of Group M8$_{10}$ following the 1st day of the pH-cycling process.

Day of pH-cycling	Assignment	Peak (cm^{-1})	Area (cm^2)	Height (cm)
6	HPO_4^{2-}	517	160.298	25.585
	υ_4 PO_4^{3-}	542	25.210	2.146
		572	27.354	3.427
		610	2.959	0.544
	OH^-	635	1.042	0.173
	υ_4 CO_3^{2-}	663	1.941	0.201
	υ_2 CO_3^{2-}	703	15.230	1.241
	F^- - OH^-	751	22.749	0.922
	υ_4 CO_3^{2-}	856	53.960	2.871
	υ_3 PO_4^{3-}	1012	101.063	3.187
		1111	8.005	0.441
		1151	56.401	1.743
	PO_2	1246	169.830	4.058
	υ_4 CO_3^{2-}	1370	27.892	1.051
	υ_3 CO_3^{2-}	1442	22.167	1.185
		1469	3.764	0.389
	C=O Stretching	1738	203.920	4.818
	HPO_4^{2-}	1991	2.832	0.238
		2091	1.164	0.074
		2119	0.467	0.061
	C-H Stretching	2989	10.583	0.389

Table A-53: FTIR results of Group $M8_{10}$ following the 6^{th} day of the pH-cycling process.

Day of pH-cycling	Assignment	Peak (cm^{-1})	Area (cm^2)	Height (cm)
11	υ_4 PO_4^{3-}	544	14.354	1.603
		565	16.916	1.695
		590	4.779	0.483
	υ_2 CO_3^{2-}	703	11.433	1.032
	F^- - OH^-	748	15.058	0.694
	υ_4 CO_3^{2-}	856	45.259	2.515
	υ_3 PO_4^{3-}	1011	62.836	2.328
		1111	9.241	0.489
		1155	48.253	1.517
	υ_3 CO_3^{2-}	1442	13.558	0.755
	C=O Stretching	1742	309.109	4.121
	HPO_4^{2-}	1993	11.098	0.693
		2087	17.545	0.475
		2118	11.527	0.327
	CO_2	2333	32.452	0.437
	C-H Stretching	2986	5.617	0.181

Table A-54: FTIR results of Group $M8_{10}$ following the 11^{th} day of the pH-cycling process.

Day of pH-cycling	Assignment	Peak (cm^{-1})	Area (cm^2)	Height (cm)
16	HPO_4^{2-}	534	36.726	5.234
	υ_4 PO_4^{3-}	551	31.156	3.185
		571	9.955	1.938
	υ_2 CO_3^{2-}	702	35.496	2.976
	F^- - OH^-	753	45.876	1.904
	υ_4 CO_3^{2-}	856	58.279	3.369
	υ_3 PO_4^{3-}	1012	123.132	3.676
		1112	7.967	0.446
		1147	76.805	2.534
	υ_4 CO_3^{2-}	1371	28.785	1.100
	υ_3 CO_3^{2-}	1441	25.489	1.313
		1653	15.521	0.378
	C=O Stretching	1734	206.343	5.205
	HPO_4^{2-}	1976	1.415	0.905
		2029	11.280	0.525
		2159	19.790	1.107
		2178	0.828	0.105
	C-H Stretching	2428	1.662	0.119
		2563	5.672	0.078
		2919	10.269	0.533

Table A-55: FTIR results of Group $M8_{10}$ following the 16th day of the pH-cycling process.

Group 8_{250}

Solutions & Treatments	Experimental Conditions
Remineralising Solution (pH)	PF (6.58)
Demineralising Solution (pH)	DW
Background F^- Concentration (ppm) (Main/ Intermediate Periods)	0.2/ 1.0
F^- Treatment Concentration (ppm)	250

Table A-56: Experimental conditions used during the pH-cycling study for the Group $M8_{250}$. Group $M8_{250}$ was treated with PF during the remineralising period, DW as the acid challenge and 250 ppm of F^- and 0.2 and 2.0 ppm of F^- during the main and intermediate remineralisation period respectively.

Day of pH-cycling	Assignment	Peak (cm^{-1})	Area (cm^2)	Height (cm)
1	HPO_4^{2-}	526	13.207	15.106
	υ_4 PO_4^{3-}	547	10.865	1.898
		575	1.335	0.421
		587	4.982	0.763
		610	5.652	0.701
	OH^-	635	4.306	0.536
	υ_2 CO_3^{2-}	702	10.436	0.990
	F^- - OH^-	749	15.862	0.741
	υ_4 CO_3^{2-}	856	48.433	2.697
	υ_3 PO_4^{3-}	1011	94.395	2.948
		1111	13.510	0.646
		1151	48.193	1.447
	υ_4 CO_3^{2-}	1371	21.842	0.899
	υ_3 CO_3^{2-}	1441	18.381	1.018
		1469	2.406	0.362
	C=O Stretching	1741	166.522	4.235
	HPO_4^{2-}	1976	8.633	1.148
		2024	1.192	0.018
		2159	36.656	1.852
	OH^- (OCP)	2440	12.137	0.215
	C-H Stretching	2920	2.032	0.138
		2985	6.862	0.314

Table A-57: FTIR results of Group $M8_{250}$ following the 1st day of the pH-cycling process.

Day of pH-cycling	Assignment	Peak (cm^{-1})	Area (cm^2)	Height (cm)
6	HPO_4^{2-}	529	78.466	10.231
	υ_4 PO_4^{3-}	544	5.175	1.000
		567	9.070	0.979
		606	2.408	0.366
	υ_2 CO_3^{2-}	702	9.503	0.854
	F^- - OH^-	755	14.037	0.623
	υ_4 CO_3^{2-}	856	33.383	1.976
	υ_3 PO_4^{3-}	1012	77.359	2.308
		1110	9.031	0.462
		1149	41.436	1.260
	υ_4 CO_3^{2-}	1370	3.063	0.322
	υ_3 CO_3^{2-}	1442	15.385	0.840
		1469	3.218	0.332
	C=O Stretching	1738	129.529	3.449
	HPO_4^{2-}	1976	4.418	0.578
		2015	1.463	0.139
		2027	5.833	0.344
		2159	198.696	2.533
	C-H Stretching	2575	0.604	0.056
		2851	1.024	0.108
		2988	5.692	0.228
	OH^-	3725	0.160	0.014

Table A-58: FTIR results of Group $M8_{250}$ following the 6th day of the pH-cycling process.

Day of pH-cycling	Assignment	Peak (cm^{-1})	Area (cm^2)	Height (cm)
11	HPO_4^{2-}	518	92.690	27.076
		534	13.240	2.711
	υ_4 PO_4^{3-}	556	6.311	1.452
		571	8.399	1.534
		614	15.839	0.924
	υ_2 CO_3^{2-}	702	10.054	0.929
	F^- - OH^-	746	21.333	1.135
	υ_4 CO_3^{2-}	856	75.822	4.365
	υ_3 PO_4^{3-}	1011	163.779	5.217
		1110	26.204	1.231
		1157	76.696	2.517
	υ_4 CO_3^{2-}	1370	34.047	1.392
	υ_3 CO_3^{2-}	1441	23.195	1.428
		1469	3.154	0.516
	C=O Stretching	1740	231.469	6.641
	HPO_4^{2-}	1976	17.823	0.711
		2159	20.959	1.104
		2212	8.949	0.134
	C-H Stretching	2587	2.489	0.054
		2921	1.844	0.108
		2991	8.457	0.336

Table A-59: FTIR results of Group $M8_{250}$ following the 11th day of the pH-cycling process.

Day of pH-cycling	Assignment	Peak (cm^{-1})	Area (cm^2)	Height (cm)
16	HPO_4^{2-}	530	15.421	2.606
	υ_4 PO_4^{3-}	543	22.039	3.167
	υ_2 CO_3^{2-}	702	50.824	4.341
	F^- - OH^-	756	74.745	2.846
	υ_4 CO_3^{2-}	856	116.022	6.746
	υ_3 PO_4^{3-}	1012	241.747	7.326
		1112	22.033	1.156
		1148	148.291	4.796
	υ_4 CO_3^{2-}	1371	60.639	2.242
	υ_3 CO_3^{2-}	1443	49.185	2.634
	C=O Stretching	1737	441.245	10.470
	HPO_4^{2-}	1976	29.382	1.014
		2023	3.653	0.172
		2159	23.831	1.287
		2177	20.473	0.141
	C-H Stretching	2921	11.672	0.520
		2989	11.329	0.436

Table A-60: FTIR results of Group $M8_{250}$ following the 16th day of the pH-cycling process.

Group M9

Solutions & Treatments	Experimental Conditions
Remineralising Solution (pH)	DW
Demineralising Solution (pH)	AC (4.90)
Background F^- Concentration (ppm) (Main/ Intermediate Periods)	N/A
F^- Treatment Concentration (ppm)	N/A

Table A-61: Experimental conditions used during the pH-cycling study for the Group M9. Group M9 was treated with DW during the remineralising period and AC during the demineralisation.

Day of pH-cycling	Assignment	Peak (cm^{-1})	Area (cm^2)	Height (cm)
1	HPO_4^{2-}	522	226.559	30.871
	υ_4 PO_4^{3-}	546	15.653	3.170
		571	11.335	1.606
		601	7.191	0.857
	OH^-	625	4.050	0.592
	υ_4 CO_3^{2-}	856	10.243	0.654
	υ_3 PO_4^{3-}	1011	18.647	0.701
		1162	13.058	0.441
	υ_3 CO_3^{2-}	1443	3.746	0.259
	C=O Stretching	1744	22.829	0.900
	HPO_4^{2-}	1977	10.525	0.923
		2027	51.991	1.429
		2160	288.476	3.639
	OH^- (OCP)	2439	2.910	0.143
	C-H Stretching	2555	8.858	0.060

Table A-62: FTIR results of Group M9 following the 1st day of the pH-cycling process.

Day of pH-cycling	Assignment	Peak (cm^{-1})	Area (cm^2)	Height (cm)
6	HPO_4^{2-}	526	46.132	9.729
	υ_4 PO_4^{3-}	538	16.794	2.923
		552	17.830	2.199
	υ_4 CO_3^{2-}	853	16.688	0.896
	υ_3 PO_4^{3-}	1009	29.241	0.982
		1110	4.981	0.295
		1157	18.274	0.571
	υ_3 CO_3^{2-}	1442	6.197	0.352
	C=O Stretching	1737	32.840	1.139
	HPO_4^{2-}	1977	18.208	0.706
		2020	2.470	0.204
		2159	13.431	0.849
		2212	10.590	0.133

Table A-63: FTIR results of Group M9 following the 6th day of the pH-cycling process.

Day of pH-cycling	Assignment	Peak (cm^{-1})	Area (cm^2)	Height (cm)
11	HPO_4^{2-}	522	80.418	9.522
	υ_4 PO_4^{3-}	545	11.095	2.261
		556	12.572	1.914
		583	14.308	1.914
	υ_4 CO_3^{2-}	855	41.006	2.254
	υ_3 PO_4^{3-}	1010	80.554	2.567
		1111	13.528	0.577
		1158	45.883	1.442
	υ_3 CO_3^{2-}	1441	14.854	0.856
	C=O Stretching	1737	117.497	3.431
	HPO_4^{2-}	1976	32.674	1.028
		2030	43.298	1.324
		2160	281.141	3.544
	OH^- (OCP)	2436	4.070	0.048
	C-H Stretching	2556	10.480	0.110
		2985	6.318	0.243

Table A-64: FTIR results of Group M9 following the 11th day of the pH-cycling process.

Day of pH-cycling	Assignment	Peak (cm^{-1})	Area (cm^2)	Height (cm)
16	HPO_4^{2-}	534	21.551	3.281
	υ_4 PO_4^{3-}	572	11.925	1.760
		615	5.391	0.670
	υ_4 CO_3^{2-}	857	10.102	0.721
	υ_3 PO_4^{3-}	1011	16.633	0.753
		1155	15.312	0.472
	υ_3 CO_3^{2-}	1743	25.994	0.969
	HPO_4^{2-}	1975	21.282	0.790
		2023	2.347	0.142
		2159	16.066	0.938
		2175	15.220	0.122
	OH^- (OCP)	2432	0.412	0.063

Table A-65: FTIR results of Group M9 following the 16th day of the pH-cycling process.

Group M10

Solutions & Treatments	Experimental Conditions
Remineralising Solution (pH)	DW
Demineralising Solution (pH)	AC (4.90)
Background F^- Concentration (ppm) (Main/ Intermediate Periods)	0.2
F^- Treatment Concentration (ppm)	N/A

Table A-66: Experimental conditions used during the pH-cycling study for the Group M10. Group M10 was treated with DW during the remineralising period, AC during the demineralisation period and added 0.2 ppm of F^- as BF.

Day of pH-cycling	Assignment	Peak (cm^{-1})	Area (cm^2)	Height (cm)
1	HPO_4^{2-}	531	20.931	3.359
	υ_4 PO_4^{3-}	548	30.628	3.941
		569	11.700	1.923
	υ_2 CO_3^{2-}	702	9.157	0.810
	F^- - OH^-	750	17.819	0.694
	υ_4 CO_3^{2-}	854	68.296	2.214
	υ_3 PO_4^{3-}	1012	66.289	1.955
		1111	7.919	0.485
		1151	28.707	0.987
	υ_4 CO_3^{2-}	1371	19.338	0.773
	υ_3 CO_3^{2-}	1441	12.510	0.695
		1653	31.997	0.857
	C=O Stretching	1736	119.051	3.253
	HPO_4^{2-}	1977	1.262	0.871
		2161	18.910	0.953
		2175	2.410	0.090
	CO_2	2362	6.006	0.432
	C-H Stretching	2923	2.665	0.157

Table A-67: FTIR results of Group M10 following the 1st day of the pH-cycling process.

Day of pH-cycling	Assignment	Peak (cm^{-1})	Area (cm^2)	Height (cm)
6	HPO_4^{2-}	527	17.540	3.984
		539	16.763	2.262
	υ_4 PO_4^{3-}	561	11.318	1.737
	υ_2 CO_3^{2-}	701	22.517	1.886
	F^- - OH^-	755	26.640	1.119
	υ_4 CO_3^{2-}	856	51.914	1.991
	υ_3 PO_4^{3-}	1013	64.832	1.901
		1147	42.809	1.419
	υ_3 CO_3^{2-}	1442	18.053	0.891
	C=O Stretching	1732	152.434	3.908
	HPO_4^{2-}	1975	26.782	1.030
		2159	83.542	2.587
	C-H Stretching	2550	0.065	0.004

Table A-68: FTIR results of Group M10 following the 6th day of the pH-cycling process.

Day of pH-cycling	Assignment	Peak (cm^{-1})	Area (cm^2)	Height (cm)
11	HPO_4^{2-}	531	150.986	13.896
	υ_4 PO_4^{3-}	563	9.053	2.225
		582	0.798	0.262
	υ_2 CO_3^{2-}	701	6.704	0.568
	F^- - OH^-	746	9.814	0.439
	υ_4 CO_3^{2-}	856	13.206	0.684
	υ_3 PO_4^{3-}	1012	9.747	0.499
		1146	14.235	0.491
	υ_2 CO_3^{2-}	1443	12.587	0.429
		1655	6.796	0.240
	C=O Stretching	1736	47.733	1.408
	HPO_4^{2-}	1976	-24.710	1.286
		2025	60.948	1.553
		2159	339.223	4.164
	C-H Stretching	2532	22.948	0.147

Table A-69: FTIR results of Group M10 following the 11th day of the pH-cycling process.

Day of pH-cycling	Assignment	Peak (cm^{-1})	Area (cm^2)	Height (cm)
16	HPO_4^{2-}	528	16.949	4.532
		537	13.802	3.295
	$\upsilon_4\ PO_4^{3-}$	589	9.286	1.084
		618	0.138	0.037
	$\upsilon_2\ CO_3^{2-}$	701	18.579	1.688
	$F^- - OH^-$	748	28.779	1.196
	$\upsilon_4\ CO_3^{2-}$	855	101.438	3.137
	$\upsilon_3\ PO_4^{3-}$	1012	95.318	2.684
		1149	46.642	1.556
	$\upsilon_4\ CO_3^{2-}$	1371	30.302	1.066
	$\upsilon_3\ CO_3^{2-}$	1442	20.630	1.061
		1650	59.573	1.458
	C=O Stretching	1738	175.144	4.447
	HPO_4^{2-}	1976	5.501	1.346
		2023	5.135	0.278
		2160	289.330	4.133
	CO_2	2362	18.029	1.226

Table A-70: FTIR results of Group M10 following the 16th day of the pH-cycling process.

Group $M11_{10}$

Solutions & Treatments	Experimental Conditions
Remineralising Solution (pH)	DW
Demineralising Solution (pH)	AC (4.90)
Background F^- Concentration (ppm) (Main/ Intermediate Periods)	N/A
F^- Treatment Concentration (ppm)	10

Table A-71: Experimental conditions used during the pH-cycling study for the Group $M11_{10}$. Group $M11_{10}$ was treated with DW during the remineralising period, AC during the demineralisation period and 10 ppm of F^-.

Day of pH-cycling	Assignment	Peak (cm^{-1})	Area (cm^2)	Height (cm)
1	HPO_4^{2-}	524	94.606	15.023
	$\upsilon_4\ PO_4^{3-}$	546	12.807	1.776
		558	5.382	1.096
		567	4.148	1.111
		581	4.897	0.993
		600	5.182	0.893
	$\upsilon_2\ CO_3^{2-}$	703	3.049	0.276
	$F^- - OH^-$	760	1.525	0.131
	$\upsilon_4\ CO_3^{2-}$	853	5.685	0.370
	$\upsilon_3\ PO_4^{3-}$	1012	5.989	0.353
		1147	3.560	0.187
	$\upsilon_3\ CO_3^{2-}$	1439	3.844	0.215
	C=O Stretching	1735	4.320	0.167
	HPO_4^{2-}	1976	22.070	0.915
		2013	2.031	0.209
		2027	6.972	0.264
		2159	59.342	1.753

Table A-72: FTIR results of Group $M11_{10}$ following the 1st day of the pH-cycling process.

Day of pH-cycling	Assignment	Peak (cm^{-1})	Area (cm^2)	Height (cm)
6	HPO_4^{2-}	527	20.040	2.873
	υ_4 PO_4^{3-}	548	12.904	1.589
		567	5.289	1.187
		583	14.433	1.900
		608	3.237	0.440
	OH^-	630	2.541	0.350
	υ_2 CO_3^{2-}	701	2.947	0.233
	F^- - OH^-	745	5.053	0.307
	υ_4 CO_3^{2-}	856	24.662	1.569
	υ_3 PO_4^{3-}	1011	60.338	1.914
		1110	8.682	0.460
		1157	30.325	1.026
	υ_4 CO_3^{2-}	1372	12.732	0.523
	υ_3 CO_3^{2-}	1442	8.144	0.493
		1543	3.421	0.293
		1650	1.691	0.146
	C=O Stretching	1739	83.952	2.469
	HPO_4^{2-}	1977	19.369	0.752
		2028	6.881	0.265
		2159	22.881	1.142
		2183	6.460	0.041
	C-H Stretching	2850	6.838	0.559
		2918	26.232	0.960

Table A-73: FTIR results of Group $M11_{10}$ following the 6th day of the pH-cycling process.

Day of pH-cycling	Assignment	Peak (cm^{-1})	Area (cm^2)	Height (cm)
11	HPO_4^{2-}	524	49.193	8.191
	υ_4 PO_4^{3-}	541	28.616	3.507
		597	6.493	0.675
	υ_2 CO_3^{2-}	702	9.872	0.812
	F^- - OH^-	756	12.400	0.496
	υ_4 CO_3^{2-}	855	21.484	1.241
	υ_3 PO_4^{3-}	1011	36.335	1.248
		1110	4.812	0.239
		1148	9.191	0.524
	υ_4 CO_3^{2-}	1369	9.600	0.401
	υ_3 CO_3^{2-}	1441	8.258	0.468
	C=O Stretching	1735	71.104	1.804
	HPO_4^{2-}	1976	15.360	0.590
		2025	12.581	0.408
		2159	48.701	1.510
		2214	7.708	0.120

Table A-74: FTIR results of Group $M11_{10}$ following the 11th day of the pH-cycling process.

Day of pH-cycling	Assignment	Peak (cm^{-1})	Area (cm^2)	Height (cm)
16	HPO_4^{2-}	525	22.342	5.567
	υ_4 PO_4^{3-}	556	7.792	1.713
	υ_2 CO_3^{2-}	702	45.255	3.852
	F^- - OH^-	756	72.924	2.690
	υ_4 CO_3^{2-}	857	110.637	6.362
	υ_3 PO_4^{3-}	1012	225.454	6.822
		1112	19.286	1.071
		1148	138.556	4.417
	υ_3 CO_3^{2-}	1443	43.571	2.413
	C=O Stretching	1739	365.440	8.847
	HPO_4^{2-}	1977	19.696	0.777
		2027	36.176	1.052
		2160	73.189	2.088
	C-H Stretching	2989	10.422	0.416

Table A-75: FTIR results of Group $M11_{10}$ following the 16^{th} day of the pH-cycling process.

Group $M11_{250}$

Solutions & Treatments	Experimental Conditions
Remineralising Solution (pH)	DW
Demineralising Solution (pH)	AC (4.90)
Background F^- Concentration (ppm) (Main/ Intermediate Periods)	N/A
F^- Treatment Concentration (ppm)	250

Table A-76: Experimental conditions used during the pH-cycling study for the Group $M11_{250}$. Group $M11_{250}$ was treated with DW during the remineralising period, AC during the demineralisation period and 250 ppm of F^-.

Day of pH-cycling	Assignment	Peak (cm^{-1})	Area (cm^2)	Height (cm)
1	HPO_4^{2-}	519	153.865	44.403
	υ_4 PO_4^{3-}	538	11.770	1.907
		559	16.531	2.532
		597	27.684	1.330
	υ_4 CO_3^{2-}	872	14.135	0.733
	υ_3 PO_4^{3-}	1021	265.824	3.681
	υ_3 CO_3^{2-}	1406	11.673	0.368
		1639	14.473	0.392
	HPO_4^{2-}	2001	1.152	0.228
		2068	4.113	0.213
		2122	4.771	0.269
	CO_2	2340	19.199	0.771
		2362	24.609	1.664

Table A-77: FTIR results of Group $M11_{250}$ following the 1st day of the pH-cycling process.

Day of pH-cycling	Assignment	Peak (cm^{-1})	Area (cm^2)	Height (cm)
6	HPO_4^{2-}	532	117.151	15.086
	υ_4 PO_4^{3-}	583	29.422	3.382
	OH^-	632	7.522	0.975
	υ_2 CO_3^{2-}	699	69.147	5.865
	F^- - OH^-	759	57.971	2.458
	υ_3 PO_4^{3-}	912	32.686	1.032
		1029	128.809	3.205
		1077	36.404	1.765
	C=O Stretching	1176	15.844	0.570
	υ_4 CO_3^{2-}	1384	31.958	1.046
	υ_3 CO_3^{2-}	1452	50.341	2.218
		1564	40.385	1.257
	C=O Stretching	1726	205.789	6.358

Table A-78: FTIR results of Group $M11_{250}$ following the 6th day of the pH-cycling process.

Day of pH-cycling	Assignment	Peak (cm^{-1})	Area (cm^2)	Height (cm)
11	HPO_4^{2-}	520	91.242	26.384
	υ_4 PO_4^{3-}	540	120.690	11.740
		579	0.000	0.989
		611	0.387	0.116
	υ_2 CO_3^{2-}	699	53.071	4.520
	F^- - OH^-	758	40.746	1.833
	υ_4 CO_3^{2-}	844	13.204	0.803
	υ_3 PO_4^{3-}	911	8.579	0.426
		1035	98.800	2.165
		1073	19.410	1.050
	C=O Stretching	1177	10.124	0.355
	υ_4 CO_3^{2-}	1382	32.885	0.962
	υ_3 CO_3^{2-}	1452	9.935	0.774
		1561	1.129	0.045
	C=O Stretching	1726	116.792	4.012
	C-H Stretching	2927	11.862	0.533

Table A-79: FTIR results of Group $M11_{250}$ following the 11th day of the pH-cycling process.

Day of pH-cycling	Assignment	Peak (cm^{-1})	Area (cm^2)	Height (cm)
16	HPO_4^{2-}	523	97.149	20.951
	υ_4 PO_4^{3-}	544	73.403	5.768
		560	48.144	5.338
		599	46.289	3.099
	υ_4 CO_3^{2-}	662	6.016	0.394
		871	38.578	1.758
	υ_3 PO_4^{3-}	1005	491.076	6.103
	υ_3 CO_3^{2-}	1405	40.270	1.029
		1452	3.960	0.160
		1557	11.107	0.397
		1649	5.392	0.178
	HPO_4^{2-}	2112	1.136	0.112

Table A-80: FTIR results of Group $M11_{250}$ following the 16th day of the pH-cycling process.

Group M12$_{10}$

Solutions & Treatments	Experimental Conditions
Remineralising Solution (pH)	DW
Demineralising Solution (pH)	AC (4.90)
Background F^- Concentration (ppm) (Main/ Intermediate Periods)	0.2/ 2.0
F^- Treatment Concentration (ppm)	10

Table A-81: Experimental conditions used during the pH-cycling study for the Group M12$_{10}$. Group M12$_{10}$ was treated with DW during the remineralising period, AC during the demineralisation period, 10 ppm of F^- and 0.2 and 2.0 ppm of BF during the main and intermediate remineralisation period respectively.

Day of pH-cycling	Assignment	Peak (cm^{-1})	Area (cm^2)	Height (cm)
1	HPO_4^{2-}	522	294.244	48.869
	υ_4 PO_4^{3-}	539	2.551	0.714
		567	12.042	1.712
	υ_2 CO_3^{2-}	698	32.060	2.482
	F^- - OH^-	758	23.347	1.146
	υ_4 CO_3^{2-}	829	7.123	0.338
	υ_3 PO_4^{3-}	913	0.091	0.019
		1016	107.459	2.173
		1077	17.421	0.714
		1156	9.221	0.594
	υ_4 CO_3^{2-}	1382	7.909	0.314
	υ_3 CO_3^{2-}	1450	22.679	0.876
	C=O Stretching	1721	55.684	1.824
	HPO_4^{2-}	1977	2.086	0.866
		2024	10.756	0.260
		2160	20.088	1.146
	OH^- (OCP)	2431	1.107	0.075
	C-H Stretching	2550	0.912	0.031
		2921	4.939	0.288

Table A-82: FTIR results of Group M12$_{10}$ following the 1st day of the pH-cycling process.

Day of pH-cycling	Assignment	Peak (cm^{-1})	Area (cm^2)	Height (cm)
6	HPO_4^{2-}	522	50.912	9.246
		534	3.880	0.968
	$\upsilon_4\ PO_4^{3-}$	551	16.392	2.467
		567	13.024	2.202
		581	4.961	1.149
		591	1.628	0.453
		612	2.560	0.573
	OH^-	627	3.435	0.363
	$\upsilon_4\ CO_3^{2-}$	649	1.274	0.205
		664	2.233	0.267
	$\upsilon_2\ CO_3^{2-}$	702	5.069	0.433
	F^- - OH^-	745	8.742	0.536
	$\upsilon_4\ CO_3^{2-}$	856	50.227	2.687
	$\upsilon_3\ PO_4^{3-}$	1010	98.827	3.073
		1110	16.066	0.806
		1154	49.264	1.668
	$\upsilon_4\ CO_3^{2-}$	1370	6.448	0.531
	$\upsilon_3\ CO_3^{2-}$	1440	16.082	0.979
		1468	2.635	0.323
		1648	1.283	0.122
	C=O Stretching	1737	150.618	4.287
	HPO_4^{2-}	1977	4.550	0.910
		2030	5.411	0.437
		2160	25.011	1.354
		2180	16.847	0.235
	C-H Stretching	2558	6.704	0.062

Table A-83: FTIR results of Group $M12_{10}$ following the 6th day of the pH-cycling process.

Day of pH-cycling	Assignment	Peak (cm^{-1})	Area (cm^2)	Height (cm)
11	HPO_4^{2-}	534	224.158	11.982
	$\upsilon_4\ PO_4^{3-}$	554	7.259	1.392
		580	4.352	0.964
		594	4.776	0.898
		617	6.460	0.917
	$\upsilon_4\ CO_3^{2-}$	857	12.470	0.727
	$\upsilon_3\ PO_4^{3-}$	1013	14.140	0.685
		1148	14.858	0.573
	$\upsilon_3\ CO_3^{2-}$	1443	5.989	0.327
	C=O Stretching	1740	4.137	0.139
	HPO_4^{2-}	1976	19.837	0.751
		2160	13.789	0.736
		2180	2.245	0.031
	OH^- (OCP)	2439	0.575	0.056

Table A-84: FTIR results of Group $M12_{10}$ following the 11th day of the pH-cycling process.

Day of pH-cycling	Assignment	Peak (cm^{-1})	Area (cm^2)	Height (cm)
16	HPO_4^{2-}	529	11.002	2.750
	$\upsilon_4\ PO_4^{3-}$	552	5.216	0.956
		569	4.367	0.630
		579	4.204	0.908
		597	8.133	0.848
	OH^-	627	1.964	0.397
	$\upsilon_2\ CO_3^{2-}$	703	14.651	1.329
	F^- - OH^-	752	21.967	0.858
	$\upsilon_4\ CO_3^{2-}$	810	1.732	0.133
		856	32.614	1.867
	$\upsilon_3\ PO_4^{3-}$	1012	45.845	1.767
		1112	5.403	0.309
		1148	39.561	1.262
	$\upsilon_4\ CO_3^{2-}$	1385	1.642	0.093
	$\upsilon_3\ CO_3^{2-}$	1444	13.442	0.721
		1470	2.473	0.225
	C=O Stretching	1738	94.811	2.471
	HPO_4^{2-}	1976	27.523	1.049
		2020	2.725	0.138
		2031	2.632	0.362
		2159	20.488	1.249
		2179	17.469	0.213
	C-H Stretching	2407	1.096	0.061
	OH^-	3646	0.775	0.160

Table A-85: FTIR results of Group $M12_{10}$ following the 16^{th} day of the pH-cycling process.

Group M12$_{250}$

Solutions & Treatments	Experimental Conditions
Remineralising Solution (pH)	DW
Demineralising Solution (pH)	AC (4.90)
Background F^- Concentration (ppm) (Main/ Intermediate Periods)	0.2/ 1.0
F^- Treatment Concentration (ppm)	250

Table A-86: Experimental conditions used during the pH-cycling study for the Group M12$_{250}$. Group M12$_{250}$ was treated with DW during the remineralising period, AC during the demineralisation period, 250 ppm of F^- and 0.2 and 2.0 ppm of BF during the main and intermediate remineralisation period respectively.

Day of pH-cycling	Assignment	Peak (cm^{-1})	Area (cm^2)	Height (cm)
1	HPO_4^{2-}	526	158.930	21.274
	υ_4 PO_4^{3-}	550	0.656	0.433
		567	12.254	2.729
	υ_3 PO_4^{3-}	1029	23.809	0.832
		1204	1.085	0.078
	υ_3 CO_3^{2-}	1676	0.976	0.074
	HPO_4^{2-}	1930	0.567	0.098
		1989	4.883	0.417
		2118	12.185	0.514
	CO_2	2338	15.307	0.458
		2363	8.065	0.603

Table A-87: FTIR results of Group M12$_{250}$ following the 1st day of the pH-cycling process.

Day of pH-cycling	Assignment	Peak (cm^{-1})	Area (cm^2)	Height (cm)
6	HPO_4^{2-}	533	54.521	8.603
	υ_4 PO_4^{3-}	547	14.212	3.059
		565	13.145	1.795
		598	40.602	2.701
	υ_4 CO_3^{2-}	870	13.739	0.791
	υ_3 PO_4^{3-}	954	9.855	0.378
		1003	179.246	2.196
	υ_3 CO_3^{2-}	1408	11.798	0.407
	HPO_4^{2-}	1912	3.867	0.136
		2113	4.239	0.253
		2287	75.587	1.936
	CO_2	2348	15.885	2.071
		2391	30.334	1.213

Table A-88: FTIR results of Group M12$_{250}$ following the 6th day of the pH-cycling process.

Day of pH-cycling	Assignment	Peak (cm^{-1})	Area (cm^2)	Height (cm)
11	HPO_4^{2-}	520	322.438	66.766
	υ_4 PO_4^{3-}	558	29.052	2.986
		601	6.227	1.013
	υ_3 PO_4^{3-}	1010	12.720	0.045
	υ_3 CO_3^{2-}	1400	1.003	0.111
	HPO_4^{2-}	2108	15.433	0.425
	CO_2	2338	9.809	0.277

Table A-89: FTIR results of Group $M12_{250}$ following the 11th day of the pH-cycling process.

Day of pH-cycling	Assignment	Peak (cm^{-1})	Area (cm^2)	Height (cm)
16	HPO_4^{2-}	532	0.000	3.122
	F^- - OH^-	757	27.775	1.128
	υ_3 PO_4^{3-}	901	73.285	3.957
		1051	83.660	3.440
		1199	82.647	2.670
	C=O Stretching	1327	232.928	5.466
	υ_4 CO_3^{2-}	1377	2.357	0.273
	υ_3 CO_3^{2-}	1462	25.959	1.397
	C=O Stretching	1794	245.580	6.489
	HPO_4^{2-}	2197	41.460	1.544

Table A-90: FTIR results of Group $M12_{250}$ following the 16th day of the pH-cycling process.

Group M13

Solutions & Treatments	Experimental Conditions
Remineralising Solution (pH)	PF (6.58)
Demineralising Solution (pH)	AC (4.90)
Background F^- Concentration (ppm) (Main/ Intermediate Periods)	N/A
F^- Treatment Concentration (ppm)	N/A

Table A-91: Experimental conditions used during the pH-cycling study for the Group M13. Group M13 was treated with PF during the remineralising and AC during the demineralising period.

Day of pH-cycling	Assignment	Peak (cm^{-1})	Area (cm^2)	Height (cm)
1	HPO_4^{2-}	525	86.229	19.859
	υ_4 PO_4^{3-}	541	1.990	0.358
		550	14.090	2.536
		568	10.719	2.130
		598	3.933	0.431
	OH^-	624	7.016	0.766
	HPO_4^{2-}	2026	11.871	0.515
		2159	13.651	0.662
		2200	3.026	0.124
	C-H Stretching	2408	0.864	0.070

Table A-92: FTIR results of Group M13 following the 1st day of the pH-cycling process.

Day of pH-cycling	Assignment	Peak (cm^{-1})	Area (cm^2)	Height (cm)
6	HPO_4^{2-}	518	74.734	27.475
		533	29.584	4.480
	υ_4 PO_4^{3-}	547	8.871	1.293
		577	7.682	1.487
		591	4.834	0.865
		604	2.805	0.562
		619	3.178	0.525
	υ_4 CO_3^{2-}	670	0.917	0.186
		853	8.037	0.548
	υ_3 PO_4^{3-}	1008	21.305	0.666
	υ_3 CO_3^{2-}	1439	3.348	0.236
	C=O Stretching	1737	27.783	0.856
	HPO_4^{2-}	1977	17.605	0.651
		2019	3.127	0.246
		2160	12.546	0.721
		2215	0.725	0.138
	CO_2	2361	4.445	0.313

Table A-93: FTIR results of Group M13 following the 6th day of the pH-cycling process.

Day of pH-cycling	Assignment	Peak (cm^{-1})	Area (cm^2)	Height (cm)
11	HPO_4^{2-}	519	78.834	18.709
	$\upsilon_4\ PO_4^{3-}$	546	63.531	4.656
		562	9.576	1.456
		587	10.775	1.177
		602	4.898	0.667
	OH^-	626	3.248	0.405
	PO_2	1276	1.985	0.135
	HPO_4^{2-}	1973	-13.315	0.576
		2025	16.816	0.605
		2159	35.229	1.381
	C-H Stretching	2573	4.202	0.057

Table A-94: FTIR results of Group M13 following the 11th day of the pH-cycling process.

Day of pH-cycling	Assignment	Peak (cm^{-1})	Area (cm^2)	Height (cm)
16	HPO_4^{2-}	532	29.097	5.034
	$\upsilon_4\ PO_4^{3-}$	545	19.122	2.988
		560	12.152	1.881
	$\upsilon_4\ CO_3^{2-}$	856	26.624	1.636
	$\upsilon_3\ PO_4^{3-}$	1012	56.053	1.923
		1111	11.087	0.519
		1157	34.062	1.118
	$\upsilon_3\ CO_3^{2-}$	1443	9.482	0.577
	C=O Stretching	1744	65.894	2.417
	HPO_4^{2-}	1975	23.144	0.866
		2029	31.467	0.955
		2160	170.671	2.254

Table A-95: FTIR results of Group M13 following the 16th day of the pH-cycling process.

Group M14

Solutions & Treatments	Experimental Conditions
Remineralising Solution (pH)	PF (6.58)
Demineralising Solution (pH)	AC (4.90)
Background F^- Concentration (ppm) (Main/ Intermediate Periods)	0.2
F^- Treatment Concentration (ppm)	N/A

Table A-96: Experimental conditions used during the pH-cycling study for the Group M14, which was treated with PF during the remineralising, AC during the demineralising period and added BF of 0.2 ppm.

Day of pH-cycling	Assignment	Peak (cm^{-1})	Area (cm^2)	Height (cm)
1	HPO_4^{2-}	521	4.953	4.910
	$\upsilon_4\ PO_4^{3-}$	540	42.009	4.212
		568	26.493	2.764
		581	0.707	0.212
		598	2.404	0.461
		610	1.854	0.426
	OH^-	637	0.886	0.124
	$\upsilon_4\ CO_3^{2-}$	656	0.380	0.076
		681	1.067	0.126
		851	1.959	0.141
	$\upsilon_3\ PO_4^{3-}$	1011	1.860	0.130
	C-H Stretching	1857	0.103	0.020
	HPO_4^{2-}	1975	3.221	0.211
		2097	1.220	0.110
		2162	4.139	0.325
		2180	1.173	0.150
	CO_2	2384	2.111	0.128
	OH^-	3743	1.221	0.282

Table A-97: FTIR results of Group M14 following the 1st day of the pH-cycling process.

Day of pH-cycling	Assignment	Peak (cm^{-1})	Area (cm^2)	Height (cm)
6	HPO_4^{2-}	524	114.911	20.379
	υ_4 PO_4^{3-}	547	3.736	1.135
		571	10.415	1.786
	υ_2 CO_3^{2-}	701	11.928	1.142
	υ_4 CO_3^{2-}	856	24.454	1.526
	υ_3 PO_4^{3-}	1012	34.263	1.548
		1112	5.626	0.337
		1147	30.335	1.053
	υ_4 CO_3^{2-}	1369	11.872	0.484
	υ_3 CO_3^{2-}	1438	13.677	0.703
	C=O Stretching	1738	111.576	2.985
	HPO_4^{2-}	1976	31.057	1.026
		2029	19.756	0.757
		2159	27.707	1.416
		2182	0.284	0.047

Table A-98: FTIR results of Group M14 following the 6th day of the pH-cycling process.

Day of pH-cycling	Assignment	Peak (cm^{-1})	Area (cm^2)	Height (cm)
11	F^- - OH^-	745	7.519	0.729
	υ_4 CO_3^{2-}	856	16.911	0.951
	υ_3 PO_4^{3-}	1012	21.642	0.918
	υ_4 CO_3^{2-}	1372	12.717	0.454
	υ_3 CO_3^{2-}	1441	8.155	0.406
		1648	10.750	0.359
	C=O Stretching	1736	72.109	1.941
	HPO_4^{2-}	1975	20.217	0.758
		2027	31.896	0.934
		2158	14.883	0.896
		2208	0.176	0.058

Table A-99: FTIR results of Group M14 following the 11th day of the pH-cycling process.

Day of pH-cycling	Assignment	Peak (cm^{-1})	Area (cm^2)	Height (cm)
16	HPO_4^{2-}	521	50.520	11.201
		534	19.167	3.577
	$\upsilon_4\ PO_4^{3-}$	561	0.269	0.075
		568	2.471	0.623
		587	2.985	0.644
		608	1.091	0.305
	$\upsilon_4\ CO_3^{2-}$	655	1.522	0.236
	$\upsilon_2\ CO_3^{2-}$	702	11.100	0.929
	F^- - OH^-	755	9.020	0.473
	$\upsilon_4\ CO_3^{2-}$	856	19.453	0.949
	$\upsilon_3\ PO_4^{3-}$	1015	33.930	1.005
		1114	1.996	0.111
		1149	12.578	0.657
	$\upsilon_4\ CO_3^{2-}$	1370	8.518	0.374
	$\upsilon_3\ CO_3^{2-}$	1444	7.960	0.437
		1650	1.108	0.109
	C=O Stretching	1731	68.974	1.928
		1842	1.068	0.125
	HPO_4^{2-}	1976	15.528	0.626
		2032	10.050	0.497
		2159	30.190	1.125
		2198	0.431	0.087
	C-H Stretching	2426	2.089	0.044
		3627	1.890	0.239
		3853	1.799	0.180

Table A-100: FTIR results of Group M14 following the 16th day of the pH-cycling process.

Group M15$_{10}$

Solutions & Treatments	Experimental Conditions
Remineralising Solution (pH)	PF (6.58)
Demineralising Solution (pH)	AC (4.90)
Background F^- Concentration (ppm) (Main/ Intermediate Periods)	N/A
F^- Treatment Concentration (ppm)	10

Table A-101: Experimental conditions used during the pH-cycling study for the Group M15$_{10}$, which was treated with PF during the remineralising, AC during the demineralising period and 10 ppm of F^-.

Day of pH-cycling	Assignment	Peak (cm^{-1})	Area (cm^2)	Height (cm)
1	HPO_4^{2-}	537	18.783	4.150
	υ_4 PO_4^{3-}	552	6.901	1.076
		570	17.491	2.232
		592	5.696	0.666
	υ_4 CO_3^{2-}	657	3.193	0.260
	υ_2 CO_3^{2-}	702	4.703	0.382
	υ_4 CO_3^{2-}	856	19.577	1.143
	υ_3 PO_4^{3-}	1011	37.542	1.267
		1108	5.082	0.277
		1148	20.255	0.691
	υ_3 CO_3^{2-}	1439	7.560	0.455
	C=O Stretching	1736	44.984	1.612
	HPO_4^{2-}	1977	29.665	1.129
		2030	50.889	1.551
		2138	300.761	3.846
	C-H Stretching	2524	23.708	0.242

Table A-102: FTIR results of Group M15$_{10}$ following the 1st day of the pH-cycling process.

Day of pH-cycling	Assignment	Peak (cm^{-1})	Area (cm^2)	Height (cm)
6	υ_4 PO_4^{3-}	548	14.493	2.383
		584	13.402	2.329
		609	1.101	0.261
	υ_2 CO_3^{2-}	702	17.250	1.439
	F^- - OH^-	755	25.685	1.010
	υ_4 CO_3^{2-}	856	43.499	2.253
	υ_3 PO_4^{3-}	1012	80.632	2.509
		1113	7.073	0.380
		1148	53.564	1.748
	υ_3 CO_3^{2-}	1443	21.948	1.135
	C=O Stretching	1733	180.236	4.456
	HPO_4^{2-}	1976	2.212	1.065
		2032	13.819	0.683
		2159	25.128	1.278
	C-H Stretching	2556	7.103	0.084
		2987	9.338	0.347

Table A-103: FTIR results of Group $M15_{10}$ following the 6th day of the pH-cycling process.

Day of pH-cycling	Assignment	Peak (cm^{-1})	Area (cm^2)	Height (cm)
11	HPO_4^{2-}	535	56.893	4.919
	υ_4 PO_4^{3-}	545	5.808	1.009
		566	21.217	2.575
		591	4.681	0.684
		602	3.032	0.517
	υ_2 CO_3^{2-}	702	32.367	2.479
	F^- - OH^-	750	44.738	1.709
	υ_4 CO_3^{2-}	856	76.610	4.351
	υ_3 PO_4^{3-}	1012	160.019	4.912
		1111	18.295	0.953
		1148	88.479	2.878
	υ_4 CO_3^{2-}	1370	39.708	1.585
	υ_3 CO_3^{2-}	1443	34.131	1.807
		1470	4.199	0.595
		1650	2.808	0.071
	C=O Stretching	1739	301.539	7.391
	HPO_4^{2-}	1976	9.305	0.953
		2026	7.822	0.318
		2159	256.515	3.193
	C-H Stretching	2425	6.752	0.087
		2851	4.720	0.367
		2920	23.481	0.720

Table A-104: FTIR results of Group $M15_{10}$ following the 11th day of the pH-cycling process.

Day of pH-cycling	Assignment	Peak (cm^{-1})	Area (cm^2)	Height (cm)
16	υ_4 PO_4^{3-}	541	51.968	4.991
		566	9.537	1.559
	υ_2 CO_3^{2-}	702	24.002	2.186
	F^- - OH^-	750	43.561	1.665
	υ_4 CO_3^{2-}	857	83.927	4.809
	υ_3 PO_4^{3-}	1012	190.555	5.606
		1111	21.830	1.051
		1150	101.744	3.154
	υ_4 CO_3^{2-}	1371	52.220	1.998
	υ_3 CO_3^{2-}	1443	41.829	2.218
	C=O Stretching	1739	365.011	9.107
	HPO_4^{2-}	1976	1.777	1.599
		2027	81.274	2.191
		2160	419.271	5.225
	OH^- (OCP)	2437	14.747	0.243
	C-H Stretching	2549	14.790	0.109
		2988	15.148	0.574

Table A-105: FTIR results of Group $M15_{10}$ following the 16^{th} day of the pH-cycling process.

Group M15$_{250}$

Solutions & Treatments	Experimental Conditions
Remineralising Solution (pH)	PF (6.58)
Demineralising Solution (pH)	AC (4.90)
Background F^- Concentration (ppm) (Main/ Intermediate Periods)	N/A
F^- Treatment Concentration (ppm)	250

Table A-106: Experimental conditions used during the pH-cycling study for the Group M15$_{250}$, which was treated with PF during the remineralising, AC during the demineralising period and 250 ppm of F^-.

Day of pH-cycling	Assignment	Peak (cm^{-1})	Area (cm^2)	Height (cm)
1	υ_4 PO_4^{3-}	558	15.549	2.374
		588	38.088	1.553
	υ_2 CO_3^{2-}	699	11.289	0.936
	υ_4 CO_3^{2-}	872	8.708	0.568
	υ_3 PO_4^{3-}	1007	501.971	5.337
	υ_3 CO_3^{2-}	1400	13.678	0.439
		1453	5.134	0.313
		1556	7.912	0.316
	C=O Stretching	1727	18.525	0.822
	HPO_4^{2-}	2160	189.261	2.322

Table A-107: FTIR results of Group M15$_{250}$ following the 1st day of the pH-cycling process.

Day of pH-cycling	Assignment	Peak (cm^{-1})	Area (cm^2)	Height (cm)
6	HPO_4^{2-}	524	58.656	11.303
	υ_4 PO_4^{3-}	545	46.183	4.228
		586	16.193	1.529
	υ_2 CO_3^{2-}	698	28.643	2.256
	F^- - OH^-	757	20.154	0.982
	υ_3 PO_4^{3-}	1019	5.819	0.194
	υ_3 CO_3^{2-}	1451	9.442	0.395
	C=O Stretching	1723	19.587	0.738
	HPO_4^{2-}	1976	-5.228	1.001
		2159	28.660	1.470
	OH^- (OCP)	2432	0.427	0.046
	C-H Stretching	2555	12.478	0.185

Table A-108: FTIR results of Group M15$_{250}$ following the 6th day of the pH-cycling process.

Day of pH-cycling	Assignment	Peak (cm^{-1})	Area (cm^2)	Height (cm)
11	HPO_4^{2-}	525	134.254	14.028
	υ_4 PO_4^{3-}	560	13.631	1.112
		569	3.663	0.894
		600	37.122	2.773
	OH^-	646	1.410	0.175
	υ_4 CO_3^{2-}	672	2.136	0.202
	υ_2 CO_3^{2-}	699	2.824	0.229
	F^- - OH^-	750	21.414	0.140
	υ_4 CO_3^{2-}	872	11.710	0.707
	υ_3 PO_4^{3-}	1012	346.430	5.067
	υ_4 CO_3^{2-}	1341	0.846	0.069
	υ_3 CO_3^{2-}	1407	16.414	0.484
		1451	6.452	0.301
		1639	0.341	0.074
	HPO_4^{2-}	2009	3.788	0.180
		2140	252.067	3.201
	C-H Stretching	2391	4.594	0.103

Table A-109: FTIR results of Group $M15_{250}$ following the 11^{th} day of the pH-cycling process.

Day of pH-cycling	Assignment	Peak (cm^{-1})	Area (cm^2)	Height (cm)
16	HPO_4^{2-}	526	14.116	1.875
	υ_4 PO_4^{3-}	543	10.031	2.429
		555	10.266	1.980
		567	8.167	1.309
		601	6.416	0.886
		620	6.702	0.688
	υ_4 CO_3^{2-}	659	2.573	0.263
	υ_2 CO_3^{2-}	698	30.390	2.455
	F^- - OH^-	756	30.229	1.286
	υ_4 CO_3^{2-}	828	7.095	0.492
	υ_3 PO_4^{3-}	914	2.102	0.134
		1015	119.335	2.332
		1070	11.122	0.384
		1157	9.469	0.597
	C=O Stretching	1317	2.064	0.106
	υ_4 CO_3^{2-}	1386	1.633	0.138
	υ_3 CO_3^{2-}	1451	21.915	0.858
		1509	4.044	0.539
		1560	11.085	0.498
	C=O Stretching	1721	46.365	1.740
	HPO_4^{2-}	1976	24.051	0.859
		2032	1.908	0.252
		2159	77.173	2.265
	OH^-	3649	1.377	0.154
		3749	1.334	0.113

Table A-110: FTIR results of Group $M15_{250}$ following the 16^{th} day of the pH-cycling process.

Group M16$_{10}$

Solutions & Treatments	Experimental Conditions
Remineralising Solution	PF (6.58)
Demineralising Solution	AC (4.90)
Background F^- Concentration (ppm) (Main/ Intermediate Periods)	0.2/ 2.0
F^- Treatment Concentration (ppm)	10

Table A-611: Experimental conditions used during the pH-cycling study for the Group M16$_{10}$, which was treated with PF during the remineralising, AC during the demineralising period, 10 ppm of F^- and added BF of either 0.2 ppm or 1.0 ppm during the main and intermediate remineralisation periods respectively.

Day of pH-cycling	Assignment	Peak (cm^{-1})	Area (cm^2)	Height (cm)
1	υ_4 PO_4^{3-}	548	6.095	0.578
		581	20.993	1.854
		605	7.558	0.831
		620	1.591	0.779
	OH^-	632	3.469	0.360
	υ_2 CO_3^{2-}	702	5.570	0.556
	$F^- - OH^-$	751	0.906	0.051
	υ_4 CO_3^{2-}	856	8.174	0.574
	υ_3 PO_4^{3-}	1011	22.484	0.686
		1109	0.405	0.057
		1145	5.542	0.304
	υ_3 CO_3^{2-}	1441	3.593	0.212
	C=O Stretching	1736	28.391	0.840
	HPO_4^{2-}	1977	2.809	0.865
		2014	2.379	0.190
		2159	15.817	0.905
		2175	10.921	0.097

Table A-117: FTIR results of Group M16$_{10}$ following the 1st day of the pH-cycling process.

Day of pH-cycling	Assignment	Peak (cm^{-1})	Area (cm^2)	Height (cm)
6	$\upsilon_4\ PO_4^{3-}$	533	208.190	15.088
		549	5.314	1.540
		560	11.828	1.836
		580	17.222	1.899
	OH^-	632	2.276	0.483
	$\upsilon_2\ CO_3^{2-}$	703	11.471	0.878
	$F^- - OH^-$	756	15.178	0.586
	$\upsilon_4\ CO_3^{2-}$	856	23.510	1.302
	$\upsilon_3\ PO_4^{3-}$	1011	48.491	1.434
		1113	5.314	0.257
		1148	25.735	0.861
	$\upsilon_3\ CO_3^{2-}$	1371	11.770	0.454
		1439	10.908	0.593
	C=O Stretching	1736	92.261	2.157
	HPO_4^{2-}	1976	8.438	0.687
		2021	2.127	0.143
		2160	16.657	1.061
		2181	22.886	0.327

Table A-118: FTIR results of Group $M16_{10}$ following the 6th day of the pH-cycling process.

Day of pH-cycling	Assignment	Peak (cm^{-1})	Area (cm^2)	Height (cm)
11	HPO_4^{2-}	531	62.268	8.675
	$\upsilon_4\ PO_4^{3-}$	566	17.658	2.839
		588	6.586	0.756
	$\upsilon_2\ CO_3^{2-}$	703	23.255	2.020
	$F^- - OH^-$	750	42.250	1.591
	$\upsilon_4\ CO_3^{2-}$	856	85.296	4.829
	$\upsilon_3\ PO_4^{3-}$	1012	186.303	5.605
		1110	25.021	1.263
		1151	94.464	2.871
	$\upsilon_4\ CO_3^{2-}$	1370	328.272	8.053
		1442	48.751	1.831
	C=O Stretching	1741	37.895	2.103
	HPO_4^{2-}	1976	360.986	8.785
		2027	3.108	1.241
		2159	336.867	4.386
	OH^- (OCP)	2433	2.324	0.019
	C-H Stretching	2947	8.144	0.275
		2990	17.383	0.661

Table A-119: FTIR results of Group $M16_{10}$ following the 11th day of the pH-cycling process.

Day of pH-cycling	Assignment	Peak (cm^{-1})	Area (cm^2)	Height (cm)
16	HPO_4^{2-}	531	29.307	4.781
	$\upsilon_4\ PO_4^{3-}$	554	6.945	0.928
		575	14.357	1.993
	$F^- - OH^-$	755	50.004	0.286
	$\upsilon_4\ CO_3^{2-}$	856	19.071	1.160
	$\upsilon_3\ PO_4^{3-}$	1011	41.679	1.384
		1105	7.370	0.365
		1157	22.454	0.737
	$\upsilon_3\ CO_3^{2-}$	1441	6.413	0.388
	C=O Stretching	1738	56.927	1.688
	HPO_4^{2-}	1976	1.935	0.864
		2032	38.513	1.220
		2159	229.012	2.947

Table A-1110: FTIR results of Group $M16_{10}$ following the 16^{th} day of the pH-cycling process.

Group M16$_{250}$

Solutions & Treatments	Experimental Conditions
Remineralising Solution	PF (6.58)
Demineralising Solution	AC (4.90)
Background F^- Concentration (ppm) (Main/ Intermediate Periods)	0.2/ 1.0
F^- Treatment Concentration (ppm)	250

Table A-1116: Experimental conditions used during the pH-cycling study for the Group M16$_{250}$, which was treated with PF during the remineralising, AC during the demineralising period, 250 ppm of F^- and added BF of either 0.2 ppm or 1.0 ppm during the main and intermediate remineralisation periods respectively.

Day of pH-cycling	Assignment	Peak (cm^{-1})	Area (cm^2)	Height (cm)
1	HPO_4^{2-}	528	30.525	6.767
	υ_4 PO_4^{3-}	545	23.897	3.731
		560	12.330	1.957
		580	5.932	0.861
		593	2.198	0.503
		615	1.997	0.325
	υ_4 CO_3^{2-}	660	1.693	0.263
	υ_2 CO_3^{2-}	698	6.878	0.545
	υ_3 PO_4^{3-}	902	1.359	0.097
		1021	3.609	0.142
	υ_3 CO_3^{2-}	1449	1.639	0.149
		1509	1.444	0.183
		1541	1.329	0.110
	C=O Stretching	1720	9.832	0.391
	HPO_4^{2-}	1976	20.403	0.760
		2025	26.879	0.887
		2066	1.307	0.111
		2159	23.211	1.082
		2186	7.950	0.162
	CO_2	23589	9.217	0.752
	OH^- (OCP)	2439	1.217	0.099
	OH^-	3629	2.866	0.300
		3806	1.520	0.123

Table A-117: FTIR results of Group M16$_{250}$ following the 1st day of the pH-cycling process.

Day of pH-cycling	Assignment	Peak (cm^{-1})	Area (cm^2)	Height (cm)
6	HPO_4^{2-}	517	2.851	2.746
		533	39.832	4.450
	$\upsilon_4\ PO_4^{3-}$	554	50.333	3.832
		600	21.490	1.733
	OH^-	642	2.009	0.286
	$\upsilon_4\ CO_3^{2-}$	662	1.367	0.175
	$\upsilon_2\ CO_3^{2-}$	697	3.137	0.230
	$F^- - OH^-$	744	0.746	0.067
	$\upsilon_4\ CO_3^{2-}$	870	14.624	0.811
	$\upsilon_3\ PO_4^{3-}$	1004	166.294	2.326
	$\upsilon_3\ CO_3^{2-}$	1450	3.638	0.178
	HPO_4^{2-}	1975	1.344	0.904
		2018	3.871	0.266
		2096	1.423	0.125
		2160	21.259	1.064
		2180	28.188	0.261
	CO_2	2348	2.511	0.243
	C-H Stretching	2417	4.688	0.034
		2578	4.166	0.074
	OH^-	3689	1.476	0.177
		3748	0.349	0.074

Table A-118: FTIR results of Group $M16_{250}$ following the 6th day of the pH-cycling process.

Day of pH-cycling	Assignment	Peak (cm^{-1})	Area (cm^2)	Height (cm)
11	HPO_4^{2-}	521	17.935	9.007
		532	34.119	4.925
	$\upsilon_4\ PO_4^{3-}$	544	6.632	1.807
		555	9.612	1.312
		580	4.717	1.046
		596	12.414	1.164
	$\upsilon_4\ CO_3^{2-}$	668	1.374	0.250
	$\upsilon_2\ CO_3^{2-}$	699	5.978	0.576
	$F^- - OH^-$	757	6.162	0.364
	$\upsilon_4\ CO_3^{2-}$	871	4.826	0.355
	$\upsilon_3\ PO_4^{3-}$	996	97.627	1.348
		1159	2.733	0.187
	$\upsilon_4\ CO_3^{2-}$	1398	4.730	0.193
		1451	5.404	0.283
	C=O Stretching	1728	11.395	0.524
	HPO_4^{2-}	1976	4.891	0.920
		2025	39.021	1.128
		2160	186.652	2.854
	CO_2	2362	13.706	0.944
	OH^-	3733	2.596	0.206

Table A-119: FTIR results of Group $M16_{250}$ following the 11th day of the pH-cycling process.

Day of pH-cycling	Assignment	Peak (cm^{-1})	Area (cm^2)	Height (cm)
16	HPO_4^{2-}	526	6.588	2.595
	υ_4 PO_4^{3-}	545	24.408	3.612
		587	18.280	1.780
	υ_2 CO_3^{2-}	699	30.657	2.270
	F^- - OH^-	756	26.371	1.085
	υ_4 CO_3^{2-}	828	6.302	0.408
	υ_3 PO_4^{3-}	1012	143.580	2.772
	υ_3 CO_3^{2-}	1451	18.324	0.738
		1561	0.552	0.098
	C=O Stretching	1722	44.786	1.570
	HPO_4^{2-}	1976	24.737	0.938
		2032	4.456	0.354
		2160	17.572	0.949
		2177	0.292	0.040
	OH^- (OCP)	2442	7.832	0.193
	C-H Stretching	2563	0.992	0.091
		2925	12.750	0.399

Table A-120: FTIR results of Group $M16_{250}$ following the 16th day of the pH-cycling process.

Group PR1$_{10}$

Solutions & Treatments	Experimental Conditions
Remineralising Solution	PF (6.58)
Demineralising Solution	AC (4.90)
Background F^- Concentration (ppm) (Main/ Intermediate Periods)	0.2/ 2.0
F^- Treatment Concentration (ppm)	10

Table A-1221: Experimental conditions used during the pH-cycling study for the Group PR1$_{10}$, which was treated with PF during the remineralising, AC during the demineralising period, 10 ppm of F^- and added BF of either 0.2 ppm or 1.0 ppm during the main and intermediate remineralisation periods respectively. The duration of the experimental procedure was 32 days instead of 16.

Day of pH-cycling	Assignment	Peak (cm^{-1})	Area (cm^2)	Height (cm)
17	HPO_4^{2-}	518	152.693	39.270
	υ_4 PO_4^{3-}	534	5.123	0.317
		560	76.315	6.351
		600	48.657	3.895
	υ_2 CO_3^{2-}	700	5.328	0.464
	$F^- - OH^-$	759	23.990	0.628
	υ_3 PO_4^{3-}	917	4.119	0.319
		962	11.778	0.842
		1021	470.968	14.536
	υ_3 CO_3^{2-}	1403	1.394	0.108
	C=O Stretching	1728	10.403	0.467
	HPO_4^{2-}	1976	21.442	1.228
		2160	356.504	4.389
	OH^- (OCP)	2437	0.310	0.051
	C-H Stretching	2555	13.070	0.163

Table A-1213: FTIR results of Group PR1$_{10}$ following the 17th day of the pH-cycling process.

Day of pH-cycling	Assignment	Peak (cm^{-1})	Area (cm^2)	Height (cm)
22	HPO_4^{2-}	517	115.347	42.262
		532	17.657	3.659
	$\upsilon_4\ PO_4^{3-}$	559	77.849	5.808
		586	6.397	1.125
		602	29.381	2.513
	$\upsilon_4\ CO_3^{2-}$	665	5.423	0.510
	$F^- - OH^-$	752	29.170	1.294
	$\upsilon_4\ CO_3^{2-}$	831	15.771	1.287
	$\upsilon_4\ CO_3^{2-}$	872	7.700	0.380
	$\upsilon_3\ PO_4^{3-}$	1024	645.839	8.867
	$\upsilon_3\ CO_3^{2-}$	1340	19.701	0.585
		1623	7.867	0.403
		1643	2.223	0.065
	HPO_4^{2-}	1976	28.167	1.411
		2020	2.605	0.132
		2159	319.811	4.021
	OH^- (OCP)	2424	3.453	0.089
	C-H Stretching	2567	6.591	0.067

Table A-1214: FTIR results of Group $PR1_{10}$ following the 22nd day of the pH-cycling process.

Day of pH-cycling	Assignment	Peak (cm^{-1})	Area (cm^2)	Height (cm)
27	HPO_4^{2-}	529	87.075	8.662
	$\upsilon_4\ PO_4^{3-}$	539	23.757	5.088
		553	34.505	4.081
		573	11.525	1.258
		603	14.975	1.432
	$F^- - OH^-$	753	33.669	0.564
	$\upsilon_4\ CO_3^{2-}$	870	0.774	0.081
	$\upsilon_3\ PO_4^{3-}$	1017	201.705	3.690
		1976	34.548	1.158
	HPO_4^{2-}	2160	292.346	3.721
	C-H Stretching	2569	5.980	0.066

Table A-1215: FTIR results of Group $PR1_{10}$ following the 27th day of the pH-cycling process.

Day of pH-cycling	Assignment	Peak (cm^{-1})	Area (cm^2)	Height (cm)
32	HPO_4^{2-}	538	64.998	6.591
	υ_4 PO_4^{3-}	555	17.454	2.445
		594	19.365	1.427
	OH^-	624	8.362	0.854
	υ_4 CO_3^{2-}	660	6.585	0.566
	υ_2 CO_3^{2-}	699	36.701	2.768
	F^- – OH^-	758	29.115	1.294
	υ_4 CO_3^{2-}	830	8.734	0.618
	υ_3 PO_4^{3-}	1022	504.480	7.131
		1157	10.463	0.752
	υ_4 CO_3^{2-}	1384	6.670	0.344
	υ_3 CO_3^{2-}	1453	23.467	1.034
		1509	6.275	0.644
		1566	13.383	0.518
	C=O Stretching	1726	9.427	2.817
	HPO_4^{2-}	1977	25.992	1.061
		2027	15.435	0.554
		2160	25.795	1.321
		2181	14.633	0.163

Table A-1216: FTIR results of Group $PR1_{10}$ following the 32nd day of the pH-cycling process.

Group PR2$_{250}$

Solutions & Treatments	Experimental Conditions
Remineralising Solution	PF (6.58)
Demineralising Solution	AC (4.90)
Background F^- Concentration (ppm) (Main/ Intermediate Periods)	0.2/ 1.0
F^- Treatment Concentration (ppm)	250

Table A-1726: Experimental conditions used during the pH-cycling study for the Group PR2$_{250}$, which was treated with PF during the remineralising, AC during the demineralising period, 250 ppm of F^- and added BF of either 0.2 ppm or 1.0 ppm during the main and intermediate remineralisation periods respectively. The duration of the experimental procedure was 32 days instead of 16.

Day of pH-cycling	Assignment	Peak (cm^{-1})	Area (cm^2)	Height (cm)
17	HPO_4^{2-}	532	61.807	6.410
	υ_4 PO_4^{3-}	546	6.821	1.127
		566	17.103	3.251
		602	20.789	1.626
	OH^-	635	2.659	0.427
	$F^- – OH^-$	755	29.135	0.294
	υ_3 PO_4^{3-}	1024	133.001	2.339
	HPO_4^{2-}	1975	4.701	1.295
		2015	3.415	0.226
		2030	13.484	0.665
		2098	3.421	0.274
		2159	344.770	4.307
	C-H Stretching	2557	0.315	0.049

Table A-127: FTIR results of Group PR2$_{250}$ following the 17th day of the pH-cycling process.

Day of pH-cycling	Assignment	Peak (cm^{-1})	Area (cm^2)	Height (cm)
22	HPO_4^{2-}	518	155.629	33.985
	υ_4 PO_4^{3-}	542	25.428	3.800
		563	81.226	6.701
		600	51.078	3.021
	OH^-	654	3.047	0.368
	$F^- - OH^-$	769	29.911	0.222
	υ_4 CO_3^{2-}	871	11.464	0.520
	υ_3 PO_4^{3-}	1024	375.915	6.447
		1219	0.227	0.043
	υ_3 CO_3^{2-}	1728	6.038	0.313
	HPO_4^{2-}	1976	13.519	1.041
		2030	41.720	1.330
		2160	204.551	3.043
	CO_2	2362	13.154	0.884
	OH^- (OCP)	2438	0.769	0.063
	C-H Stretching	2541	13.147	0.123

Table A-128: FTIR results of Group $M16_{250}$ following the 22nd day of the pH-cycling process.

Day of pH-cycling	Assignment	Peak (cm^{-1})	Area (cm^2)	Height (cm)
27	HPO_4^{2-}	535	8.405	2.098
	υ_4 PO_4^{3-}	541	2.113	0.701
		567	19.045	2.873
		602	18.501	1.714
	υ_2 CO_3^{2-}	701	14.470	1.195
	$F^- - OH^-$	757	29.781	0.559
	υ_4 CO_3^{2-}	862	0.389	0.070
	υ_3 PO_4^{3-}	1019	330.957	4.163
	υ_4 CO_3^{2-}	1453	10.316	0.449
	υ_3 CO_3^{2-}	1728	33.859	1.256
	HPO_4^{2-}	1976	29.134	1.193
		2032	15.767	0.883
		2160	327.811	4.100
	OH^- (OCP)	2419	0.146	0.031

Table A-129: FTIR results of Group $PR2_{250}$ following the 27th day of the pH-cycling process.

Day of pH-cycling	Assignment	Peak (cm^{-1})	Area (cm^2)	Height (cm)
32	HPO_4^{2-}	530	76.472	11.921
	υ_4 PO_4^{3-}	549	17.862	3.958
		580	7.322	1.173
	υ_2 CO_3^{2-}	601	33.728	2.603
	F^- - OH^-	757	28.573	1.218
	υ_4 CO_3^{2-}	871	10.206	0.429
	υ_3 PO_4^{3-}	1024	408.971	6.975
	HPO_4^{2-}	1976	3.141	1.233
		2031	65.824	1.831
		2160	360.632	4.489
	OH^- (OCP)	2434	0.071	0.019

Table A-130: FTIR results of Group $PR2_{250}$ following the 32nd day of the pH-cycling process.

Group PMix

Solutions & Treatments	pH Cycling Rounds
Remineralising Solution (pH)	PF (6.58)
Demineralising Solution (pH)	AC (4.90)
Days 1 - 6	
Background F^- Concentration (ppm)	0.2/ 2.0
Brushing F^- Concentration (ppm)	10.0
Days 7 - 16	
Background F^- Concentration (ppm)	0.2/ 1.0
Brushing F^- Concentration (ppm)	250

Table A-1831: Experimental conditions used during the pH-cycling study for the Group PMix, which was treated with PF during the remineralising, AC during the demineralising period, 10 ppm of F^- for the first 6 and 250 ppm of F^- for the remaining days and added BF of either 0.2 ppm and 2.0 or 1.0 ppm (depending on the F^- treatment) during the main and intermediate remineralisation periods respectively.

Day of pH-cycling	Assignment	Peak (cm^{-1})	Area (cm^2)	Height (cm)
1	HPO_4^{2-}	522	423.379	47.017
	υ_4 PO_4^{3-}	565	13.541	2.297
	F^- - OH^-	751	11.194	0.595
	υ_4 CO_3^{2-}	830	108.335	2.746
	υ_3 PO_4^{3-}	1023	23.065	0.463
	PO_2	1276	44.353	2.429
	υ_4 CO_3^{2-}	1370	5.123	0.254
	υ_3 CO_3^{2-}	1455	5.303	0.303
		1644	92.778	2.459
	C=O Stretching	1729	44.660	1.247
	HPO_4^{2-}	1975	26.262	0.990
		2027	47.656	1.354
		2159	24.195	1.181
	C-H Stretching	2552	10.009	0.107

Table A-132: FTIR results of Group PMix following the 1st day of the pH-cycling process.

Day of pH-cycling	Assignment	Peak (cm^{-1})	Area (cm^2)	Height (cm)
6	HPO_4^{2-}	540	19.723	3.110
	υ_4 PO_4^{3-}	559	8.983	1.369
	υ_2 CO_3^{2-}	700	12.141	1.245
	F^- – OH^-	753	26.878	1.213
	υ_4 CO_3^{2-}	830	241.224	5.611
	υ_3 PO_4^{3-}	1022	31.192	0.621
		1062	3.850	0.063
		1158	9.608	0.716
	PO_2	1276	85.025	4.536
	υ_4 CO_3^{2-}	1370	8.173	0.411
	υ_3 CO_3^{2-}	1455	10.378	0.545
		1641	14.735	4.436
	C=O Stretching	1727	81.236	2.149
	HPO_4^{2-}	2160	16.465	0.837

Table A-133: FTIR results of Group PMix following the 6th day of the pH-cycling process.

Day of pH-cycling	Assignment	Peak (cm^{-1})	Area (cm^2)	Height (cm)
11	HPO_4^{2-}	525	75.885	11.723
	$\upsilon_4\ PO_4^{3-}$	543	17.779	3.421
		559	11.993	1.521
		579	7.548	1.312
		603	2.753	0.529
		614	3.095	0.253
	$\upsilon_2\ CO_3^{2-}$	700	21.731	1.846
	$F^- - OH^-$	753	33.871	1.480
	$\upsilon_4\ CO_3^{2-}$	830	282.691	6.425
	$\upsilon_3\ PO_4^{3-}$	916	2.175	0.262
		1022	62.084	1.339
		1057	16.548	0.527
		1118	3.729	0.330
		1157	11.401	0.887
		1183	5.766	0.499
	PO_2	1276	89.149	4.987
	$\upsilon_4\ CO_3^{2-}$	1371	9.889	0.472
	$\upsilon_3\ CO_3^{2-}$	1453	11.455	0.581
		1510	5.250	0.561
		1640	2.398	1.260
	C=O Stretching	1726	96.128	2.575
	HPO_4^{2-}	1977	3.468	0.946
		2025	47.108	1.274
		2096	1.506	0.162
		2159	246.515	3.263
	OH^- (OCP)	2441	7.383	0.154
	C-H Stretching	2521	1.158	0.102
		2566	2.524	0.020
		2875	3.849	0.183
		2933	4.524	0.193
		2959	6.375	0.357
	OH^-	3676	1.425	0.126
		3710	0.931	0.089

Table A-134: FTIR results of Group PMix following the 11th day of the pH-cycling process.

Day of pH-cycling	Assignment	Peak (cm^{-1})	Area (cm^2)	Height (cm)
16	HPO_4^{2-}	518	97.171	29.556
	υ_4 PO_4^{3-}	538	37.762	4.852
		572	3.906	0.606
		594	3.480	0.437
	υ_4 CO_3^{2-}	670	3.093	0.534
	υ_2 CO_3^{2-}	700	29.789	2.313
	F^- - OH^-	753	42.317	1.884
	υ_4 CO_3^{2-}	829	36.366	8.322
	υ_3 PO_4^{3-}	1022	68.226	1.358
		1059	21.469	0.728
		1119	6.792	0.515
		1157	16.291	1.216
		1183	7.625	0.687
	PO_2	1276	131.297	6.884
	υ_4 CO_3^{2-}	1371	13.219	0.645
	υ_3 CO_3^{2-}	1453	16.540	0.831
		1509	7.685	0.805
		1640	91.901	1.216
	C=O Stretching	1726	137.854	3.650
	HPO_4^{2-}	1976	24.328	1.177
		2030	59.024	1.704
		2159	259.315	4.002
	CO_2	2340	8.670	0.559
	OH^- (OCP)	2360	24.014	1.638
	C-H Stretching	2875	5.367	0.292
		2932	6.819	0.304
		2960	5.012	0.442
	OH^-	3627	1.464	0.149
		3731	2.397	0.226

Table A-135: FTIR results of Group PMix following the 16th day of the pH-cycling process.

4. pH Cycling Studies Using Natural Primary Bovine Enamel

Primary Enamel

Group p1$_{10}$

Solutions & Treatments	Experimental Conditions
Remineralising Solution	PF (6.58)
Demineralising Solution	AC (4.90)
Background F^- Concentration (ppm) (Main/ Intermediate Periods)	0.2/ 2.0
F^- Treatment Concentration (ppm)	10

Table A-1936: Experimental conditions used during the pH-cycling study for the Group p1$_{10}$, which was treated with PF during the remineralising, AC during the demineralising period, 10 ppm of F^- and added BF of either 0.2 ppm or 1.0 ppm during the main and intermediate remineralisation periods respectively.

Day of pH-cycling	Assignment	Peak (cm^{-1})	Area (cm^2)	Height (cm)
1	HPO_4^{2-}	522	8.718	2.398
		523	42.029	8.089
	$\upsilon_4\ PO_4^{3-}$	547	11.879	1.692
		566	16.381	2.205
		585	2.369	0.368
		605	3.328	0.586
	OH^-	624	2.702	0.389
	$\upsilon_2\ CO_3^{2-}$	700	7.387	0.698
	$F^- - OH^-$	752	12.753	0.642
	$\upsilon_4\ CO_3^{2-}$	831	129.800	3.086
	$\upsilon_3\ PO_4^{3-}$	1021	14.350	0.261
		1059	6.211	0.226
		1118	2.653	0.222
		1158	5.163	0.377
		1183	2.151	0.177
	PO_2	1276	40.755	2.333
	$\upsilon_4\ CO_3^{2-}$	1370	5.068	0.243
	$\upsilon_3\ CO_3^{2-}$	1454	5.270	0.295
		1510	2.501	0.240
		1644	94.505	2.406
	C=O Stretching	1729	43.625	1.225
	HPO_4^{2-}	1976	41.959	1.352
		2030	48.089	1.512
		2159	242.864	3.582
	CO_2	2362	6.201	0.494
	OH^- (OCP)	2423	1.460	0.082
	C-H Stretching	2876	1.382	0.114
		2958	2.499	0.135

Table A-137: FTIR results of Group $p1_{10}$ following the 1st day of the pH-cycling process.

Day of pH-cycling	Assignment	Peak (cm^{-1})	Area (cm^2)	Height (cm)
4	HPO_4^{2-}	523	99.650	17.580
	υ_4 PO_4^{3-}	543	11.278	2.233
		554	9.609	1.339
	υ_2 CO_3^{2-}	700	8.854	0.733
	$F^- - OH^-$	750	11.273	0.623
	υ_4 CO_3^{2-}	831	131.193	2.994
	υ_3 PO_4^{3-}	1022	20.832	0.476
		1057	8.694	0.287
	PO_2	1275	41.770	2.292
	υ_3 CO_3^{2-}	1639	14.696	0.493
	C=O Stretching	1725	4.327	0.214
	HPO_4^{2-}	1976	15.368	0.515
		2030	5.755	0.345
		2159	17.190	0.842
		2218	16.766	0.193
	OH^- (OCP)	2423	0.523	0.048

Table A-138: FTIR results of Group $p1_{10}$ following the 4th day of the pH-cycling process.

Day of pH-cycling	Assignment	Peak (cm^{-1})	Area (cm^2)	Height (cm)
7	HPO_4^{2-}	541	31.520	3.126
	υ_4 PO_4^{3-}	563	16.404	2.170
		577	12.826	1.721
		607	12.687	1.182
		699	12.025	1.078
	$F^- - OH^-$	752	20.098	0.932
	υ_4 CO_3^{2-}	829	192.937	4.826
	υ_3 PO_4^{3-}	1023	303.124	4.282
	PO_2	1276	79.094	4.077
	υ_4 CO_3^{2-}	1454	8.254	0.426
		1644	161.480	4.055
	C=O Stretching	1730	68.973	2.038
	HPO_4^{2-}	1977	9.797	1.221
		2031	56.397	1.713
		2159	322.330	4.155
	C-H Stretching	2555	9.551	0.087

Table A-139: FTIR results of Group $p1_{10}$ following the 7th day of the pH-cycling process.

Day of pH-cycling	Assignment	Peak (cm^{-1})	Area (cm^2)	Height (cm)
10	HPO_4^{2-}	520	18.695	6.185
		531	11.088	2.885
		538	5.858	1.420
	$\upsilon_4\ PO_4^{3-}$	553	6.415	0.998
		572	8.463	1.210
		601	18.993	1.379
		619	4.384	0.518
	$\upsilon_2\ CO_3^{2-}$	699	20.245	1.680
	$F^- - OH^-$	751	34.124	1.553
	$\upsilon_4\ CO_3^{2-}$	829	30.271	6.801
	$\upsilon_3\ PO_4^{3-}$	917	2.219	0.257
		1021	452.463	6.207
		1116	0.964	0.067
		1156	10.234	0.800
		1183	5.915	0.473
	PO_2	1276	95.429	5.333
	$\upsilon_4\ CO_3^{2-}$	1371	12.155	0.618
	$\upsilon_3\ CO_3^{2-}$	1434	2.333	0.218
		1454	14.228	0.745
		1509	5.826	0.609
		1640	39.953	6.080
	C=O Stretching	1729	120.362	3.245
	HPO_4^{2-}	1976	21.133	1.331
		2014	2.188	0.176
		2031	14.978	0.793
		2097	2.019	0.195
		2160	364.921	4.634
	OH^- (OCP)	2427	2.602	0.100
	C-H Stretching	2538	0.977	0.082
		2874	4.962	0.267
		2931	7.816	0.328
		2960	8.748	0.476

Table A-140: FTIR results of Group $p1_{10}$ following the 10^{th} day of the pH-cycling process.

Group p2$_{250}$

Solutions & Treatments	Experimental Conditions
Remineralising Solution	PF (6.58)
Demineralising Solution	AC (4.90)
Background F^- Concentration (ppm) (Main/ Intermediate Periods)	0.2/ 1.0
F^- Treatment Concentration (ppm)	250

Table A-2041: Experimental conditions used during the pH-cycling study for the Group p2$_{250}$, which was treated with PF during the remineralising, AC during the demineralising period, 250 ppm of F^- and added BF of either 0.2 ppm or 1.0 ppm during the main and intermediate remineralisation periods respectively.

Day of pH-cycling	Assignment	Peak (cm^{-1})	Area (cm^2)	Height (cm)
1	υ_4 PO_4^{3-}	541	125.687	8.654
		574	0.684	0.192
		596	6.957	0.775
		609	3.268	0.520
	OH^-	629	4.124	0.491
	υ_2 CO_3^{2-}	700	4.032	0.367
	υ_4 CO_3^{2-}	833	62.005	1.540
	υ_3 PO_4^{3-}	1001	2.969	0.150
		1052	3.294	0.058
		1118	2.023	0.149
		1159	2.657	0.192
	PO_2	1277	24.409	1.254
	υ_4 CO_3^{2-}	1370	0.857	0.084
	υ_3 CO_3^{2-}	1452	2.038	0.151
		1644	3.065	0.339
	C=O Stretching	1731	21.277	0.633
	HPO_4^{2-}	1976	37.222	1.272
		2019	2.175	0.124
		2031	3.874	0.434
		2098	0.154	0.036
		2160	302.084	3.909
	CO_2	2366	1.520	0.138
	OH^- (OCP)	2446	1.277	0.083
	C-H Stretching	2551	1.027	0.079
	OH^-	3669	1.961	0.184

Table A-142: FTIR results of Group p2$_{250}$ following the 1st day of the pH-cycling process.

Day of pH-cycling	Assignment	Peak (cm^{-1})	Area (cm^2)	Height (cm)
4	HPO_4^{2-}	519	31.591	10.388
		530	47.457	7.112
	$\upsilon_4\ PO_4^{3-}$	556	37.915	3.410
		576	5.266	0.814
		600	1.244	0.311
		610	1.940	0.352
		624	1.261	0.350
	OH^-	635	1.737	0.338
	$\upsilon_2\ CO_3^{2-}$	700	0.908	0.149
	$F^- - OH^-$	750	1.696	0.161
	$\upsilon_4\ CO_3^{2-}$	833	4.480	0.193
	$\upsilon_3\ PO_4^{3-}$	1021	80.315	1.449
		1090	0.992	0.082
		1152	1.072	0.079
	PO_2	1277	8.283	0.461
	$\upsilon_3\ CO_3^{2-}$	1650	16.193	0.457
	C=O Stretching	1730	0.017	0.005
	HPO_4^{2-}	1977	18.900	0.649
		2010	1.407	0.154
		2161	8.673	0.487
		2176	0.899	0.089
		2197	2.033	0.085
	C-H Stretching	2573	0.599	0.026
	OH^-	3644	0.857	0.083
		3666	1.264	0.119

Table A-143: FTIR results of Group $p2_{250}$ following the 4th day of the pH-cycling process.

Day of pH-cycling	Assignment	Peak (cm^{-1})	Area (cm^2)	Height (cm)
7	HPO_4^{2-}	528	39.696	7.537
		539	17.469	2.990
	$\upsilon_4\ PO_4^{3-}$	563	27.958	2.882
		579	8.291	1.681
		599	4.663	0.876
		609	1.752	0.327
	OH^-	628	3.836	0.677
	$\upsilon_4\ CO_3^{2-}$	662	2.146	0.240
	$\upsilon_2\ CO_3^{2-}$	699	5.343	0.484
	$F^- - OH^-$	753	10.095	0.476
	$\upsilon_4\ CO_3^{2-}$	829	96.669	2.279
	$\upsilon_3\ PO_4^{3-}$	1023	24.652	0.526
		1060	7.577	0.327
		1117	2.110	0.154
		1158	3.967	0.305
		1183	2.164	0.177
	PO_2	1276	38.149	1.944
	$\upsilon_4\ CO_3^{2-}$	1371	3.734	0.193
	$\upsilon_4\ CO_3^{2-}$	1454	4.973	0.255
		1512	2.680	0.200
		1645	74.683	2.010
	C=O Stretching	1731	34.038	1.004
	HPO_4^{2-}	1974	15.723	0.558
		2028	19.481	0.823
		2101	0.594	0.071
		2160	14.400	0.796
		2179	1.629	0.161
	C-H Stretching	2876	1.810	0.095
		2932	3.318	0.163
		2961	2.815	0.180

Table A-144: FTIR results of Group $p2_{250}$ following the 7th day of the pH-cycling process.

Day of pH-cycling	Assignment	Peak (cm^{-1})	Area (cm^2)	Height (cm)
10	HPO_4^{2-}	528	22.447	5.400
		538	8.156	2.007
	$\upsilon_4\ PO_4^{3-}$	550	3.515	0.753
		569	11.405	1.459
		594	2.920	0.501
		610	1.679	0.312
	OH^-	621	2.309	0.196
	$\upsilon_2\ CO_3^{2-}$	699	13.364	1.132
	F^- - OH^-	751	24.909	1.153
	$\upsilon_4\ CO_3^{2-}$	831	23.479	5.044
	$\upsilon_3\ PO_4^{3-}$	1022	43.803	0.851
		1061	6.228	0.207
		1117	3.778	0.288
		1157	8.947	0.658
		1183	5.141	0.456
	PO_2	1276	79.094	4.162
	$\upsilon_4\ CO_3^{2-}$	1371	7.887	0.419
	$\upsilon_3\ CO_3^{2-}$	1454	9.249	0.538
		1509	4.217	0.426
		1643	165.898	4.312
	C=O Stretching	1730	81.695	2.269
	HPO_4^{2-}	1977	15.647	1.256
		2024	2.398	0.046
		2099	1.706	0.153
		2160	327.644	4.776
	CO_2	2338	1.490	0.230
		2360	12.686	0.979
	OH^- (OCP)	2426	2.018	0.117
	C-H Stretching	2930	2.740	0.138
		2961	3.798	0.255

Table A-145: FTIR results of Group $p2_{250}$ following the 16th day of the pH-cycling process.

Group pMix

Solutions & Treatments	pH Cycling Rounds
Remineralising Solution (pH)	PF (6.58)
Demineralising Solution (pH)	AC (4.90)
Days 1 – 4	
Background F^- Concentration (ppm)	0.2/ 2.0
Brushing F^- Concentration (ppm)	10.0
Days 4 - 10	
Background F^- Concentration (ppm)	0.2/ 1.0
Brushing F^- Concentration (ppm)	250

Table A-2146: Experimental conditions used during the pH-cycling study for the Group pMix, which was treated with PF during the remineralising, AC during the demineralising period, 10 ppm of F^- for the first 4 and 250 ppm of F^- for the remaining days and added BF of either 0.2 ppm and 2.0 or 1.0 ppm (depending on the F^- treatment) during the main and intermediate remineralisation periods respectively.

Day of pH-cycling	Assignment	Peak (cm^{-1})	Area (cm^2)	Height (cm)
1	HPO_4^{2-}	517	3.574	3.430
		529	92.526	12.598
	$\upsilon_4\ PO_4^{3-}$	546	5.290	1.314
		557	17.282	1.912
		583	15.885	1.759
		618	3.339	0.366
	OH^-	631	1.772	0.277
	$\upsilon_2\ CO_3^{2-}$	698	3.380	0.234
	F^- - OH^-	756	0.268	0.013
	$\upsilon_4\ CO_3^{2-}$	836	29.884	0.824
	$\upsilon_3\ PO_4^{3-}$	1160	1.604	0.112
	PO_2	1277	10.989	0.633
	$\upsilon_3\ CO_3^{2-}$	1659	1.065	0.077
	C=O Stretching	1729	8.052	0.270
	HPO_4^{2-}	1977	9.951	0.366
		2023	6.631	0.219
		2159	27.378	0.927
		2260	2.138	0.069
	OH^- (OCP)	2403	2.393	0.106
	C-H Stretching	2599	2.025	0.069
	OH^-	3657	1.103	0.089

Table A-147: FTIR results of Group PMix following the 1st day of the pH-cycling process.

Day of pH-cycling	Assignment	Peak (cm^{-1})	Area (cm^2)	Height (cm)
4	HPO_4^{2-}	517	17.687	2.186
		538	36.747	4.344
	υ_4 PO_4^{3-}	555	3.628	0.923
		574	4.198	1.179
	υ_2 CO_3^{2-}	700	7.927	0.642
	$F^- - OH^-$	753	13.322	0.604
	υ_4 CO_3^{2-}	833	123.717	2.813
	υ_3 PO_4^{3-}	1023	1.895	0.192
		1057	9.642	0.373
		1156	4.868	0.375
		1185	3.718	0.261
	PO_2	1276	42.924	2.397
	υ_4 CO_3^{2-}	1371	4.866	0.244
	υ_3 CO_3^{2-}	1454	5.749	0.321
		1510	3.096	0.273
		1645	92.713	2.529
	C=O Stretching	1730	45.609	1.325
	HPO_4^{2-}	1976	6.032	1.243
		2027	54.352	1.524
		2159	332.525	4.092
	OH^- (OCP)	2432	0.311	0.029
	C-H Stretching	2549	11.930	0.119
		2962	3.145	0.175

Table A-148: FTIR results of Group pMix following the 4th day of the pH-cycling process.

Day of pH-cycling	Assignment	Peak (cm^{-1})	Area (cm^2)	Height (cm)
7	HPO_4^{2-}	536	67.800	6.012
	υ_4 PO_4^{3-}	557	16.586	1.981
		620	6.029	0.854
	υ_2 CO_3^{2-}	700	12.147	1.114
	$F^- - OH^-$	753	22.640	0.985
	υ_4 CO_3^{2-}	829	205.992	4.498
	υ_3 PO_4^{3-}	1022	36.921	0.600
		1057	13.682	0.453
		1157	7.568	0.575
	PO_2	1275	68.300	3.667
	υ_4 CO_3^{2-}	1370	8.079	0.403
	υ_3 CO_3^{2-}	1455	9.176	0.477
		1640	158.689	4.186
	C=O Stretching	1726	77.930	2.197
	HPO_4^{2-}	1976	22.459	1.271
		2028	56.228	1.613
		2159	320.668	4.168
	C-H Stretching	2543	14.406	0.080

Table A-149: FTIR results of Group pMix following the 7th day of the pH-cycling process.

Day of pH-cycling	Assignment	Peak (cm^{-1})	Area (cm^2)	Height (cm)
10	HPO_4^{2-}	531	12.722	4.171
	$\upsilon_4\ PO_4^{3-}$	544	14.367	2.644
		553	0.023	0.092
		579	20.269	1.968
	$\upsilon_2\ CO_3^{2-}$	700	15.044	1.301
	$F^- - OH^-$	751	27.933	1.249
	$\upsilon_4\ CO_3^{2-}$	829	234.478	5.136
	$\upsilon_3\ PO_4^{3-}$	1021	32.377	0.473
		1060	15.401	0.601
		1157	8.782	0.690
	PO_2	1275	79.729	4.241
	$\upsilon_4\ CO_3^{2-}$	1371	9.170	0.466
	$\upsilon_3\ CO_3^{2-}$	1455	11.839	0.626
		1641	191.326	4.837
	C=O Stretching	1728	97.271	2.603
	HPO_4^{2-}	1977	28.426	1.095
		2023	65.027	1.591
		2159	298.919	4.138
	CO_2	2360	13.309	0.912
	C-H Stretching	2555	8.810	0.086
		2931	6.197	0.256

Table A-150: FTIR results of Group pMix following the 10th day of the pH-cycling process.

5. Development of Enamel Proxies & Comparison with Natural Bovine Enamel

Bovine Enamel

Powdered Bovine Enamel

Assignment	Peak (cm^{-1})	Area (cm^2)	Height (cm)
$\upsilon_4\ PO_4^{3-}$	544	153.647	23.234
	556	16.763	3.378
	562	349.504	17.575
	602	129.580	9.292
$\upsilon_4\ CO_3^{2-}$	873	60.779	2.778
$\upsilon_3\ PO_4^{3-}$	959	6.209	1.905
	1025	1858.726	25.103
$\upsilon_3\ CO_3^{2-}$	1414	29.156	1.275
	1452	45.518	1.274

Table A-151: FTIR results of powdered mature bovine enamel.

Bovine Enamel Blocks

Assignment	Peak (cm^{-1})	Area (cm^2)	Height (cm)
$\upsilon_4\ PO_4^{3-}$	548	153.865	44.403
	559	16.531	2.532
	597	27.684	1.330
$\upsilon_4\ CO_3^{2-}$	872	14.135	0.733
$\upsilon_3\ PO_4^{3-}$	1021	265.824	3.681
$\upsilon_3\ CO_3^{2-}$	1406	11.673	0.368
	1639	14.473	0.392
HPO_4^{2-}	2001	1.152	0.228
	2068	4.113	0.213
	2122	4.771	0.269
CO_2	2340	19.199	0.771
	2362	24.609	1.664

Table A-152: FTIR results of bovine mature enamel block.

Bovine enamel blocks treated with a PF proxy for 5 days

Assignment	Peak (cm^{-1})	Area (cm^2)	Height (cm)
HPO_4^{2-}	519	55.316	25.938
	533	41.278	6.747
$\upsilon_4\ PO_4^{3-}$	546	11.437	2.408
	570	1.443	0.433
	595	13.216	1.287
$\upsilon_4\ CO_3^{2-}$	670	1.433	0.082
$\upsilon_2\ CO_3^{2-}$	700	42.244	3.469
$\upsilon_4\ CO_3^{2-}$	831	588.100	13.718
$\upsilon_3\ PO_4^{3-}$	915	4.832	0.451
	1021	71.183	1.547
	1059	77.109	2.583
	1120	11.077	0.834
	1157	28.865	2.144
PO_2	1183	14.159	1.291
	1276	207.888	11.792
$\upsilon_4\ CO_3^{2-}$	1370	21.034	1.043
$\upsilon_3\ CO_3^{2-}$	1455	28.640	1.435
	1509	13.789	1.468
	1641	460.348	11.924
C=O Stretching	1727	262.262	6.416
CO_2	2360	2.775	0.190
C-H Stretching	2874	4.260	0.446
	2934	11.274	0.464
	2959	12.768	0.799
OH^-	3676	2.390	0.241

Table A-153: FTIR results of bovine mature enamel block immersed for 5 days in a PF proxy (pH: 6.58).

Bovine enamel blocks treated with an AC for 5 days

Assignment	Peak (cm^{-1})	Area (cm^2)	Height (cm)
HPO_4^{2-}	532	33.144	4.946
$\upsilon_4\ PO_4^{3-}$	555	5.566	1.248
	570	15.236	1.972
	595	12.418	0.968
OH^-	626	16.022	1.284
$\upsilon_2\ CO_3^{2-}$	700	75.253	3.362
$\upsilon_4\ CO_3^{2-}$	831	416.085	9.626
$\upsilon_3\ PO_4^{3-}$	916	3.452	0.328
	1021	69.924	1.365
	1061	39.719	1.491
	1119	9.268	0.658
	1157	18.510	1.401
PO_2	1183	10.138	0.867
	1276	134.543	7.933
$\upsilon_4\ CO_3^{2-}$	1371	15.621	0.789
$\upsilon_3\ CO_3^{2-}$	1454	18.871	1.036
	1510	8.648	0.857
	1644	314.984	8.271
C=O Stretching	1729	173.451	4.479
HPO_4^{2-}	1976	12.881	1.004
	2026	47.104	1.264
	2160	27.849	1.400
CO_2	2362	5.558	0.481
OH^- (OCP)	2441	0.500	0.067
C-H Stretching	2927	14.585	0.598
	2959	5.956	0.499

Table A-154: FTIR results of bovine mature enamel block immersed for 5 days in an AC (pH: 4.90).

Bovine enamel blocks treated with 250 ppm of F^- for 5 days

Assignment	Peak (cm^{-1})	Area (cm^2)	Height (cm)
HPO_4^{2-}	523	18.748	4.886
	537	13.101	2.175
υ_4 PO_4^{3-}	592	11.069	1.403
OH^-	635	12.713	1.143
υ_2 CO_3^{2-}	700	78.200	5.989
F^- - OH^-	754	88.671	4.132
υ_4 CO_3^{2-}	835	966.867	23.436
υ_3 PO_4^{3-}	1022	105.018	3.138
	1062	102.786	3.876
	1119	25.164	1.746
	1158	41.969	3.258
PO_2	1184	22.676	1.979
	1277	390.890	22.165
υ_4 CO_3^{2-}	1371	33.221	1.674
υ_3 CO_3^{2-}	1454	41.774	2.160
	1505	18.758	1.957
	1647	731.540	18.719
C=O Stretching	1730	391.887	10.122
HPO_4^{2-}	2116	0.839	0.091
C-H Stretching	2932	18.603	0.809
	2959	18.927	1.353

Table A-155: FTIR results of bovine mature enamel block immersed for 5 days in 250 ppm of F^-.

Synthetic HA

FD-HA Powder

Assignment	Peak (cm^{-1})	Area (cm^2)	Height (cm)
υ_4 PO_4^{3-}	544	101.032	12.796
	563	230.376	11.613
	602	55.543	4.585
OH^-	628	13.047	0.700
υ_3 PO_4^{3-}	962	7.825	0.696
	1029	486.419	13.329
υ_3 CO_3^{2-}	1420	3.649	0.204
HPO_4^{2-}	2231	2.512	0.228
CO_2	2386	6.080	0.352
OH^-	3743	2.301	0.196

Table A-156: FTIR results of freeze dried synthetic HA powder.

HD-HA Powder

Assignment	Peak (cm^{-1})	Area (cm^2)	Height (cm)
υ_4 PO_4^{3-}	548	307.338	75.011
	558	332.470	21.294
	573	20.821	3.072
υ_3 PO_4^{3-}	972	94.316	2.021
	1082	44.117	0.247
HPO_4^{2-}	2113	0.390	0.088
CO_2	2303	25.526	0.631
	2390	15.412	0.732

Table A-157: FTIR results of oven dried synthetic HA powder.

FD-HA Pellets

Assignment	Peak (cm^{-1})	Area (cm^2)	Height (cm)
υ_4 PO_4^{3-}	540	74.319	6.794
	578	22.167	1.874
	611	3.002	0.557
υ_4 CO_3^{2-}	661	2.270	0.333
υ_3 PO_4^{3-}	975	77.370	2.121
	1083	37.043	0.816
υ_3 CO_3^{2-}	1143	15.662	0.365
CO_2	2395	1.628	0.065

Table A-158: FTIR results of freeze dried synthetic HA pellets.

FD-HA Pellets Sintered at 500°C

Assignment	Peak (cm^{-1})	Area (cm^2)	Height (cm)
$\upsilon_4\ PO_4^{3-}$	546	15.815	3.275
	558	42.373	3.788
	584	4.925	1.402
	598	20.844	2.234
$\upsilon_3\ PO_4^{3-}$	1020	202.595	4.578
$\upsilon_3\ CO_3^{2-}$	1424	1.073	0.092
HPO_4^{2-}	1977	0.346	1.142
	2025	57.430	1.468
	2159	328.389	4.136
C-H Stretching	2430	7.154	0.122
	2567	1.828	0.073

Table A-159: FTIR results of freeze dried synthetic HA pellets sintered for 3 hours at 500°C.

FD-HA Pellets Sintered at 800°C

Assignment	Peak (cm^{-1})	Area (cm^2)	Height (cm)
$\upsilon_4\ PO_4^{3-}$	546	102.232	19.912
	552	617.748	27.988
	598	138.326	13.099
OH^-	629	136.527	8.321
$\upsilon_3\ PO_4^{3-}$	959	49.840	3.359
	990	218.403	6.667
	1056	79.692	4.040
	1089	36.857	3.162
HPO_4^{2-}	1976	32.226	1.227
	2021	2.774	0.129
	2160	92.515	2.762

Table A-160: FTIR results of freeze dried synthetic HA pellets sintered for 3 hours at 800°C.

FD-HA Pellets Sintered at 1100°C

Assignment	Peak (cm^{-1})	Area (cm^2)	Height (cm)
$\upsilon_4\ PO_4^{3-}$	543	5.029	0.179
	551	29.389	7.200
	564	49.855	6.182
	588	19.398	2.085
	614	8.951	1.603
OH^-	639	8.707	0.741
$\upsilon_3\ PO_4^{3-}$	914	7.184	0.116
	971	15.049	0.705
	1082	18.233	0.467
	1153	0.557	0.074
HPO_4^{2-}	2025	2.981	0.334

Table A-161: FTIR results of freeze dried synthetic HA pellets sintered for 3 hours at 1100°C.

HD-HA Pellets

Assignment	Peak (cm^{-1})	Area (cm^2)	Height (cm)
υ_4 PO_4^{3-}	544	115.121	24.680
	559	461.733	19.957
	599	111.887	9.544
υ_4 CO_3^{2-}	872	7.108	0.529
υ_3 PO_4^{3-}	1004	284.882	10.052
	1047	29.849	1.105
HPO_4^{2-}	1977	5.247	0.349
	2160	7.334	0.604
	2276	10.925	0.281
CO_2	2390	12.097	0.566

Table A-162: FTIR results of oven dried synthetic HA pellets.

HD-HA Pellets Sintered at 500°C

Assignment	Peak (cm^{-1})	Area (cm^2)	Height (cm)
υ_4 PO_4^{3-}	544	21.610	4.736
	615	14.690	1.812
υ_2 CO_3^{2-}	696	440.720	23.518
υ_4 CO_3^{2-}	875	24.796	2.199
υ_3 PO_4^{3-}	907	33.285	2.008
	966	41.473	2.491
	1079	26.465	0.886
	1154	41.727	1.165
υ_3 CO_3^{2-}	1451	133.176	6.033
	1492	39.959	4.722
HPO_4^{2-}	1977	5.884	0.567
	2160	17.671	1.171
C-H Stretching	2850	37.852	2.245
	2920	173.189	5.198
OH^-	3025	23.695	1.875

Table A-163: FTIR results of oven dried synthetic HA pellets sintered for 3 hours at 500°C.

HD-HA Pellets Sintered at 800°C

Assignment	Peak (cm^{-1})	Area (cm^2)	Height (cm)
υ_4 PO_4^{3-}	542	58.019	6.323
	555	202.736	11.085
	598	68.357	7.280
OH^-	628	83.297	4.658
υ_3 PO_4^{3-}	957	69.778	1.807
	976	57.994	2.230
	1066	59.063	2.540
	1090	16.811	1.189

Table A-164: FTIR results of oven dried synthetic HA pellets sintered for 3 hours at 800°C.

HD-HA Pellets Sintered at 1100°C

Assignment	Peak (cm^{-1})	Area (cm^2)	Height (cm)
υ_4 PO_4^{3-}	542	21.008	1.921
	554	57.013	5.270
	580	10.809	1.783
	603	5.494	0.997
OH^-	631	7.804	0.666
υ_4 CO_3^{2-}	642	0.922	0.276
	664	1.746	0.367
υ_4 CO_3^{2-}	859	4.919	0.253
υ_3 PO_4^{3-}	914	0.143	0.041
	924	18.356	0.464
	970	19.271	1.285
	1158	8.206	0.196
υ_4 CO_3^{2-}	1361	2.988	0.081
HPO_4^{2-}	2061	6.838	0.585

Table A-165: FTIR results of oven dried synthetic HA pellets sintered for 3 hours at 1100°C.

FD-HA pellets treated with a PF proxy for 5 days

Assignment	Peak (cm^{-1})	Area (cm^2)	Height (cm)
υ_4 PO_4^{3-}	547	34.571	3.631
	572	17.594	2.212
	600	7.823	0.959
υ_2 CO_3^{2-}	700	9.290	0.720
υ_4 CO_3^{2-}	831	101.396	2.513
υ_3 PO_4^{3-}	1020	15.907	0.641
	1056	7.902	0.256
PO_2	1276	36.281	2.022
υ_3 CO_3^{2-}	1454	4.467	0.303
	1644	73.992	1.970
C=O Stretching	1727	35.002	0.996
HPO_4^{2-}	1977	6.560	0.361
	2158	9.571	0.488
	2263	3.408	0.183

Table A-166: FTIR results of freeze dried synthetic HA pellets immersed for 5 days in a PF proxy (pH: 6.58).

FD-HA pellets sintered at 500°C & treated with a PF proxy for 5 days

Assignment	Peak (cm^{-1})	Area (cm^2)	Height (cm)
HPO_4^{2-}	533	97.909	11.594
υ_4 PO_4^{3-}	557	13.245	2.244
	569	11.716	1.581
	595	8.931	0.912
OH^-	629	3.746	0.672
υ_2 CO_3^{2-}	700	13.462	1.210
υ_4 CO_3^{2-}	830	186.531	4.623
υ_3 PO_4^{3-}	1021	54.457	1.138
	1055	14.202	0.405
	1117	5.060	0.334
	1157	7.607	0.576
PO_2	1183	4.176	0.377
	1276	75.723	4.003
υ_4 CO_3^{2-}	1371	6.944	0.353
υ_3 CO_3^{2-}	1454	8.182	0.435
	1509	4.316	0.399
	1644	149.302	3.810
C=O Stretching	1728	65.413	1.787
HPO_4^{2-}	1977	9.258	0.479
	2157	12.167	0.655
	2255	2.808	0.142
CO_2	2362	7.152	0.503
C-H Stretching	2958	3.903	0.226

Table A-167: FTIR results of freeze dried synthetic HA pellets sintered at 500°C for 3 hours and immersed for 5 days in a PF proxy (pH: 6.58).

FD-HA pellets sintered at 800°C & treated with a PF proxy for 5 days

Assignment	Peak (cm^{-1})	Area (cm^2)	Height (cm)
HPO_4^{2-}	527	23.049	5.253
υ_4 PO_4^{3-}	538	11.378	1.812
	555	14.905	1.853
	593	19.734	1.527
υ_4 CO_3^{2-}	676	6.421	0.289
υ_2 CO_3^{2-}	700	45.975	3.747
υ_4 CO_3^{2-}	831	621.190	14.167
υ_3 PO_4^{3-}	1022	142.228	2.921
	1059	43.385	1.511
	1119	14.110	1.053
	1157	27.738	2.131
PO_2	1184	14.302	1.248
	1276	215.191	11.989
υ_4 CO_3^{2-}	1371	21.061	1.066
υ_3 CO_3^{2-}	1454	28.551	1.518
	1510	13.898	1.423
	1644	437.928	11.684
C=O Stretching	1729	230.737	5.910
HPO_4^{2-}	1976	7.713	0.883
	2158	25.141	1.360
	2178	1.409	0.017
OH^- (OCP)	2434	0.733	0.075
C-H Stretching	2932	13.607	0.546
	2960	10.168	0.735

Table A-168: FTIR results of freeze dried synthetic HA pellets sintered at 800°C for 3 hours and immersed for 5 days in a PF proxy (pH: 6.58).

FD-HA pellets sintered at 1100°C & treated with a PF proxy for 5 days

Assignment	Peak (cm^{-1})	Area (cm^2)	Height (cm)
HPO_4^{2-}	524	100.655	27.686
υ_4 PO_4^{3-}	533	7.473	2.424
	556	7.997	1.806
υ_2 CO_3^{2-}	700	9.077	0.907
υ_4 CO_3^{2-}	833	176.371	4.155
υ_3 PO_4^{3-}	1023	39.694	1.042
	1061	11.355	0.433
	1119	5.893	0.377
	1158	6.060	0.475
PO_2	1277	62.812	3.411
υ_4 CO_3^{2-}	1371	5.148	0.281
υ_3 CO_3^{2-}	1455	6.935	0.319
	1646	106.033	2.932
C=O Stretching	1731	56.001	1.476
HPO_4^{2-}	2161	1.826	0.190

Table A-168: FTIR results of freeze dried synthetic HA pellets sintered at 1100°C for 3 hours and immersed for 5 days in a PF proxy (pH: 6.58).

HD-HA pellets treated with a PF proxy for 5 days

Assignment	Peak (cm^{-1})	Area (cm^2)	Height (cm)
HPO_4^{2-}	519	345.911	69.798
υ_4 PO_4^{3-}	549	47.003	3.372
	586	12.924	1.183
υ_2 CO_3^{2-}	700	40.615	3.423
υ_4 CO_3^{2-}	831	611.472	13.904
υ_3 PO_4^{3-}	1021	124.195	2.526
	1059	55.362	2.005
	1119	13.958	1.010
	1157	24.773	1.916
PO_2	1183	14.895	1.261
	1276	208.956	11.651
υ_4 CO_3^{2-}	1371	20.917	1.076
υ_3 CO_3^{2-}	1454	26.339	1.416
	1509	11.973	1.233
	1643	476.463	11.915
C=O Stretching	1729	244.196	6.100
HPO_4^{2-}	2118	11.667	0.473
	2220	6.152	0.147
CO_2	2331	12.134	0.234
C-H Stretching	2932	12.426	0.544
	2959	12.954	0.758

Table A-169: FTIR results of oven dried synthetic HA pellets immersed for 5 days in a PF proxy (pH: 6.58).

HD-HA pellets sintered at 500°C & treated with a PF proxy for 5 days

Assignment	Peak (cm^{-1})	Area (cm^2)	Height (cm)
HPO_4^{2-}	517	92.491	0.907
$\upsilon_4\ PO_4^{3-}$	547	40.851	4.579
	582	4.541	1.027
	595	6.206	0.618
$\upsilon_4\ CO_3^{2-}$	676	2.810	0.261
$\upsilon_2\ CO_3^{2-}$	700	20.356	1.715
$\upsilon_4\ CO_3^{2-}$	831	307.381	6.924
$\upsilon_3\ PO_4^{3-}$	1021	33.645	1.415
	1054	18.949	0.478
	1119	9.529	0.603
	1157	11.572	0.913
PO_2	1184	5.881	0.521
	1276	103.993	5.812
$\upsilon_4\ CO_3^{2-}$	1372	11.155	0.561
$\upsilon_3\ CO_3^{2-}$	1454	13.093	0.723
	1510	5.670	0.592
	1644	233.947	5.905
C=O Stretching	1729	109.424	2.935
HPO_4^{2-}	1977	8.267	0.427
	2021	1.943	0.104
	2033	3.510	0.245
	2159	12.486	0.647
	2226	0.754	0.088
C-H Stretching	2935	4.869	0.226
	2961	6.603	0.388

Table A-170: FTIR results of oven dried synthetic HA pellets sintered at 500°C for 3 hours and immersed for 5 days in a PF proxy (pH: 6.58).

HD-HA pellets sintered at 800°C & treated with a PF proxy for 5 days

Assignment	Peak (cm^{-1})	Area (cm^2)	Height (cm)
HPO_4^{2-}	526	49.012	8.011
	536	7.323	1.637
υ_4 PO_4^{3-}	562	1.471	0.344
	578	9.234	1.117
	597	2.748	0.512
	609	2.124	0.341
OH^-	633	2.113	0.287
υ_4 CO_3^{2-}	675	2.472	0.246
υ_2 CO_3^{2-}	701	8.392	0.730
υ_4 CO_3^{2-}	832	149.154	3.521
υ_3 PO_4^{3-}	1022	15.511	0.418
	1063	18.136	0.647
	1124	3.312	0.213
	1159	6.252	0.489
PO_2	1185	2.547	0.229
	1277	50.470	2.775
υ_4 CO_3^{2-}	1371	3.984	0.195
υ_3 CO_3^{2-}	1455	4.939	0.303
	1509	2.973	0.229
	1645	91.684	2.492
C=O Stretching	1731	42.777	1.118
HPO_4^{2-}	1920	5.459	0.161
	1993	5.931	0.448
	2074	3.342	0.077
	2090	1.003	0.113
	2111	16.659	0.490
	2191	2.154	0.157
CO_2	2332	9.832	0.275
C-H Stretching	2665	1.409	0.077
	2963	2.746	0.173
OH^-	3479	0.615	0.102
	3508	0.666	0.072

Table A-171: FTIR results of oven dried synthetic HA pellets sintered at 800°C for 3 hours and immersed for 5 days in a PF proxy (pH: 6.58).

HD-HA pellets sintered at 1100°C & treated with a PF proxy for 5 days

Assignment	Peak (cm^{-1})	Area (cm^2)	Height (cm)
HPO_4^{2-}	519	345.911	69.798
$\upsilon_4\ PO_4^{3-}$	549	47.003	3.372
	586	12.924	1.183
$\upsilon_2\ CO_3^{2-}$	700	40.615	3.423
$\upsilon_4\ CO_3^{2-}$	831	611.472	13.904
$\upsilon_3\ PO_4^{3-}$	1021	124.195	2.526
	1059	55.362	2.005
	1119	13.958	1.010
	1157	24.773	1.916
PO_2	1183	14.895	1.261
	1276	208.956	11.651
$\upsilon_4\ CO_3^{2-}$	1371	20.917	1.076
$\upsilon_3\ CO_3^{2-}$	1454	26.339	1.416
	1509	11.973	1.233
	1643	476.463	11.915
C=O Stretching	1729	244.196	6.100
HPO_4^{2-}	2118	11.667	0.473
	2220	6.152	0.147
CO_2	2331	12.134	0.234
C-H Stretching	2932	12.426	0.544
	2959	12.954	0.758

Table A-172: FTIR results of oven dried synthetic HA pellets sintered at 1100°C for 3 hours and immersed for 5 days in a PF proxy (pH: 6.58).

FD-HA pellets treated with an AC for 5 days

Assignment	Peak (cm^{-1})	Area (cm^2)	Height (cm)
$\upsilon_4\ PO_4^{3-}$	544	7.454	1.273
	562	12.862	2.581
	572	0.191	0.072
OH^-	639	1.539	0.222
$\upsilon_2\ CO_3^{2-}$	699	6.473	0.604
$\upsilon_4\ CO_3^{2-}$	830	129.725	2.865
$\upsilon_3\ PO_4^{3-}$	1018	28.453	0.764
	1057	4.298	0.056
	1157	5.336	0.420
PO_2	1276	43.108	2.381
$\upsilon_3\ CO_3^{2-}$	1407	21.769	0.623
	1452	2.810	0.145
	1642	86.840	2.376
C=O Stretching	1729	40.822	1.164
HPO_4^{2-}	1977	9.537	0.452
	2160	14.917	0.734

Table A-173: FTIR results of freeze dried synthetic HA pellets immersed for 5 days in an AC (pH: 4.90).

FD-HA pellets sintered at 500°C & treated with an AC for 5 days

Assignment	Peak (cm^{-1})	Area (cm^2)	Height (cm)
HPO_4^{2-}	521	43.772	11.675
υ_4 PO_4^{3-}	550	17.799	2.141
	566	9.048	1.449
	580	12.021	1.739
	616	5.934	0.615
υ_2 CO_3^{2-}	699	16.516	1.472
υ_4 CO_3^{2-}	829	269.871	6.235
υ_3 PO_4^{3-}	1020	56.821	1.085
	1057	26.878	0.891
	1118	5.604	0.329
	1156	10.800	0.843
PO_2	1183	4.921	0.467
	1276	90.138	5.043
υ_4 CO_3^{2-}	1371	5.666	0.372
υ_3 CO_3^{2-}	1454	8.292	0.477
	1509	4.200	0.480
	1560	9.374	0.361
	1644	172.520	4.623
C=O Stretching	1729	77.722	2.225
HPO_4^{2-}	1976	24.596	0.837
	2018	0.875	0.044
	2160	20.127	0.950
OH^- (OCP)	2404	0.410	0.009
C-H Stretching	2934	3.409	0.137
	2960	6.015	0.299

Table A-174: FTIR results of freeze dried synthetic HA pellets sintered at 500°C for 3 hours and immersed for 5 days in an AC (pH: 4.90).

FD-HA pellets sintered at 800°C & treated with an AC for 5 days

Assignment	Peak (cm^{-1})	Area (cm^2)	Height (cm)
HPO_4^{2-}	520	734.141	287.027
υ_4 PO_4^{3-}	566	25.482	3.400
υ_4 CO_3^{2-}	828	75.831	1.727
υ_3 PO_4^{3-}	1028	26.036	0.923
υ_3 CO_3^{2-}	1540	100.228	2.251
	1646	21.184	0.743
C=O Stretching	1740	29.950	0.971
HPO_4^{2-}	2030	54.524	1.572
	2159	28.622	1.507
CO_2	2340	24.496	1.225
OH^- (OCP)	2360	48.712	3.232
C-H Stretching	2921	39.563	1.757

Table A-175: FTIR results of freeze dried synthetic HA pellets sintered at 800°C for 3 hours and immersed for 5 days in an AC (pH: 4.90).

FD-HA pellets sintered at 1100°C & treated with an AC for 5 days

Assignment	Peak (cm^{-1})	Area (cm^2)	Height (cm)
υ_4 PO_4^{3-}	542	9.394	1.831
	556	10.766	1.408
υ_2 CO_3^{2-}	699	10.215	0.893
υ_4 CO_3^{2-}	829	179.769	4.146
υ_3 PO_4^{3-}	1020	21.432	0.622
	1039	29.525	0.496
	1154	7.044	0.549
PO_2	1276	75.632	3.877
υ_3 CO_3^{2-}	1408	46.732	1.562
	1554	52.685	1.627
	1640	125.144	3.540
C=O Stretching	1727	60.545	1.633
HPO_4^{2-}	1975	14.686	0.584
	2160	10.097	0.612

Table A-176: FTIR results of freeze dried synthetic HA pellets sintered at 1100°C for 3 hours and immersed for 5 days in an AC (pH: 4.90).

HD-HA pellets treated with an AC for 5 days

Assignment	Peak (cm^{-1})	Area (cm^2)	Height (cm)
HPO_4^{2-}	530	74.536	11.684
υ_4 PO_4^{3-}	552	5.091	1.178
	575	10.541	1.846
υ_2 CO_3^{2-}	700	14.694	1.195
υ_4 CO_3^{2-}	830	203.635	4.747
υ_3 PO_4^{3-}	1021	37.394	0.726
	1056	23.284	0.777
	1157	8.091	0.596
PO_2	1183	4.185	0.377
	1275	76.377	3.945
υ_4 CO_3^{2-}	1370	6.714	0.341
υ_3 CO_3^{2-}	1456	7.644	0.434
C=O Stretching	1724	6.844	0.020
HPO_4^{2-}	2113	0.029	0.006
CO_2	2332	6.851	0.316
	2359	6.414	0.415

Table A-176: FTIR results of oven dried synthetic HA pellets immersed for 5 days in an AC (pH: 4.90).

HD-HA pellets sintered at 500°C & treated with an AC for 5 days

Assignment	Peak (cm^{-1})	Area (cm^2)	Height (cm)
HPO_4^{2-}	525	101.495	21.314
	537	4.437	1.439
$\upsilon_4\ PO_4^{3-}$	551	12.717	1.271
	577	6.991	0.779
OH^-	626	4.577	0.511
$\upsilon_4\ CO_3^{2-}$	679	7.724	0.340
$\upsilon_2\ CO_3^{2-}$	700	43.791	3.771
$\upsilon_4\ CO_3^{2-}$	831	719.629	16.333
$\upsilon_3\ PO_4^{3-}$	916	5.688	0.574
	1022	101.189	1.838
	1059	92.975	3.137
	1119	13.944	1.037
	1157	28.822	2.226
PO_2	1184	17.053	1.457
	1276	247.977	13.923
$\upsilon_4\ CO_3^{2-}$	1371	27.765	1.388
$\upsilon_3\ CO_3^{2-}$	1454	33.368	1.707
	1510	14.081	1.439
	1643	590.432	14.576
C=O Stretching	1728	292.679	7.512
HPO_4^{2-}	1978	19.127	0.619
	2030	5.083	0.345
	2160	15.948	0.805
	2180	3.101	0.088
C-H Stretching	2874	10.495	0.577
	2933	18.127	0.705
	2960	11.571	0.889

Table A-177: FTIR results of oven dried synthetic HA pellets sintered at 500°C for 3 hours and immersed for 5 days in an AC (pH: 4.90).

HD-HA pellets sintered at 800°C & treated with an AC for 5 days

Assignment	Peak (cm^{-1})	Area (cm^2)	Height (cm)
HPO_4^{2-}	520	43.800	13.981
	537	95.087	8.070
$\upsilon_4\ PO_4^{3-}$	562	6.583	1.112
	584	9.228	1.213
	608	8.288	0.980
OH^-	632	8.338	1.002
$\upsilon_4\ CO_3^{2-}$	674	1.653	0.172
$\upsilon_2\ CO_3^{2-}$	699	16.990	1.367
$\upsilon_4\ CO_3^{2-}$	828	228.589	5.313
$\upsilon_3\ PO_4^{3-}$	1003	10.057	0.282
	1059	25.871	0.877
	1119	3.811	0.299
	1157	9.823	0.756
PO_2	1183	3.179	0.308
	1275	77.094	3.910
$\upsilon_4\ CO_3^{2-}$	1372	6.238	0.329
$\upsilon_3\ CO_3^{2-}$	1452	7.327	0.336
	1509	3.106	0.418
	1639	10.917	0.846
C=O Stretching	1722	5.653	0.344
HPO_4^{2-}	1911	1.100	0.087
	1992	2.333	0.212
	2121	1.353	0.033
CO_2	2321	2.232	0.095
	2354	1.293	0.153
OH^- (OCP)	2372	1.423	0.100
C-H Stretching	2924	7.479	0.345

Table A-178: FTIR results of oven dried synthetic HA pellets sintered at 800°C for 3 hours and immersed for 5 days in an AC (pH: 4.90).

HD-HA pellets sintered at 1100°C & treated with an AC for 5 days

Assignment	Peak (cm^{-1})	Area (cm^2)	Height (cm)
HPO_4^{2-}	542	0.489	0.350
υ_4 PO_4^{3-}	553	17.302	2.635
OH^-	628	7.364	0.279
υ_2 CO_3^{2-}	700	51.251	4.306
υ_4 CO_3^{2-}	831	60.591	17.374
υ_3 PO_4^{3-}	1021	113.045	2.163
	1059	102.823	3.411
	1119	16.348	1.190
	1157	33.429	2.569
PO_2	1184	19.043	1.628
	1276	256.149	14.717
υ_4 CO_3^{2-}	1371	27.228	1.442
υ_3 CO_3^{2-}	1454	34.308	1.782
	1510	15.720	1.613
	1643	56.460	15.123
C=O Stretching	1729	28.520	8.033
HPO_4^{2-}	2117	2.846	0.178
C-H Stretching	2874	13.421	0.663
	2960	18.434	1.119

Table A-179: FTIR results of oven dried synthetic HA pellets sintered at 1100°C for 3 hours and immersed for 5 days in an AC (pH: 4.90).

FD-HA pellets treated with 250 ppm of F^- for 5 days

Assignment	Peak (cm^{-1})	Area (cm^2)	Height (cm)
HPO_4^{2-}	525	38.334	7.494
	538	16.429	2.439
υ_4 PO_4^{3-}	565	3.516	0.430
	573	3.619	0.473
	599	5.375	0.627
OH^-	627	9.153	0.709
υ_2 CO_3^{2-}	700	106.730	4.683
F^- - OH^-	753	59.018	2.724
υ_4 CO_3^{2-}	833	691.855	16.549
υ_3 PO_4^{3-}	916	4.868	0.457
	1023	64.430	1.684
	1061	96.936	3.263
	1118	12.312	0.913
	1158	26.516	2.048
PO_2	1184	15.085	1.282
	1277	274.449	15.125
υ_4 CO_3^{2-}	1371	21.844	1.146
υ_3 CO_3^{2-}	1434	4.007	0.374
	1454	24.464	1.313
	1510	9.647	1.045
	1647	501.773	12.699
C=O Stretching	1730	231.587	6.159
HPO_4^{2-}	1977	2.692	0.793
	2031	44.105	1.297
	2160	18.683	1.129
	2175	3.342	0.131
CO_2	2360	7.919	0.542
C-H Stretching	2932	11.129	0.494
	2960	10.882	0.749

Table A-180: FTIR results of freeze dried synthetic HA pellets immersed for 5 days in 250 ppm of F^-.

FD-HA pellets sintered at 500°C & treated with 250 ppm of F^- for 5 days

Assignment	Peak (cm^{-1})	Area (cm^2)	Height (cm)
υ_4 PO_4^{3-}	544	55.779	4.355
	575	18.533	2.564
υ_2 CO_3^{2-}	700	47.194	4.025
F^- - OH^-	753	71.448	3.263
υ_4 CO_3^{2-}	832	756.164	17.793
υ_3 PO_4^{3-}	1023	85.172	1.918
	1059	56.289	2.031
	1118	12.098	0.966
	1157	32.649	2.427
PO_2	1184	17.357	1.532
	1277	288.670	15.847
υ_4 CO_3^{2-}	1371	22.814	1.246
υ_3 CO_3^{2-}	1454	38.223	1.907
	1509	11.958	1.307
	1645	598.633	15.012
C=O Stretching	1730	292.157	7.544
HPO_4^{2-}	1975	1.906	0.243
	2160	8.900	0.464
C-H Stretching	2925	26.847	1.098

Table A-181: FTIR results of freeze dried synthetic HA pellets sintered at 500°C for 3 hours and immersed for 5 days in 250 ppm of F^-.

FD-HA pellets sintered at 800°C & treated with 250 ppm of F^- for 5 days

Assignment	Peak (cm^{-1})	Area (cm^2)	Height (cm)
HPO_4^{2-}	532	11.741	2.317
υ_4 PO_4^{3-}	553	23.356	2.575
	570	9.354	1.276
υ_2 CO_3^{2-}	700	25.818	2.152
F^- - OH^-	752	42.079	1.840
υ_4 CO_3^{2-}	832	399.408	9.212
υ_3 PO_4^{3-}	1022	52.191	1.081
	1059	33.316	1.152
	1157	20.822	1.529
PO_2	1184	8.830	0.830
	1276	131.973	7.878
υ_4 CO_3^{2-}	1370	13.297	0.700
υ_3 CO_3^{2-}	1455	22.291	1.204
	1543	16.070	1.005
	1641	292.487	7.862
C=O Stretching	1726	154.198	3.980
HPO_4^{2-}	1977	20.555	0.904
	2160	26.738	1.279
C-H Stretching	2933	9.227	0.389

Table A-182: FTIR results of freeze dried synthetic HA pellets sintered at 800°C for 3 hours and immersed for 5 days in 250 ppm of F^-.

FD-HA pellets sintered at 1100°C & treated with 250 ppm of F^- for 5 days

Assignment	Peak (cm^{-1})	Area (cm^2)	Height (cm)
HPO_4^{2-}	534	108.039	10.897
υ_4 PO_4^{3-}	564	18.789	2.994
	586	16.036	1.457
υ_2 CO_3^{2-}	700	8.598	0.740
F^- - OH^-	754	14.637	0.611
υ_4 CO_3^{2-}	831	142.072	3.492
υ_3 PO_4^{3-}	1021	16.080	0.361
	1060	14.201	0.520
PO_2	1276	58.015	3.158
υ_3 CO_3^{2-}	1456	6.673	0.361
	1647	116.505	3.051
C=O Stretching	1731	63.559	1.673
HPO_4^{2-}	2160	10.546	0.600

Table A-183: FTIR results of freeze dried synthetic HA pellets sintered at 1100°C for 3 hours and immersed for 5 days in 250 ppm of F^-.

HD-HA pellets treated with 250 ppm of F^- for 5 days

Assignment	Peak (cm^{-1})	Area (cm^2)	Height (cm)
HPO_4^{2-}	518	77.947	19.583
υ_4 PO_4^{3-}	540	17.971	2.291
	555	5.784	1.128
	564	2.455	0.664
	575	4.996	0.997
	591	4.530	0.729
OH^-	631	13.501	0.897
υ_4 CO_3^{2-}	676	3.383	0.269
υ_2 CO_3^{2-}	700	35.891	2.946
F^- - OH^-	752	54.191	2.454
υ_4 CO_3^{2-}	831	569.453	13.079
υ_3 PO_4^{3-}	915	3.154	0.377
	1022	79.571	1.593
	1059	70.360	2.504
	1119	10.880	0.774
	1157	21.547	1.662
PO_2	1184	13.404	1.130
	1276	205.631	11.400
υ_4 CO_3^{2-}	1370	20.107	1.044
υ_3 CO_3^{2-}	1454	24.721	1.294
	1510	10.786	1.107
	1644	465.940	11.687
C=O Stretching	1729	230.266	5.925
HPO_4^{2-}	1976	16.935	0.642
	2031	6.137	0.397
	2161	13.351	0.701
C-H Stretching	2930	15.764	0.631

Table A-184: FTIR results of oven dried synthetic HA pellets immersed for 5 days in 250 ppm of F^-.

HD-HA pellets sintered at 500°C & treated with 250 ppm of F^- for 5 days

Assignment	Peak (cm^{-1})	Area (cm^2)	Height (cm)
HPO_4^{2-}	532	15.654	3.504
υ_4 PO_4^{3-}	566	6.734	0.826
	589	9.357	1.104
υ_4 CO_3^{2-}	678	6.933	0.285
υ_2 CO_3^{2-}	700	56.633	4.704
F^- - OH^-	753	81.099	3.572
υ_4 CO_3^{2-}	833	778.097	18.210
υ_3 PO_4^{3-}	1022	85.440	1.865
	1061	102.168	3.460
	1119	14.349	1.046
	1158	38.218	2.840
PO_2	1277	289.015	16.148
υ_4 CO_3^{2-}	1371	27.633	1.375
υ_3 CO_3^{2-}	1454	35.946	1.923
	1510	16.633	1.706
	1645	603.195	15.399
C=O Stretching	1729	313.375	8.106
HPO_4^{2-}	1978	14.978	0.494
	2023	17.154	0.557
	2160	9.821	0.548
C-H Stretching	2960	16.183	0.995

Table A-185: FTIR results of oven dried synthetic HA pellets sintered at 500°C for 3 hours and immersed for 5 days in 250 ppm of F^-.

HD-HA pellets sintered at 800°C & treated with 250 ppm of F^- for 5 days

Assignment	Peak (cm^{-1})	Area (cm^2)	Height (cm)
HPO_4^{2-}	524	79.797	17.044
υ_4 PO_4^{3-}	543	36.306	3.528
	565	7.402	1.498
	575	7.650	1.673
	602	4.624	0.863
OH^-	632	11.011	0.847
υ_2 CO_3^{2-}	700	36.682	2.973
F^- - OH^-	753	50.345	2.292
υ_4 CO_3^{2-}	832	524.695	12.372
υ_3 PO_4^{3-}	917	4.142	0.384
	1021	97.433	1.929
	1061	48.718	1.812
	1119	9.567	0.684
	1158	23.131	1.797
PO_2	1277	178.867	10.178
υ_4 CO_3^{2-}	1371	16.049	0.815
υ_3 CO_3^{2-}	1454	20.924	1.109
	1509	9.352	0.942
	1645	340.381	9.065
C=O Stretching	1730	170.305	4.334
HPO_4^{2-}	1996	0.546	0.094
	2090	7.316	0.120
	2119	2.518	0.042
OH^- (OCP)	2362	7.174	0.530
C-H Stretching	2925	15.560	0.667

Table A-186: FTIR results of oven dried synthetic HA pellets sintered at 800°C for 3 hours and immersed for 5 days in 250 ppm of F^-.

HD-HA pellets sintered at 1100°C & treated with 250 ppm of F^- for 5 days

Assignment	Peak (cm^{-1})	Area (cm^2)	Height (cm)
HPO_4^{2-}	524	49.490	10.719
	537	19.547	3.713
υ_4 PO_4^{3-}	555	21.435	2.727
	575	8.977	0.911
OH^-	628	7.716	0.678
υ_4 CO_3^{2-}	677	5.769	0.288
υ_2 CO_3^{2-}	700	71.906	5.759
F^- - OH^-	754	75.781	3.953
υ_4 CO_3^{2-}	835	1048.462	25.419
υ_3 PO_4^{3-}	917	7.380	0.739
	1023	107.528	2.734
	1062	171.557	5.934
	1119	22.523	1.620
	1158	44.376	3.424
PO_2	1184	25.861	2.218
	1277	435.288	24.341
υ_4 CO_3^{2-}	1371	33.848	1.767
υ_3 CO_3^{2-}	1454	47.335	2.400
	1510	17.937	1.895
	1648	752.738	20.140
C=O Stretching	1731	387.629	10.552
HPO_4^{2-}	1994	1.461	0.144
	2117	9.725	0.242
CO_2	2332	11.934	0.246
C-H Stretching	2874	20.338	0.779
	2929	31.781	1.319

Table A-187: FTIR results of oven dried synthetic HA pellets sintered at 1100°C for 3 hours and immersed for 5 days in 250 ppm of F^-.

6. pH-Cycling Experiments Using Synthetic Hydroxylapatite Pellets

Synthetic HA Pellets

Group FD_{10}

Solutions & Treatments	Experimental Conditions
Remineralising Solution	PF (6.58)
Demineralising Solution	AC (4.90)
Background F^- Concentration (ppm) (Main/ Intermediate Periods)	0.2/ 2.0
F^- Treatment Concentration (ppm)	10

Table A-2288: Experimental conditions used during the pH-cycling study for the Group FD_{10}, which was treated with PF during the remineralising, AC during the demineralising period, 10 ppm of F^- and added BF of either 0.2 ppm or 1.0 ppm during the main and intermediate remineralisation periods respectively.

Day of pH-cycling	Assignment	Peak (cm^{-1})	Area (cm^2)	Height (cm)
1	HPO_4^{2-}	525	110.252	16.244
	$\upsilon_4\ PO_4^{3-}$	558	28.561	2.109
		590	6.541	1.031
		616	5.219	0.578
	$\upsilon_2\ CO_3^{2-}$	701	6.497	0.442
	$F^- - OH^-$	753	2.569	0.240
	$\upsilon_4\ CO_3^{2-}$	829	61.264	1.612
	$\upsilon_3\ PO_4^{3-}$	1156	3.833	0.299
		1184	2.225	0.168
	PO_2	1276	25.886	1.362
	$\upsilon_4\ CO_3^{2-}$	1371	3.174	0.173
	$\upsilon_3\ CO_3^{2-}$	1649	4.569	0.153
	C=O Stretching	1730	25.537	0.709
	HPO_4^{2-}	1977	27.763	1.484
		2025	71.245	1.896
		2098	2.254	0.240
		2159	421.157	5.308
	OH^- (OCP)	2438	10.992	0.118
	C-H Stretching	2549	1.054	0.046

Table A-189: FTIR results of Group FD_{10} following the 1st day of the pH-cycling process.

Day of pH-cycling	Assignment	Peak (cm^{-1})	Area (cm^2)	Height (cm)
6	υ_4 PO_4^{3-}	558	28.180	2.881
	F^- – OH^-	750	5.890	0.340
	υ_4 CO_3^{2-}	832	48.910	1.410
	υ_3 PO_4^{3-}	1025	161.769	3.668
	PO_2	1277	16.976	0.946
	υ_3 CO_3^{2-}	1647	22.284	0.697
	HPO_4^{2-}	1977	16.171	0.665
		2028	9.082	0.382
		2159	10.633	0.623
		2214	1.275	0.094

Table A-190: FTIR results of Group FD_{10} following the 4th day of the pH-cycling process.

Day of pH-cycling	Assignment	Peak (cm^{-1})	Area (cm^2)	Height (cm)
11	HPO_4^{2-}	528	47.511	9.536
	υ_4 PO_4^{3-}	548	53.900	5.122
		571	13.041	1.483
	F^- – OH^-	753	12.755	0.658
	υ_4 CO_3^{2-}	831	13.094	3.318
	υ_3 PO_4^{3-}	1024	158.233	2.218
	PO_2	1276	47.131	2.553
	υ_4 CO_3^{2-}	1644	93.619	2.433
	C=O Stretching	1729	44.417	1.213
	HPO_4^{2-}	2159	28.168	1.307
		2219	0.629	0.031
	OH^- (OCP)	2364	9.078	0.641

Table A-191: FTIR results of Group FD_{10} following the 7th day of the pH-cycling process.

Day of pH-cycling	Assignment	Peak (cm^{-1})	Area (cm^2)	Height (cm)
16	HPO_4^{2-}	526	64.736	13.983
		538	81.805	8.998
	υ_4 PO_4^{3-}	567	28.601	3.273
		606	12.210	1.389
	F^- – OH^-	753	15.083	0.823
	υ_4 CO_3^{2-}	831	14.871	4.075
	υ_3 PO_4^{3-}	1023	252.958	3.830
	PO_2	1276	59.293	3.191
	υ_3 CO_3^{2-}	1640	120.460	3.164
	C=O Stretching	1726	52.414	1.475
	HPO_4^{2-}	1977	27.013	0.992
		2159	358.163	4.426
	OH^- (OCP)	2426	6.335	0.121
	C-H Stretching	2536	26.639	0.249

Table A-192: FTIR results of Group FD_{10} following the 10th day of the pH-cycling process.

Group FD_{250}

Solutions & Treatments	Experimental Conditions
Remineralising Solution	PF (6.58)
Demineralising Solution	AC (4.90)
Background F^- Concentration (ppm) **(Main/ Intermediate Periods)**	0.2/ 1.0
F^- Treatment Concentration (ppm)	250

Table A-2393: Experimental conditions used during the pH-cycling study for the Group FD_{250}, which was treated with PF during the remineralising, AC during the demineralising period, 250 ppm of F^- and added BF of either 0.2 ppm or 1.0 ppm during the main and intermediate remineralisation periods respectively.

Day of pH-cycling	Assignment	Peak (cm^{-1})	Area (cm^2)	Height (cm)
1	HPO_4^{2-}	529	40.796	7.041
	$\upsilon_4\ PO_4^{3-}$	542	12.542	2.316
		558	22.584	2.710
		578	18.868	2.284
		620	7.823	0.697
	OH^-	642	2.572	0.295
	$\upsilon_2\ CO_3^{2-}$	700	7.289	0.572
	$F^- - OH^-$	754	8.805	0.406
	$\upsilon_4\ CO_3^{2-}$	828	65.991	1.771
	$\upsilon_3\ PO_4^{3-}$	920	0.992	0.143
		1025	14.398	0.317
		1059	3.376	0.075
		1158	3.979	0.278
	PO_2	1276	26.020	1.394
	$\upsilon_3\ CO_3^{2-}$	1456	2.976	0.181
		1643	43.626	1.313
	C=O Stretching	1729	19.999	0.629
	HPO_4^{2-}	1976	32.506	1.128
		2029	20.932	0.816
		2159	268.950	3.381
	OH^- (OCP)	2404	1.223	0.023
	C-H Stretching	2961	2.586	0.150

Table A-194: FTIR results of Group FD_{250} following the 1st day of the pH-cycling process.

Day of pH-cycling	Assignment	Peak (cm^{-1})	Area (cm^2)	Height (cm)
6	HPO_4^{2-}	517	169.325	43.928
		537	15.109	3.333
	$\upsilon_4\ PO_4^{3-}$	557	18.099	2.192
		585	6.480	1.466
		596	7.345	0.883
	$\upsilon_2\ CO_3^{2-}$	700	5.115	0.545
	$F^- - OH^-$	753	9.018	0.436
	$\upsilon_4\ CO_3^{2-}$	831	83.655	2.144
	$\upsilon_3\ PO_4^{3-}$	1022	21.314	0.584
	PO_2	1276	29.046	1.611
	$\upsilon_3\ CO_3^{2-}$	1457	3.115	0.157
		1644	52.190	1.492
	C=O Stretching	1731	23.947	0.723
	HPO_4^{2-}	1976	5.011	0.561
		2027	10.668	0.405
		2161	51.482	1.485

Table A-195: FTIR results of Group FD_{250} following the 6th day of the pH-cycling process.

Day of pH-cycling	Assignment	Peak (cm^{-1})	Area (cm^2)	Height (cm)
11	HPO_4^{2-}	523	12.292	6.763
		533	23.654	5.303
	$\upsilon_4\ PO_4^{3-}$	563	25.899	1.580
		592	10.714	1.057
	$F^- - OH^-$	754	13.605	0.624
	$\upsilon_4\ CO_3^{2-}$	829	134.185	3.219
	$\upsilon_3\ PO_4^{3-}$	1023	320.457	4.609
	PO_2	1276	50.421	2.619
	$\upsilon_4\ CO_3^{2-}$	1645	85.202	2.338
	C=O Stretching	1729	38.610	1.068
	HPO_4^{2-}	1977	20.315	0.739
		2028	10.300	0.486
		2159	11.408	0.663
		2207	10.128	0.143

Table A-196: FTIR results of Group FD_{250} following the 11th day of the pH-cycling process.

Day of pH-cycling	Assignment	Peak (cm^{-1})	Area (cm^2)	Height (cm)
16	$\upsilon_4\ PO_4^{3-}$	540	29.051	3.390
		566	40.022	4.200
		604	12.721	1.349
	$\upsilon_4\ CO_3^{2-}$	670	4.875	0.475
	$\upsilon_2\ CO_3^{2-}$	700	13.275	1.268
	$F^- - OH^-$	752	24.957	1.181
	$\upsilon_4\ CO_3^{2-}$	831	24.163	5.276
	$\upsilon_3\ PO_4^{3-}$	1024	485.469	6.596
		1156	7.114	0.574
		1184	3.914	0.382
	PO_2	1276	75.342	3.996
	$\upsilon_4\ CO_3^{2-}$	1370	7.654	0.347
	$\upsilon_3\ CO_3^{2-}$	1454	9.147	0.469
		1509	4.612	0.454
		1646	10.517	3.858
	C=O Stretching	1728	5.788	1.905
	HPO_4^{2-}	1977	16.275	1.322
		2027	18.753	0.720
		2159	278.230	4.142
	CO_2	2339	2.093	0.279
	OH^- (OCP)	2425	1.563	0.120
	C-H Stretching	2931	4.769	0.219
		2963	4.118	0.256
	OH^-	3034	1.612	0.125

Table A-197: FTIR results of Group FD_{250} following the 16th day of the pH-cycling process.

Group FD_{Mix}

Solutions & Treatments	pH Cycling Rounds
Remineralising Solution (pH)	PF (6.58)
Demineralising Solution (pH)	AC (4.90)
Days 1 – 6	
Background F^- Concentration (ppm)	0.2/ 2.0
Brushing F^- Concentration (ppm)	10.0
Days 7 - 16	
Background F^- Concentration (ppm)	0.2/ 1.0
Brushing F^- Concentration (ppm)	250

Table A-2498: Experimental conditions used during the pH-cycling study for the Group pMix, which was treated with PF during the remineralising, AC during the demineralising period, 10 ppm of F^- for the first 6 and 250 ppm of F^- for the remaining days and added BF of either 0.2 ppm and 2.0 or 1.0 ppm (depending on the F^- treatment) during the main and intermediate remineralisation periods respectively.

Day of pH-cycling	Assignment	Peak (cm^{-1})	Area (cm^2)	Height (cm)
1	$\upsilon_4\ PO_4^{3-}$	542	103.794	6.519
		558	8.006	1.063
		570	7.852	1.598
		585	12.306	1.712
	$\upsilon_2\ CO_3^{2-}$	697	5.450	0.389
	$F^- - OH^-$	749	7.727	0.389
	$\upsilon_4\ CO_3^{2-}$	827	59.496	1.366
	PO_2	1276	22.695	1.180
	$\upsilon_3\ CO_3^{2-}$	1640	45.926	1.284
	C=O Stretching	1729	24.842	0.719
	HPO_4^{2-}	1977	12.188	0.645
		2033	14.258	0.712
		2160	23.363	1.140
		2211	13.500	0.180

Table A-199: FTIR results of Group FD_{Mix} following the 1st day of the pH-cycling process.

Day of pH-cycling	Assignment	Peak (cm^{-1})	Area (cm^2)	Height (cm)
6	HPO_4^{2-}	519	10.948	9.915
		528	84.259	12.629
	$\upsilon_4\ PO_4^{3-}$	555	40.184	3.703
		571	11.126	1.647
		590	4.020	0.571
		615	3.221	0.502
	OH^-	630	0.992	0.232
	$\upsilon_2\ CO_3^{2-}$	700	6.729	0.674
	$F^- - OH^-$	753	11.117	0.615
	$\upsilon_4\ CO_3^{2-}$	827	138.830	3.064
	$\upsilon_3\ PO_4^{3-}$	1020	2.580	0.263
		1053	8.210	0.193
		1119	2.846	0.194
		1157	4.679	0.382
		1182	3.032	0.276
	PO_2	1276	48.210	2.512
	$\upsilon_4\ CO_3^{2-}$	1371	4.545	0.243
	$\upsilon_3\ CO_3^{2-}$	1454	5.625	0.250
		1510	2.562	0.258
		1641	97.569	2.565
	C=O Stretching	1727	47.291	1.293
	HPO_4^{2-}	1976	21.703	0.916
		2024	43.390	1.197
		2158	229.766	2.953
	C-H Stretching	2929	1.857	0.092

Table A-200: FTIR results of Group FD_{Mix} following the 6^{th} day of the pH-cycling process.

Day of pH-cycling	Assignment	Peak (cm^{-1})	Area (cm^2)	Height (cm)
11	HPO_4^{2-}	523	163.220	20.047
	$\upsilon_4\ PO_4^{3-}$	553	11.195	2.332
		571	11.848	1.660
		598	6.186	0.767
		611	4.319	0.510
	OH^-	629	1.239	0.300
	$\upsilon_4\ CO_3^{2-}$	672	3.122	0.328
	$\upsilon_2\ CO_3^{2-}$	900	17.346	1.503
	$F^- - OH^-$	752	25.777	1.155
	$\upsilon_4\ CO_3^{2-}$	831	25.177	5.522
	$\upsilon_3\ PO_4^{3-}$	1023	277.302	4.354
		1118	6.397	0.408
		1156	8.854	0.664
		1183	4.190	0.368
	PO_2	1276	77.401	4.353
	$\upsilon_4\ CO_3^{2-}$	1371	8.020	0.401
	$\upsilon_3\ CO_3^{2-}$	1454	9.097	0.499
		1510	4.064	0.397
		1644	14.599	4.127
	C=O Stretching	1730	76.076	2.038
	HPO_4^{2-}	1976	1.539	0.831
		2026	0.089	0.025
		2160	28.379	1.365
		2181	13.467	0.193
	OH^- (OCP)	2443	7.605	0.142
	C-H Stretching	2874	3.819	0.182
		2933	5.253	0.202

Table A-201: FTIR results of Group FD_{Mix} following the 11th day of the pH-cycling process.

Day of pH-cycling	Assignment	Peak (cm^{-1})	Area (cm^2)	Height (cm)
16	HPO_4^{2-}	534	8.020	1.525
	$\upsilon_4\ PO_4^{3-}$	543	6.230	1.302
		563	12.313	2.329
		572	7.431	1.891
		598	6.101	0.620
	$\upsilon_2\ CO_3^{2-}$	699	17.955	1.300
	F^- - OH^-	752	21.287	0.966
	$\upsilon_4\ CO_3^{2-}$	831	18.348	4.906
	$\upsilon_3\ PO_4^{3-}$	1025	81.934	2.111
		1053	10.481	0.215
		1105	4.127	0.105
		1157	7.131	0.584
		1181	4.601	0.394
	PO_2	1276	76.895	4.090
	$\upsilon_4\ CO_3^{2-}$	1371	7.962	0.395
	$\upsilon_3\ CO_3^{2-}$	1454	9.251	0.501
		1509	4.521	0.479
		1644	14.510	3.929
	C=O Stretching	1729	70.296	2.032
	HPO_4^{2-}	1911	0.326	0.061
		1975	22.874	0.801
		2032	3.880	0.194
		2159	28.320	1.200
		2216	0.608	0.112
	C-H Stretching	2928	4.283	0.219
		2959	6.021	0.334

Table A-202: FTIR results of Group FD_{Mix} following the 16th day of the pH-cycling process.

Appendix II

Conferences

1. **GlaxoSmithKline Science Symposium 2012: Weybridge, UK, Poster Presentation**:
   Maturation and ageing in biominerals with application to enamel maturation
   A. G. Papadiamantis, R. J.M. Lynch, E. Valsami-Jones
2. **School of Geography, Earth and Environmental Sciences 2012: Birmingham, UK, Poster Presentation**:
   Maturation and ageing in biominerals with application to enamel maturation
   A. G. Papadiamantis, R. J.M. Lynch, E. Valsami-Jones
3. **The Geological Society. Frontiers Meeting 2012: London, UK, Oral Presentation**:
   Maturation and ageing in biominerals with application to enamel maturation
   A. G. Papadiamantis, R. J.M. Lynch, E Valsami-Jones
4. **GlaxoSmithKline Science Symposium 2013: Weybridge, UK, Oral Presentation**:
   Maturation and ageing in biominerals with application to enamel maturation
   A. G. Papadiamantis, R. J.M. Lynch, E. Valsami-Jones
5. **60th Congress of the European Organisation for Caries Research (ORCA), 2013: Liverpool, UK, Poster & Oral Presentation**:
   Maturation and ageing in biominerals with application to enamel maturation
   A. G. Papadiamantis, R. Willson, R. J.M. Lynch, E. Valsami-Jones
6. **School of Geography, Earth and Environmental Sciences 2013: Birmingham, UK, Poster Presentation**:
   Maturation and ageing in biominerals with application to enamel maturation
   A. G. Papadiamantis, R. Willson, R. J.M. Lynch, E. Valsami-Jones
7. **GlaxoSmithKline Science Symposium 2014: Weybridge, UK, Oral Presentation**:
   Maturation and ageing in biominerals with application to enamel maturation
   A. G. Papadiamantis, R. J.M. Lynch, E. Valsami-Jones